MARTIN MARIETTA ENERGY SYSTEMS LIBRARIES

3 4456 0351204 5

ORNL-2839
Metallurgy and Ceramics

METALLURGY DIVISION

ANNUAL PROGRESS REPORT

FOR PERIOD ENDING SEPTEMBER 1, 1959

LIBRARY
REFERENCE COPY

OAK RIDGE NATIONAL LABORATORY
operated by
UNION CARBIDE CORPORATION
for the
U.S. ATOMIC ENERGY COMMISSION

LEGAL NOTICE

This report was prepared as an account of Government sponsored work. Neither the United States, nor the Commission, nor any person acting on behalf of the Commission:

A. Makes any warranty or representation, expressed or implied, with respect to the accuracy, completeness, or usefulness of the information contained in this report, or that the use of any information, apparatus, method, or process disclosed in this report may not infringe privately owned rights; or

B. Assumes any liabilities with respect to the use of, or for damages resulting from the use of any information, apparatus, method, or process disclosed in this report.

As used in the above, "person acting on behalf of the Commission" includes any employee or contractor of the Commission, or employee of such contractor, to the extent that such employee or contractor of the Commission, or employee of such contractor prepares, disseminates, or provides access to, any information pursuant to his employment or contract with the Commission, or his employment with such contractor.

ORNL-2839
ERRATA

METALLURGY DIVISION ANNUAL PROGRESS REPORT FOR PERIOD ENDING SEPTEMBER 1, 1959

Page	Line	Errata
16	3	Sentence referring to Fig. 1.10 deleted by author
19	Legend	for Slip-Line read Twin
31	Fig. 1.13	for ● Zr-In α read ● Zr-In α'
		for ▲ Zr-Sn α read ▲ Zr-Sn α'
36	Fig. 1.18	for b read bR
		for a read aR
41	4	for 001 read 002
44	Fig. 1.25	for RT ln P read RT ln γ
67	Fig. 1.30	for 28 Å read 280 Å
74	Legend	for Figs. 1.30 and 1.31 read Figs. 1.32 and 1.33
134	Table 2.4	delete footnote
		for ~ 40 read ~ 80
223	Fig. 3.29	for 8000 to 4000 read 8000/4000
		for -4400 to 4000 read -4400/4000
		for 6000 to 4000 read 6000/4000
		for -2300 to 4000 read -2300/4000
118	Fig. 2.2	Sched 8: for k_{yz} read k_{xz}
		Sched 10: for $k_{yx} = 0.675$ read $k_{xy} = 0.675$
		Sched 62: for $k_{xy} = 0.414$ read $k_{xz} = 0.414$

ORNL-2839
Metallurgy and Ceramics
TID-4500 (15th ed.)

Contract No. W-7405-eng-26

METALLURGY DIVISION

ANNUAL PROGRESS REPORT

for Period Ending September 1, 1959

J. H. Frye, Jr., Director
W. D. Manly, Associate Director
J. E. Cunningham, Assistant Director

DATE ISSUED

NOV 16 1959

OAK RIDGE NATIONAL LABORATORY
Oak Ridge, Tennessee
operated by
UNION CARBIDE CORPORATION
for the
U. S. ATOMIC ENERGY COMMISSION

MARTIN MARIETTA ENERGY SYSTEMS LIBRARIES

3 4456 0351204 5

SUMMARY

PART I. FUNDAMENTAL METALLURGY

Physicometallurgical Research

The use of axis charts for representing the textures of cold-rolled thorium sheet was compared with conventional pole figures. Four texture components were deduced from the axis charts and shown to be consistent with the pole figures. It was shown that consideration of the pole figures alone could lead to an apparent component which is the average of two actually present. It was also shown that the spread about the "ideal" textures and the amount of material associated with each could be readily obtained from the axis chart method.

Deformation twins were found in single crystals and coarse-grained specimens of high-purity niobium deformed by impact or slow compression at -196°C. The twinning elements were established to be: K_1 (twin plane) $\{112\}$ and η_1 (shear direction) $< 11\bar{1} >$. Cleavage fracture at -196°C was found always to occur on $\{100\}$ planes.

An apparent phase transformation has been detected in high-purity gallium deformed at 4.2°K. The crystal structure of the new phase has not yet been determined.

The specific heats of the group IVA metals and alloys of zirconium-indium and zirconium-tin have been measured from 1.2 to 4.5°K. As in other transition metals, a large electronic term is found which, for the sequence titanium, zirconium, and hafnium, decreases with increasing atomic number. The Debye temperatures decrease with increasing atomic mass, as would be expected from the central force model; however, the ratios of the Debye temperatures indicate that the atomic force constants for hafnium are some 50% larger than for titanium and zirconium. For the alloys, both the densities of states and the Debye temperatures are electron concentration dependent if zirconium is assumed to have a valency of 1.5 to 2.0.

In the zirconium-rich portion of the zirconium-gallium phase diagram, the α/β phase boundaries of zirconium are depressed by additions of gallium and the β phase decomposes by a eutectoid reaction. The normal rise

of the allotropic boundaries with a higher-valent solute is apparently overcome in this case by a large size-factor effect, a characteristic of the system also suggested by rapid hardening of the alloys and abnormally low solubility of the gallium in β zirconium.

The cadmium pressures of α- and β-zirconium alloys containing 1 to 11% cadmium have been measured between 1090 and 1325°K. The partial excess free energies of the β alloys obey Henry's law, implying equivalence in the Zr-Zr, Zr-Cd, and Cd-Cd interactions. In the α phase, on the other hand, the excess free energies appear to increase slightly with cadmium content. The partial excess entropies are negative in both α and β forms with the more negative values for the β phase. This entropy difference could easily account for the slight rise in the α/β boundaries.

A measurement of the axial ratio of several zirconium-cadmium α alloys shows that the axial ratio increases with cadmium concentration almost as rapidly as with tin concentration. The axial ratio would thus appear to depend upon zirconium content and upon numbers of d electrons in these alloys.

X-Ray Diffraction

Crystal structures of several unreported transition-metal fluorides, rare earth hydrides and nitrides have been determined.

Progress in the study of phase transitions in β-quenched zirconium-niobium alloys aged below the eutectoid temperature is reported. A metastable ω + niobium-enriched β system forms at 400°C, but discontinuous or continuous precipitation of equilibrium phases occurs at 500 and 600°C. The formation and reversion of ω in 25 and 33 wt % niobium alloy crystals has been observed. The effect of low-temperature in-pile irradiation on a 15 wt % niobium alloy is primarily an acceleration of the rate of ω formation.

Structural changes in the ω phase during its development have been followed through observation of selected x-ray reflections. A gradual change in the degree of "rumpling" of the close-packed midplane is noted.

A high-temperature investigation of the order-disorder phase transition of a Cu–31 at. % Au alloy has revealed an intermediate periodic

antiphase condition. A structure for this phase is proposed and calculated diffraction maxima compared with observations.

Microstrains in Crystals

A previously described x-ray diffraction technique for the measurement of the thickness and strain of thin oxide films has been applied to a series of five Cu_2O films grown on copper single crystals. The method makes use of the shapes of the Bragg reflections. The results of these measurements are described and discussed.

A new x-ray diffraction method for measuring film thickness, based on the integrated intensities of the Bragg maxima, is shown to agree very well with the thickness as determined from the line-shape analysis.

In order to determine the film thickness from the integrated intensity, the crystal structure factor and the Debye temperature factor must be known. A separate experiment has been performed to determine these quantities in absolute units for the various reflections. The results of the experiment are given.

High-Temperature Reactions

A determination was made of the influence which electrostatic interactions with neighboring ions have on the energy of the $n \rightarrow \pi^*$ transition in the nitrate ion. A large mass of data relative to the influence of cationic size on this process has been collected and will be analyzed.

The charge-transfer band for I^- dissolved in the LiCl-KCl eutectic was measured and, in contrast to the results of other investigators, found to be in agreement with current theory.

Some information on the behavior of solute species in dilute solutions of bismuth in $BiCl_3$ was obtained from absorption spectra.

Reactions at Metal Surfaces

Studies of the gaseous oxidation of niobium and zirconium in the ORNL Graphite Reactor indicated that neutron fluxes of $\sim 10^{12}$ nv had no effect on the oxidation processes for these two metals. Two primary ways in which irradiation may influence the oxidation of metals are through

changes in the defect concentration in the oxide and through the activation of nucleation stages in the oxidation process. Calculations are presented to show that the former is unlikely with currently available flux levels but that the density in the oxide of regions of localized disorder produced by neutron bombardment is of the same order as the number of oxide nuclei normally observed on oxide films.

Efforts aimed at the characterization of thin oxide films on copper single crystals were continued. These investigations included an x-ray diffraction study of strain distribution in thin Cu_2O films; in addition, a chemical method for the analysis of Cu_2O films is under study, and a spectrophotometric investigation of the optical anisotropy of such films was initiated.

A variety of new techniques was applied to the study of the oxidation of tantalum. It was shown that previously observed platelets of oxide which extended into the metal are formed at temperature rather than during cooling. The very early stages of oxidation were characterized over a temperature range from 300 to 700°C.

Crystal Physics

Efforts to grow macroscopic single crystals of ceramic-type materials have been initiated. With the resulting crystals, studies will be made of crystalline perfection, of growth mechanisms, and of magnetic behavior. A hydrothermal crystal-growth system is in operation. Systems for crystal growth by several other methods are in varying stages of completion.

PART II. HRP METALLURGY

An intensive study of the effects of fabrication variables on the anisotropy of mechanical properties and the preferred orientation in Zircaloy-2 has shown that the control of the preferred orientation and anisotropy is quite important in extending the use of the alloy as an engineering material. The study has shown that the use of the usual tensile test properties, for example, yield and tensile strengths, elongation, and reduction of area, are of little value in separating the effects

of the fabrication variables. All values fall, without appreciable order, within a scatter band only slightly larger than that found for duplicate tests of the same fabrication schedule. A new evaluation method has been developed which not only separates the effects of the fabrication variables but which can be used to predict the degree and nature of the preferred orientation and the anisotropy of mechanical properties for all directions in the plate or sheet, including the normal. The technique involves the measuring of the shape and area of cross section of fractured longitudinal and transverse tensile specimens at the fracture and at several points along their length and the plotting of the true contraction strains vs the true axial strains. The slopes of the resulting straight lines characterize the preferred orientation and anisotropy of mechanical properties in the particular lot of material. The analysis should be extensible to pipe and tubing fabrication studies.

The transformation sequence study of the Zr-Nb-X alloys has shown that the metastable transformation of quenched and retained β phase is to a hexagonal metastable ω phase and an enriched β phase (progressively enriched in Nb to above 45% with increased aging time) followed by the coprecipitation of α zirconium and the equilibrium bcc 85 Nb-15 Zr phase. The formation of α zirconium in the Zr-15 Nb binary alloy does not occur in three weeks of aging at 400°C but does occur in less than 24 hr at 500°C. The metastable formation of ω phase does not occur above 525°C. The structure of the martensitic Widmanstätten phase formed on quenching, previously reported as tetragonal, has actually been found to be monoclinic, the angle α being approximately 85°.

A detailed macro- and micro-examination has been completed on samples and debris removed from the core vessel of the Homogeneous Reactor. Subsize mechanical-property specimens of zirconium and titanium alloys which were suspended on a titanium holder within the core vessel during operation of the reactor had been severely damaged. Both the mechanical-property specimens and the holder contained areas that had either been molten or very close to it. Near the molten areas, wide ranges of structures were found indicating temperature gradients from less than 800 to

over 1800°C in lengths of not more than 3/16 in. The structures indicated, and it was confirmed by laboratory tests, that the time at the elevated temperature was very limited and that the quenching rate was very rapid. The "burning" was never general but was restricted to specific areas. It was concluded that no evidence existed for a direct reaction between either zirconium or titanium and the normal reactor environment. The damage that occurred was a result of overheating caused by a poor flow pattern and was not a function of the alloys. Even when started by external means, the reaction was quenched as soon as the heat source was removed.

During a visual examination of the core vessel it appeared that considerable attack had occurred to the Zircaloy-2 screens within the vessel. Therefore, samples were cut from the centers of the six top screens, and five of these were submitted for metallurgical study. While considerable damage was noted, it was shown to be an accentuation of damage which had occurred during the fabrication. A single, very small spot showed evidence of being at high temperature, but this is thought to have resulted from contact with the specimen holder. No other section had been above 550°C during operation (this is only a limit that was not reached and is not an operating temperature). These studies have gone far to relieve the anxieties that had lately arisen concerning the use of zirconium or titanium in homogeneous reactor applications.

The samples removed from the blanket region, none of which showed any damage, were broken as scheduled. For both zirconium and titanium, small increases in yield and ultimate strengths and decreases in elongation were shown. The maximum exposure was still low, being only 2×10^{18} nvt.

For optimum operation of the present homogeneous reactor it may be desirable to remove the Zircaloy-2 screens now welded to the inside of the core vessel. The screens, some of which are almost 2 ft in diameter, would have to be removed through a 2-in.-dia hole. Underwater electric-arc cutting, using a specially designed small heliarc torch, has been developed as a method for cutting the screens into strips. A screen may be cut at rates approaching 100 in./min, and all particles, except the

1-1/2-in. strips being cut, are small enough to be flushed through the 3/8-in. holes. The method appears to be readily adaptable to the remote operation that would be required. No evidence of a reaction between the molten particles and the water was noted.

A considerable improvement has been made in the fabrication of Zircaloy-2 vessels. The existing vessel was fabricated by several cycles of pressing small segments, welding them together, and repressing, but it now appears to be possible to form an entire hemisphere from a flat plate. Such hemispheres have been fabricated by a warm power-spinning operation. It was also possible, by warm pressing, to press a reverse curvature into the polar region of a hemisphere. Such a reverse flare would serve as the transition from the vessel to a flared pipe. It has also been possible to eliminate the expensive root-insert type of welds and their very close fitup tolerances used for the present vessel. By using a butt, fusion-type joint with no root gap and with root faces up to half the plate thickness, it was possible to make satisfactory full-penetration welds with offsets as great as 0.045 in. with 5/16-in. plate. All welding has been machine-type, with protection from the atmosphere achieved by careful design of inert-gas trailers attached to the torch and backup devices designed for each joint.

Type 312 stainless steel has been found to be a satisfactory barrier material in making tube-to-header welds in Inconel—type 347 stainless steel composites. Without a barrier, diffusion of nickel into the stainless steel weld resulted in an all-austenitic structure and cracking. A layer of type 312 stainless steel placed upon the Inconel root minimized diffusion and permitted the desired amount of ferrite to remain in the type 347 stainless steel weld.

PART III. REACTOR METALLURGY

Corrosion Engineering

The scope of the materials compatibility program in support of the Gas-Cooled Reactor was increased by the modification of static pots to contain independently heated test specimens which provide metal surface

temperatures in excess of 1600°F. Two high-pressure thermal-convection- and one forced-convection test facilities have also been constructed in order to afford high-pressure and high-velocity conditions, respectively.

Examinations were made of low-alloy and stainless steels following their exposure to impurities outgassed by graphite in these test facilities. Corrosion films that formed on stainless steels were quite protective in these tests; however, in certain cases, films formed on low-alloy steels were poorly adherent, and specimens of these materials showed appreciable weight losses.

A three-phase out-of-pile corrosion test program is continuing in order to evaluate the behavior of Inconel and INOR-8 in contact with fluoride salt mixtures in terms of such variables as time, temperature, and flow rate. Results of the tests completed to this date show Inconel to be quite susceptible to the corrosive attack of the various fused fluoride mixtures, while INOR-8 continues to show excellent corrosion resistance. Excellent compatibility of INOR-8 was also demonstrated in a forced-convection test containing graphite together with fused salt.

Metallurgical support has been supplied to the Reactor Projects Division in the form of inspection of welds, material, and fabricated components. An evaluation of drawings for weld design, inspectability, and materials selection, as well as an analysis of component failures, also was conducted. A summary of results of material and welds inspected is given.

Materials Compatibility

Inconel and INOR-8 specimens carburized in the sodium-graphite system show an appreciable decrease in their room-temperature ductility, compared with control specimens subjected to argon for the same temperature and time. The ductility at 1250°F (677°C) was not seriously affected.

Metallography, chemical results, and tensile test data on INOR-8 subjected to a static fuel 130—graphite system for 6000 hr at 1300°F show that carburization does not occur under these conditions.

The nickel-base Coast Metals Nos. 52 and 53, the 82 Au–18 Ni, and the pure copper brazing alloys show no attack when subjected to fuel 130 for 1000 hr at 1300°F.

It was found that $LiF-BeF_2-UF_4$ (62-37-1 mole %, fuel 130) would precipitate part of its uranium as UO_2 when in contact with graphite at 1300°F (704°C). The graphite was the source of the oxide contamination. The precipitation of the uranium as UO_2 was essentially complete in a relatively short time. High purity and careful handling of the graphite appeared to reduce the quantity of uranium that precipitated from the fuel.

Initial tests to determine whether oxygen contaminants could be removed from graphite by gettering them with molten fuel 130 appeared to be partially successful.

Graphite grades GT-123, 186, CCN, R-0013, AGOT, and TSF were exposed in 100-hr static permeation tests to molten fluoride salts at 1300°F (704°C) under a 150-psig pressure. All were penetrated by the molten salts; grade GT-123 was the only one that met the permeability requirements for the Molten-Salt Reactor.

Hot-pressed UO_2 pellets show no corrosion after being subjected to pure lead, pure bismuth, the 55 Bi–45 Pb eutectic alloy, and the Pb–0.69 Li eutectic alloy in separate tests at 650 and 750°F. Type 304 stainless steel capsules were used in each test and showed no corrosion. Uranium compounds were detected on the surface of the solidified bath that contained bismuth and on the surface of the solidified lead from the higher temperature lead test.

High-Temperature Alloy Development

The reactions of type 304 stainless steel with CO and CO_2 have been studied at high temperatures. At 1500°F, both CO and CO_2 oxidize the metal, forming various complex oxides. In static CO_2 or CO, carburization as well as oxidation occur. In flowing CO_2, carburization did not occur.

The attractive nuclear properties of beryllium have created interest in its use as a container material for uranium oxide and/or uranium carbide fuel elements for future gas-cooled reactors. Beryllium tubing has

been requested on a purchase order basis to help supply the needs for determining its potential for this application.

The stability of INOR-8 was determined in the temperature range between 1000–1400°F for periods up to 10,000 hr. The variations observed in the tensile properties of the alloy after aging indicate that the alloy does not embrittle under these conditions. This investigation has shown that chemical-constituent variations from heat to heat has a larger effect on the tensile properties than does the aging heat treatments.

Studies have been made to determine the feasibility of fabricating a triplex heat exchanger tube made up of two concentric tubes separated by a porous metal annulus to enable the passage of a gas for leak detection. A promising method of fabrication involves the cladding of a core consisting of prefabricated porous nickel tubing. The cladding material used to date has been Inconel because of its immediate availability.

Liquid-Metal Research

The diffusion coefficients of silver and nickel in liquid lead were measured by the capillary reservoir technique and found to have the values

$$D\ (0.165\ \text{wt}\ \%\ \text{Ni in Pb}) = 2.43 \times 10^{-3} \exp\left[-(7000 \pm 3700)/RT\right]$$

and

$$D\ (2.25\ \text{wt}\ \%\ \text{Ag in Pb}) = 5.14 \times 10^{-3} \exp\left[-(6800 \pm 5300)/RT\right] \quad .$$

The small difference in the diffusion coefficients of silver and nickel in lead is surprising, in view of the large differences in the atomic radii of the two species. The results add credence to the theory that the mechanism of liquid metal diffusion involves the cooperative movement of a large number of atoms where the average displacement of an individual atom is much smaller than the radii of the solute or solvent atoms.

The mass transfer constant, k, varied from 2.8×10^{-3} to 8.9×10^{-4} cm/sec in a liquid mercury–nickel thermal-convection loop in the temperature range of 205–280°C. The solubility of nickel in liquid mercury was measured between 120 and 330°C and found to have a heat of solution of 15,200 cal/mole.

Nondestructive Test Development

Work on the eddy-current inspection of tubing has been concentrated primarily on the inspection of EGCR (Experimental Gas-Cooled Reactor) fuel capsule tubing and has included the development of reference standards, the study of test conditions and parameters, and the development of inspection procedures for use in the tubing manufacturer's plant. A technique for inspecting the austenitic stainless steel sheath of Kanthal heater wires has been developed.

Empirical studies have been made on several types of eddy-current probe coils in the accomplishment of phase 1 of a three-phase program being conducted to produce adequate probe-design information for the future development of eddy-current inspections.

Two ultrasonic techniques have been developed for the evaluation of the bonding in flat, compartmented fuel plates. Both of these techniques capitalize on the inability of a poor bond to readily transmit ultrasonic energy.

Difficulties which have been encountered in ultrasonic inspections for laminations and nonbond in thin material have led to the measurement and study of the fields of ultrasonic transducers. Techniques were developed for the field studies, and the irregular nature of the ultrasonic fields has been observed.

Some preliminary investigations have indicated that magnetostrictive ferrites have some promise as ultrasonic transducers in the high-frequency range. The measurement of ultrasonic velocity has been investigated because of its effect on inspections and because of its anticipated use as a tool for metallurgical research. Two promising measurement techniques have been investigated. One of these is a comparison method which can be accomplished with present equipment to an accuracy of about 99%; the other is an absolute measurement method which requires some development but which promises extreme accuracy and amenability to automation.

The high-resolution, electronic, x-ray imaging system has been further investigated and found to exhibit an unsharpness of 0.001 and usable contrast sensitivity.

Low-voltage radiography has been studied as an inspection tool for beryllium, graphite, and thin sections of other materials. Techniques which employ a helium atmosphere have been developed and show promise.

Techniques, procedures, and standards for the inspection of EGCR fuel elements have been developed, and a considerable quantity of fuel-capsule tubing has been evaluated.

Mechanical Properties

Problems studied in connection with the Experimental Gas-Cooled Reactor include creep buckling, creep burst, and gas-metal reactions. In the past year, the conditions of configuration, temperature, and external pressure required to achieve uniform collapse of the fuel element capsule have been established. Tube-burst results have been obtained through the temperature range of interest and are found to correlate well with published uniaxial creep data. It has been concluded that creep tests performed in an inert environment provide more conservative data than those obtained in the pure gases which may be present as contaminants in the helium stream.

The test program for evaluating INOR-8 as a structural material for the Molten-Salt Reactor has been completed. A summary report describes these results.

Research has continued on the study of the effects of stress state and environment in the deformation and fracture of metals. Some progress has been made toward obtaining an analytical model for predicting, from simple laboratory experiments, the behavior of metal under service conditions.

Efforts in this group have been directed toward problems in connection with the Gas-Cooled Reactor, the Molten-Salt Reactor, and the Aircraft Nuclear Propulsion Project. In addition, research was conducted on the fracture of metals as affected by the stress state and environment. A resume of the progress on the other activities is given.

Welding and Brazing

The progress of the Welding and Brazing Group during the past reporting period has been published in the Reactor Projects Division

progress and design reports and in various topical reports. The investigations have been highly diversified and cannot be summarized under a general subject. Abstracts covering the pertinent results of each study are presented under appropriate headings.

PART IV. APPLIED METALLURGY

Process Metallurgy

Development work during the past year has been mainly centered on advancements in fuel element technology for the Army Reactors Branch, the Maritime Reactors Branch, and the Division of Reactor Development of the AEC.

Metallurgical development in the Army Package Power Reactor (SM-1) Project was confined primarily to problems associated with the burnable poison boron, which as B_4C is homogeneously distributed in the UO_2–stainless steel fuel core. An extensive analysis of boron losses in the Core I fuel plates, which contained 0.13 wt % B_4C, revealed an average loss of 22.4%. Initial experiments, aimed at determining the mechanism of boron losses, indicated that rather high losses are associated with an oxidation mechanism, and it is quite apparent that the moisture content of the sintering atmosphere must be maintained at a low and controlled level. Studies of an alternative boron compound, SrB_6, showed that when this compound was dispersed in stainless steel and heat treated at 1150°C that it reacted in a manner analogous to previously observed reactions between ZrB_2, B_4C, BN, and stainless steel.

Additional accomplishments included publication of specifications for manufacturing control-rod fuel elements and europium-bearing neutron absorber sections for Core II of the SM-1 reactor, followed by the production of eight of each of these components.

The APPR (Army Package Power Reactor) irradiation test program was stimulated by shipment to the MTR (Materials Testing Reactor) of miniature plates containing 20, 30, and 40 wt % Eu_2O_3 dispersed in stainless steel, as well as by the post-irradiation examination of the B^{10}-Fe neutron absorber sections and fuel elements from Core I of SM-1. The 3%

B^{10}–Fe section exhibited significant swelling and localized splitting of the cladding. The fuel elements appeared to be undamaged.

The Maritime Ship Program continued in support of work associated with construction of the NS "Savannah." In addition to evaluating brittle-fracture characteristics of the reactor pressure vessel, studies were also conducted on the usefulness of electroless nickel as the brazing alloy for joining the NS "Savannah" reference fuel tubes. The results confirmed similar work conducted by Babcock and Wilcox and led to the selection of this alloy as the reference material.

Other studies were directed principally to possible advancements in fuel element design. These included the potentially economical cold- and hot-swaging of bulk oxide into fuel rods; the application of lead or low melting alloys as heat transfer mediums in rods containing sintered UO_2 pellets; and the development of a compartmented plate containing UO_2 platelets. The results revealed that (1) rods containing high density UO_2 can be prepared by hot-swaging, and, if lower densities can be tolerated, cold-swaging may suffice; (2) lead may be a feasible heat transfer medium for pellet-containing rods operating at a surface temperature in the vicinity of 525°F. If the rod develops a leak, no drainage of lead will occur up to 650°F, and if the lead becomes exposed to 525°F water, it will not corrode catastrophically; (3) the compartmented plate appears attractive because of lower central-fuel-temperatures for the same specific power, or because of higher specific power with the central temperatures presently estimated for the rod design. Both brazing and resistance-welding techniques are being investigated for joining cover plates to the compartmented plate. Brazing with electroless nickel has met with relatively little success.

The majority of the effort in the Fuel Element Development Program (Activity 4420) was confined to the research-reactor aluminum fuel element, although a study was initiated to investigate the feasibility of ferritic stainless steel fuel elements. The development of a fuel compound for foreign research-reactor fuel elements utilizing 20%-enriched uranium was climaxed with the selection of U_3O_8 as the dispersoid for two experimental fuel element loadings to be produced for the Puerto Rico

Nuclear Center. Irradiation tests indicate that fuel elements containing U_3O_8 can withstand as high as 50% burnup of the U^{235} atoms without apparent damage and that this dispersion-type material is relatively corrosion resistant to 60 and 90°C water. Manufacturing specifications are in process.

Twenty-four alloy- and dispersion-type irradiation specimens were prepared and then irradiated in the Materials Testing Reactor. The alloy specimens contained 48 wt % of 20%-enriched uranium, 3 wt % silicon, and the balance was aluminum. The dispersion specimens were of two types: 60 wt % UC_2 in aluminum, and 63 wt % U_3O_8 in aluminum. No gross damage to any of the specimens has yet been observed.

Additional work on UO_2 dispersions in aluminum, in which high-fired titanium-bearing UO_2 was used as the fuel compound, confirmed the results of the previous, more extensive, study of the UO_2-Al system by R. C. Waugh that UO_2 will react rather rapidly with aluminum at 600°C.

Alloy-type elements have been examined for uranium surface-contamination, and the results strongly indicate that even with careful housekeeping, surface contamination may occur during 600°C heat treatments by diffusion of uranium from the alloy core. It is possible that by use of vacuum cast alloys in combination with high strength age-hardenable alloys and mechanical joining that many of the presently specified high-temperature treatments can be decreased or eliminated and that problems of this nature can be circumvented. The feasibility of using vacuum cast U-Al alloys in combination with both Alclad 6061 and 6951 aluminum has been demonstrated.

Studies have revealed that no great problems exist in incorporating UO_2 in type 430 ferritic stainless steel and rolling into composite plate. However, it was observed that subsequent heat treatments should be confined to 800°C in order to avoid possible sensitization of the cladding as well as rapid grain coarsening at higher temperatures.

Among the reactor components produced this year was a loading of stainless steel fuel elements for the Bulk Shielding Reactor. The design and fabrication procedures were similar to those specified for APPR fuel elements.

Advanced Engineering and Development of Reactor Materials

The ORR (Oak Ridge Reactor) fuel-irradiation program will investigate the effects of exposure temperature and fission burnup on thorium-base materials irradiated in temperature-controlled capsules. Initial test materials will be thorium alloys containing 0–10% of fully enriched uranium. Preliminary work necessary to develop facilities and techniques for the irradiations has continued. Capsule-fabrication techniques have been developed, and standard nondestructive methods of inspection have been applied. The required instruments, including an automatic withdrawal mechanism have been designed, fabricated, and partially installed in the ORR. A thin-walled aluminum access tube has been made and installed. A capsule carrier, having an inside diameter of about 2-1/2 in. and an internal length of 23 in., with a minimum shielding of about 10 in. of lead, has been designed and fabricated. An experiment to determine the gamma heating in the assigned ORR lattice position soon will be performed. Thorium and thorium alloyed with 1, 3, 6, and 10% depleted uranium have been cast to 1/2-in. diameter, swaged to 1/8-in. diameter, and heat treated for various times and temperatures. Metallographic studies of these alloys will be used to ascertain the heat treatments required to produce desired preirradiation microstructures.

Corrosion tests of zirconium and Zircaloy-2 intergranularly penetrated by magnesium at 625°C were continued in order to investigate a possible method of removing zirconium and Zircaloy-2 cladding from fuel elements. Specimens were completely disintegrated by intergranular corrosion in 6 M HCl. About 95% of each specimen was recovered as small granular particles.

Ceramic Materials

The primary aim of the Gas-Cooled Reactor fuel program is to develop a relatively cheap UO_2 body which is capable of consistently withstanding a fission burnup in excess of 10,000 Mwd/ton at the expected operating temperature. Numerous specimens have been prepared in support of the test program in order to evaluate the influence of starting material, product density, shape, heat flux, and other operating variables

on the behavior of UO_2 bodies during exposure to reactor-induced radiation. Studies are also in progress on the characterization of UO_2 powder resulting from the conversion of UF_6 by the ammonium diuranate process, optimization of processing conditions for consolidation, sintering of the powder to a density 95% of theoretical, and the establishment of permissible dimensional tolerances for economic production of UO_2 fuel bushings. Exploratory tests are also in progress to develop a UO_2 powder which is capable of 97% densification by the conventional cold pressing and sintering method.

A permanent deformation of approximately 1% was observed in bulk-oxide fuel bushings after compression at 5000 psi for 1 hr at 1500°C.

The technical feasibility of producing UO_2 fuel bodies by the extrusion process is being investigated under subcontract at the Auto-Lite Company. Results of the initial runs are encouraging and indicate that extrusion yields a high-density product.

The reduction of UO_2 by graphite has been observed to occur at temperatures as low as 1300°C, under certain environmental conditions.

Cursory studies on the chemical reactions of eight different oxides in contact with Nb, Mo, Ta, W, and Re at elevated temperatures indicate that thoria is the most stable of the oxides tested and that Nb is the most reactive metal. Alumina appears to be quite stable up to its melting point, whereas beryllia shows good stability with the elements molybdenum, tungsten, and tantalum. Urania seems compatible up to 2000°C with all metals tested, except rhenium. Zirconia, on the other hand, shows instability in contact with molybdenum and rhenium at temperatures below 2000°C.

A study of the sintering characteristics of the lanthanide oxides reveal that CeO_2 is the most refractory of the group and is stable toward air and boiling water. Similar tests show that a temperature of 1650–1700°C is required to achieve complete sintering of Sc_2O_3 in an oxygen atmosphere.

X-ray diffraction work on the UO_2-Y_2O_3 system shows that a single region of solid solubility of Y_2O_3 in UO_2 exists up to about 28 wt % Y_2O_3 and the presence of a two-phase region in the range of 28 to 45 wt %

Y_2O_3. X-ray diffraction measurements reveal the presence of the compound $Ca_2Be_3O_5$ in the CaO-BeO system. Densities, as determined from x-ray data, are reported for the compounds $LiYF_4$, $Li_7U_6F_{31}$, and Rb_2ThF_6.

Metallography

Metallography continues to play an important role in the support of various research and development activities. Techniques have been developed to aid in the microstructural analysis of UO_2 and U_3O_8 fuel-bearing bodies. Electron microscopy has been utilized to determine the nature of surface films on anodized aluminum and to examine topographical difference occurring on the surface of zirconium samples exposed to reactor-induced radiation and fission-recoil neutrons.

The linear expansion characteristics of several reactor materials have been investigated. Additions of U_3O_8 to aluminum, for instance, reduce the linear expansion of the resulting powder compact by an amount which is proportional to the volume percentage of U_3O_8 added, in the temperature range of 50 to 425°C. Thermal expansion data on Hastelloy B reveal that an inflection in the curve occurs at a temperature of 600°C on both heating and cooling. Similar data have been obtained on selected samples from the Ni-Mo and Ni-Mo-Fe systems to determine whether the inflection observed is related to a phase transformation in the Ni-Mo system.

Design criteria have been established on a micro-hot-hardness tester. Work on the ultrasonic apparatus for removal of microconstituents and on the equipment designed for hot- and cold-stage microscopy has continued. Layout and equipment design for remote metallographic equipment to be operated in the hot cells has progressed to an advanced stage.

CONTENTS

SUMMARY iii

PART I. FUNDAMENTAL METALLURGY

PHYSICOMETALLURGICAL RESEARCH 3

Structure of Metals 3
Use of Axis Distribution Charts to Represent Sheet Textures ... 3
Twinning and Cleavage in Niobium 10
Structure of Metals at Low Temperatures 17

Theory of Alloying 21
Low-Temperature Specific Heats of Group IVA Elements and Their Alloys 21
Constitution of Zirconium-Gallium 33
Vapor Pressures and Constitution of Zirconium-Cadmium 36

X-RAY DIFFRACTION 49

Routine Analyses 49
Aging Transformations of Zirconium-Niobium Alloys 51
Ordering of a Copper–31 at. % Gold Alloy 58
Preliminary Considerations for the X-Ray Diffraction Facility of the High-Level Radiation Examination Laboratory 64

MICROSTRESSES IN CRYSTALS 66

X-Ray Diffraction Studies of Cu_2O Films Grown on Copper 66
Determination of the Atomic Scattering Factors and Debye Factors in Cuprous Oxide 71

HIGH-TEMPERATURE REACTIONS 76

Absorption Spectra of Fused Salts 76

REACTIONS AT METAL SURFACES 80

Topography of Oxide Films Formed on Tantalum 80

The Effect of Radiation on the Oxidation of Metals 97

Oxidation Studies on Copper 100

FUNDAMENTAL CERAMIC STUDIES 103

Crystal Physics 103

PART II. HRP METALLURGY

HRP METALLURGY 109

Introduction 109

HRT Metallurgical Research 110
Examination of Samples and Components Removed from the Homogeneous Reactor Core 110

Physical Metallurgy..... 113
Zirconium Alloy Development..... 113
Zircaloy-2 Fabrication Study..... 115

Engineering Metallurgy..... 127
Forming of Zircaloy-2..... 127
Zircaloy-2 Welding Development..... 129
Electric-Arc Cutting of Zircaloy-2..... 131
Duplex Inconel—Stainless Steel Welds..... 135
Effect of Reactor Environment on Zirconium and Titanium Alloys..... 140
Combustion of Zirconium and Titanium..... 143

PART III. REACTOR METALLURGY

CORROSION ENGINEERING 147

Molten-Salt Reactor Program..... 147
Engineering Support..... 157
GCR Materials Compatibility Tests..... 158

MATERIALS COMPATIBILITY..... 162

Molten-Salt Reactor Program..... 162
Corrosion Research in Support of Maritime Ship Reactor Project..... 171
Aircraft Nuclear Propulsion..... 171

HIGH-TEMPERATURE ALLOY DEVELOPMENT..... 172

Materials for GCR Fuel Capsules..... 172
High-Temperature Stability of INOR-8..... 175
Aircraft Nuclear Propulsion Project..... 178
Molten-Salt Reactor Project..... 178
Gas-Cooled Reactor..... 181

LIQUID METAL RESEARCH..... 183

The Diffusion of Silver and Nickel in Liquid Lead..... 183
The Mass Transfer of Nickel in Liquid Mercury..... 187

METAL PROCESSING..... 192

Electron-Beam-Melting Laboratory..... 192

NONDESTRUCTIVE TEST DEVELOPMENT..... 192

Eddy-Current Development: Tubing..... 192
Eddy-Current Development: Probe Coils..... 193
Ultrasonic Bond-Evaluation Studies..... 197
Ultrasonic Field Measurements..... 205
Ultrasonic Transducer Development..... 207
Ultrasonic Velocity Studies..... 208
X-Ray Imaging System..... 212
Low-Voltage Radiography..... 212
Gas-Cooled Reactor Development..... 213
Gas-Cooled Reactor Program Materials Evaluation..... 215

MECHANICAL PROPERTIES 216

Gas-Cooled Reactor 216
Molten-Salt Reactor Program 219
Research on Fracture of Metals 220
Aircraft Nuclear Propulsion Program 229

WELDING AND BRAZING 229

Molten-Salt Reactor Program 229
Gas-Cooled Reactor Program 230
Sherwood Project 232
Aircraft Nuclear Propulsion Program 233
Chemical Technology Division Liaison 233

PART IV. APPLIED METALLURGY

PROCESS METALLURGY 237

Army Package Power Reactor (APPR) Project 237
Development of Europium-Bearing Absorber Rods 237
Development of Control-Rod Fuel Element with Eu_2O_3 Flux Suppressor 238
Aqueous Corrosion Studies 238
Determination of Boron Loss in Core I Fuel Plates 239
Mechanism Studies of Boron Sintering Losses 240
Compatibility of SrB_6 and Type 304LB Stainless Steel 243

Maritime Ship Reactor (MSR) Project 244
Brazing Alloy Development 245
Brittle-Fracture Evaluation 245
Pyrometer-Wire Studies 245
Swaging of UO_2 in Stainless Steel Capsules 246
Metal Bonding of Stainless Steel-Clad UO_2 Fuel Rods 248
Compartmented Fuel-Plate Development 249

Fuel Element Development 253
Utilization of High-Strength Aluminum 254
Uranium Contamination on Surfaces of Alclad Plates Containing Uranium-Aluminum Alloys 256
Compatibility of Alclad Fuel Plates Containing UO_2 Dispersed in Aluminum 258
Alclad Plates Containing Dispersions of U_3O_8 in Aluminum 261
Aqueous Corrosion Tests of Aluminum-Base Fuels Containing High Concentrations of UAl_3, UC, and U_3O_8 262
Ferritic Stainless Steel-Base Fuel Plates 264

Irradiation Testing 266
Examination of Irradiated SM-1 Core I Fuel and Control-Rod Components 266
Miniature Specimens of SM-1 Stainless Steel-Clad Absorber Plates Containing 3 wt % Enriched Boron Dispersed in Iron 268
Miniature Alclad Plates Containing High Investments of 20% Enriched Uranium 268

Miniature Specimens of SM-1 Core II Absorber Plates Containing Various Percentages of Eu_2O_3 in Stainless Steel Clad with Stainless Steel 270
Full-Size, Plate-Type Elements Containing 20% Enriched U_3O_8-Al Dispersions 270

Bulk Shielding Reactor (BSR) Stainless Steel Fuel Elements 271

ADVANCED ENGINEERING AND DEVELOPMENT OF REACTOR MATERIALS 274

Fuel Irradiation Program 274
Intergranular Diffusion of Zirconium and Zircaloy-2 by Magnesium 277

CERAMIC MATERIALS 278

Uranium Dioxide Technology Studies 279
Fabrication of GCR Fuel Bushings 279
High-Temperature Compression Testing of UO_2 281
Literature Survey on Thermal Conductivity 281
Equipment for Thermal-Conductivity Measurement 283
Fabrication of MSR Fuel Platelets 283
Extrusion of Uranium Dioxide 283
Compatibility of Graphite and UO_2 285
Preparation of Hydrothermal Oxide Particles 285

Beryllium Oxide Technology Studies 286
ANP Reactor Work 286
Lithium-Release Experiments 286
Preparation of High-Density Beryllium Oxide Shot 287

Ceramics Research 287
X-Ray Diffraction Studies 287
Refractory-Property Studies 289
ThO_2-UO_2-Al_2O_3 Systems 290

Studies on Other Ceramic Bodies 291
Si-SiC Fuel Plates 291
Uranium Monocarbide 292
Spherical Thorium Oxide Particles 292
Compatibility of Various Oxides with Selected Metals 292

METALLOGRAPHY 295

Dilatometry 295
Electron Microscopy 301
Metallography of Ceramic Fuel Materials 307
Reactor Support Activities 317
Equipment Development 326
Metallography of Irradiated Materials 328

PUBLICATIONS 333

Part I

FUNDAMENTAL METALLURGY

PHYSICOMETALLURGICAL RESEARCH

L. K. Jetter
C. J. McHargue J. O. Betterton, Jr. G. D. Kneip, Jr.

STRUCTURE OF METALS

C. J. McHargue L. K. Jetter

Use of Axis Distribution Charts to Represent Sheet Textures

Because of the crystallographic nature of the deformation mechanisms in metals, plastic flow results in the alignment of certain crystallographic directions with the primary flow directions. In the study of the "preferred orientation" thus developed, one wishes to discern the distribution of the crystallographic directions with respect to some reference direction, usually a direction related to the fabrication procedure, such as the rolling direction.

The pole figure method, introduced by Wever,[1] involves the plotting of the distribution of the poles of some family of planes on a stereographic projection which places the reference direction (s) at the north pole and/or in the center. By noting the angles between the reference directions and concentrations of poles on several such pole figures, the crystallographic directions which are aligned with the reference directions can be deduced. If the preferred orientation is relatively simple and well developed, two or three pole figures may be sufficient for obtaining the desired information; however, if there are several texture components, more pole figures may be needed.

A significant improvement in the method of representing the textures in wires and rods resulted from the introduction of the "inverse pole figure" or axis distribution chart by Harris.[2] Such a chart gives directly the distribution of the reference axis relative to the standard stereographic projection. There has been widespread acceptance of this method for the

---

[1]F. Wever, Trans. Am. Inst. Mining, Met. Petrol. Engrs. 93, 51 (1931).
[2]G. B. Harris, Phil. Mag. 43 (7), 113 (1952).

representation of fiber textures, and methods have been proposed for converting observed diffraction intensities into axis densities.[2–6]

The suggestion by Mitchell and Rowland[7] and Jetter, McHargue, and Williams[5] that sheet textures could be represented as distributions of rolling, normal, and transverse directions has been criticized on the basis that they offer no significant advantage over a combination of two ordinary pole figures and that it has not been proved that sheet textures can be treated as quasi fiber textures.[6]

If the purpose of a texture determination is to study some property which is related to the orientation of a particular crystallographic plane or direction, then conventional pole figures certainly are sufficient. For example, the distribution of the slip planes in face-centered cubic metals (the {111} pole figure) serves to indicate the variation in mechanical properties of sheet. On the other hand, if the study is directed at an understanding of the factors influencing texture formation, it is desirable to know not only the preferred orientation but the kind and degree of spread from it and the relative amounts of material in each component if there is more than one. Axis charts give this information as well as the orientations distribution.

Consider the procedure for deducing a texture component from a pole figure for the {111} planes of a face-centered cubic metal. If there is a concentration of poles at ϕ_1, α_1, where ϕ is the angle between the reference direction and diffracting plane pole and α is the azimuthal angle, it is obvious that any crystallographic direction which lies ϕ_1 degrees from {111} could be aligned with the rolling direction. By consideration of several concentrations, a direction can be found which lies ϕ_1, ϕ_2, ϕ_3, and ϕ_4 deg from the rolling direction. The crystallographic direction which has these angular relationships to the {111} poles is taken to be

---

[3]C. M. Mitchell and J. F. Rowland, Acta Met. 2, 559 (1954).

[4]C. G. Dunn, J. Appl. Phys. 25, 233 (1954).

[5]L. K. Jetter, C. J. McHargue, and R. O. Williams, J. Appl. Phys. 27, 368 (1956).

[6]W. Mueller, W. Chernock, and P. A. Beck, Trans. Met. Soc. AIME 212, 39 (1958).

[7]C. M. Mitchell and J. F. Rowland, Acta Met. 2, 559 (1954).

aligned with the rolling direction. In a similar manner, the plane which lies parallel to the rolling plane is deduced. If there are several components, the problem becomes more complicated. It is to be emphasized that the so-called "ideal" texture is deduced from the distribution of the poles of a few planes with respect to the reference directions.

The use of the axis distribution method for the determination of the distribution of the rolling, normal, or transverse direction in sheet material is no different in principle from its application for a fiber-axis distribution.[5] Each reference direction is considered in turn as a separate problem. In order to be used most effectively, the data from all three distributions can be combined. As long as the orientation distributions are relatively sharp, the requirement that the rolling, normal, and transverse directions be mutually perpendicular allows one to deduce an "ideal" texture from the three charts. Results on a thorium specimen obtained by the pole figure and axis-distribution method are compared.

Procedure. — The material studied was thorium having the following composition: 0.009% C, 0.14% O_2, 0.006% N_2, 0.01% Fe, and 0.005% Si. A 3.125-in.-dia billet was extruded to a 1- × 2-in. bar at 850°C, and a portion of the bar was reduced 95% in thickness by straight-rolling parallel to the extrusion direction at room temperature. This extrusion operation resulted in a texture which influenced the final orientation in the cold-rolled sheet.

An 0.200-in.-dia spherical x-ray diffraction specimen was prepared from a laminate of 0.050-in.-thick sheet which had been bonded with an adhesive. In order to remove metal disturbed by the machining operation, 0.010 in. of material was electropolished from the diameter. This specimen was used to obtain x-ray data for the pole figures and the axis distribution charts.

Conventional pole figures were prepared for the {222} and {400} planes by using the method described by Jetter and Borie[8] whereby the specimen is rotated simultaneously through the angles Φ and α, thus producing a spiral path on the sterographic projection. These pole figures are shown in Fig. 1.1 where the intensity contours are in arbitrary units.

---

[8]L. K. Jetter and B. S. Borie, J. Appl. Phys. 24, 532 (1953).

UNCLASSIFIED
ORNL-LR-DWG 36704

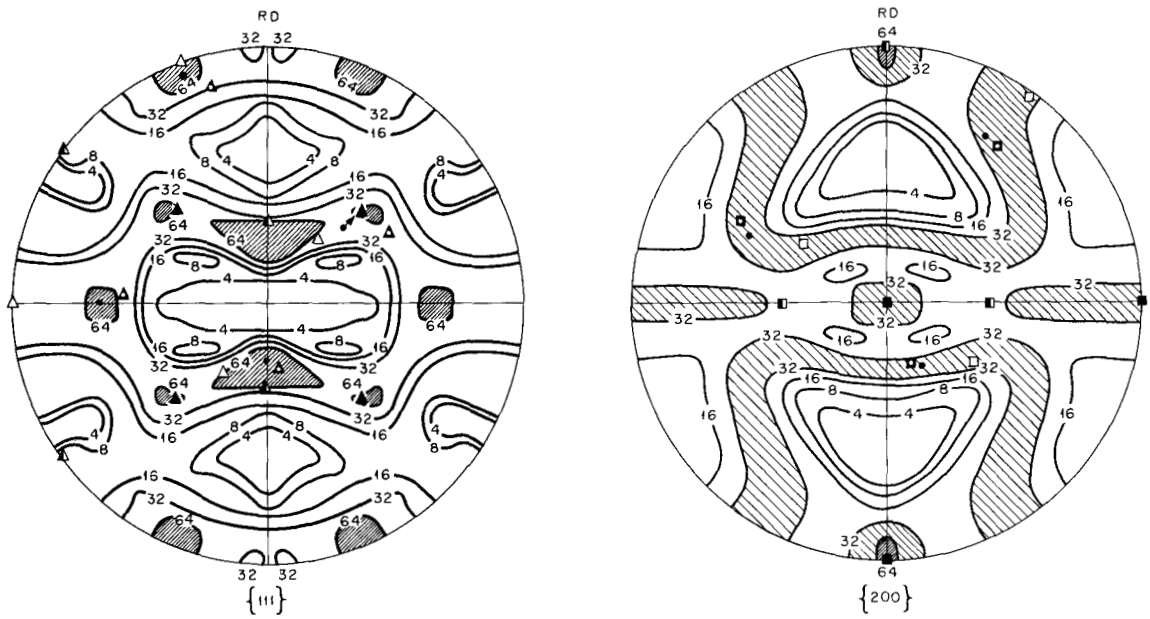

TEXTURE COMPONENTS ARE NOTED BY:
▲■ {001} <$\bar{1}$00>; ▲◧ {011} <$\bar{1}$00>; △□ NEAR-{011} <$\bar{2}\bar{1}$1>;
△◪ NEAR-{113} <$\bar{2}\bar{1}$1>; • NEAR-{7,12,22} <$\bar{8}\bar{4}$5>.

Fig. 1.1. Conventional Pole Figures for Thorium Sheet Reduced 95% in Thickness by Cold Rolling.

Axis distribution charts for the rolling, normal, and transverse directions were deduced from pole charts (I vs ϕ).[5] These pole charts were experimentally obtained for the following planes: {111}, {200}, {220}, {113}, {222}, {400}, {133}, {420}, {422}, and {135}. The specimen was rotated rapidly around the reference axis (in turn the rolling, normal, or transverse direction), while the specimen was scanned slowly through ϕ, the angle between the reference axis and the diffracting plane pole. The data from $\phi = 0°$ to $\phi = 90°$ for each of the ten pole charts were used in constructing the axis chart; thus each axis chart contains the information contained in eight conventional pole figures. The axis charts for the rolling and normal directions are shown in Fig. 1.2 and have previously been published.[9] The units in this figure are times random, for example, the axis density for a random texture is unity.

---

[9]L. K. Jetter and C. J. McHargue, The Metal Thorium, p 161, American Society for Metals, Cleveland, Ohio, 1958.

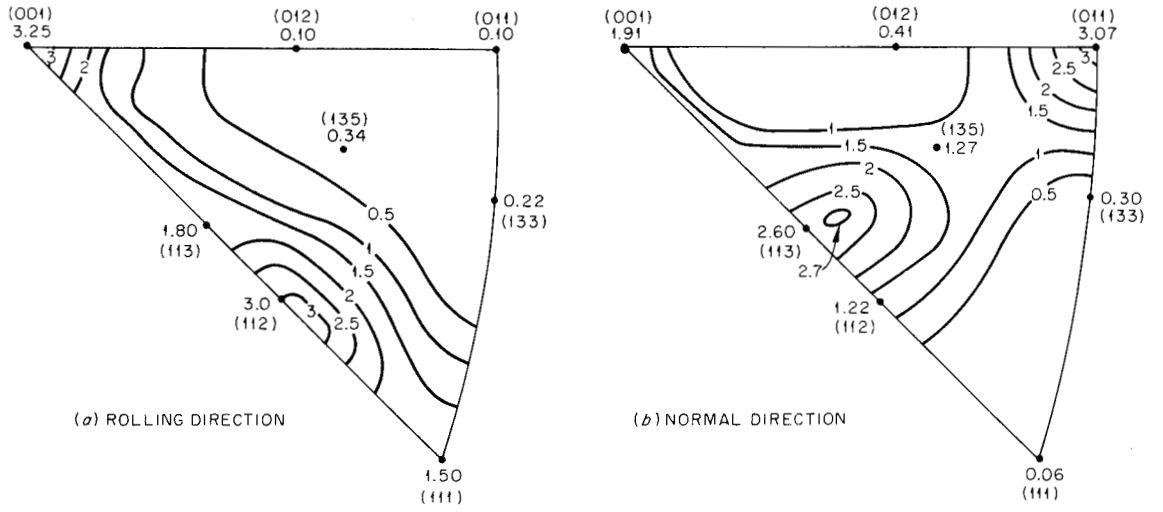

Fig. 1.2. Axis Distribution Charts for Rolling and Normal Directions.

Discussion. – The procedure of rotating the specimen rapidly through the angle α when obtaining pole charts is equivalent to averaging the intensities in a pole figure for $\alpha = 0°$ to $\alpha = 360°$ at constant values of ϕ. Thus one check of the data is the correspondence of pole charts experimentally obtained and those averaged from Fig. 1.1. Typical results are shown for the $\{200\}$ reflection. Agreement of this nature between the x-ray data (solid line) and that calculated from pole figures (dotted line) was found for several planes.

These data show that pole charts (I vs ϕ) can be obtained directly from pole figures. It has been shown also that pole charts can be obtained directly from axis distribution charts.[10] The reverse procedure, for example, to obtain axis charts or pole figures from pole charts, can be accomplished only by trial-and-error solutions at the present time. In each case, a distribution is assumed and the pole chart calculated and compared with the observed data. An important point in the construction of the axis charts is the use of x-ray data for the range $\phi = 0°$ to $90°$ for at least eight families of planes in the face-centered cubic case. An acceptable axis chart is one which leads to the reproduction of the pole chart for

[10] L. K. Jetter, C. J. McHargue, and R. O. Williams, J. Appl. Phys. 27, 368 (1956).

each plane for the whole range. The agreement for one such chart used in the present study is indicated in Fig. 1.3.

The axis distribution charts of Fig. 1.2 show the distribution of the normal directions to have maxima at < 011 >, < 001 >, and at a direction 3° from < 113 >, and the rolling direction maxima to be at < 001 >, < 111 >, and 2° from < 112 >. Since each point on the normal direction chart would be consistent with rolling directions which lie at any position on the locus 90° away, there is introduced an element of uncertainty. However, if we wish to consider "ideal" textures, for example, the center of each maxima, this can be accomplished by considering those mutually perpendicular on the axis charts for the three reference directions: rolling, normal, and transverse. Such considerations lead to the conculsion that there are orientations centered about the four components $\{001\} < \bar{1}00 >$, $\{011\} < \bar{1}00 >$, near - $\{011\} < 211 >$, and near - $\{113\} < \bar{2}\bar{1}1 >$. An examination of the axis charts shows that there is a continuous spread of orientations between the $\{001\} < \bar{1}00 >$ and near - $\{113\} < \bar{2}\bar{1}1 >$ components.

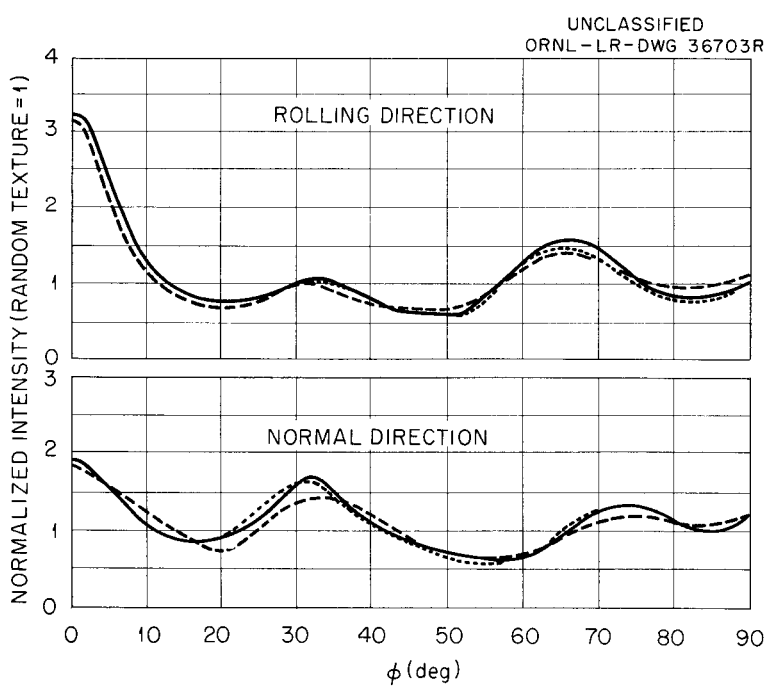

Fig. 1.3. Normalized Pole Charts for {400} Reflections. Solid lines derived from data used in constructing Fig. 1.2. Dashed lines calculated from Fig. 1.1. Dotted lines calculated from axis charts of Fig. 1.2.

One orientation of each of these four components is shown on the pole figures of Fig. 1.1. The orientation near - $\{7,12,22\} < \bar{8}\bar{7}45 >$ which was used by Hu, Sperry, and Beck[11] to describe the pole figures for cold-rolled aluminum and used by Smallman[12] to describe roughly the texture of cold-rolled thorium (99.5% pure) is also indicated. These two pole figures could be described by either the four components deduced from the axis charts or the near - $\{7,12,22\} < \bar{8}\bar{7}45 >$ component plus $\{001\} < \bar{1}00 >$. However, the spread of the high-intensity regions of the pole figures is better described by the four components.

Consideration was given to the possibility that the pole charts could give rise to axis charts containing only near - $\{7,12,22\} < \bar{8}\bar{7}45 >$ and $\{001\} < \bar{1}00 >$. The observed value of the axis density for the normal direction at the orientation $\{135\}$ is shown to be 1.27 in Fig. 1.2b. Since data for the $\{135\}$ planes were recorded, and since the axis density at $\phi = 0°$ is equal to the normalized x-ray diffraction intensity at $\phi = 0°$, this value of 1.27 contains no assumptions as to the type of axis distribution. Since the orientation $\{135\}$ is closer to $\{7,12,22\}$ than either $\{113\}$ or $\{011\}$, it is apparent that the high values of axis density observed at these latter positions (2.60 and 3.07, respectively) cannot be due to spread from an orientation peaked near $\{7,12,22\}$.

To further check this point, the axis density value at $\{135\}$ was ignored and an axis distribution was assumed which had a maximum at $\{7,12,22\}$ and fell to the observed values shown in Fig. 1.2b for the points $\{011\}$, $\{113\}$, $\{112\}$, and $\{133\}$. Pole charts calculated from such an axis distribution did not show reasonable agreement with the observed pole charts.

It is concluded that the four components deduced from the axis distribution charts were actually present in the specimen of cold-rolled thorium sheet studied. While these four components are consistent with the pole figures, three of them would not have been deduced without the axis charts. It should be pointed out that the near - $\{7,12,22\} < \bar{8}\bar{7}45 >$ component is an approximate average orientation between the near - $\{113\}$

---

[11] H. Hu, P. R. Sperry, and P. A. Beck, Trans. Am. Inst. Mining, Met. Petrol. Engrs. 194, 76 (1952).

[12] R. E. Smallman, J. Inst. Metals 83, 408 (1955).

$< \bar{2}\bar{1}1 >$ and near - $\{011\} < \bar{2}\bar{1}1 >$ orientations. It is not implied that $\{7,12,22\} < \bar{8}\bar{4}5 >$-type textures reported for many face-centered cubic metals may not exist in some cases. In the present case, the presence of several components can be explained in terms of the texture in the extruded bar from which the sheet was cold rolled.

Using the plots of I sin ϕ vs ϕ which were obtained in normalizing the observed intensities, the amount of each texture component was calculated by the method previously described.[13] The relative amount of material which contained either the $< \bar{1}00 >$ or the $< \bar{2}\bar{1}1 >$ directions parallel to the rolling direction was determined from the charts for the rolling direction; the amount associated with $\{011\}$, $\{113\}$, and $\{011\}$ was determined from the normal-direction data. The figures obtained were 10% $\{001\} < \bar{1}00 >$, 13% $\{011\} < \bar{1}00 >$, 20% near - $\{011\} < \bar{2}\bar{1}1 >$, and 50% near - $\{113\} < \bar{2}\bar{1}1 >$. These figures represent the amount of material oriented within 15° of the "ideal" textures. The remaining 7% lies outside these limits.

Conclusion. — An example has been cited whereby four texture components were deduced from axis distribution charts for the normal, rolling, and transverse directions of cold-rolled thorium sheet. These components were shown to be consistent with the conventional pole figures for the $\{222\}$ and $\{400\}$ planes except that one component deduced from the pole figure was an average of two of these and was not consistent with the observed pole charts. In addition, it was shown that the symmetry and degree of spread about the "ideal" textures, as well as the relative amount of each component, could be readily deduced from the axis charts.

Twinning and Cleavage in Niobium

C. J. McHargue

Determinations of the mechanical properties of tantalum, niobium, and vanadium have shown these metals to retain a high degree of ductility at temperatures as low as that of liquid nitrogen, and it has been suggested that this group of body-centered cubic metals do not deform by mechanical

[13] L. K. Jetter, C. J. McHargue, and R. O. Williams, J. Appl. Phys. 27, 368 (1956).

twinning.[14] Since this is an unexpected behavior for a body-centered cubic metal, Barrett and Bakish[15] deformed tantalum (99.9% pure) under conditions favorable to twinning rather than slip, for example, impact loading on large-grained specimens at low temperature. Impact deformation at -196°C produced both slip lines and twin bands, but tests at -77 and at 25°C produced only slip markings. Clough and Pavlovic[16] found twin markings in commercially pure vanadium deformed by impact at temperatures of -77°C and lower. However, in this case, the twins were present only within one or two grains of a cleaved surface.

Because of the potential importance of niobium, it appeared desirable to define the conditions under which mechanical twins and cleavage might occur.

Single crystals were cut from an ingot of electron-beam-melted niobium whose analysis was reported to be (in ppm) B, < 1; C, 10; Fe, < 100; N, 60; O, 32; Si, < 100; Ta, 1000; and Ti, < 150. These crystals varied from 0.50 × 0.25 × 0.25 in. to 0.75 × 0.50 × 0.50 in. In order to determine any grain-size effects, tests were also conducted on sheet rolled from a section of the ingot and recrystallized at 1600°C. Deformation was applied by hammer blows on an anvil or by slow compression on a hydraulic press. In each case, the specimen and anvils were immersed in the coolant (liquid nitrogen or dry ice and acetone mixture).

At -196°C, deformation twins were produced by both impact loading and slow compression. The slow-compression result is rather surprising in view of general experience with body-centered cubic metals. Two-surface analysis of each crystal showed the twin plane to be of the $\{112\}$ family and the twin directions to be of the $\langle 11\bar{1} \rangle$ family, the usual plane and direction for this class of metals.

No twins were found in specimens deformed at -77 and 25°C. It is possible that much higher rates of loading might cause this mode of deformation to become operative.

---

[14] C. S. Barrett, Trans. Am. Soc. Metals 49, 53 (1957).

[15] C. S. Barrett and R. Bakish, Trans. Met. Soc. AIME 212, 122 (1958).

[16] W. R. Clough and A. S. Pavlovic, Flow Fracture and Twinning of Commercially Pure Vanadium, Am. Soc. Metals Preprint 125 (1959).

Two specimens of coarse-grained sheet were tested at -196°C. The average grain diameter was about 3 mm. Deformation twins were found in about one-third of the grains and their traces were identified as $\{112\}$ planes. Deformation in the remaining grains was by slip and deformation-band formation.

The profusion of twinning is shown in Fig. 1.4 which shows photomacrographs of the crystal deformed in slow depression at -196°C. Compression was normal to face 4.

Many of the twin bands resembled the Neumann bands of iron, having a thin lens shape and serrated edges. However, many of them contained a large amount of unusual structure, and others had a laminated appearance. The electron micrographs of Fig. 1.5 show some of these features. Both figures indicate an extremely inhomogeneous state of deformation. Figure 1.5a shows very thin strips of untwinned crystal between twins as well as some details of the serrations. Figure 1.5b illustrates in more detail the markings within the twin; these markings seem to be associated with the formation of the serrations.

It was noted that much of the structure within the twin bands was orientation dependent. A detailed analysis of a crystal deformed slowly in compression yielded the following tentative picture. Figure 1.6a and 1.6b contains the sterographic projections of the two crystal faces sketched in Fig. 1.6c and contain the traces of deformation markings. Electron micrographs of representative areas of these faces are shown in Fig. 1.7.

The approximately horizontal twin on face 1 (Fig. 1.7a) is on the $(\bar{1}\bar{1}2)$ plane and probably formed in the late stages of deformation. From Fig. 1.6a it can be seen that the $[1\bar{1}1]$ direction which is both the shear direction for twinning on $(1\bar{1}\bar{2})$ and for slip on $(\bar{1}01)$ and $(0\bar{1}\bar{1})$ lies only 7° from the plane of the projection. Moreover, the traces of the $(\bar{1}01)$ and $(0\bar{1}\bar{1})$ slip planes lie only 5.5 to 6° from the trace of $(1\bar{1}\bar{2})$ on this surface. Thus, neither slip nor twinning will have a large shear component out of face 1, and the deformation marking should be relatively faint. The diagonal markings shown in Fig. 1.7a have been interpreted as traces of $(\bar{1}01)$ and $(0\bar{1}\bar{1})$ slip planes within the $(1\bar{1}\bar{2})$ twin, whose width can be seen from the extent of the slip markings as well as from the displacement of the scratch running from lower left to upper right. The view of these

UNCLASSIFIED
Y-29682

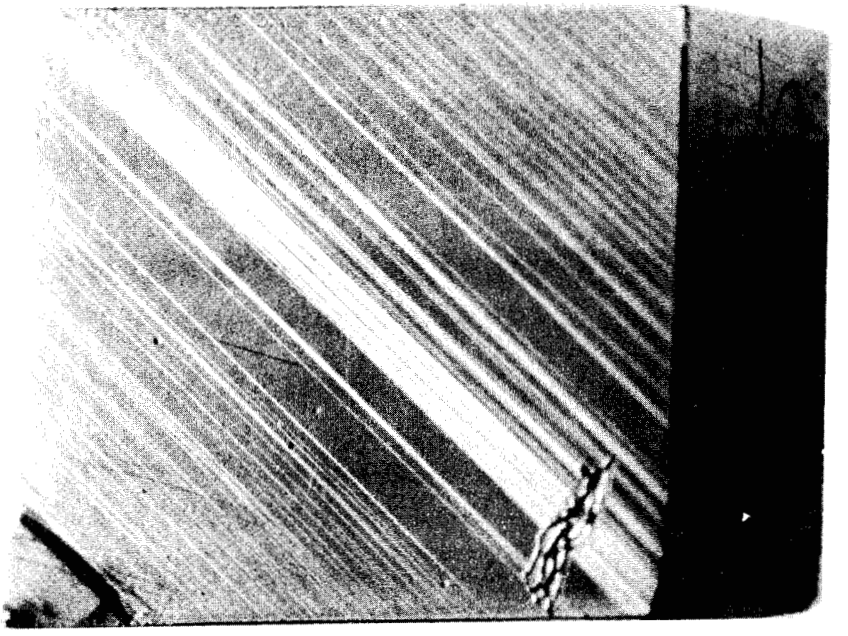

UNCLASSIFIED
Y-29685

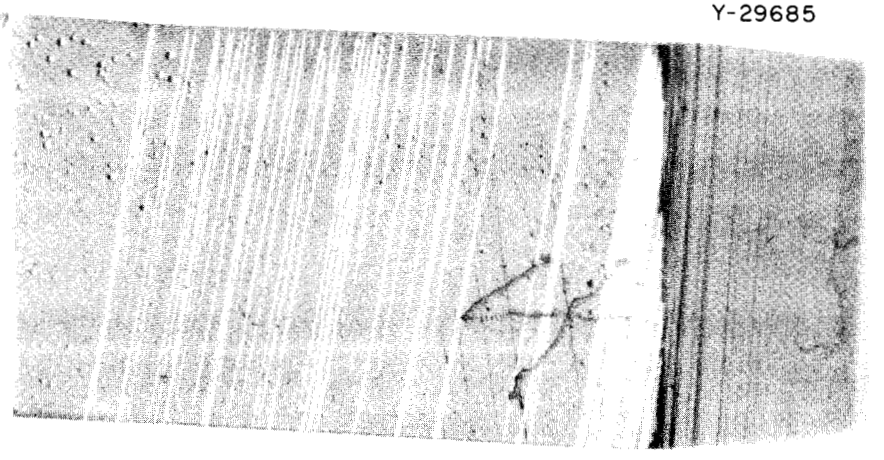

Fig. 1.4. Photomacrographs Showing Deformation Markings in Niobium Single Crystal Deformed by Slow Compression at −196°C.

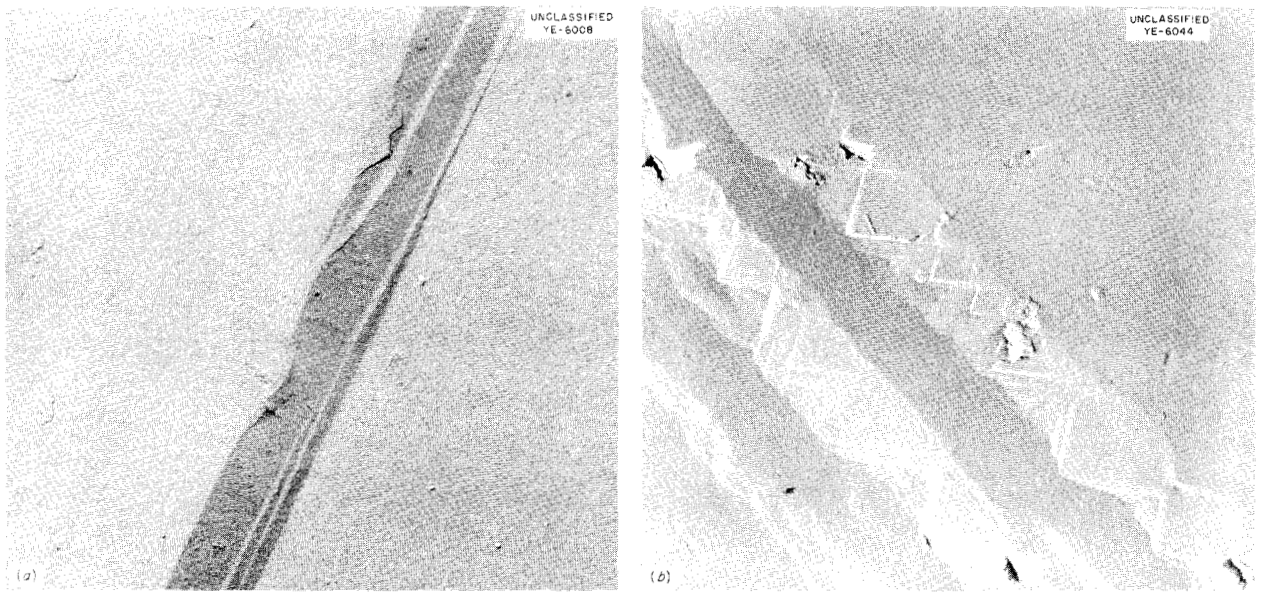

Fig. 1.5. Electron Micrographs of Mechanical Twins in Niobium Single Crystals. Specimen unetched after deformation; preshadowed indirect carbon replica. (*a*) 17,000X, (*b*) 9700X. Reduced 55%.

markings on face 6 is shown in Fig. 1.7b. The diagonal bands are the twins, and the slip lines form the notches within them. A small amount of $(0\bar{1}\bar{1})$ slip is seen in the adjacent matrix. For this orientation, the $(\bar{1}01)$ slip plane of the twin coincides with a $(0\bar{1}\bar{1})$ slip plane of the matrix. These markings are identified on the sketch of Fig. 1.6c.

Further evidence of the inhomogeneous nature of twin deformation is illustrated by Fig. 1.8 and it is seen here that markings of some sort are present in the matrix to the left of the twin. These markings appear to be associated with areas of the twin which later form serrations. The exact nature of these markings is not yet known, but that they represent a shear of the crystal face is shown by the displacement of the scratch. It is felt that they are connected with the nucleations of parallel twin bands or with the growth of the existing twin.

Many photographs indicated that relief of stresses at the tips of twins in niobium takes place by slip rather than by kinking or crack formation, as in many substances. A typical case is shown in Fig. 1.9 where there is profuse slip between the tips of adjacent twins.

Although much of the deformation at -196°C occurred by twinning, it was possible to find many areas which contained slip lines not associated

UNCLASSIFIED
ORNL-LR-DWG 42647

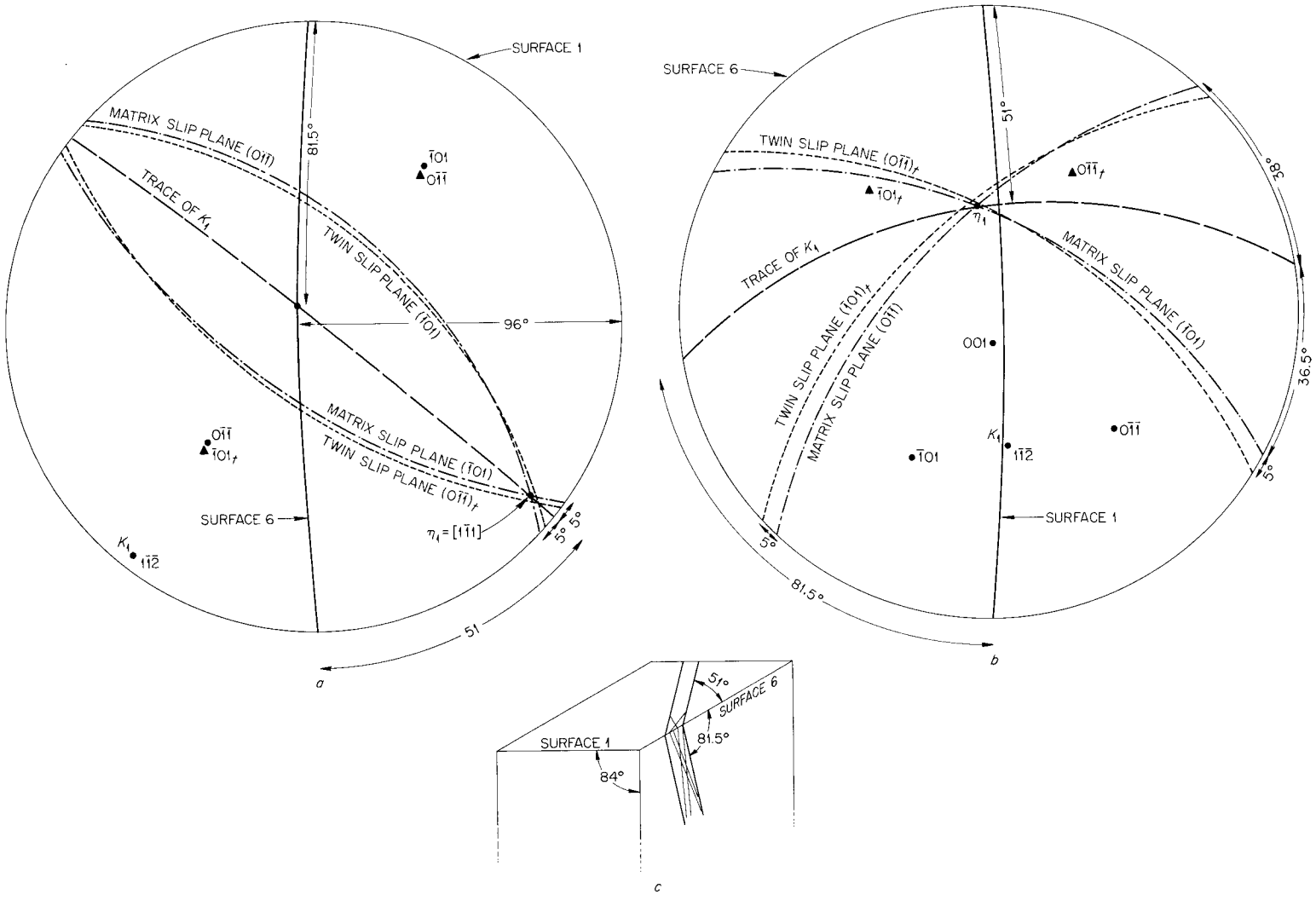

Fig. 1.6. Stereographic Projection of (*a*) Face 1, and (*b*) Face 6 of Niobium Crystal Deformed at −196°C Showing Two Surface Solution of Deformation Markings Sketched in (*c*).

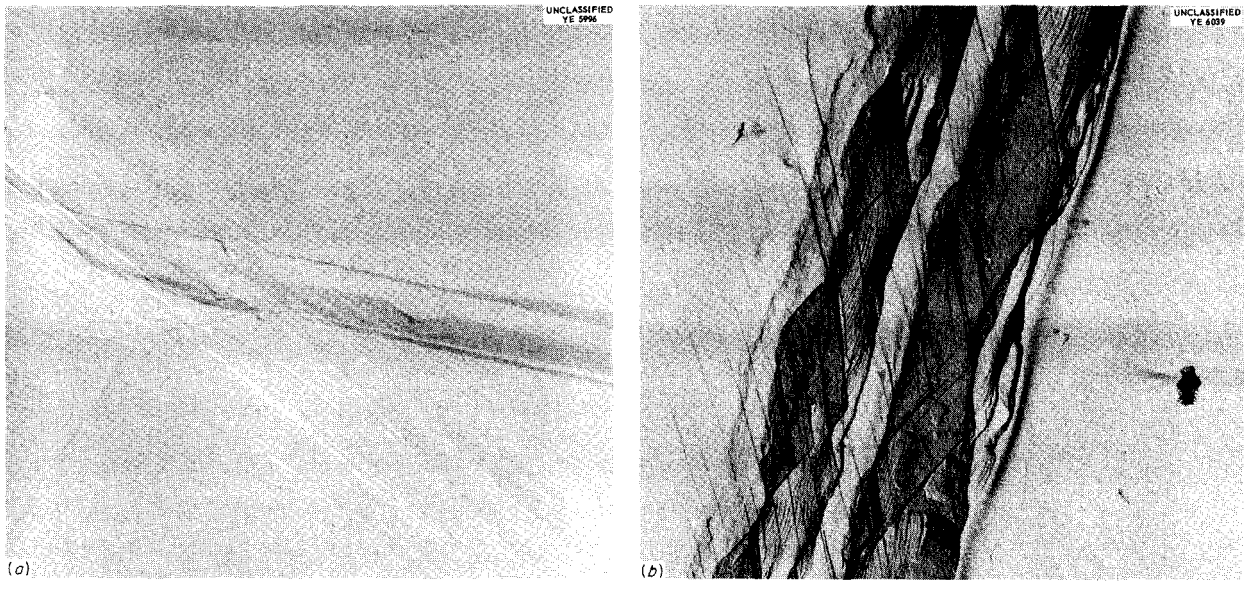

Fig. 1.7. Electron Micrographs of Areas of (*a*) Face 1, and (*b*) Face 6. Preshadowed indirect carbon replica. 9700X. Reduced 55.5%.

with twins. In many of these regions the slip lines appear as short segments alternating on parallel planes, these segments being joined by cross slip. ~~A typical area is shown in Fig. 1.10.~~ *

Cleavage in body-centered cubic metals is found usually to be on only {100} planes, and it has been suggested that the unusual low-temperature ductility of tantalum might be associated with the fact that the primary cleavage of this metal is on {110} planes.[17] Cleavage fracture on both families of planes has been reported for vanadium.[18]

The results of experiments on a limited number of niobium crystals in this study show only {100} cleavage to occur at -196°C. It is possible that crystals oriented in other positions relative to the stress axis might cleave on {110} planes. However, one specimen was machined such that the normal stress would be approximately equal on (001) and (011). A back-reflection Laue photograph of the cleaved surface showed only {001} facets. It must be concluded that even in a group of metals as similar as tantalum, niobium, and vanadium the cleavage habit varies for reasons as yet unknown.

---

[17] C. S. Barrett and R. Bakish, Trans. Met. Soc. AIME 212, 122 (1958).

[18] W. R. Clough and A. S. Pavlovic, Flow Fracture and Twinning of Commercially Pure Vanadium, Am. Soc. Metals Preprint 125, (1959).

 * See errata

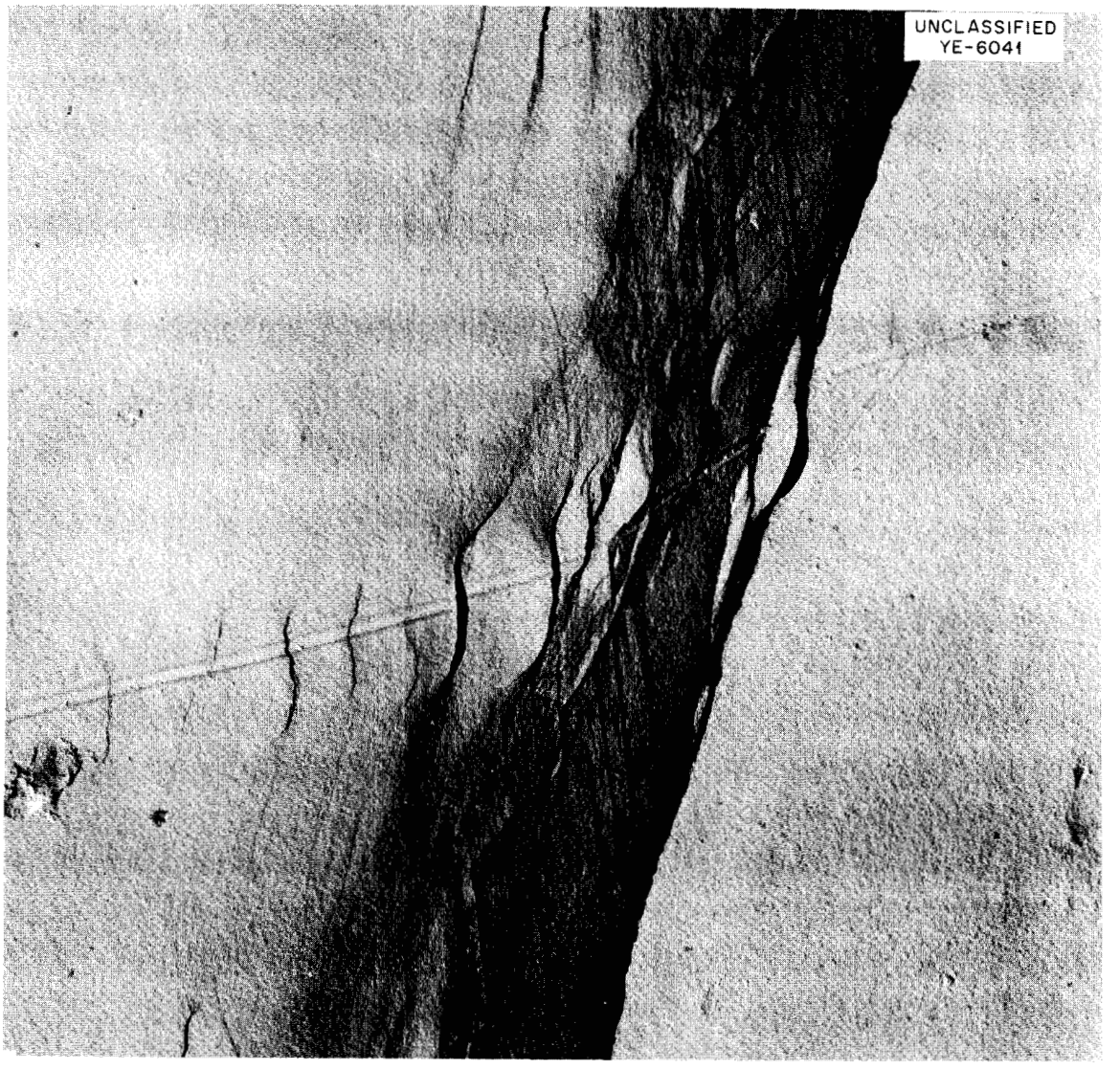

Fig. 1.8. Electron Micrograph of Mechanical Twin in Niobium Single Crystal. Preshadowed indirect carbon replica. 9700X. Reduced 17%.

Structure of Metals at Low Temperatures

C. J. McHargue H. L. Yakel, Jr.

In order to learn more of the factors influencing allotropic transformations, a study was started to determine the structure of elements at low temperatures with the use of the liquid helium x-ray diffractometer. No transformations were observed in titanium, hafnium, zirconium, thorium, or mercury. A specimen of gallium, however, gave indications of a transformation.

Fig. 1.9. Electron Micrograph Showing Slip Between Tips of Twins. Preshadowed indirect carbon replica. 22,700X. Reduced 17%.

The gallium studied was obtained from McKay, and their analysis stated it to be 99.9% pure. A specimen was cast in place in the x-ray diffractometer. The structure was orthorhombic at room temperature, 77 and 4.2°K. After the surface had been scratched a few times at 4.2°K with the tool built into the cryostat, eight additional diffraction lines appeared in the x-ray pattern. Efforts to determine the crystal structure from these

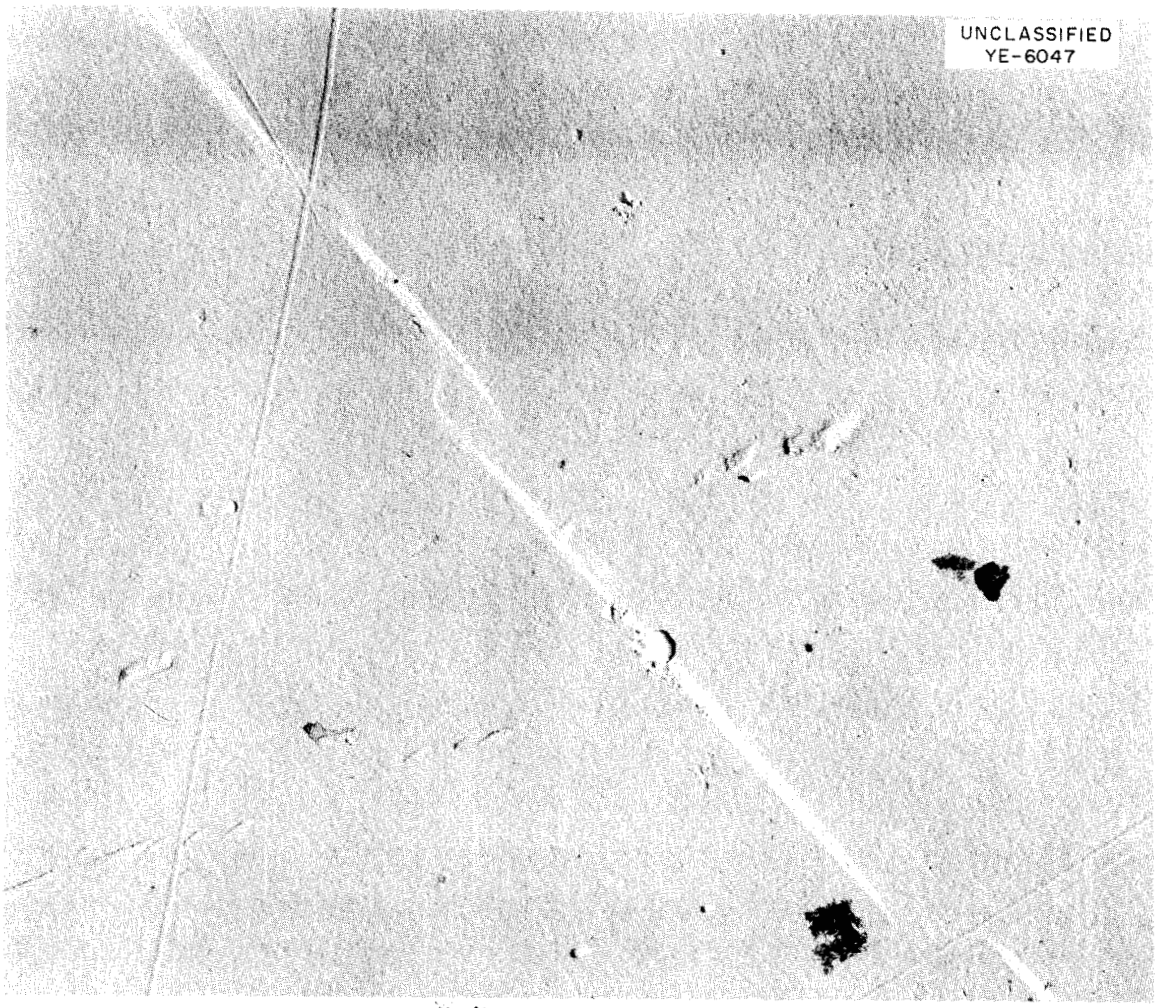

Fig. 1.10. Electron Micrograph of ~~Slip~~ Line Segments Showing Cross Slip. Preshadowed indirect carbon replica. 9700X. Reduced 17%.

so far have not been successful. The Bragg angle and intensities of the extra lines are:

2θ	Intensity
25.75	10
28.4	> 100
32.7	24
35.75	28
40.35	7
44.0	7
44.9	10
53.15	15

The extra lines disappeared at a temperature below 200°K when the specimen was heated, and only the diffraction lines corresponding to the orthorhombic structure remained.

The appearance of the specimen indicates that it had undergone a transformation and that the stresses involved had been large. Because of the apparent inability of the specimen to plastically deform, extensive cracking occurred, as is shown in Fig. 1.11.

Fig. 1.11. X-Ray Specimen of Gallium After Being Deformed at 4.2°K.

THEORY OF ALLOYING

Low-Temperature Specific Heats of Group IVA Elements and Their Alloys

G. D. Kneip, Jr. J. O. Betterton, Jr.

The relative freedom of electrons in metals to move throughout the entire lattice is responsible for many of the distinguishing features of the pure metals and controls their alloying behavior. According to band theory, the electrons in metals are pictured as occupying a series of closely spaced energy levels such that the energy of the highest occupied level, the Fermi energy, is several electron volts above the lowest occupied level. Not all energies are allowed, due to the periodic potential field of the nuclei. Hence, in a real metal, the permissible electronic energies may be considered to be bands of closely spaced energy levels which may overlap or may have a range of forbidden energies between the bands. Only the electrons at the top of the band can be thermally excited into adjacent unoccupied energy levels and hence contribute to the specific heat. This electronic part of the specific heat then is proportional to the density of electronic states at the Fermi surface, and if the electronic wave functions are chosen to be combinations of one-electron functions, then the electronic specific heat is[19]

$$C_{V_e} = \frac{\pi^2}{3} k^2 N (E_{max}) T. \tag{1}$$

At liquid-helium temperatures, the approximately equal magnitudes and different temperature dependence of the electronic and lattice contributions to the specific heats of metals make possible the separation of the two components. At sufficiently low temperatures, where the lattice heat capacity can be accurately represented by the Debye approximation, the total heat capacity is[19]

$$C_V = \gamma T + \frac{12}{5} \pi^4 N k \left(\frac{T}{\theta_D}\right)^3 , \tag{2}$$

---

[19]A. H. Wilson, Theory of Metals, p 141–44, 2d ed., Cambridge University Press, Cambridge, 1953.

where the linear and T^3 terms are the electronic and lattice contributions, respectively, and the coefficient of the linear term is proportional to the density of electronic states at the Fermi surface.

Bands arising from both d and s atomic electrons are expected to contribute to the electronic specific heats of the group IVA elements, titanium, zirconium, and hafnium. As in the other transition metals with unfilled d shells, the d band should exist over a narrow energy range and have a high density of states compared to the s band, leading to a high density of states and thus a high electronic specific heat in the pure metals. If the rigid-band model is assumed to be valid for alloying, then the addition of other elements to the group IVA solvent allows the filling of the band to be changed in proportion to the difference in valency of the two metals; thus, it should be possible to investigate the pure metal band shape in the vicinity of Fermi surface by measuring the electronic specific heat.

Recently it has been proposed that titanium[20,21] and zirconium[21] are divalent in the metallic state with respect to the effects of substitutional solutes on the allotropic transformation temperature. The density of electronic states as derived for the experimental low-temperature heat capacities of zirconium-indium and zirconium-tin alloys is in reasonable agreement with this hypothesis.

The low-temperature calorimeter and the appropriate experimental techniques have been described in an earlier report.[22] Earlier investigations have reported rather widely scattered results for the low-temperature specific heats of titanium and zirconium,[23,24] due either to impurities in the metals or to inadequate experimental techniques. The

---

[20]J. M. Denney, Electron Effects in Solid Solution Alloys of Titanium, Sixth Technical Report, ONR-N6onr-24430, Project NR 031-355, Calif. Inst. of Tech., Pasadena, Calif. (1955).

[21]J. O. Betterton, Jr., and J. H. Frye, Jr., Acta Met. 6, 205 (1958); Met. Semiann. Prog. Rep. Apr. 10, 1954, ORNL-1727, p 108 (classified).

[22]G. D. Kneip, Jr. and J. O. Betterton, Jr., Met. Ann. Prog. Rep. Oct. 10, 1958, ORNL-2632, p 11.

[23]I. Estermann, S. H. Friedberg, and J. E. Goldman, Phys. Rev. 87, 582 (1952).

[24]N. M. Wolcott, Conference de Physique des Basses Temperatures, Paris 1955, p 286, Centre National de la Recherche Scientifique, and UNESCO, Paris, 1956.

specific heat of copper has been measured in order to show that the experimental techniques used yield results that are in good agreement with those of Corak.[25] These results are listed in Table 1.1 along with other recently reported values. Both calorimeter specimens were prepared from 99.999% copper (American Smelting and Refining Company) by vacuum melting

[25]W. S. Corak et al., Phys. Rev. 98, 1699 (1955).

Table 1.1. Low-Temperature Specific Heat of Copper

Reference	γ (millijoules • mole^{-1} • deg^{-2})	θ_D (°K)
This work	0.692 ± 0.003	341.9 ± 0.6
This work	0.693 ± 0.004	341.4 ± 0.8
Corak[a]	0.688 ± 0.002	343.8 ± 0.5
Rayne[b]	0.686 ± 0.005	345.1 ± 0.9
Phillips[c]	0.69	342
Griffel[d]	0.691	347 ± 2
Estermann[e]	0.75	315

[a]W. S. Corak et al., Phys. Rev. 98, 1699 (1955).

[b]J. A. Rayne, Australian J. Phys. 9, 189 (1956).

[c]N. E. Phillips, p 414 in Proceedings of the Fifth International Conference on Low Temperature Physics and Chemistry, ed. by J. R. Dillinger, University of Wisconsin Press, Madison, 1958.

[d]M. Griffel, R. W. Vest, and J. F. Smith, J. Chem. Phys. 27, 1267 (1957).

[e]I. Estermann, S. H. Friedberg, and J. E. Goldman, Phys. Rev. 87, 582 (1952).

(10^{-6} mm Hg) in a graphite crucible, machining to size, vacuum annealing for 1 hr at 1000°C, and finally, slowly cooling to room temperature.

Specimens suitable for the calorimeter were prepared from iodide process titanium, zirconium, and hafnium with appropriate heat treatments. The source of the materials as well as their heat treatments are shown in Table 1.2. The annealing procedures were similar to those used by Betterton and Easton[26] for the study of the zirconium-silver phase diagram and include suitable precautions to avoid contamination of these reactive metals. Two zirconium specimens (Zr α1 and Zr α2) were prepared from different lots of zirconium and a third (Zr O In) was fabricated in the same manner as the zirconium-indium and zirconium-tin alloys to investigate the sensitivity of the measurements to minor impurities. The fourth zirconium specimen, Zr α', was water quenched from the high-temperature BCC structure in order to show the effect of severe lattice distortions on the specific heats. Table 1.3 lists the significant impurity concentrations in the specimens.

The zirconium for the zirconium-indium alloys came from the same crystal bar (iodide zirconium) as the pure specimen, Zr α1, while that for the zirconium-tin alloys was taken from the same material as specimen Zr α2. The indium and tin were both of 99.99% purity and were supplied by American Smelting and Refining Company and Alpha Metals, Inc., respectively. Uniform solute composition in the alloys was attained by repetitive arc melting on alternate sides of the ingot, then shearing to small pieces and remelting. Each ingot was cut up at least twice and melted a minimum of 12 times. The more dilute indium and tin alloys were annealed at 1100°C for a minimum of five days to remove minor concentration gradients, annealed in the α solid-solution region for a minimum of 25 days, and then quenched in water to retain the α solid-solution structure. The more concentrated alloys were annealed in the β solid-solution region for periods between ten days at 1100°C and one day at 1200°C and then quenched in water. This heat treatment yields a distorted hexagonal structure with the solute atoms randomly distributed, designated α', which is similar to

---

[26]J. O. Betterton, Jr., and D. S. Easton, Trans. Met. Soc. AIME 212, 470 (1958).

Table 1.2. Heat Treatment of Calorimeter Specimens

	Titanium	Zirconium	Zirconium	Zirconium	Zirconium	Hafnium
Specimen designation	Ti	Zr $\alpha 1$	Zr α'	Zr O In*	Zr $\alpha 2$	Hf
Vendor	New Jersey Zinc Company		Westinghouse Atomic Power Division			Battelle Memorial Institute
Vendors No.	IT-160	1436-C	1436-C	1436-C	1688	8496
Hydrogen removal treatment	10^{-6} mm Hg at 1100°C	10^{-6} mm Hg at 1100°C	10^{-6} mm Hg at 1100°C	10^{-6} mm Hg at 1100°C	10^{-6} mm Hg at 1100°C	10^{-6} mm Hg at 1100°C
Arc melting	No	No	No	9 times	Cast by WAPD	2 times
Homogenization anneal	No	No	No	1100°C, 7 days	No	No
Final anneal						
Temp., °C	800	800	1100	845	800	800
Time	1 hr	1 hr	1 hr	25 days	2 hr	1 hr
Cooling rate	Slow	Slow	Water quench	Slow	Slow	Slow

*Control for the indium system.

Table 1.3. Impurity Content of Specific Heat Specimens

Metallic impurities determined by neutron-activation analysis, gases determined by vacuum-fusion analysis. All specimens were 99.9% pure; impurities are given in parts per million.

Impurity	Specimen Designation				
	Ti	Zr α1	Zr O In*	Zr α2	Hf
Ti		NA**	NA	NA	NA
Zr	183				3
Hf	NA	130	NA	NA	
Si	3	2	NA	NA	NA
Cr	NA	2	NA	NA	NA
Fe	200	23	NA	NA	200
Ni	<4	11	NA	NA	7
Cu	2	0.8	14	3	3
Mo	4	4	NA	NA	43
W	2	0.4	8	8	1
H	<1	<1	NA	<1	<1
N	7	3	NA	<5	<5
O	100	26	NA	10	18
C	190	56	30	80	130
			Vickers hardness		
	63	63	68	75	120

*Control for indium system.

**Not analyzed.

the equilibrium α solid-solution. All annealing treatments were carried out in evacuated or argon-filled silica capsules by using procedures which introduce a minimum of impurities into the alloy.[26] The composition of each alloy was determined by chemical analysis.[27] Most of the specimens were analyzed at three different parts of the ingot, the variation in analytical values indicating a maximum inhomogeneity of ± 0.20 at. %.

[27]Johnson, Matthey and Company, Ltd., London, Eng.

In order to facilitate the separation of the electronic and vibrational specific heats, Eq. (2) is written in the form:

$$\frac{C}{T} = \gamma + \beta T^2, \tag{3}$$

and the constants γ and β are determined by a least-squares analysis of the data. A typical set of data is shown in Fig. 1.12 plotted as C/T vs T^2. Except in the case of the 7.5 and 9% tin alloys, where a superconducting transition was observed at approximately 1.2°K, the data fit Eq. (2) with a scatter of a few tenths of a per cent, indicating that at temperatures below 4.5°K the Debye T^3 relation is valid for the group IVA elements. The coefficients of the electronic specific heats and the Debye temperatures of the group IVA elements, the zirconium-indium alloys, and the zirconium-tin alloys are listed in Tables 1.4, 1.5, and 1.6, respectively. The probable errors shown were estimated from the least-squares analysis of the data at a 99% confidence level.

The electronic specific heats of the three group IVA metals decrease with increasing atomic number, as might be expected from the progressively larger degree of electronic interaction in the sequence, titanium, zirconium, and hafnium. The Debye temperatures also decrease with increasing atomic number through the sequence, as expected from the increasing atomic masses. The Debye temperature is expected to vary as the square root of an average interatomic force constant and inversely as the square root of the atomic

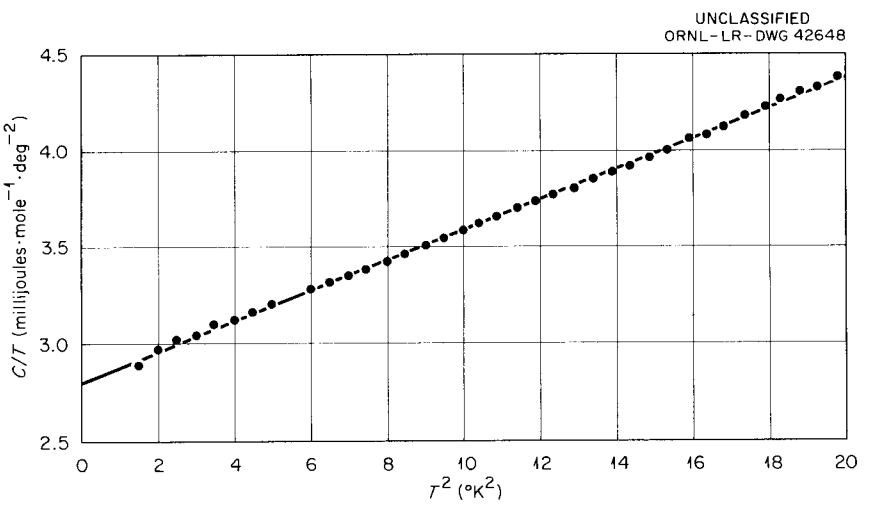

Fig. 1.12. Specific Heat of Zirconium (α-1) from 1.1 to 4.5°K.

Table 1.4. Low-Temperature Specific Heats of the Group IVA Metals

	γ (millijoules · mole^{-1} · deg^{-2})	θ_D (°K)	Reference
Titanium	3.329 ± 0.014	420.3 ± 6.3	This work
	3.35	280	Estermann[b]
	3.56	430	Wolcott[c]
Zirconium			
Zr α1	2.798 ± 0.012	291.1 ± 1.2	This work
Zr α'	2.806 ± 0.014	290.4 ± 1.5	This work
Zr 0 In[a]	2.827 ± 0.014	292.6 ± 1.5	This work
Zr α2	2.804 ± 0.012	291.3 ± 1.2	This work
	2.90	265	Estermann[b]
	3.03	310	Wolcott[c]
Hafnium	2.169 ± 0.013	251.3 ± 0.8	This work
	2.64	261	Wolcott[c]

[a]Control for indium system.

[b]I. Estermann, S. H. Friedberg, and J. E. Goldman, Phys. Rev. 87, 582 (1952).

[c]N. M. Wolcott, Conférence de Physique des Basses Températures, Paris, Sept. 2–8, 1955, p 286, Centre National de la Recherche Scientifique, and UNESCO, Paris, 1956.

mass, on the basis of a central-force model of lattice vibrations. The Debye temperatures of titanium and zirconium are very nearly inversely proportional to the ratio of the atomic masses to the one-half power, so that the force constants must be approximately equal for these two metals. The Debye temperature of hafnium, however, is considerably higher than its atomic weight would indicate, and, thus, the force constant for hafnium

Table 1.5. Low-Temperature Specific Heats of Zirconium–Indium Alloys

Indium Content (at. %)	Structure	γ (millijoules · mole^{-1} · deg^{-2})	θ_D (°K)
1.79	α	2.858 ± 0.012	289.3 ± 1.1
3.65	α	2.956 ± 0.015	287.7 ± 1.5
5.33	α	3.090 ± 0.015	286.8 ± 1.5
8.19	α	3.243 ± 0.014	284.5 ± 1.2
8.19	α'	3.223 ± 0.024	284.1 ± 2.2
9.40	α'	3.271 ± 0.015	283.4 ± 1.4
11.26	α'	3.319 ± 0.017	282.6 ± 1.6

Table 1.6. Low-Temperature Specific Heats of Zirconium–Tin Alloys

Tin Content (at. %)	Structure	γ (millijoules · mole^{-1} · deg^{-2})	θ_D (°K)
1.60	α	2.952 ± 0.019	290.6 ± 1.9
3.09	α	3.043 ± 0.015	287.5 ± 1.3
4.58	α	3.152 ± 0.015	282.6 ± 1.4
6.11	α'	3.242 ± 0.023	278.2 ± 1.9
7.60	α'	3.329 ± 0.018	277.5 ± 1.5
9.06	α'	3.376 ± 0.035	275.3 ± 2.7

must be approximately 50% larger than those of the other two group IVA metals. Table 1.4 also shows that there is no significant difference in either the electronic specific heats or the Debye temperatures for the different zirconium samples, indicating that small variations in the amounts of impurities do not affect these measurements and that, from the standpoint of the electronic and vibrational specific heats, the metastable α' and the equilibrium α structures are equivalent.

For alloys, Friedel[28] has shown that in the first-order approximation where the perturbing potential is localized around the impurity, the electronic energy band is shifted without change in shape. Furthermore, for low concentrations of solute the Fermi level is unchanged, since the potential field of the impurity is screened at small distances by a local heaping up of charge from the conduction band. The density of states, however, is changed, and if the conduction band is assumed to be parabolic, the change in the density of states upon alloying is the same as that computed from the rigid band model. Where that is assumed, the Fermi level shifts with the change in electron-to-atom ratio. If the usual chemical valences of 3 for indium and 4 for tin and zirconium are chosen, then either of the theories predicts that the addition of tin to zirconium would leave the electron concentration and the density of states unchanged, and thus the electronic coefficient of the specific heat would not be altered by the addition of tin to zirconium. Furthermore, the addition of indium to zirconium would decrease the electron concentration and hence the electronic specific heat. Figure 1.13 shows that the observed electronic specific heats do not behave in this manner at all. It has been suggested that zirconium is divalent in the metallic state, from the study of various alloying elements on the allotropic transformation of zirconium.[29] The observed electronic specific heats are in much better agreement with this hypothesis, the effect of tin being nearly twice that of indium. In order to make the observed densities of states coincide for a given electron-to-atom ratio, it is necessary to choose a valency of 1.5 for zirconium, and the experimental densities of states are plotted on this basis in Fig. 1.14. The

---

[28] J. Friedel, Advances in Physics, vol 3, p 465, Taylor and Francis, London, 1954.

[29] J. O. Betterton, Jr., and J. H. Frye, Jr., Acta Met. 6, 205 (1958).

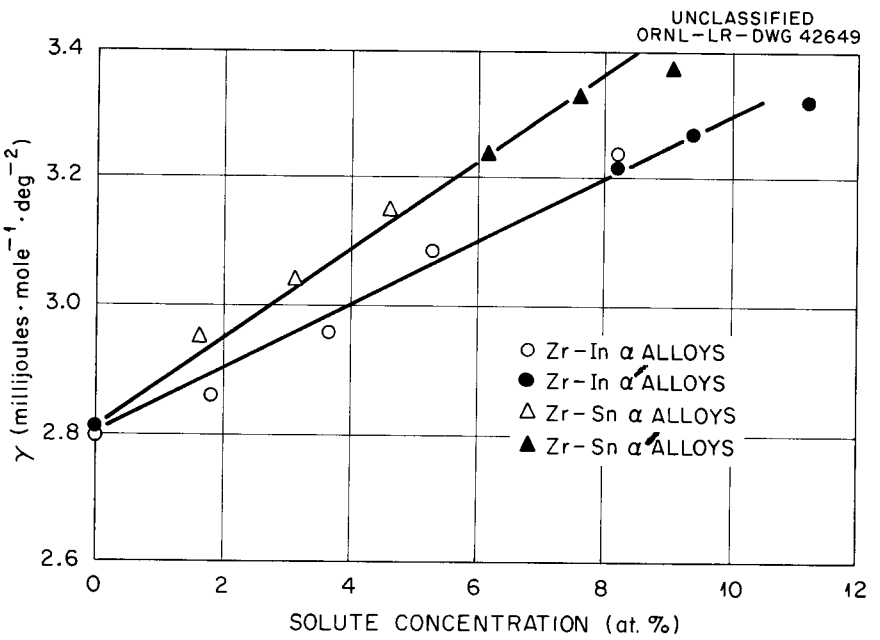

Fig. 1.13. The Electronic Specific Heat Coefficient of Zirconium-Indium and Zirconium-Tin Alloys as a Function of Concentration.

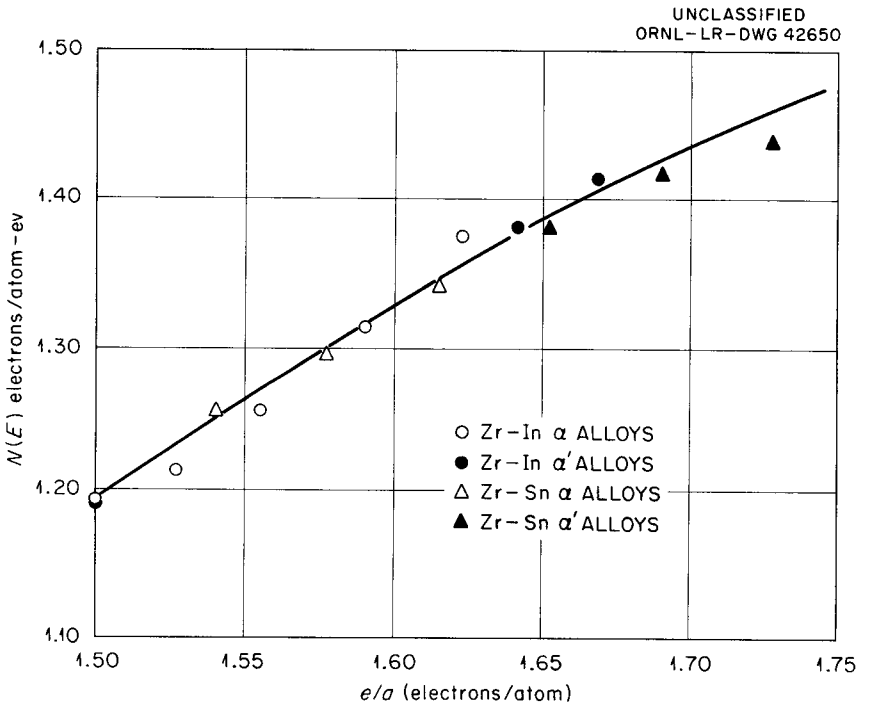

Fig. 1.14. Density of States in Zirconium Alloys as a Function of Electron-to-Atom Ratio.

solid line in the figure has been computed on the basis of a parabolic conduction band with a value of 2.50 for the effective mass. The band structure of zirconium then could be imagined to consist of a narrow bound d-band containing 2 to 2.5 electrons/atom and a conduction band consisting of a broad s band overlapping a partially filled d band. A similar band structure has been proposed for titanium by Denney.[30]

The Debye temperatures of the same series of alloys are shown in Fig. 1.15 plotted in the same manner. Unfortunately, the scatter is much larger than for the density of states, but the experimental values show a definite correlation with the electron concentration indicating the importance of the electronic energies in determining the elastic properties and hence the vibrational specific heat of the zirconium alloys.

---

[30]J. M. Denney, Electron Effects in Solid Solution Alloys of Titanium, Sixth Technical Report, ONR-N6onr-24430, Project NR 031-355, Calif. Inst. of Tech., Pasadena, Calif. (1955).

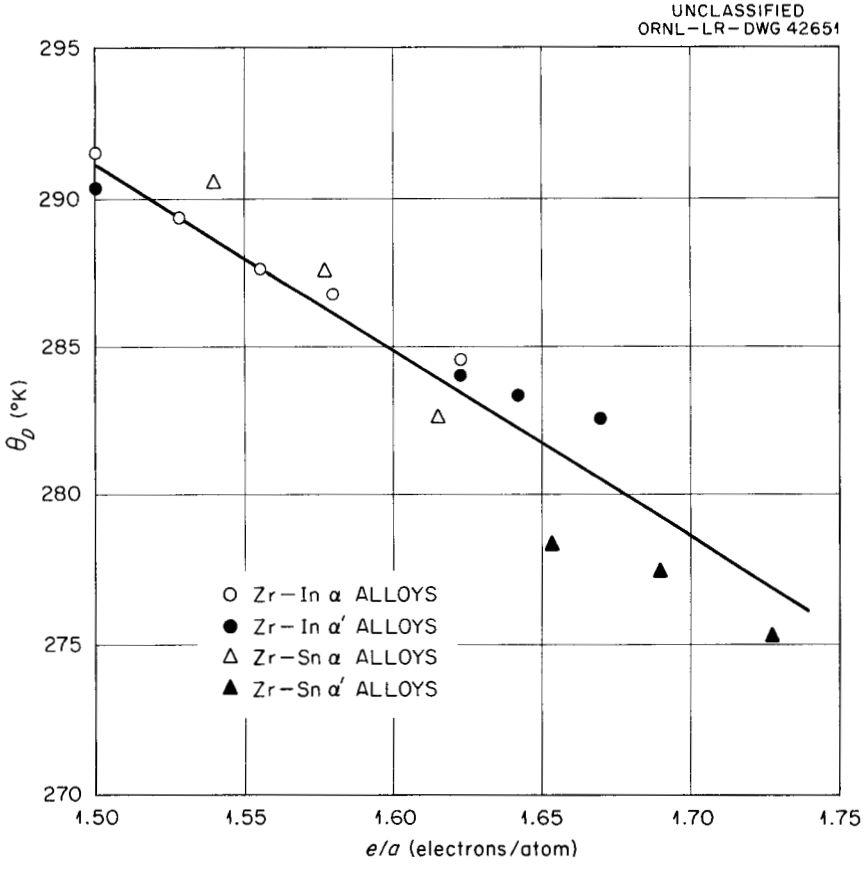

Fig. 1.15. Debye Temperatures of Zirconium Alloys as a Function of Electron Concentration.

Other interpretations of these results can of course be given, and the valence of zirconium as the solvent in metallic solutions cannot be precisely established in view of the possibility of incomplete ionization of the solvents. The extension of the measurements to the zirconium-silver and zirconium-cadmium alloy systems should provide valuable information about the electronic structures of zirconium.

Constitution of Zirconium-Gallium

J. O. Betterton, Jr. D. S. Easton

A study of the zirconium-gallium system was made to extend the knowledge of the effects of B-subgroup solutes on the allotropic transition temperature of zirconium to a new element. Previous investigations of these alloys had been made in the intermediate phase region by Wallbaum,[31] who found a $ZrGa_3$ phase of tetragonal structure ($TiAl_3$ type), and by Anderko,[32] who reported a peritectically formed Zr_5Ga_3 phase with a hexagonal $D8_8$ structure (Mn_5Si_3 type) and a probable phase, Zr_3Ga, of unknown structure. A preliminary account of the present work on the zirconium-rich portion of the system was given previously.[33]

This work has been continued and the new results are shown in the form of a partial phase diagram in Fig. 1.16. The experimental methods and the purity of the metals are similar to those used in the zirconium-silver investigation.[34] In order to illustrate the sensitive indication of the solid solubility limit which was obtained during quenching experiments with these alloys, a typical ($\beta + \gamma$) microstructure is shown in Fig. 1.17. The rectangular crystals are the Zr_3Ga phase formed in a body-centered cubic zirconium matrix which has exceeded the solubility limit by 0.6% Ga. The β matrix transforms to the α form upon cooling, with a typical transformation pattern.

---

[31] H. J. Wallbaum, Z. Metallk. 34, 118 (1942).

[32] K. Anderko, Z. Metallk. 49, 165 (1958).

[33] Met. Ann. Prog. Rep. Oct. 10, 1958, ORNL-2632, p 17 (classified).

[34] J. O. Betterton, Jr., and D. S. Easton, Trans. Met. Soc. AIME 212, 470 (1958).

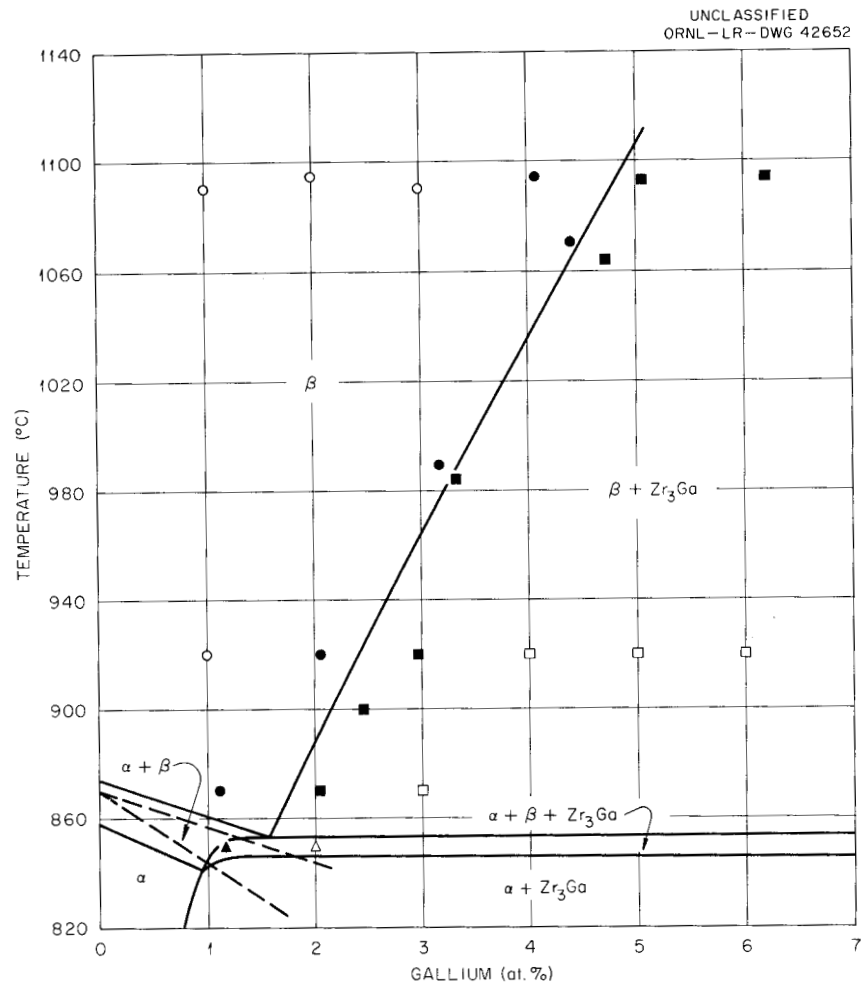

Fig. 1.16. Constitution of Zirconium-Gallium in the Region 0 to 7 at. % Ga. Dotted lines are calculations assuming 15% size factor.

Two significant features of this partial zirconium-gallium phase diagram are the eutectoid decomposition of the β phase and the restricted solid solubility of the terminal zirconium phases. Trivalent and tetravalent solutes which previously depressed the allotropic transition temperature of a group IVA element have always been associated with a large size factor. Since the detailed phase boundaries of the (α + β) region have not been established, α/β phase boundaries have been calculated as shown by the dotted lines on Fig. 1.16 by using average α/β boundary parameters[29] for a trivalent solute and a size factor of 15%. The approximate size factor indicated in this way agrees fairly well with the size of the gallium atom obtained by an average of the interatomic distances of the seven nearest neighbors in the irregular gallium structure. The unfavorable size ratio

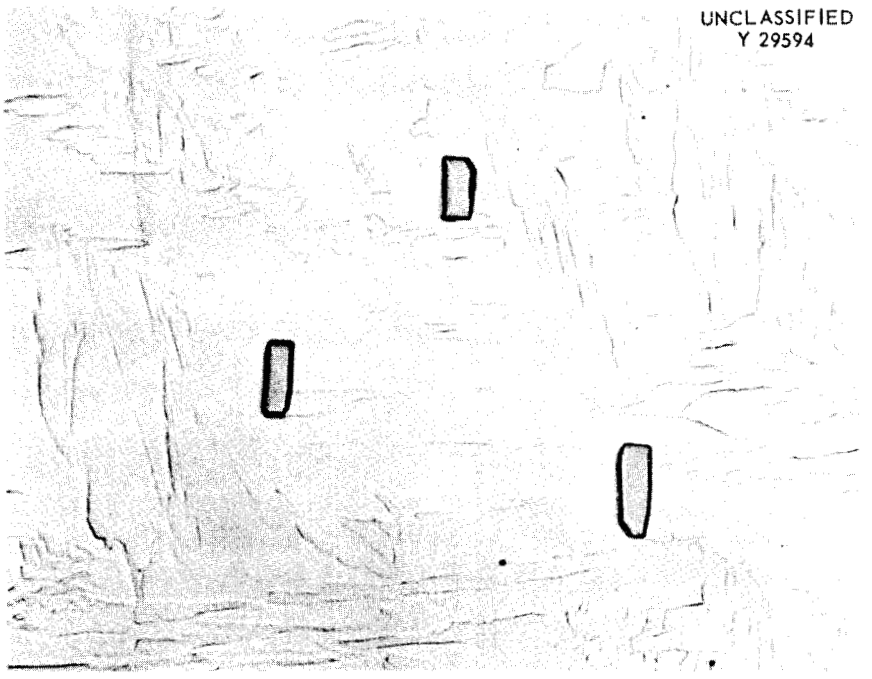

Fig. 1.17. Zirconium–2.4% Gallium Alloy with a ($\beta + \gamma$) Microstructure After Quenching from 900°C. Etchant mixture: 50 ml conc HNO_3, 30 ml H_2O, and 3 ml conc HF. 500X.

for zirconium-gallium is also implied by the restricted β-phase solid solubility, which is only one-third that of aluminum or indium, and by the rapid hardening effect[33] of gallium in zirconium.

Unusually large values of the constants a, b occur when the β solid-solubility limit is plotted as $x_\beta = \exp(a - b/T)$. When solid solutions obey Henry's law, a and b are proportional to the partial molal excess entropy and heat of the solute in the β phase relative to the partial molal entropy and heat of the solute in the intermediate phase. In terms of Zener's theory, a solute with a large size-factor lattice strain would be expected to have a large positive entropy contribution.[35] The constants from zirconium-gallium are compared with other zirconium systems in Fig. 1.18. Increase of the constants a, b corresponds to greater valency difference and to greater size difference in an interesting way, although, of course, there is no way to know the degree of deviation from Henry's law in each of these systems.

---

[35]C. Zener, Acta Cryst. 2, 163 (1949).

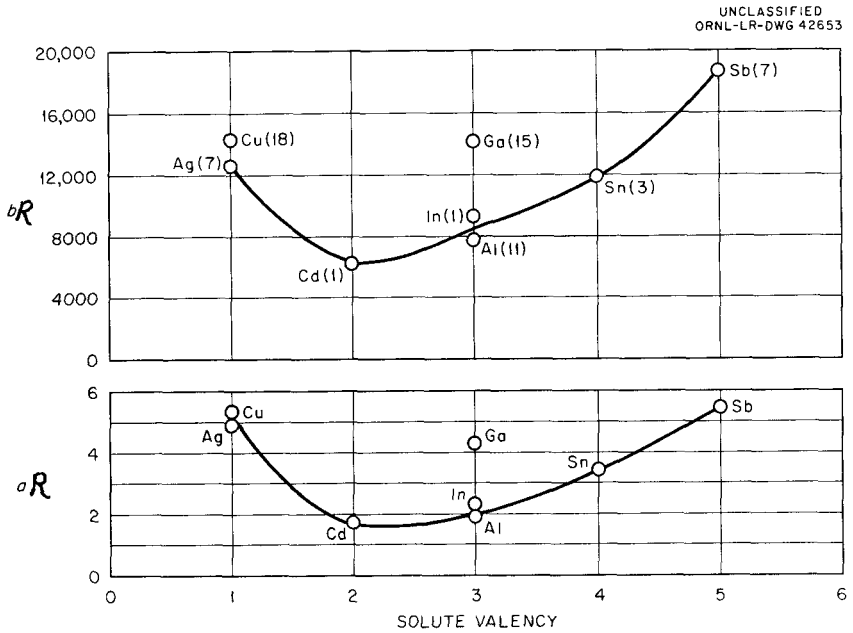

Fig. 1.18. The Coefficients from the $\beta/(\beta + \gamma)$ Phase Boundaries of Various Zirconium Systems when Plotted in the Form: exp [a − (b/T)]. The numbers inserted are atomic size factors. The cadmium-zirconium data are for the $\alpha/(\alpha + \gamma)$ boundary.

A microscopical examination was made of alloys containing 25, 29, 33.2, and 37.5% Ga in the cast condition. Between 25 and 33.2 at. % Ga, the alloys appeared as primary crystals of Zr_5Ga_3 surrounded by a eutectic. The proportions of the phases in these and earlier alloys indicate the eutectic reaction, liquid (~21% Ga) $\rightleftharpoons$ β (~8%) + Zr_5Ga_3. The 37.5% alloy contained primary crystals of a third phase, a small amount of eutectic, and a matrix of Zr_5Ga_3. The volume percentage of the primary phase would place its composition near 50% Ga. This information and that obtained earlier are summarized in the form of a hypothetical phase diagram in Fig. 1.19, and since no temperatures were determined, the temperature scale has not been specified.

The zirconium-gallium intermediate phases were very hard and brittle. The Vickers hardness values were as high as 657 on the 37.5% alloy, and the samples were easily crushed in a mortar.

Vapor Pressures and Constitution of Zirconium-Cadmium

J. O. Betterton, Jr. D. S. Easton

The zirconium-cadmium system is important in the study of group IVA element alloys as it represents a case of small valency and size-factor

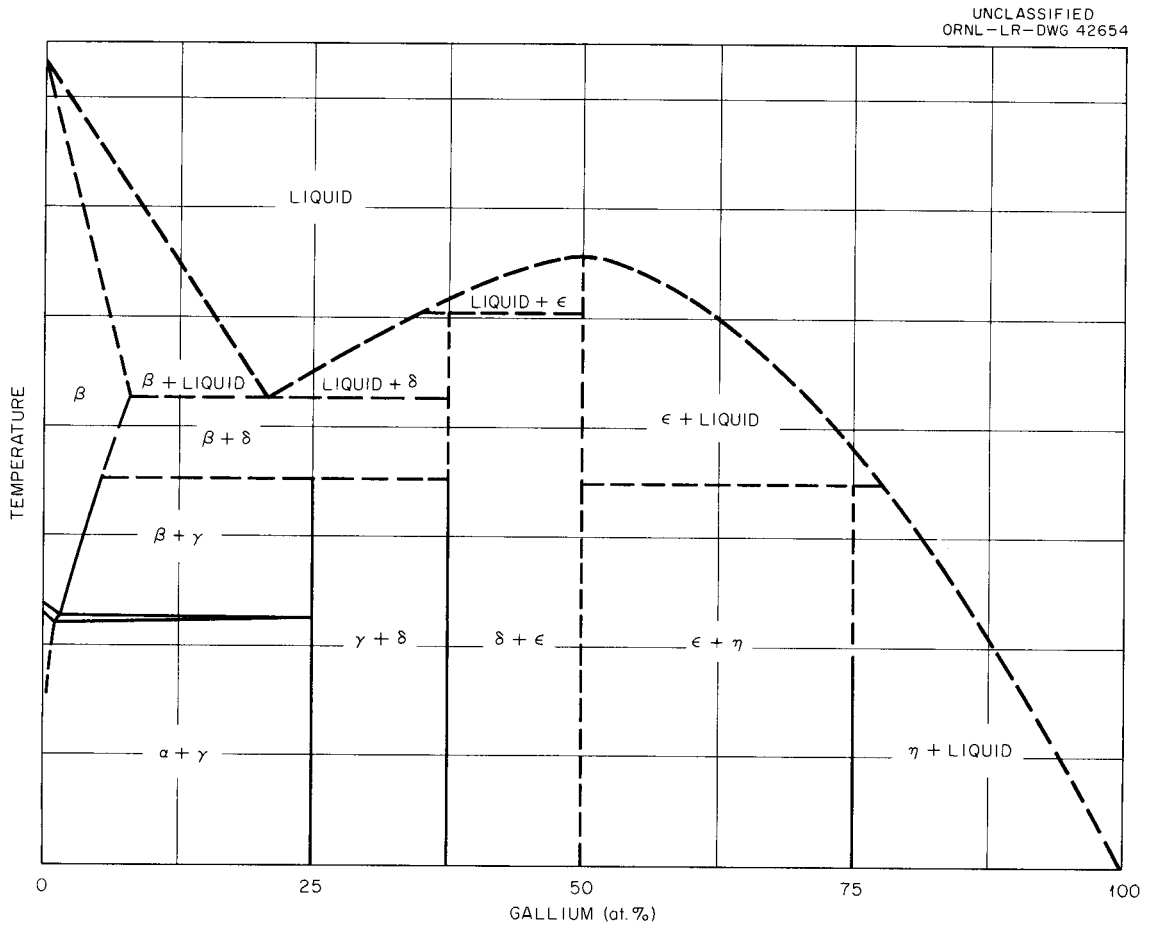

Fig. 1.19. Hypothetical Phase Diagram of the Zirconium-Gallium System.

change. This assumes that the numbers of d-type electrons, two in zirconium and ten in cadmium, are of little importance in determining the free energies of the alloys. The first test of this idea was an investigation of the effect of cadmium on the α/β transition.

The zirconium-rich part of the zirconium-cadmium phase diagram is shown in Fig. 1.20, and as reported earlier,[36] the α/β transition temperature rises only gradually. This indicated that cadmium affected the relative free energies of the two phases only slightly, in agreement with the absence of valency change. As shown in Fig. 1.20, a new determination of the $\alpha/(\alpha + \gamma)$ boundary by the quenching method has revealed recently a solubility as high as 17% Cd in the α phase. This solubility decreases with

[36]Met. Ann. Prog. Rep. Oct. 10, 1958, ORNL-2632, p 19 (classified).

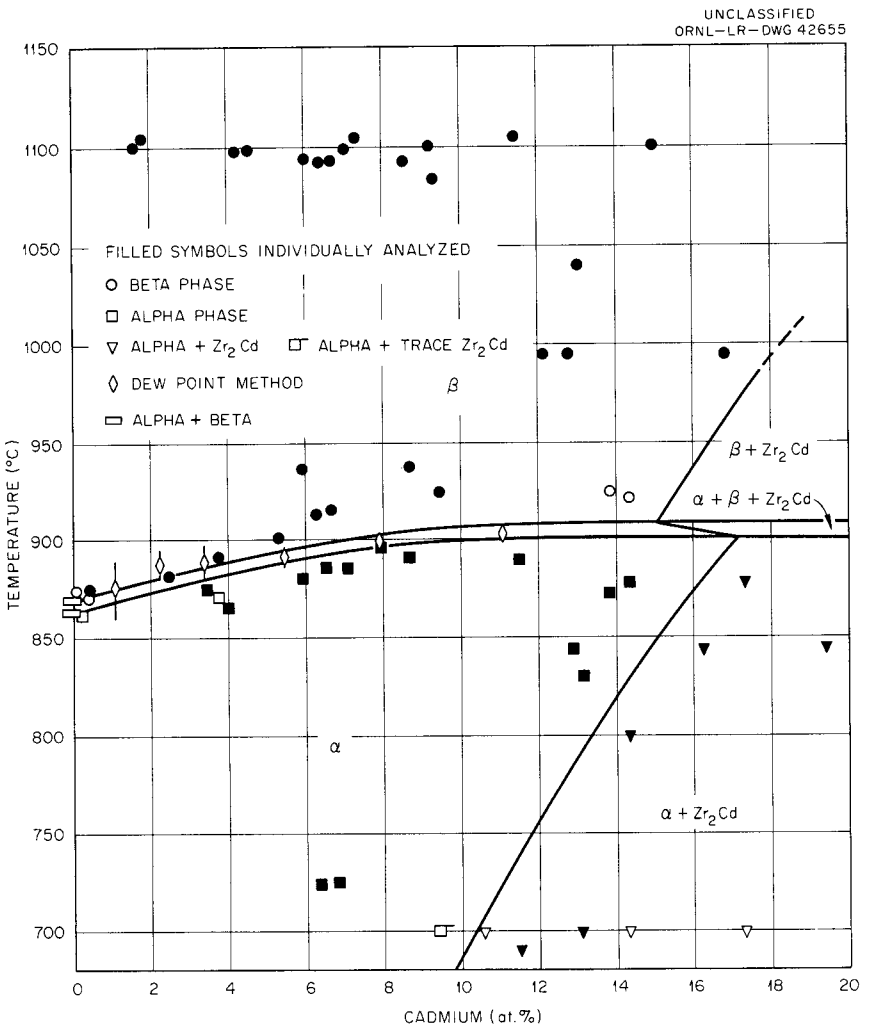

Fig. 1.20. Zirconium-Rich Region of the Zirconium-Cadmium Phase Diagram.

temperature to approximately 9% Cd at 700°C. The position and curvature of the boundary when plotted in the form, exp (a + b/T), reveal low values of the constants a and b when compared with the other zirconium systems in Fig. 1.18. The significance of this should become evident when the thermodynamic properties of this system have been more completely measured. The techniques for the preparation of cadmium-zirconium alloys of precise composition are just now becoming satisfactory. The preparation is done in the β region at constant cadmium pressures of 1 to 2 atm provided by an isothermal liquid bath of pure cadmium. Depletion is prevented at intermediate temperatures 890 to 1000°C by similar isothermal baths. It is hoped in this way to determine more completely the boundaries of the α and β phases. A

typical homogeneous α alloy containing a substantial amount of cadmium is illustrated in Fig. 1.21. Microstructures of $(\alpha + \gamma)$ alloys that contained a very characteristic Widmanstätten structure are illustrated in Fig. 1.22. Platelets of Zr_2Cd form on the basal plane of the hexagonal α phase in the same manner as was previously observed in the $\alpha + \gamma$ alloys of the zirconium-indium system. The elongated crosses which are shown on the phase diagram represent the position of the $(\alpha + \beta)$ region as indicated by the vapor-pressure measurements.

A second test which has been made with zirconium-cadmium alloys is a measurement of the axial ratios of α-zirconium with additions of cadmium. Axial ratios of hexagonal phases have been shown to depend upon the number of electrons in the conduction band of hexagonal brasses,[37] in magnesium alloys,[38] and in titanium alloys.[30] The theory of the effect is that a

---

[37]H. Jones, Proc. Roy. Soc., (London) A147, 396 (1934).

[38]H. Jones, Phil. Mag. 41, 663 (1950); W. Hume-Rothery and G. V. Raynor, Proc. Roy. Soc. (London) A177, 27 (1940); D. Hardie, R. N. Parkins, Phil. Mag. 4, 815 (1959).

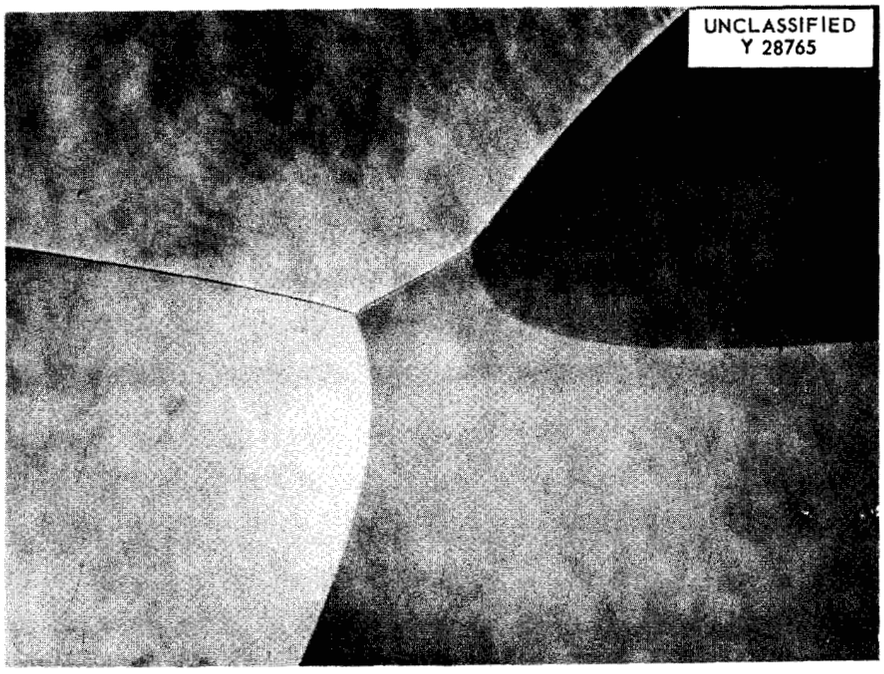

Fig. 1.21. Zirconium Alloy Containing 12.9 at. % Cadmium After Annealing 33 Days at 845°C.

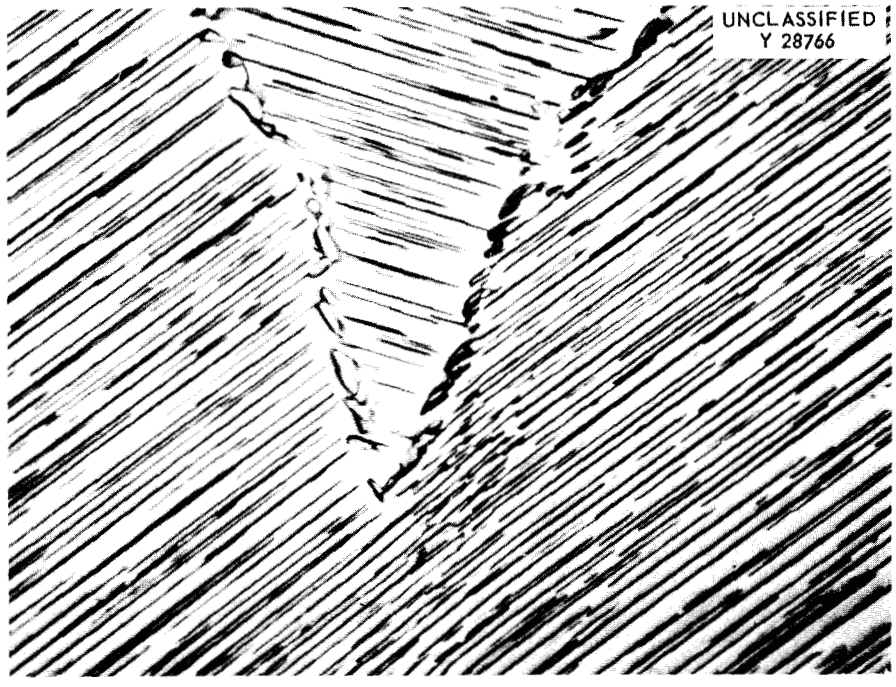

Fig. 1.22. Typical Laminar Widmanstätten Structure of the $\alpha/(\alpha+\gamma)$ Alloys.

minimization of the Fermi energy can be obtained by allowing axial ratios to deviate from the ideal value when the Fermi surface is near or has just overlapped a Brillouin zone.[37,38] Since the axial ratio corresponding to the minimum energy would be expected to be dependent on the degree of the filling of the zone, the axial ratio varies with the electron concentration of the alloy. In earlier discussion,[30,39] it was believed that the effects of Ag, Al, Ga, and Sn in Ti and of Ag, In, and Sn in Zr were fairly well interpreted in this way, although the argument was never completely satisfactory. That was because a different overlap, {100}, had to be assumed to account for the effect of silver rather than the {002} overlap, which was assumed to account for the effects of the other solutes. Recently Debye-Scherrer measurements with alpha phase alloys of zirconium-cadmium show that the electron-concentration relationship is incorrect. The increase in axial ratio with cadmium is approximately equal to that of indium, whereas with valencies Ag 1, Cd 2, Zr 2, In 3, and Sn 4, cadmium should not change the axial ratio. The data are plotted in Fig. 1.23 with earlier data[39] from the Zr-Ag, Zr-In, and Zr-Sn systems. It is thus probable that the strongly

[39] Met. Semiann. Prog. Rep. Apr. 10, 1956, ORNL-2080, p 228 (classified).

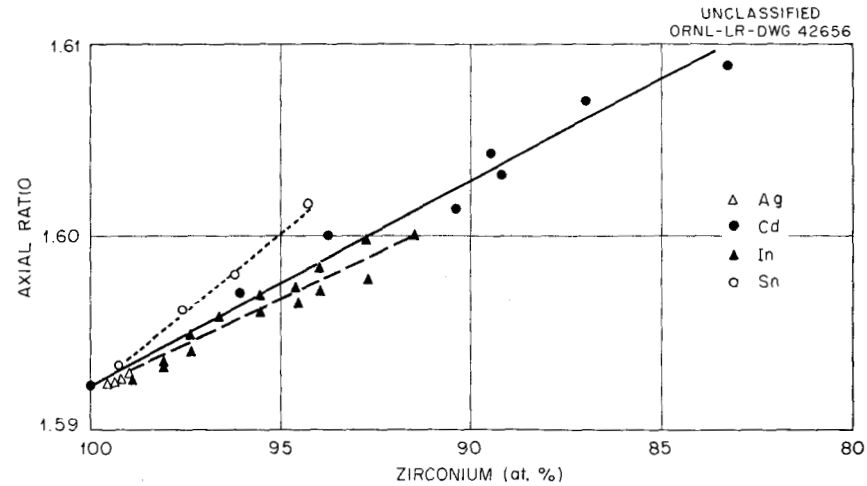

Fig. 1.23. Axial Ratios of α-Zirconium Alloys at Room Temperature, Plotted as a Function of Zirconium Content.

interacting S-type electron bands which are believed responsible for allotropic transactions are not so effective in determining the axial ratio of α-zirconium, possibly because of a simultaneous competition in the {100} and {002} overlaps. The deviation of group IVA elements from ideal packing may instead be a d-electron effect arising from weakly interacting electrons in these metals. This effect would be proportional to the zirconium concentration in the alloys where alloying is done with solutes which have no d-electrons or in which the d-shell is filled. Data which are available are plotted against zirconium composition in Fig. 1.23. The accuracy of the measurements is still not sufficient to make certain the correctness of the relationship. It is of interest to note that the axial ratios of the hexagonal elements scandium and yttrium are also depressed (1.585 and 1.588, respectively)[40] so that any simple dependence on d-electron number would require similar numbers of these electrons in the metallic state of these group IIIA and the IVA elements.

A third test of absence of valency and size effects in the cadmium-zirconium alloys was a determination of the thermodynamic properties by measurement of cadmium vapor pressures. This serves the additional purpose of providing information on whether the phase diagrams of this type depend

---

[40]W. Hume-Rothery and G. Raynor, The Structure of Metals and Alloys, p 88, Institute of Metals, London, 1956.

upon thermal entropies or upon the energies of the phases at low temperature. The relationship between composition, pressure, and temperature is also essential to the preparation of cadmium-zirconium alloys for other purposes.

As indicated earlier,[36] a series of experiments has been started, using a dewpoint method. Since many of the details of this investigation were discussed before, the present discussion will be limited to new points on the pressure curves. These data are shown in Fig. 1.24, where the quantity RT $\ln$ P, with P as the cadmium pressure in millimeters of mercury, is plotted against temperatures. The dashed lines through the center of this figure represent the $(\alpha + \beta)$ region as taken from Fig. 1.20. Aside from this, the data on Fig. 1.24 are entirely within the homogeneous β region at higher temperatures and the homogeneous α region at lower temperatures. The positions of the curves represent the partial molar free energies of the cadmium in the alloys, with the assumption that the gas phase is ideal and monatomic over this pressure and temperature range. The slope of the curves represents the partial molar entropy of the cadmium in the alloy relative to pure cadmium gas at 1 mm Hg. Partial molar enthalpies relative

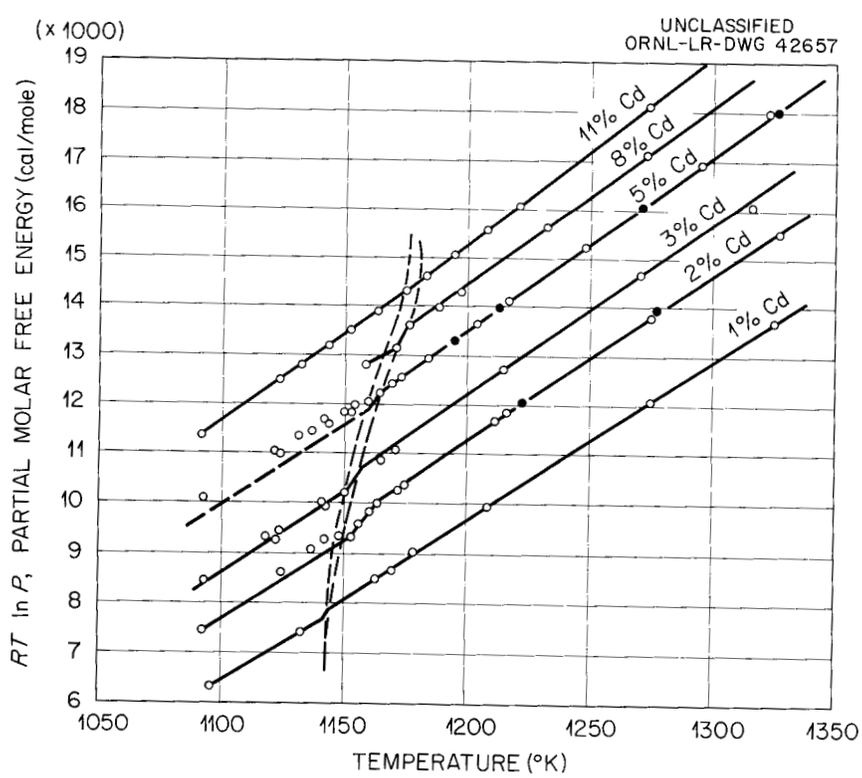

Fig. 1.24. Free Energies of Zirconium-Cadmium Alloys as a Function of Temperature.

to the gas are indicated by the intercepts on the vertical axis at zero temperature. Preliminary data taken with the alloys containing 2 and 5 at. % cadmium were not held for sufficient time during the cooling cycle of these experiments, and some of the points lie above the curves because of nonequilibrium concentration of cadmium on the surface of the foil. These experiments are being repeated, and some of the new data are indicated by filled symbols on Fig. 1.24.

In zirconium-rich alloys, the vertical position of RT $\ln$ P curves corresponds approximately to the first derivative of the integral free energy of the alloy. Thus, to account for the initial elevation of the α/β boundaries with cadmium in Fig. 1.20, the free energy should be increasing less rapidly in the α phase than in the β phase, and the pressures should be lower in the α phase than in the β phase. This condition is fairly well satisfied, as shown in Fig. 1.24, aside from the 5% alloy which is not thought to be in equilibrium until the 11% alloy is reached. Here, as can be seen on both Figs. 1.20 and 1.24, the α/β boundaries have actually stopped rising near this composition.

Examination of Fig. 1.24 will show that the free energies are decreasing very rapidly with lower cadmium contents. In order to put the data in a form convenient for integration and for comparison to the entropy expected from random mixing, it is customary to express the data as the excess quantities defined below:

$$F_1^{E\beta} = \frac{\partial F^\beta}{\partial n_1} - F_\beta^0 - RT \ln X_{1\beta} ,$$

$$H_1^{M\beta} = \frac{\partial H^\beta}{\partial n_1} - H_\beta^0 ,$$

$$S_1^{E\beta} = \frac{\partial S^\beta}{\partial n_1} - S_\beta^0 + R \ln X_{1\beta} .$$

Here the subscript 1 refers to cadmium; n is a mole; and $X_{1\beta}$ is the mole fraction of cadmium in phase β; F_β^0, H_β^0, and S_β^0 refer to solid, pure cadmium in a body-centered cubic form. Since cadmium does not exist in this form, the terms of the type $(H_\beta^0 - H_\alpha^0)$ have to be estimated theoretically. In the

present discussion these terms have been neglected. It may be seen in the above formulas that effects as large as 500 cal/mole or of fractions of a cal·mole^{-1}·deg^{-1} may appear in the resulting partial excess quantities. Where differences between the α and β phases are of interest, this is of less importance. The excess quantities in this discussion will be calculated by subtracting first the quantity RT $\ln P^0$ from the RT $\ln P$, where P^0 is the pressure of pure, solid cadmium, and then subtracting the quantity RT $\ln X_{1\beta}$. The resulting relative partial molal excess free energy is plotted against temperature in Fig. 1.25.

The data are reduced to a much narrower range of values and the singularity at $X_{1\beta} = 0$ appears to be removed. This condensation has frequently been found when excess free energies are used in other alloy systems. The experiments now indicate, within the limitations of about ± 100 cal/mole, that the β phase alloys obey Henry's law. This law states that the activity of the solution is proportional to the composition and, hence, the excess free energy, RT $\ln \gamma_{1\beta}$, is independent of composition. Integration to integral free energies $F^{E\beta} = X_1 F_1^{E\beta} + (1 - X_1) F_2^{E\beta}$ is simple, since Henry's law in the solute implies Raoult's law in the solvent,[41] so $F_2^{E\beta}$ for the zirconium vanishes. The scatter about this curve depends upon the accuracy of the synthetic compositions used since RT $\ln X_{1\beta}$ changes rapidly with

[41] L. S. Darken and R. W. Gurry, Physical Chemistry of Metals, p 260, McGraw-Hill, New York, 1953.

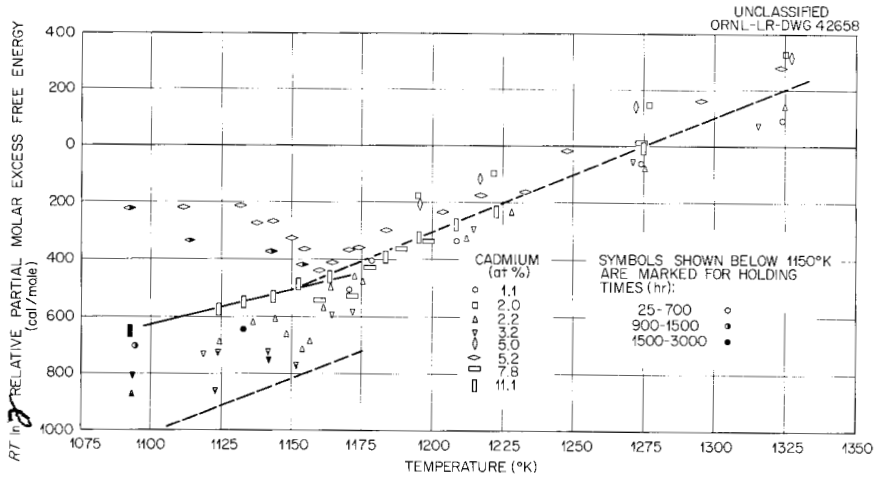

Fig. 1.25. Excess Free Energies of Zirconium-Cadmium Alloys.

See Mater

composition. If the composition of an alloy specimen is slightly enriched or depleted of cadmium on the surface, the data deviate widely. This is believed to account for the upward scatter of the 5.2% alloy in the α region in the left side of Fig. 1.25. During cooling into the α region, this alloy was held for 50 to 250 hr at each temperature, whereas present alloys are found to reach equilibrium in the α region only after 600 to 2700 hr, the shorter time applying only to the 11% alloy which was found to have a faster diffusion rate than the more dilute alloys.

When the results of the 5% alloy in the α region are omitted, the average excess free energies of the cadmium in the α are somewhat lower and with smaller slope than those of the β phase. The scatter in the data obscures the effect of composition in this region, but a gradual rise in RT $\ln \gamma_\alpha$ is thought to exist for the following reasons. The activities of the cadmium at a given temperature are equal on both boundaries of the $(\alpha + \beta)$ region. Since $a_{1\alpha} = \gamma_{1\alpha} X_{1\alpha}$, RT $\ln \gamma_{1\alpha}$ = RT $\ln X_{1\beta}/X_{1\alpha}$ + RT $\ln \gamma_{1\beta}$. If the α/β phase boundaries in Fig. 1.20 are represented by two straight lines intersecting at pure zirconium, then RT $\ln X_{1\beta}/X_{1\alpha}$ = AT, where A is a constant. The β phase follows Henry's law; so RT $\ln \gamma_{1\beta}$ is a function of T, - 5217 + 4.091T. It follows that RT $\ln \gamma^*_{1\alpha}$ is also a function of temperature only, where the asterisk has been introduced to indicate along the phase boundary only. In order to evaluate RT $\ln \gamma^*_{1\alpha}$ = AT - 5217 + 4.091T, it is necessary to know only the constant A. The width of the $(\alpha + \beta)$ region can be found by expanding the exponentials in α/β phase boundary relations[29] under conditions corresponding to Henry's law with the result that

$$X^*_{1\alpha} - X_{1\beta} \cong \frac{\Delta S^0}{R} \quad (1 - T_0/T) \ .$$

Using the values $\Delta S^0/R = 0.405$, $T_0 = 1143.2°K$, and $T = 1173.2°K$, the phase boundary width is found to be 0.010. Taking the experimental value of $X_{1\beta} = 0.07$, the value of A is -0.265 cal•mole^{-1}•deg^{-1}, and RT $\ln \gamma^*_{1\alpha}$ = -5217 + 3.83T.[42] The assumption of Henry's law in the alpha phase extends this

---

[42]The calculation of the free energy of the α Zr-Cd alloys by Henry's law and two straight lines for the $(\alpha + \beta)$ region was suggested to us by J. L. Gregg.

expression to compositions away from the phase boundary. This limiting relation is drawn as a dashed line below the experimental data on Fig. 1.25. The experimental points lie above this line and, in the 11.2% Cd alloy, in which we have considerable confidence because of more rapid diffusion, the excess energies have reached equality with the α phase at the same composition. Thus, a deviation from Henry's law is probable in the α phase even at a cadmium content of 1%, and RT $\ln \gamma_{1\gamma}$ appears to rise with composition until the point is reached where the activities of the α phase are equal to those of the β phase.

It is worthwhile to consider briefly the meaning of these effects. Since Henry's law is obeyed in the β phases over a range of temperatures, the integral excess free energy, heat of formation, and excess entropy of formation will all be linear in X. This is likely to only occur under two conditions: (1) where the alloys are so dilute that Cd-Cd interactions do not occur, and (2) where Zr-Cd and Cd-Cd interactions are the same. This, of course, is what one might hope to obtain in Cd-Zr on the basis of the small valency and size effects in this system. This is not true at all temperatures, however, since a small deviation from Henry's law occurs in the α phase and because of the existence of a significant and constant negative deviation from ideal mixing entropy in the β phase.

The slopes of the curves in Fig. 1.25 are $-S_1^E$ or the excess of the relative partial molal entropy of the cadmium in the alloy phase less the partial molal entropy from ideal mixing. In the β region from 1 to 11% Cd, this slope is within the accuracy of the data represented by one value, $S_1^{E\beta} = -4.09$ cal·mole^{-1}·deg^{-1}. A similar constancy of the entropy deviation has been found also in α-brass in the Cu-Zn system over the range 10 to 38% Zn (ref 43). The intersection of the excess free-energy curve with the vertical axis at zero temperature is the relative partial molal heat of mixing, 5200 cal/mole for the β phase. By integration, it can be seen that 0.9 mole zirconium and 0.1 mole cadmium would combine with the heat evolution of 520 cal. This is of the same order of magnitude as the heat of formation in systems such as Au-Ag or Au-Cu.[43]

---

[43] R. Hultgren, Selected Values of Thermodynamic Properties of Alloys, University of California, 1956.

In the α-phase region, the excess entropies from the various alloys range from -2.8 cal·mole^{-1}·deg^{-1} for 11% Cd to -1.2 cal·mole^{-1}·deg^{-1} for 3.2% Cd. The time required for equilibrium has not been fully established for the α region, although it is clear that some of the experiments for the 2.2% alloy and, apparently, all of the experiments for the 5.2% alloy were held for insufficient time during the cooling cycle. Annealing times in the 1500 to 3000 hr range are now being used. For the present, based on the alloys held for long periods, the tentative conclusion can be drawn that $S_1^{E\alpha}$ is greater than $S_1^{E\beta}$. If this is true, the α phase with a higher partial molal entropy would be stablized relative to the β phase as cadmium is added. This could account for the gradual rise in the Cd-Zr α/β boundaries, since only 1/4 cal·mole^{-1}·deg^{-1} higher entropy in the α phase would give a phase diagram parameter, in agreement with the initial portion of the α/β boundaries.

The constancy of the relative partial molal excess entropy of cadmium in the β phase has been discussed earlier[36] and the suggestion was made that is was of thermal rather than configuration origin. T. Usui, of the University of Tokyo, was consulted on the variation of excess entropy with composition which would be expected from short-range order. He offered the opinion that the effect of short-range order would be given by the approximate formula

$$-S + S^{ideal} \cong K\ N\ (\frac{Z}{2})\ \sigma^2 X^2,$$

where Z is the number of nearest neighbors, X is the atomic concentration, and σ is the short-range order assumed here independent of X. This expression is certainly not linear in X and would support some other origin for the entropy deviation observed.

Cadmium-zirconium alloys are being prepared for specific heat investigations at low temperatures. One of the objects will be to compare the high-temperature pressure results with those extrapolated from lower temperatures assuming the Debye model. Here, other effects, such as those related to volume changes, are assumed to be equal to the linear expression of a heterogeneous mixture of the pure elements. Typical results, Table 1.7, calculated from the low-temperature specific heats of Zr-In and Cu-Zn show negative integral excess entropy of the same order of magnitude as that observed at high temperatures in Zr-Cd and Cu-Zn. Thus, it may be that the

Table 1.7. A Comparison of the Thermodynamic Properties Calculated from Low-Temperature Specific Heats with the Experimental Values at High Temperatures

Alloy	Temperature (°K)	F^E	H^M	S^E
			Calculated	
0.88 Zr-0.12 In	1000	428	56	-0.39
0.90 Cu-0.10 Zn	773	119	-8	-0.17
			Experimental	
0.90 Zr-0.10 Cd	1200	-30	-520	-0.41
0.90 Cu-0.10 Zn	773	-617	-745	-0.17

entropy deviations in the Zr-Cd β phase are of thermal origin and can be interpreted in terms of the long-wavelength part of the vibrational spectra revealed at low temperatures and the electronic specific heat.

The data shown in Table 1.7 for the low-temperature specific heats of the Cu-Zn alloy are from J. A. Rayne,[44] and the experimental data for the Cu-Zn alloy are from R. Hultgren.[43] The remaining information is from work done during this report period.

There is a good possibility that careful chemical analysis following the present experiments will reduce the scatter of the data in Fig. 1.25. At the same time, a comparison of the synthetic and the final composition will help determine if any systematic drift of composition occurred during the time of the experiment. Temperature-cycling processes have so far indicated no effect of this kind. If the data can be improved by chemical analysis, it may be possible to consider more seriously the tendency, or the absence of a tendency, for curvature to appear in the RT $\ln \gamma$ plots. Since the slope of these graphs is $-S_1^{E\beta}$, the second derivative is $-C_1^{M\beta}/T$, and the curves can be analyzed for the existence of alloying effects on specific heat at high temperatures. At present there is no definite indication of this effect.

[44] J. A. Rayne, Phys. Rev. 108, 22 (1957).

X-RAY DIFFRACTION

H. L. Yakel, Jr.
O. B. Cavin R. M. Steele

Routine Analyses

H. L. Yakel, Jr.
O. B. Cavin R. M. Steele

The Metallurgy X-Ray Laboratory has examined over 600 specimens submitted for routine analysis during the period of this report. Following is a brief description of several problems that have been given more extensive study.

In conjunction with C. E. Curtis of the Ceramics Group, a systematic examination of phase transitions and lattice parameters of the lanthanide sesquioxides has been completed. The results have been submitted for publication in the Journal of the American Ceramic Society.

The techniques developed by Jetter, McHargue, and Williams[45] for the measurement and representation of preferred orientation in rolled sheet have been applied to the problem of the establishment of optimum rolling schedules for Zircaloy-2. The results and interpretation of these measurements are described in another section of this report.[46] In the period of the report, 12 specimens have been studied completely by texture determinations about rolling, normal, and transverse directions.

Further measurements of the density of rhombohedral MoF_3, and improved chemical analysis, have confirmed the results tentatively reported last year.[47] Experiments suggest that the cubic material with ReO_3 type of structure examined by Gutmann and Jack[48] was actually an oxyfluoride of uncertain composition. This data has been submitted for publication in co-authorship with M. K. Wilkinson and D. E. LaValle.

---

[45] L. K. Jetter, C. J. McHargue, and R. O. Williams, J. Appl. Phys. 27, 368 (1956).

[46] M. L. Picklesimer, P. L. Rittenhouse, and R. L. Stephenson, Part II of this report.

[47] H. L. Yakel, Jr., et al., Met. Ann. Prog. Rep. Oct. 10, 1958, ORNL-2632, p 25 (classified).

[48] V. Gutmann and K. H. Jack, Acta Cryst. 4, 244 (1951).

Some other compounds of previously uncertain structure which have been examined at the request of the Physics Division include: $CrCl_2$, CrF_2, $TbH_{2.95}$, and a series of nitrides of the heavy lanthanide elements. The crystallographic data for the chromous halides are summarized in Fig. 1.26. The results for CrF_2 are in good agreement with those recently reported by Jack.[49] Note that both structures are derived from the rutile structure by distortions which produce four short and two long Cr-F bonds about each octahedrally coordinated chromous ion, as would be predicted by ligand field theory.[50] Terbium hydride ($TbH_{2.95}$) was found to have the hexagonal trihydride structure formed by lanthanides heavier than gadolinium[51] (SmH_3 also has this structure). Lattice parameters, $a_o = 3.70 \pm 0.02$ Å, $c_o = 6.60 \pm 0.03$ Å, $c_o/a_o = 1.78$, give an x-ray density (Z = 2 formula weights per

---

[49]K. H. Jack and R. Maitland, Proc. Chem. Soc., p 232 (August 1957).

[50]J. D. Dunitz and L. E. Orgel, Phys. Chem. Solids 3, 20 (1957).

[51]A. S. Coffinberry and F. H. Ellinger, U.S.A. Rep. A/Conf. 8/P/826 (1955).

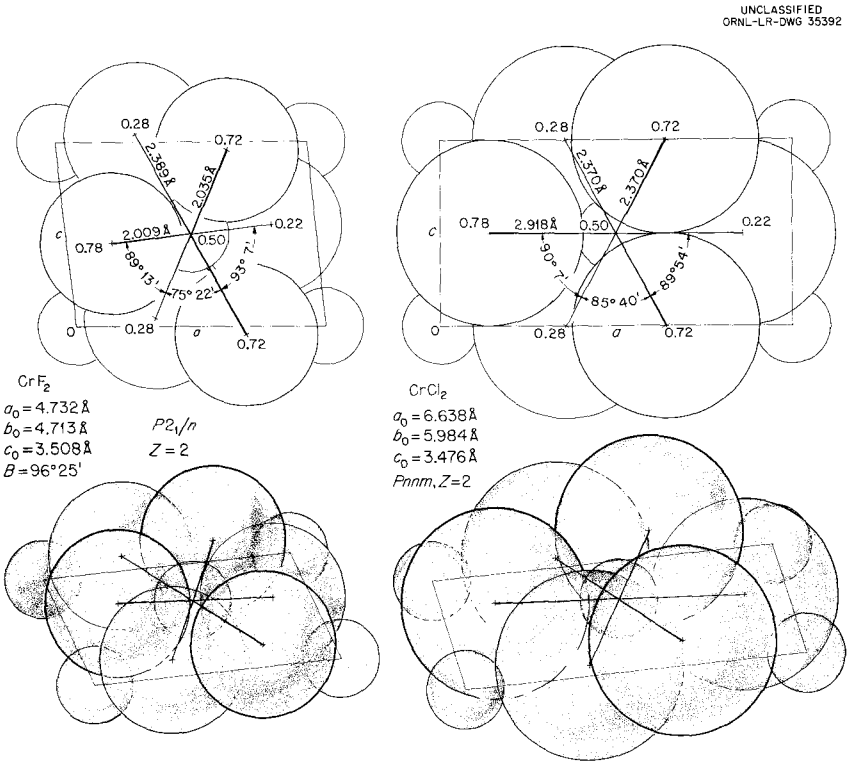

Fig. 1.26. Crystallographic Data and Structures of CrF_2 and $CrCl_2$.

cell) of 6.88 g/cm^3, in excellent agreement with that predicted by a linear density vs atomic number function for similar trihydrides.[52]

Aging Transformations of Zirconium-Niobium Alloys[53]

H. L. Yakel, Jr.

X-ray diffraction investigations of structural changes occurring on aging of β-quenched zirconium-niobium alloys have followed two principal courses during the period of this report.

First, a more intensive study has been made of the transitions of 15 wt % Nb alloy single crystals[54] aged at 400, 500, and 600°C. Similar experiments have been performed with 25 and 33 wt % Nb crystals heat treated at 250, 325, 425, and 650°C. Examination of the effects of in-pile irradiation on the aging behavior of a 15 wt % Nb crystal has also been initiated.

Second, detailed analyses of the structures of the metastable ω and Widmanstätten phases observed in the zirconium-niobium system have been attempted. For the ω phase, the calculations were directed toward the determination of atomic parameters — the subject of some disagreement in titanium ω-phase alloys.[55,56]

Experimental Details. — Techniques of crystal preparation and diffraction examination have been described previously.[57] Out-of-pile heat treatments were conducted by standard methods.

---

[52]R. N. R. Mulford, A.E.C.U.-3813 (1950).

[53]Data on mechanical properties and transformation kinetics of these alloys are given in "HRP Metallurgy — Zirconium Alloy Development," Part II of this report. This program is being carried out in cooperation with the HRP Metallurgy Group. Crystals were prepared and heat treated by M. L. Picklesimer, P. L. Rittenhouse, and R. L. Stephenson of that Group.

[54]The term "crystal" here denotes a single retained-β matrix grain which may undergo several transformations in the aging process. The word is therefore not crystallographically correct, but its use is justified merely as a literary convenience.

[55]J. M. Silcock, Acta Met. 6, 481 (1958).

[56]I. A. Bagariatskii and G. I. Nosova, Kristallografiya 3, 15 (1958).

[57]H. L. Yakel, Jr., Met. Ann. Prog. Rep. Oct. 10, 1958, ORNL-2632, p 29 (classified).

Two quartz-encapsulated 15 wt % Nb as-β-quenched crystals, one sealed in air, the other in a 1-μ vacuum, were irradiated to 10^{21} nvt during a four-month exposure in the LITR at 85°C. A residual activity of 10–20 mr/hr at contact was observed in each crystal after a three-week "cooling" period. This activity, primarily hard gamma radiation due to a small amount of iron contamination, produced a moderate background on diffraction films exposed 1–4 hr, but did not interfere with the observation of scattering maxima.

Results. –

1. Phase Transitions. As noted in the last report,[57] successive aging of an as-quenched 15 wt % Nb crystal at 250, 400, and 500°C partially transforms the retained body-centered cubic β phase to a metastable ω lattice which then reverts to virtually the as-quenched condition. The critical temperature for reversion of this alloy composition was located between 400 and 500°C.

Extended aging treatments have now been given separate, as-quenched, 15 wt % Nb crystals at 400, 500, and 600°C. Examination of room-temperature diffraction patterns at various stages of these treatments yielded the following results:

A. A crystal aged 360 hr at 400°C showed only diffractions of the four ω lattice orientations obtainable from an original β grain and those of a niobium-enriched residual β lattice. The latter were diffused and, assuming size broadening only, indicated crystallites of the order of 100 Å in linear dimension. The lattice parameter of the residual β phase decreased, therefore its niobium content increased, with increasing aging time at 400°C. The effect was asymptotic to a composition near 55 wt % Nb. No evidence of formation of hexagonal α from ω was observed in these experiments, which leaves the isolated instance reported last year in doubt.[57]

B. An as-quenched crystal aged a total of 96 hr at 500°C passed through two distinct transition stages. The first, occurring within the first hour of aging, was an ω formation resembling behavior at lower temperatures. This stage was succeeded by a second which may be described as a discontinuous precipitation of hexagonal α and niobium-rich β phases from a β matrix. Though discontinuous, the precipitation was oriented, Burgers' $\alpha\beta_M$ relations being observed as well as a $(100)_{\beta Nb}$ // $(100)_{\beta M}$,

$[100]_{\beta Nb}$ // $[100]_{\beta M}$ relation between the two body-centered cubic lattices. Reflections of all three phases in this stage were diffuse. Lattice parameters of both body-centered cubic phases decreased with increasing aging period up to 40 hr, at which time a matrix of 40 wt % Nb disappeared and a niobium-rich β phase of 80 wt % Nb was attained. No variation was observed on additional aging up to 96 hr.

C. A crystal aged 524 hr at 600°C gave diffractions characteristic of a continuous, oriented precipitation of the hexagonal α phase from a β matrix whose niobium content slowly increased (24 wt % Nb after 524 hr). The contrasted 500 and 600°C aging behavior is illustrated by diffraction patterns shown in Fig. 1.27.

The effects of in-pile irradiation to 10^{21} nvt at 85°C were assessed by comparison of diffraction patterns of the irradiated 15 wt % Nb crystal with patterns of a control crystal aged out-of-pile for four months at 85°C. As seen in Fig. 1.28, the most significant effect of pile irradiation at this temperature is an acceleration of ω formation.

Aging of β-quenched 25 and 33 wt % Nb crystals at 325 and 425°C has shown that:

(a) Omega precipitation in the 25 wt % Nb alloy, first observed after 168 hr at 250°C, proceeds at 325°C with a gradual niobium enrichment of the residual β phase (31 wt % Nb after 120 hr). Reaging at 425°C produces a partial reversion (the amount of ω phase decreases; the lattice parameter of the residual β phase increases) which is not complete after 20 hr.

(b) Omega precipitation in the 33 wt % Nb alloy is first observed after 48 hr aging at 325°C. Whereas the ω-precipitation process in 15 and 25 wt % Nb alloys is continuous, it is discontinuous in the 33 wt % Nb alloy, being accompanied by formation of a niobium-enriched β phase distinct from the residual β matrix. Partial reversion of this system is also observed on reaging at 425°C. The reversion rate is greater than that noted for the 25 wt % Nb alloy.

Measured lattice parameters of ω phases formed by 25 and 33 wt % Nb crystals are only slightly smaller than those of ω formed by a 15 wt % Nb alloy. The ω compositions corresponding to these parameters are 4 ± 1 wt % Nb (original 15 wt % Nb matrix) and 6 ± 1 wt % Nb (original 33 wt % Nb matrix).

UNCLASSIFIED
Y 30161

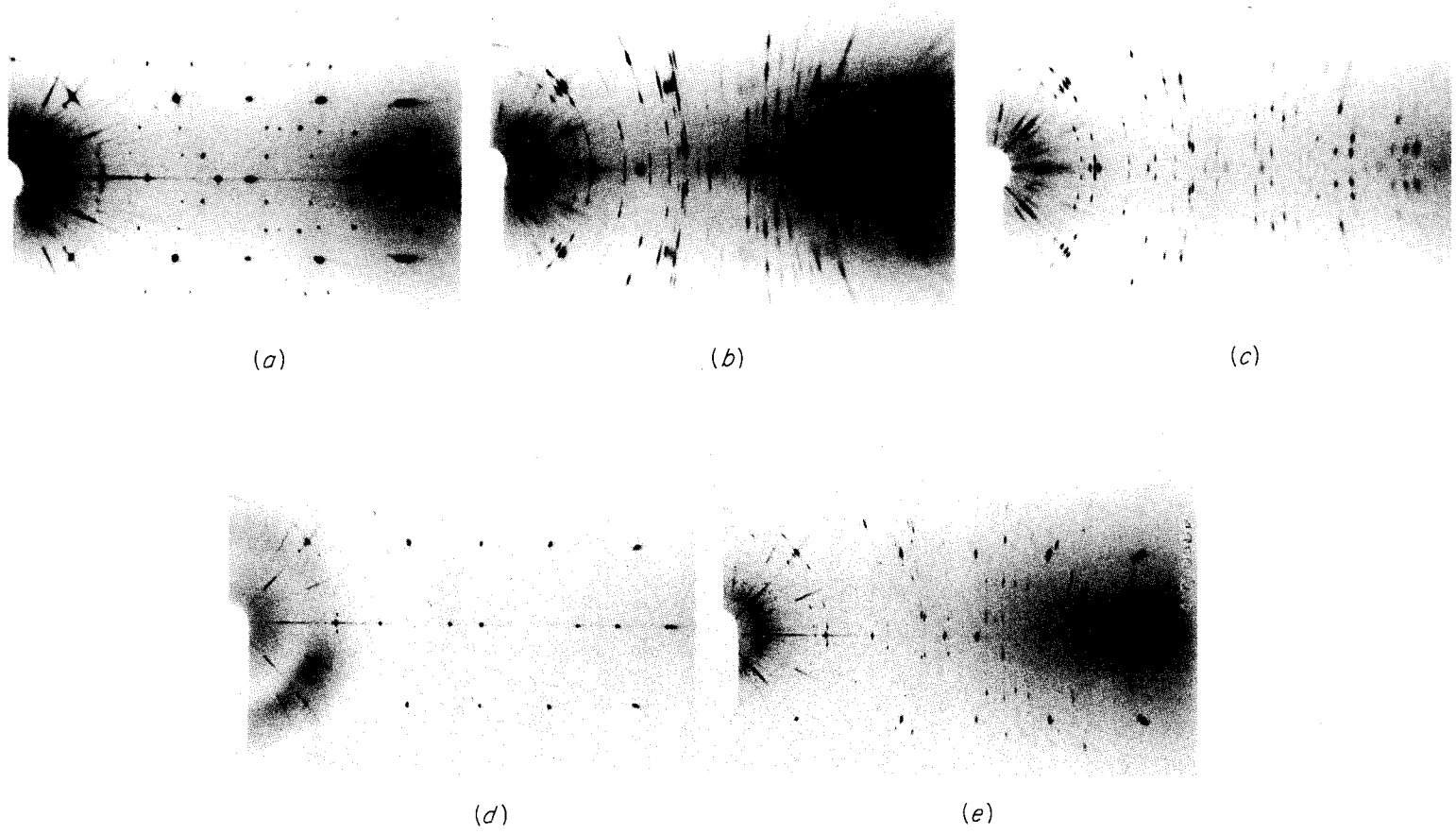

Fig. 1.27. Rotation Patterns (Cu K_α Radiation, λ = 1.5418 Å) of β-Quenched Zr–15 wt % Nb Crystals Aged (*a*) 1 hr, (*b*) 24 hr, and (*c*) 96 hr at 500°C; (*d*) 1 hr, and (*e*) 524 hr at 600°C.

UNCLASSIFIED
Y 31583

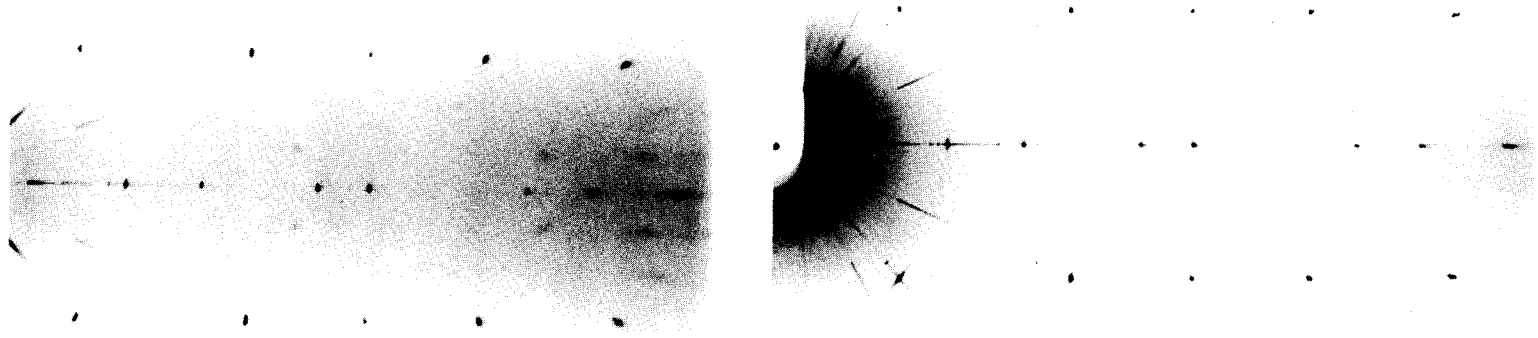

(*a*) (*b*)

Fig. 1.28. Rotation Patterns (Cu K_α Radiation, $\lambda = 1.5418$ Å) of β-Quenched Zr–15 wt % Nb Crystals. (*a*) Aged in-pile to 10^{21} nvt at 85°C during a four-month period, and (*b*) aged out-of-pile for four months at 85°C.

2. The Structure of ω. A hexagonal unit cell of the disordered ω lattice is simply related to that of the body-centered cubic β lattice by the following vector equations:

$$\vec{a_1}(\omega) = \vec{a_1}(\beta) - \vec{a_2}(\beta) \quad ,$$

$$\vec{a_2}(\omega) = \vec{a_2}(\beta) - \vec{a_3}(\beta) \quad ,$$

$$\vec{a_3}(\omega) = - \vec{a_1}(\beta) + \vec{a_3}(\beta) \quad ,$$

$$\vec{c}(\omega) = 1/2\ [\vec{a_1}(\beta) + \vec{a_2}(\beta) + \vec{a_3}(\beta)] \quad ,$$

which lead to the ideal axial relationships,

$$a_o(\omega) = \sqrt{2} \cdot a_o(\beta) \quad ,$$

$$c_o(\omega) = \frac{\sqrt{3}}{2} \cdot a_o(\beta) \quad ,$$

$$c_o(\omega)/a_o(\omega) = \frac{\sqrt{3}}{2\sqrt{2}} = 0.6124 \quad .$$

The original body-centered cubic β structure could be described on the basis of this hexagonal cell with atomic parameters 000, 1/3 2/3 1/3, 2/3 1/3 2/3. The β → ω transition involves equal movement of the atoms at z = 1/3 and 2/3 toward z = 1/2 (ref 58). If this z parameter is 1/2, the symmetry of the structure is hexagonal, space group D^1_{6h}, P 6/mmm, as proposed by Silcock.[55] If, however, the atomic parameters are ± (1/3 2/3u), with 1/3 < u < 1/2, the symmetry is trigonal, space group D^3_{3d}, p$\bar{3}$ml, as proposed by Bagariatskii.[56]

A consequence of trigonal symmetry would be that F^2 (hk·ℓ) is not equal to F^2 (kh·ℓ) for given h, k, ℓ (ℓ ± 0). Relative corrected intensities of pairs of such reflections are thus critical tests of the true structure symmetry.

---

[58]Note that these movements may be considered as displacements of atoms on {112} β planes in < 111 > β directions, just as in the Burgers' mechanism for converting a body-centered cubic to a hexagonal close-packed lattice. But, whereas in the Burgers' mechanism, all {112} planes are sheared in the same direction, the β → ω transition involves movement of two out of three consecutive {112} β planes in opposite < 111 > β directions.

A careful examination of selected reflections of the ω phase formed in a Zr–15 wt % Nb crystal shows that:

A. Omega present in the as-β-quenched crystal is trigonal with u = 0.45.

B. As aging progresses at 250°C, the parameter u approaches 0.50, and after a few hours at 400°C it is equal to 0.50, within the error of visual observation.

3. The Structure of the Widmanstätten Precipitate. Somewhat contradictory evidence has been presented concerning the formation conditions and crystal structure of the Widmanstätten precipitate appearing in as-quenched zirconium-niobium alloys above 10 wt % Nb.[57,59] While a few experiments point to identification of this phase as an interstitial impurity, other experiments, especially vacuum annealing and cathodic etching, have suggested that it is a true metastable transition structure, characteristic of the binary system.

A careful analysis of the diffraction patterns of the several orientations of the Widmanstätten phase produced in a β-quenched Zr–15 wt % Nb–5 wt % Mo crystal has indicated its structure to be orthorhombic, or monoclinic with a rhombic B plane, rather than tetragonal, as previously reported.[57] Lattice parameters are:

Monoclinic	Orthorhombic
$a_o = c_o = 3.55 \pm 0.01$ Å	$a_o = 5.29 \pm 0.01$ Å
$b_o = 3.92 \pm 0.01$ Å	$b_o = 4.74 \pm 0.01$ Å
$\beta = 96° 13' \pm 30'$	$c_o = 3.92 \pm 0.01$ Å
Z = 2, lattice is body-centered	Z = 4, lattice is face-centered
$V = 49.11 \pm 0.50$ Å^3	$V = 98.22 \pm 1.00$ Å^3

Final structural details, such as deviations of atomic parameters from ideal body-centered cubic (or face-centered cubic) positions and the ordering of atoms, are not obtainable. The substructure noted in electron micrographs of individual Widmanstätten platelets[59] is postulated to be a twinned configuration in the monoclinic B plane.

---

[59]G. M. Adamson et al., Met. Ann. Prog. Rep. Oct. 10, 1958, ORNL-2632, p 68 (classified).

Discussion. – Single-crystal diffraction experiments with specimens aged at 425°C and below have demonstrated the unique stability of the metastable ω + Nb-enriched β systems formed at such temperatures by zirconium alloys containing from 15 to 33 wt % Nb.

Clear evidence of structural changes in the ω lattice in passing from an as-β-quenched to a fully aged condition was found in the 15 wt % Nb alloy crystals. This result clarifies the previous discrepancy between the published data of Silcock and Bagariatskii on titanium ω alloys since Silcock analyzed aged alloys, while Bagariatskii studied as-quenched alloys. The ultimate reason for the varying degree of "rumpling" of the mid-plane of the ω structure may be associated with a change in degree of atomic order, an effect which cannot be followed with x rays in these alloys.

Reversion of the metastable ω-containing system on overaging is probably a characteristic common to all ω-forming zirconium or titanium alloys. Course and rate of postreversion dissociation of the alloy are dependent on the difference between the dissociation temperature and the eutectoid temperature. The free energy available to drive the reaction is clearly a prominent factor.

It is too soon to generalize about the effect of pile irradiation on the various aging transformations of zirconium-niobium alloys, but a general increase in reaction rates and a lowering of metastable transition temperatures are anticipated.

Ordering of a Copper-31 at. % Gold Alloy

B. S. Borie
C. J. Sparks H. L. Yakel, Jr.

The observation of intermediate equilibrium structures occurring in the temperature intervals separating the disordered and fully ordered phases of nonstoichiometric copper-gold alloys near Cu_3Au has been made by Rudman[60] and by Scott.[61] These structures have been described as arising from periodic anti-phase regions of the same general type found near

[60]P. S. Rudman, S. B. Thesis, Physics Dept., MIT.
[61]R. E. Scott, Ph.D. Thesis, Physics, MIT (1958).

CuAu (the CuAu II · structure) by Johansson and Linde.[62] Since the reported experiments leave several questions concerning the thermodynamic character of the transitions unanswered, high-temperature x-ray diffraction studies of a Cu-31 at. % Au alloy were begun at this laboratory.

Filings, -200 mesh, were prepared from a melt-grown single crystal homogenized 21 days at 860°C. The filings were placed in a thin-walled 0.3-mm quartz capillary, which was evacuated, sealed, and cemented into the sample holder of a Unicam S.150 high-temperature camera.[63] The sample was annealed for 1 hr at 420°C (above T_c for ordering); then, the temperature was lowered to 290°C (below T_c) for 21 hr. Debye-Scherrer photographs (Cu K_α radiation, λ = 1.5418 Å) at 14°C after this heat treatment revealed a partially ordered structure with no evidence of the satellited superlattice reflections characteristic of the anti-phased transition structure. The measured lattice parameter corresponded to approximately 31 at. % Au.[64]

The results to date of the high-temperature x-ray diffraction study of the order-disorder transition in this alloy may be summarized as follows:

1. No clear indication of a two-phase region at any temperature within the transition range could be found, based on broadening or splitting of fundamental reflections at high-scattering angles.[65]

2. Satellited superlattice reflections are observed to appear at a temperature between 340 and 335°C, on cooling. They persist to a temperature between 306 and 300°C, though below 318 ± 4°C they gradually diminish in intensity relative to the associated superlattice reflection. The reverse transition on heating is sluggish; the satellites first reappear at about 317°C. The cooling observations are similar to those reported in a 320-350°C range for a 31 at. % Au alloy by Scott.[61]

A crystal structure, based on Scott's single-crystal measurements of the intensity distribution in the OKℓ plane of reciprocal space, has been proposed. It is illustrated in Fig. 1.29. The unit cell is tetragonal,

---

[62] C. H. Johansson and J. O. Linde, Ann. Physik 28, 1 (1936).

[63] H. L. Yakel, Jr., Met. Ann. Prog. Rep. Oct. 10, 1958, ORNL-2632, p 26 (classified).

[64] Metals Handbook, 1948 ed., p 1170, American Society for Metals, Cleveland, Ohio.

[65] F. N. Rhines and J. B. Newkirk, Trans. Am. Soc. Metals 45, 1029 (1953).

UNCLASSIFIED
ORNL-LR-DWG 42659

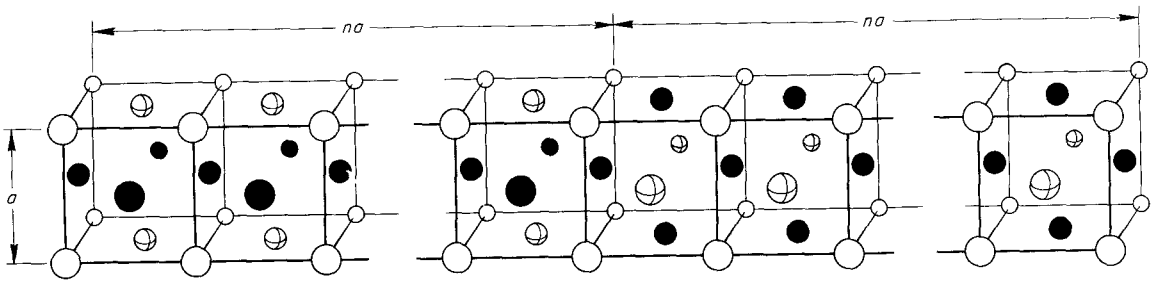

Fig. 1.29. Proposed Crystal Structure of Intermediate Phase of Cu–31 at. % Au. Shaded sites represent copper; open sites represent half gold, half copper; crossed sites represent approximately three-quarters gold, one-quarter copper.

c/a = 2n where n is an integer on the order of 9. The proposed structure contains three kinds of sites, A, B, and C. To match the relative intensities reported by Scott, A sites were populated with copper atoms, B sites were half copper and half gold, and C sites were approximately three-quarters gold and one-quarter copper.

The structure factor may be readily derived, and the following extinction rules determined:

1. If h and k are both even, ℓ must be either an even multiple of 2n (strong fundamental reflections) or an odd multiple of 2n (weak superstructure reflections).

2. If h and k are both odd, ℓ must be either an even multiple of 2n (weak superstructure reflections) or an odd multiple of 2n (strong fundamental reflections).

3. If h and k are mixed (one even and one odd), ℓ must be a multiple of 2n (weak superstructure reflections) or ℓ may differ from a multiple of 2n by one (weak satellites). Actually, for this case, all reflections for odd ℓ are allowed, but the intensities for all of them except those nearest the normal superstructure reflections are negligibly small.

The powder data reported here provide a more general test for the extinction rules than do Scott's measurements. Table 1.8 compares intensities and $\sin^2 \theta$ observed at 323 ± 2°C with Cu K_α radiation, λ = 1.5418 Å, with those computed from the above described crystal structure. The lattice constant, a_o, was chosen to fit the data at approximately 2θ = 90°,

Table 1.8. Calculated and Observed Diffraction Data for the Intermediate Ordered Structure in a Cu–31 at. % Au Alloy

(Cu K_α radiation, λ = 1.5418 Å)

hkℓ	$\sin^2\theta_{calc}$	$\sin^2\theta_{obs}$	I_{obs}
1,0,0	0.0411	0.0417	MW[a]
0,0,18	0.0411		
1,0,1	0.0413		
1,0,17	0.0779	0.0787	W[b]
1,0,18	0.0823	0.0831	W
1,1,0	0.0823		
1,0,19	0.0870	0.0880	W
1,1,18	0.1234	0.1242	VS[c]
0,0,36	0.1646	0.1655	S[d]
2,0,0	0.1646		
1,0,35	0.1967	0.1970	VW[e]
1,0,36	0.2057	0.2064	W
2,0,18	0.2057		
2,1,0	0.2057		
2,1,1	0.2059		
1,0,37	0.2150	0.2164	VW
2,1,17	0.2424	0.2428	W
2,1,18	0.2469	0.2476	W
1,1,36	0.2469		
2,1,19	0.2516	0.2525	W
2,0,36	0.3292	0.3300	MS[f]
2,2,0	0.3292		
2,1,35	0.3613	0.3614	VW
2,1,36	0.3703	0.3705	W
2,2,18	0.3703		
3,0,0	0.3703		
0,0,54	0.3703		
3,0,1	0.3705		
2,1,37	0.3796	0.3805	VW

Table 1.8 (continued)

hkℓ	$\sin^2 \theta_{calc}$	$\sin^2 \theta_{obs}$	I_{obs}
1,0,53	0.3979		
3,0,17	0.4070		
1,0,54	0.4115		
3,1,0	0.4115		
3,0,18	0.4115		
3,0,19	0.4162		
1,0,55	0.4253		
3,1,18	0.4526	0.4530	MS
1,1,54	0.4526		
2,2,36	0.4938	0.4945	M^g
3,0,35	0.5259		
3,2,0	0.5349	0.5355	VW
2,0,54	0.5349		
3,0,36	0.5349		
3,2,1	0.5351		
3,0,37	0.5442		
2,1,53	0.5625	0.5613	VW
3,2,17	0.5716		
3,2,18	0.5761	0.5755	VW
3,1,36	0.5761		
2,1,54	0.5761		
3,2,19	0.5808	0.5902	VW
2,1,55	0.5899		
4,0,0	0.6584	0.6581	M
0,0,72	0.6584		
1,0,71	0.6814		
3,2,35	0.6905		
4,1,0	0.6995	0.6980	VW
4,0,18	0.6995		
3,2,36	0.6995		
2,2,54	0.6995		
1,0,72	0.6995		
4,1,1	0.6996		

Table 1.8 (continued)

hkℓ	$\sin^2 \theta_{calc}$	$\sin^2 \theta_{obs}$	I_{obs}
3,2,37	0.7088		
1,0,73	0.7179		
3,0,53	0.7271		
4,1,17	0.7362		
3,3,0	0.7407		
4,1,18	0.7407		
3,0,54	0.7407		
1,1,72	0.7407		
4,1,19	0.7454		
3,0,55	0.7545		
3,3,18	0.7818	0.7811	S
3,1,54	0.7818		
4,2,0	0.8230		
4,0,36	0.8230	0.8222	S
2,0,72	0.8230		
2,1,71	0.8459	0.8435	VVW[h]
4,1,35	0.8551	0.8542	VVW
4,1,36	0.8641		
2,1,72	0.8641	0.8631	VW
4,2,18	0.8641		
4,1,37	0.8734	0.8726	VW
2,1,73	0.8825	0.8817	VW
3,2,53	0.8917	0.8897	VW
3,2,54	0.9053	0.9044	VW
3,3,36	0.9053		
3,2,55	0.9191	0.9181	VW
2,2,72	0.9876	0.9853	VS
4,2,36	0.9876		

[a]Moderately weak
[b]Weak
[c]Very strong
[d]Strong
[e]Very weak
[f]Moderately strong
[g]Medium
[h]Very, very weak

and c/a was taken to be 18. The agreement is reasonably good, though it might have been somewhat improved had c/a been chosen to be 17.

Recent very briefly reported work[66] suggests that this structure may exist even at the composition Cu_3Au. Future plans include a study of this interesting and unexpected possibility and a more complete exploration of the equilibrium diagram up to 40 at. % Au.

Preliminary Considerations for the X-Ray Diffraction Facility of the High-Level Radiation Examination Laboratory

H. L. Yakel, Jr.
W. C. Ulrich[67] V. A. McKay[68]

During the past year, responsibility for design and operation of in-cell experiments and associated equipment of the High-Level Radiation Examination Laboratory was delegated to the Metallurgy Division. The following paragraphs summarize current plans and preliminary experiments for the X-Ray Diffraction Facility of this laboratory.

Observation of x-ray diffraction patterns from radioactive materials poses problems both in basic design and operational technique. Perhaps the most obvious difficulty arises from the attempt to discern low-energy (5–20 kev) x-ray photons diffracted from samples which are also sources of high α, β and/or γ background. If the detector (film or counter) is to detect only the desired x rays, a discriminator must be used to either (a) deflect only photons of a narrow wavelength band into a heavily shielded detector, or (b) render the detector sensitive only to x rays of certain wavelength.

"Hot" x-ray diffraction equipment described to date has usually utilized method (a) in the form of a monochromator in the diffracted beam path.[69–71] In only one case has the natural discrimination of a propor-

---

[66] A. Pianelli and R. Faivre, Bull. Soc. Chim. Fr. (1), 8 (1959).

[67] On loan from Reactor Experimental Engineering Division.

[68] Member of Instrumentation and Controls Division.

[69] W. V. Cummings, Jr., D. C. Kaulitz, and M. J. Sanderson, HW-28331, June 9, 1953; Rev. Sci. Instr. 26, 5 (1955).

[70] J. Adam, A.E.R.E.M. and C/R 2751 (November 1958).

[71] R. W. M. D'Eye, I. F. Ferguson, and R. S. Street, A.E.R.E. C/R 2807 (January 1959).

tional counter been relied upon to record only desired x-ray pulses without monochromatization.[72]

If method (b) is used, radiation damage of the detector must be considered. In order to obtain some estimates of this damage, scintillation counter components (phototubes and crystals) have been subjected to 150-kev, 1-Mev, and 15-Mev x rays. Results indicate that while massive doses (e.g., 10^6 r) in one period destroy the photocathode of the phototube and probably damage the diodes; smaller doses (e.g., 30,000 r) interspersed with recovery periods do not materially affect phototube operation, although accumulative doses may exceed 10^5 r.

Pending further experiments to be carried out in the hot cells of the Solid State Division, detector designs center on a well-collimated, diffracted beam path leading to an ultrathin crystal scintillation counter, perhaps with the phototube set at an angle to the beam path. For abnormally active samples, the counter would be interchangeable with a bent-ground monochromator, the detector then being set at an alternative position properly oriented with the monochromator.

Goniometer design is being approached from the viewpoint of absolute containment of the sample for particulate radiation, but limited accessibility to x-ray tube and detector components. A sample holder contained within a small beryllium-windowed projection connected with a high-level cell by means of a suitable transport mechanism is envisioned. A rotatable x-ray tube and stationary detector will be external to the sample projection but within a partially demountable gamma shield. Such problems as θ-2θ coupling between sample and x-ray tube remain to be solved in detail. Useful preliminary models of a transfer elevator and powdered-sample holder are under development.

---

[72]M. A. Bredig, G. E. Klein, and B. S. Borie, Jr., Rev. Sci. Instr. 26, 610 (1955).

MICROSTRESSES IN CRYSTALS

B. S. Borie C. J. Sparks

X-Ray Diffraction Studies of Cu_2O Films Grown on Copper

B. S. Borie
C. J. Sparks J. V. Cathcart

Line Contour Analysis. — A method for the interpretation of the shapes of the Bragg maxima of very thin oxide films in terms of their thickness and strain has been reported elsewhere.[73] The line shapes were represented by a Fourier series, and it was shown that the Fourier coefficients are given by

$$C_L = \frac{\sin 2\pi B\ell L(T-L)}{2\pi B\ell LT} . \qquad (1)$$

The quantity $L=na_3$ where n is the order number of the coefficients and a_3 the average unit cell dimension normal to the reflecting planes. The reflection has Miller indices 00ℓ. The thickness of the film is given by T, and B is a parameter related to the strain in the film. To derive Eq. (1) it was assumed that the film is of uniform thickness and that the strain is such that the lattice constant varies linearly from one interface of the film to the other.

A series of cuprous oxide films grown on flat (110) faces of copper single crystals at 250°C in 1 atm of oxygen have been examined by the above method. The shapes of the 110 and 220 reflections from the oxide (planes of the type hh0 are parallel to the copper surface) were carefully measured, corrected for instrumental contributions to their contours, and reduced to Fourier coefficients C_L.

Figure 1.30 compares the experimentally determined values of LC_L for the two reflections for five different films with Eq. (1), the parameters B and T having been chosen in each case for a best fit. Thus, the thickness and strain distribution have been determined in each film.

Integrated Intensities from Thin Films. — It is desirable to have some independent check of the film thickness determined as described above from

[73]B. S. Borie and J. V. Cathcart, Met. Ann. Prog. Rep. Oct. 10, 1958, ORNL-2632, p 34 (classified).

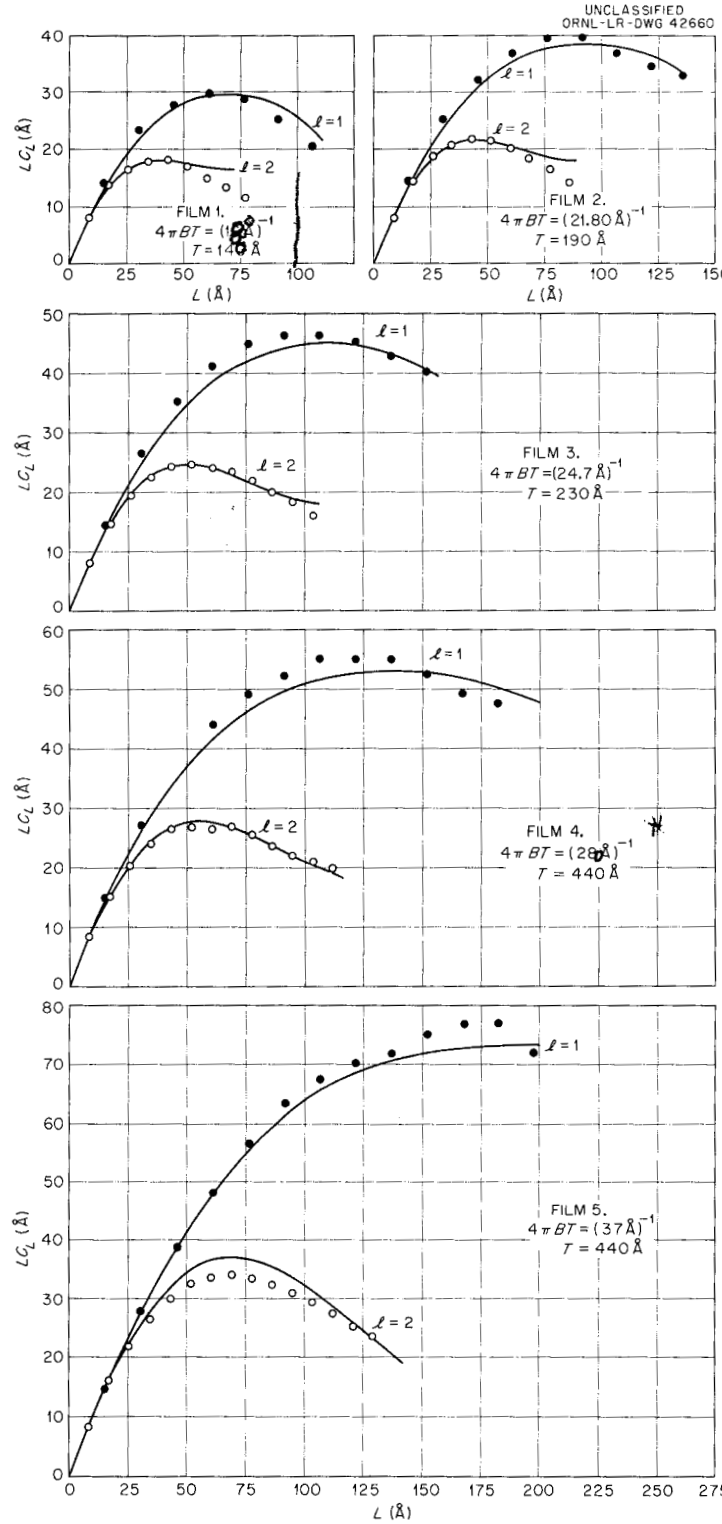

Fig. 1.30. Comparison of Experimentally Determined Values of LC_L for the 110 and 220 Reflections for Five Cu_2O Films with Eq. (1). The measurements for 110 are shown by closed circles, those for 220 by open circles, and the curves given by theory are shown as solid lines.

the shapes of the Bragg maxima. It was felt for some time that such a second measurement of the film thickness was provided by the polarizing spectrometer. However, recent work[74] has cast considerable doubt on the reliability of this instrument, and it became important to find a third method for measuring the film thickness. Described here is such an independent thickness determination from the integrated intensities of the Bragg reflections.

If a very small single crystal is bathed by an x-ray beam of uniform intensity I_0, if the detector is sufficiently large to intercept the entire diffracted beam, and if the crystal is rotated about an axis perpendicular to the x-ray beam through its entire range of diffraction, then the total energy diffracted by the crystal is simply related to the structure factor $F_{hk\ell}$ of the Bragg reflection and the volume V of the crystal. Let α be the angle between the normal to the diffracting planes and the x-ray beam, and let $P(\alpha)$ be the power detected by the counter for a crystal orientation given by α. Then,

$$\int P(\alpha)\, d\alpha = \frac{I_0 e^4}{m^2 c^4} \frac{\lambda^3 F^2_{hk\ell} e^{-2M} V}{v_a^2 \sin 2\theta} \left(\frac{1 + \cos^2 2\theta_M \cos^2 2\theta}{1 + \cos^2 2\theta_M} \right) . \quad (2)$$

The integral is carried out over the entire range of α for which diffraction occurs. The electronic charge and mass are e and m; the velocity of light is c; and the wavelength of the x rays is λ. The volume of the unit cell is v_a, e^{-2M} is the Debye temperature factor; the Bragg angle of the diffracting planes is θ, and that of the monochromator is θ_M. This well-known result presumes that the crystal is so small that there is no extinction and that absorption is negligible.

The geometry of our instrument is such that the entire incident beam is intercepted by the flat sample, the surface of which makes an angle θ with the incident beam. The diffracting planes are parallel to the surface. If the cross sectional area of the beam is A, then the area of the film irradiated is $A/\sin\theta$; and the volume V irradiated is $AT/\sin\theta$, where T is the thickness of the film. So, $I_0 V = P_0 T/\sin\theta$ where P_0 is the total power

---

[74] J. V. Cathcart, "Metal Surface Studies," this part of report.

in the primary beam. Hence, Eq. (2) becomes

$$\int P(\alpha)\, d\alpha = \frac{P_0 e^4}{m^2 c^4} \frac{\lambda^3 F^2_{hk\ell} e^{-2MT}}{v_a^2 \sin\theta \sin 2\theta} \left(\frac{1 + \cos^2 2\theta_M \cos^2 2\theta}{1 + \cos^2 2\theta_M} \right). \qquad (3)$$

We wish to measure $\int P(\alpha)\, d\alpha$ and from it obtain a value of T by using Eq. (3). Since P_0 is very much greater than $P(\alpha)$, it is difficult to measure both directly with the same detector. Hence, we measure P_0 indirectly by measuring the scattering from an amorphous sample. For this situation, with a flat sample of polystyrene making equal angles with the incident and scattered beams, the scattered intensity I_s is given by

$$I_s = \frac{P_0 e^4}{m^2 c^4} \frac{N_A I_{eum}}{2M_s R^2 (\mu/\rho)} \left(\frac{1 + \cos^2 2\theta_M \cos^2 2\theta_s}{1 + \cos^2 2\theta_M} \right), \qquad (4)$$

where $2\theta_s$ is the scattering angle, μ/ρ the mass absorption coefficient of polystyrene, R the specimen-to-detector distance, M_s the molecular weight of polystyrene, and N_A Avogadro's number. The total coherent and incoherent scattering in electron units per molecule is given by I_{eum}. It is assumed that the sample is infinitely thick, and that its atoms scatter independently of each other.

If one divides Eq. (3) by Eq. (4) and solves for T, there results

$$T = \frac{\int P(\alpha)\, d\alpha}{I_s} \frac{v_a^2 N_A I_{eum} \sin\theta \sin 2\theta}{2R^2 F^2_{hk\ell} e^{-2M} \lambda^3 M_s (\mu/\rho)} \left(\frac{1 + \cos^2 2\theta_M \cos^2 2\theta_s}{1 + \cos^2 2\theta_M \cos^2 2\theta} \right). \qquad (5)$$

A measurement of $F^2_{hk\ell} e^{-2m}$ by using bulk Cu_2O is described in the following portion of this report. All other quantities on the right of Eq. (5) are either known or readily measured.

Compared in Table 1.9 are T_{110} and T_{220}, the thickness determined from integrated intensity measurements, with T_s, that determined from the line-shape analysis. It is seen that T_{110} and T_{220} agree quite closely with each other, while T_s is 10 to 15% smaller. The agreement among these three independent thickness measurements confirms the accuracy of the line-shape analysis.

Discussion. – The line-shape analysis yields not only the thickness of the film, but also the strain distribution. Figure 1.31 is a plot of interplanar spacing as a function of position through the film thickness as determined from the line shapes of the five films here studied.

Table 1.9. Comparison of Film Thickness Measured by Three Methods

Film No.	T_{110} (Å)	T_{220} (Å)	T_s (Å)
1	153	146	140
2	237	227	190
3	285	275	230
4	319	321	280
5	527	496	440

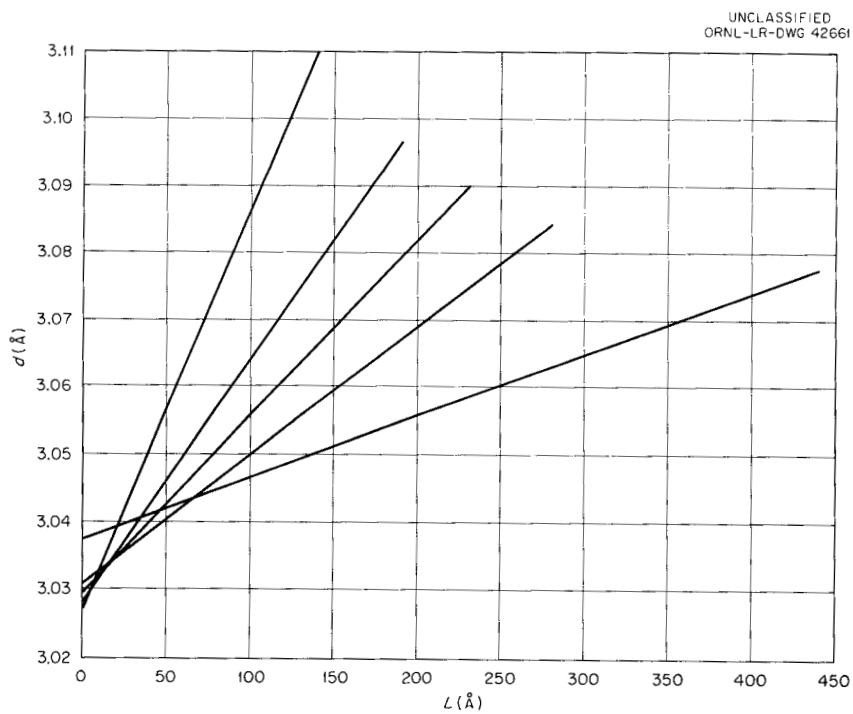

Fig. 1.31. The Variation of the Interplanar Spacing of the 110 Planes Through the Film Thickness for Five Films. The corresponding spacing in bulk Cu_2O is 3.019 Å.

For all the films, the interplanar spacing is everywhere greater than that of bulk Cu_2O, though at one interface the spacing is very nearly that of the bulk material, and very nearly the same for all five films. It is not possible to determine from the x-ray diffraction experiment whether this is the gas-oxide interface or that of the oxide-metal. Figure 1.31 shows that the strain in the film decreases from a large value in thin films to a very much smaller value as the film grows, in much the same way that the growth rate varies. It may be that the two are in some way related.

Future work will include efforts to understand the cause of the strain in the film, to relate it to the growth rate of the oxide, and to extend the study to other orientations and perhaps to other systems.

Determination of the Atomic Scattering Factors and Debye Factors in Cuprous Oxide

B. S. Borie C. J. Sparks

For the thickness determination of thin single-crystal oxide films, described elsewhere in this report, it is necessary to know the structure factors of the Bragg reflections, along with the Debye temperature factor. Though atomic scattering factors computed from theory are satisfactory, a lack of knowledge of the Debye factor requires an experimental determination of these quantities.

The data necessary are measurements of the integrated intensities of the Bragg reflections from a random powder sample and of the temperature diffuse scattering, both in absolute units. Copper $K\alpha$ radiation with an LiF monochromator and balanced Ni-Co filters were used. The power of the primary beam was measured by scattering it from polystyrene $(C_8H_8)_x$ at a scattering angle sufficiently large that the scatterer may be assumed to be structureless. This allows the measurements of intensity to be converted to absolute units and the Compton scattering subtracted.

An expression developed by Warren[75] was used to fit the temperature diffuse scattering away from the Bragg reflections and to compute the diffuse scattering under the Bragg maxima, so that the diffuse background could be unambiguously separated from the peaks. A comparison of the thus computed

---

[75] B. E. Warren, Acta Cryst. 6, 803 (1953).

and observed diffuse scattering is shown in Fig. 1.32. The integrated Bragg reflections were then converted to absolute units according to the method of Warren.[76]

Cuprous oxide is cubic, with four copper atoms in the unit cell at 000, 1/2 1/2 0, 1/2 0 1/2, 0 1/2 1/2, and two oxygen atoms at ± 1/4 1/4 1/4. Four types of crystal structure factor are readily derived. The integrated intensity measurements then are determinations in abolute units of the quantities $f_O \exp[-M_O]$, $f_{Cu} \exp[-M_{Cu}]$, $2 f_{Cu} \exp[-M_{Cu}] - f_O \exp[-M_O]$, and $2 f_{Cu} \exp[-M_{Cu}] + f_O \exp[-M_O]$. The atomic form factors of copper and oxygen are f_{Cu} and f_O, and the Debye temperature factors are M_{Cu} and M_O.

Plotted in Fig. 1.33 are the experimentally determined values of the first three of these quantities. For an internal consistency check, the first two were used to compute the third. The agreement is seen to be quite good.

Figure 1.34 shows $2M_{Cu}$ determined experimentally as a function of $\sin^2 \theta/\lambda^2$. This was done by using the curves of the diffuse scattering of Fig. 1.32 and the atomic form factors of Fig. 1.33. It was assumed that the extremely small contribution of oxygen to the diffuse background could be

[76]B. E. Warren, Norelco Reptr. 2, 63 (1955).

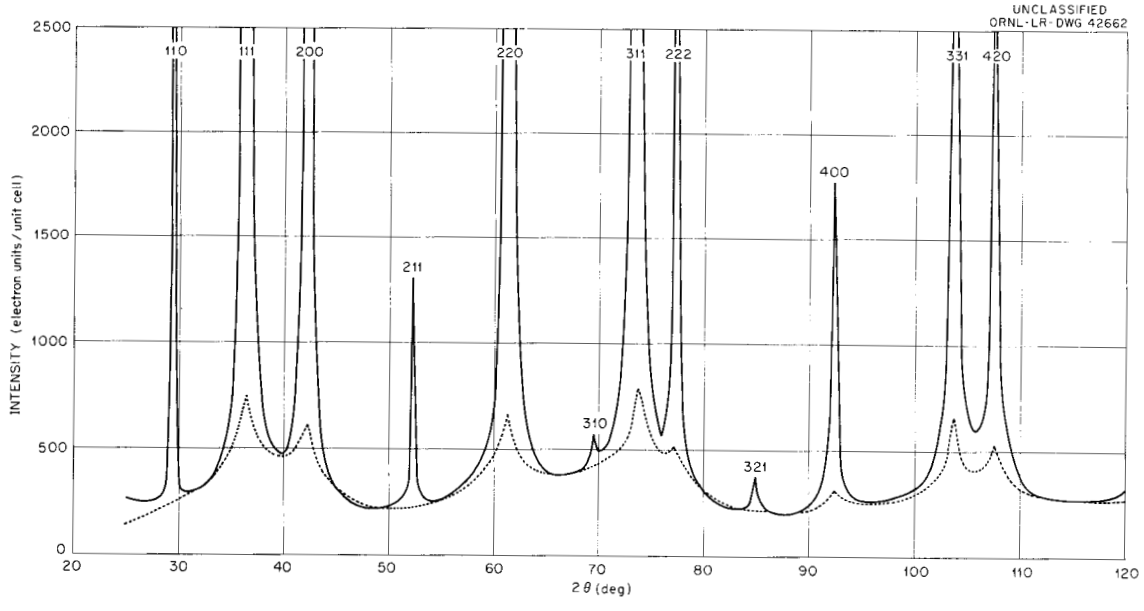

Fig. 1.32. Comparison of Observed (Solid Line) and Computed (Dashed Line) Diffuse Scattering for Cu_2O.

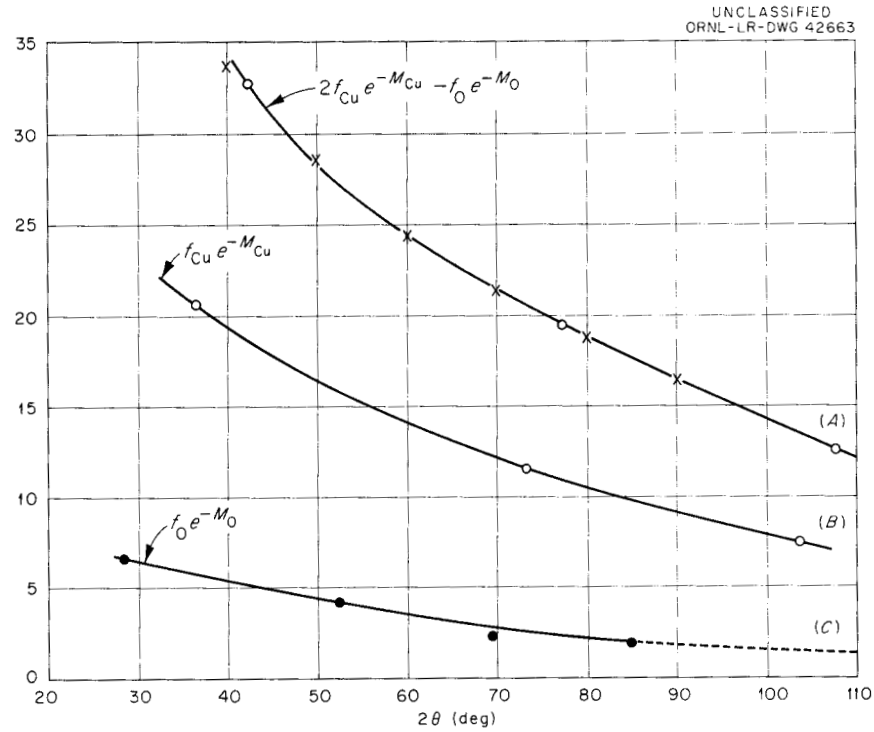

Fig. 1.33. Form Factors and Debye Factors for Cu_2O as Determined from Integrated Intensity Measurements. Crosses are points for curve (*A*) computed from curves (*B*) and (*C*).

sufficiently well approximated by letting $M_O = M_{Cu}$, and it was further assumed that the diffuse scattering is well described by the Warren theory for face-centered cubic elements. The only justification for this latter assumption is that such a treatment of this data is internally self-consistent, and that the resultant $2M_{Cu}$ is linear with $\sin^2 \theta/\lambda^2$.

With the experimentally determined $2M_{Cu}$, one may finally reduce the data of Fig. 1.33 to f_{Cu}. This quantity is compared in Fig. 1.35 with the theoretical values given by Berghuis et al.[77] Such a separation of the form factor and the Debye factor for oxygen is not possible because the diffuse scattering is very insensitive to the thermal motion of these atoms.

---

[77]J. Berghuis et al., Acta Cryst. 8, 478 (1955).

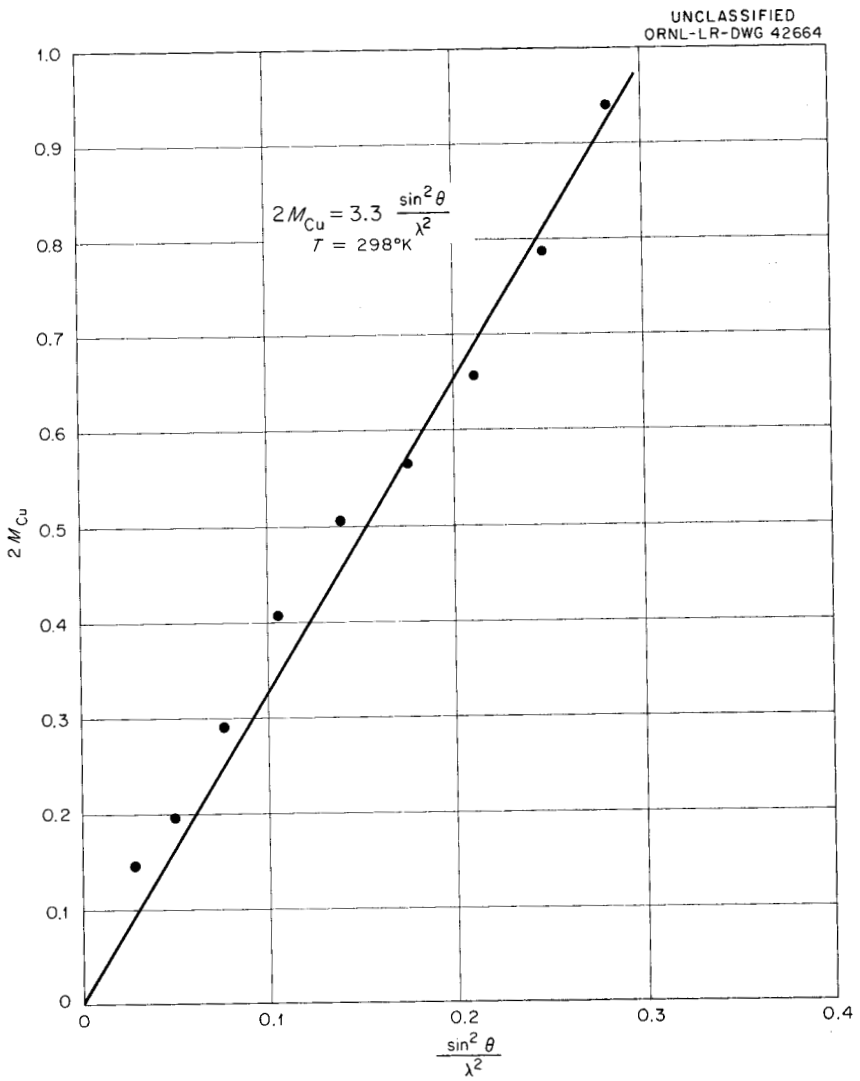

Fig. 1.34. The Debye Factor for Copper in Cu_2O as Determined from the Data of Figs. 1.~~30~~ 32 and ~~1.31~~ 1.33

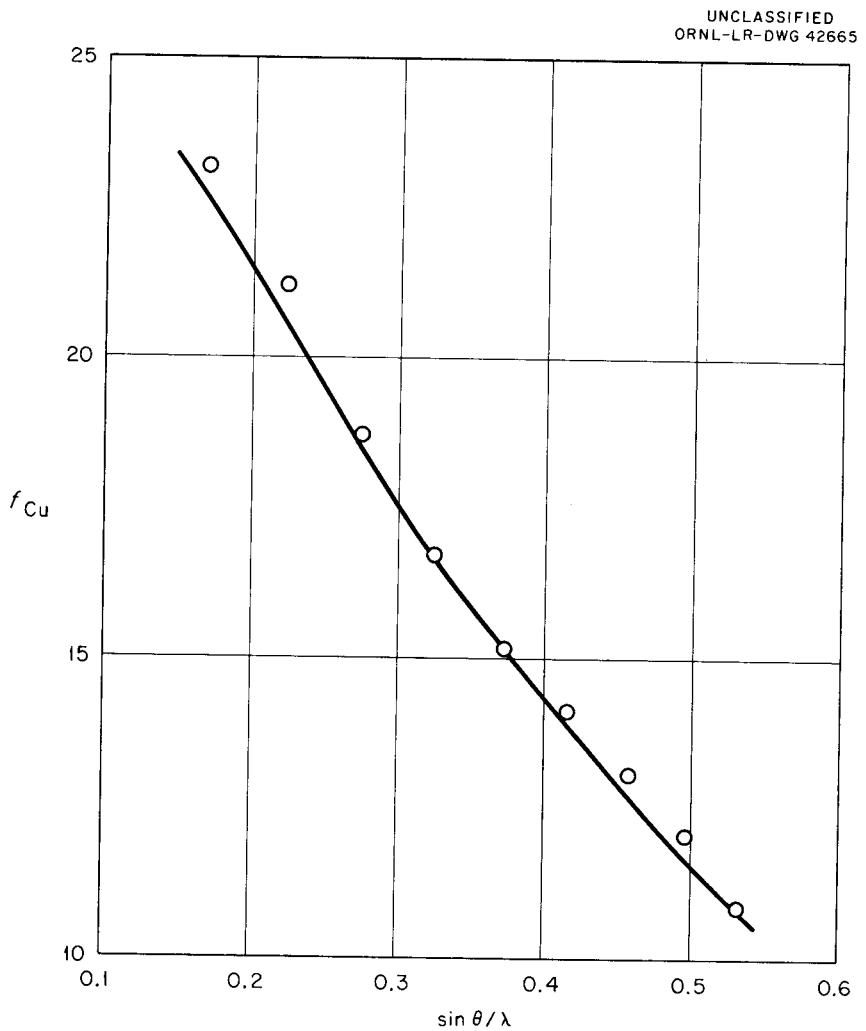

Fig. 1.35. Comparison of Observed Atomic Scattering Factor for Copper with That Computed by Berghuis et al. Observed factors shown as circles, computed factors shown as solid line.

HIGH-TEMPERATURE REACTIONS

G. P. Smith, Jr.

C. R. Boston J. V. Cathcart G. W. Clark
J. J. McBride G. F. Peterson

Absorption Spectra of Fused Salts

G. P. Smith, Jr.
C. R. Boston J. J. McBride

Influence of Cation Potential on the Energy of an Anion Transition. — As an initial phase of a study of ion-ion interactions in fused salts, a determination was made of the influence which electrostatic interactions have on the energy of an $^1A \rightarrow {}^1U$ type of $n \rightarrow \pi^*$ transition in the nitrate ion. From studies of the pure, molten alkali nitrates it was found that the energy of this transition increases linearly with the reciprocal of the cationic radius (1/r). In order to show that this is an effect of cationic potential (Ze/r) it was necessary to obtain measurements on ions of rare-gas electronic configuration with charge Z greater than unity. The pure, alkaline earth nitrates, the obvious choice, do not melt without decomposition. Consequently, it was necessary to study them in mixtures with the more stable alkali nitrates. Such studies established rules for extrapolating to the behavior of the pure materials. In this manner it was possible to show that the energy of the $n \rightarrow \pi^*$ transition of NO_3^- is a linear function of the cation potential for values of Z/r from about 0.6 to about 2.0.

The direction of this effect is predicted by McConnell's theory[78,79] of the influence of intermolecular interactions on $n \rightarrow \pi^*$ transitions. Previously, this theory has been verified only for hydrogen bonding. The present work extends this to include electrostatic effects.

It was also found that the temperature coefficient of the mean transition energy is negative and progressively increases in magnitude with increasing cation potential. This effect may be rationalized in terms of McConnell's theory when account is taken of the randomizing effect of thermal motions.

---

[78] H. McConnell, J. Chem. Phys. 20, 700 (1952).

[79] J. W. Sidman, Chem. Revs. 58, 689 (1958).

When the above conclusions are applied to aqueous and organic solutions of nitrates, many of the complex solvent effects which have been reported are readily rationalized. The supposedly anomalous red shift of the $n \rightarrow \pi^*$ nitrate band for solvents of progressively increasing polarity may be accounted for very simply in terms of ion-cluster formation.

A very large mass of data has been collected from which it will be possible to assess the influence of cations which do not have rare-gas electron configurations and from which transition probabilities may be obtained. These data must be subjected to extensive computations before physically meaningful numbers are forthcoming. These calculations are incomplete at the present time.

The Iodide Ion Charge-Transfer Band. – Recent attempts at measuring the charge-transfer bands of I^- and Br^- in fused mixtures of the KBr-LiBr and KCl-LiCl eutectics[80] gave results which are difficult to reconcile with any current theories of the charge-transfer process. Particularly striking were the molar extinction coefficients, ϵ, of the band maxima with values of the magnitude of 50 and less (values of ϵ are not listed in ref 80 but are easily computed from the number given), indicating a forbidden transition, whereas the charge-transfer process is expected to be strongly allowed with values of ϵ of the magnitude of 10,000.

We have, accordingly, checked these measurements for the case of KI dissolved in the molten LiCl-KCl eutectic and obtained results which were quite different from the foregoing and which are much more nearly in line with what would be anticipated. In these measurements, we reproduced the experimental conditions of the above authors (0.29 M KI and 2 mm path length) and also made measurements under conditions more favorable for determining the high absorbancies involved (0.047 M KI and 0.06 mm path length).

We were able to measure an absorption edge down to a wavelength of 215 mμ with a clear inflection point indicating the nearness of the band maximum. This absorption edge had a very accurate Gaussian profile. Consequently, the coordinates of the band maximum were computed by assuming exact Gaussian character and found to be 8,500 for ϵ and 210 mμ for the wavelength. Greenberg

---

[80] J. Greenberg and B. R. Sundheim, J. Chem. Phys. 29, 1029 (1958).

and Sundheim reported the low-energy band maximum at about 280 mμ. As a consequence of possible errors in I^- concentration, arbitrary error limits of ± 10% are placed on ε. The spectra reported by Greenberg and Sundheim can be accounted for in a semiquantitative way on the basis of stray-light errors.

The charge-transfer band of I^- in LiCl-KCl is thus established as having the anticipated strongly allowed character. Further analysis is postponed until more extensive data are available.

Bismuth Metal in Molten Bismuth Trichloride. — A basic postulate of most solution chemistry is that all electron orbitals may be regarded as localized on atoms, bonds, or, at most, small molecular units. For many solutions of metals in their molten halides this postulate is not even approximately correct. However, for some metal-salt systems it appears plausible that in going from metal-rich to salt-rich compositions, valency electrons from the metal atoms undergo a transition from delocalized to localized orbitals. The existence of the diamagnetic compounds of Bi(I), BiCl, and $AlBiCl_4$ suggests that the bismuth-bismuth trihalide systems are likely candidates for this behavior. For example, Bredig[81] postulates that metallic bismuth in dilute Bi-BiX_3 (X = Cl, Br) solutions is largely partitioned between Bi_2 molecules and Bi_2^{++} molecule ions.

A first problem in the study of such transitional systems is that of establishing the species formed by the metal in dilute solution. As a contribution to this problem, preliminary results have been obtained on the visible absorption spectrum of solutions of bismuth in $BiCl_3$ up to 0.7 M (about 6 mole %) over the temperature range from 260 to 360°C. A strong, easily measured absorption band was found at 560 mμ (260°C) and another strong band at about 420 mμ. The second band lay within the very strong background absorption of the $BiCl_3$ solvent, where precise measurement is difficult. Consequently, only order-of-magnitude statements can be made about the 420 mμ band.

The absorption coefficients (internal absorbance per unit path length) of these bands were different nonlinear functions of the formal concentration of bismuth. This result shows that bismuth in $BiCl_3$ is partitioned into at least two different species. As the formal concentration of bismuth changed from 0.009 M to 0.7 M, the formal extinction coefficient (absorption coefficient/

---

[81] M. A. Bredig, J. Phys. Chem. 63, 978 (1959).

formal M of bismuth) decreased rapidly. This shows that with increasing total concentration, a rapidly decreasing fraction of bismuth is partitioned into the 560 mμ species. The absorption of the 560 mμ band changed with temperature in such a way as to indicate that the concentration of the associated species increases with increasing temperature at constant total bismuth concentration. Quantitative statements must await detailed numerical analysis. An attempt will be made to fit these data to the Bredig equilibrium, $2\ Bi_2 + 2\ Bi^{3+} = 3\ Bi_2^{++}$.

The qualitative changes, when interpreted by the Bredig model, suggest assignment of the 560 mμ band to Bi_2 molecules. It is interesting to note that there is a good correspondence between the 560 mμ band and the lowest-energy band of Bi_2 molecules in the vapor phase.

Bredig has postulated that the Bi_2^{++} molecule ion has a 4-electron bond. Hence, the Bi_2 molecule should also be multiply bonded. This postulate is of general chemical interest because multiple bonds between heavy-metal atoms are uncommon. Ordinarily, one expects such bonding to arise from a single, 2-electron, σ bond with the π orbitals essentially nonbonding. However, it is possible that in the cases of Bi_2 and Bi_2^{++} there is some mixing of d character in the π orbitals to give enough overlap so that one obtains a relatively weak π-type bond. Such bonding would split the otherwise accidentally degenerate π and π^* levels. This splitting would be manifest in the lowest-energy band in different ways, depending on the strength of the bond. At present, band assignments are too tenuous to justify elaboration on these matters, but the above comments point toward the possible utility of electronic spectra in understanding the species and bonding in dilute solutions of metals in salts, provided that the present, rather serious experimental difficulties can be overcome.

REACTIONS AT METAL SURFACES

J. V. Cathcart
R. E. Pawel G. F. Petersen W. O. Harms[82]

TOPOGRAPHY OF OXIDE FILMS FORMED ON TANTALUM

R. E. Pawel J. V. Cathcart

Previous work at this laboratory[83,84] has shown that the gaseous oxidation of tantalum takes place in a nonuniform fashion, characterized at least in the initial stages by the formation in the metal of discrete platelets of oxide resembling a typical Widmanstätten structure. The tendency for this metal to react in such a heterogeneous manner illustrates the need for consideration of oxide morphology in any interpretation of the oxidation mechanism for tantalum.

The present oxidation research with tantalum consists of work in two major areas. Measurements were made of the oxidation rate at temperatures betweel 475 and 530°C, and a phenomenological study of the first-stage oxidation characteristics of tantalum was undertaken at temperatures between 300 and 700°C.

Specimen Preparation and Experimental Procedures. – Tantalum specimens (nominal analysis: Ta, 99.71%; Nb, 0.15%; Fe, 0.03%; C, 0.03%; and W, 0.05%) were cut from 0.5 mm sheet in the form of coupons, 1 × 2 cm. In most of the work reported here, the specimens were preannealed in vacuum for 1 hr at 1200°C; some specimens were strain annealed for longer periods at 1200 and 1300°C to yield a larger grain size. The specimens were mechanically polished through 0.3-μ levigated alumina and finally electropolished in a 90% H_2SO_4–10% HF solution. The specimens were then placed in quartz reaction tubes and annealed at a pressure of $\sim 2 \times 10^{-6}$

---

[82] Consultant from University of Tennessee.

[83] J. V. Cathcart, Met. Ann. Prog. Rep. Oct. 10, 1957, ORNL-2422, p 76 (classified); Oct. 10, 1958, ORNL-2632, p 58 (classified).

[84] J. V. Cathcart and R. Bakish, J. Electrochem. Soc. (to be published).

mm Hg at the reaction temperature for approximately 16 hr prior to oxidation. Except as noted, all oxidations were performed in purified oxygen at approximately atmospheric pressure.

The surface topography of the oxidized tantalum specimens was examined by both optical and electron microscopy. Two methods of specimen replication were used. Direct carbon replication, with chromium preshadowing, could be used on all but the heaviest oxide films. An indirect method involving carbon replication of a Parlodion intermediate was used with success even on the roughest films. Comparative tests indicated that both methods reproduced surface features equally well; however, for the sake of convenience and specimen preservation, the latter technique has been favored.

Characteristic of the electropolished specimens was the presence of a "bubble raft" type of structure on the specimen surface even before oxidation (see Fig. 1.43). These surface features developed during either electrolytic or chemical polishing, but nothing is known concerning the mechanism of their formation. The "bubble raft" structure was preserved unchanged on the surfaces of oxidized specimens. Thus, the simple oxidation of a tantalum specimen constituted a marker experiment, and the fact that this texture persisted after oxidation was evidence that anion diffusion was the predominant mode of diffusion in tantalum oxide films.

Experimental Results. — 1. Oxidation-rate measurements. A manometric system, similar to that previously used in rate measurements on the alkali metals,[85] was employed for the oxidation-rate determinations for tantalum. Typical rate curves at 475, 515, and 530°C are shown in Figs. 1.36 and 1.37, where the number of moles of oxygen consumed per square centimeter of surface area is plotted against the time of oxidation. In this temperature range, tantalum characteristically formed initially a protective oxide film; however, as the reaction proceeded, the rate of oxidation increased, and the rate curve became approximately

---

[85] J. V. Cathcart, L. L. Hall, and G. P. Smith, Acta Met. 5, 245 (1957).

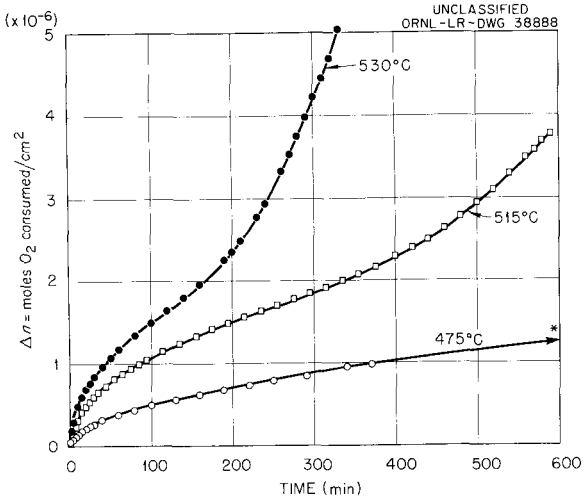

Fig. 1.36. Oxidation-Rate Curves for Tantalum at 475, 515, and 530°C. See Fig. 1.37 for complete rate curve at 475°C.

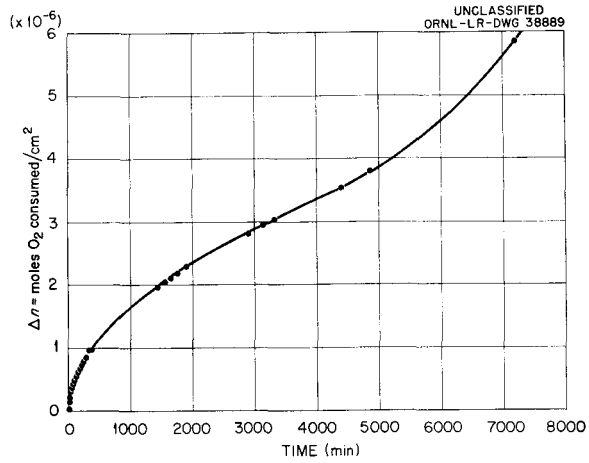

Fig. 1.37. Oxidation-Rate Curve for Tantalum at 475°C.

linear. The mechanism associated with this "breakaway" phenomenon appeared to be similar to that previously proposed for niobium[86] in that the diminution of the protective qualities of the initial oxide film could be correlated with the formation of microscopic, blister-like cracks in the oxide film. Figure 1.47 shows a typical example of such cracks.

2. Mode of oxide platelet formation. The morphology of tantalum and niobium oxide films differed considerably up to the stage of blister formation. Where the early stages of oxidation of niobium showed reasonably uniform, though wrinkled, oxide surfaces, tantalum oxide films were covered with needle-shaped structures as indicated in Fig. 1.38. Taper sections, Fig. 1.39, and cross sections, Fig. 1.40, of oxidized tantalum specimens showed that these needles were actually traces of platelets of oxide extending into the metal. Hereafter, these features will be referred to as "platelets." Bakish[87] has reported that these

---

[86] J. V. Cathcart, J. J. Campbell, and G. P. Smith, J. Electrochem. Soc. 105, 442–46 (1958).

[87] R. Bakish, J. Electrochem. Soc. 105, 71 (1958).

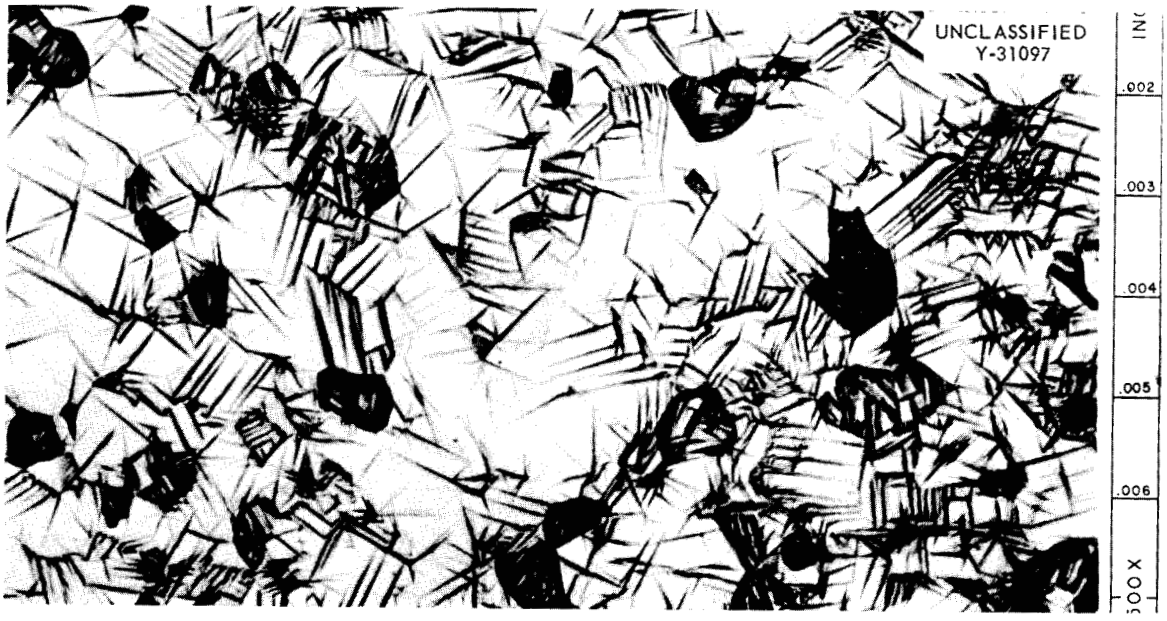

Fig. 1.38. Typical Platelet Growth of Oxide on Tantalum Specimen. Preannealed 1 hr at 1200°C; oxidized 96 hr at 320°C.

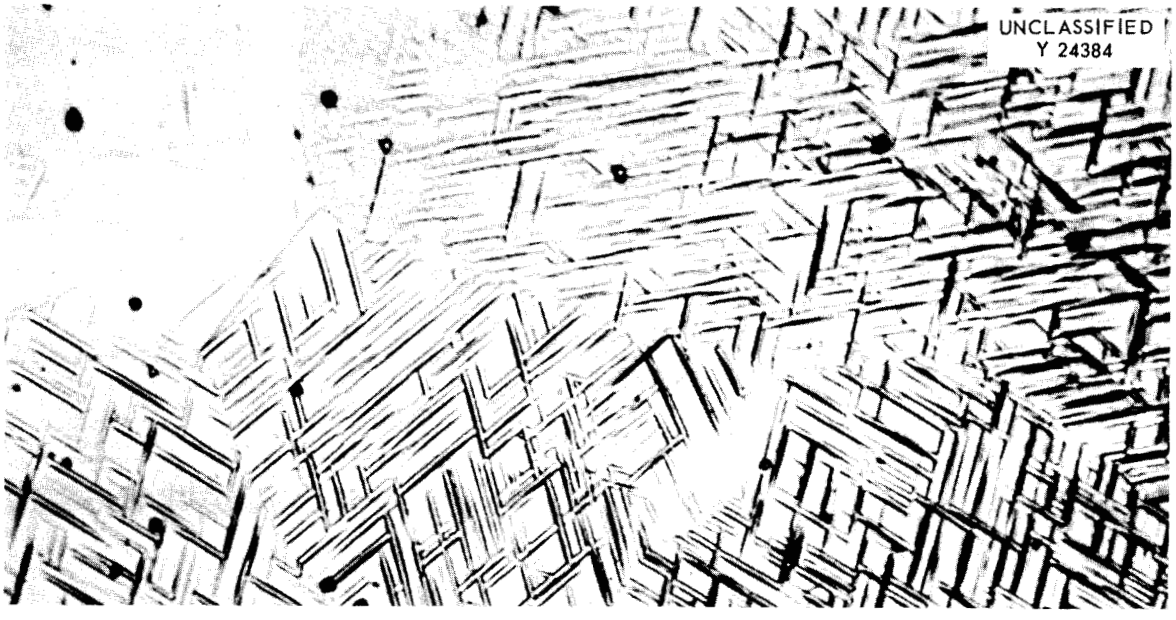

Fig. 1.39. Taper Section Through Platelet Structure on Oxidized Tantalum Surface, Showing Depth of Platelets. Oxidized 4 hr at 500°C. 500X.

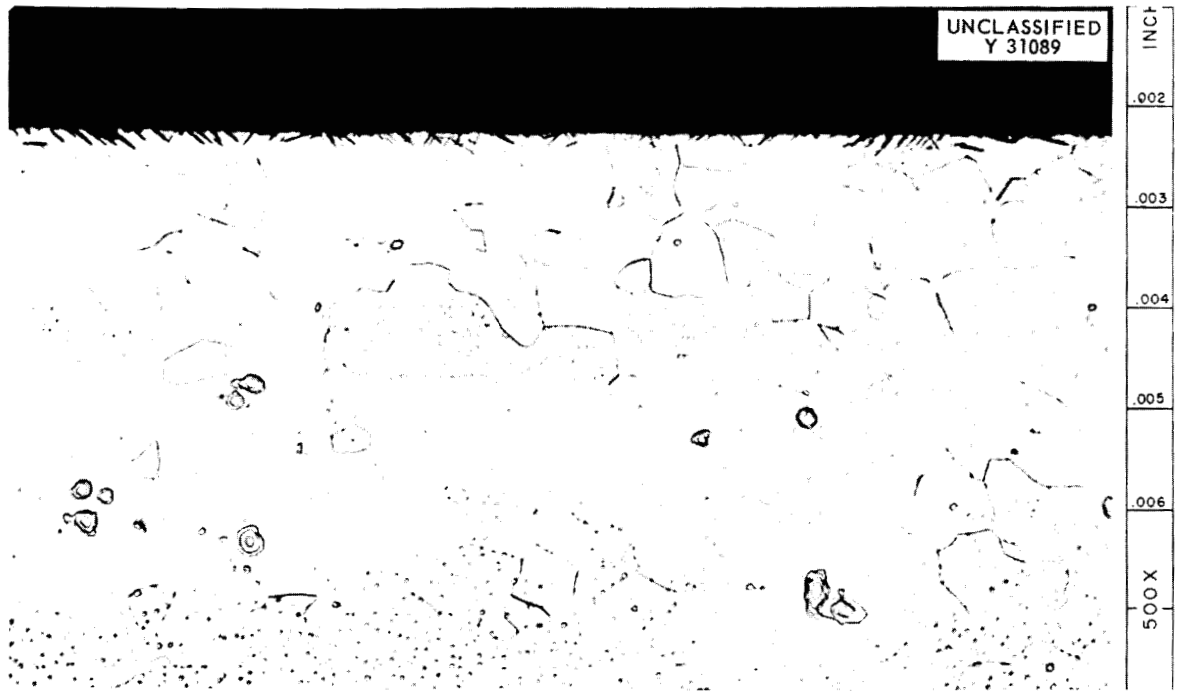

Fig. 1.40. Cross Section of Oxidized Tantalum Specimen Showing Platelet Growth into the Metal. Preannealed 1 hr at 1200°C; oxidized 6 hr at 500°C. Etched for 2 sec in 50% H_2SO_4–25% HNO_3–25% HF.

platelets form on the {100} planes of the metal and grow in < 100 > directions. It is of interest to observe that other gas-tantalum reactions, notably those with sulfur[88] and nitrogen,[89] have also shown this characteristic structure.

The resemblance of the platelet structure to the Widmanstätten pattern observed in many precipitation systems suggested the possibility that the platelets formed during the cooling of the specimen from the reaction temperature. For this reason, the effect of varying the cooling rate was studied; hot-replication techniques and hot-stage microscopy methods were also applied to the problem.

The results obtained by varying the cooling rate from the oxidation temperature were inconclusive. Cooling rates were varied from approximately 2°/min to an estimated > 200°C/min. Although some difference in

---

[88] J. V. Cathcart and J. B. Wagner, Met. Ann. Prog. Rep. Oct. 10, 1957, ORNL-2422, p 87 (classified).

[89] R. Bakish, J. Electrochem. Soc. 105, 574 (1958).

structure existed between specimens treated in these ways, no correlation of morphology with cooling rate could be made.

The results of replicating the specimens before cooling from the reaction temperature were more definite. A small hot-plate was constructed and mounted in the vacuum evaporator normally used for specimen replication. The specimen was oxidized in air at 400°C, on the hot plate. After the evacuation of the system, with the specimen still at 400°C, a direct carbon replica, preshadowed with gold or palladium, was made of the oxide surface. The hot replica was then removed and the specimen re-replicated in the normal way at room temperature. The resulting two sets of replicas were examined in the electron microscope. No differences in surface topography could be detected in the replicas. Figure 1.41 is an electron micrograph of the specimen replicated at temperature. Figure 1.42 shows another area from the same specimen replicated after cooling. It was concluded that the platelet growths occurred during oxidation.

The formation of the platelet structure was also observed directly at temperature with a hot-stage microscope. Although the magnification and resolution of the microscope were not sufficient to permit the observation of very fine details, the progress of the reaction could be described as follows: A gradual darkening of scattered grains in the specimen occurred. As this darkening progressed, platelets became visible in other lighter grains. Some platelets definitely were nucleated at grain boundaries, while others seemed to develop wholly in situ and grew slightly in thickness as a function of time. As oxidation continued, the platelets frequently developed small, needle-like subplatelets. No detectable changes in surface topography occurred when the specimens were cooled to room temperature in vacuum.

Thus, hot-replication methods and hot-stage microscopy showed that the platelet structure originated during oxidation and not during cooling from the reaction temperature. It should be indicated that these specimens were all oxidized in air and that temperature control was poorer than with the standard apparatus; however, the morphology of these specimens compared favorably with that of the more carefully oxidized samples.

Fig. 1.41. Platelet Structure Existing on Oxidized Tantalum Surface Before Cooling from Reaction Temperature. Preannealed 1 hr at 1200°C; oxidized 1 hr at 400°C. Replicated at temperature; direct replica; 6800X.

3. Oxide morphology, 300–700°C. The first stages of tantalum oxidation were studied over the temperature range 300–700°C at 100° increments. Particular attention was paid to the initial oxidation behavior and its possible influence on the onset of blistering or rupturing of the oxide film.

Only the very initial stages of oxide formation occurred on specimens oxidized at 300°C for times varying up to 95 hr. In the electron

Fig. 1.42. Platelet Structure on Tantalum Surface After Cooling from Reaction Temperature. Preannealed 1 hr at 1200°C, oxidized 1 hr at 400°C. Replicated at room temperature; indirect replica; 9600X.

microscope, the oxide appeared as fine needles originating in the grain boundaries and extending into the grains along definite crystallographic directions. Figure 1.43 shows a typical electron micrograph of these grain-boundary growths. At 400 and 500°C, the growth process was similar, although the rate of oxidation was much increased, and prolonged oxidation at 500°C resulted in the formation of blister-like cracks in the oxide. Figures 1.44, 1.45, and 1.46 illustrate a typical sequence of

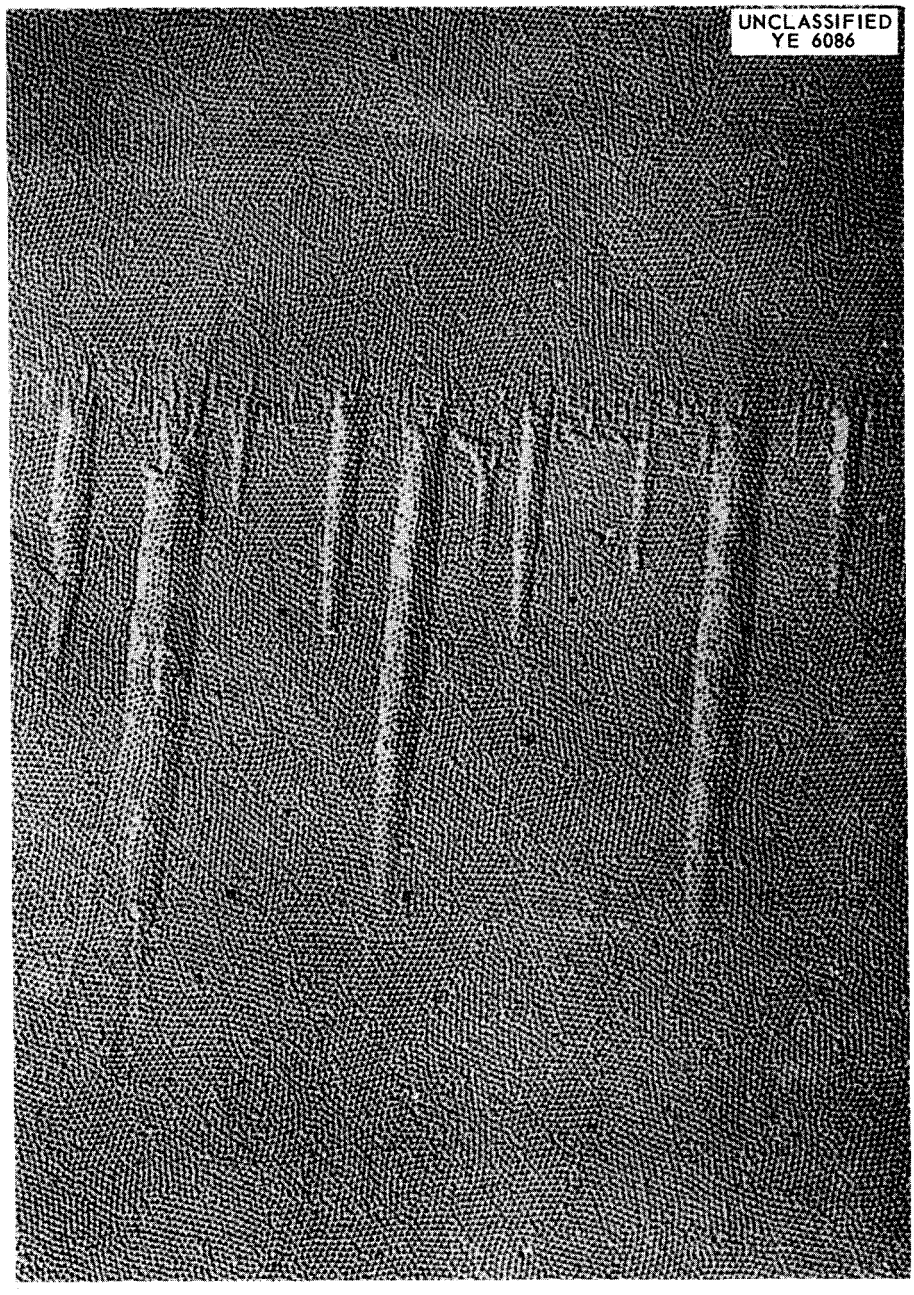

Fig. 1.43. Typical Grain-Boundary Platelet Growth on Tantalum Oxidized at Low Temperature. Note "bubble raft" background texture. Preannealed 1 hr at 1200°C; oxidized 95 hr at 300°C; indirect replica; 16,800X.

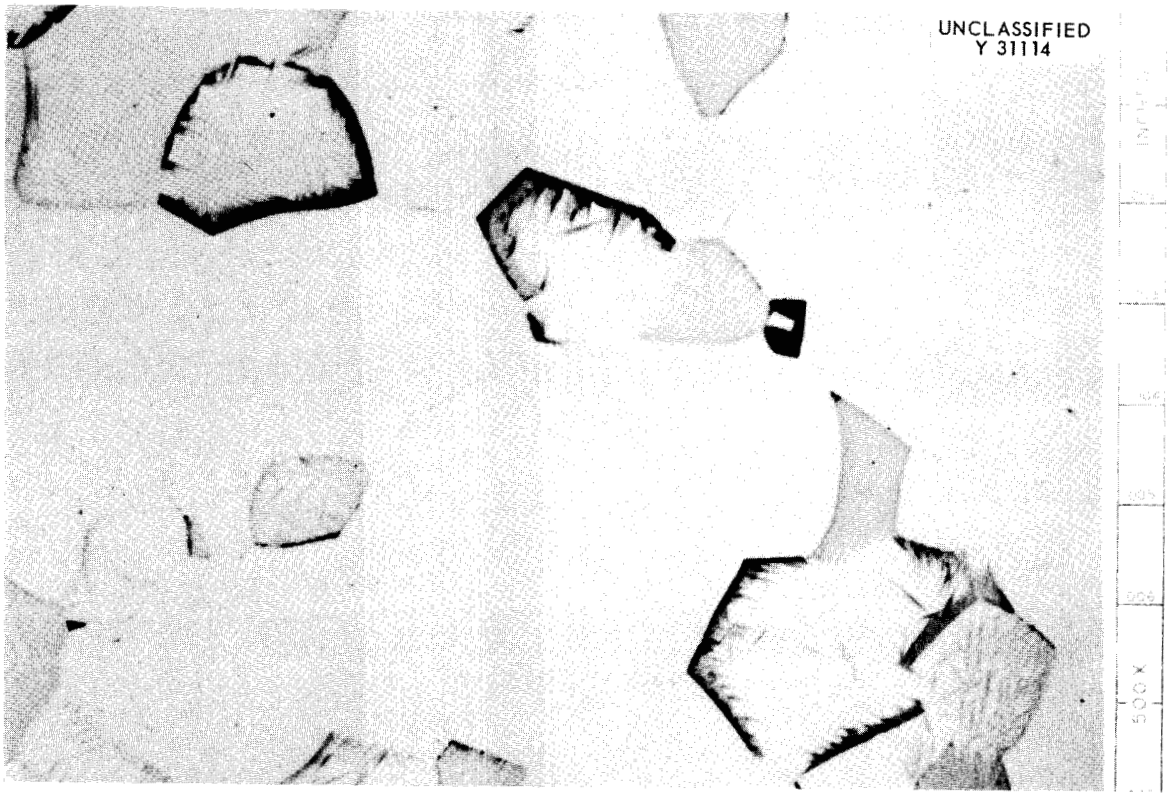

Fig. 1.44. Early Stage of Oxidization on Coarse-Grained Tantalum at 500°C. Preannealed 16 hr at 1200°C; oxidized 15 min at 500°C.

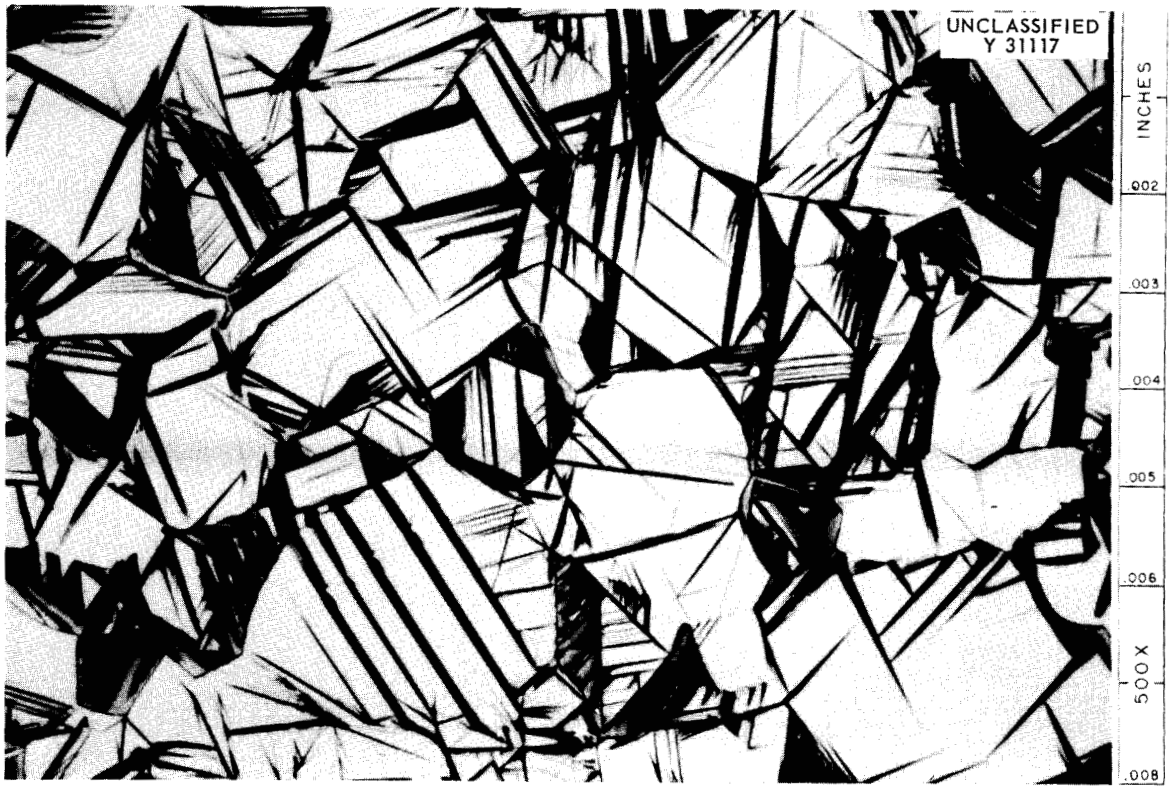

Fig. 1.45. Platelet Growth on Coarse-Grained Tantalum at 500°C. Preannealed 16 hr at 1200°C; oxidized 60 min at 500°C.

Fig. 1.46. Surface Structure of Tantalum After Period of Longer Oxidation at 500°C. Pre-annealed 1 hr at 1200°C; oxidized 5 hr at 500°C.

specimens oxidized at 500°C, and an example of crack formation in the oxide is shown in Fig. 1.47.

At 600°C a change in the oxide morphology was first observed. On some grains, nodular oxide growths were interspersed with platelets. In some instances the nodular growths showed crystallographic character and even the tendency to develop in the manner of a platelet. These characteristics are illustrated in Figs. 1.48-1.51. At 700°C, the nodular growth was even more pronounced, and the first stages of oxidation consisted almost entirely of nodular-type attack. Figures 1.52-1.54 illustrate these features.

These sequences of photographs also demonstrate the marked variation of the oxidation behavior of tantalum with crystallographic orientation. In many specimens, a grain which had progressed to the blister stage of oxidation was adjacent to grains which showed little or no evidence of oxide formation.

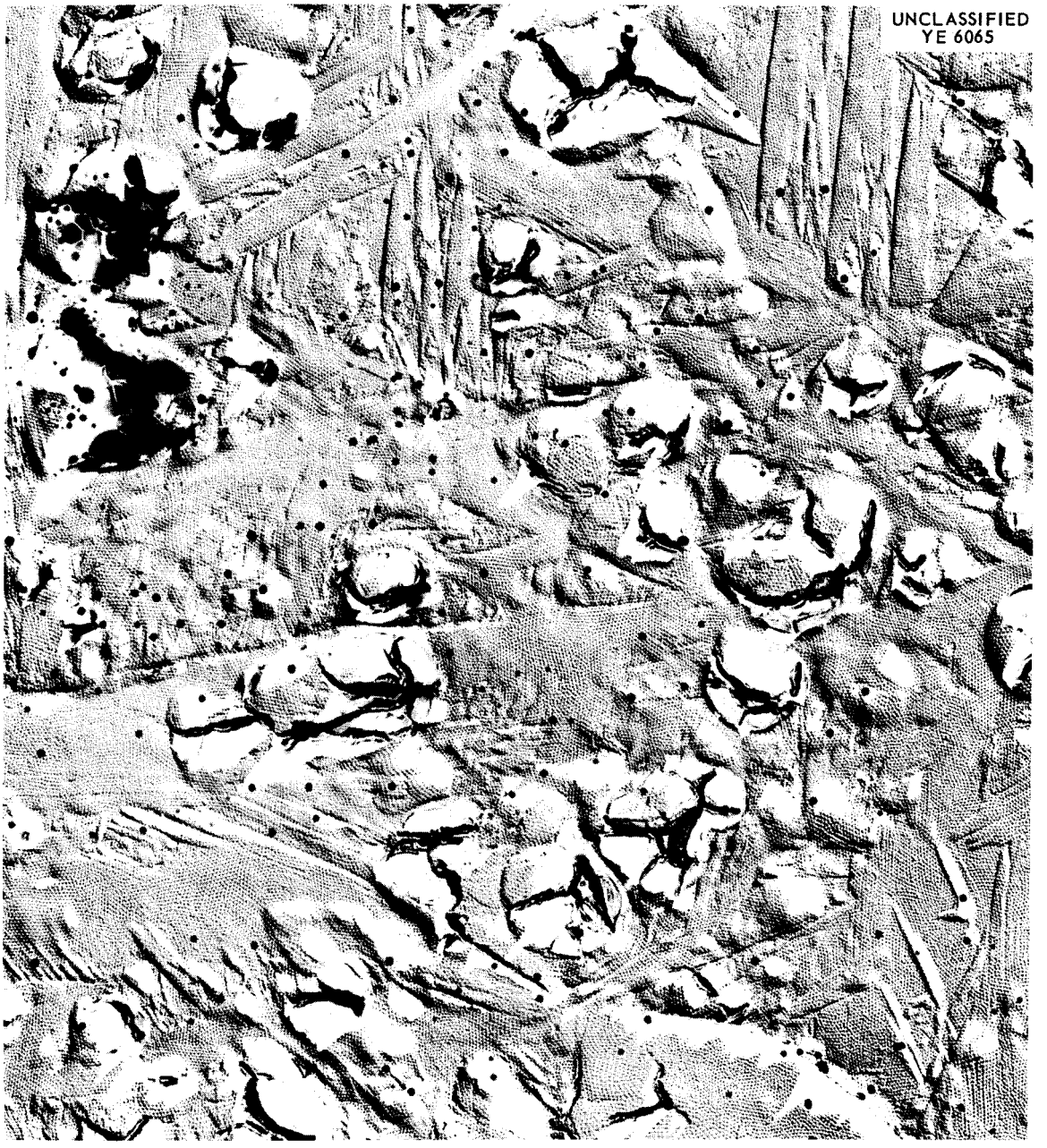

Fig. 1.47. Blisters Observed on Oxidized Tantalum Surface in Later Stages of Oxidation. Preannealed 1 hr at 1200°C; oxidized 7 hr at 500°C. Indirect replica; 9700X.

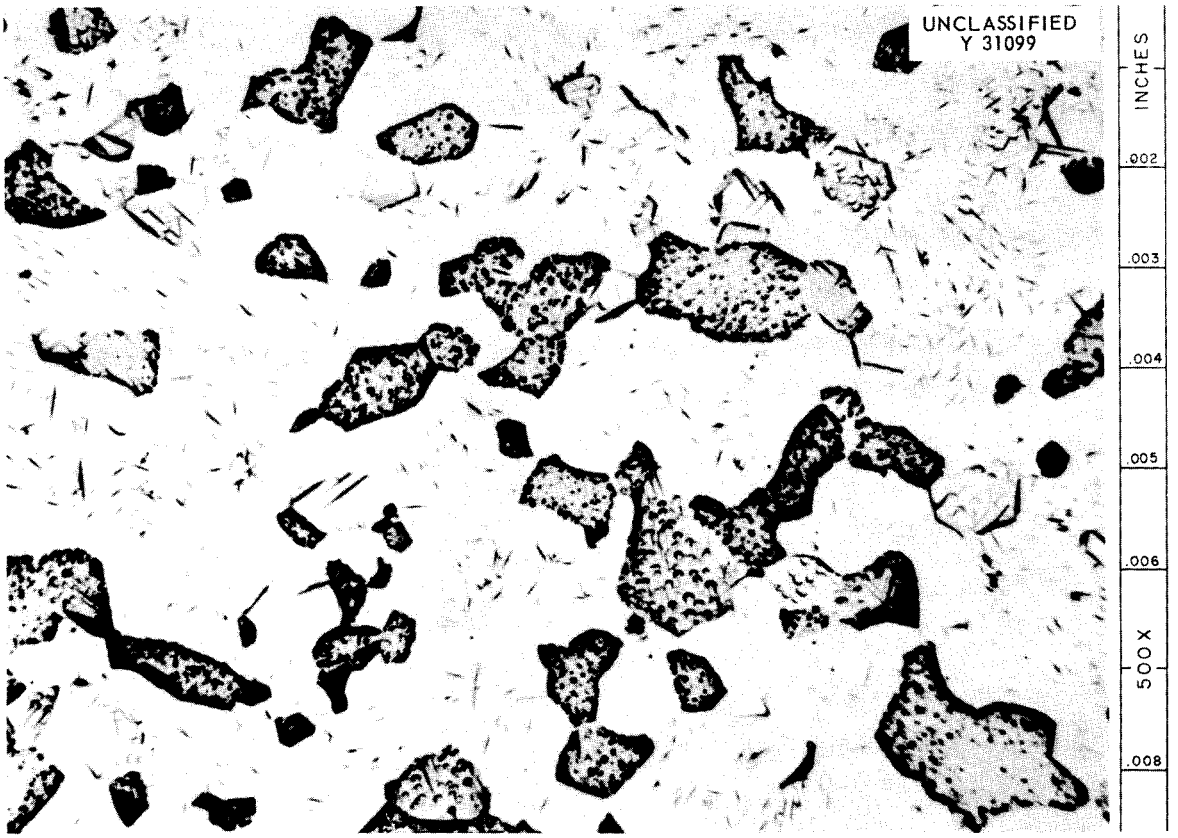

Fig. 1.48. Early Stage Platelet-Nodule Oxide Growth at 600°C. Preannealed 1 hr at 1200°C; oxidized 3 min at 600°C.

Fig. 1.49. Continuation of Platelet-Nodule Oxide Growth at 600°C. Preannealed 1 hr at 1200°C; oxidized 4 min at 600°C.

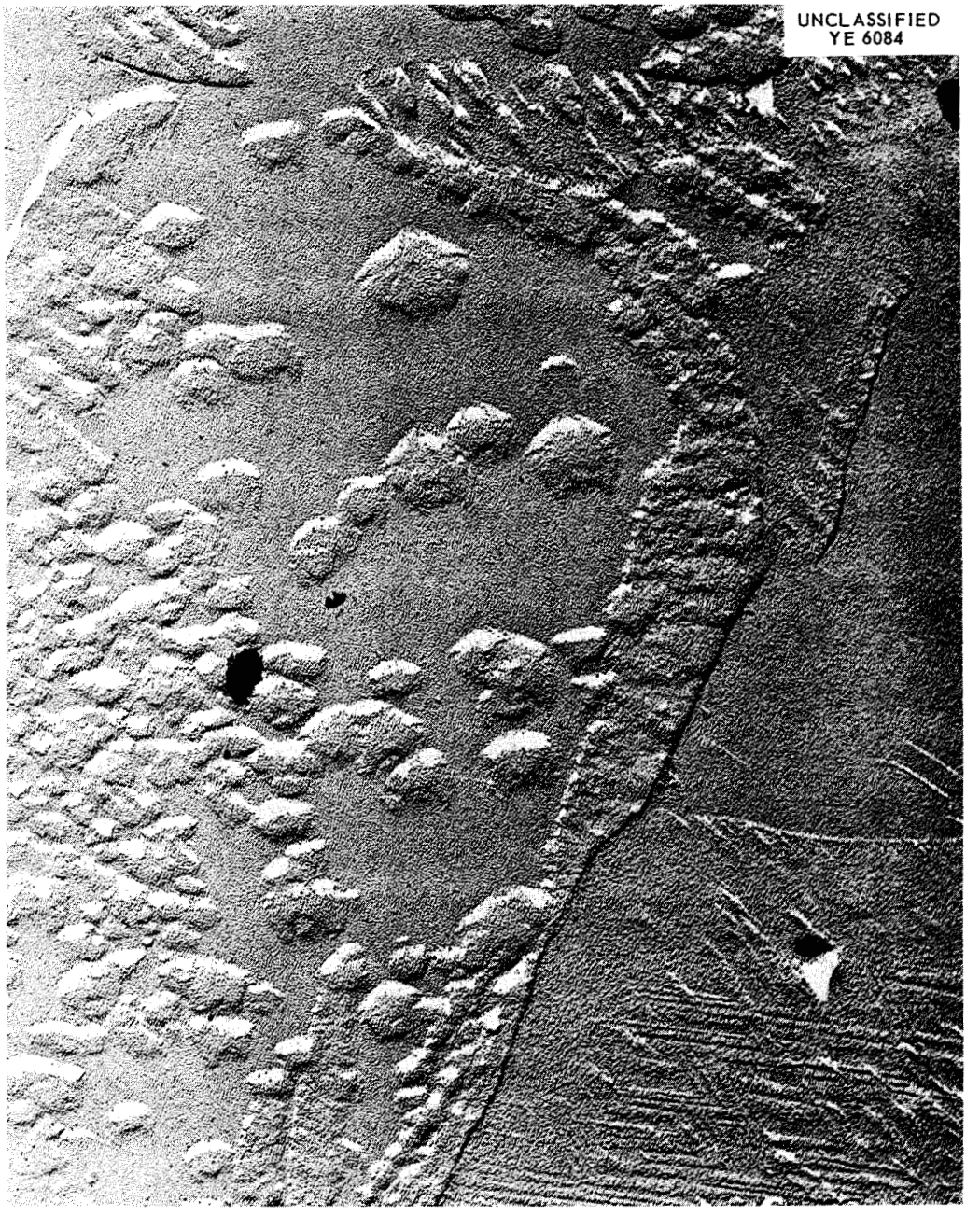

Fig. 1.50. Electron Micrograph of Nodular Growth on Tantalum at 600°C. Preannealed 1 hr at 1200°C; oxidized 1 min at 600°C. Indirect replica. 9700X.

Fig. 1.51. Electron Micrograph of Grain Showing Both Platelets and Nodules of Oxide. Pre-annealed 1 hr at 1200°C; oxidized 1 min at 600°C. Indirect replica. 6900X.

Fig. 1.52. Nodular Growths Appearing in First Stages of Oxidation at 700°C. Preannealed 16 hr at 1200°C; oxidized 6 to 10 sec at 700°C.

Fig. 1.53. Nodular and Platelet-Nodule Growth of Oxide at 700°C. Preannealed 1 hr at 1200°C; oxidized 6 to 10 sec at 700°C.

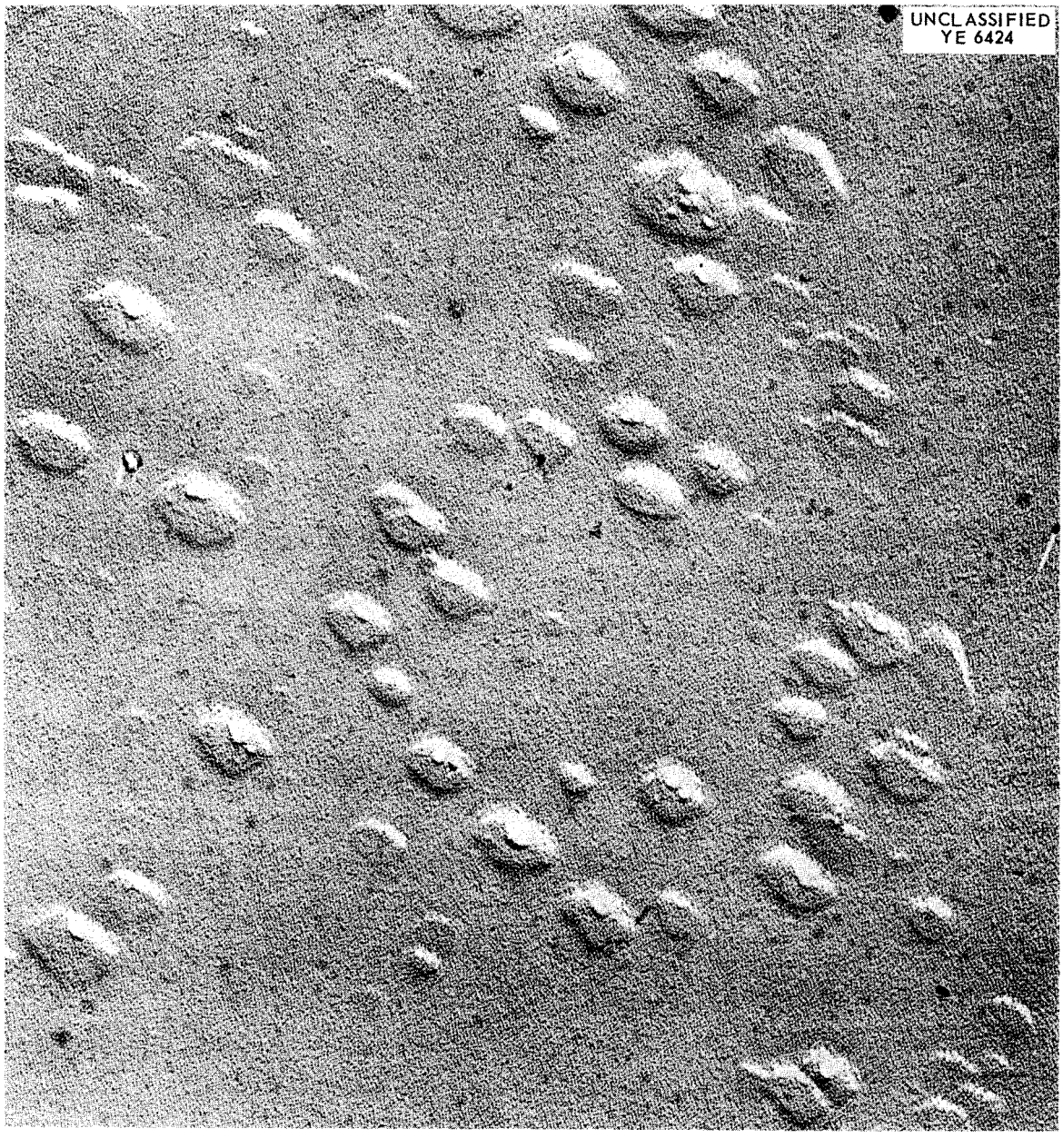

Fig. 1.54. Electron Micrograph of First-Stage Oxide Nodules Formed at 700°C. Preannealed 16 hr at 1200°C; oxidized 6 to 10 sec at 700°C. Indirect replica. 9600X.

Conclusions. — On the basis of these results, the following conclusions appear to be justified.

1. Oxide platelet formation on tantalum occurred at the temperature of oxidation and seemed to involve a type of precipitation process.

2. At lower temperatures, the nucleation of platelets occurred at grain boundaries, but at 600°C and higher, nodular growths were observed whose nucleation was not a grain boundary phenomenon.

3. Tantalum exhibited a pronounced dependence of oxidation rate on crystallographic orientation.

4. Some form of anion diffusion was shown to predominate in the oxide films during the protective stage of oxidation.

5. A correlation was established between the oxide morphology and the oxidation rate curves for tantalum. The occurrence of anion diffusion, the large oxide/metal volume ratio, and the geometry of the platelet and nodular growth forms in the oxide films suggested that these latter features should be centers of regions of stress in the oxide and, hence, preferred sites for crack formation in the oxide. Cracks were formed preferentially at nodular growths at 600°C and above. At lower temperatures, however, the correlation was more ambiguous; many of the cracks produced in regions of platelet growth were sufficiently large so as to encompass parts of several platelets.

THE EFFECT OF RADIATION ON THE OXIDATION OF METALS[90]

J. V. Cathcart

Two primary ways in which nuclear radiation might influence the gaseous oxidation of metals are (1) through a change in the total number of lattice defects in the oxide film, and (2) by the alteration of some nucleation step in the oxidation process. In instances where the oxide film formed on a metal is relatively thick and nonporous, the rate-determining step is usually the diffusion of lattice defects across the oxide film; thus, a significant increase in defect concentration should produce an increase in the rate of oxidation. With regard to the second effect, the

---

[90] This research was performed jointly with F. W. Young, Jr., of the Solid State Division.

formation of a crack or some other relatively gross discontinuity in the oxide film is usually associated with a nucleation process. Highly localized additions of energy to the oxide lattice might then be expected to trigger certain types of nucleation steps and again produce an increase in the oxidation rate.

These ideas were tested through a study of the in-pile oxidation of niobium. In the neighborhood of 400°C and in the absence of radiation, niobium initially forms a protective oxide film but, as oxidation proceeds, the protective character of the film decreases due to the formation of microscopic, blister-like cracks in the oxide.[91] Therefore, the in-pile oxidation of niobium in this temperature range permitted a study of the effect of radiation both on the oxidation rate of niobium and as a trigger for the nucleation of cracks in the oxide.

Electrolytically polished, polycrystalline niobium coupons[92] were oxidized in the ORNL Graphite Reactor at temperatures from 380 to 450°C and for times ranging from 1 to 6 hr. The fast neutron flux during oxidation was $\sim 10^{12}$ nv. After oxidation, the specimens were replicated and examined with an electron microscope. Both the time required for the initiation of blister formation and the blister density were essentially the same as reported previously[93] for out-of-pile experiments.

Possible changes in the rate of oxidation under irradiation were investigated by oxidizing a spherical single crystal of niobium in-pile. In the absence of radiation, a pattern of oxide interference colors, reflecting a variation of oxide-film thickness, formed over the sphere as a result of the marked variation in oxidation rate with crystallographic plane. Areas near the < 100 > poles oxidized most slowly, while the oxidation rate was a maximum at < 111 > and < 110 > poles. Because of a lack of information regarding the index of refraction of Nb_2O_5, no absolute thickness

---

[91] J. V. Cathcart, J. J. Campbell, and G. P. Smith, J. Electrochem. Soc. 105, 442–46 (1958); J. V. Cathcart, Met. Ann. Prog. Rep. Oct. 10, 1957, ORNL-2422, p 76–90 (classified).

[92] For specimen preparation and details of the oxidation apparatus, see Met. Ann. Prog. Rep. Oct. 10, 1958, ORNL-2632, p 63 (classified).

[93] J. V. Cathcart, Met. Ann. Prog. Rep. Oct. 10, 1957, ORNL-2422, p 76 (classified).

values could be assigned to these oxide films. However, after 1 hr at 400°C, third-order interference colors were evident around the < 111 > and < 110 > poles, while the < 100 > poles still exhibited first-order colors. This same pattern was observed when the crystal was oxidized in-pile; therefore, it was concluded that the radiation had not significantly altered the rate of oxidation.

A similar set of in-pile experiments was performed with polycrystalline zirconium specimens. Samples were oxidized for 2 hr at temperatures from 450 to 500°C. Again, however, electron microscopic examination revealed no differences between specimens oxidized in-pile and those oxidized in the absence of radiation.

Discussion. – In attempting to evaluate the essentially negative results described above, it is necessary to ascertain whether the neutron flux was sufficiently high to have a measurable effect on the oxidation process. A precise determination of the change in defect concentration in the oxide film as a function of neutron flux would require a knowledge of the normal defect concentration in the film in the absence of radiation. This latter quantity is not available, but an order-of-magnitude estimate of the changes to be expected as a result of neutron bombardment may be obtained in the following way. Assume that each neutron produces 10 defects/cc of oxide[94] and that each defect contributes to the oxidation process. Then for a niobium oxide film 5000-Å thick and growing at a rate of 10 Å/hr and for a flux of 10^{12} nv, approximately 2×10^{11} defects$\cdot$hr$^{-1}\cdot$cm^{-2} could be formed in the film. However, the stipulated growth rate requires the addition to the film of $\sim 10^{16}$ oxygen ions$\cdot$hr$^{-1}\cdot$cm^{-2} and, hence, the generation of $\sim 10^{16}$ defects$\cdot$hr$^{-1}\cdot$cm^{-2}. It is to be expected, therefore, that exposures to fluxes of the order of 10^{15}–10^{16} nv would be required before the oxidation rate could be changed appreciably as a result of a shift in defect concentration. These calculation have been based on 5000-Å films, since it is at this approximate thickness that crack formation is initiated in the oxide.

In a similar manner, a rough estimate of the number of localized regions of disorder introduced into the film by neutron bombardment may also

---

[94] F. Seitz and J. S. Koehler, Solid State Physics 2, 307 (1956).

be obtained. Assume that 10^{-1} such regions are created per cubic centimeter of oxide per unit of flux.[94] Then a flux of 10^{12} nv would produce $\sim 2 \times 10^{10}$ regions of disorder per square centimeter of a 5000-Å film in 1 hr. The maximum number of blister-like cracks usually observed on niobium oxide films, however, is only $\sim 10^7/cm^2$ and the density of other types of oxide nuclei generally ranges from 10^7 to $10^{10}/cm^2$.

It was therefore concluded that extremely high neutron fluxes would be required to produce a measurable effect on the oxidation rate of metals as a result of changing the defect concentration in the oxide film. On the other hand, a neutron flux of only 10^{12} nv could in 1 hr generate potential nucleation sites in the oxide in numbers at least of the same order of magnitude as the number of nuclei normally found in oxide films. However, the results obtained with niobium and zirconium suggest that the nucleation processes in the oxidation of these metals is not affected by nuclear radiation. Further experiments will be required to determine the applicability of these results to other metal-oxide systems.

OXIDATION STUDIES ON COPPER

J. V. Cathcart W. O. Harms

Studies designed to characterize thin oxide films on various crystallographic planes of copper single crystals have been continued. The research has been confined to three major areas: an investigation of the apparent optical anisotropy of thin Cu_2O films, the development of a chemical method for the determination of the thickness of such films, and an x-ray diffraction study of strain distribution in thin Cu_2O films. The last area was undertaken in cooperation with the Microstresses in Crystals Group of the Metallurgy Division and is described elsewhere in this report.

The crystal lattices for both copper and Cu_2O are cubic, and, consequently, an optical method[95] involving the use of a polarizing spectrometer should be applicable in the determination of oxide film thicknessess on copper. This technique has for some time been used with

---

[95] O. Kubaschewski and B. E. Hopkins, Oxidation of Metals and Alloys, p 106-10, Academic Press, New York, 1953.

success for very thin Cu_2O films, but recently it was found that at least for films 200 to 800 Å thick formed at 250°C, significant variations in apparent oxide thickness were obtained, depending on the orientation of the specimen relative to the plane of incidence of the polarizing spectrometer. A typical plot of apparent film thickness as a function of the angle of rotation about the normal to the specimen surface is shown in Fig. 1.55. The periodic variation of the thickness measurements is apparent from the graph, 90° of rotation separating maxima and minima.

These data were taken with an oxide film formed on the (110) of a copper crystal. The oxide film was itself a pseudo single crystal, and the epitaxial relationship between oxide and metal is such that the crystal lattices are parallel to one another. It was found that the maxima in the thickness curve occurred when a [110] direction lay in the plane of incidence. The minima corresponded to those orientations for which a [100] direction lay in the plane of incidence.

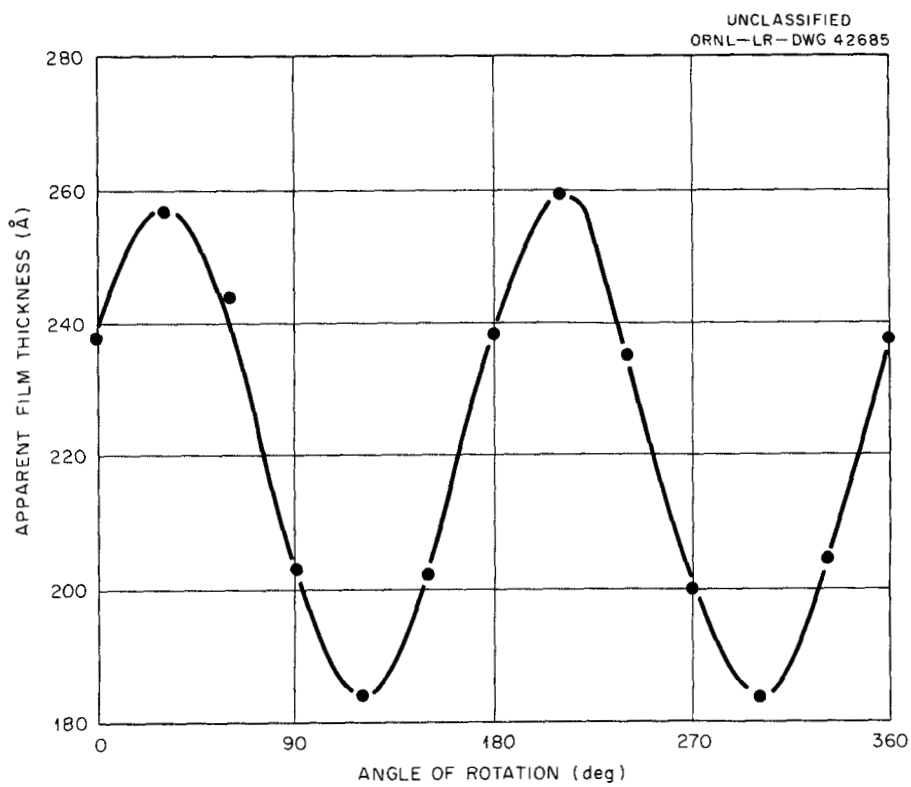

Fig. 1.55. The Variation of Spectrometer Thickness Measurements as a Function of the Angle of Rotation of the Specimen About the Normal to the Specimen Surface.

It would appear that the optical anisotropy exhibited by the oxide films may be related to the lattice distortions detected in these films by the x-ray diffraction studies mentioned above. While the full significance of the results is not understood, it is felt that further investigations may produce useful data relative to strain, and possibly, defect distribution in the films.

An analytical method is being developed whereby thin Cu_2O films can be dissolved either directly or after electrolytic stripping and analyzed for copper content. The information so derived could be used in at least two ways: (1) to determine the thickness of cuprous oxide films formed under various conditions of time and temperature, and (2) to investigate the validity of the electrolytic stripping procedure used in connection with previous electron optical studies of the films.[96] To date only tentative results have been obtained, but these preliminary studies indicate that the method shows promise as a useful tool in thin-film research.

The solvent for the oxide films is freshly de-aerated 0.01 M ethylenediamine solution. In the absence of dissolved oxygen, the ethylenediamine forms a chelated complex with the copper of the oxide films but does not react with the copper substrate. The solution is then analyzed spectrophotometrically by a method described by Smith and McCurdy[97] in which the specific complexing reagent is 2,9-dimethyl-1,10-phenanthroline and for which the limit of detection is 0.04 μ of copper per milliliter. The experimental technique was suggested by methods developed by L. H. Jenkins[98] of the Solid State Division, ORNL, whose assistance in this research is gratefully acknowledged.

---

[96] J. V. Cathcart, Met. Ann. Prog. Rep. Oct. 10, 1958, ORNL-2632, p 60 (classified).

[97] G. F. Smith and W. H. McCurdy, Anal. Chem. 24, 371–73 (1952).

[98] L. H. Jenkins and F. W. Young, Jr., J. Electrochem. Soc. (in press).

FUNDAMENTAL CERAMIC STUDIES

G. W. Clark

CRYSTAL PHYSICS

G. W. Clark O. C. Kopp[99]

To use more skillfully the currently available ceramic materials and to aid in designing special properties into new ceramics, basic scientific information is seriously needed. In order to characterize unambiguously certain physical phenomena associated with transport, magnetic, mechanical, and optical properties of many materials, the utilization of single crystals is required. The mechanisms of crystallization have proved difficult to establish. In fact, the significance of defect structure in crystal growth and its influence on physical properties has only recently been recognized. The availability of macroscopic single crystals of high-melting-point ceramics is almost nil.

It is the aim of this program to explore methods for growing ceramic-type crystals, to study the defect structure of the crystals, and to study the magnetic properties of certain of these crystals.

Major attention has been directed toward preparing the laboratory space and equipment for growing crystals. A hydrothermal autoclave has been constructed and is in operation. In addition, the following systems are in varying stages of completion: a flame fusion furnace, a constricted-arc furnace, and an arc-image furnace. Also being built is an apparatus which will permit the investigation of crystal growth from fused halide solutions.

The hydrothermal system has as its upper design limit 650°C and 1200 atm. In anticipation of studying acidic systems, especially those with the fluoride ions, one autoclave was fabricated from INOR-8.

In order to adjust the hydrothermal system, single crystals of quartz (SiO_2) were grown according to the method described by A. C. Walker.[100] A basket of nutrient quartz was placed at the bottom of an

---

[99] Summer research participant from University of Tennessee.

[100] A. C. Walker, Ind. Eng. Chem. 46, 1670–76 (1954).

autoclave and covered with a baffle. Quartz seed-plates were suspended above the basket, and the autoclave was filled to 80% of its free volume with 0.5 N NaOH. The sealed autoclave was placed in a furnace and the temperature controlled so that the nutrient region was at 410°C and the seed region at 390°C. Under these conditions the estimated internal pressure was 1200 atm.

When, after seven days, the autoclave was opened, the original 1-mm-thick seed-plates had grown to a thickness of 7 to 9 mm. Thus, the average growth rate was 1 mm/day (about 80% of the optimum rate reported by Walker).[100]

Upon the successful completion of this preliminary test, attention was given to the problem of growing quartz hydrothermally under retrograde conditions. For most conditions of temperature and pressure, the solubility of SiO_2 in water increases with the temperature; however, in the region between 150 and 600 atm, and above the critical temperature for water, the solubility is a negative function of temperature[101] (that is, retrograde conditions exist). Even though unfavorable results were reported in previous attempts[102] to grow quartz crystals under retrograde conditions, the potential advantages of working in this pressure-temperature region appeared to warrant further experimental efforts in this area.

Preliminary experiments were successful. Best results to date were obtained when the autoclave was filled to 40% of its free volume with 0.1 N NaOH and with the seeds being located in a region having an indicated temperature 5°C above that of the nutrient, which was controlled at 410°C. The estimated internal pressure was 350 atm.

In one of the first experiments, quartz single-crystal whiskers (confirmed by x ray) were grown on the seed support. In subsequent runs, two minerals, tentatively identified as acmite and osannite (both sodium-iron silicates), were synthesized. Additional work, designed to confirm these results, is in progress.

---

[101] G. C. Kennedy, Econ. Geol. 45, 629–53 (1950).

[102] A. C. Walker, J. Am. Ceram. Soc. 36, 250–56 (1953).

A second hydrothermal furnace has been completed and will be used in an attempt to grow MgO crystals.

The second phase of this program will include studies of crystal perfection, growth mechanisms, and specific physical properties relating to magnetic behavior. In cooperation with the X-Ray Group of the Metallurgy Division, a double crystal spectrometer is now being set up. With this spectrometer and by other means, crystal perfection will be evaluated.

Part II

HRP METALLURGY

HRP METALLURGY

G. M. Adamson, Jr.
M. L. Picklesimer E. S. Bomar, Jr.
S. G. Nelson F. W. Cooke
P. L. Rittenhouse W. J. Leonard
R. L. Stephenson J. J. Prislinger
C. H. Wodtke

INTRODUCTION

The principal responsibility of the Homogeneous Reactor Metallurgy Section is to furnish metallurgical assistance to the Homogeneous Reactor Project. The Project is attempting to develop an aqueous homogeneous power reactor[1] which is also capable of breeding uranium from thorium. The fuel is an acidified solution of uranyl sulfate and the thorium is used in the form of a thoria slurry. The Project has built and is now operating its second experimental reactor which is known as the Homogeneous Reactor Test (HRT).

The majority of the metallurgical problems in this system arise from the use of a zirconium alloy as a core vessel which separates the uranyl sulfate core solution from the thoria blanket slurry. This member must have a low thermal-neutron cross section, be corrosion resistant to both uranyl sulfate and to thoria slurry under radiation, and act as a pressure vessel at 300°C. A zirconium alloy is the only material that appears possible for such a use. Zircaloy-2 is satisfactory for the lower-power, short-lived experimental reactors; but, from a corrosion-resistant standpoint, it is marginal for the proposed large-power reactors.

The external reactor system would most likely be constructed from type 347 stainless steel, with the reactor itself being made from a type 347 stainless-steel-clad—pressure-vessel steel. These conventional engineering materials offer no serious metallurgical problems other than those likely to be encountered in the fabrication of any complex structure. Type 347 stainless steel offers corrosion problems, and some metallurgical studies have been made on the possibilities of using a titanium alloy for the external system or for selected portions of it.

---

[1]J. A. Lane, H. G. MacPherson, and F. Maslan (eds.), Fluid Fuel Reactors, p 11, Addison-Wesley, Reading, Mass., 1958.

HRT METALLURGICAL RESEARCH

Examination of Samples and Components Removed from the Homogeneous Reactor Core

M. L. Picklesimer
P. L. Rittenhouse R. L. Stephenson

At the conclusion of run 17, the core of the homogeneous reactor was opened for an examination and for the removal of the mechanical-property—corrosion samples which had been exposed during the run.[2] The samples had been suspended on an A55 titanium holder,[3] with six samples at each of four positions. The holder had extended up into the neck region (outlet) of the reactor, and 24 samples had also been exposed there. A third array of 24 samples had been exposed in the blanket region. The samples were subsize multiple-break tensile and impact samples which also served as corrosion samples. The materials tested included Zircaloy-2, zirconium alloys, various alloys of titanium, austenitic stainless steels, and welds of Zircaloy-2 and type 347 stainless steel. On removal, only two of the 24 core samples remained on the holder, with many of the others visible on the top screen. The holder itself contained three holes and showed areas that appeared to have melted.

The Zircaloy-2 screens welded inside the lower core also had been changed. The top screen contained holes caused by missing ligaments, and most of the surface showed considerable attack. An apparatus was developed by the Reactor Experimental Engineering Division, and disks 2 in. in diameter were cut from the center of the six top screens.

The core holder, the core samples that had been recovered, and the screen disks were turned over to Metallurgy for examination. The examination, macroscopic and microscopic, was made in the hot cells of the Solid State Division with the assistance of their personnel.

Sections cut from the specimen holder were examined macroscopically and metallographically for evidence of damage. In all, three sections

---

[2]S. E. Beall et al., HRP Quar. Prog. Rep. Oct. 31, 1958, ORNL-2654, p 3–13.

[3]R. M. Warner et al., HRT Corrosion Specimens and Holder: Core Region of Pressure Vessel (Loading No. 1), ORNL CF-58-7-68 (Aug. 15, 1958).

from the highest-flux regions, stations F, G, and H, and one from the low-flux neck region, station D, were carefully examined for evidence of surface attack, for changes in microstructure, and for hydrogen-deuterium contents.

It was concluded that the holes in the web were "melted" through by an external heat source,[4,5] that the spike tip and specimen support brackets were "burned" off in a similar fashion, that the pits observed were formed by corrosive attack, and that the "burning" of the titanium was not caused by the reaction of the titanium with its environment but was the result of an external heat source heating the titanium to or above its melting point. The high-temperature reaction of titanium and the fuel solution or steam was not self-sustaining and quenched out once the external heat source was removed. It was further concluded that a similar event would have occurred regardless of the metal used for the construction of the specimen holder. The heat source was undoubtedly a concentration of uranium caused by the shape of the holder. Such a concentration could be caused either by hot spots and resulting second-phase formation caused by poor cooling or by stagnant solution in eddies or pockets. Once such reactions start they would very rapidly result in very high temperatures. In all cases the reactions were very brief and were probably quenched as soon as the melting changed the flow pattern.

Specimens of Zircaloy-2 and Ti-A40 (ref 6) were among those suspended on the holder. Three of the Zircaloy-2 and one of the Ti-A40 multiple-tensile specimens were recovered from the top screen after the run and were examined macroscopically and metallographically.[7] All except the titanium specimen contained defects of a size that prevented obtaining mechanical-property data.

---

[4]J. C. Griess et al., HRP Quar. Prog. Rep. Apr. 30, 1959, ORNL-2743, p 103–8.

[5]H. C. Claiborne, Hole Formation in HRT Core Tank, ORNL CF-58-11-49 (Dec. 4, 1958).

[6]R. M. Warner et al., HRT Corrosion Specimens and Holder: Core Region of Pressure Vessel (Loading No. 1), ORNL CF-58-7-68 (Aug. 15, 1958).

[7]G. M. Adamson et al., HRP Quar. Prog. Rep. Apr. 30, 1959, ORNL-2743, p 168–80.

The conclusions drawn were that the damage to the Zircaloy-2 and Ti-A40 tensile specimens examined was caused by the "burning" of the titanium specimen holder on which they were assembled, that the duration of the "burning" events was not more than a few seconds, and that the "burning" reaction of the specimens was not self-sustaining, quenching out once the external heat source was removed.

Cross-section metallography of the Zircaloy-2 screen specimens and of a section of scrap trimmed from one of the screens before installation in the core tank has shown that the exfoliation of the surfaces during exposure in the reactor was caused primarily by an enlargement of defects in the material as installed. Cold working, cracking, and intermettalic stringers were present in the screens, as fabricated. The cold working and cracking were caused primarily by the punching operation used for forming the holes. Thermal cycling, corrosion in cracks extending to the surface of the holes, and local boiling in a crack can explain the exfoliation.

The major conclusions reached were: (1) the "hot spot" observed on the top screen specimen was caused by contact with the "burning" tip of the Ti-A55 specimen holder; (2) the reaction of the Zircaloy-2 screen with its environment ceased as soon as the external heat source was removed, quenching out very rapidly; (3) none of the other portions of the top screen nor those from any of the other screen specimens showed any evidence of having been at a temperature higher than 550–600°C during reactor operation (as yet no samples have been removed from areas near the wall); (4) all the screen specimens showed a cold-worked, cracked, and stringered microstructure, indicative of cold working during the punching of the holes in the screens; and (5) the exfoliation of the surfaces observed on all screen specimens was caused by enlargement of cracks formed during the punching of the holes.

The metallographic examination of samples and debris removed from the core of the Homogeneous Reactor Test has explained much of what happened during operation of the reactor and allayed the fears which had arisen concerning the use of zirconium and titanium under such conditions. While many areas were found in which "burning" or melting of these metals

had occurred, in all cases the reaction had been quenched out and appeared to have been started by an external heat source. It seems very likely that, locally, the temperatures were sufficiently high so that the more conventional structural materials would also have melted. It is assuring that in spite of considerable molten metal being present, no evidence of a self-sustaining reaction was found even with these active metals. The reactions that did occur were not of sufficient magnitude to require shutdown of the reactor.

PHYSICAL METALLURGY

M. L. Picklesimer
S. G. Nelson P. L. Rittenhouse
R. L. Stephenson

Zirconium Alloy Development

Zirconium-niobium-X alloys have shown promise in having an in-pile corrosion resistance superior to that of Zircaloy-2 in aqueous uranyl sulfate fuel solutions. An alloy development study has been under way for the past several years with the major objective of developing such a zirconium-base alloy as an engineering material for the construction of the core tank of the reactor vessel. The study has required the determination of the physical metallurgy of the alloy systems, and the prior work has been reported elsewhere.[8-10]

The metastable transformation, in quenched and reheated samples, of the retained high-temperature β phase to $\omega + \beta$ phase enriched in niobium has been studied in considerable detail by the use of single-crystal rotation x-ray diffraction techniques; details of the study are reported by

---

[8]M. L. Picklesimer et al., Met. Ann. Prog. Rep. Oct. 10, 1957, ORNL-2422, p 117; Oct. 10, 1958, ORNL-2632, p 67–70 (classified).

[9]G. M. Adamson et al., HRP Quar. Prog. Rep. Oct. 31, 1956, ORNL-2222, p 114–16; Jan. 31, 1957, ORNL-2272, p 119–23; Apr. 31, 1957, ORNL-2331, p 124–28; July 31, 1957, ORNL-2379, p 122–26; Oct. 31, 1957, ORNL-2432, p 131–33; Jan. 31, 1958, ORNL-2493, p 141–43; Apr. 30 and July 31, 1958, ORNL-2561, p 245; Oct. 31, 1958, ORNL-2654, p 188.

[10]H. L. Yakel, "Aging Transformations of Zirconium-Niobium Alloys," Part I of this report.

H. L. Yakel in another section of this report.[10] The specimens were 0.010-in.-dia wires formed from large-grained sheet by filing and chemical polishing. The transformation on aging of retained β at less than 525°C has been found to occur by the formation of the hexagonal metastable ω phase, containing approximately 5–6% niobium, and a body-centered cubic β phase which is progressively enriched in niobium with increased aging time at temperature. The composition of the ω phase does not change after the quenched-in ω phase has aged for a few minutes, but the volume of ω phase present increases progressively with aging time. The composition of the enriched β phase, however, changes progressively with aging (and the volume present decreases) to higher and higher niobium contents until, eventually, at about 45% niobium, the α phase and the equilibrium niobium-rich phase are precipitated simultaneously. The latter coprecipitation has not been observed after three weeks of aging at 400°C but has been observed in one day of aging at 500°C.

When the β Zr–Nb-X alloys are rapidly quenched to below 200°C, a martensitic Widmanstätten-type phase forms on the (100) planes of the retained β matrix. The Widmanstätten phase will revert without decomposition to the original β phase on reheating to 250°C or above. It was reported previously that the Widmanstätten phase had been identified as a body-centered tetragonal phase with the c axis in a [100] direction. Recent studies with a specimen cut from a Zr–15% Nb–5% Mo alloy sheet in which only one (100) trace could be found in each grain have shown that the Widmanstätten phase is actually monoclinic ($\alpha = 85°$), such that only a 5° distortion is required of the unit cell of the original identification of body-centered tetragonal. The formation of α from ω has not yet been shown to be the sequence of transformation, the data obtainable to date being too inconclusive for the determination.

Recent determinations of the aging behavior of the binary and ternary alloys at temperatures intermediate to those previously studied have caused only minor revisions of the time-temperature-transformation diagrams previously prepared. The determinations have also shown that relatively minor amounts of cold working (10% and less of cold reduction) decrease appreciably the incubation time for the formation of ω phase.

Zircaloy-2 Fabrication Study

The principal applications of Zircaloy-2 have been as cladding of fuel elements and as tubing for the water-cooling of reactors. Only limited use has been made of the alloy for other engineering applications, for example, in the construction of the core tank of the homogeneous reactor. No effort has been made to use the alloy as a general engineering construction material.

The effects of the fabrication variables on the preferred orientation and the anisotropy of the mechanical properties of Zircaloy-2 are being investigated in order to better understand the properties and textures observed and to obtain the background information necessary for the prediction and control of texture. Control of texture, and thereby the anisotropy of mechanical properties, may be as important, if not more so, as the randomization of texture in the material for use as pipe and tubing, in spherical and cylindrical pressure vessels, and in certain forming operations.

Fabrication variables which have been considered are: rolling and forging temperatures, final and intermediate annealing temperatures, cross rolling, reduction between anneals, and final reduction. The effects of these variables have been studied by standard tensile tests, by impact energy tests, by determination of the preferred orientation with x-ray diffraction techniques, and by a newly developed axial strain—contractile strain analysis. Data obtained in the standard tensile tests have not shown differences between fabrication schedules sufficient to determine the effect of any specific variable.[11,12] The tensile- and yield-strength values for the longitudinal specimens for 18 fabrication schedules fell within bands of 10,000 psi, showing the difficulty of this type of analysis. As will be shown, differences do, however, exist and may be revealed by other tests.

Preliminary examination of the cross sections of fractured tensile specimens showed that the originally circular specimen cross sections became elliptical during straining and that the degree of ellipticity seemed

---

[11] G. M. Adamson et al., HRP Quar. Prog. Rep. Oct. 31, 1958, ORNL-2654, p 184–85.

[12] G. M. Adamson et al., HRP Quar. Prog. Rep. Apr. 30, 1959, ORNL-2743, p 182–91.

to be characteristic of both the particular fabrication schedule and the specimen orientation in the plate. Optical comparator measurements of the cross sectional diameter of the specimens every 5° of rotation at several points between the fracture and the shoulder have proved that the cross sections are truly elliptical wherever plastic flow has occurred. Measurements of the elliptical cross sections of specimens from 18 fabrication schedules have shown that the contraction strain for each of the major and minor axes of the ellipse of cross section is a linear function of the axial tensile strain, at all points along fractured specimens whose axes lie on the principal deformation directions. The functional relationships can be evaluated by using the rolling, transverse, and normal directions for the plate or sheet as reference axes x, y, and z and conventional three-dimensional vector notation for the natural strains, as shown in Fig. 2.1. In each case, regardless of the orientation of the specimen axis, the axial tensile natural strain is defined as $\bar{\epsilon}_{ii}$, and the contraction natural strains as $\bar{\epsilon}_{ij}$ and $\bar{\epsilon}_{ik}$. The axial and contractile strains are related by a linear function which can then be expressed as

$$\bar{\epsilon}_{ij} = k_{ij}\,\bar{\epsilon}_{ii} \quad , \tag{1}$$

and

$$\bar{\epsilon}_{ik} = k_{ik}\,\bar{\epsilon}_{ii} \quad , \tag{2}$$

where k_{ij} and k_{ik} are the respective slopes of the strain-strain plots.

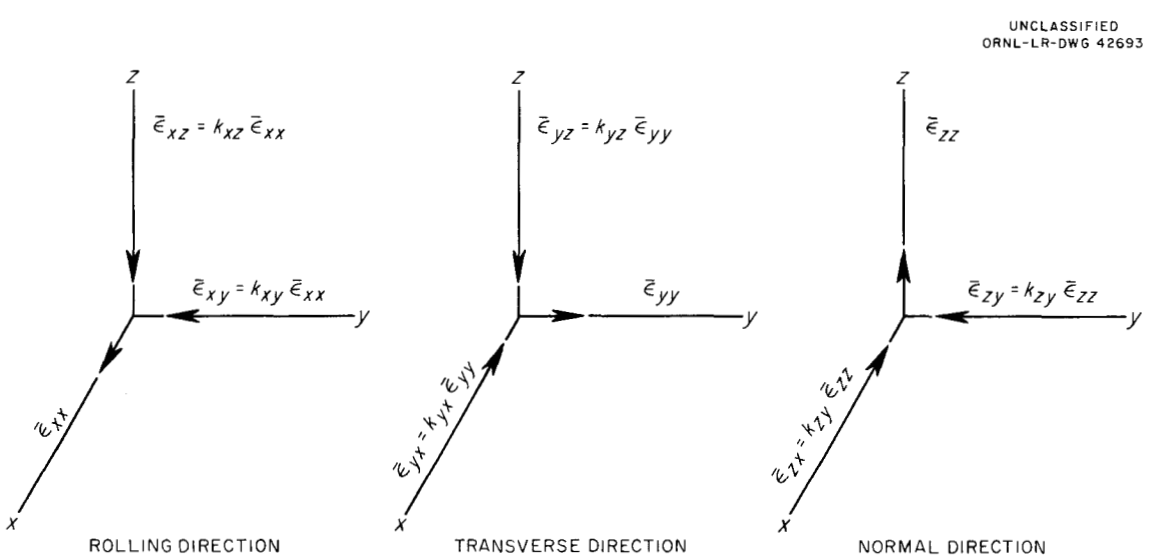

Fig. 2.1. Coordinate Systems for Tensile Axes.

For an isotropic material,

$$\bar{\epsilon}_{ij} = \bar{\epsilon}_{ik} = \frac{-\bar{\epsilon}_{ii}}{2} , \tag{3}$$

and

$$k_{ij} = k_{ik} = -0.5 \quad . \tag{4}$$

Such a relationship would be the limiting case for Zircaloy-2 and as the values approach 0.5 it would become more nearly isotropic.

Values for k_{xy}, k_{xz}, k_{yx}, and k_{yz} can be determined experimentally from fractured tensile specimens with axes in the rolling and transverse directions. In order to determine the strain behavior of a specimen with an axis in the normal direction of the plate, for example, to calculate k_{zx} and k_{zy}, it is necessary to establish at least two relationships between the k values. Since the volume of the specimen remains constant during plastic flow,

$$\bar{\epsilon}_{ii} + \bar{\epsilon}_{ij} + \bar{\epsilon}_{ik} = 0 \quad . \tag{5}$$

Substituting from Eqs. (1) and (2), for $\bar{\epsilon}_{ij}$, $\bar{\epsilon}_{ik}$, then

$$k_{ij} + k_{ik} = -1 \quad . \tag{6}$$

It is also possible to show that[13]

$$\frac{k_{xy}\ k_{yz}\ k_{zx}}{k_{xz}\ k_{yx}\ k_{zy}} = 1 \quad . \tag{7}$$

The values of k_{zx} and k_{zy} may be calculated by using Eqs. (6) and (7). Strain-strain plots for four experimental fabrication schedules are shown in Fig. 2.2 with the predicted strain behavior for the normal-direction specimens. The details of the fabrication schedules are presented in Table 2.1. Similar plots have been made for a total of 18 fabrication schedules and have shown that the k values are specific for each schedule and appear to be related to the preferred orientation and mechanical anisotropy in the material.

---

[13]R. Hill, Proc. Roy Soc. (London) 193, 281–97 (1948).

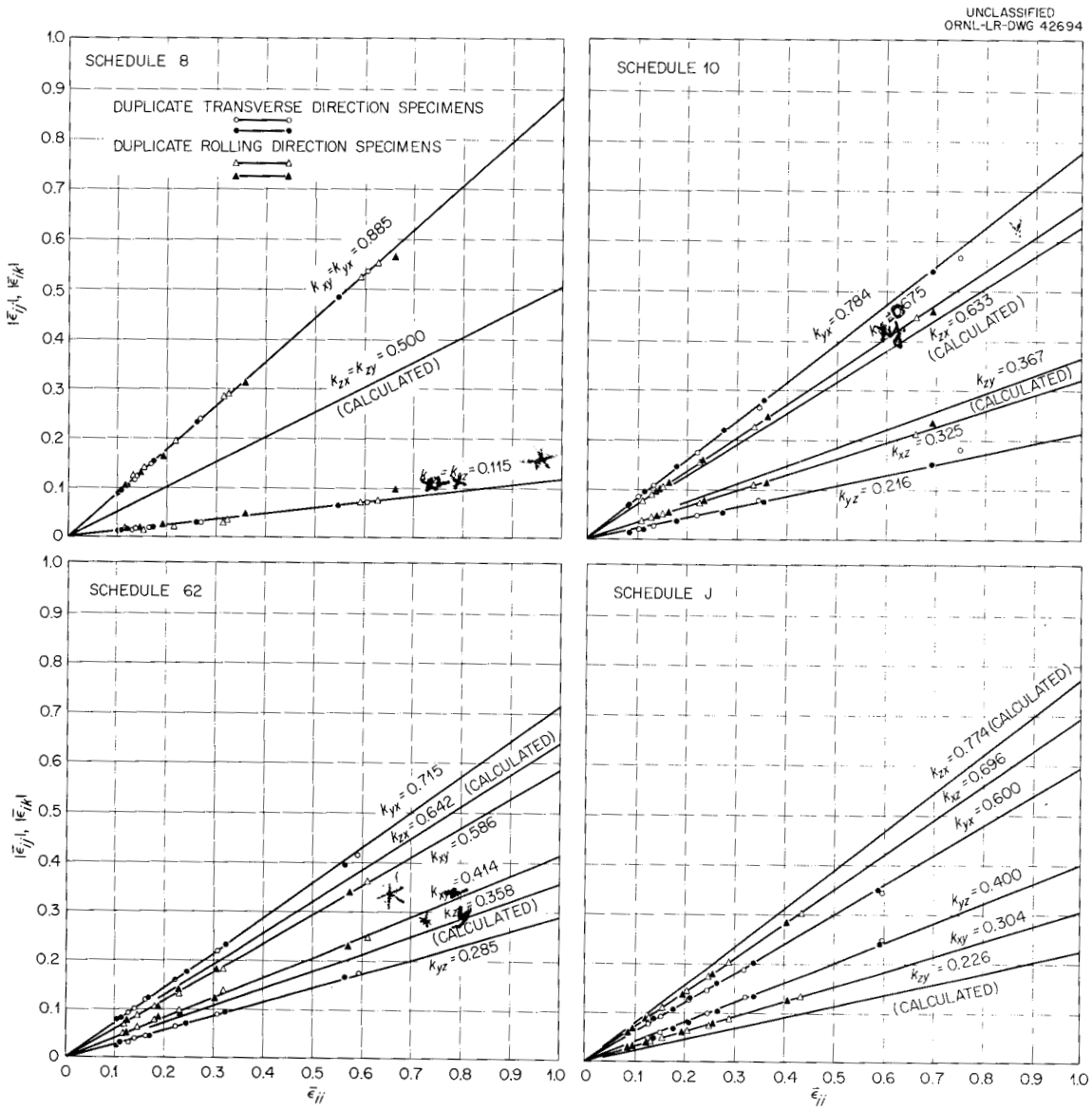

Fig. 2.2. Strain-Strain Plots for Zircaloy-2 Produced by Four Schedules: 8, 10, 62, and J.

Preferred orientation determinations by x-ray diffraction have shown the effects of the fabrication variables on the texture developed and have afforded a qualitative check on the k values determined. By considering the deformation systems available for slip and twinning and the determined textures, it is possible to predict relative cross-sectional shapes, yield strengths, and probable bend ductilities. Since the inverse pole figures

* See errata

 * k_{zy}

Table 2.1. Working and Annealing Temperature for Four Zircaloy-2 Fabrication Schedules

Schedule	Ingot Breakdown Temperature (°C)	Major Reduction Temperature (°C)	Intermediate Annealing Temperature (°C)	Final Working Temperature (°C)	Comments*
8	1050	800	800	540	Reduction at 1050°C, 55%; 800°C, 40%; 540°C, 70%; straight rolled. Ingot breakdown by forging
10	1050	750	1000	540	Reduction at 1050°C, 75%; 750°C, 40%; 540°C, 40%; cross rolled during final working. Ingot breakdown by forging
J	1000	780	1000	540	Reduction at 1000°C, 65%; 780°C, 80%; 540°C, 30%; cross rolled during ingot breakdown
62	1000	780	1000	540	Same as schedule J, except for cross rolling

*Working by rolling except where indicated.
All material annealed at 775°C for 30–45 min after final working.

present a quantitative measure of the degree of preferred orientation,[14,15] the effects of the fabrication variables can be easily seen. The inverse pole figures for four experimental fabrication schedules (Table 2.1) are presented in Figs. 2.3–2.6. The pole figures shown are consistent with the k values determined for the schedules concerned.

Impact energy tests have also served as an indication of the effects of the fabrication variables on the mechanical anisotropy of Zircaloy-2.[16] If transverse and longitudinal specimens are tested with notches both in and perpendicular to the rolling plane, considerable differences in energy absorption and transition temperature are seen, both in-schedule and between schedules. Impact energy curves are presented in Fig. 2.7 for the four experimental fabrication schedules discussed previously. Prediction and rationalization of the relative positions of the curves is quite difficult, for, although both the preferred orientation and the deformation systems are known, neither the effect of temperature on the activity of the deformation systems nor the form of progression of the triaxiality of stresses developed at the root of the notch are known with any confidence.

Analyses of the data from all schedules have shown that the texture varies greatly with the fabrication procedure, especially for the variables of intermediate annealing and cross rolling. Comparison of textures for schedules 8 and 62 (Figs. 2.3 and 2.5) shows the effect of annealing temperature. The schedules are essentially identical (Table 2.1) except that the intermediate anneal for schedule 8 was at 800°C (in the α-phase region) while that for schedule 62 was 1000°C (in the β-phase field). The α-annealed material had a very high concentration of basal poles normal to the rolling plane, whereas the β-annealed material had the basal poles spread into a band containing both the normal and transverse direction of the plate. If the β-annealed material is cross-rolled as the final cold

---

[14] L. K. Jetter and B. S. Borie, Jr. J. Appl. Phys. 24(5), 532–35 (1953).

[15] L. K. Jetter, C. J. McHargue, and R. O. Williams, J. Appl. Phys. 27(4), 368–74 (1956).

[16] G. M. Adamson et al., HRP Quar. Prog. Rep. Apr. 30, 1957, ORNL-2331, p 132.

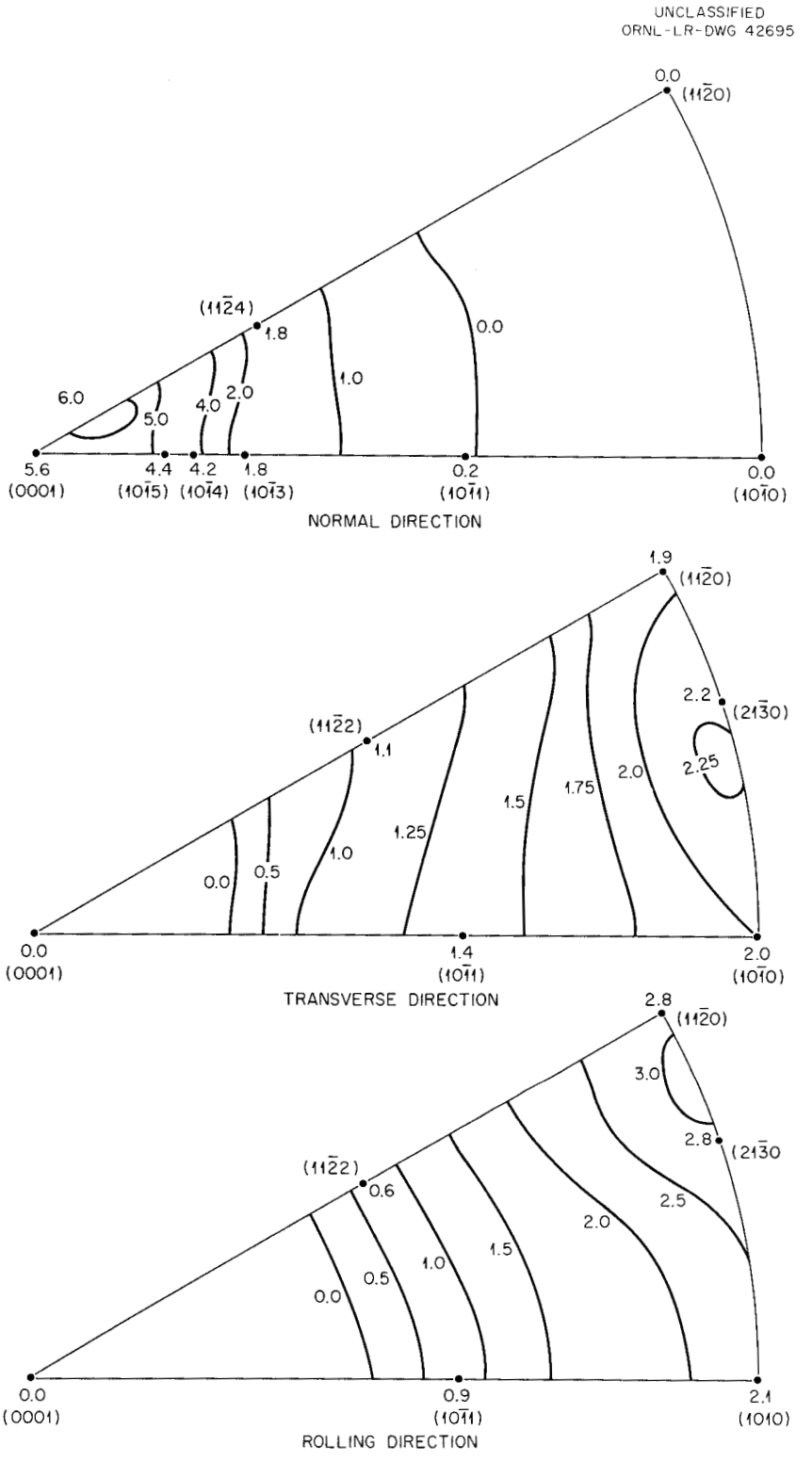

Fig. 2.3. Schedule 8 Inverse Pole Figures for Zircaloy-2.

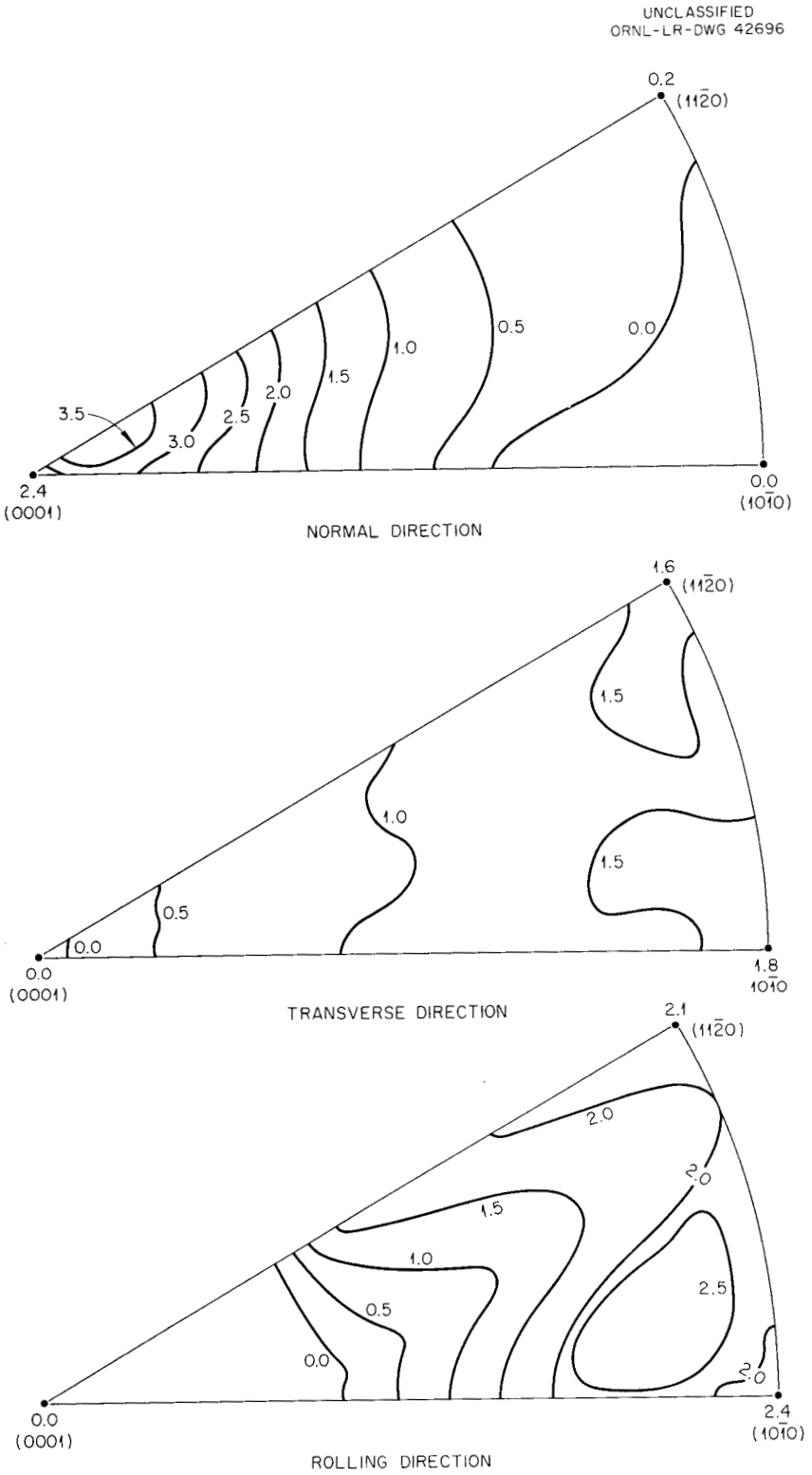

Fig. 2.4. Schedule 10 Inverse Pole Figures for Zircaloy-2.

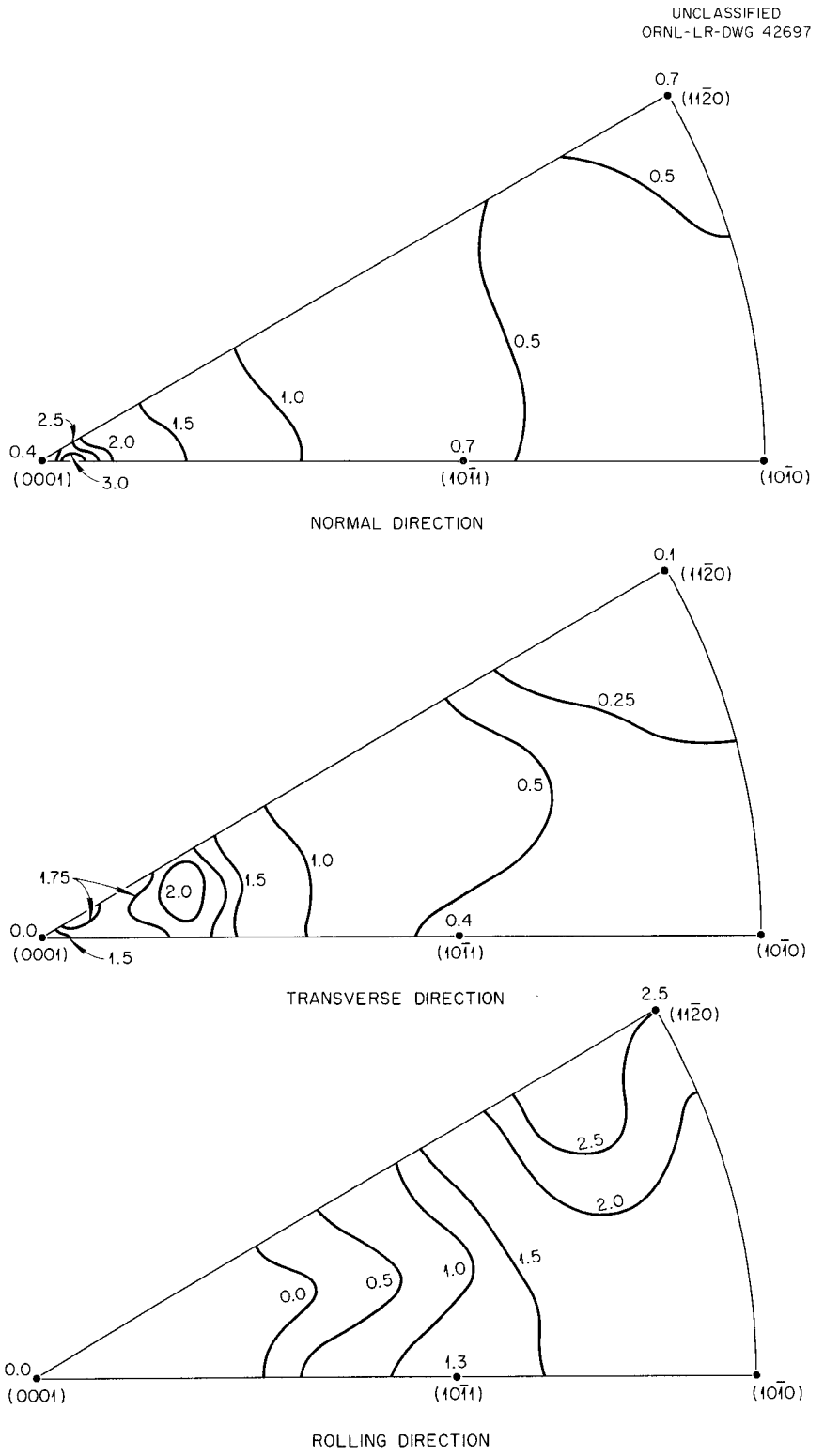

Fig. 2.5. Schedule 62 Inverse Pole Figures for Zircaloy-2.

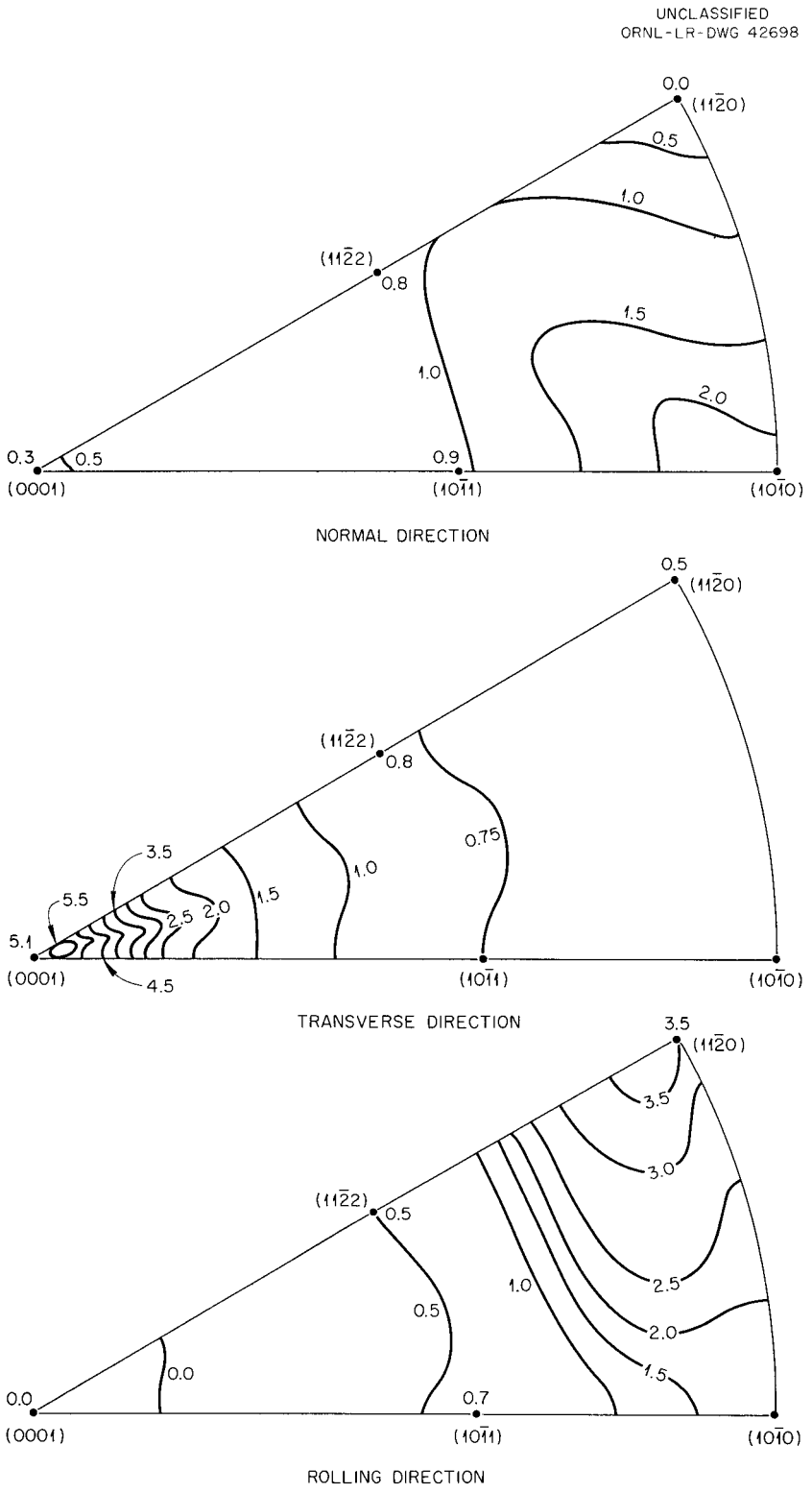

Fig. 2.6. Schedule J Inverse Pole Figures for Zircaloy-2.

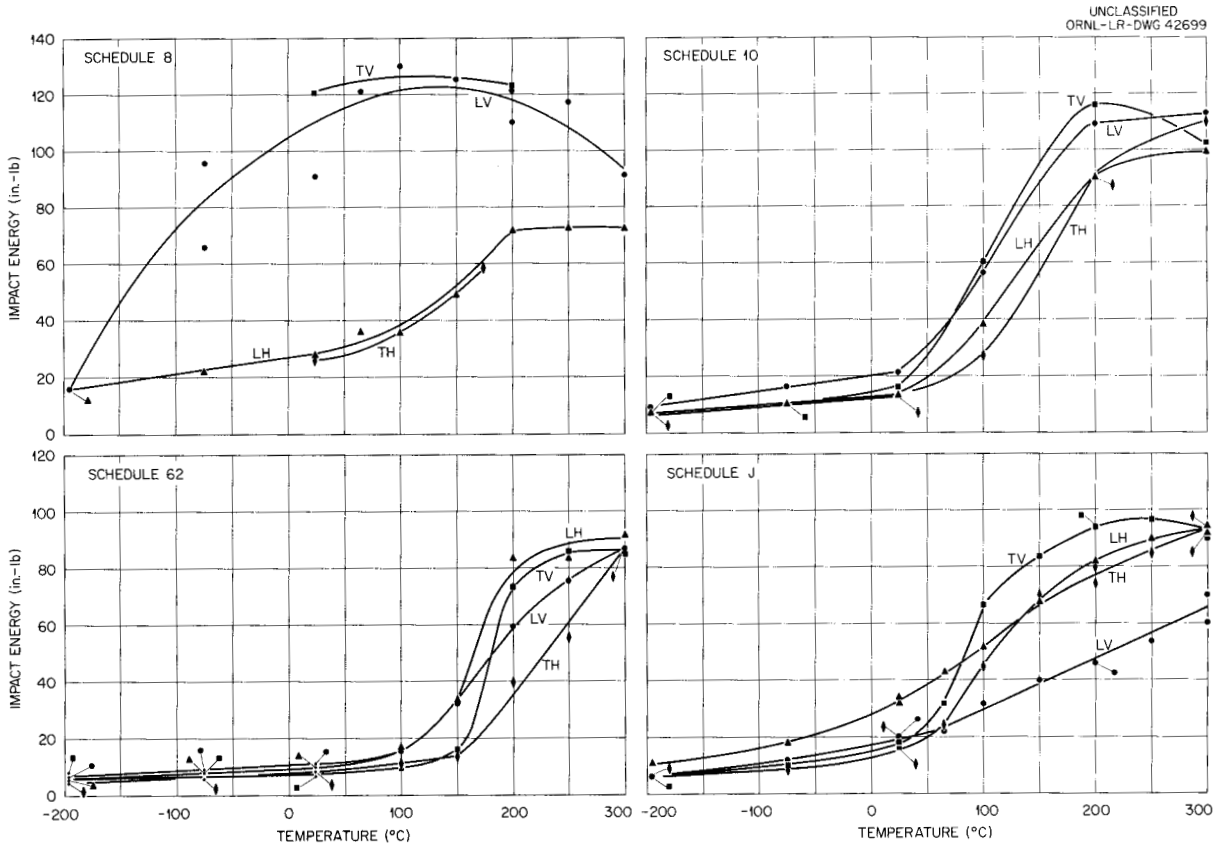

Fig. 2.7. Subsize Izod V-Notch Impact Energy Curves for Zircaloy-2 Produced by Four Schedules: 8, 10, 62, and J.

reduction after the β anneal (schedule 10), the texture tends toward that found for the α-annealed material (schedule 8), as shown in Fig. 2.3. Although any combination of variables which leads to a concentration of basal planes in the rolling plane will tend to equalize the tensile properties in directions in the plane of the plate, the contraction strain in the normal direction will be small, indicating that considerable anisotropy exists which will not be detected if the usual tensile-property values are used as criteria.

Cross rolling during ingot breakdown and the major reduction before an intermediate β anneal (schedule J) produces a preferred orientation texture such that no basal planes lie in the plane of the plate. Instead, the basal poles are concentrated in the transverse direction, as shown in Fig. 2.6. This texture leads to a very high yield strength in the transverse direction relative to that in the rolling direction, as shown in

Table 2.2. A large amount of contraction strain also occurs in the direction of the plate normal for a tensile specimen with the tensile axis in the rolling direction. A transverse tensile specimen of schedule J has the same texture as a normal direction specimen from schedule 10, permitting an estimation of the tensile properties for that orientation.

A complete analysis of all data obtained to date in the fabrication study is in progress. Of particular interest are attempts to derive a quantitative relationship between the k values and the inverse pole figures, to describe the complete stress-strain curve in terms of the k values,

Table 2.2. Tensile Properties of Zircaloy-2 Plate Produced by Four Fabrication Schedules[a]

Schedule	Testing Temperature (°C)	Specimen Orientation	Tensile Strength	Yield Strength	% Extension in 1 in.	Reduction in Area (%)
			$\times 10^3$ psi	$\times 10^3$ psi		
8	25	TD[b]	68.0	58.3	19.5	44
	25	RD[c]	67.8	54.9	24.2	47
	150	RD	47.6	36.4	29.0	52
	300	RD	33.4	22.5	32.0	64
10	25	TD	73.5	66.6	21.7	52
	25	RD	75.0	57.0	22.5	49
	150	RD	58.0	42.4	26.5	53
	300	TD	35.6	28.5	34.0	71
	300	RD	38.0	24.6	32.5	63
62	25	TD	74.2	63.2	22.2	44
	25	RD	75.8	55.8	22.5	45
	150	TD	52.0	43.3	23.0	
	150	RD	57.2	34.8	26.0	50
J	25	TD	78.1	70.0	21.5	45
	25	RD	74.9	52.0	22.0	34
	150	TD	56.6	48.4	23.5	51
	150	RD	55.9	32.9	20.0	37
	300	TD	36.3	30.9	29.0	66
	300	RD	36.7	25.0	26.5	57

[a]See Table 2.1 for rolling schedules.

[b]Transverse direction.

[c]Rolling direction.

and to obtain the stress tensor—strain tensor relationships and thereby predict accurately the behavior of a specimen with any tensile axis orientation. It is hoped that the information obtained in this study will lead finally to a theory of elastic and plastic deformation in polycrystalline hexagonal metals.

It has been concluded, so far in the study, that the control of the preferred orientation and resulting anisotropy of the mechanical properties by choice of fabrication schedule is a necessary prerequisite for the development of Zircaloy-2 as a general engineering material and for evaluation of the usual engineering tests such as tensile properties, impact properties, notch sensitivity, bend tests, creep tests, stress rupture, and tube-burst tests. The data being determined should be extensible to other fabrication methods and, particularly, to the development of tube and pipe fabrication schedules.

ENGINEERING METALLURGY

E. S. Bomar W. J. Leonard
F. W. Cooke J. J. Prislinger
C. H. Wodtke

Forming of Zircaloy-2

The Zircaloy-2 core vessel used in the present Homogeneous Reactor was fabricated by the slow and expensive process of forming small segments, welding them together, reforming, welding to other sections and again reforming.[17] Such a procedure requires a large number of welds in a metal that is easily contaminated, and such contamination is difficult to detect by nondestructive testing. Such contamination may result in decreased corrosion resistance and in poor mechanical properties. Development work with other forming processes has therefore been undertaken to simplify the operation and to reduce the number of welds required.

By using existing equipment at Titanium Fabricators, Inc., attempts were made to power spin 15-in.-dia hemispheres (approximately 1/2 size) of

[17]Newport News Shipbuilding and Dry Dock Company, Fabrication History of HRT Core Tank, ORNL CF-58-12-6 (Jan. 2, 1959).

Zircaloy-2 from flat plate. Twelve sheets with starting thicknesses varying from 0.126 in. to 0.300 in. were successfully spun into hemispheres. Difficulties were encountered with laps and with earing, but both were corrected by slight changes in procedure. Data showing the average quality of the hemispheres are presented in Table 2.3.

Good reproducibility with similar starting thicknesses was obtained with the values for springback and for equatorial thinout but not for maximum thinout (wall thickness) or for ellipticity. To meet the fit-up tolerances for a girth weld, the variation in ellipticity would require either careful selection and hand fitting of the hemispheres or the spinning of thicker walls and machining to size. Six of the hemispheres were successfully welded to form three spheres with high-quality welds.

In an effort to further reduce the number of welds, a program is under way to develop techniques for forming a reverse-curvature flare into the polar region of a hemisphere. Such a flare would serve as a transition from the vessel to the inlet or outlet piping.

By using warm pressing (1200–1400°F) in simple steel dies, it was possible to press a 3-in.-radius flare with no earing and with a high degree of symmetry (Fig. 2.8). The tendency of the shell to draw up the male die

Table 2.3. Dimensional Variations of Spun 15-in.-Diameter Zircaloy-2 Hemispheres

Original Thickness (in.)	Average Equatorial Thinout (%)	Maximum Thinout (%)	Average Radial Springback at Equator (in.)	Average* Diametral Ellipticity at Equator (in.)
0.300	30	34	0.175	0.101
0.285	24	29	0.175	0.062
0.218	18	32	0.118	0.050
0.126	38	42	0.040	0.050

*Major diameter minus minor diameter.

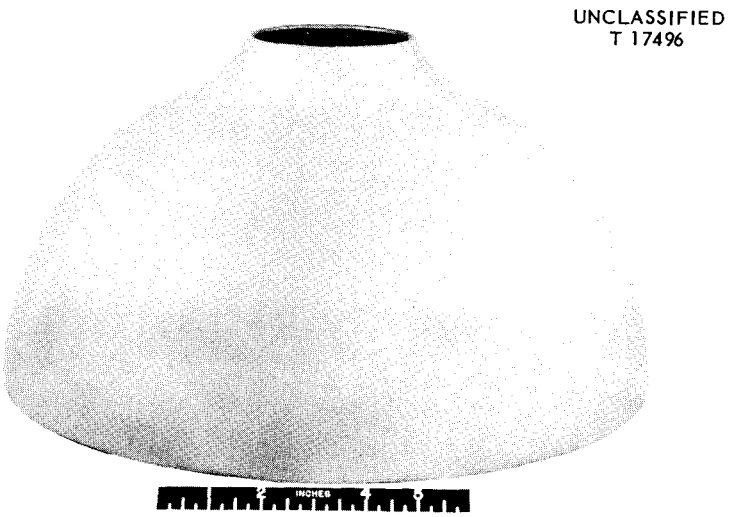

Fig. 2.8. Zircaloy-2 Hemispheres Spun from Simple Flat Plate.

reduced the thinout in the region of maximum deformation from an expected 36% to only 13.5%. The springback found was relatively small and could be corrected easily by die design. A similar procedure was also used to flare the end of an extruded Zircaloy-2 pipe having an outside diameter of 3 in. and a 0.200-in. wall. Equal success was achieved, and the thinout measured 13.7% rather than a predicted 40%.

The success of these forming operations shows that it is quite likely that a Zircaloy-2 core vessel could be produced which would contain only three welds and that they would all be of a simple configuration. Whether the vessel could be formed directly or would have to be machined to final size would depend upon the tolerances placed upon the vessel. In either case, a considerable savings in cost and an increase in integrity would be achieved.

Zircaloy-2 Welding Development

In previous years[18] techniques have been developed by which Zircaloy-2 may be successfully welded by using any of three methods: in a dry box, with a protective trailer on the torch, or with only conventional welding equipment. The latter method has now been used to fabricate components for both in-pile loops and corrosion-testing loops.

---

[18]W. J. Leonard, Met. Ann. Prog. Rep. Oct. 10, 1958, ORNL-2632, p 83 (classified).

While the use of conventional welding equipment is desirable for making loop components and test pieces which require a wide variety of sizes and types of welds, this is not true for a core vessel. It is likely that such a vessel will contain only a limited number of welds of relatively simple configuration; all welds must, however, be of high quality and uncontaminated. While it is possible to make uncontaminated welds with the conventional equipment, highly skilled welders are required. Until a nondestructive test is developed that will reveal weld contamination, it is not likely that such a seemingly straightforward method would be used for a reactor vessel. Efforts have therefore been made to improve the other methods, especially that of the protective trailer, in order to provide a simple but reliable procedure for welding the next core vessel. One aim of the program has been to increase the tolerances on the weld joint fit-ups and thereby simplify fabrication procedures.

Both the protective-trailer and dry-box welding methods are awkward and inefficient when used for hand welding, therefore efforts have been concentrated on the development of machine welding techniques. Equivalent welds were made in Zircaloy-2 plates and hemispheres, up to 5/16-in. thick, when the work was moved past a stationary torch or when the torch was moved over the work. The major accomplishment of this study has been the replacement of the expensive root-insert type of weld with a simple fusion root pass. The root-insert type of joint had previously been chosen as being more reliable than a filler metal root pass.[19] The two root faces are now butted together, without gap, and have a thickness up to half of the plate thickness. This heavy-root fusion pass requires an increase in power input and thereby increases the possibility of contamination, but this may be avoided with carefully designed trailers and backup devices. With the thick root faces, the tolerances on joint alignment may be relaxed. With 5/16-in. plate, full-penetration root passes were obtained with misalignments as high as 0.045 in., compared with the 0.005 in. allowed in the present procedure. Additional filler passes are made by using a machine-driven filler wire.

---

[19]Newport News Shipbuilding and Dry Dock Company, Fabrication History of HRT Core Tank, ORNL CF-58-12-6 (Jan. 2, 1959).

Electric-Arc Cutting of Zircaloy-2

In one proposed series of tests for the HRT it would be necessary to remove the Zircaloy-2 screens now attached by ligament welds to the inner surfaces of the cones. Such screens are 1/8-in. thick and are perforated with 3/8-in. holes on a 1/2-in. triangular pitch.[19] The largest screen is approximately 24 in. in diameter. Major complications in such a removal are that the only access is from the top and through a 2-in. hole and that the reactor has been in operation for a considerable time, resulting in a tremendous residual activity after shutdown. Underwater electric-arc (tungsten electrode) cutting was investigated as a possible means of reducing the screens to a size that would allow them to be removed.

Such a process was used on other metals by Oyler,[20] and trial underwater cuts on a Zircaloy-2 plate had been made by Linde. Early trial cuts were made by using the standard Linde Heliarc manual cutting torch and control equipment. The torch was mounted for mechanical movement across a Zircaloy-2 screen submerged in water. All cutting was done using argon gas only. It was found that a single screen could be readily cut at nearly 100 in./min at a current of 425 amp. Up to four stacked screens were cut also, but at a much slower speed.

An experimental torch (Fig. 2.9) was designed and built small enough to pass through a 2-in. hole. This greatly simplified torch retained only features believed essential to the underwater cutting process. The cutting-tip orifice dimensions of the Heliarc torch were preserved. Cooling water lines and "pilot arc" circuit were eliminated, and only argon was used. Control circuits were modified to provide a high-frequency test switch, continuous hold-in of cutting-current contactor, and continuous application of high frequency currents during cutting. The power source was two standard 300-amp d-c welding machines connected in series, as normally done in Heliarc cutting.

Features found necessary and added to the standard Heliarc equipment were: (a) a separate supply of argon continuously flowing at 5 cfh to keep

---

[20] G. W. Oyler, R. L. O'Brian, and J. Maier III, Welding J. 35, 1214 (1956).

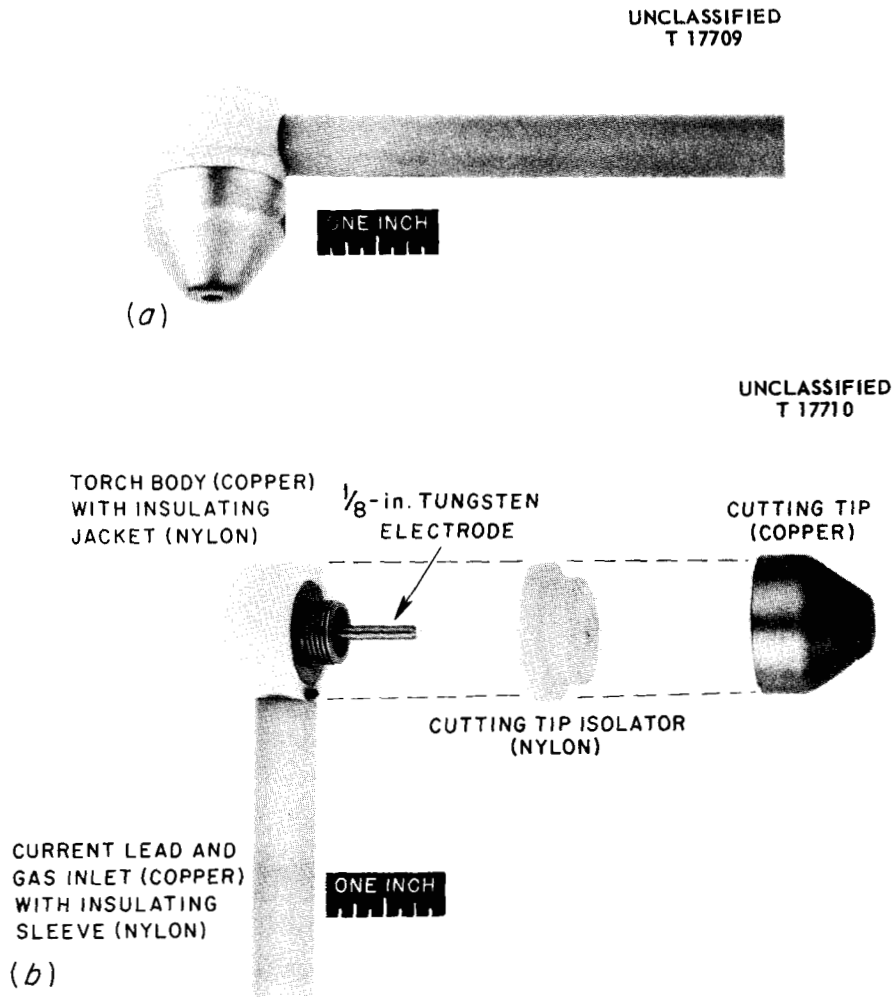

Fig. 2.9. Experimental Tungsten-Arc Torch for Underwater Cutting. (*a*) Assembled, (*b*) disassembled.

water out of the torch and preserve electrode life, (b) a higher-than-normal voltage supply to the high-frequency generator for reliable arc starting under water, and (c) flexibility in the support arm to permit the experimental torch to bounce. A Teflon skid and positive pressure were used to maintain a constant arc length during cutting.

In the operating cycle of the torch, arc starting and all cutting was done submerged. With the torch positioned below the screen, cutting circuits were energized, and argon flow started. Torch travel was then started at full cutting speed. When the torch was opposite the screen edge, the cutting arc was self-established. The arc was maintained until it was self-extinguished when the torch passed off the screen at the end of the cut. A photograph of the torch in operation is shown in Fig. 2.10.

Fig. 2.10. Experimental Tungsten-Arc Torch in Action, Cutting Screen Under Water. Photo made through Lucite tank. Torch is traveling upward 90 in./min. A Teflon skid (white half-moon-shaped part behind tip) was used to provide constant arc length. Scale: screen thickness, $\frac{1}{8}$ in.; hole diameter, $\frac{3}{8}$ in.

After preliminary trials for optimizing cutting conditions, a life test of torch and electrode was made. Operating data are given in Table 2.4. The series of cuts was intentionally terminated with the torch head, cutting orifice, and electrode still in satisfactory and usable condition.

At no time during the operation was there any evidence of self-ignition, of continuing combustion of the Zircaloy or of a reaction with the water, even though the drops remained molten for several seconds. As shown by Fig. 2.11, the solidified metal particles removed from the kerf are small and spherical and could easily be flushed through the 3/8-in. holes. The condition of the cut screen may be seen in Fig. 2.12. No attempt was made to obtain clean cuts since in this operation the slag and solidified metal on the underside would not present a problem.

It now appears feasible to use an underwater tungsten-arc cutting process for removing the Zircaloy-2 screens from the HRT, provided that a satisfactory apparatus can be developed for remote manipulation of the torch. It

Table 2.4. Life Test Data of An Experimental Underwater Cutting Torch

Tungsten-electrode dia, in.	1/8
Tip orifice dia, in.	5/32
Tip-to-base metal space, in.	1/4
Argon flow, cutting, cfh	60
Argon flow between cuts, cfh	~ 5
Current DCSP, amp	350 to 425*
Volts, open circuit	155
Volts, cutting	~ 80*
Travel speed, in./min	~ 90
Cutting direction	Up
Depth at start of cut, in.	28
Length of cut, minimum–maximum, in.	11–22
Total number of cuts	137
Approximate total length of cut, in.	~ 2306

*~~Varied with line load of primary power source.~~

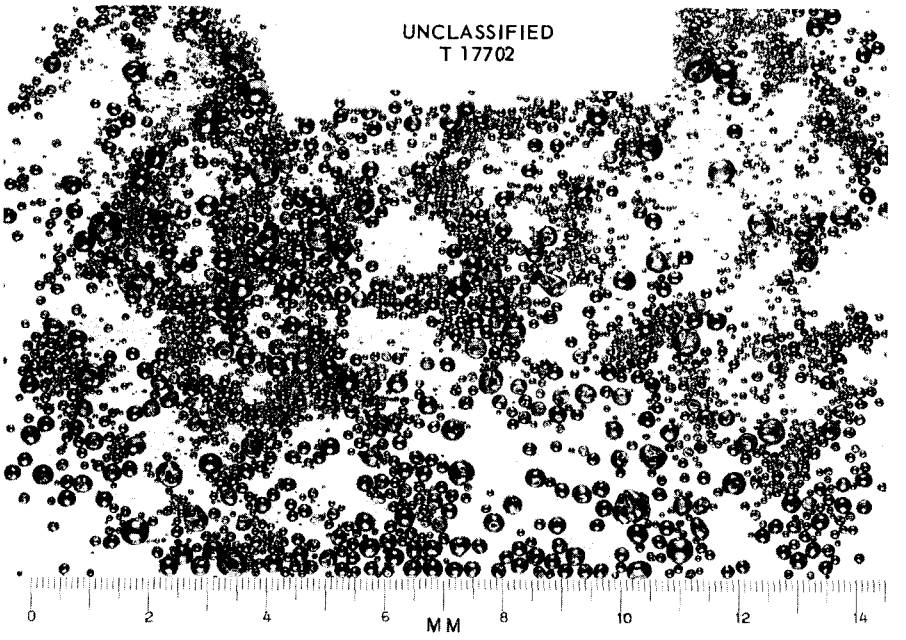

Fig. 2.11. Size Range of Drops of Metal and Slag Removed from the Kerf. Some fines (dust) not recovered; test No. 56X.

is also visualized that such a process will have other applications in the nuclear field. Cutting under water should simplify the control of the spatter of molten metal and of dust and residue in cutting radioactive materials, factors of major importance in reactor maintenance or disassembly operations. The use of the water should also provide rapid quenching and thereby limit the heat-affected areas where such control is needed.

Duplex Inconel—Stainless Steel Welds

The heat exchangers in a homogeneous reactor system will be exposed to uranyl sulfate on the primary side, which therefore must be of stainless steel or titanium, and to water or steam on the secondary side. Sufficient activity will be present from the uranyl sulfate to cause dissociation of the water and thereby complicate the control of oxygen, which is the usual method for the prevention of stress-corrosion cracking in stainless steels.[21] One answer to these corrosion problems would be found in the use of composite materials, with type 347 stainless steel being used

[21] J. A. Lane, H. G. MacPherson, and F. Maslan (eds.), Fluid Fuel Reactors, p 283, Addison-Wesley, Reading, Massachusetts, 1958.

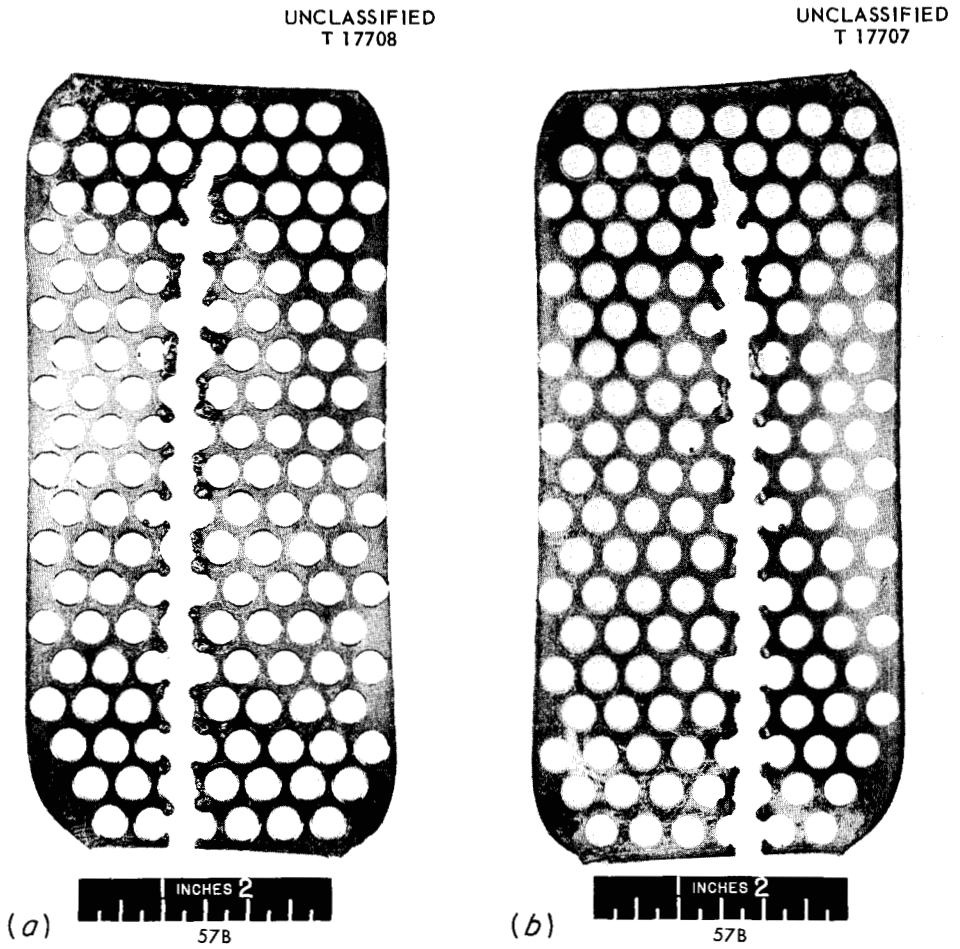

Fig. 2.12. Appearance of $\frac{1}{8}$-in. Zircaloy-2 Screen After Cutting. Presence of resolidified metal and slag unimportant in intended application. (*a*) Back side; (*b*) torch side.

for exposure to the uranyl sulfate, and Inconel for exposure to the water. Such a system does, however, present many welding difficulties, especially for the tube-to-header welds.

In this system, the most corrosion-resistant stainless steel is type 347; however, in welding this alloy, close control of the composition, and especially the nickel-chromium ratio, is required to prevent weld cracking. When Inconel—type 347 stainless steel composites are welded, control of this ratio becomes very difficult and cracking is encountered. Cracks were found when thick deposits of stainless steel were deposited on a single layer of Inconel and when a single layer of type 347 stainless steel was deposited on a joint filled with Inconel. Use of other stainless steels, such as type 316 or 304L in place of type 347, alleviated but did not completely eliminate the cracking. Efforts have

therefore been spent in finding a suitable barrier material for use between the two deposits.

The initial tests were single welds made by using 1/2-in.-dia, 1/16-in.-wall stainless steel tubing, clad exteriorly with Inconel (88% Inconel, 12% stainless steel), and a tube sheet 1-1/4 in. square and 1/2 in. thick. All welding was inert-gas tungsten-arc welding. Hastelloy W (24% Mo, 6% Cr, 5% Fe, balance Ni), INOR-8 (16% Mo, 5% Cr, 1.5% Ti, 0.5% Al, balance Ni), and Incoloy (16% Cr, 29% Ni, balance Fe) were evaluated as being the most likely barrier metals. After some development in welding techniques, these three alloys were all successfully deposited on the Inconel root pass. However, on the deposition of the type 347 stainless steel cover passes, under-bead cracking was observed with the first two alloys but not with Incoloy. Cracking was always observed at crater positions (arc extinguishment and restarting) for all three alloys, but was much less severe with the Incoloy. However, by use of current tapering and filler-metal additions at the crater, crater cracking was eliminated for the Incoloy barrier metal but not for the other two.

Additional welds were made by using a larger-size tube sheet in which three tubes were inserted on 1/2-in. triangular centers. Tubing of the same dimension was used, but the Inconel—stainless steel ratio was 60/40. Incoloy and stainless steel type 312 (29% Cr, 9% Ni) were evaluated as barrier materials. On deposition of type 347 stainless steel cover passes on Incoloy, under-bead cracking occurred in the second weld made on a tube sheet. Figure 2.13 illustrates such cracking and shows an all-austenitic structure; such structures are known to lead to cracking in the welding of type 347 stainless steel. Type 312 stainless steel barrier metal showed no cracking at any location.

Tube-sheet welds were then made in headers containing six tube positions with the same geometry as before, and with the material combinations listed in Table 2.5.

Cracking was found only at the transition from Inconel to Incoloy. Figure 2.14 shows typical structures of the two transition regions in the sound welds. Ferrite networks were present in all these structures, compared with the all-austenitic structure previously shown in Fig. 2.13.

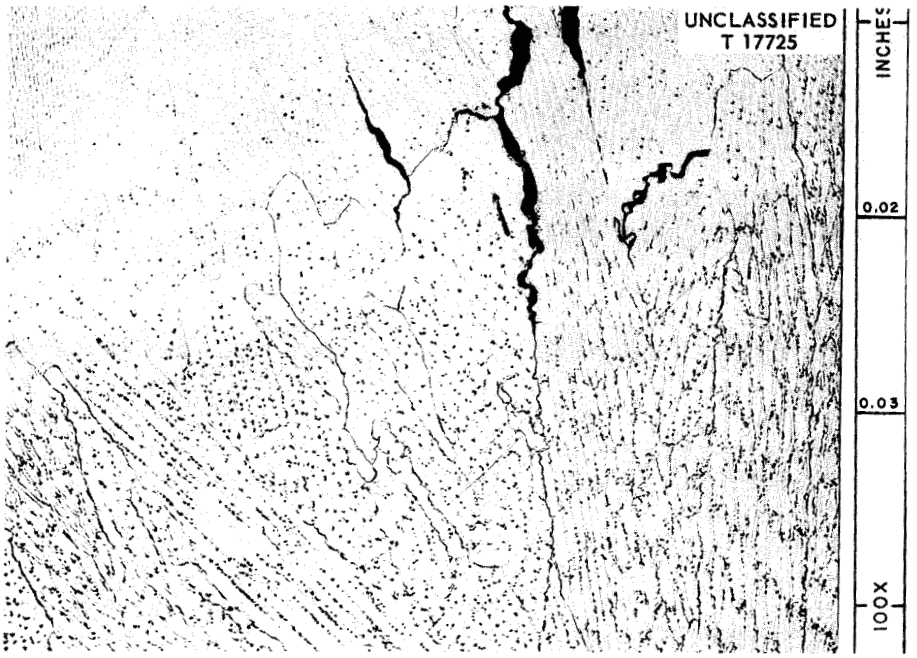

Fig. 2.13. Cracks in Type 347 Stainless Steel Weld Deposited on Incoloy. Note the all-austenitic microstructure.

Table 2.5. Composite Inconel–Stainless Steel, Six-Tube, Tube-To-Header Welds

Root Pass	Barrier Pass	Cover Pass	Comments
Inconel	Type 312 SS	Type 312 SS	Sound weld
Inconel	Type 312 SS	Type 308L SS	Sound weld
Inconel	Type 312 SS	Type 347 SS	Sound weld
Inconel	Incoloy		Under-bead cracking

Excessive dilution by nickel has been prevented by the high-chromium barrier alloy.

The cracking found between the Inconel and the Incoloy is typical of the hot shortness found in welds in high-nickel alloys. Such cracking has not been studied in this program but usually may be prevented by the addition of niobium or titanium.

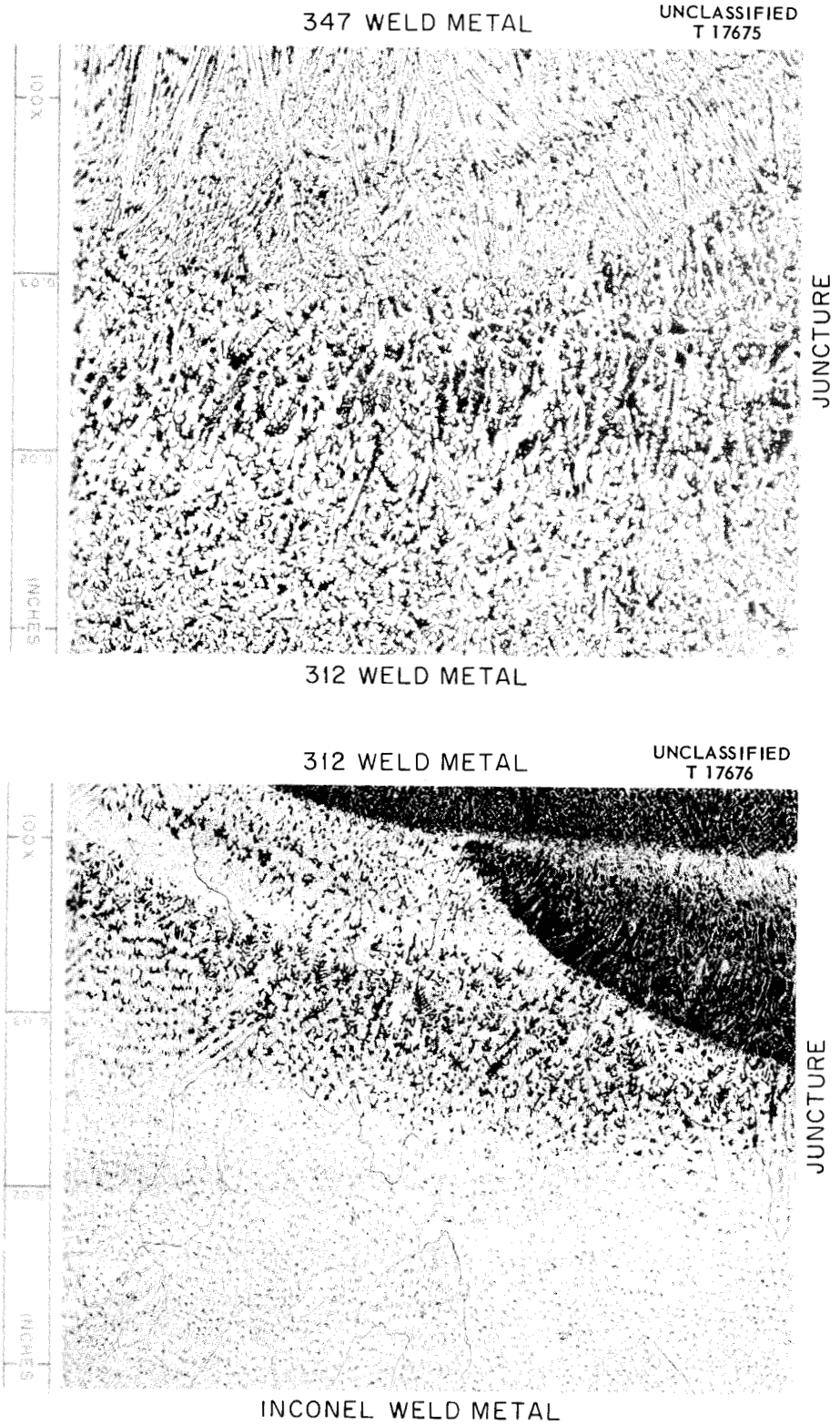

Fig. 2.14. Microstructure in Transition Region of Inconel–Type 347 Stainless Steel Tube-to-Header Weld, with Type 312 Stainless Steel as Barrier. Note ferrite networks.

It appears to be possible to make high quality tube-to-header welds in heat exchangers with composite stainless steel—Inconel structures if type 312 stainless steel is used as a barrier between the two. Incoloy may also be used as a barrier in systems having low restraint, but some changes in composition would be required for the more complex systems.

Effect of Reactor Environment on Zirconium and Titanium Alloys

In the operation of a homogeneous reactor, materials are exposed directly to fissioning uranyl sulfate solution. Such materials might undergo changes caused by either radiation damage from fast neutrons or by reactions with the environment, such as corrosion or deuterium pickup from dissociation of the heavy-water solution. No evidence of such changes was found in samples exposed in in-pile LITR loops,[22] but the exposures were low. Additional and more reliable confirmation of the absence of such changes has been sought by exposing mechanical-property samples within the blanket and core regions of the HRT.

Multiple-break, sub-size tensile and impact samples were exposed in the reactor core, the reactor outlet (same solution, much lower flux), and in the blanket. A variety of alloys of zirconium, titanium, and stainless steels were exposed (Table 2.6). As planned, some samples would be exposed for the life of the reactor, while others would be exposed for various shorter periods; these samples will also provide corrosion information.

At present, only samples exposed in the blanket region have been broken. The first group of samples was exposed in D_2O but only for a short period; the second group was exposed in uranyl sulfate during the period of essentially single-region operation. Samples exposed in the center of the core and in the neck region during this latter period are either not suitable for breaking (see HRT Metallurgical Research in this Part) or are not yet available.

---

[22] J. J. Prislinger, Met. Ann. Prog. Rep. Oct. 10, 1958, ORNL-2632, p 78–80 (classified).

Table 2.6. Average Tensile Properties of Materials Exposed in the Homogeneous Reactor Blanket

Material	When Exposed	Breaks (Averaged)	0.2% Offset Yield Strength (psi)	Ultimate Tensile Strength (psi)	Total Elongation (%)	Uniform Elongation (%)	Necking Elongation (%)	Reduction of Area (%)	Fracture Diameter (in.)*		
									Major	Minor	Major/Minor
Zircaloy-2 (cross rolled, commercial)	Controls	4	65,300	71,000	23.6	7.8	15.8	55.2	0.1536	0.0945	1.627
Zircaloy-2 (cross rolled, commercial)	First loading	2	66,000	70,800	23.4	8.2	15.2	57.2	0.1518	0.0917	1.660
Zircaloy-2 (cross rolled, commercial)	Second loading	2	68,300	71,800	20.6	6.8	13.8	53.7	0.1546	0.0987	1.584
Zircaloy-2 (experimental)	Controls	2	55,100	73,500	30.3	18.8	11.6	37.4	0.1512	0.1343	1.126
Zircaloy-2 (experimental)	Second loading	2	58,100	77,900	25.5	15.8	9.8	35.5	0.1536	0.1358	1.132
Zircaloy-2 (E,β-Q)	Controls	2	66,600	81,100	21.7	11.5	10.2	28.8	0.1600	0.1447	1.106
Zircaloy-2 (E,β-Q)	Second loading	2	73,600	86,000	17.0	10.2	6.8	26.7	0.1621	0.1469	1.108
Zircaloy-2 (E,weld)	Controls	4	56,800	66,600	13.1	7.0	6.1	37.5	0.1480	0.1369	1.082
Zircaloy-2 (E,weld)	First loading	2	59,600	66,400	11.8	6.0	5.9	38.4	0.1469	0.1363	1.080
Zircaloy-2 (E,weld)	Second loading	2	61,200	68,400	10.6	5.4	5.2	37.7	0.1484	0.1366	1.087

Table 2.6 (continued)

Material	When Exposed	Breaks (Averaged)	0.2% Offset Yield Strength (psi)	Ultimate Tensile Strength (psi)	Total Elongation (%)	Uniform Elongation (%)	Necking Elongation (%)	Reduction of Area (%)	Fracture Diameter (in.)*		
									Major	Minor	Major/Minor
Ti-A40	Controls	4	39,700	48,000	44.7	11.3	33.9	67.6	0.1452	0.0724	2.008
Ti-A40	First loading	4	41,300	51,500	39.7	11.1	31.1	71.4	0.1395	0.0666	2.11
Ti-A40	Second loading	2	46,600	57,500	32.8	11.6	21.2	68.6	0.1403	0.0721	1.948
Ti-A110AT	Controls	2	122,400	132,100	19.8	10.6	9.2	44.1	0.1433	0.1266	1.131
Ti-A110AT	First loading	2	124,100	133,100	20.2	11.1	9.6	39.2	0.1473	0.1339	1.10
Ti-6Al-4V	Controls	2	149,500	156,200	14.9	8.8	6.2	43.9	0.1392	0.1307	1.064
Ti-6Al-4V	Second loading	2	168,100	172,800	8.6	6.4	2.8	15.1	0.1683	0.1638	1.025
347 SS	Controls	4	44,700	95,600	74.8	69.4	11.6	61.4	0.1136	0.1104	1.029
347 SS	First loading	4	47,600	97,000	74.4	63.3	11.2	62.6	0.1114	0.1086	1.025
347 SS	Second loading	2	46,600	88,600	82.9	70.0	11.9	76.8	0.0874	0.0860	1.018
347 SS (weld)	Controls	4	44,000	87,000	87.2	77.0	12.9	77.3	0.0868	0.0859	1.011
347 SS (weld)	Second loading	2	62,400	101,100	52.6	44.4	8.4	65.7	0.1089	0.1037	1.050
Incoloy	Controls	2	48,400	86,300	57.8	46.5	11.2	61.5	0.1128	0.1107	1.021
Incoloy	Second loading	2	48,600	93,000	55.5	45.2	10.2	65.7	0.1077	0.1039	1.038
304 ELC	Controls	2	64,900	94,400	70.8	59.1	11.8	74.1	0.0925	0.0907	1.020
304 ELC	Second loading	2	67,700	96,200	61.6	50.6	10.9	75.5	0.0894	0.0884	1.012
309 SCb	Controls	4	58,400	96,000	59.2	46.2	12.9	64.8	0.1079	0.1055	1.024
309 SCb	Second loading	2	59,500	99,400	49.8	39.2	10.6	69.8	0.0998	0.0984	1.015

*Original gage diameter was 0.180 in.

During the first loading, the specimens accumulated a calculated maximum fast dose of only 1.2×10^{17} nvt while exposed in D_2O. No significant changes in the tensile properties were noted, as shown in Table 2.6.

Specimens in the second loading were exposed to an oxygenated uranyl sulfate solution and to a maximum fast dose of 2.6×10^{18} nvt. The zirconium and titanium specimens showed small increases in the yield and ultimate strengths and decreases in elongation. The changes are small and are within the expected accuracy; however, they are consistent for all materials tested and appear to be real (Table 2.6).

Metallographic examination and equilibrium pressure analyses were made on many of the broken specimens, but no evidence of deuterium pickup or other chemical or metallurgical changes was noted.

Combustion of Zirconium and Titanium

During this year, the responsibility for the work on the combustion of titanium and zirconium being carried out by Stanford Research Institute was taken over by the Reactor Safety Branch of the AEC. The work under ORNL direction was summarized in a final report.[23]

In a limited amount of work with titanium, the relationship between the minimum oxygen pressure required for spontaneous ignition of titanium and the temperature of the sample was determined. Exposure of a fresh surface resulted in autoignition at an oxygen pressure of 350 psi at room temperature, 130 psi at 600°C, and 70 psi at 1220°C.

Work with zirconium has been considerably hampered by difficulty in obtaining reproducible results. Ignition of fracture tensile-test specimens occurred with oxygen pressures ranging from 650 to 1500 psi. With the development of a technique for cleaning the surface by dissolving the oxide in the sample itself and then exposing the renewed surface to oxygen, ignition took place at 250 psi of oxygen without requiring fracture of the specimen. Difficulty was also encountered in obtaining reproducible results in the dynamic tests, the lowest value being 50 psi of oxygen.

---

[23] F. E. Littman and F. M. Church, Reactions of Metals with Oxygen and Steam, Stanford Research Institute, AUCE-3882 (Oct. 22, 1958).

Part III

REACTOR METALLURGY

CORROSION ENGINEERING

J. H. DeVan
A. J. Rosenberg R. C. Schulze
G. M. Tolson

Molten-Salt Reactor Program

J. H. DeVan R. C. Schulze

A three-phase test program[1] to evaluate the corrosion resistance of Inconel and INOR-8 when in contact with fused fluoride mixtures has been continued. Ten additional tests were completed under the first phase, which is intended to establish the relative corrosion properties of different salt mixtures in thermal-convection loops over a 1000-hr test period. Also, 27 phase-2 tests were completed and examined. These latter tests were carried out in thermal-convection loops for a test period of one year and at two maximum temperature levels – 1250 and 1350°F. Results were obtained also for three tests operated under phase 3, which utilizes forced-convection loops at flow rates and temperature conditions intended to simulate reactor operation.

Inconel Thermal-Convection-Loop Tests.[2–4] – The attack found in Inconel loops operated under phase-1 conditions ranged from surface roughening to 3 mils of void formation, as shown in Table 3.1. To evaluate the effects of salt purity on test scatter, three loops were operated with a similar salt composition (No. 130) but having had different pretreatments. Two of the loops, 1222 and 1223, circulated mixtures obtained from a common 5-lb batch. However, the salt circulated in loop 1223 was extensively purged with HF and H_2 to remove sulfur contamination. The third loop, 1230, contained a salt mixture prepared as a 250-lb batch. Although no sulfur could be detected in the gas bubbled through the salt used in loop 1223, this mixture resulted in the lowest depth of

---

[1] Met. Ann. Prog. Rep. Oct. 10, 1958, ORNL-2632, p 89–92 (classified).
[2] MSR Quar. Prog. Rep. Jan. 31, 1959, ORNL-2684, p 75–76.
[3] MSR Quar. Prog. Rep. Apr. 30, 1959, ORNL 2723, p 51–54.
[4] MSR Quar. Prog. Rep. July 31, 1959, ORNL-2799 (in press).

Table 3.1 Operating Conditions and Metallographic Results of Inconel Thermal-Convection-Loop Tests

Loop No.	Salt No.	Salt Composition (mole %)	Temperature (°F)	Time (hr)	Metallographic Results, Hot Leg
			Phase 1 Tests		
1223	130	62 LiF–37 BeF_2–1 UF_4	1350	1000	Light intergranular voids to 1-1/2 mils
1230	130	62 LiF–37 BeF_2–1 UF_4	1350	1000	Moderate intergranular voids to 2-1/2 mils
1234	133	71 LiF–16 BeF_2–13 ThF_4	1250	1000	A few scattered intergranular voids to less than 1 mil
1232	134	62 LiF–36.5 BeF_2–0.5 UF_4–1 ThF_4	1250	1000	Moderate intergranular voids; maximum depth 3 mils, mostly 1-1/2 mils
1243	135	53 NaF–45.5 BeF_2–0.5 UF_4–1 ThF_4	1250	1000	Light surface roughening and pitting
			Phase 2 Tests		
1217	122	57 NaF–42 KF–1 UF_4	1350	8760	Moderate intergranular voids, maximum depth 7 mils; average, 4 mils
1225	123	53 NaF–46 BeF_2–1 UF_4	1250	8760	Moderate intergranular voids, maximum depth 7 mils; average, 4 mils
1218	123	53 NaF–46 BeF_2–1 UF_4	1350	8760	Heavy intergranular voids to 18 mils
1198	126	53 LiF–46 BeF_2–1 UF_4	1250	8760	Moderate to heavy intergranular voids; maximum depth 7 mils; average, 5 mils
1199	126	53 LiF–46 BeF_2–1 UF_4	1350	8760	Heavy intergranular voids to 15 mils
1182	126	53 LiF–46 BeF_2–1 UF_4	1350	8760	Heavy intergranular voids to 15 mils
1184	129	55.3 NaF–40.7 ZrF_4–4 UF_4	1350	8760	Heavy intergranular voids; maximum depth 7 mils; average, 3 mils
1201	126	53 LiF–46 BeF_2–1 UF_4	1250	8664	Heavy intergranular voids; maximum depth 7 mils, mostly 5 mils

Table 3.1 (continued)

Loop No.	Salt No.	Salt Composition (mole %)	Temperature (°F)	Time (hr)	Metallographic Results, Hot Leg
1189	130	62 LiF–37 BeF_2–1 UF_4	1250	8760	Moderate intergranular voids; maximum depth 5 mils; average, 2 mils
1180	130	62 LiF–37 BeF_2–1 UF_4	1350	8760	Heavy intergranular voids to 14 mils
		Fused Salts with Thorium			
1202	125	53 NaF–46 BeF_2–0.5 UF_4–0.5 ThF_4	1250	8332	Heavy intergranular voids to 13 mils
1211	125	53 NaF–46 BeF_2–0.5 UF_4–0.5 ThF_4	1350	8760	Moderate intergranular voids to 15 mils
		Blanket Salts			
1210	128	71 LiF–29 ThF_4	1250	8760	Light scattered subsurface voids, maximum depth 5 mils; average, 2 mils
1181	128	71 LiF–29 ThF_4	1350	8760	Moderate intergranular voids; maximum depth 6-1/2 mils; average, 3 mils
		Coolant Salts			
1214	12	11.5 NaF–42 KF–46.5 LiF	1250	4670	Heavy intergranular voids to 13 mils
1188	84	27 NaF–35 LiF–38 BeF_2	1250	8760	Heavy general and intergranular voids; maximum depth 9 mils; average, 4 mils

attack (1-1/2 mils) among the three loops. Approximately the same depth of attack was observed in loops 1222 and 1230, ranging from 2-1/2 to 3 mils.

Inconel thermal-convection loops operated for one year under the second test phase revealed considerably greater depths of attack than loops containing comparable salts operated for 1000 hr. As shown in Table 3.1, phase-2 tests revealed attack in the form of void formation to depths of 5 to 13 mils at a hot-leg temperature of 1250°F, and 7 to 18 mils at a hot-leg temperature of 1350°F. The difference in attack between loops operated at 1250°F and at 1350°F was much greater in the case of salt mixtures containing UF_4 than for salt mixtures containing ThF_4 or for salt mixtures containing no fissile or fertile components. The attack produced by the blanket-salt mixture 128 ($LiF-ThF_4$, 71-29 mole %) is noticeably the lowest among the many types of salt mixtures tested.

INOR-8 Thermal-Convection Loops.[2,5,6] – The INOR-8 loops operated for 1000 hr under the phase-1 program were unattacked except for extremely light surface roughening, as shown in Table 3.2. No evidence of mass transfer was found in any of the loops operated.

The surfaces of INOR-8 loops operated for one year under the phase-2 program again showed no evidence of attack other than slight roughening, as shown in Table 3.2. Loop 1208, which circulated salt 12 (NaF-LiF-KF, 42-46.5-11.5 mole %) for 8760 hr at 1250°F, did show evidence of subsurface void formation of 1/2 mil; however, this attack was traced to the contamination of the salt by water. By direct comparison, Inconel loop 1214 (Table 3.1), which circulated salt 12 under the same conditions as loop 1208, underwent 14 mils of void formation after 4670 hr of operation. The excessive attack in this loop also was traced to water contamination of the salt.

On several of the long-term INOR-8 loops, surface layers were present on the surfaces exposed to the salt circulating after operation for one year, and were found to vary in thickness from just barely visible

---

[5] MSR Quar. Prog. Rep. Apr. 30, 1959, ORNL-2723, p 52–54.

[6] MSR Quar. Prog. Rep. July 31, 1959, ORNL-2799 (in press).

Table 3.2. Operating Conditions and Metallographic Results of INOR-8 Thermal-Convection-Loop Tests

Loop No.	Salt No.	Salt Composition (mole %)	Temperature (°F)	Time (hr)	Metallographic Results
			Phase 1 Tests		
1228	133	71 LiF–16 BeF_2–13 ThF_4	1250	1000	Light surface roughening
1227	134	62 LiF–36.5 BeF_2–0.5 UF_4–1 ThF_4	1250	1000	Light surface roughening
1229	135	53 NaF–45.5 BeF_2–0.5 UF_4–1 ThF_4	1250	1000	Light surface roughening
1241	136	70 LiF–10 BeF_2–20 UF_4	1250	1000	No attack
1242	136	70 LiF–10 BeF_2–20 UF_4	1350	1000	Moderate surface roughening
			Phase 2 Tests		
			(Fuel Salts)		
1219	122	57 NaF–42 ZrF_4–1 UF_4	1350	8760	No attack
1224	123	53 NaF–46 BeF_2–1 UF_4	1350	8760	Moderate surface roughening and surface pitting to 1 mil
1185	126	53 LiF–46 BeF_2–1 UF_4	1250	8760	No attack
1206	126	53 LiF–46 BeF_2–1 UF_4	1350	8760	Light surface pitting
1200	130	62 LiF–37 BeF_2–1 UF_4	1250	8760	Moderate surface roughening, surface layer < 1/2 mil thick
1196	130	62 LiF–37 BeF_2–1 UF_4	1350	8760	Light surface roughening, extremely thin surface layer

Table 3.2. (continued)

Loop No.	Salt No.	Salt Composition (mole %)	Temperature (°F)	Time (hr)	Metallographic Results
		(Fuel Salts with Thorium)			
1212	125	53 NaF–46 BeF_2–0.5 UF_4–0.5 ThF_4	1250	8760	Moderate pits to 1 mil; surface layer present < 1/2 mil thick
1215	125	53 NaF–46 BeF_2–0.5 UF_4–0.5 ThF_4	1350	8760	Moderate surface roughening, surface layer present, < 1/2 mil thick
		(Blanket Salts)			
1190	127	58 LiF–35 BeF_2–7 ThF_4	1250	8760	Light surface roughening, a few pits to less than 1 mil
1209	128	71 LiF–29 ThF_4	1350	8760	Heavy surface roughening
		(Coolant Salts)			
1208	12	11.5 NaF–46.5 LiF–42 KF	1250	8760	A few subsurface voids to 1/2 mil, surface roughening

at a magnification of 250X to approximately 1/4 mil thick. These layers presently are being examined by x-ray diffraction, electron diffraction, and spectrographic techniques.

Forced-Convection Loops. — Chemical and metallographic examinations have been completed on two forced-convection loops, Inconel loop 9344-1 and INOR-8 loop 9354-5, each of which completed one year of operation. Also, one hot-leg specimen was examined after being removed from INOR-8 loop 9354-4 following 5000 hr of operation (operation of the loop was resumed after removal of the specimen). Operating conditions and metallographic results for the three loops are shown in Table 3.3.

Inconel loop 9344-1 was very heavily attacked along hot-leg sections, to a maximum depth of 38 mils. Accompanying this attack was a large increase in chromium concentration of the fused salt mixture. Petrographic and x-ray examinations of this salt also showed the presence of large amounts of UO_2. This finding provides strong evidence that contamination of the salt occurred either before or during the test and, in some measure, contributed to the high attack observed.

INOR-8 loop 9354-5 (ref 6) was operated to provide data on the compatibility of INOR-8 and graphite in a rapidly circulating molten-salt medium. A box constructed of INOR-8 and containing graphite rods was incorporated into the loop at the end of the second heater leg. As shown in Table 3.3, no evidence of carburization could be found in metallographic examinations of loop sections examined after test. However, as in the case of INOR-8 thermal-convection loops described above, a surface layer, as yet unidentified, was apparent in hot-leg sections of the loop. The appearance of this layer at the point of maximum loop temperature is illustrated in Fig. 3.1. Chemical analysis of the after-test salt showed little change in the concentration of impurities except for an expected increase in the chromium concentration. Examinations of the after-test salt were also made under the petrographic microscope and x-ray diffraction unit to detect the presence of oxides. These analyses showed the salt to be apparently unaffected by impurities contained in the graphite.

Removal of a hot-leg specimen from INOR-8 loop 9354-4 was effected in order to measure accurately the weight loss occurring after 5000 hr at surfaces operating at the maximum loop temperature.[6] The specimen was one

Table 3.3. Operating Conditions and Results of MSRP Forced-Convection-Loop Tests

Maximum salt-metal interface temperature, 1300°F
Minimum fluid temperature, 1100°F
ΔT, 200°F

Loop No.	Material	Salt No.	Salt Composition (mole %)	Time Operated (hr)	Reynolds Number	Flow Rate (gpm)	Metallographic Results
9344-1	Inconel	123	53 NaF–46 BeF_2–1 UF_4	8823	3250	2	Heavy voids ranging from 18–34 mils in first hot leg, 18–38 mils in second hot leg
9354-4*	INOR-8	130	62 LiF–37 BeF_2–1 UF_4	5000	3000	2	No attack
9354-5**	INOR-8	130	62 LiF–37 BeF_2–1 UF_4	8760	2200	1	Light surface roughening and surface pitting

*This pump-loop was equipped with three inserts designed to provide weight-loss data.

**This pump-loop had a box containing graphite rods.

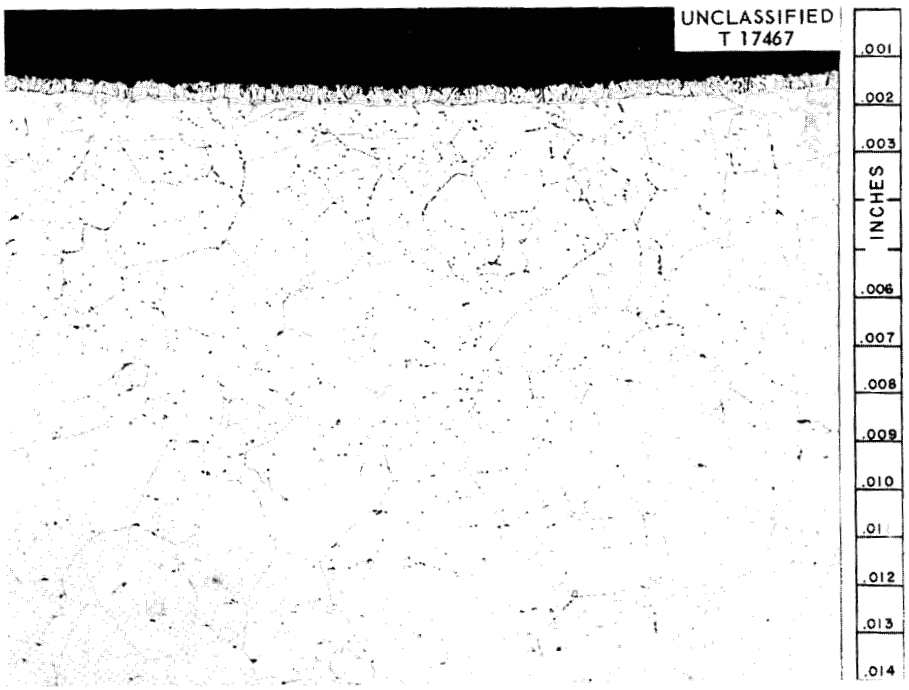

Fig. 3.1. Specimen Taken from Hot Leg of INOR-8 Forced-Convection Loop 9354-5 at Point of Maximum Loop Temperature (1350°F). Loop was operated for one year with salt mixture $LiF-BeF_2-UF_4$ (62-37-1 mole %). Etchant: 3 vol HCl, 2 vol H_2O, 1–10% CrO_3. 250X.

of three carefully weighed inserts incorporated at the end of the second (last) heater leg. The other two inserts are scheduled to be removed after 10,000 and 15,000 hr of operation, respectively. Weight measurements of the 5000-hr insert after test revealed a slight weight loss, which averaged 1.7 mg ± 2% per square centimeter over the 4-in. specimen length. This weight loss corresponds to a loss in wall thickness of 0.08 (±2%) mil if uniform surface removal is assumed. Metallographic examination of the insert showed a very thin surface layer similar to that shown in Fig. 3.1, with no additional indications of attack.

The status of five Inconel and eleven INOR-8 thermal-convection loops which presently are being operated with various fluoride mixtures is summarized in Table 3.4.

Table 3.4. Status of MSRP Forced-Circulation-Loop Tests

Loop No.	Material	Salt Composition (mole %)	Time Operated (hr)	Maximum Salt-Metal Interface Temperature (°C)	Minimum Fluid Temperature (°C)	ΔT	Reynolds No.	Flow Rate (gpm)	Remarks
9344-2	Inconel	11.5 NaF–46.5 LiF–42 KF	8,800	1200	1100	200	8200	2.5	Terminated; no results
9377-3	Inconel	60 LiF–36 BeF_2–4 UF_4	8,823	1300	1100	200	3400	2	Terminated; no results
9377-4	Inconel	62 LiF–37 BeF_2–1 UF_4	9,231	1300	1100	200	2600	1.8	Operating
9377-5	Inconel	62 LiF–36.5 BeF_2–0.5 UF_4–1 ThF_4	6,570	1300	1100	200	2300	1.8	Operating
9377-6	Inconel	71 LiF–16 BeF_2–13 ThF_4	4,384	1300	1100	200	3100	1.8	Operating
9354-1	INOR-8	53 LiF–46 BeF_2–1 UF_4	12,319	1300	1100	200	2000	2.5	Operating
9354-3	INOR-8	27 NaF–35 LiF–38 BeF_2	14,328	1200	1050	150	3000	2	Operating
9354-4	INOR-8	62 LiF–37 BeF_2–1 UF_4	9,516	1300	1100	200	3000	2.5	Operating
MSRP-6	INOR-8	62 LiF–36.5 BeF_2–0.5 UF_4–1 ThF_4	8,847	1300	1100	200	2300	1.5	Operating
MSRP-7	INOR-8	71 LiF–16 BeF_2–13 ThF_4	9,070	1300	1100	200	3100	1.8	Operating
MSRP-8	INOR-8	58 NaF–35 BeF_2–7 ThF_4	8,621	1300	1100	200	4000	2	Operating
MSRP-9	INOR-8	62 LiF–36.5 BeF_2–0.5 UF_4–1 ThF_4	8,455	1300	1100	200	2300	1.8	Operating
MSRP-10	INOR-8	53 NaF–45.5 BeF_2–0.5 UF_4–1 ThF_4	8,284	1300	1100	200	3400	2	Operating
MSRP-11	INOR-8	53 NaF–46 BeF_2–1 UF_4	7,881	1300	1100	200	3200	2	Operating
MSRP-12	INOR-8	62 LiF–36.5 BeF_2–0.5 UF_4–1 ThF_4	7,384	1300	1100	200	3900	2	Operating
MSRP-13	INOR-8	70 LiF–10 BeF_2–20 UF_4	3,438	1300	1100	200	3900	2	Operating

Engineering Support

G. M. Tolson J. H. DeVan

Metallurgical support is being supplied to the Reactor Projects Division for the purpose of inspecting materials and fabricated components used in conjunction with various power reactor programs. These inspections are intended to evaluate fabrication methods and to locate defective conditions which could result in failure of components under test. Included under this program is an evaluation of engineering drawings for adequacy of weld design, inspectability, and materials selection. Also, an analysis of component failures that occur during service is made to determine and correct conditions leading to failure.

Materials which were inspected during the report period are summarized in Table 3.5. The intended application of the materials was used as a criterion for both the acceptability and the amount and type of inspection performed. As can be seen, the rejection rate was quite low for all forms of materials except bar stock. Stainless steel bar stock in sizes 1/2 in. or under in particular contributed to the high rejection rate for the latter item. These results and others obtained

Table 3.5. Material Inspection

Item	Type of Material	Quantity Inspected	Quantity Rejected	Percentage Rejection
Tubing	INOR-8	2,235 ft	66 ft	3.0
	Inconel	434 ft	5 ft	1.2
	Stainless steel	16,292 ft	765 ft	4.7
Bar	INOR-8	5 ft	None	0
	Stainless steel	249 ft	100 ft	40
Machined parts	Stainless steel	1,675 units	24 units	1.4
	INOR-8	34 units	4 units	11.8

on materials previously inspected were compiled and presented at the National Exposition and Congress of the Society for Nondestructive Testing, Cleveland, Ohio, October 27–31, 1958.[7]

Table 3.6 lists the number and rejection rates of welds inspected during the report period in support of reactor programs. The four weld types designated in Table 3.6 were assigned on the basis of the following criteria of quality:

Type C – For all critical welds wherein optimum soundness is required (e.g., for sealing between corrosive environments, to meet thermal gradients or high strength requirements).

Type CN – For welds which normally would be designated "C" but which cannot be given a complete inspection due to design or fabrication requirements.

Type B – For welds which need only to meet the integrity requirements of an X-Ray ASME Boiler and Pressure Vessel Code weld.

Type BN – For welds which normally would be designated "B" but which either cannot be given a complete inspection due to design or fabrication requirements or where inspection by all methods is not necessary.

Type S – For structural welds wherein leaktightness is not required.

In addition to weld inspections given in Table 3.6, 23 fuel elements containing three welds each for in-pile tests in the Oak Ridge Research Reactor and Engineering Test Reactor were inspected, and only one weld was found rejectable.

GCR Materials Compatibility Tests

J. H. DeVan G. M. Tolson
A. J. Rosenberg

The GCR out-of-pile materials compatibility program, initiated to evaluate the outgassing characteristics of graphite and the effects of various combinations of gaseous impurities in helium on reactor structural materials, was continued in four types of test facilities.[8–11]

---

[7] G. M. Tolson, A. Taboada, and R. Stepp, J. Soc. Nondestructive Testing 16(5), 416 (1958).

[8] The ORNL Gas-Cooled Reactor – Materials and Hazards, ORNL-2505, p 13.33 (May 22, 1958).

[9] GCR Semiann. Prog. Rep. Dec. 31, 1958, ORNL-2676, p 138–46.

[10] GCR Semiann. Prog. Rep. June 30, 1959, ORNL-2767, p 188–90.

[11] Met. Ann. Prog. Rep. Oct. 10, 1958, ORNL-2632, p 89 (classified).

Table 3.6. Weld Inspection Data

Weld Type		Project					Total
		MSRP[a]		GCR[b]	ANP[c]	MSR[d]	
		INOR-8	Other Material				
C	Number inspected	169	128	1420	13	11	1741
	Number rejected	42	15	208	3	3	271
	Percentage rejected	24.9	11.8	14.7	23.1	36.7	15.6
CN	Number inspected	144	818	275	56	5	1298
	Number rejected	10	24	11	1	0	46
	Percentage rejected	6.9	2.9	4.0	1.8	0	3.5
B	Number inspected	2	74	11	0	4	91
	Number rejected	0	19	1	0	0	20
	Percentage rejected	0	39.2	9.1	0	0	22
S	Number inspected	0	253	83	0	58	394
	Number rejected	0	22	4	0	2	28
	Percentage rejected	0	8.7	4.8	0	3.5	7.1

[a]Molten-Salt Reactor.

[b]Gas-Cooled Reactor; predominantly, the welds were of type 304 stainless steel.

[c]Aircraft Nuclear Propulsion; predominantly, the welds were of Inconel and stainless steel.

[d]Maritime Ship Reactor; predominantly, the welds were of type 347 stainless steel.

Two static-pot assemblies have been modified to enable the insertion of independently heated type 304 stainless steel specimens which are capable of generating metal surface temperatures up to 1800°F (ref 12). Two high-pressure thermal-convection- and one forced-convection-loop facilities were also constructed to allow testing under high-pressure and high-velocity conditions, respectively.

Isothermal tests have been operated in the static-pot facilities with TSF and AGOT grades of graphite at temperatures of 1100, 1250, and 1400°F. In addition, tests with independently heated test specimens have been completed with AGOT graphite at specimen temperatures of 1500 and 1600°F and at a gas pot temperature of 1100°F. One long-term (3580 hr) low-pressure thermal-convection test of AGOT graphite was operated at 1400°F. Short-term (1000 hr) tests were also completed at 1300°F with TSF graphite and at 1100 and 1400°F with AGOT graphite. One high-pressure thermal-convection test and one forced-convection test were operated at 1225 and 1400°F, respectively. The materials exposed in these tests included four types of stainless steel (304, 310, 316, and 410), three types of low-alloy steel (Croloy 2-1/4, Croloy 3M, and T-1), and one iron-aluminum base alloy.

The analyses of gaseous impurities in these tests were consistent with those of earlier tests, the major impurities being CO, CO_2, H_2, H_2O, and CH_4 (ref 10). Each of these impurities increased rapidly because of outgassing of the graphite as the test vessel was heated to the test temperature; however, upon reaching this temperature the impurity level immediately decreased. The level ultimately reached as a result of this decrease was considerably lower in tests operated at 1400 than at 1100°F. It is interesting to note that the gas analyses for the static-heated-specimen tests were comparable to those obtained for similar isothermal static tests at 1100°F (ref 12).

In agreement with earlier tests, all unheated samples of austenitic stainless steels exposed in the gas streams of these tests showed no surface changes other than a thin, tightly adherent, gray-to-black oxide tarnish, which was accompanied by a very small weight gain.[11,12] The heated

---

[12] GCR Quar. Prog. Rep. Sept. 30, 1959, ORNL-2835 (in press).

Fig. 3.2. Photograph of T-1 Steel Specimen After Exposure in Low-Pressure Thermal-Convection Loop at 1100°F for 1000 hr. Oxide layers on base-metal surface are evident. Electron microscopy and electron and x-ray diffraction analyses showed scale to consist of four layers, the surface (*A*) and first subsurface (*B*) layers being Fe_3O_4 and the following two subsurface layers (*C* and *D*) being Fe_3O_4 plus α iron. (Photograph and scale analyses courtesy of T. E. Willmarth, Analytical Chemistry Division.) 20X. Reduced 8%.

elements, however, showed varied attack. A type 304 stainless steel section heated to 1500°F in a static pot formed a loosely adherent, silvery gray, nonmagnetic layer. In areas where spalling of the outer layer had occurred, a thin, gray underlayer was apparent. In contrast, a type 304 stainless steel test section that was held at 1500°F in another static pot showed a typical, adherent, black reaction layer. The conditions of the two static tests differed only in that the former had a slightly higher metal volume. The surface appearance of a type 304 stainless steel section heated to 1600°F in a static test varied noticeably along the length of the element. The hotter upper portion of the assembly exhibited a bright-green surface film, while two removable sleeves near the cooler bottom portion were dark gray.

The low-alloy steels generally showed good resistance to attack, although they were more heavily oxidized and more susceptible to decarburization than the stainless steels. However, in one low-pressure- and one high-pressure thermal-convection test, the low-alloy steels showed heavy silvery-gray reaction films. These films tended to spall off both during testing and when handled, and revealed powdery black layers beneath. The appearance of the latter specimens is illustrated in Fig. 3.2.

MATERIALS COMPATIBILITY

E. E. Hoffman
W. H. Cook J. R. DiStefano
D. H. Jansen

Molten-Salt Reactor Program

W. H. Cook D. H. Jansen E. E. Hoffman

Introduction. – An unclad graphite moderator would be a definite advantage in the Molten-Salt Power Reactor.[13] This would require that portions of the structural alloys of the reactor be exposed to the molten salt in contact with the graphite at the reactor operating temperature of

[13]H. G. MacPherson et al., A Preliminary Study of Molten-Salt Power Reactors, ORNL CF-57-4-27 (Apr. 29, 1957).

approximately 1200°F (649°C).[13] The compatibility and permeability of the unclad graphite with the molten salt, plus the effects of carburization, if any, on the structural alloys, at operating conditions must be known before these components can be incorporated into the design of the reactor.

At the beginning of the investigation of the preceding questions, Inconel and INOR-8 were considered as potential structural alloys, and $LiF-BeF_2-UF_4$ (62-37-1 mole %, fuel 130) was the fuel generally considered for use in the Molten-Salt Power Reactor. A test temperature of 1300°F (704°C) was chosen so that there would be a small, built-in safety factor.

Carburization of Inconel and INOR-8 in Sodium-Graphite Systems (W. H. Cook, D. H. Jansen). – Carburization studies on Inconel and INOR-8 in a sodium-graphite medium were conducted at the following conditions: 1200°F (649°C) for 40, 400, and 4000 hr; 1400°F (760°C) for 40, 400, and 4000 hr; and 1600°F for 40 hr. The relative carburizing rates of Inconel and INOR-8 were studied as a function of time and temperature. A detailed description of the test assembly was reported previously.[14]

The results of room-temperature tensile tests on duplicate carburized specimens indicated that the room-temperature ductility was appreciably decreased, compared with control specimens heat treated in argon for the same temperatures and times. There was no appreciable decrease in the 1250°F (677°C) tensile strengths of these carburized specimens.

The approximate diffusion coefficient at 1200°F of carbon in Inconel and in INOR-8 was calculated from the carbon analyses of a series of millings taken from the Inconel and INOR-8 exposed to sodium and graphite for 4000 hr.[15] The diffusion coefficient of carbon in Inconel was calculated to be approximately 7×10^{-12} cm^2/sec, and the diffusion coefficient for carbon in INOR-8 was 3.5×10^{-12} cm^2/sec. These results indicate that the carbon content at the midpoint of an INOR-8 tube having a wall 50 mils thick would be approximately 0.2 wt % after the inside diameter was exposed for 20 years to the sodium-graphite carburizing system at 1200°F

[14]E. E. Hoffman, W. H. Cook, and D. H. Jansen, MSR Quar. Prog. Rep. June 30, 1958, ORNL-2551, p 59.

[15]W. H. Cook and D. H. Jansen, A Preliminary Summary of Studies of INOR-8, Inconel, Graphite, and Fluoride Systems for the MSRP for the Period from May 1, 1958 to Dec. 31, 1958, ORNL CF-59-1-4.

(649°C). More studies are necessary to determine whether the mechanical properties of the tube would be detrimentally affected by this amount of carburization. Information available at present indicates that carburization of this extent would be detrimental to the room-temperature tensile properties of the tube but that the 1250°F (677°C) tensile properties of the tube would not be seriously affected. This was found for 40-mil-thick INOR-8 sheet specimens that had been carburized to depths of 6 to 10 mils and in which a 10-mil-thick surface layer analyzed from 0.3 to 0.4 wt % carbon.[16]

Inconel and INOR-8 in the Fuel 130–Graphite Test Systems (D. H. Jansen, W. H. Cook). – The advantages of having the fuel in contact with an unclad graphite moderator in the Molten-Salt Reactor has been indicated earlier.[17] Consequently, Inconel and INOR-8 were statically tested in fuel 130 ($LiF-BeF_2-UF_4$, 62-37-1 mole %), which was in contact with bare graphite to determine whether the system would carburize the alloys. A test configuration similar to those used in previously reported sodium-graphite tests[18] was employed. The ratio of the surface area of Inconel and INOR-8 to the volume of fuel was 1.3 $in.^{-1}$ while the ratio of the surface area of the graphite to the volume of fuel was 0.43 $in.^{-1}$. A series of eight such tests was initiated. The 2000-, 4000-, and 6000-hr tests were terminated as scheduled, while those scheduled for 8000, 10,000, 12,000, 14,000 hr, and one for a longer period, are still in operation.

Results of Fuel-Graphite Tests in INOR-8. – No evidence of carburization was detected metallographically in any of the three completed tests. Chemical results of millings from the specimens in the 6000-hr test showed no significant carburization.

The effects of exposure time on the mechanical properties of INOR-8 are shown in Table 3.7. It can be seen that there were no appreciable

---

[16]E. E. Hoffman, W. H. Cook, and D. H. Jansen, MSR Quar. Prog. Rep. Oct. 31, 1958, ORNL-2626, p 57–60.

[17]Molten Salt Reactor Program Status Report, ORNL CF-58-5-3, p 6 (May 1, 1958).

[18]E. E. Hoffman, W. H. Cook, and D. H. Jansen, MSR Quar. Prog. Rep. June 30, 1958, ORNL-2551, p 59.

Table 3.7. Tensile Results of INOR-8 Control* and Test** Specimens from Fuel 130–Graphite Tests

Time of Exposure (hr)	Control Specimens		Test Specimens	
	Tensile Strength (psi)	Elongation (% in 2 in.)	Tensile Strength (psi)	Elongation (% in 2 in.)
	Room Temperature Tensile Tests			
	x 10^3		x 10^3	
2000	123.2	42.5	124.8	41.0
4000	123.0	42.0	124.5	43.0
6000	124.7	39.0	124.2	36.0
	1250°F Tensile Tests			
2000	74.6	18.0	75.6	18.5
4000	75.9, 76.0	19.0, 20.0	76.2, 74.3	18.5, 18.5
6000	72.8	16.5	74.5	16.0

*Control specimens exposed to argon at 1300°F for the times indicated.

**Test specimens exposed to fuel 130–graphite system at 1300°F for the times indicated.

differences in the mechanical properties of the control and test specimens from these tests.

No corrosion of the INOR-8 test specimens was observed except for a slight roughening of less than 1 mil in depth on specimens tested for 4000 and 6000 hr.

Results of Fuel-Graphite Tests on Inconel. — Metallographic examination of Inconel specimens tested in the fuel-graphite system for 2000 and 4000 hr showed that they were attacked to depths of 3 and 5 mils, respectively. Attack of this magnitude on Inconel by fuel 130 has not been observed in graphite-free, thermal-convection-loop corrosion systems.[19]

Results of tensile tests show a sharp decrease in elongation and tensile strength due to the heavy corrosion, thus masking any possible minor effect of carburization on the tensile properties.

[19] J. H. DeVan and J. R. DiStefano, MSR Quar. Prog. Rep. June 30, 1958, ORNL-2551, p 57.

INOR-8 Thermal-Convection Loop Containing Graphite and Fuel 130. – An INOR-8 thermal-convection-loop test circulating fuel 130 ($LiF-BeF_2-UF_4$, 62-37-1 mole %) with a TSF graphite tube-insert in the hot leg has been operated for 4000 hr. The hot-leg temperature of this loop was 1300°F. The purpose of the test was to investigate possible carbon pickup by INOR-8 in a nonisothermal circulating system. No evidence of carburization could be detected by metallography, microhardness measurements, or chemical analyses.[20]

Brazing Alloys Tested in Loop Circulating Fuel 130 (D. H. Jansen). – Brazing alloys have been corrosion tested in the hot-leg section of a thermal-convection loop circulating fuel 130 for 1000 hr.[21] The hot-leg temperature of the loop was 1300°F (704°C).

Inconel and INOR-8 lap joints were brazed with these alloys, making a total of ten specimens which were suspended in an expanded section in the hot leg. The alloys, their compositions, and metallographic results after test are listed in Table 3.8.

No attack was found on the nickel-base Coast Metals alloys or the pure copper alloy after test. Similar tests for 5000- and 10,000-hr periods are in progress.

Uranium Precipitation from Fuel 130 in Contact with Graphite at 1300°F (704°C) (W. H. Cook). – The fact that part of the uranium in $LiF-BeF_2-UF_4$ (62-37-1 mole %, fuel 130) precipitated as UO_2 when this fuel was contained in graphite crucibles at 1300°F (704°C) under a vacuum has been reported; no precipitate was observed in $NaF-ZrF_4-UF_4$ (56-40-4 mole %, fuel 30) under similar conditions.[22]

Results have indicated that the source of the oxygen which caused the precipitation from fuel 130 was the graphite.[23] Graphite grades TSF, AGOT, CCN, ATJ, and C-18 have been used to fabricate test crucibles.

---

[20]"General Corrosion Studies," MSR Quar. Prog. Rep. Apr. 30, 1959, ORNL-2723, pp 61, 62, 64.

[21]E. E. Hoffman and D. H. Jansen, MSR Quar. Prog. Rep. June 30, 1958, ORNL-2551, p 62.

[22]W. H. Cook, Met. Ann. Prog. Rep. Oct. 10, 1958, ORNL-2632, p 105 (classified).

[23]MSR Quar. Prog. Rep. Apr. 30, 1959, ORNL-2723, p 58.

Table 3.8. Metallographic Results of Brazing Alloys Tested in Thermal-Convection Loop Circulating Fuel 130

Test Conditions: Hot-leg temperature, 1300°F; time, 1000 hr

Alloy	Composition (%)	Metallographic Results of Alloy Brazed to: Inconel	INOR-8
Coast Metals No. 52	89 Ni–5 Si–4 B–2 Fe	No attack	No attack
Coast Metals No. 53	81 Ni–8 Cr–4 B–4 Si–3 Fe	No attack	No attack
General Electric No. 81	70 Ni–20 Cr–10 Si	6 mils of uniform attack	No attack
Gold-Nickel	82 Au–18 Ni	Diffusion voids to a depth of 3 mils	Diffusion voids to a depth of 4 mils
Copper	100 Cu	No attack; a few porous areas in fillet	No attack; minute porosity in fillet

The ratio of the bulk volume of a crucible to the volume of fuel it contained in test was 27:1. The range of the portion of the uranium that precipitated from fuel 130 charges has been from approximately 4% for fuel contained in a TSF graphite crucible to 54% for fuel contained in a C-18 graphite crucible.

The quantity of UO_2 precipitated from fuel 130 varied for the same grade of graphite in crucibles that had been machined from different stocks, indicating that manufacturing variables and/or subsequent handling were responsible for the variations. Reproducible results were obtained by using crucibles machined from a single stock of graphite. This indicated that graphite contamination and subsequent UO_2 precipitation could be appreciably controlled by proper handling of the graphite during and following its fabrication.

In general, the smaller quantities of precipitate were associated with the graphite that had been manufactured to have the smallest amount of metal contaminants, such as the TSF and AGOT grades.

The fraction of uranium that precipitated from fuel 130 in contact with graphite grades TSF, AGOT, and CCN appeared to occur quickly, generally within a 5-hr exposure.

Removal of Oxide Contamination from Graphite (W. H. Cook). — Previous tests have shown that exposing graphite to fuel 130 at 1300°F (704°C) would result in the precipitation of a fraction of the uranium as UO_2. This precipitation reaction had occurred in fuel 130 in vacuum, where the graphite was not in direct contact with the fuel, as well as in the tests where the fuel was contained in graphite crucibles.[24–26] These results suggested that it might be feasible to remove oxide contaminants from the graphite by gettering or flushing the graphite with a suitable medium, such as fuel 130, itself.

Initial tests were conducted in a vacuum, with graphite crucibles exposed for 20 hr to fuel 130 both in proximity to and also in direct

---

[24] MSR Quar. Prog. Rep. Oct. 31, 1958, ORNL-2626, p 62.
[25] MSR Quar. Prog. Rep. Jan. 31, 1959, ORNL-2684, p 80.
[26] MSR Quar. Prog. Rep. Apr. 30, 1959, ORNL-2723, p 58.

contact with the fuel. Both methods appeared to remove small amounts of oxide, and additional experiments are planned.[27]

Permeation of Various Grades of Graphite by Molten Fluoride Salts (W. H. Cook). – Six grades of graphite have been subjected to permeation tests with three different fluoride compositions, and results are summarized in Table 3.9.

The methods were the same for each test. The graphite specimens were ultrasonically washed in absolute ethyl alcohol to remove machining dust and then dried for at least 15 hr at 248°F (120°C). The specimens were evacuated at less than 12 μ Hg for 15 hr at 572°F (300°C), plus half an hour during which the temperature was increased to 752°F (400°C). The evacuated graphite was flooded and completely covered with the test salt at the liquidus temperature of the salt. The temperature was raised to 1300°F (704°C) and then pure argon was used to create a salt pressure of 150 psig. The temperature and pressure were maintained for 100 hr; the salt was drained from the graphite, the test unit was cooled to room temperature, and the graphite was examined for salt permeation.

The mixture $LiF-BeF_2-ThF_4-UF_4$ (67-18.5-14-0.5 mole %, BULT 14-.5U) is typical of the salts now being considered for the Molten-Salt Reactor. Until recently, fuel 130 was used for most of the permeation tests; fuel 30 was included to determine whether a different salt composition was a factor in the degree of penetration. The data in Table 3.9 indicate that, under the test conditions, the extent of permeation was not dependent on the types of salt represented by fuels 30, 130, or BULT 14-.5U.

Graphite grades GT-123 and 186 were the only ones tested that were fabricated as low-permeability graphite.

The permeation tests (Table 3.9) were all separate tests except for the one involving BULT 14-.5U; all six grades of graphites (three specimens of each) were exposed at the same time to this medium.

Of the graphite tested, only grade GT-123 appeared to meet the Molten-Salt Reactor permeability requirement that the bulk volume of the graphite permeated by salt be less than 0.5%.

The preceding are initial tests; future work consists in evaluating the salt permeabilities of the many grades of "low permeability" graphite

[27] MSR Quar. Prog. Rep. July 31, 1959, ORNL-2799 (in press).

Table 3.9. Permeation of Various Grades of Graphite by Molten Salts

Graphite specimens tested in BULT 14-.5U were 0.500 in. in diameter and 1.500 in. long; those tested in the other two salts were 1.875-in. OD × 0.250-in. ID × 2.00 in. long

All values are averages of three except those with the numerical superscripts; the numerical superscripts denote the number of values averaged

Test Conditions: Temperature, 1300°F (704°C)
Pressure, 150 psig
Exposure period, 100 hr

Graphite Grade	Bulk Density (g/cc)	Percentage of Voids in Graphite	Percentage of Voids Permeated by Fuel Salts			Percentage of Bulk Volume of Graphite Permeated by Fuel Salts		
			Fuel 30[a]	Fuel 130[b]	BULT 14-.5U[c]	Fuel 30	Fuel 130	BULT 14-.5U
GT-123	1.92	15.8			1.02			0.13
186	1.86	18.6		26.4(1)	21.2		4.6(1)	4.0
CCN	1.92	16.0	29.2(1)		26.2	4.9(1)		4.2
R-0013	1.87	18.0			33.5			6.0
AGOT	1.68	26.2	58.4(1)	58.2	54.3	14.9(1)	14.8	14.2
TSF	1.67	26.7		49.6(2)	53.7		13.2(2)	14.4

[a] $NaF-ZrF_4-UF_4$ (56-40-4 mole %).

[b] $LiF-BeF_2-UF_4$ (62-37-1 mole %).

[c] $LiF-BeF_2-ThF_4-UF_4$ (67-18.5-14-0.5 mole %).

and establishing the effects of temperature, time, and pressure on the permeabilities of the most promising grades of graphite.

The graphite specimens will be taken from bulk shapes, pipes, and tubes that are suitable for reactor construction without major changes in their shapes and sizes.

Corrosion Research in Support of Maritime Ship Reactor Project

D. H. Jansen W. H. Cook

A fuel element proposed for possible application in maritime reactors incorporates a low-melting liquid metal as the thermal bonding agent between the UO_2 pellets and the stainless steel can.

The compatibility of various low-melting metals with UO_2 and type 304 stainless steel was determined.

Small, hot-pressed UO_2 cylinders were exposed to lead, bismuth, the 55 Bi–45 Pb eutectic, and the Pb–0.69 Li eutectic for 500 hr at 650°F (343°C) and 750°F (399°C) in type 304 stainless steel containers.

Metallography shows no corrosion of the stainless steel containers after test. A black powdery substance was observed on the surface of each solidified bath after test. Results of x-ray examination on this powdery material are listed in Table 3.10. Uranium compounds were found only in tests containing bismuth and in the higher-temperature (750°F) lead test.

The presence of UC_2 in the 650°F Pb-Bi test is probably due to carbon contamination present in the UO_2 pellet prior to testing.

Metallography of as-received and tested specimens did not show any indications that any of the heat-transfer media had attacked the UO_2 specimens.

Aircraft Nuclear Propulsion

E. E. Hoffman
W. H. Cook J. R. DiStefano
D. H. Jansen

The research performed by the Materials Compatibility Group during this reporting period has been reported elsewhere.[28]

---

[28] ANP Semiann. Prog. Rep. Oct. 31, 1959, ORNL-2840 (in press) (classified).

Table 3.10. Results of X-Ray Examinations of Solidified Heat-Transfer Media Following Exposure to UO_2 in Type 304 Stainless Steel Capsules

Test Conditions: Temperature, as indicated
Time, 500 hr

Heat Transfer Medium	Temperature of Test (°F)	Identified Compounds* Detected in the Powdery Material Found on Solidified Heat-Transfer Media
Lead	650	Pb, PbO
Lead	750	Pb, PbO, UO_2
Bismuth	650	Bi, UO_2, Bi_2O_3
Bismuth	750	Bi, UO_2
55 Bi–45 Pb	650	Bi, Pb, UO_2, Bi_2O_3
55 Bi–45 Pb	750	Bi, Pb, UO_2, Bi_2O_3
Pb–0.69 Li	650	Pb, PbO
Pb–0.69 Li	750	Pb, PbO

*Compounds are listed in order of decreasing intensities.

HIGH-TEMPERATURE ALLOY DEVELOPMENT

H. Inouye
T. K. Roche D. O. Hobson
W. J. Werner

Materials for GCR Fuel Capsules

H. Inouye

The Reactions Between Type 304 Stainless Steel and Gases. – This investigation is concerned with determining the compatibility of type 304 stainless steel with low concentrations of impurity gases which accompany helium. Since the helium is in contact with graphite at high temperatures, the impurity species assumed for this study are CO, CO_2, H_2O, H_2, and CH_4. The temperature range of interest is from 500 to 1850°F. The thermodynamic

aspects of the gas-metal reactions and the results of preliminary experiments have been reported.[29,30]

The objectives of this study are (1) to establish the effects of these gases singly and in combination with respect to oxidation, carburization, and decarburization, and (2) to establish the permissible limits of these gases which will not seriously cause deterioration of the mechanical properties of the alloy after exposure for extended periods.

Reactions with Flowing CO_2. – The principal reaction between type 304 stainless steel and CO_2 was oxidizing, at 1500°F. Tests were run in flowing mixtures of Ar and CO_2 containing between 0.1 and 0.6% CO_2. At a flow rate of 300 cc/min the bulk oxide was 3 $Cr_2O_3 \cdot Fe_2O_3$, which was magnetic and green. Analysis of the metal for changes in the carbon content did not indicate carburization or decarburization (see Table 3.11). Based on these tests, the approximate reaction was assumed to be

$$2\ Fe + 6\ Cr + 12\ CO_2 \rightarrow 3\ Cr_2O_3 \cdot Fe_2O_3 + 12\ CO \qquad (1)$$

The rates of reaction at the various pressures studied were not significantly different, ranging from 109 to 117 $\mu g/cm^2$ per hundred hours.

Reactions with CO. – Thermodynamically, CO will oxidize stainless steel at 1500°F. The possibility of carburization exists, however, if the oxide film is not impervious to CO.

Tests run in static CO showed that Fe_3O_4 was the oxide film at the gas interface and that various spinels formed at the metal-oxide interface. Starting with an initial CO pressure of 20.5 cm Hg, the final pressure after 120 hr was about 0.0020 cm Hg. Analysis of the stainless steel after testing showed that carburization had occurred. In order to account for the nearly complete consumption of gases, the reaction was assumed to be approximately

$$4\ Fe + 34\ Cr + 8\ CO \rightarrow Fe_3O_4 + FeO \cdot Cr_2O_3 + 8\ Cr_4C \qquad (2)$$

Reactions with Static CO_2. – Since it was found that type 304 stainless steel does not carburize in flowing CO_2 and that carburization does

[29] GCR Semiann. Prog. Rep. Dec. 31, 1958, ORNL-2676, p 85–90.

[30] GCR Semiann. Prog. Rep. June 30, 1959, ORNL-2767, p 114–15.

Table 3.11. Reactions of Type 304 Stainless Steel with CO and CO_2 at 1500°F

Atmosphere	Flow Rate (cc/min)	Test Duration (hr)	Weight Gain ($\mu g/cm^2$)	Principal Oxide Film	Weight Per Cent Carbon in Stainless Steel	
					Before	After
0.1% CO_2 + Ar	300	120	109		0.097	0.086
0.6% CO_2 + Ar	300	90	117	$3\ Cr_2O_3 \cdot Fe_2O_3$	0.11	0.12
CO at 20.5 cm Hg	Static	118	93	Fe_3O_4	0.098	0.26
CO_2 at 70 cm Hg	Static	304			0.098	0.41
CO at 20.5 cm Hg*	Static	168			0.41	0.72

*Sample from static CO_2 test re-exposed to CO.

occur with CO, the possibility of carburization in static CO_2 was assumed on the basis of reaction (1). As shown in Table 3.11, carburization did occur, indicating that CO might be a metastable corrosion product. The instability of CO resulting from the decomposition of CO_2 in contact with stainless steel was demonstrated by the fact that with starting pressure of 25 mm Hg, the final pressure was reduced to 0.020 mm.

In a recent report by Bockros and Wallace,[31] the oxidation rates of various stainless steels were determined in static CO_2 at 2000 psi and 1500°F. They found that for the 18-8 stainless steel, the weight gain was 2.2 mg/cm^2 in 168 hr under these conditions. The present available data indicate that the reaction rate increased from 0.1 to 2.2 mg/cm^2 per 150 hr as the CO_2 pressure was increased from 0.088 psi to 2000 psi. The above authors conclude that the CO_2 reaction with type 304 stainless steel results from the dissociation of CO_2 to CO and O_2, with subsequent oxidation of the metal by the O_2 in accordance with reactions (3) and (4).

$$2\ CO_2 \rightarrow 2\ CO + O_2 \qquad (3)$$

$$\text{Metal} + O_2 \rightarrow \text{Metal oxide} \qquad (4)$$

The proposed reactions are not in agreement with this investigation.

High-Temperature Stability of INOR-8

H. Inouye

A nickel-base alloy containing 16 to 18% Mo–6 to 8% Cr–0.04 to 0.08% C–4% (max) Fe has been developed for containing fused fluoride salts at high temperatures. This alloy, designated as INOR-8, was developed for service at temperatures in excess of 1500°F. Presently the alloy is contemplated for use below 1500°F. In order to determine the suitability of the alloy with respect to stability at these temperatures, the tensile properties of the alloy were determined for aging times up to 10,000 hr in the temperature range between 1000–1400°F.

The compositions of the heats studied are listed in Table 3.12. Heat SP-19 was a 10,000-lb melt from an electric furnace. Heat 8-M-1

[31] J. C. Bockros and W. P. Wallace, The Oxidation of Metals by CO_2 at Temperatures of 1100°F to 1700°F and Pressures of 1000–2000 psi, GA-700 (Mar. 25, 1959).

Table 3.12. Percentage Chemical Composition of INOR-8

Element	Haynes Heat SP-19	Westinghouse Heat 8-M-1	Westinghouse Heat 8-M-1 AC
C	0.06	0.14	0.144
Mn	0.48	0.69	0.73
Si	0.40	0.21	0.19
S	0.015	0.006	0.001
P	0.010	0.002	0.001
Fe	4.83	6.1	5.10
Cr	7.43	7.47	7.00
Mo	16.65	16.20	17.20
Ti		0.11	0.075
Ni	70.00	70.60	70.60
V	0.10		
Cu	0.02		
W	Trace		
Co	0.51		

was a 5000-lb air-induction melt, and heat 8-M-1 AC was a vacuum arc remelt of heat 8-M-1. Tensile tests were conducted on 0.045-in. sheet specimens which were aged 500, 1000, 2000, 5000, and 10,000 hr at room temperature and at the aging temperatures.

Table 3.13 lists the tensile properties of the alloy in the annealed condition and after aging times of 1000 and 10,000 hr. The variations from heat to heat are apparent in the yield point and ductility after the various heat treatments. From previous studies of nickel-molybdenum alloys, it has been shown that the mechanical properties are influenced significantly by the carbon content. The lower yield point and higher ductility of heat SP-19 (C = 0.06%) compared with that of 8-M-1 and/or 8-M-1 AC (C = 0.14%) are probably due to the difference in carbon content.

Table 3.13. Tensile Properties of INOR-8*

Test Temperature (°F)	Haynes Heat SP-19 Ultimate Tensile Strength (psi)	Haynes Heat SP-19 0.2% Yield Strength (psi)	Haynes Heat SP-19 Percentage Elongation	Westinghouse Heat 8-M-1 Ultimate Tensile Strength (psi)	Westinghouse Heat 8-M-1 0.2% Yield Strength (psi)	Westinghouse Heat 8-M-1 Percentage Elongation	Westinghouse Heat 8-M-1 AC Ultimate Tensile Strength (psi)	Westinghouse Heat 8-M-1 AC 0.2% Yield Strength (psi)	Westinghouse Heat 8-M-1 AC Percentage Elongation
				Annealed					
Room	114,400	44,700	50	117,100	51,900	39	113,300	48,500	33
1000	93,000	28,300	46	101,000	34,200	40	104,100	35,500	34
1100	93,000	28,900	50	102,600	37,600	37	100,900	35,900	36
1200	82,400	27,500	37	83,100	38,400	16	87,900	37,000	19
1300	69,900	28,000	24	70,500	38,400	18	78,400	37,800	14
1400	61,800	26,200	21	63,900	38,500	14	64,900	35,000	21
				Aged 1000 hr**					
1000	94,800	30,400	51	98,600	35,000	42	105,800	39,100	39
1100	88,400	31,700	43	87,350	36,300	27	101,600	42,300	34
1200	75,700	29,740	29	72,300	35,700	14	83,500	39,600	14
1300	73,200	28,900	29	74,900	36,400	14	80,600	37,800	21
1400	64,900	29,000	18	65,200	36,100	14	62,700	29,200	26
				Aged 10,000 hr**					
1000	97,700		46	101,600		32			
1100	90,500		40	86,000		19			
1200	81,900		32	78,800		16			
1300	76,100		24	78,000		15			
1400	65,100		20	60,600		16			

*0.045 in. sheet specimens; annealed 1 hr at 2100°F; air cooled; strain rate 0.05 in./min.

**Aged at testing temperature in quartz capsules.

In general, these differences are of minor proportions with respect to the serviceability of the alloy in this temperature range. For a particular heat, aging does not significantly affect the tensile properties. As a result of this study, it was concluded that embrittlement by aging does not occur and that the variations observed from heat to heat are due to the chemical composition.

Aircraft Nuclear Propulsion Project

H. Inouye D. O. Hobson W. J. Werner

The research performed in the High-Temperature Alloy Development Laboratory on the Aircraft Nuclear Propulsion Project has been reported.[32,33]

Molten-Salt Reactor Project

Fabrication of Triplex Heat Exchanger Tubing (T. K. Roche). – Studies have been made in order to determine the feasibility of fabricating a triplex heat exchanger tube according to a design proposed by the Reactor Projects Division. The tube is made up of two concentric tubes separated by a porous-metal annulus which is intended to provide thermal contact between a hot, low-pressure fluid on one side of the tube and high-pressure steam on the other. At the same time, the porous-metal annulus would effectively isolate the two fluids in the event of a wall failure. Static helium at an intermediate pressure within the porous annulus would serve as a leak detector. In case of failure of either wall, an increase or decrease in the helium pressure will be observed. The introduction of a positive means of leak detection, in addition to providing an attractive feature for liquid-metal-to-steam heat exchangers, could offer the advantage of direct transfer of heat from liquid fuel to steam, thereby eliminating secondary cooling circuits.

The proposed requirements of the triplex tube are (1) that the annular core be sufficiently porous, perhaps 25 to 50% by volume, to allow gas passage; (2) that the core be bonded to the cladding tubes for optimum heat transfer; and (3) that the core have sufficient ductility to allow a

[32] ANP Semiann. Prog. Rep. Mar. 31, 1959, ORNL-2711, p 3–10.

[33] ANP Semiann. Prog. Rep. Oct. 31, 1959, ORNL-2840 (in press).

7- to 8-ft length of triplex to be bent into a U-configuration of approximately 27 in. radius without causing excessive core damage. Successful fabrication of seven such tubes would enable the construction of a heat exchanger[34] designed for heat transfer and reliability evaluation tests. Development studies for the welding and back brazing of triplex tubes into tube sheets have been made.[35]

Materials presently being considered for fabricating such tubing are a porous nickel core clad with Inconel or INOR-8. Inconel cladding tubes have been used exclusively to date because of their immediate availability.

Two methods for making triplex tubing have been considered: first, by tamping powdered nickel into the annular space formed by the concentric cladding tubes and then developing a porous core bonded to the cladding tubes by suitable drawing and sintering operations; and second, by bonding a prefabricated porous core to the cladding tubes, also by suitable drawing and sintering operations.

Results obtained by the first method have been described.[36] Difficulties were encountered with an oxide layer that formed at the core-clad interface, causing a poor-quality bond (see Fig. 3.3). These difficulties were attributed to oxygen contamination in the nickel powder. As a result, this method has been discontinued, for the present, in favor of the second method.

Porous nickel tubing of approximately 50–60% of theoretical density is available from the Micro Metallic Corporation. This tubing is prepared by rolling powder-metallurgy sheet stock. One-sixteenth-inch-thick sheet stock can be rolled into a 3/4-in.-OD tube.

An attempt to Inconel-clad a sample of porous nickel received from Micro Metallic showed that a clean bond could be achieved between the components.[37,38] A 9-ft length of triplex tubing was subsequently made by assembling six 18-in. lengths of porous nickel tubing in the annular space

---

[34] MSR Quar. Prog. Rep. Jan. 31, 1959, ORNL-2684, p 54.

[35] MSR Quar. Prog. Rep. Jan. 31, 1959, ORNL-2684, p 88.

[36] MSR Quar. Prog. Rep. Jan. 31, 1959, ORNL-2684, p 85–87.

[37] MSR Quar. Prog. Rep. Apr. 30, 1959, ORNL-2723, p 67–68.

[38] MSR Quar. Prog. Rep. July 31, 1959, ORNL-2799 (in press).

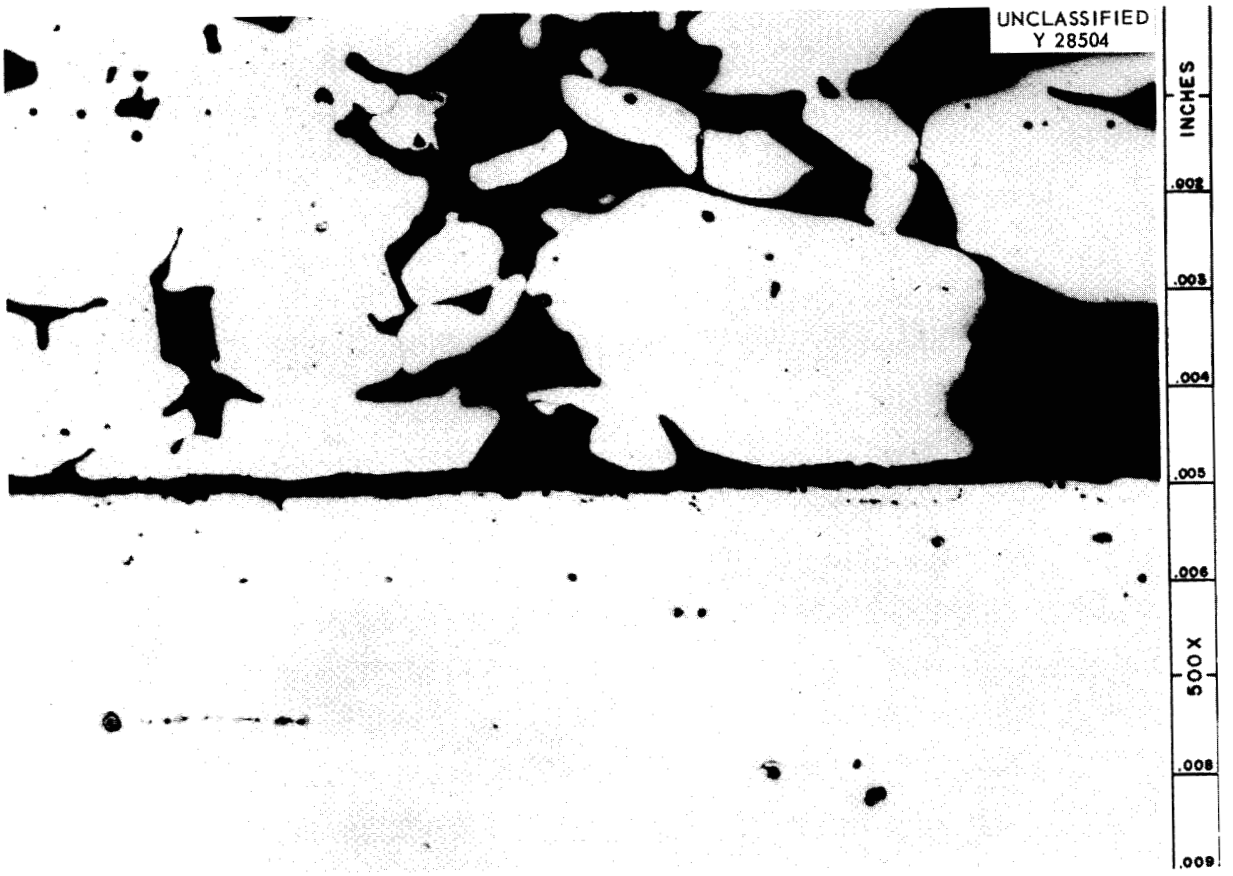

Fig. 3.3. Oxide Layer (Cr_2O_3) Formation at Interface Between Inconel Cladding Tube and Nickel-Powder Core. Triplex fabricated by tamping nickel powder between concentric Inconel tubes, then sintering, drawing, and resintering. As-polished.

between Inconel cladding tubes, cold drawing the assembly, and sintering 1 hr at 2200°F (ref 38). Figure 3.4 shows a macrograph of a transverse section of this tube. Metallography showed evidence of bonding between clad and core, as shown in Fig. 3.5. Preliminary evaluation of the tube after bending into a U-configuration of 26-1/2-in. radius has shown the core-clad bonding to be retained.

One difficulty has been encountered in carrying through this method of triplex tubing fabrication. A radiograph made of the tube after drawing and sintering revealed that two of the five core-to-core joints had separated to a maximum of 3/8 in. At present it is not known if the core separations occurred during assembly, the pointing operation (swaging), or drawing.

Future work will be directed toward the immediate aim of securing seven tubes acceptable for incorporating into a test heat exchanger.

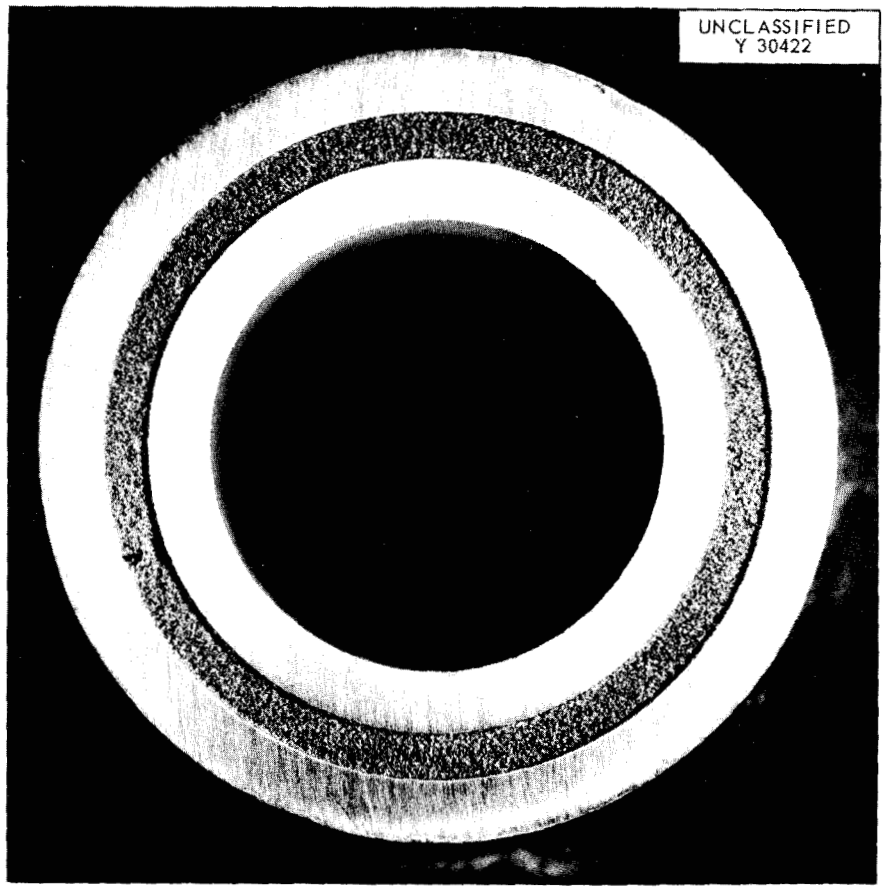

Fig. 3.4. Transverse Section of 9-ft Triplex Tube Fabricated by Cladding Prefabricated Porous Nickel Tubes with Inconel. Approximately 5X.

Gas-Cooled Reactor

T. K. Roche

Procurement of Beryllium Tubing. — The attractive nuclear properties of beryllium have created interest in the application of this metal as a container material for uranium oxide and/or uranium carbide fuel elements for future gas-cooled reactors. To initially assess beryllium for this application will require that tubing be procured preferably from vendors experienced in the handling and fabrication of the metal. At present, an attempt is being made to obtain 500 ft of tubing having an ID of 0.300 in. and a wall thickness of 0.040 in. from each of three sources on a purchase-order basis.

1. English source, Chesterfield Tube Company, Ltd. One hundred feet of tubing extruded from hot-pressed beryllium rod and 400 ft extruded from virgin beryllium powder have been requested.

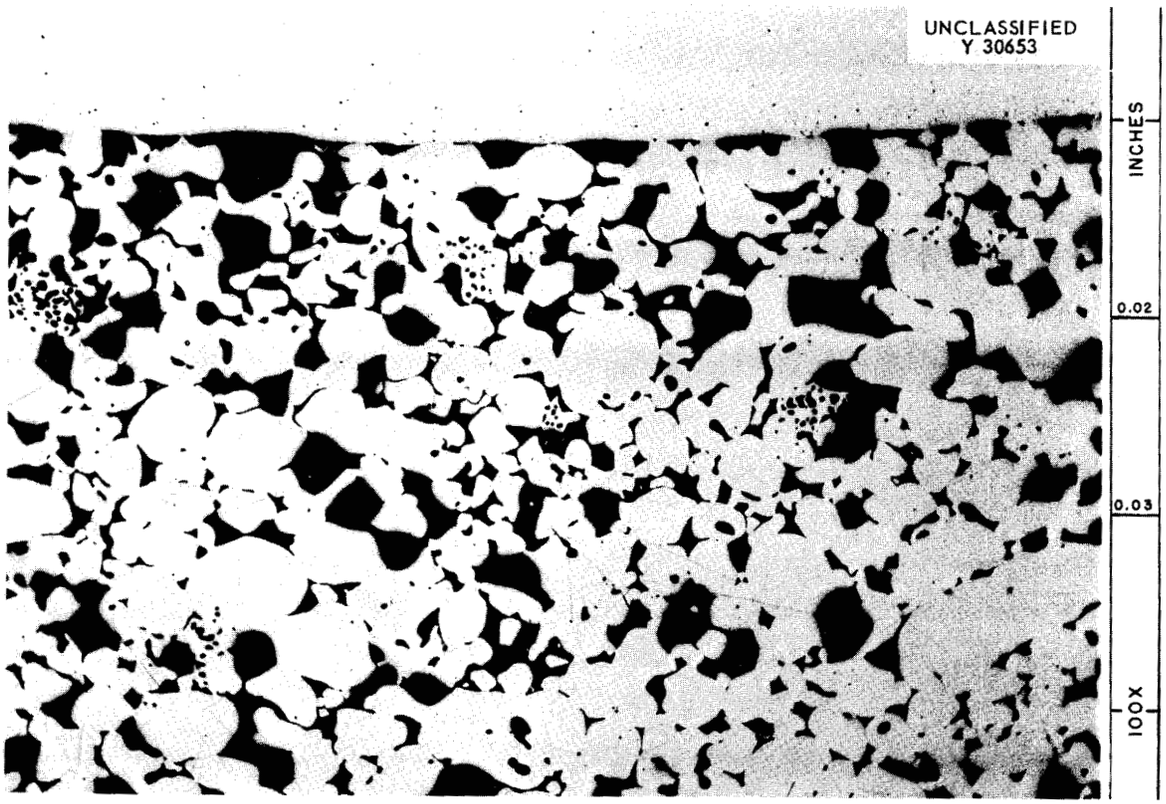

Fig. 3.5. Interface Between Inconel Cladding-Tube and Prefabricated Porous-Nickel Core, Showing Evidence of Bonding. As-polished.

2. French source, Pechiney. Beryllium tubes of the above-mentioned size are not currently available, but Pechiney is considering an attempt to produce tubes of this size. The smallest beryllium tubes on hand at present have an ID of 0.520 in. and a wall thickness of 0.040 in. An inquiry has been issued for procuring 50 ft of this tubing.

3. United States source, Brush Beryllium Company. Brush proposes to fabricate 500 ft of beryllium tubing from their immediate or best grade of beryllium powder by the following methods: (a) machining from hot-pressed block; (b) warm extrusion; (c) hot extrusion; and (d) swaging the powder, followed by sintering and extrusion. The product to be delivered would represent the best results of variations of process conditions for each of these methods. It is felt that this approach would give a better product to evaluate for tests as well as provide the vendor with knowledge of the fabrication problems and eventual manufacturing costs for larger quantities.

As soon as beryllium tubing is made available, it will be evaluated nondestructively to determine the quality of tubing produced by the various suppliers, the percentage of rejection, and the type of defects encountered. The tubing will be examined by x-ray diffraction techniques to determine the degree of preferred orientation in the material which, in turn, will be correlated with the ductility of the material. Tests will be conducted on the weldability, brazability, and mechanical strength of the tubing prior to an in-pile irradiation test program.

In addition, samples of the beryllium tubing are to be evaluated for their corrosion rates in potential gas coolants, specifically helium and carbon dioxide. Corrosion rates will be correlated with manufacturing history and chemical composition of the material.

LIQUID METAL RESEARCH

J. L. Scott D. F. Toner

The Diffusion of Silver and Nickel in Liquid Lead

J. L. Scott

Strauss, White, and Brown[39] proposed recently that solutes occupy interstitial sites in liquid metal solvents when the solvent-to-solute radius ratio exceeds a value of about 1.4. They proposed that at lower values of the radius ratio the solute occupies substitutional sites. If this theory is true, and if the activated-complex theory of liquid metal diffusion of Eyring[40] applies, marked differences would be expected in the diffusion coefficients for solutes which occupy interstitial sites in the liquid compared with those of solutes which occupy substitutional

---

[39] S. W. Strauss, J. L. White, and B. F. Brown, Acta Met. 6(9), 604 (1958).

[40] S. Glasstone, K. Laidler, and H. Eyring, The Theory of Rate Processes, p 477, McGraw-Hill, New York, 1941.

sites. Since the only data for checking this conclusion were for substitutional and interstitial solutes in molten iron,[41] and since the measurement of diffusion coefficients at the temperatures of molten iron is subject to large experimental errors, the writer felt that a definitive experiment was needed to check the validity of the above line of reasoning.

Dilute solutions of silver and nickel in lead were selected for study. The solvent-to-solute radius ratio for silver in lead is 1.18, if the data of Pauling[42] are used and if twelvefold co-ordination is assumed. The corresponding value for nickel in lead is 1.27. Though this value is slightly lower than 1.4, Strauss, White, and Brown[39] place nickel in lead in the interstitial category. Since an interstitial atom has sixfold co-ordination and since a 4% contraction in the radius occurs when the co-ordination changes from twelve- to sixfold,[43] the true solvent-to-solute radius ratio for interstitial nickel atoms in lead is 1.43. In addition to satisfying the atomic size requirements, silver and nickel in lead are amenable to chemical analysis and the measurement of diffusion coefficients.

The apparatus used for diffusion-coefficient measurements is shown in Fig. 3.6. Pyrex capillary tubes having a 2-mm bore were filled with alloys of 0.165 wt % nickel or 2.25 wt % silver in an auxiliary apparatus. The capillaries were then placed in a stainless steel holder and admitted to the apparatus under a hydrogen atmosphere. Initially the capillary was placed in the bath in such a way that the mouth of the capillary was slightly above the surface of the pure lead bath and was held in this position until the temperature of the bath returned to its equilibrium value. The mouth of the capillary was then submerged in the bath, and a run of predetermined duration was made. The capillary was then removed from the bath and chilled. After the capillary had cooled, the metal sample was removed and sectioned, and each section was chemically analyzed. Diffusion coefficients were determined by a comparison with theoretical curves of experimental normalized-concentration-distance data.

---

[41] R. E. Grace and G. Derge, Trans. Met. Soc. AIME 212, 331 (1958).

[42] L. Pauling, Trans. Am. Soc. Metals 48A, 220 (1956).

[43] C. J. Smithells, Metals Reference Book, p 165, Butterworth, London, 1949.

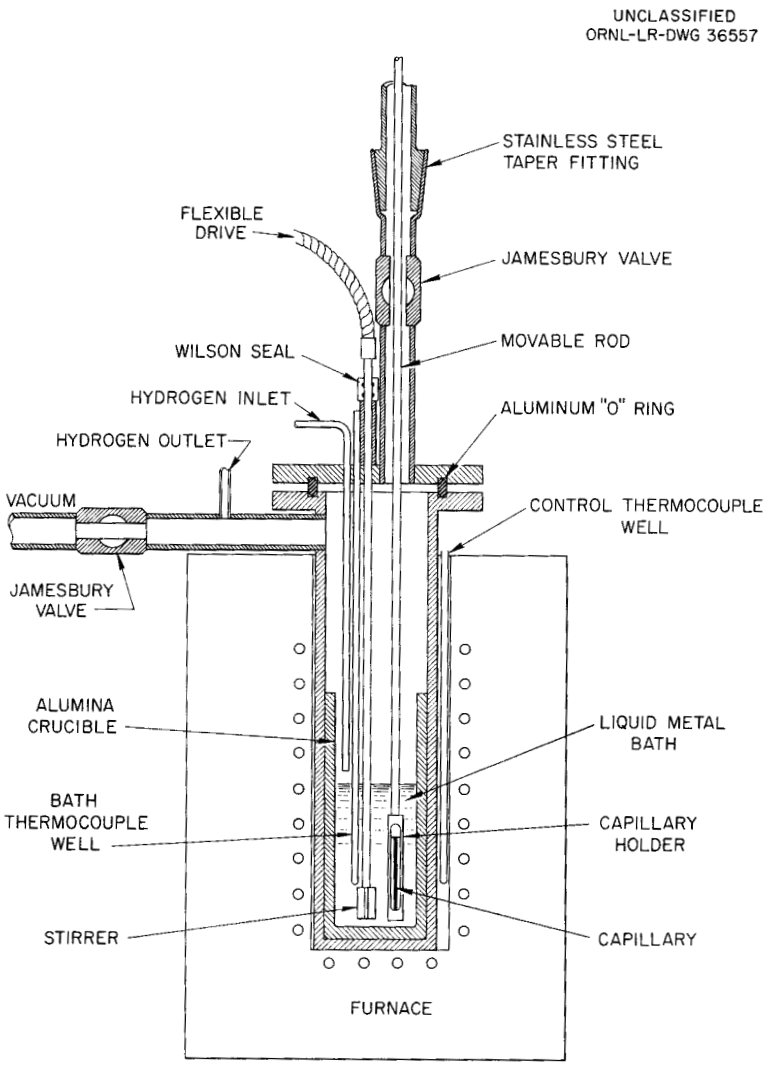

Fig. 3.6. Apparatus for Measuring Diffusion Coefficients in Liquid Metals.

In order to reduce end effects at the mouth of the capillary, the lead bath was stirred vigorously during a few of the runs. No significant differences in diffusion coefficients were observed between runs made with and without stirring.

Measured diffusion coefficients are compared to self-diffusion coefficients for liquid lead[44] in Fig. 3.7. The scatter in the data is inherent in the method, and the close agreement of successive runs at some temperatures is fortuitous. The least-squares expressions for the two sets of data

[44]S. Rothman and L. Hall, Trans. Am. Inst. Mining, Met. Petrol. Engrs. 206, 199 (1956).

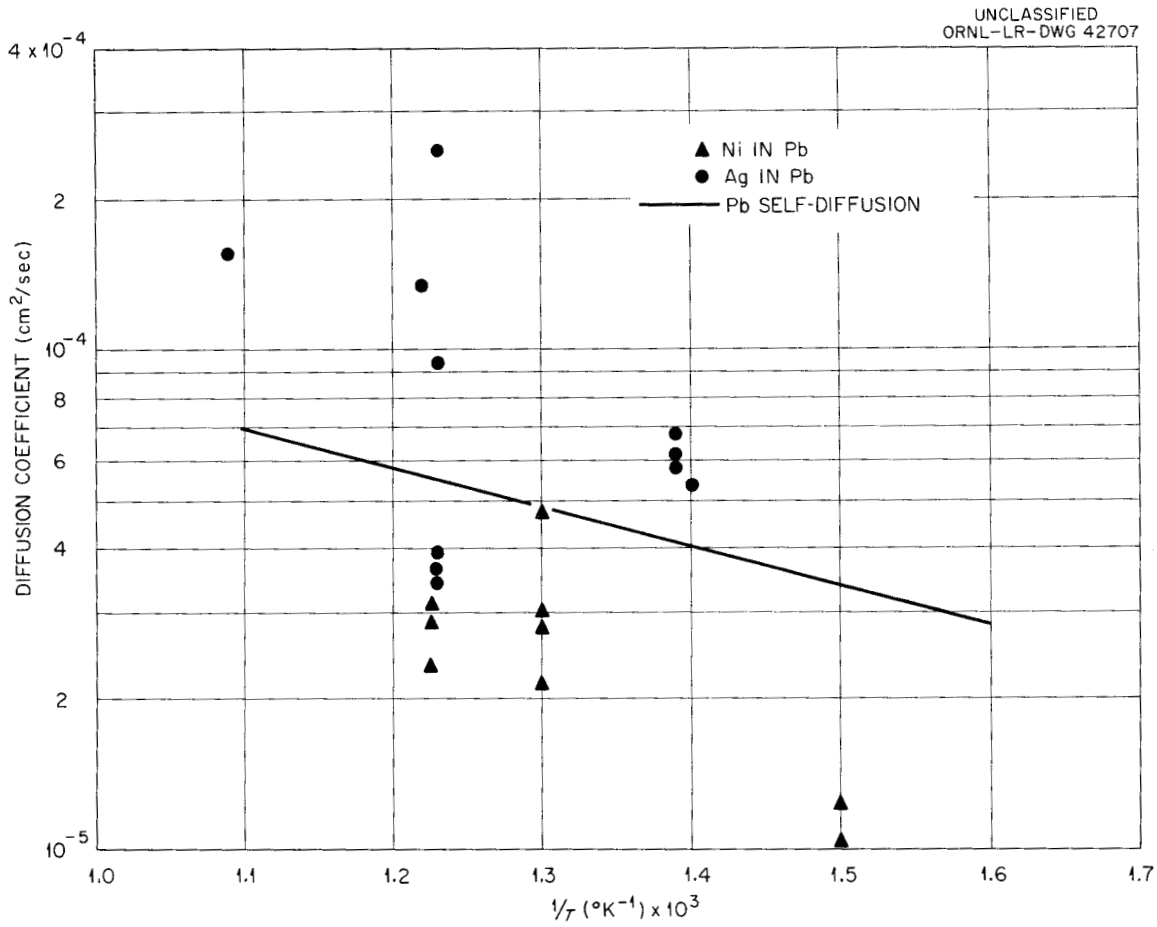

Fig. 3.7. Diffusion Coefficients of Silver and Nickel in Liquid Lead.

were computed to be:

$$D\ (0.165\ \text{wt}\ \%\ \text{Ni in Pb}) = 2.43 \times 10^{-3} \exp\left[-(7000 \pm 3700)/RT\right] \quad , \quad (1)$$

$$D\ (2.25\ \text{wt}\ \%\ \text{Ag in Pb}) = 5.14 \times 10^{-3} \exp\left[-(6800 \pm 5300)/RT\right] \quad . \quad (2)$$

The large spread in the activation energies for diffusion, which were calculated with 90% confidence limits, is a result of the scatter in the data and the small number of observations.

It may be observed in Fig. 3.7 that the measured diffusion coefficients of nickel in lead are lower, not higher, than those of silver in lead at corresponding temperatures. Although this rather surprising result may be a result of random errors, it is clear that the diffusion coefficients of nickel in lead are not markedly higher than those of silver in lead. Thus,

the results are not in agreement with the predictions of the combined theories of Strauss, White, and Brown,[45] and Eyring.[40] A reasonable explanation for these results has been given by Nachtrieb,[46] who proposed recently that the process of liquid metal diffusion involves much smaller readjustments than the discrete jumps of 3 to 4 Å proposed by Eyring,[40] and also involves the co-operative movement of many atoms. If this theory is true, liquid metal diffusion coefficients should be characterized by the rate of movement of the solvent rather than the solute, for dilute solutions.

The Mass Transfer of Nickel in Liquid Mercury

D. F. Toner

A quantitative analysis of the rates of mass transfer of container materials in liquid metal systems has heretofore been hampered by a lack of data concerning mass-transfer rate constants and the variables, such as flow rate, temperature, surface preparation, etc., which govern their magnitudes. Because of the lack of information, a program was initiated at ORNL to measure mass-transfer rate constants of different solid metal–liquid metal systems for a variety of operating conditions. The system nickel-mercury was selected for initial studies because of the relative simplicity of the experimental work and the fact that an inert quartz apparatus could be used with these metals.

The apparatus is shown in Fig. 3.8. A cylindrical nickel specimen, instrumented with a calibrated thermocouple, was inserted into the isothermal hot zone of a mercury thermal-convection loop. Before insertion, the sample was mechanically polished with 4/0 grit paper or electropolished in a sulfuric acid bath[47] to achieve a standard surface preparation. The system operated under a hydrogen atmosphere to prevent the oxidation of the nickel sample. A series of thermocouples placed in wells around the loop indicated the temperature profile.

---

[45] S. W. Strauss, J. L. White, and B. F. Brown, Acta Met. 6(9), 604 (1958).

[46] N. H. Nachtrieb, Trans. Am. Soc. Metals 50A, 49 (1958).

[47] A. W. Hothersall and R. A. F. Hammond, J. Electrodepositors' Tech. Soc. 16, 83 (1940).

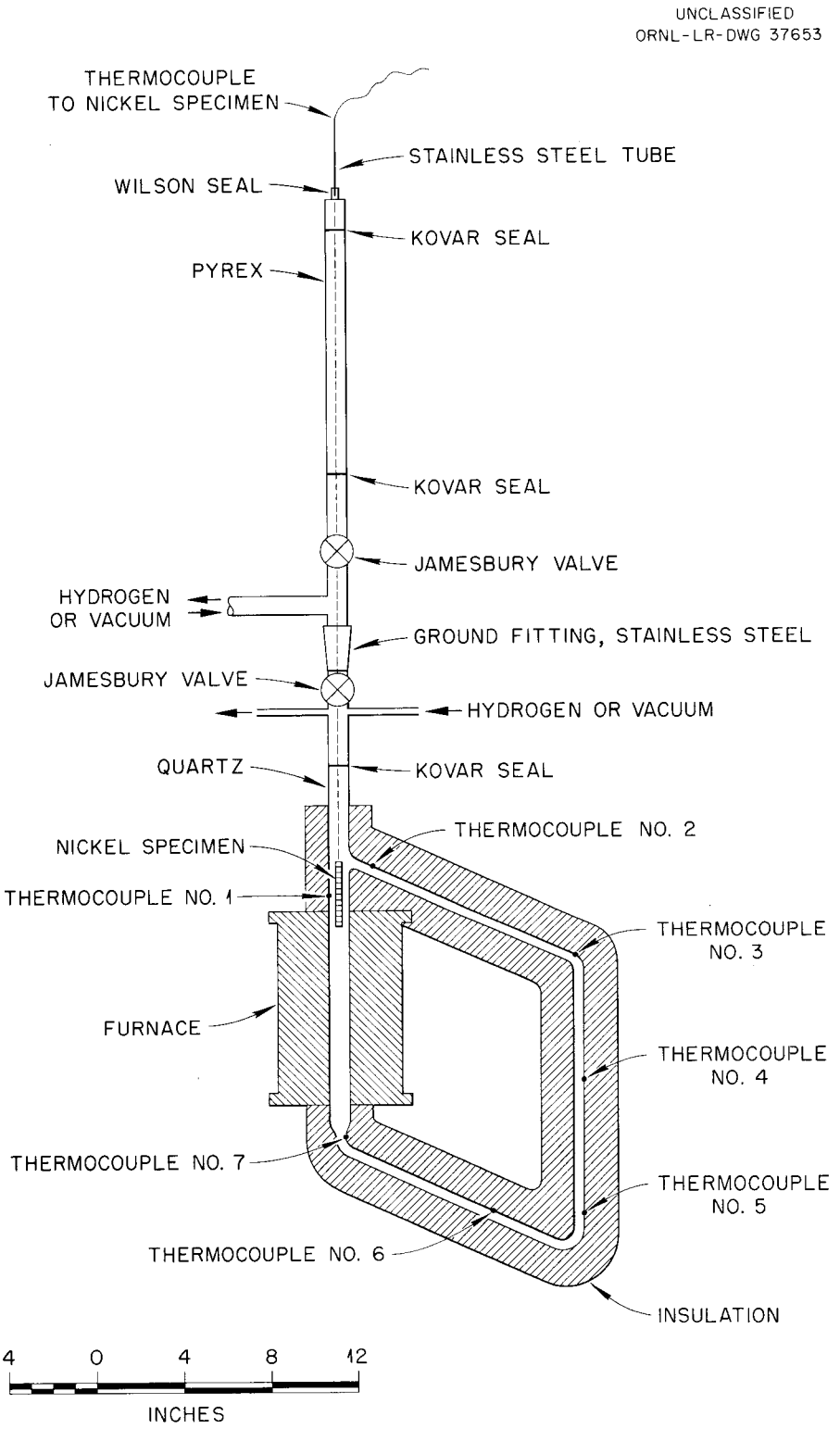

Fig. 3.8. Liquid-Metal Thermal-Convection Loop.

The following procedure was used to obtain mass-transfer rate constants. The change in mass of the nickel sample was measured as a function of time by withdrawing it periodically from the loop, removing the mercury by vacuum distillation and weighing. Following each nickel withdrawal, a liquid mercury specimen was extracted through a fritted disk and then chemically analyzed. The nickel concentration in the mercury, together with the previously determined solubility-temperature curve for the nickel-mercury system, served to define the concentration driving force. The area of the sample was computed from the measured dimensions. Typical sample-weight-loss and nickel-in-mercury concentration curves are shown in Fig. 3.9. Mass-transfer rate constants were computed by the equation

$$k = \frac{\Delta W}{A(C^* - C)} \quad , \tag{3}$$

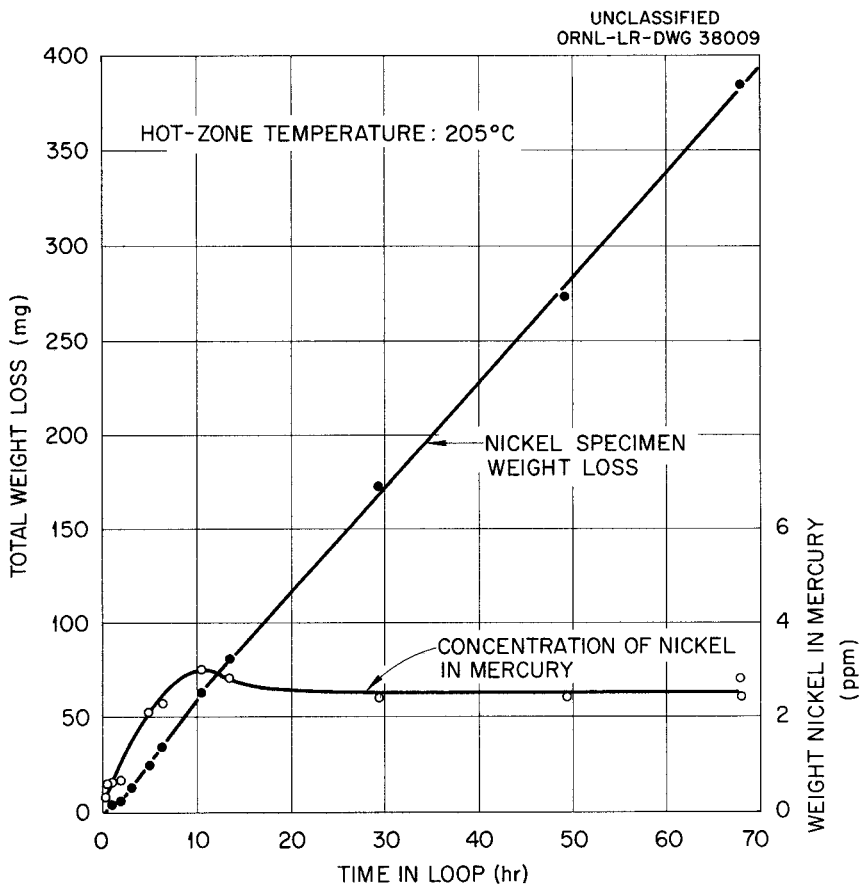

Fig. 3.9. Weight Loss of Nickel Specimen and Concentration of Nickel in Mercury in a Thermal-Convection Loop.

where

ΔW = weight loss of nickel, mg/sec,

A = area of specimen, cm^2,

C^* = saturation concentration of nickel in the hot zone, mg/cm^3,

C = actual concentration, mg/cm^3,

k = mass-transfer rate constant, cm/sec.

The solubility of nickel in mercury is shown in Fig. 3.10 as a function of temperature. The discontinuity at 280°C is in agreement with the reported peritectic decomposition of $NiHg_4$ (ref 48). The heat of solution of nickel in liquid was computed to be 15,200 cal/mole. Mass-transfer rate constants for nickel in mercury (Table 3.14) were compared with values obtained according to the assumption that the mass-transfer process was liquid-diffusion controlled. The mass-transfer rate constant for a diffusion-controlled process is given by the expression $k = D/\delta$, where D = coefficient of diffusion of the solute through the solvent and δ =

[48] F. Lihl, Z. Metallk. 44, 160–66 (1953).

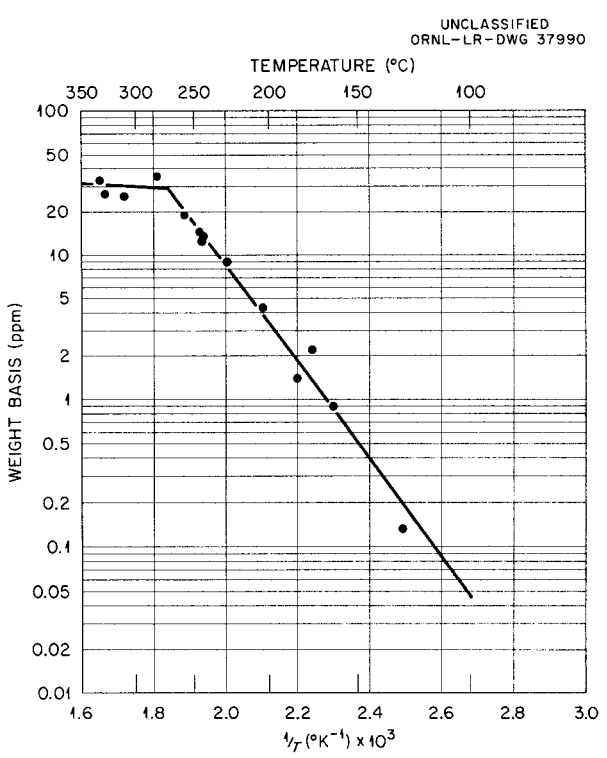

Fig. 3.10. Solubility of Nickel in Mercury.

the thickness of solvent through which diffusion is taking place. Values of δ were obtained from the data of Ward and Taylor,[49] who observed that the mass transfer of copper in bismuth was diffusion controlled within the same range of flow rates as those observed in the present investigation.

Results showed that the measured values of the mass-transfer rate constant of nickel in mercury were an order of magnitude lower than those predicted by a diffusion-controlled mechanism and that they varied erratically from run to run. These variations are believed to be a result of incomplete wetting of the nickel samples. Although the samples appeared to be completely wet, it is possible that residual oxygen dissolved in the mercury oxidized a portion of the surface and prevented wetting. Future tests should be done with vacuum-distilled mercury and with an electropolished, hydrogen-annealed nickel sample.

---

[49]A. G. Ward and J. W. Taylor, Dynamic Solution-Rate Studies of Solid in Liquid Metals, AERE-MR-2113 (Jan. 1957).

Table 3.14. Thermal Gradient Mass-Transfer Data for the Liquid-Mercury–Nickel System

Hot-Zone Temperature (°C)	Type of Surface Preparation	Flow Rate* (fpm)	k (cm/sec)	Identification
205	4/0 grit paper	2.6	2.8×10^{-3}	A
252	4/0 grit paper	3.4	5.7×10^{-4}	B
232	Electropolished	3.3	3.9×10^{-4}	C
280	Electropolished	3.0	2.4×10^{-4}	D
255	Electropolished	2.9	8.9×10^{-4}	E
255	Electropolished	2.9	6.8×10^{-4}	F

*Average of two or more determinations.

METAL PROCESSING

T. Hikido

The research performed in the Metal Processing Laboratory on the Aircraft Nuclear Propulsion Project has been reported elsewhere.[50,51]

Electron-Beam-Melting Laboratory

An electron-beam-melting furnace for melting refractory-metal ingots has been purchased and is now being installed. Work on this furnace is supported by ANP; therefore, the details of the furnace are being reported elsewhere.[51]

---

[50]T. Hikido, ANP Semiann. Prog. Rep. Mar. 31, 1959, ORNL-2711, p 3 (classified).

[51]T. Hikido, ANP Semiann. Prog. Rep. Oct. 31, 1959, ORNL-2840 (in press) (classified).

NONDESTRUCTIVE TEST DEVELOPMENT

J. W. Allen
R. W. McClung R. A. Nance

Eddy-Current Development: Tubing

R. A. Nance J. W: Allen

A major portion of the encircling-coil development in the past year has centered about the inspection of type 304 stainless steel tubing (3/4 in. in diameter, 0.020-in. wall) for GCR fuel capsules.[52] In continuation of the policy of developing inspection techniques by using commercial instruments when feasible, a Radac model 302 eddy-current instrument was purchased. Although this instrument is designed for production inspections, it is sufficiently versatile for extensive use in development work.

The development effort has been divided into three major portions: (1) development of reference standards, (2) a study of the parameters of coil systems, and (3) the development of inspection procedures. In order to specify an inspection procedure, it is first necessary to develop a

---

[52]GCR Quar. Prog. Rep. Sept. 30, 1959, ORNL-2835 (in press).

standard defect which can be used as a reference for calibrating eddy-current instruments for the detection of defects. Several types of standard defects have been examined. An interim standard consisting of a transversely filed notch on the outside surface of the tube has been chosen for use until this investigation is completed. The study of coil systems has been limited to an investigation of spacing between differential encircling coils. It was found that the best signal-to-noise ratio was obtained when the differential coils were in intimate contact. The information obtained from all these investigations has been used to formulate an inspection procedure for the eddy-current inspection of thin-wall austenitic stainless steel tubing.

An encircling-coil technique has been developed for the inspection of the sheath on heater and thermocouple wires used in high-temperature fuel element irradiation studies. The heater wire (Kanthal – 5.5% Al, 22% Cr, 0.5% Co, 78% Fe) and thermocouple wire (Chromel-Alumel) are packed in magnesium oxide and contained in a type 347 stainless steel sheath, 1/16 in. in diameter and having a 0.015-in. wall. As both heater and thermocouple wires are magnetic, normal inspection techniques could not be used. By using a saturating d-c field, it was possible to eliminate the signals produced by variations in the magnetic properties of the wire, thereby permitting the detection of defects 0.0025 in. deep on the outside surface of the sheath. This is illustrated in the signal traces of Fig. 3.11, in which the signals are displayed vertically as a function of the tubing length.

Eddy-Current Development: Probe Coils

R. A. Nance J. W. Allen

A program has been initiated to conduct empirical studies of eddy-current probe coils and their application to inspection problems. This program includes: (1) a study of probe-coil induction fields and the resultant eddy-current flow in test specimens, (2) examination of various probe-coil design parameters, and (3) the determination of techniques for focusing the field of probe coils.

This program has been prompted by the lack of adequate detailed design information needed for the development of eddy-current inspections.

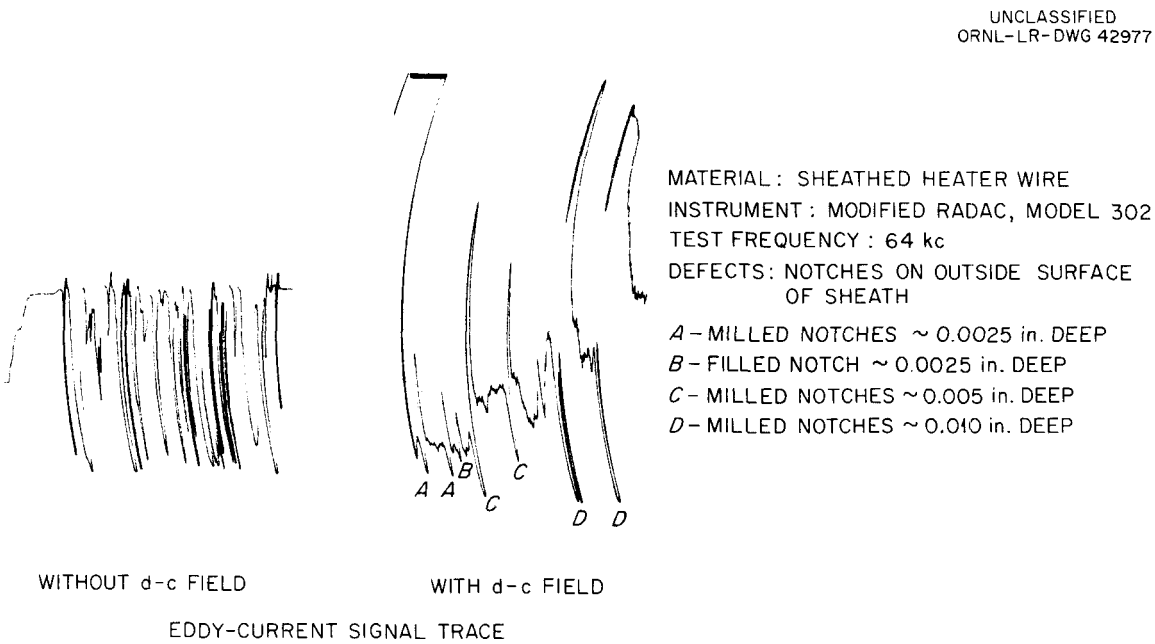

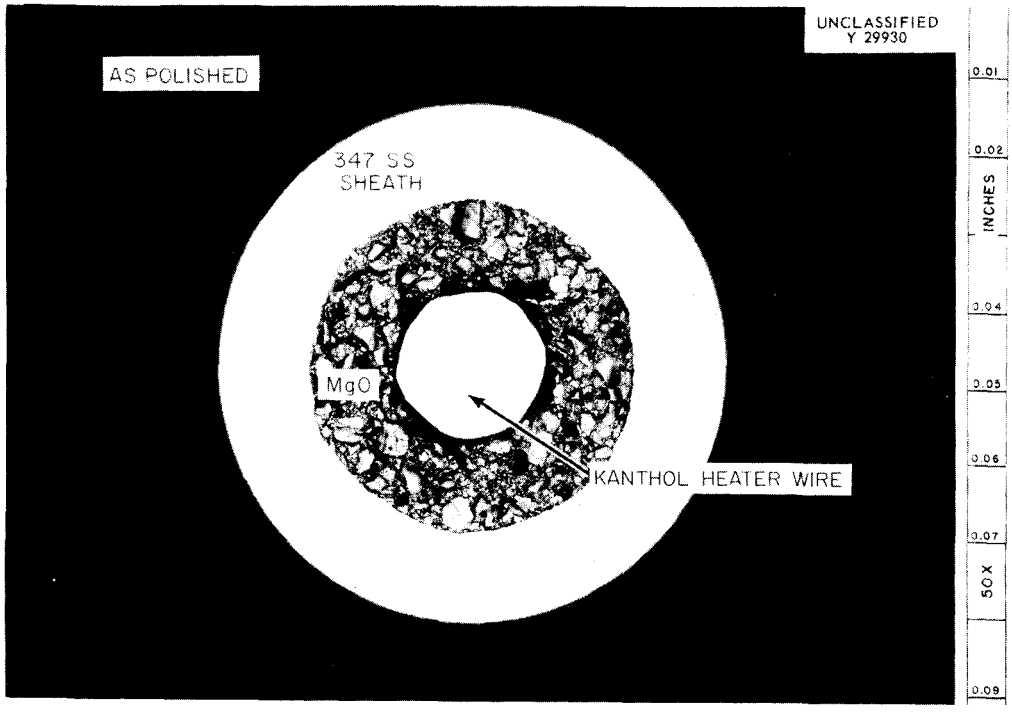

Fig. 3.11. Eddy-Current Inspection of Sheathed Heater Wire. 50X. Reduced 20%.

Although theoretical studies[53] have served to provide a general background of understanding of the various parameters, they have not produced sufficient analytical results to be applied in practice. The present empirical

[53]R. B. Oliver et al., Met. Ann. Prog. Rep. Oct. 10, 1957, ORNL-2422, p 38 (classified).

studies will provide detailed information for the design of probes for specific applications, such as:

1. core location in flat fuel elements,
2. weld penetration depth,
3. metal identification and conductivity measurements,
4. cladding integrity and thickness measurements,
5. tubing and rod inspection.

This program is divided into three phases:

Phase 1. A study of the induction-field shape and intensity of various probe coils, both with and without field focusing and extension devices.

Phase 2. A study of the eddy-current flow produced in metal specimens by the induction field of probe coils. This is accomplished by using a miniature search coil within a liquid metal specimen.

Phase 3. Evaluation of the data obtained from phases 1 and 2 as they apply to the design of probe coils. The criteria by which the various coil systems are evaluated are their ability to:

1. concentrate or focus an induction field into a smaller effective area to produce an inspection more sensitive to small defects,
2. project the field deeper into a metal to provide a more sensitive inspection for defects below the surface of the metal,
3. contract the field and confine eddy-current flow to regions near the surface of a metal for the examination of thin metal sections,
4. produce relatively large areas in an induction field having a constant potential which would alleviate some of the probe-coil-to-specimen spacing problems.

At present, phase 1 is almost complete. The measurement of the induction field parameters was facilitated by mounting the probe coil on a lathe and mounting a small search coil on the tool post. The test setup is shown in Fig. 3.12. Figure 3.13 is a block diagram of the instrumentation.

The coils examined thus far include (1) a single-layer long solenoid, (2) a multilayer short solenoid, (3) a triangular coil, and (4) a flat, single-layer coil spirally wound, using flat wire. Several field extension devices were also examined. Some of the data obtained are shown in Figs. 3.14–3.17, illustrating the field intensity, direction, and attenuation as a function of distance from the probe coil. Although these data

UNCLASSIFIED
Y 31075

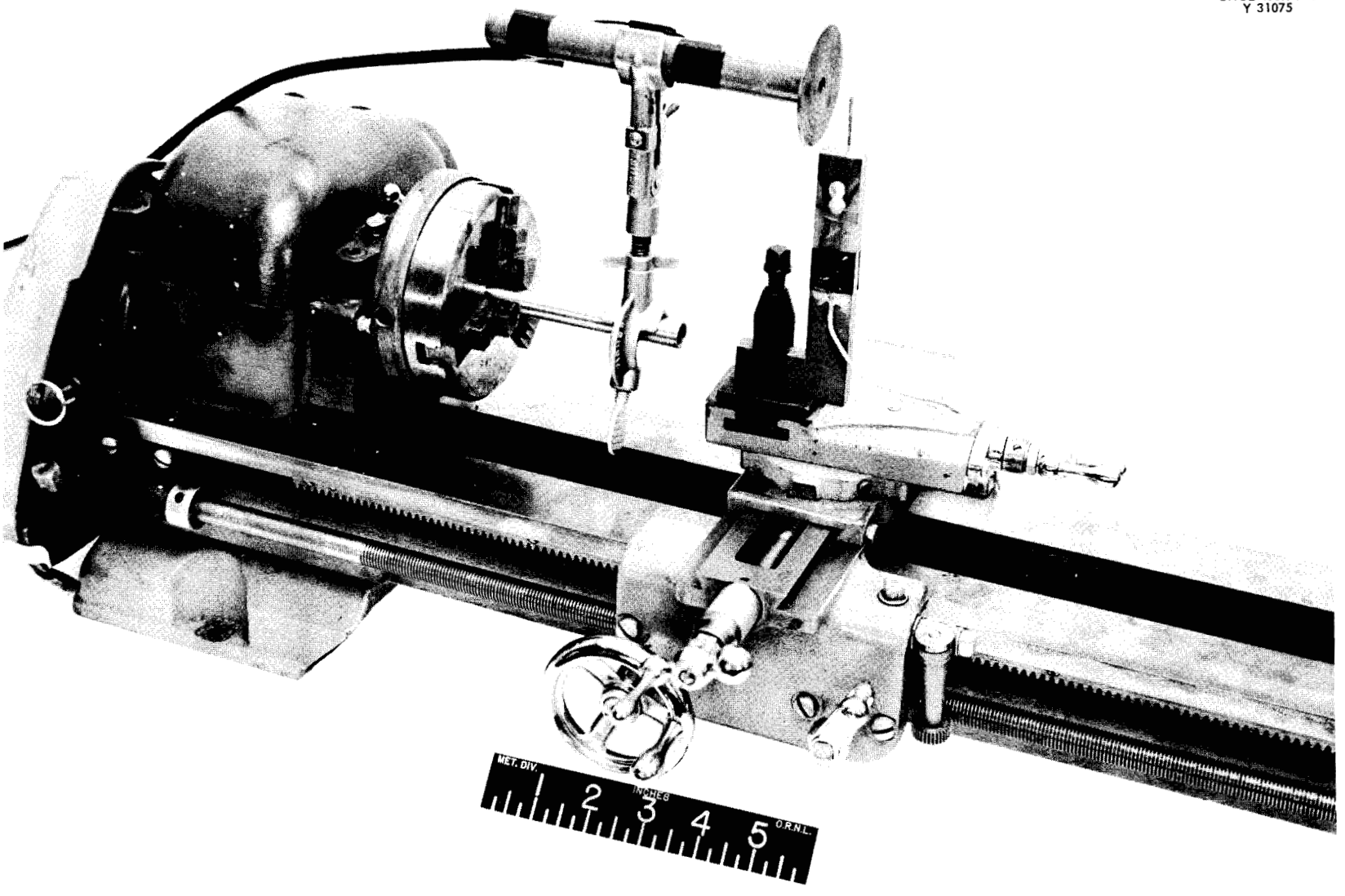

Fig. 3.12. Device for Measurement of Induction Field of Probe Coils.

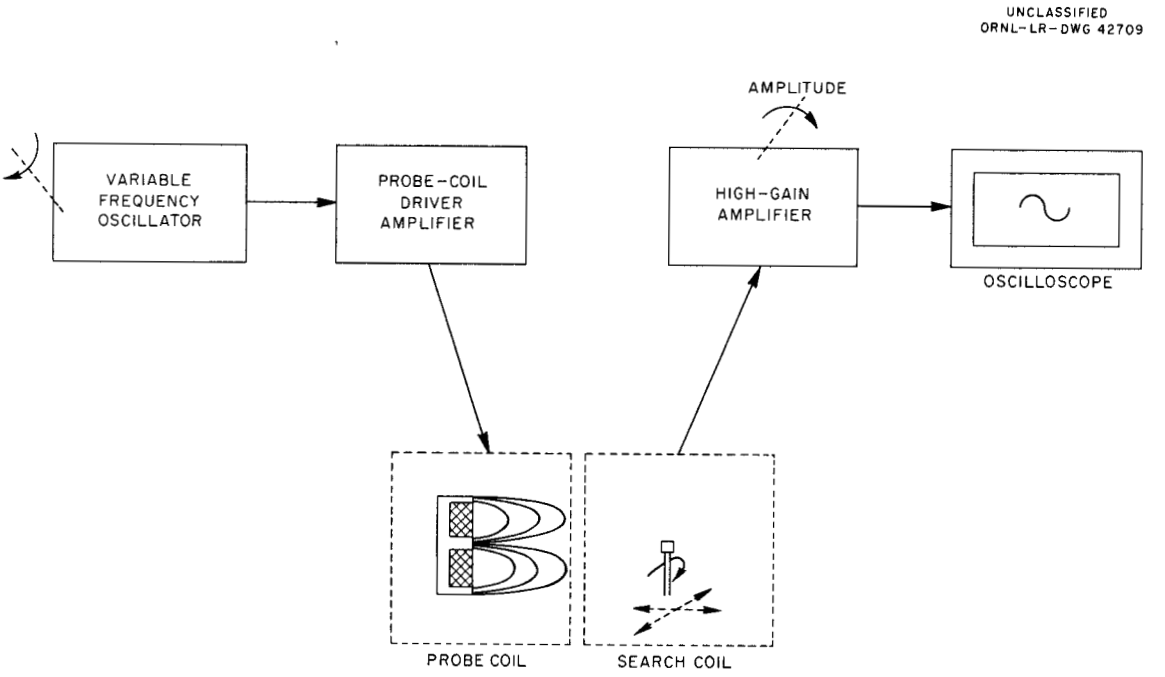

Fig. 3.13. Block Diagram of Induction-Field Measurement Instrumentation.

cannot be considered conclusive until phase 2 is completed, some general observations can be made. It is apparent that a field extension piece, such as shown in Fig. 3.15, effectively concentrates the field of the coil in a smaller area and produces a field which attenuates relatively slowly with distance from the probe. In opposition to this, the flat coil of Fig. 3.16 has a large, evenly distributed field which attenuates rapidly with distance from the probe coil. Some work has also been done on focusing fields by the use of a second coil whose field modifies the field of the primary coil. This technique has met with some success but requires further investigation before concrete conclusions can be reached.

Work on phase 2 has begun, but insufficient data have been obtained to be discussed at present.

Ultrasonic Bond-Evaluation Studies

R. W. McClung

Technique development and applications work has been accomplished for the detection of nonbond in a mockup of a compartmented flat-plate fuel element having a modified honeycomb structure. An exploded view

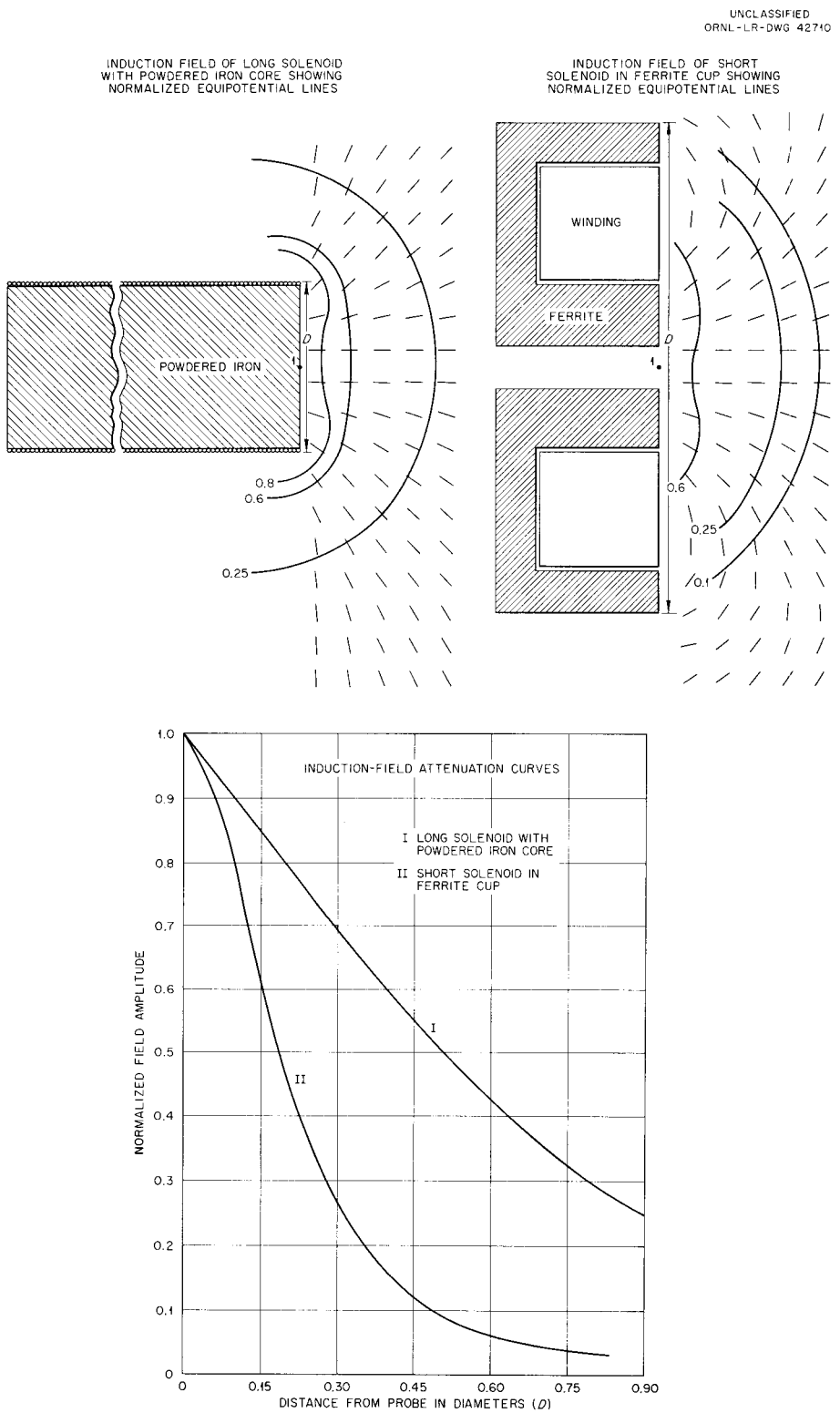

Fig. 3.14. Induction Fields of Probe Coils.

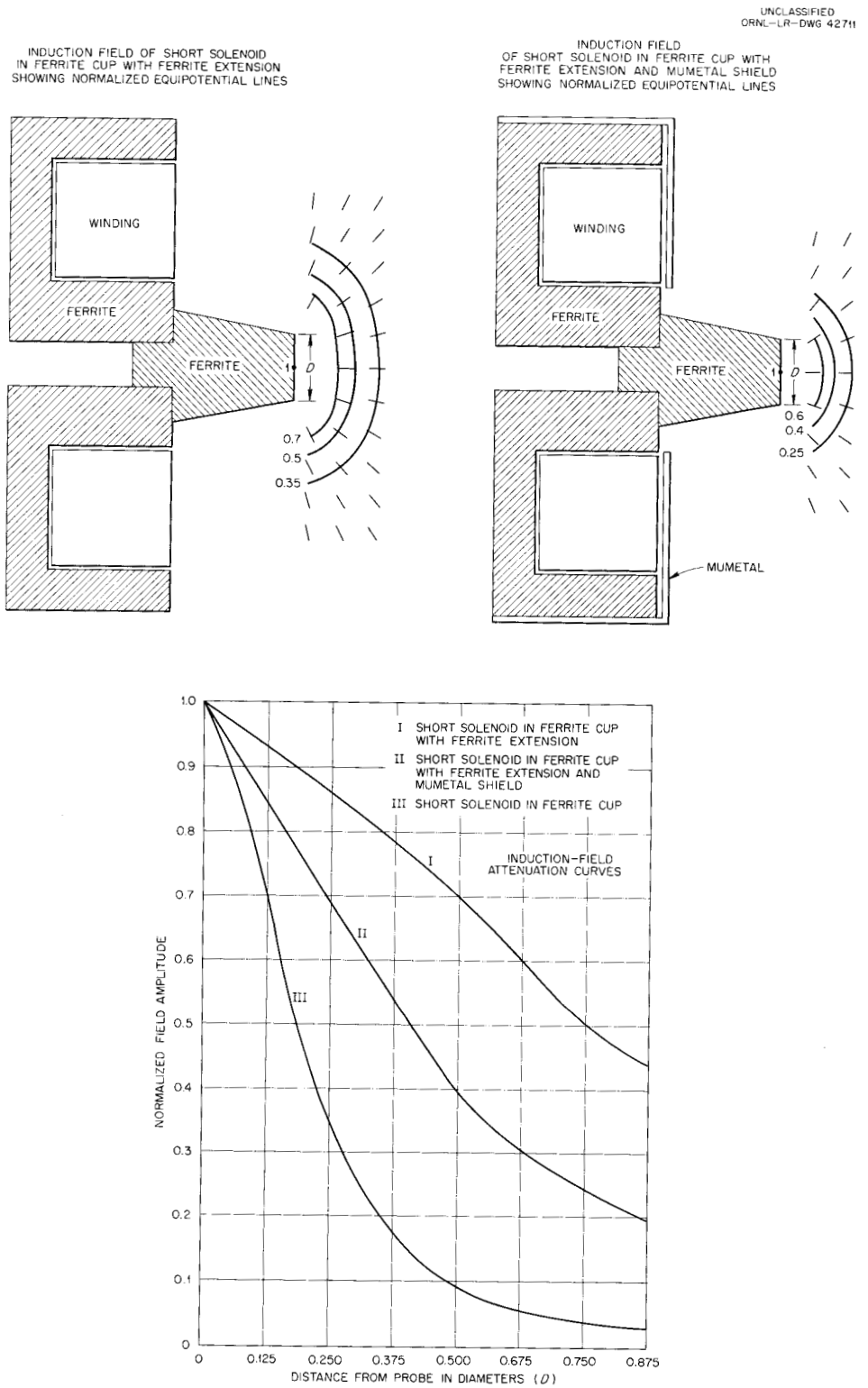

Fig. 3.15. Induction Fields of Probe Coils.

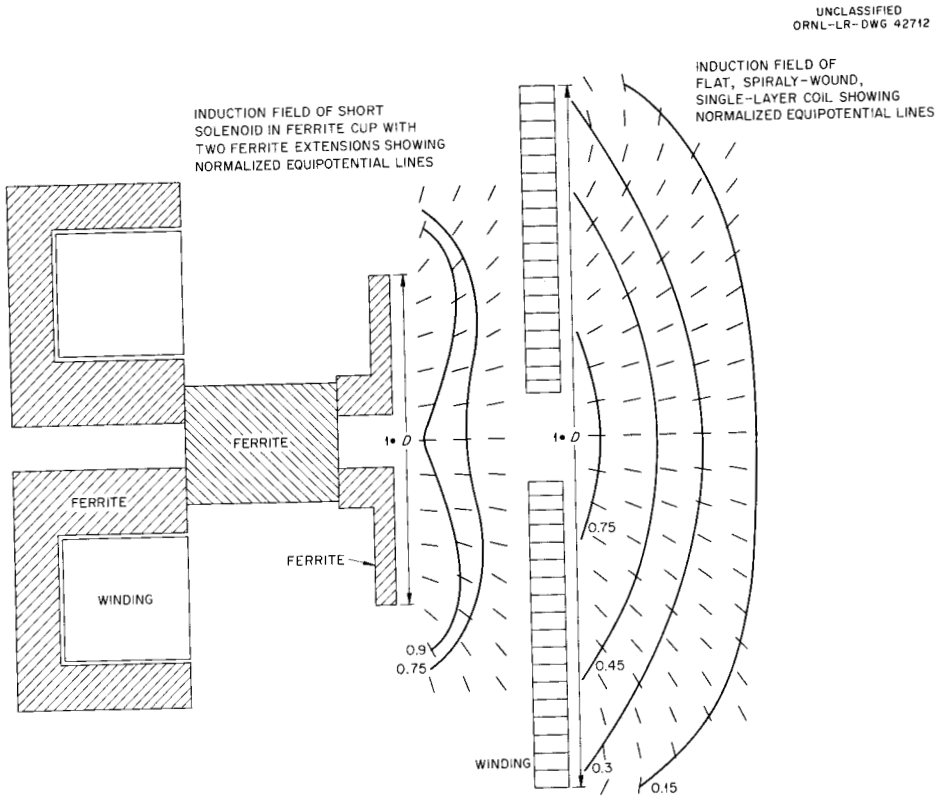

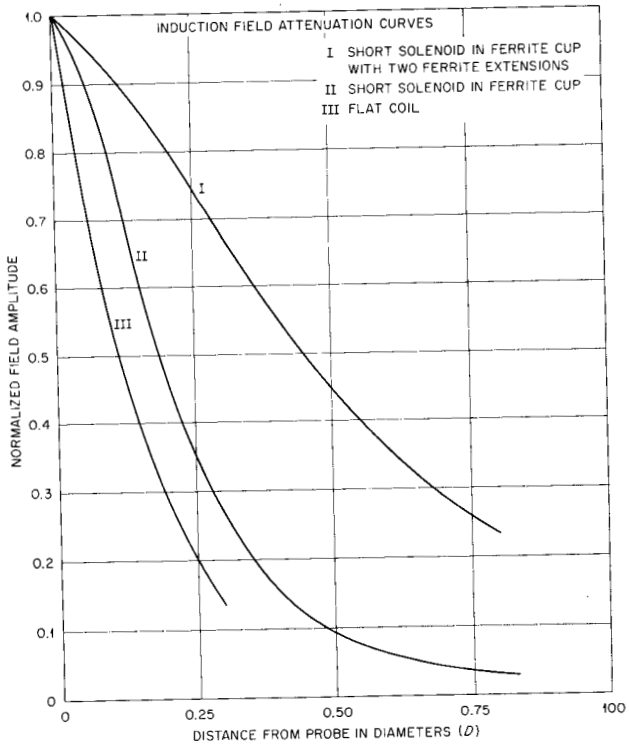

Fig. 3.16. Induction Fields of Probe Coils.

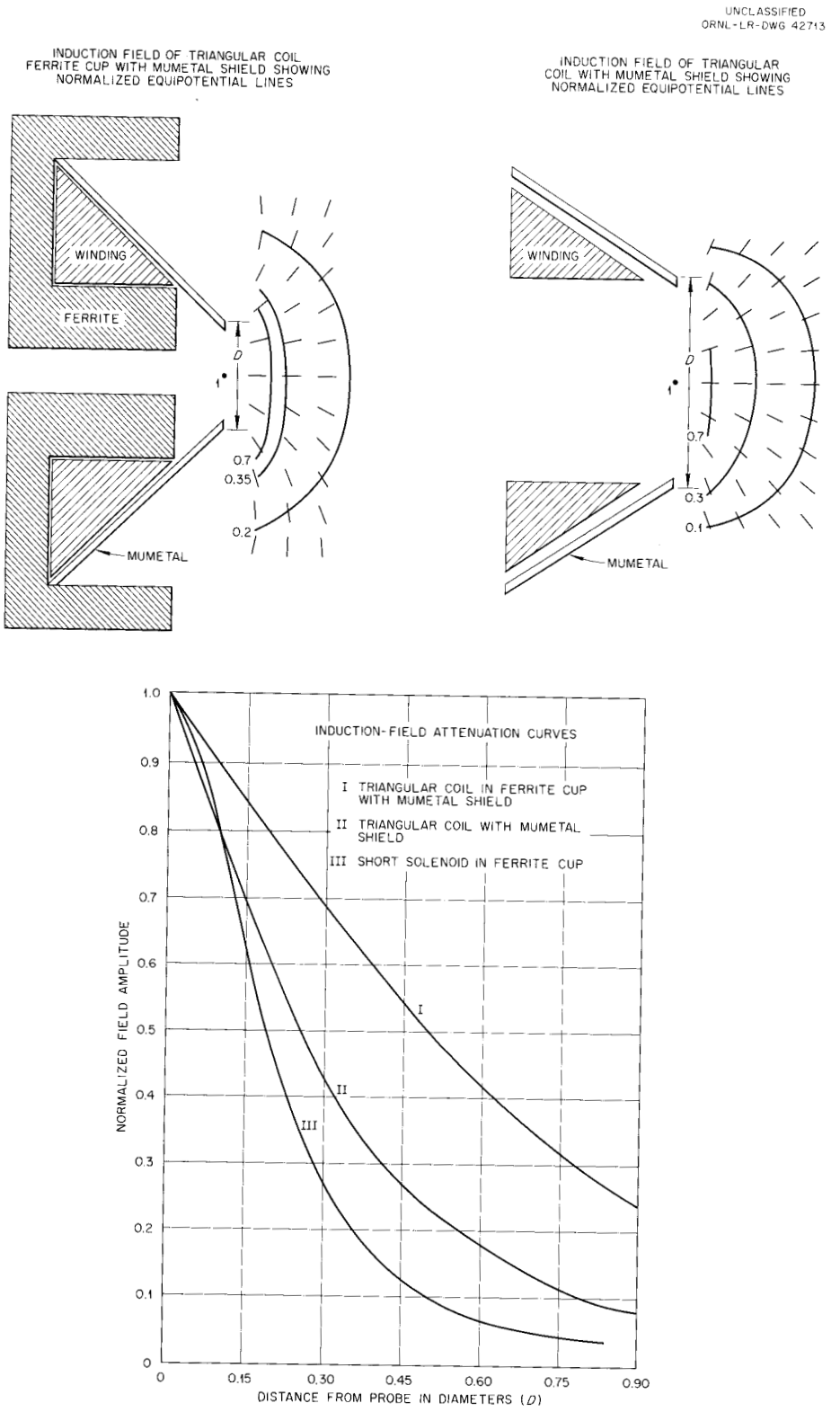

Fig. 3.17. Induction Fields of Probe Coils.

of this element showing the ribbed structure and the cover sheets is shown in Fig. 3.18. One technique which was evaluated consisted in projecting a finely collimated ultrasonic beam perpendicularly onto the thin cover sheet of the element. By proper selection of the frequency, a modified "ringing" was produced which was observed as an extended pulse length in the received echo. Any area which is well bonded to the structure beneath should change the ringing characteristic of the cover sheet, and the resultant would then be a damped or shortened echo pulse. Figure 3.19 illustrates the typical oscilloscope trace, showing the extended pulse length associated with the nonbond which is pictured. Figure 3.20 is a composite which demonstrates the damped pulse length of the echo associated with the bonded condition.

Since this was a pulse-echo technique with a finely collimated beam, difficulties arose when the surface was uneven such that the echo was not returned directly to the transducer. Because of these difficulties, another technique was established in which the sound beam was transmitted through the fuel plate and detected by a second transducer. Bonded areas

UNCLASSIFIED
Y 28449

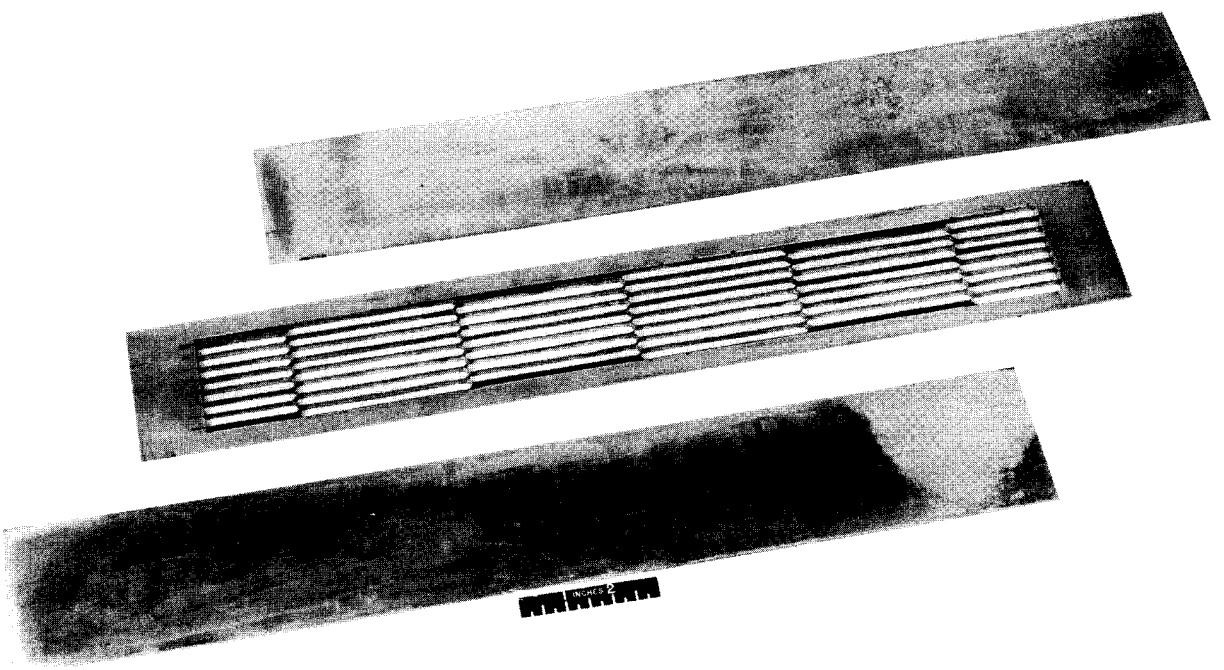

Fig. 3.18. Exploded View of Compartmented Fuel-Element Mockup.

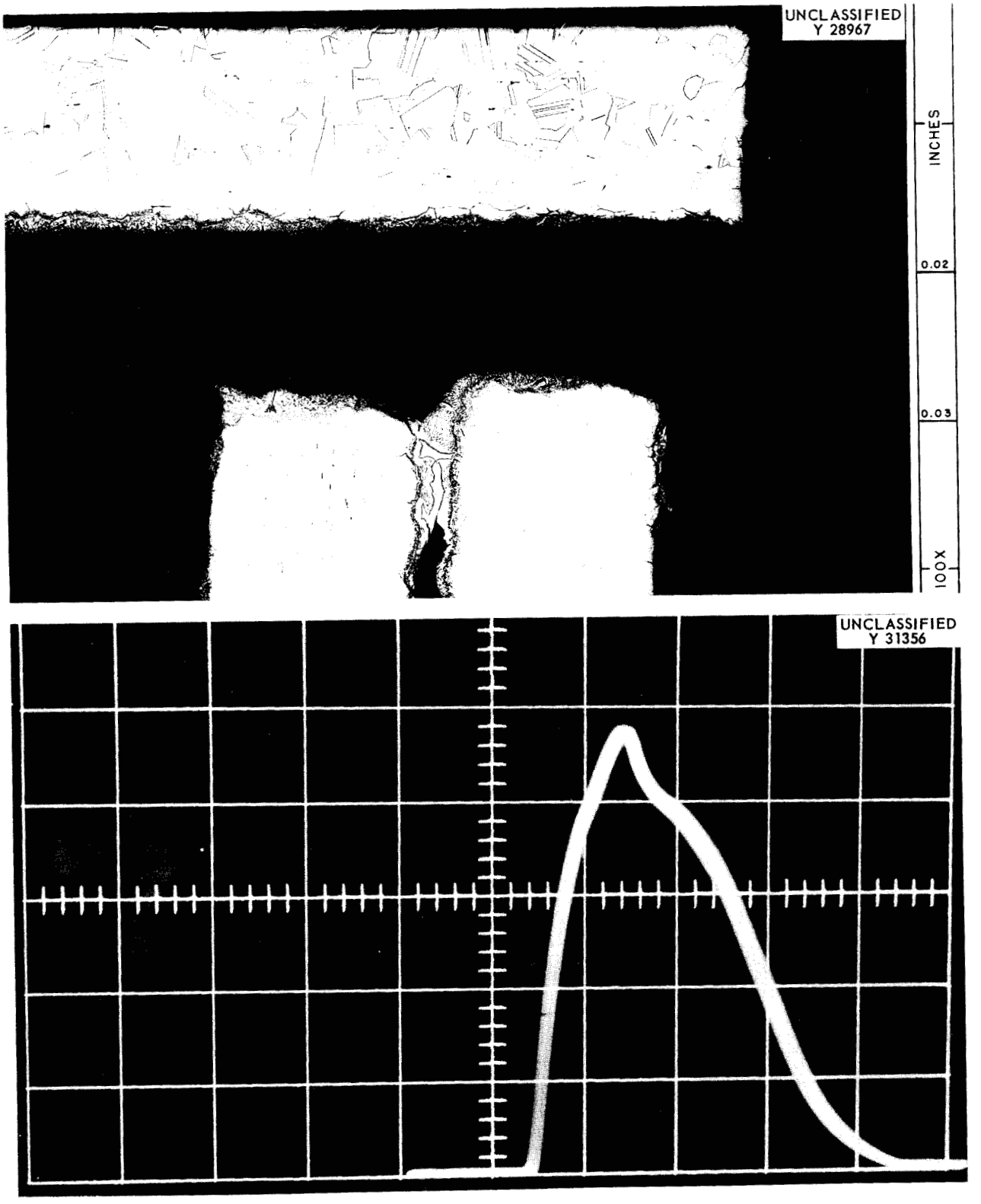

Fig. 3.19. Ultrasonic Oscilloscope Trace and Associated Lack of Bond in Ribbed Section of Compartmented Fuel Element. Etchant: 5% CrO_3, electrolytic.

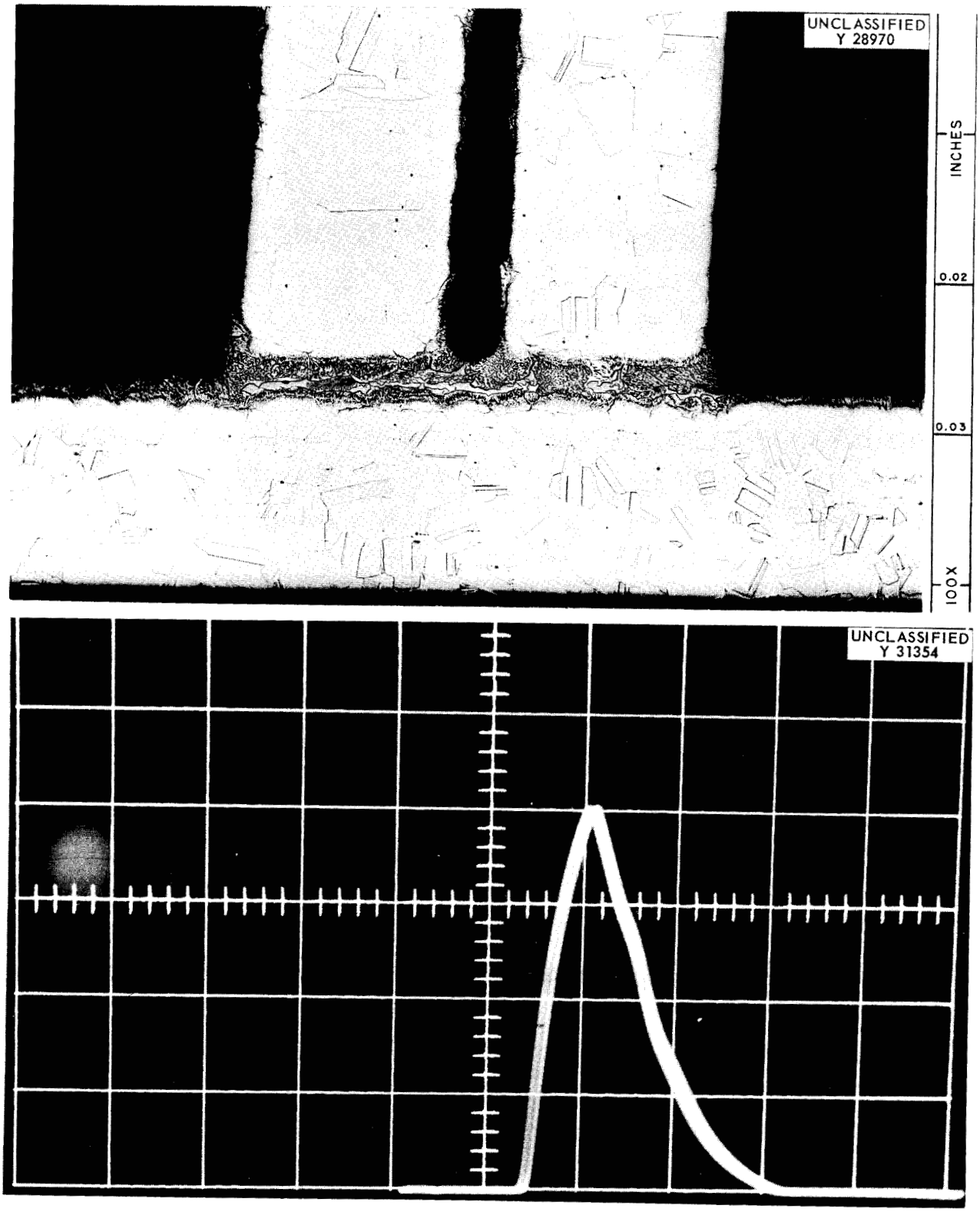

Fig. 3.20. Ultrasonic Oscilloscope Trace and Photomicrograph of Associated Bond in Ribbed Section of Compartmented Fuel Element. Etchant: 5% CrO_3, electrolytic.

would transmit the sound, but poorly bonded regions would offer an acoustic barrier, and no sound would be received by the second transducer. By this technique, the bond at both cover sheets was evaluated simultaneously. Figure 3.21 is a recording of a section of such a plate. The darkened area is that of good bond. Note the small unbonded area in the frame at the top and that the two outer ribs give no evidence of bonding.

Ultrasonic Field Measurements

R. W. McClung

Because of the need for well-defined angular relationships between incident ultrasound beams and thin-metal sections during inspection for laminations or nonbond,[54] a study was begun in order to make quantitative pro-

[54] R. W. McClung, Met. Ann. Prog. Rep. Oct. 10, 1958, ORNL-2632, p 124–26 (classified).

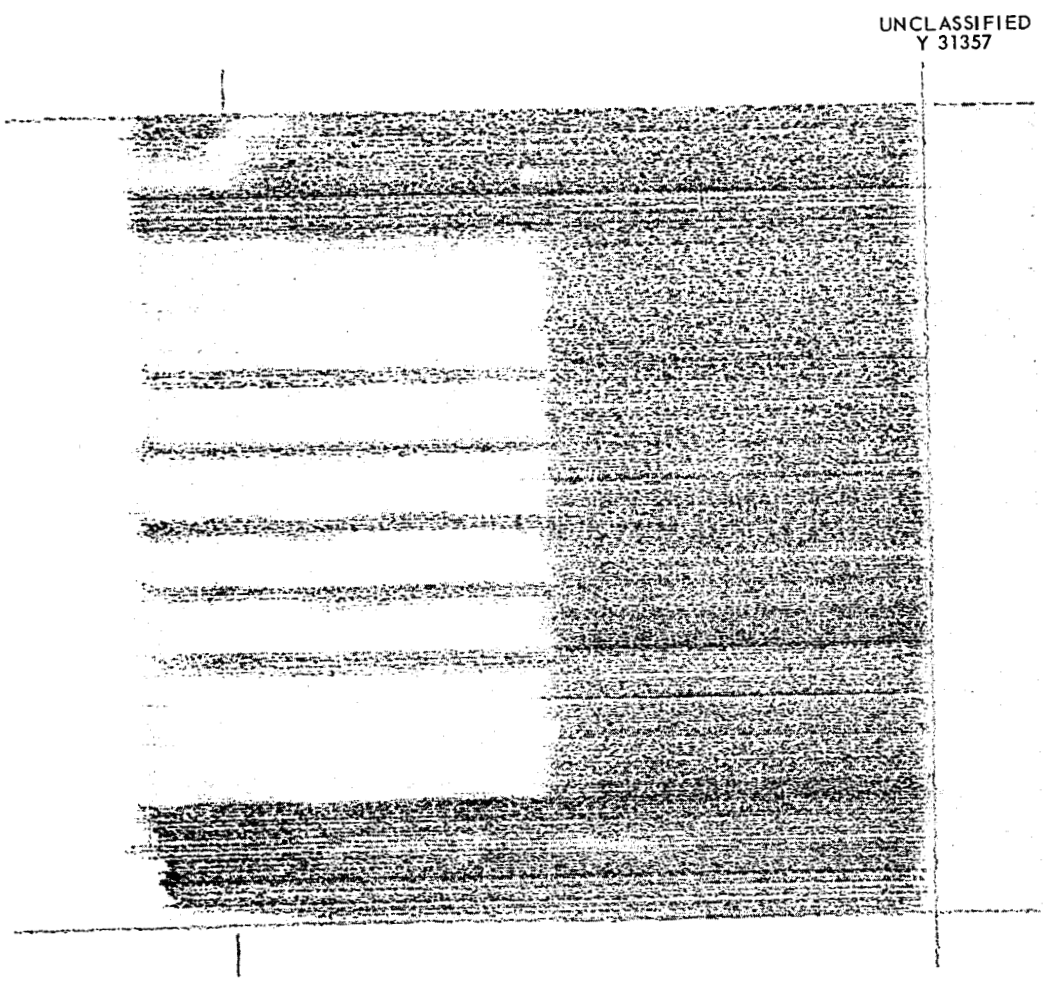

Fig. 3.21. Recording from Through-Transmission Ultrasonic Inspection on Section of Compartmented Fuel Element.

files of sonic beam intensities for the ultrasonic transducers which are used. This was accomplished by means of two transducers and some special mechanical devices which provided for scanning in the x, y, and z directions as well as making angular adjustment. Figure 3.22 shows the relative position of the transducers. The receiving transducer was masked rather severely in order to approach a unidirectional response. It then could be scanned in any direction through the sound field being emitted by the transmitting transducer. The angular components in the field are determined by adjusting the attitude of the receiver about the pivot point. Thus, a rather comprehensive study of the ultrasonic field intensities is allowed.

In the initial investigations, the relative ultrasonic intensities were determined across planes perpendicular to the direction of propagation for different distances from the emitting transducer. The results demonstrated that the electromechanical efficiency of the transducer varies across the crystal face, which produces somewhat irregular lobes of energy, and that each transducer varies somewhat from the others in having its own characteristic radiation pattern.

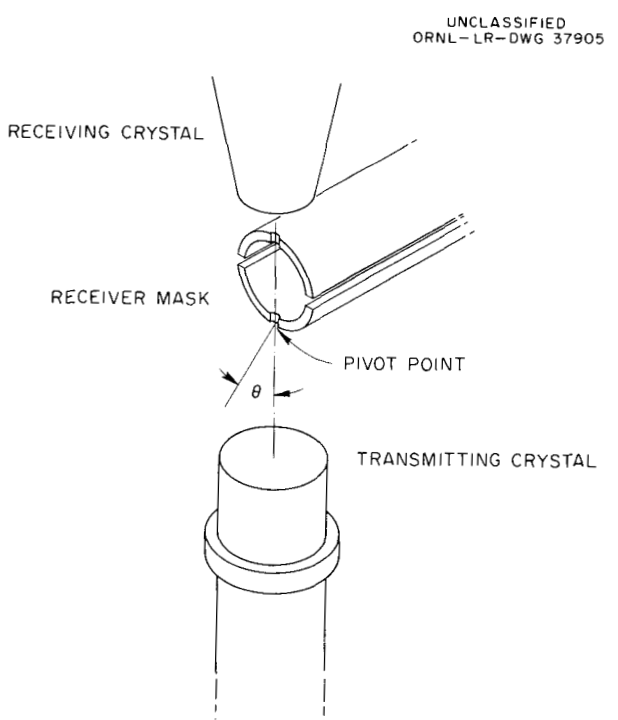

Fig. 3.22. Transducer Alignment for Sound-Beam Evaluation.

Measurements have been taken across the most uniform portion of a transducer to determine the angular components which are present. Figure 3.23 is a plot of the angular components and their amplitude at discrete positions across the transducer diameter. At each position, the amplitude was measured and recorded with the receiver transducer being adjusted at 1° intervals on either side of the setting normal to the beam axis.

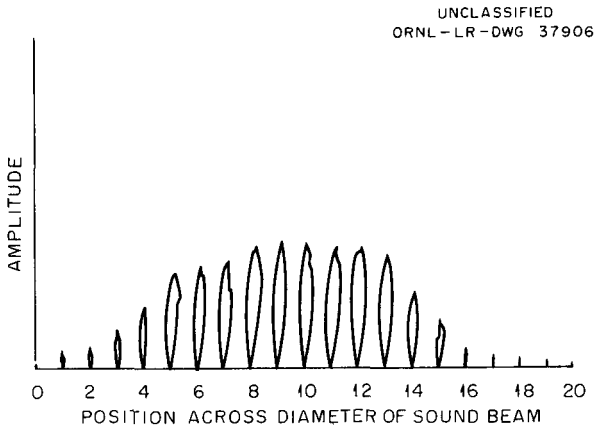

Fig. 3.23. Amplitude of Angular Components Across the Diameter of an Ultrasonic Beam.

By use of these data, attempts were made to mask or collimate the sound beam in order to reduce the angular components and to optimize the axial portion of the beam. The best method determined to date has consisted of a combination of orifice masks, one at the transmitter and one at the receiver or specimen.

Ultrasonic Transducer Development

J. W. Allen R. W. McClung

Some preliminary investigations were made in order to determine the feasibility of ultrasonic transducers which utilize the magnetostrictive effect. For this study, several magnetostrictive cermet disks have been obtained which have been cut for ultrasonic resonance at frequencies of 0.5, 1, and 2.25 Mc. The transducers are of interest since it is theoretically possibly to obtain ultrasonic pulses of much greater power than can be obtained with conventional piezoelectric transducers. The interest

in high-power transducers has been prompted by the very high ultrasonic attenuation which has been encountered in weldments of several alloys.[55,56]

Using existing test equipment and several exciting-coil configurations, preliminary tests have shown promising results. The most promising coil configuration has been a flat-type coil wound in a ferrite cup core. Test results have shown that as ultrasonic transmitters, the cermet disks produce approximately five times more power than quartz transducers of comparable size, using existing ultrasonic instruments. However, the magnetostrictive cermet disks are comparatively poor receivers of ultrasonic energy. When used in ultrasonic through-transmission-type tests, this disadvantage is overcome through the use of a quartz receiving transducer. Consideration is being given to the fabrication of sandwiches of magnetostrictive and piezoelectric transducers which would possibly be superior to the conventional piezoelectric transducers presently used.

Ultrasonic Velocity Studies

J. W. Allen R. W. McClung

A program of study and development has been initiated on the measurement of the velocity of the propagation of ultrasonic energy through various materials of interest. There are two reasons for this interest: (1) more and better velocity information is needed in the application of ultrasonics to nondestructive inspection; and (2) the measurement of ultrasonic velocity may be used in metallurgical research. Ultrasonic techniques are amenable to the measurement of the elastic constants of both single crystals and polycrystalline material and offer several advantages over other techniques in the making of such determinations.[57–60] Although a considerable

---

[55] R. W. McClung and E. A. Reed, Jr., Met. Ann. Prog. Rep. Oct. 10, 1958, ORNL-2632, p 123 (classified).

[56] J. K. White, R. W. McClung, and J. W. Allen, Met. Ann. Prog. Rep. Oct. 10, 1958, ORNL-2632 (classified).

[57] M. B. Reynolds, Trans. Am. Soc. Metals 45, 839 (1953).

[58] H. J. McSkimin, J. Acoust. Soc. Am. 22(4), 413 (1950).

[59] P. E. Armstrong, O. N. Carson, and J. F. Smith, J. Appl. Phys. 30(1), 36 (1959).

[60] H. J. McSkimin, J. Appl. Phys. 24(8), 988 (1953).

quantity of experimental apparatus has been described in the literature, there is no commercial equipment for the very accurate measurement of ultrasonic velocity. Therefore, considerable effort has gone into the study and development of suitable equipment.

One exception to the lack of commercial equipment is the water-path comparator system illustrated in Fig. 3.24. In this technique, a standard ultrasonic reflectoscope (a pulse-echo inspection instrument) is used to excite two transducers with a pulse of high-frequency energy, one of the transducers being coupled to the metal sample and the other in a water bath having a calibrated, variable-length water path. The resultant echo pulses from each source are fed through a common receiver, and the water-path length is varied for time coincidence of the echoes. The velocity in the sample can then be related to the velocity in the water by the path lengths. The precision of measurements by this technique is about 0.1%, which is adequate for many comparative measurements. The absolute accuracy, however, is difficult to analyze in a given instance, and the error may be several per cent. This is due to the effect of dissolved gases on the velocity of sound in water, to the transit time of the ultrasound through the couplant used to couple the transducer to the sample, and to the uncertainty of the time coincidence of the echo pulses. The presence of a

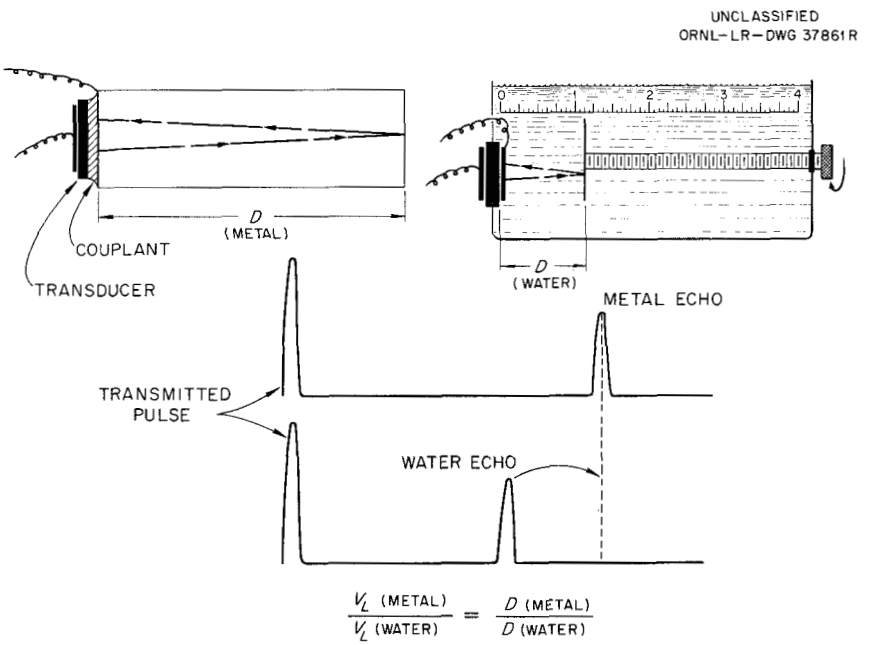

Fig. 3.24. Water-Path Comparator Technique of Velocity Determination.

sizable error on which it is difficult to establish limits, plus the fact that the technique is not amenable to automation, has indicated a need to investigate other systems.

A system is under development which alleviates many of these difficulties by making a direct measurement of the elapsed time between echo pulses. As shown in Fig. 3.25, this system is composed of an Immerscope, a time-interval electronic counter, and a two-channel gated system (dual-channel analyzer). The time between any two echo pulses which are selected by use of the gating system, t_2 and t_6 (as illustrated in Fig. 3.25),

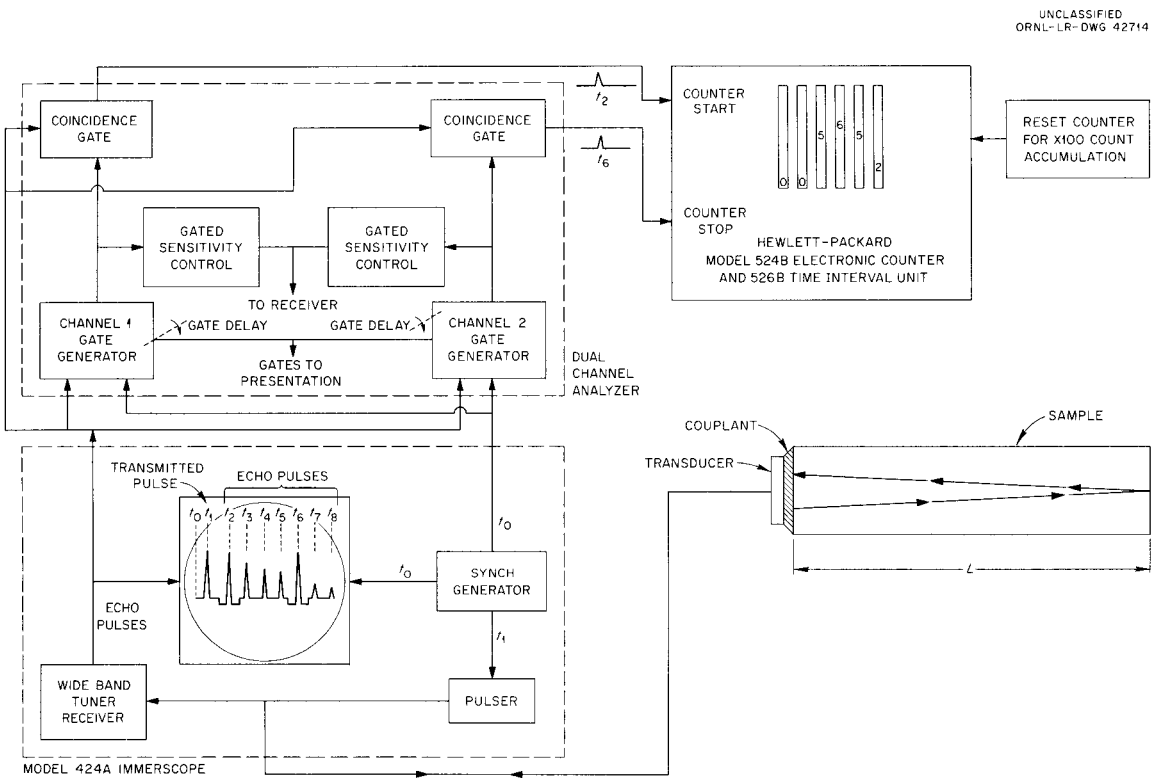

Fig. 3.25. Velocity Determination by Direct Time-Interval Measurement.

is measured by using these two pulses to start and stop a very accurate (1 part in 10^5) 10-Mc signal which is counted by a high-speed electronic counter. The interval is thus counted to within ± 0.1 μsec. Since the pulse excitation is repetitive (at about 600 pps), a reset counter was designed for use with the time-interval counter which allows the count to accumulate for 100 successive intervals. Thus, the interval is statistically measured to within ± 0.001 μsec. The 10-Mc signal is gated on and

off to the counter by the leading edge of the echo pulses at a preselected amplitude and processed through circuitry of identical time response. To produce the two selected pulses identical in amplitude, gated sensitivity controls are utilized, thus allowing the receiver sensitivity during each gate interval to be varied independently.

The velocity in this system is determined by

$$V = \frac{2nL}{T} \quad ,$$

where

T = measured time interval,

n = number of echo intervals used,

L = length of sample.

It is advantageous to measure the time of more than one echo interval since, for thin samples, each echo interval is only a very few microseconds, and greater accuracy is obtained by measuring a longer interval. It should be noted that the error introduced by the transit time of the ultrasound through the couplant is eliminated by the expedient of measuring between echoes rather than between the transmitted pulse and an echo.

It has become evident during this development that the Immerscope, while an excellent tool for ultrasonic inspection, is not well suited for use in this system for several reasons:

1. A small amount of short-term drift and pulse-time jitter contribute to inaccuracy.

2. Because of the receiver design, errors up to one-half cycle of the ultrasonic wave may exist, depending on the character of the leading edge of the echo pulses.

3. The transmitted pulse is too long and too irregular in shape for use on thin samples.

Because of these difficulties, the accuracy of the system is limited to about 99%. Future development of replacement equipment is planned which should allow absolute velocity measurements with accuracies of 99.9 to 99.99%.

X-Ray Imaging System

J. W. Allen R. W. McClung

An x-ray imaging system[61] consisting of an x-ray-sensitive Vidicon in a closed-circuit television system has been further investigated. It has been demonstrated[62] that this system exhibits an unsharpness of less that 0.001, which is comparable to class I radiographic film. Also, the contrast sensitivity, though generally lower than that attainable with film technique, is adequate for many inspection problems: contrast and detail sensitivities of 1 to 2% have been demonstrated in 0.5- to 1.5-in. thick aluminum. At the present stage of development, the system is plagued with anomalies in the selenium photoconductor Vidicon target, which detract from the image quality. Further development will be required before this system is suitable for the high-quality radiographic performance demanded for the inspection of nuclear reaction components.

Low-Voltage Radiography

R. W. McClung J. W. Allen

A program of study has begun for the development of radiographic technology for the inspection of low-absorption materials, such as beryllium and graphite, and of very thin sections of aluminum, stainless steel, or other materials. To accomplish this, equipment has been procured which is capable of emitting long-wavelength x radiation in the range from 0 to 50 kvp. Since all materials exhibit greater linear absorption coefficients for longer wavelength radiation, these problem materials then become fit subjects for radiography in the low-energy range. However, because of this increased absorption by all materials, conventional radiographic techniques and accessories are not applicable, since the normally used film holders, filters, etc., will absorb much more radiation than the specimen. Therefore, a mottled radiograph of very poor contrast would result. For this reason, most of the work has been

[61] J. W. Allen and R. W. McClung, Met. Ann. Prog. Rep. Oct. 10, 1958, ORNL-2632, p 120 (classified).

[62] J. W. Allen and R. W. McClung, An Electronic, High-Resolution, X-Ray Imaging System, ORNL-2671 (Aug. 11, 1959).

accomplished by darkroom techniques, with the object being placed directly on the bare film.

At these very low energies, even the absorption by the air becomes a large factor in the total absorption by the inspection system. For this reason, techniques have been evolved which utilize a helium atmosphere through which the radiation is passed. This may consist of complete dry-box radiography with specimen and film being in the helium atmosphere or may involve the use of a helium-filled chamber placed between the x-ray tube and the specimen. Of course, thin, low-absorption diaphragms must be used as radiation windows on the chamber. This permits the radiography of sections of much larger or longer items than could be accomplished readily by dry-box techniques. The advantages of a helium atmosphere are illustrated in Fig. 3.26, which is a plot of the radiographic film-density variation as a function of helium-purging time in the small chamber. Thus, it could be considered as density vs per cent helium. Of course, this technique greatly enhances the available contrast sensitivity (the ability to detect changes in thickness). Figure 3.27 is a graph of the radiographic film density vs thickness of aluminum for both helium and air atmospheres for 6.5-kvp x radiation.

Much work remains to be done to establish optimum techniques, sensitivity levels, etc. But, already, practical applications have been made in the measurement of localized wall-thickness variations, inspection of very thin-walled tubing,[63,64] and for the evaluation of beryllium tubing.[65]

Gas-Cooled Reactor Development

R. W. McClung J. W. Allen R. A. Nance

One of the major efforts of the Nondestructive Test Development Group has been the development of adequate techniques, procedures, and standards for the inspection of the EGCR (Experimental Gas-Cooled Reactor) components, with particular emphasis being placed upon the fuel element. One of the

---

[63] GCR Semiann. Prog. Rep. Dec. 31, 1958, ORNL-2676, p 92.

[64] GCR Semiann. Prog. Rep. June 30, 1959, ORNL-2767, p 125.

[65] GCR Quar. Prog. Rep. Sept. 30, 1959, ORNL-2835 (in press).

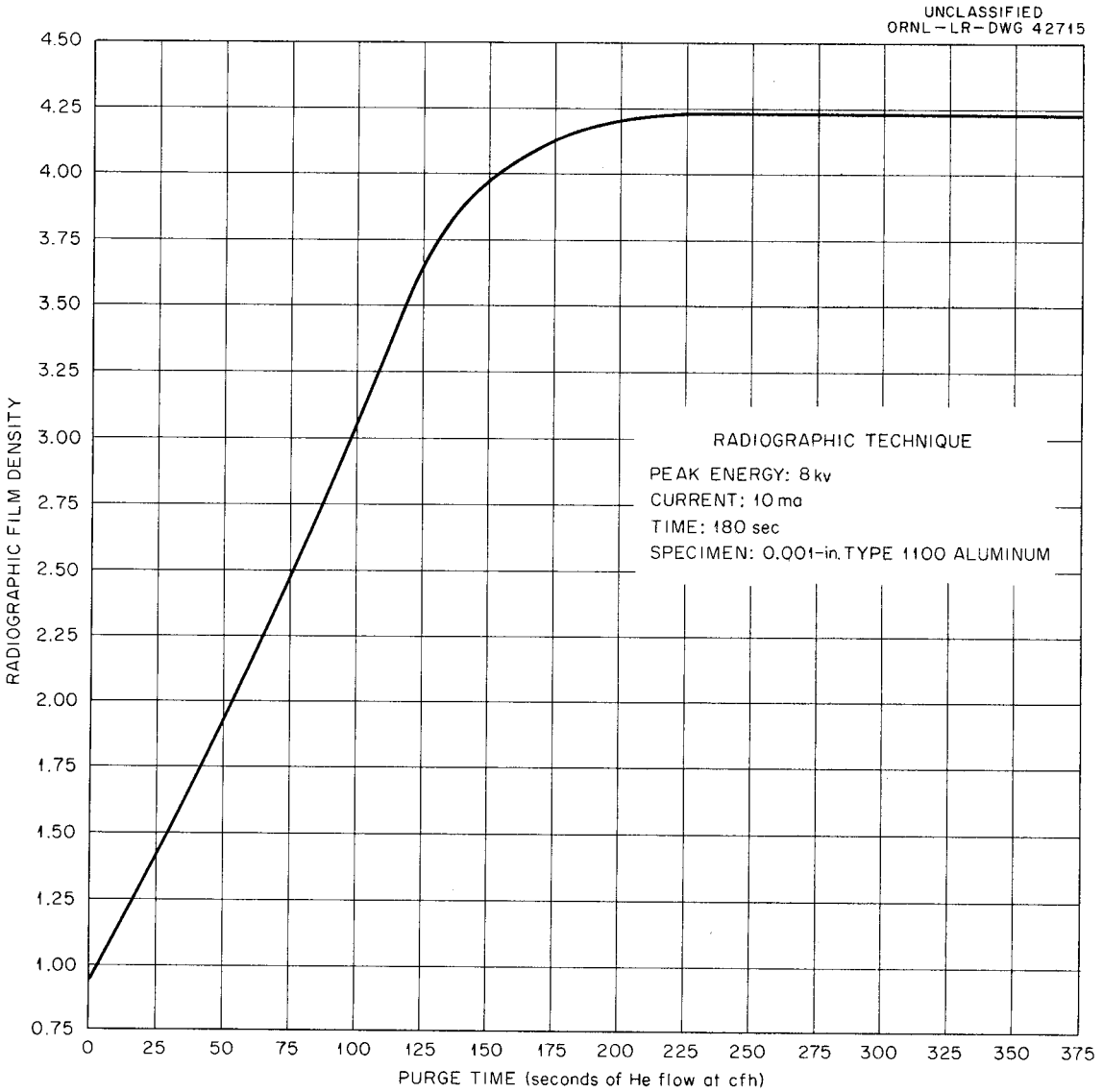

Fig. 3.26. Effect of Helium Atmosphere on Radiographic Density.

major inspection problems has been that of the type 304 stainless steel tubing (3/4-in. OD × 0.020-in. wall) which will be used as the cladding. For the detection of discontinuities, eddy-current and penetrant inspections are believed to be adequate.[66] According to the Title I design, the tubing will conform to dimensional tolerances of 0.710 (+ 0.002, - 0.000) in. on the inside diameter and 0.020 ± 0.002 in. on the wall. Air gaging will be

[66] GCR Semiann. Prog. Rep. Dec. 31, 1958, ORNL-2676, p 90-91.

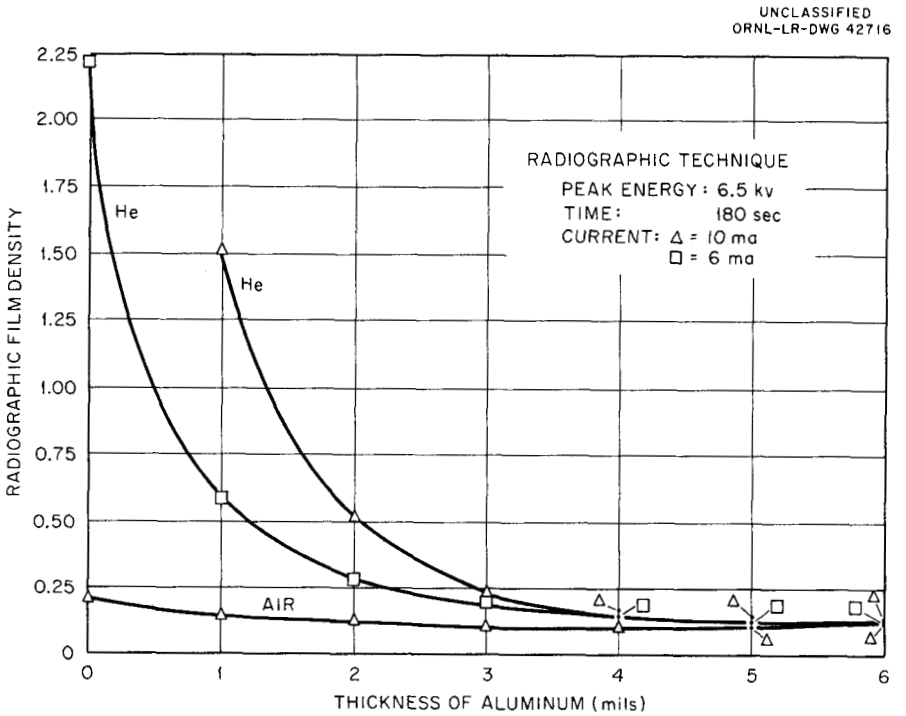

Fig. 3.27. Comparison of Air and Helium Atmospheres for Radiography of Thin Aluminum.

used to measure the inside diameter, and a resonance ultrasonic technique will be used to evaluate the wall thickness variations.[65]

Development efforts for the inspection of the closure weld for the capsule have been primarily directed toward the use of helium leak-testing, penetrants, and radiography.[67] Procedure specifications for these inspections have been written or are being prepared to ensure that the welds on the capsules will be of high quality.

A considerable amount of work has been expended for the development and evaluation of an ultrasonic inspection technique for the heavy pressure-vessel weldments. Preliminary results indicate that this will be a very good, definitive inspection for this purpose.[65]

Gas-Cooled Reactor Program Materials Evaluation

R. W. McClung R. A. Nance J. W. Allen

As an aid in developing inspection techniques and to determine quality levels available in reactor materials, a quantity of type 304 stainless

[67] GCR Semiann. Prog. Rep. June 30, 1959, ORNL-2767, p 121.

steel tubing has been thoroughly evaluated by nondestructive methods, including penetrants, pulse-echo and resonance ultrasonics, radiography, eddy-currents and dimensional gaging. Some of the sizes have included 3/4 × 0.020 in. (refs 63, 65, 68), 1/2 × 0.014 in. (ref 63), 1/2 × 0.003 in. (ref 68), and 3/4 × 0.004 in. (ref 65).

Most of the evaluation has centered around the 3/4 × 0.020 in. type 304 stainless steel tubing, this being the proposed cladding size for the Title I design. One batch of approximately 1300 ft was inspected in the vendor's plant and subsequently inspected at ORNL.[68] The greatest discrepancy in this tubing was the failure to meet the wall-thickness tolerance. A second batch of approximately 1500 ft which was purchased without vendor inspection was completely evaluated at ORNL, with a rejection rate of about 45% (ref 65).

Several small batches of beryllium tubing from domestic and foreign fabricators have been nondestructively evaluated.[65,68] Thus, the most definitive inspection method seems to be that of low-voltage radiography.

---

[68] GCR Semiann. Prog. Rep. June 30, 1959, ORNL-2767, p 124–25, 128.

MECHANICAL PROPERTIES

D. A. Douglas, Jr.
C. R. Kennedy R. W. Swindeman
H. E. McCoy, Jr. J. R. Weir
J. W. Woods

Gas-Cooled Reactor

H. E. McCoy, Jr. J. R. Weir J. W. Woods

Tube-Burst Tests. – One of the more predictable circumstances leading to failure of the fuel element capsule in the EGCR (Experimental Gas-Cooled Reactor) occurs when the pressure within the capsule exceeds the external pressure. This may occur through the release of a large percentage of fission gas from the UO_2, thus producing pressures in excess of 300 psi. Or it may occur as a result of an accident leading to the loss of the primary

coolant pressure. In these circumstances, the time interval before failure is a function of the pressure differential, the temperature of the metal, and the structural changes produced by the service environment. These variables are being investigated on type 304 stainless steel tubes having a 0.020-in. wall. Some of the results obtained in air have been reported.[69–71] These stress-rupture curves agree quite well with conventional tension creep-rupture curves reported in the literature[72] except for the 1800°F data, which are considerably lower in the ORNL tests.

Since there is an economic advantage to using welded and drawn tubing instead of seamless tubing, specimens from this type of stock have also been tested. Rupture life was significantly shorter for this material under test conditions similar to those used for seamless tubes, and all failures occurred in the weld seam. Metallography indicates that the metal in the fusion-welded area has a much finer grain size than that in the rest of the tube. Since a metal is generally weaker in creep in the fine-grain condition, the early failure of the welded tubes can be attributed to this factor. Attempts will be made to equalize the grain size by thermal treatment, and additional burst tests will be made.

Creep Buckling. – Early in the service life of a fuel element, the maximum principal stress is a compressive one acting in the tangential direction. There is a possibility that a substantial gap may exist between the ceramic fuel and the inside of the capsule walls. Under such conditions, the unsupported wall will deform until resistance is offered by the UO_2 pellets. As previously discussed,[73] this deformation may be either uniform or nonuniform, depending on the size of the gap, the temperature of the capsule, the circumferential temperature distribution, and the thickness of the capsule wall.

Strain Fatigue. – Failure of a fuel element may result from repeated strains imposed either thermally or mechanically. Creep and relaxation

---

[69] GCR Semiann. Prog. Rep. Dec. 31, 1958, ORNL-2676, p 81–85.

[70] GCR Semiann. Prog. Rep. June 30, 1959, ORNL-2767, p 103–5.

[71] GCR Quar. Prog. Rep. Oct. 31, 1959, ORNL-2840 (in press).

[72] Digest of Steels for High Temperature Service, p 58, The Timken Roller Bearing Company, 6th ed., 1957.

[73] Met. Ann. Prog. Rep. Oct. 10, 1958, ORNL-2632, p 129 (classified).

are prominent factors in the temperature range of interest, and considerable plastic strain can be induced by rather rapid stress reversals. Consequently, an investigation of the isothermal strain-cycling capacity of type 304 stainless steel is being conducted. Initial results indicate that its fatigue strength is about the same as Inconel's. Using the plastic strain per cycle as a measure of damage, no change in properties is noted within the temperature range from 1300 to 1600°F.

Environmental Effects on Creep. – Although the major constituent of the coolant stream in the EGCR will be helium, small quantities of other gases will be present due to the outgassing of the large quantity of graphite present and due to inleakage during operation. Hence, small quantities of CO, CO_2, H_2, H_2O, CH_4, O_2, and N_2 will be present in the helium coolant. The concentration of each of these impurities will depend upon the time the reactor has been in operation, the operating temperature, the purification system used, and the particular location in the reactor system. Hence, the exact service environment to which the material is exposed is not precisely known. The approach taken to this problem has been that of studying the physical behavior of the material in the pure gases which will appear as contaminants in the reactor environment, with the long-range objective of prescribing "safe contaminant limits" within which fuel elements of the type proposed will operate satisfactorily.

Creep tests carried out to date on type 304 stainless steel at 1300, 1500, and 1700°F in CO, CO_2, H_2, N_2, air, and Ar indicate that data obtained in argon represent the most conservative values for design purposes. The other environments decrease the creep rate and increase the rupture life. The details of this study have been reported.[74,75]

An extensive amount of carburization occurred in specimens tested in pure CO_2. This was, of course, unexpected. To study this further, a number of unstressed samples, 0.020 in. thick, were annealed in a ceramic tube at 1500°F in flowing CO_2. In approximately 140 hr, the average carbon content of the samples was increased from 0.04 to 0.18%. The effect of flow rate was examined, and variations of 0.75 to 1.5 cfh did not alter the above

---

[74] GCR Semiann. Prog. Rep. June 30, 1959, ORNL-2767, p 106–8.

[75] GCR Quar. Prog. Rep. Sept. 30, 1959, ORNL-2835 (in press).

results. In a comparable time, similar samples annealed in flowing CO at 1500°F increased in carbon content from 0.04 to 0.30%. Preoxidation and thin copper films were found to effectively reduce the carburization rates in CO and CO_2, although neither completely prevented carbon pickup.

It is difficult to predict whether the reactions which occur in the pure gases will present problems in an environment composed primarily of helium plus small partial pressures of contaminant gases. Flowing environments of this type are difficult to meter, and the problem of controlling the composition over long periods makes static environments undesirable. Equipment is currently being developed for the mixing of dynamic environments containing helium and five contaminant gases in concentrations as low as 0.1 vol %. The gas-metal reactions which occur in these environments will be studied, and the effects of these reactions upon the mechanical properties of type 304 stainless steel will be evaluated.

Molten-Salt Reactor Program

R. W. Swindeman

The alloy INOR-8 developed specifically for the Molten-Salt Reactor has been under study by the Mechanical Properties Group to evaluate its high-temperature strength properties. This investigation includes tensile, creep, and relaxation tests on several heats of metal. A detailed report on the results of this study has been written.[76] A brief review of the mechanical properties described in this report will be presented here.

It has been found that the tensile properties of INOR-8, especially the yield stress and ductility, vary significantly from heat to heat. In general, the difference may be explained by variations in the grain size and carbon content. Fine-grained and high-carbon heats exhibit the greatest strength but the lowest ductility.

All solution-annealed heats exhibit a minimum ductility around 1500°F, with the tensile elongation for some heats being less than 10%. This loss in ductility appears to be caused by carbide precipitation along grain boundaries.

---

[76]R. W. Swindeman and D. A. Douglas, The Mechanical Properties of INOR-8, ORNL-2780 (to be published).

Creep data in air and in molten salt have been presented in several Molten-Salt Reactor progress reports.[77–79] Comparative tests between salt and air do not indicate any significant weakening in the fused-salt environment. Metallography of ruptured specimens tested in salt reveals no evidence of intergranular corrosion up to 1800°F, although surface roughening has been observed, especially at the higher temperatures.

Design stresses for INOR-8, based on a minimum creep rate of 10^{-5}%/hr, compare favorably with the ASME Boiler Code stress for type 316 stainless steel between 1100 and 1300°F. The allowable stress at each temperature varies slightly according to the heat, specimen configuration, and environment. For example, at 1250°F the stress ranges from 5000 to 5600 psi. The maximum allowable stress for type 316 stainless steel at this temperature is 5300 psi.

The fatigue properties of INOR-8 in air have also been investigated.[80] In the rotating-beam fatigue test, both frequency and grain size were found to be important variables affecting the rupture life. This alloy was shown to be markedly superior to Inconel in fatigue strength.

Research on Fracture of Metals

C. R. Kennedy H. E. McCoy, Jr. R. W. Swindeman

One of the primary goals of this research program is the establishment of failure criteria applicable to complex service conditions, but based upon conventional test data. Previous results[81] obtained from testing tubes with internal pressure and axial loads demonstrated that the creep rates in the principal directions can be determined from uniaxial data by means of a simple formulation. The rupture-life results tended to indicate that, although the shear stresses controlled the strain rates, the rupture life followed a maximum-principal-stress criterion. The test program in the past

[77] D. A. Douglas, MSR Quar. Prog. Rep. June 30, 1958, ORNL-2551, p 64.

[78] R. W. Swindeman and D. A. Douglas, MSR Quar. Prog. Rep. Oct. 31, 1958, ORNL-2626, p 64.

[79] MSR Quar. Prog. Rep. Jan. 31, 1959, ORNL-2684, p 82.

[80] R. G. Carlson, Fatigue Studies of INOR-8, BMI-1354 (June 26, 1959).

[81] C. R. Kennedy, W. O. Harms, and D. A. Douglas, Multiaxial Creep Studies on Inconel at 1500°F, ORNL-2622 (Jan. 19, 1959).

year has been directed toward expanding the failure criterion to more complex and dynamic stress states.

Multiaxial Stresses. – This test program consists of two types of tests, both designed to critically evaluate the maximum-principal-stress criterion for rupture life. The first type of test evaluates the effect of prior creep under a uniaxial stress in one principal direction on the rupture life when subsequently stressed in a second principal direction. This was accomplished by creep testing Inconel tubes at 1500°F first with an axial tensile stress of 4,000 psi to a given axial strain of 1% and 3%. The axial stress was then released and the test continued to rupture with a pure tangential stress of 4,000 psi. The axial creep curves of the two tests are shown in Fig. 3.28 in comparison with a test specimen which had no prior axial strain. The small deviation in results is considered within the normal experimental error. It appears then that a metal can absorb considerable strain or damage along one principal stress axis without seriously affecting the resistance to creep and fracture in other principal directions.

The purpose of the second type of test was to determine the effect of superposition of a constant stress concurrent with strain cycling on the rupture life of Inconel at 1500°F. This again was accomplished by testing tubes with internal pressure and axial loading. Two stress states were calculated for each test such that each state would produce the same axial strain rates, one in tension and the other in compression, with a constant internal pressure or tangential stress. The time per cycle was chosen so that the strain per cycle would be essentially the same for each test. The nominal strain per cycle was chosen to be 0.75%. A schematic drawing shown in Fig. 3.29 demonstrates the stress states with time. Table 3.15 lists the test conditions and results.

The analysis of the test results is made by considering the maximum principal stress as the criterion for fracture and by assuming that creep damage in one direction is additive but is not affected by stresses in the other directions. The time to failure is then predicted by the total time under the maximum principal stresses. The total time that the axial tensile stress is applied will be $1/2\ t_{\sim} N = t$, where t = total time, N = number of cycles, and $t_{\sim}$ = time per cycle, since this stress is only applied

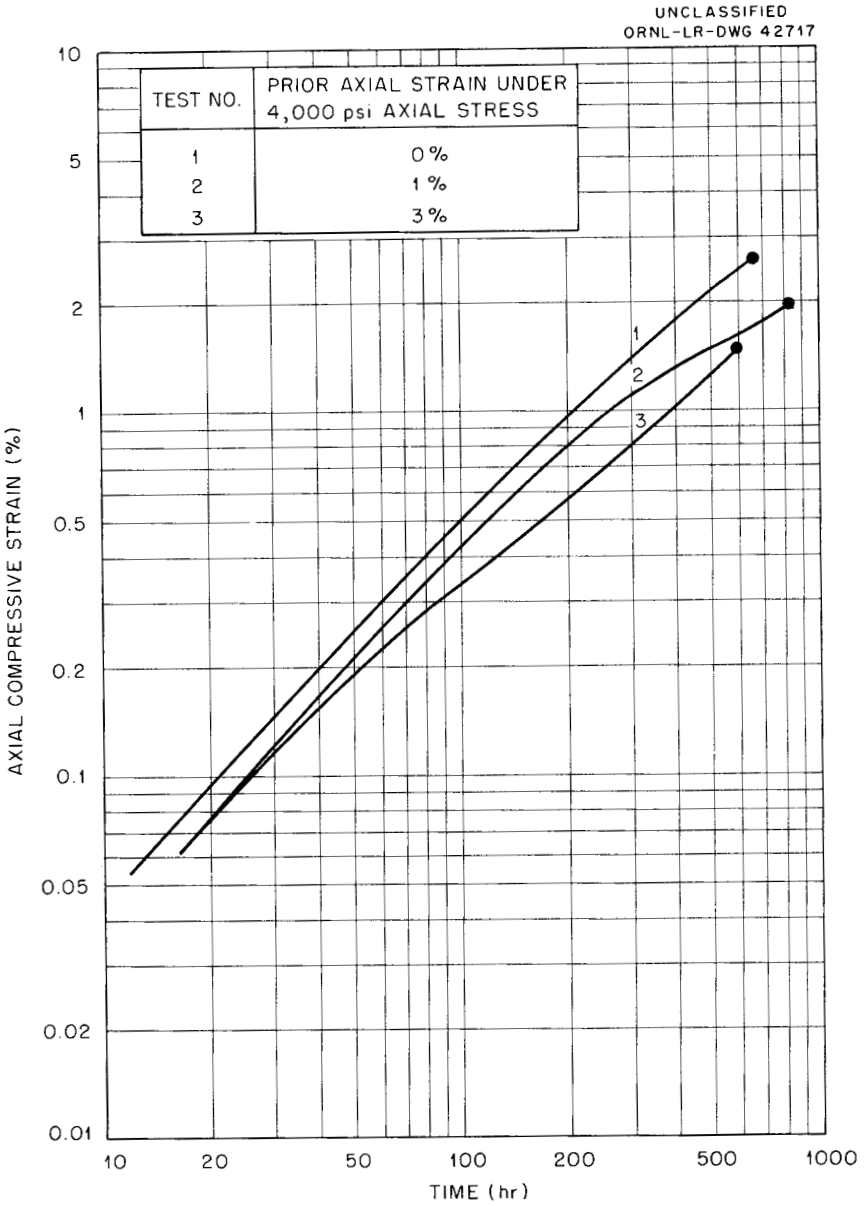

Fig. 3.28. Effect of a Prior Axial Creep Stress on Creep in the Tangential Direction.

half of the time. The total time that the tangential stress is applied is equal to the time in test, since it is applied continuously. Therefore, if the axial tensile stress causes failure, the time to failure is twice the rupture life determined by conventional uniaxial testing. If the tangential stress causes failure, the time to failure is equal to the conventional rupture life. The rupture-life results of the tests are compared with predicted values in Fig. 3.30, indicating a very close agreement. It should be

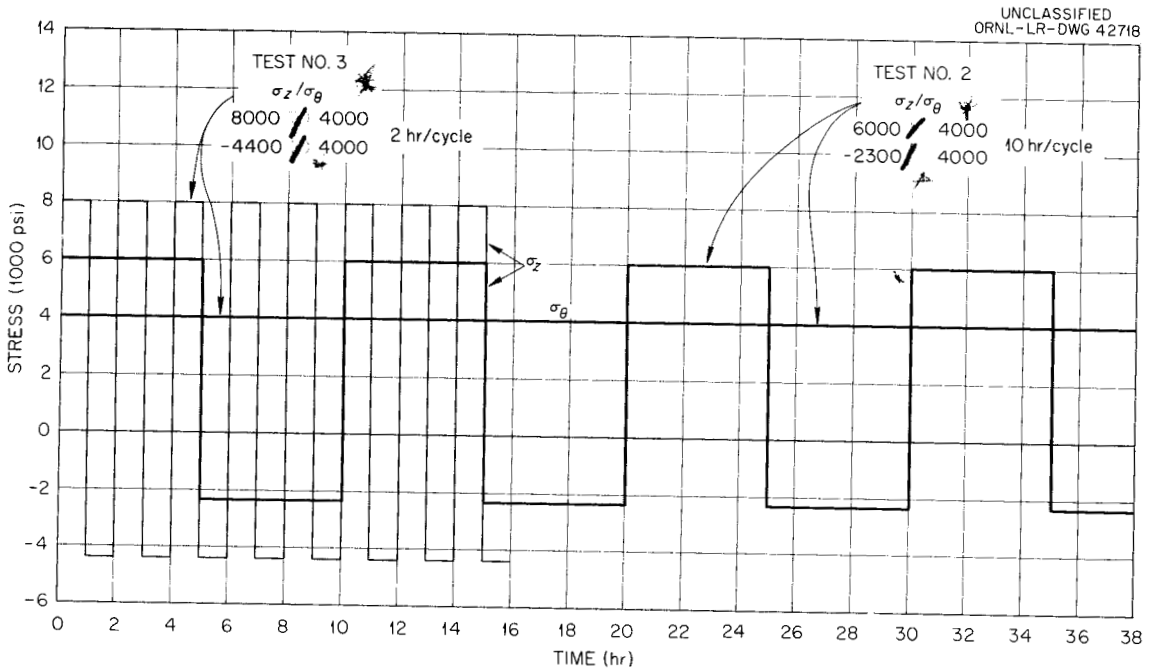

Fig. 3.29. Stress States vs Time for Inconel Tubes under Superimposed Creep and Strain Cycling.

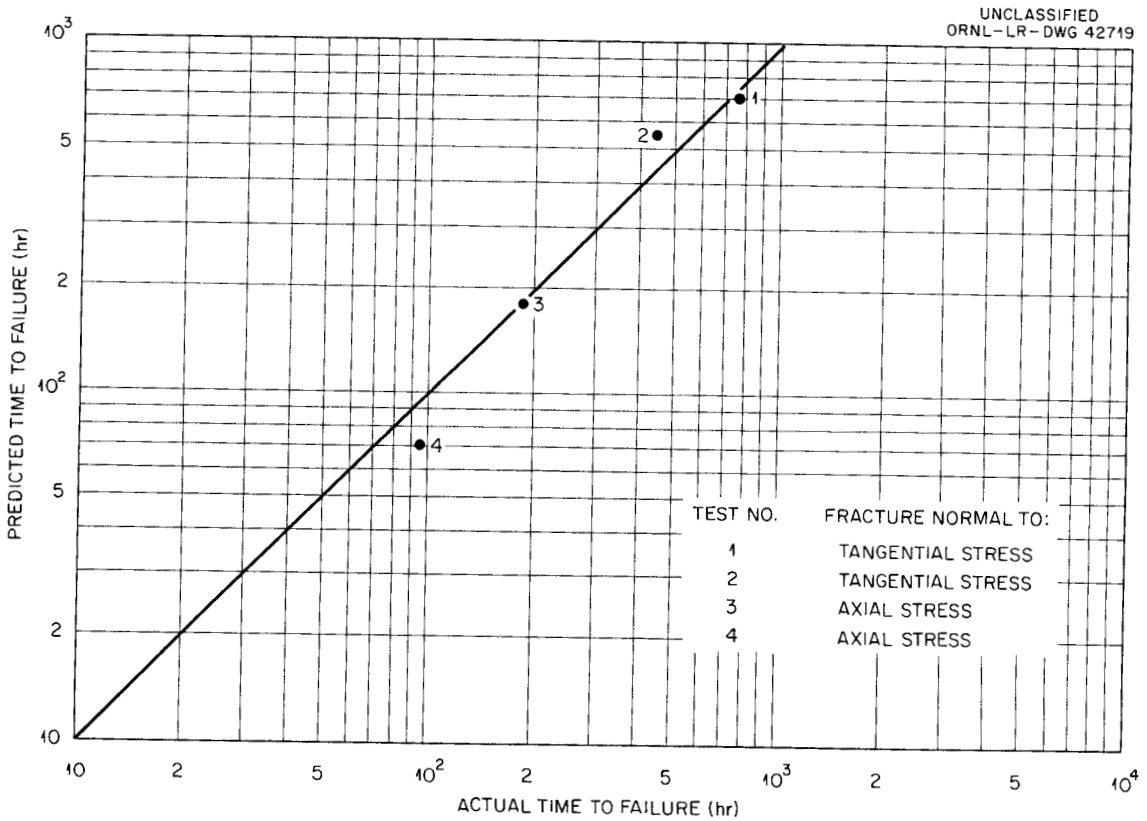

Fig. 3.30. Comparison of Predicted and Observed Rupture Results Obtained by Testing under Superimposed Creep and Strain Cycling.

See note

Table 3.15. Test Conditions and Results of Testing Inconel Tubes Under Superimposed Creep and Strain Cycling

Test Number	Stress States (psi) (axial stress/tangential stress)		Time/Cycle (hr)	Axial Plastic Strain/Cycle (%)	Time to Rupture (hr)	Number of Cycles to Failure
1	4000/4000,	0/4000	96	0.75	750	7.5
2	6000/4000,	-2300/4000	10	0.43	441	44
3	8000/4000,	-4400/4000	2	0.66	188	94
4	10000/4000,	-6400/4000	1.1	0.80	99	87

emphasized that these cyclic tests were performed with fairly slow frequencies and that this analysis may not be applicable to high-frequency fatigue problems. One of the several problems which remains to be resolved is that, in high-frequency fatigue tests, the stress is not applied in a square wave but is applied in a sine wave. Therefore, the true effect of the applied stress or the fraction of the life used each cycle is not simply the time under the maximum stress in the cycle.

Strain Fatigue. – For the last several years the Mechanical Testing Group has been studying the problem of high-temperature fatigue. Particular emphasis has been placed on low-cycle fatigue where failures occur in less than 10^5 cycles. Because measurable plastic strains must be introduced in order to fail a material in less than 10^5 cycles, low-cycle fatigue is often termed strain-cycling. The strain-cycling behavior must be considered where cyclic creep or cyclic thermal stresses occur, since these stresses often produce appreciable plastic strain.

Two reports have been published concerning the low-frequency mechanical strain-cycling properties of Inconel between 1300 and 1650°F.[82,83] It was found that the number of cycles to failure, N, could be related to the plastic strain per cycle, ϵ_p, by the relation

$$N^{\alpha}\epsilon_p = K \quad , \tag{1}$$

where K and α are constants. Investigations at the University of Alabama show that this equation also holds for thermal-cycling conditions.[84]

Recent work on the strain-cycling problem has been aimed at exploring the effect of frequency on the constants of Eq. (1). Both the thermal and mechanical strain-cycling tests have shown that longer time cycles tend to decrease the number of cycles to failure. Fatigue tests at the Battelle Memorial Institute also indicate this behavior.[85]

---

[82] C. R. Kennedy and D. A. Douglas, Plastic Strain Absorption as a Criterion for High-Temperature Design, ORNL-2360 (Apr. 17, 1958).

[83] R. W. Swindeman and D. A. Douglas, Trans. Am. Soc. Mech. Engrs. Series D, 81(2), 203 (1959).

[84] J. F. Goree, Jr., Thermal Fatigue Tests – III, Memorandum Report No. 9, Bur. Engr. Res., Univ. of Ala., University, Alabama (Aug. 1957).

[85] R. G. Carlson, Fatigue Studies of Inconel, BMI-1355 (June 26, 1959).

The existence of a frequency effect indicates that strain absorption is not the sole mechanism controlling fracture. Since strain rate affects the ductility at high temperatures, as is often observed in creep testing, it may be possible to explain the frequency effects on this basis. This subject will be pursued during the next year.

A second approach is one of considering the cyclic stress-rupture properties.

Currently, strain-cycling tests are being performed by imposing cyclic creep stresses on the specimens. It has been found that the frequency has no significant effect on the curve relating the cyclic stress to the rupture life. Considerably more study must be given to this approach before it can be considered useful from an engineering viewpoint.

Environmental Effects on Creep. – Several recent investigations have shown that the creep and stress-rupture properties of metals are not only dependent upon such normal factors as temperature, stress, and prior history, but that they also may be dependent upon the testing environment. Although creep tests are quite effective in pointing out such environmental effects, they are not very informative as to the mechanisms responsible for the observed behavior. Hence, in order to obtain information of a more definitive nature concerning these mechanisms, it has become necessary to consider properties such as thermal expansion, electrical resistivity, and internal friction, which are more refined measurements of atom movements than are gross deformation rates.

During the past year a detailed study has been made of the various techniques in use for making internal-friction measurements. It was concluded from this investigation that the use of the specimen as the suspension member for a torsional pendulum was a technique which had been used with considerable success and did not pose serious problems for making measurements at elevated temperatures in a controlled environment. An apparatus of this type has been constructed during the past year. It is now possible to measure the internal friction of wire specimens as large as 0.060 in. in diameter and 8 in. long, at temperatures up to 1000°C. Preliminary measurements on 2S aluminum in vacuum at several temperatures agree well with those found in the literature. From these experiments, it is concluded that this device has the required degree of accuracy and sensitivity for the study of gas-metal reactions.

The torsional pendulum has the limitation of not being able to describe the elastic properties of the test specimen as completely as is possible by other methods, where the specimen is driven at a higher frequency. Equipment has been purchased which will make it possible to determine the elastic properties and the damping capacity of rod test specimens up to 1000°C in air. This equipment is being modified to operate with the specimen in a controlled environment.

Another apparatus has been constructed whereby the electrical resistivity of wire specimen can be determined as a function of strain. Specimens can be tested at temperatures as high as 1000°C in controlled environments.

High-temperature test equipment has been developed which has a sensitivity of $5 \times 10^{-7}\%$ for measuring the expansion or contraction, as a function of time, of a metal specimen in a controlled environment. Such measurements are informative as to the long-range isothermal stability of a material.

A quartz reaction chamber has been constructed for studying gas-metal reactions. Reaction environments are generated by a metering system capable of mixing up to five contaminants with an inert carrier gas, in concentrations as low as 0.1 vol %. Weight changes are measured by observing the elongation of a calibrated spring.

It is felt that the information obtained from these experimental apparatus, combined with additional information from x-ray and metallographic examination of test specimens, will lead to a more basic understanding of the effects of certain gaseous environments upon the deformation process.

The Relaxation Phenomena. — Stress-relaxation tests have been used to provide information for the design of bolted flange joints or shrinkage assemblies operating at elevated temperatures. Similarly, the data can be used to indicate the effectiveness of stress-relief treatments. In the past year it has also been determined that, by direct computation, reliable creep-rate values can be obtained from the relaxation-test results. Thus, creep-strength values can be derived over a wide range of stresses in tests of relatively short duration and with the use of a single specimen. It is not proposed that the relaxation test will supplant the constant-stress creep test, but rather that it provide an additional means for the evaluation of the high-temperature properties of metals.

Relaxation results are compared with constant-stress creep data in Fig. 3.31 by use of an expression originally proposed by Kanter:[86]

$$t = \frac{A^n}{E(n - 1)} \sigma^{1-n} \quad , \tag{2}$$

where

σ = stress,

t = time in hours to relax to stress σ,

E = modulus of elasticity,

A,n = creep constants.

The creep constants, A and n, are those which fit into the expression

$$\dot{\epsilon} = \left(\frac{\sigma}{A}\right)^n \quad , \tag{3}$$

where $\dot{\epsilon}$ = strain rate corresponding to stress σ.

[86] J. J. Kanter, Trans. Am. Soc. Metals 24, 900 (1936).

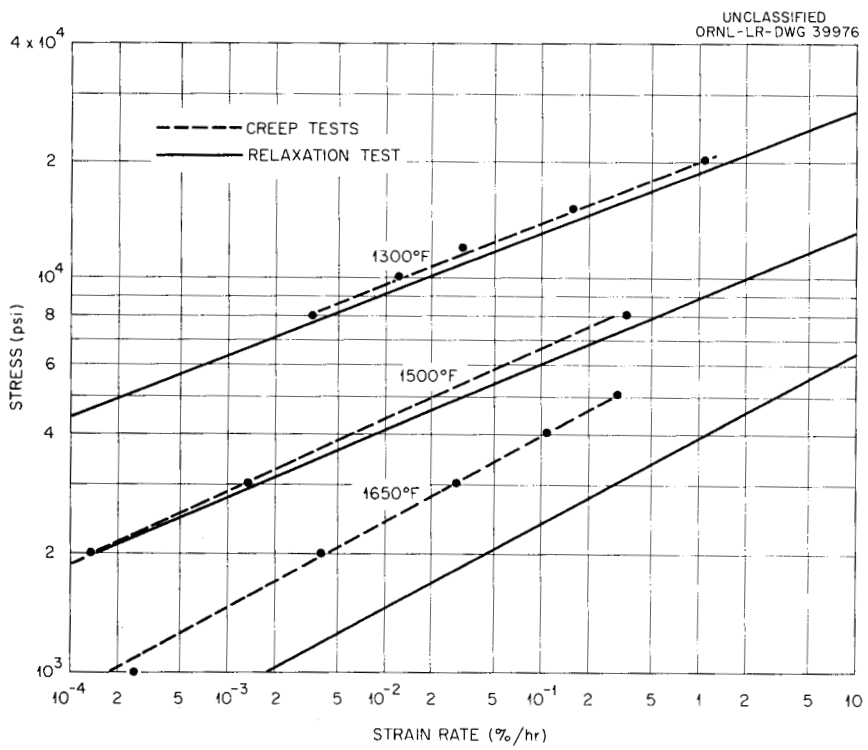

Fig. 3.31. Stress vs Strain Rate for As-Received Inconel.

Equation (3) is a common expression used in machine design because of its simplicity. The agreement shown in Fig. 3.31 between the constant-stress and the relaxation results demonstrates the validity of Eq. (2) at temperatures where primary creep is negligible and the material is metallurgically stable. However, at 1650°F, the results demonstrate the value of the relaxation test in checking the applicability of the creep constant determined by constant-stress creep tests. In this case, the constant-stress tests produced optimistic strength values due to the effects of an unstable metallurgical structure.

The relaxation test, therefore, has the unique advantages of (1) obtaining reliable creep data over a wide range of stresses in a relatively short time and with a single specimen; (2) furnishing a check as to the accuracy of the law assumed to fit constant-stress creep data; and (3) furnishing a complete stress-strain history, which is recorded automatically.

Aircraft Nuclear Propulsion Program

Progress on the ANP Program has been described elsewhere.[87,88]

[87] ANP Semiann. Prog. Rep. Mar. 31, 1959, ORNL-2711, p 23–27 (classified).

[88] ANP Semiann. Prog. Rep. Oct. 31, 1959, ORNL-2840 (in press) (classified).

WELDING AND BRAZING

P. Patriarca

R. E. Clausing
R. G. Donnelly
E. A. Franco-Ferreira
R. G. Gilliland
A. E. Goldman
R. L. Heestand
A. P. Litman
J. J. Prislinger
G. M. Slaughter
J. W. Tackett

Molten-Salt Reactor Program

Welding of Nickel-Molybdenum Alloys (G. M. Slaughter). – A summary report[89] was prepared, describing the results of welding studies on two age-hardenable alloys (Hastelloy B and Hastelloy W) and a non-age-hardenable alloy (INOR-8). The all-weld-metal mechanical properties of these

[89] G. M. Slaughter, P. Patriarca, and R. E. Clausing, Welding of Nickel-Molybdenum Alloys, ORNL-2760 (Aug. 11, 1959).

alloys at room temperature and at 1200°F were presented for both the as-welded and welded-and-aged conditions. Hastelloy B welded joints were also aged in the temperature range of 1100–1500°F, and the effects upon the room temperature hardness profiles of the weld metal and parent plate were discussed.

Since the ductility of commercial INOR-8 weld metal in the 1300–1500°F temperature range is 10% or less, a program was conducted to develop improved filler metal compositions. Several approaches to the problem were investigated, including (1) improved melting practices during the casting of the original ingot, (2) weld postheat treatment, (3) carbon content reductions, and (4) additions of other elements.[90–92] A 2% addition of niobium to INOR-8 appears to be very promising, since the ductility of this alloy at 1500°F is approximately 30% (ref 93).

Brazing of Graphite (R. G. Donnelly and G. M. Slaughter). – A program is under way to investigate various techniques for producing graphite-to-graphite and graphite-to-metal joints for Molten-Salt Reactor service.[94,95] Several brazing alloys containing carbide-forming elements wet graphite, and one alloy (48 wt % Ti–48 wt % Zr–4 wt % Be) is very promising for the brazing of graphite components. However, the corrosion resistance of this alloy to molten salts is poor, and other alloys having improved corrosion resistance are under development.

Gas-Cooled Reactor Program

Fuel Element Fabrication (R. L. Heestand and A. E. Goldman). – A study of the influence of design and manufacturing variables upon the fabricability of tubular fuel elements was conducted with particular emphasis on methods of effecting the end closures.[96] Optimum joint designs

---

[90] MSR Quar. Prog. Rep. Oct. 31, 1958, ORNL-2626, p 68–71.

[91] MSR Quar. Prog. Rep. Jan. 31, 1959, ORNL-2684, p 90–96.

[92] MSR Quar. Prog. Rep. Apr. 30, 1959, ORNL-2723, p 68–72.

[93] MSR Quar. Prog. Rep. July 31, 1959, ORNL-2799 (in press).

[94] MSR Quar. Prog. Rep. Apr. 30, 1959, ORNL-2723, p 73–74.

[95] G. M. Slaughter, Brazing of Graphite – Prog. Rep. No. 1, ORNL CF-59-8-42 (Aug. 13, 1959).

[96] GCR Semiann. Prog. Rep. Dec. 31, 1958, ORNL-2676, p 73.

and welding conditions were determined for three basic types of end closures, and capsules containing these types of closures were fabricated. Tube burst, thermal cycling, and tensile tests on these capsules revealed no significant differences in joint behavior.[97]

Irradiation test capsules and prototype fuel elements were then fabricated, using the optimum conditions.[98] Additional investigations to determine the influence of other manufacturing variables will be carried out during the manufacture of fuel elements for the Chemical Technology Division's power reactor fuel-reprocessing program.

Welding and Brazing Laboratory personnel were in residence at the General Electric Vallecitos Laboratory (GEVAL) for approximately two months to observe and assist in the fabrication of irradiation capsules. Several GEVAL-type prototype capsules were fabricated at ORNL prior to the period of assistance.

Beryllium-Joining Studies (R. L. Heestand and R. G. Gilliland). — Studies of methods for joining beryllium for fuel-cladding applications are continuing.[98–100] Approximately 100 ft of tubing, 3/4-in. OD × 0.040-in. wall, was procured from Nuclear Metals Corporation and from Chesterfield Tube, Ltd., for evaluation. Fusion welding has been utilized to join end caps to this tubing, and the resultant weld characteristics were similar to those previously observed in welds on material machined from hot-pressed QMV beryllium.

A brazing-alloy development program has been initiated for beryllium-joining applications where temperatures in the 600–700°C range are to be expected. The flowability and general brazing characteristics of a variety of alloys are being investigated in vacuum-brazing equipment which has been installed in an isolated beryllium-joining facility. One of the alloy systems which has indicated promise for joining beryllium is the zirconium-titanium-beryllium system. A pressure-bonding experimental program is also being planned.

---

[97] GCR Semiann. Prog. Rep. June 30, 1959, ORNL-2767, p 120.

[98] GCR Quar. Prog. Rep. Sept. 30, 1959, ORNL-2835 (in press).

[99] GCR Semiann. Prog. Rep. Dec. 31, 1958, ORNL-2676, p 97–104.

[100] GCR Semiann. Prog. Rep. June 30, 1959, ORNL-2767, p 129.

Pressure-Vessel Fabrication (P. Patriarca and J. J. Prislinger). — A number of problems associated with the use of thick plates of ASTM A212B steel for field fabrication of a GCR pressure vessel have been recognized. One of the more important problems is the determination of the pre- and postirradiation notch toughness of weldments prepared by using field-erection welding procedures.[98]

A plate, 144 × 48 × 4 in., was purchased from the Lukens Steel Company with a limit on the carbon content of 0.25% in order to promote good weldability. Three test weldments were fabricated by Chicago Bridge and Iron Company, using suitable welding procedures and E7018 electrodes. Notch-toughness tests will be used to determine the pre- and postirradiation properties of the parent plate, weld deposits, and heat-affected zones.

Sherwood Project

Valve Development (J. W. Tackett). — The development of suitable seal materials for use in high-vacuum valves and flanges is continuing. The types of demountable seals under study are (1) gasket seals of soft, low-vapor-pressure materials, (2) cast-metal seals, and (3) seals of metals which are liquid at room temperature.[101,102] A literature survey indicated that most high-vacuum apparatus incorporated the use of gaskets of copper, gold, aluminum, and Teflon. However, in view of the 400°C bake-out temperature required in service, the investigation of the latter two types of seals was considered necessary.

A program is under way to develop low-vapor-pressure brazing alloys which have melting points in the temperature range 425–600°C. Joint seals involving a circumferential pool of filler metal and a circumferential sintered-metal compact impregnated with filler alloy are under study, the latter design being promising since it is applicable to seals in the vertical as well as the horizontal direction.

Seals utilizing metals which are liquid at room temperature appeared promising in preliminary tests. However, compatibility tests between the

---

[101] R. E. Clausing, J. W. Tackett, and J. D. Hudson, TED Semiann. Prog. Rep. Jan. 31, 1959, ORNL-2693, p 86–93.

[102] R. E. Clausing and J. W. Tackett, TED Semiann. Prog. Rep. July 31, 1959, ORNL-2802 (in press).

In-Ga-Sn eutectic alloy and several potential structural materials at temperatures up to 450°C indicated that corrosion would be encountered. The refractory metals appeared the most promising, but some reaction was observed on these materials after 1000 hr at 400°C.

Materials Outgassing Studies (R. E. Clausing). – Gas-metal reaction studies are being conducted in an effort to (1) measure both qualitatively and quantitatively the outgassing characteristics of materials used in ultrahigh-vacuum systems and (2) investigate the adsorption and desorption of gases on metal surfaces.[101,102] The outgassing characteristics of graphite have been primarily studied to date, and extensive qualitative data have been obtained; quantitative data will be obtained by use of a mass spectrograph. Experimental techniques are still under development for the adsorption and desorption studies.

Aircraft Nuclear Propulsion Program

E. A. Franco-Ferreira R. G. Gilliland

The research performed in the Welding and Brazing Laboratory on the Aircraft Nuclear Propulsion Project has been reported elsewhere.[103,104]

Chemical Technology Division Liaison

A. P. Litman A. E. Goldman

Assistance was given to the Chemical Technology Division in connection with corrosion, selection of materials of construction, welding and brazing, and failure analysis. The majority of this support was for the Pilot Plant and Unit Operations Sections as well as for Chemical Development, Section A, concerning their work on the Fused-Salt Fluoride Volatility Process for recovering uranium from spent reactor fuels.

Summaries of corrosion analyses and experimental work done at ORNL, Argonne National Laboratory, and Battelle Memorial Institute associated

---

[103] ANP Semiann. Prog. Rep. Mar. 31, 1959, ORNL-2711, p 17–22 (classified).

[104] ANP Semiann. Prog. Rep. Oct. 31, 1959, ORNL-2840 (in press) (classified).

with the fluorination and hydrogen fluoride dissolution phases of the process are being prepared.[105,106]

Numerous drawings have been reviewed, most of which pertained to vessels built at ORNL and supplementary equipment presently being installed in the Volatility Pilot Plant's Hydrofluorination Addition. This new equipment will enable the plant to handle zirconium-clad heterogeneous fuels. The hydrofluorinator was made of INOR-8.

To date, corrosion of the fluorination vessel has been of primary concern. Examinations of the two full-size units used in the Volatility Pilot Plant and fabricated from L nickel disclosed extensive attack, at a rate > 1 mil/hr, based on fluorine sparge time. Loss of protective fluoride films plus intergranular attack resulting from sulfur in the system seem to be the major modes of attack. Scouting tests of several nickel-rich alloys containing iron, cobalt, and/or molybdenum have shown promise in the fluorinator's environment, especially because of their lesser susceptibility to intergranular attack.[105] Similar tests will be continued in the next fiscal year.

---

[105]A. P. Litman and A. E. Goldman, Corrosion Associated with Fluorination in the Fluoride Volatility Process, ORNL-2832 (to be published).

[106]A. E. Goldman and A. P. Litman, Corrosion Associated with Hydrogen Fluoride Dissolution in the Fluoride Volatility Process, ORNL-2833 (to be published).

Part IV

APPLIED METALLURGY

PROCESS METALLURGY

R. J. Beaver

C. F. Leitten W. C. Thurber
W. J. Kucera J. T. Lamartine
J. H. Cherubini J. H. Erwin
D. T. Bourgette

ARMY PACKAGE POWER REACTOR (APPR) PROJECT

C. F. Leitten J. H. Cherubini

This section of the report is concerned with materials technology work undertaken in support of the Army's Pressurized Water Reactor programs. A year-end report covering the major metallurgical developments during 1958 was presented in March.[1] Recent efforts have been directed toward developing improved materials combinations for potential application in advanced core loadings of SM-1, formerly designated as APPR-1 (Army Package Power Reactor-1). Progress on these activities are reported below.

Development of Europium-Bearing Absorber Rods

The use of europium as the neutron-absorbing material for reactivity control in Core II of SM-1 has been investigated. Techniques are available for incorporating Eu_2O_3 as a dispersoid in elemental austenitic stainless steel and cladding by roll bonding with wrought stainless steel for corrosion protection.

Specifications and fabrication procedures for the prototype absorber component have been established.[2] Eight absorber sections were manufactured to demonstrate technical feasibility of the process. These units will be employed for reactor control in the second core loading of SM-1. The essential difference between absorber rods designed for service in Core I and Core II is that a 37 wt % dispersion in elemental stainless steel of type 304 composition will replace the 3 wt % B^{10} dispersion in iron as the neutron-absorbing material.

---

[1] APPR Prog. Rep., ORNL-2703, p 3–49 (Mar. 24, 1959) (classified).

[2] C. F. Leitten et al., Specifications and Fabrication Procedures on Europium-Bearing Absorber Rods for Reactivity Control in Core II of SM-1, ORNL-2733 (July 29, 1959).

Despite the fact that the development work on europium-bearing components appears complete, an exploratory effort will continue on the system to evaluate more closely the effect of silicon on the chemical stability of Eu_2O_3 in type 304 stainless steel.

Development of Control-Rod Fuel Element with Eu_2O_3 Flux Suppressor

Fabrication studies were conducted to determine the feasibility of incorporating an internal flux-suppressor in the control-rod fuel assembly. The function of a neutron-absorber integral with the fuel is to minimize flux peaking, due to the Wilkins effect, at the void junction between the fuel and absorber sections of the control-rod assembly. Flux peaking in Core I was minimized by utilizing Haynes-25 combs located at one end of the control-rod fuel element, but this contributed to cobalt activity in the primary coolant loop. The studies indicated that a dispersion containing 26 wt % Eu_2O_3 in elemental type 304 stainless steel can be successfully incorporated directly at the end of the fuel-bearing section of the composite fuel plate.

This task also culminated with the manufacture of eight full-size control-rod fuel elements containing a built-in flux suppressor for service in Core II of SM-1. The specifications and fabrication procedures for preparing the component have been reported previously.[3]

Aqueous Corrosion Studies

The corrosion testing of a large variety of brazed stainless steel joints and miniature fuel plates containing deliberate defects has been completed. This testing program was initiated several years ago to evaluate the corrosion resistance of various brazing alloys in direct contact with the cladding material as well as to determine the behavior of defective fuel plates in pressurized water, in the event of a cladding failure. A topical report covering the conditions of test as well as the results

---

[3]C. F. Leitten *et al.*, Specifications and Fabrication Procedures for SM-1 Core II Control Rod Fuel Elements, ORNL-2726 (July 29, 1959).

obtained from the autoclave screening-program is in process of publication.[4]

Determination of Boron Loss in Core I Fuel Plates

During the manufacture of Core I fuel plates, it was observed that some loss of boron was occurring. A cursory examination at the time revealed that the loss was occurring during sintering and that the magnitude of loss ranged between 0 and 15% of the intended boron content, with an arithmetic average of 7%. As an expedient to compensate for this observed loss, 3.5% excess boron was added to each fuel plate.

More recently, controlled experiments have been performed to establish the reliability of the analytical procedure for determinations of small quantities of boron in UO_2-stainless steel mixtures and to firmly establish the magnitude of loss which occurred during the processing of Core I fuel plates. It was desirable to know, for example, the boron content in Core I fuel plates in order to facilitate the physical analysis of certain discrepancies which appeared between the calculated and the observed nuclear lifetime of Core I and to establish more accurately the level of boron required for proper control of future reactors scheduled for construction in the Army's pressurized water program.

Synthetic samples containing 188.0 mg B_4C, 35.09 g UO_2, and 203.8 g of type 304 stainless steel powders were prepared and forwarded to L. Pitkin Company and to The Martin Company for boron determinations. Similar determinations were made on the same sample in the Analytical Chemistry Division of ORNL. Results of the cooperative program to evaluate the accuracy of low-level boron analysis in such mixtures are listed in Table 4.1.

The boron content was determined by systematic chemical analyses of 15 fuel plates which had been fabricated for the Core I loading, but which had been rejected because of failure to meet dimensional specifications. The Martin Company had previously calculated that, based on their reactivity measurements, there was an average boron deficiency of (29 ± 3)% in

---

[4]C. F. Leitten *et al.*, *Corrosion Investigations of Brazing Alloys and Austenitic Stainless Steel Fuel Composites for Army Package Power Reactor*, ORNL-2834 (in press).

Table 4.1. Percentage Deviation of Boron Analyses in Synthetic Samples Containing 0.188 g of Boron, 35.09 g of UO_2, and 203.8 g of Type 304B Stainless Steel

Analytical Laboratory	Percentage Deviation
ORNL	- 6.01
	- 5.94
	- 4.01
	- 2.49
The Martin Company	+ 0.8
	- 8.1
	- 3.3
	- 9.9
L. Pitkin Company*	- 0.55
	+ 1.52
	+ 0.28
	- 0.68

*Samples did not contain UO_2.

the fuel plates fabricated for the SM-1 (ref 5). The results of the present study, based on chemical analysis of each plate, are listed in Table 4.2. An arithmetical average boron content of 112.4 mg per plate, corresponding to a 22.4% boron loss, can therefore be computed. Considering the distribution of the results, the boron content of any individual plate can be predicted as 112.4 ± 21 mg, with 66% confidence.

Mechanism Studies of Boron Sintering Losses

As previously reported, erratic losses of boron from boron-bearing stainless steel compacts have been observed on sintering in a hydrogen

[5] J. F. O'Brian, Some Aspects of a Boron Determination for the APPR-1, MNO-E-1718-1 (February 1959).

Table 4.2. Reported Boron Content of Fabricated SM-1 Fuel Plates*

Plate No.	Analytical Laboratory	Boron Reported (mg)	Boron Loss (%)
991	ORNL	96.7	33.2
992	ORNL	118.2	18.4
994	ORNL	131.5	9.2
1030	ORNL	79.0	45.5
1045	ORNL	89.1	38.5
1400	ORNL	128.5	11.3
1510	ORNL	119.9	10.3
1541	ORNL	121.5	16.1
1648	ORNL	86.2	40.5
1649	ORNL	77.0	50.3
983	The Martin Company	127.8	11.5
986	The Martin Company	125.3	13.2
992	The Martin Company	131.2	9.2
1260	The Martin Company	148.7	- 2.6
1278	The Martin Company	99.4	30.6

*Originally charged with 0.188 g of B_4C.

atmosphere.[6] Analogous experiments and the variance of boron in SM-1 Core I fuel plates confirm this trend. The erratic deviation of boron losses from hydrogen-sintered compacts of different experiments, and the consistent losses of samples in an experiment, are illustrated in Table 4.3. This suggests that minor changes in the sintering environment can induce disproportionate variances in boron loss.

The first variables studied in order to determine the nature of the loss have been sintering atmosphere and matrix materials. Compacts containing 0.0485 g of high-purity boron and 1.000 g each of Cr, Ni, Si, Fe, Cr_2O_3, NiO, SiO_2, or Fe_2O_3 have been sintered in vacuum ($< 0.1\mu$), helium

[6]Met. Ann. Prog. Rep. Oct. 10, 1958, ORNL-2632, p 140.

Table 4.3. Boron Losses from Hydrogen-Sintered, 0.05 Wt % Boron–Stainless Steel Compacts Prepared from a 0.25 Wt % Boron–Stainless Steel Alloy

Experiment No.	Alloy Base (Type of Stainless Steel)	Boron Loss (Wt %)				
		Individual Compacts				Average
1	304	27	30	23	29	27
2	304	24	26	20	26	24
3	304	40	41	40	36	32
4	347	60	59	60	64	61
5	304*	68	68	72	71	70
	304	75	66	69		70
6	304*	79	75	71		74
	304	77	72	74	76	75
7	304	59	60	58	53	57.5

*Contained 25 wt % UO_2.

(+ 70°F dew point) and argon (< 1 ppm H_2O) for 1-1/4 hr at 1135°C. Table 4.4 lists the analytical results obtained to date. If a loss of less than 6% (3 mg) of boron is considered to be within experimental error, appreciable losses have occurred only in an oxidizing environment. This behavior suggests the following reaction sequence:

$$3/x\ MO_x + 2B \rightleftharpoons B_2O_3(\ell) + 3/x\ M \text{ (ref 7)} \qquad (1)$$

and

$$B_2O_3(\ell) \rightleftharpoons B_2O_3(g) \qquad (2)$$

where reaction (2) is the rate-controlling process. This sequence may explain the larger losses incurred when sintering the metal oxide–boron compacts in vacuum, compared with the argon environment.

[7]Thermodynamically, $\Delta F°$ for the reaction is negative in all cases except for SiO_2.

Table 4.4. Average Boron Sintering Losses From Compacts Containing 5% Boron, Balance Matrix Material, Sintered at 1135°C

Matrix Material	Boron Loss (%)		
	Vacuum*	Argon*	Wet Helium*
Si	2.6	3.4	10.1
SiO_2	12.3	9.1	7.2
Ni	2.6	5.3	9.3
NiO	31.5	8.6	41.5
Cr	1.7	3.0	
Cr_2O_3	2.1	3.3	
Fe	5.1	3.0	
Fe_2O_3	**	**	

*Sintering environment.

**Compacts reacted and spattered.

Compatibility of SrB_6 and Type 304LB Stainless Steel

The stability of SrB_6 in stainless steel at 1150°C was evaluated as a normal extension of the boron compound-stainless steel compatibility program. A compact of 87.3 g of -100 mesh type 304LB stainless steel powder and 0.4035 g of -325 mesh SrB_6 was fabricated by employing conventional powder-metallurgical techniques. The sintering operation was performed at 1150°C for 1-1/4 hr in hydrogen (inlet dew point < -60°F). After roll cladding at 1150°C into a composite plate, the plate was sectioned and the samples were heat treated for 1, 2, and 3 cycles at 1150°C. Each cycle consisted in heating at a rate of 150°C/hr in the temperature range of 500 to 1150°C, holding for 1 hr at 1150°C, then furnace cooling. Figure 4.1 depicts the core-clad interface of a sample heat treated for 3 hr. The dark, ovate phase is believed to be unreacted SrB_6. The light-grey phase, which in some cases is intimate with the SrB_6 particle, is also dispersed throughout the stainless steel and appears to be a product of reaction between the compound and stainless steel. A small amount of this phase can also be observed in the clad area. A similar precipitate

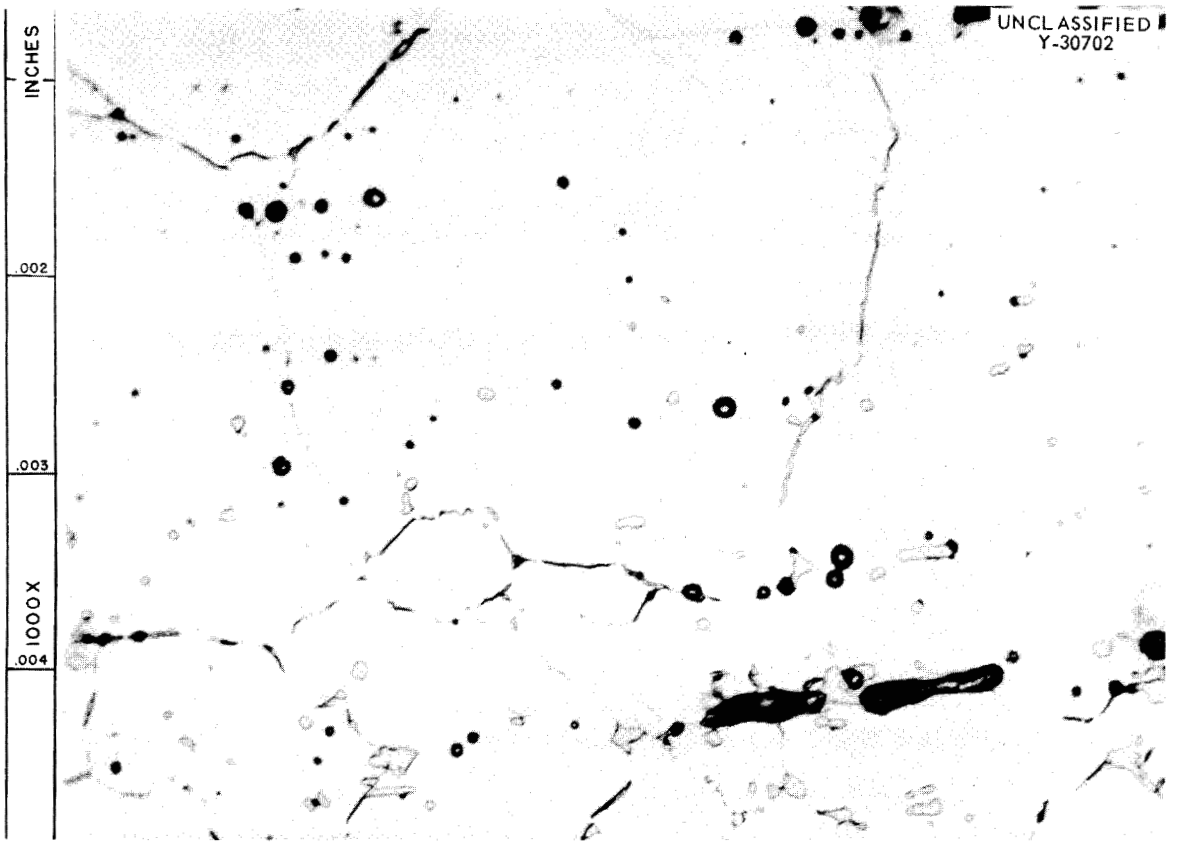

Fig. 4.1. Type 304LB Stainless Steel Containing 0.56 wt % SrB_6, Heat Treated for 3 hr at 1150°C. Depicted is the ovate SrB_6 and a light-grey phase, which appears to be a product of reaction between SrB_6 and stainless steel. Etchant: aqua regia.

has been found in past studies of ZrB_2, B_4C, and BN in stainless steel, indicating analogous reaction mechanisms.

MARITIME SHIP REACTOR (MSR) PROJECT

W. C. Thurber J. T. Lamartine

The Metallurgy Division continued to provide technical assistance to the Maritime Reactors Branch of the Atomic Energy Commission. The scope of the assistance included design review as well as experimental work. The experiment program consisted in materials studies related to the immediate needs of the NS "Savannah" Project and the development of fuel elements for advanced cores for the NS "Savannah." Progress on the program is reported below.

Brazing Alloy Development

The main effort in this study consisted in determining the applicability of electroless nickel (Kanigen) process plate as the brazing material for the NS "Savannah" fuel bundles. Results of this study with this brazing substance, which is really a nickel-phosphorus alloy, are reported in the literature[8] and indicate that electroless nickel is generally suited for the proposed application. This alloy has been subsequently selected by Babcock and Wilcox Company for use in assembling Core-I fuel bundles for the NS "Savannah."

Brittle-Fracture Evaluation

Scrap material from the upper and lower closure heads of the NS "Savannah" pressure vessel was obtained from the Babcock and Wilcox Company to evaluate the tendency of the A212B steel toward brittle-fracture initiation. Testing involved measurement of the nil-ductility-transition (NDT) temperature by using both full-size and subsize drop-weight specimens and correlation of this temperature with impact energy of standard Charpy V-notch specimens at the same temperature. Results of this study are reported elsewhere.[9]

Pyrometer-Wire Studies

The feasibility of using small-diameter wires placed at strategic radial locations in UO_2 pellets for temperature monitoring during in-pile experiments was examined. Melting of the wires, as determined by post-irradiation metallography, was chosen as the criterion for temperature measurement. To select wires best suited for this application, the compatibility of Au, Cu, Ni, Fe, Pt, V, and Nb with UO_2 was examined. It was found that nickel, vanadium, and platinum reacted with UO_2 at temperatures well below the respective melting points of these metals. Gold,

---

[8] J. T. Lamartine and W. C. Thurber, Status Report – Application of Electroless Nickel Brazing to Tubular Fuel Elements for the N.S. Savannah, ORNL CF-59-6-55 (June 2, 1959).

[9] W. C. Thurber and J. T. Lamartine, Determination of the Nil-Ductility-Transition Temperature for A212B Steel Used in the N.S. Savannah Pressure Vessel, ORNL CF-59-7-143 (July 23, 1959).

copper, and iron reacted with UO_2 at temperatures slightly above their melting points. Niobium, on the other hand, was compatible with UO_2 to 1800°C, which was the highest temperature examined. On the basis of these studies, which are reported in detail elsewhere,[10] it appears that this technique is not particularly promising.

Swaging of UO_2 in Stainless Steel Capsules

A program for studying the influence of type of UO_2, swaging temperatures, total reduction, and UO_2 particle size on the maximum oxide density attainable by compaction in rotary swaging machines has been completed, and a status report describing the work to date has been submitted for publication.[11] In conjunction with this study, the nature and extent of swaged fuel-rod cladding defects were investigated. Results, although not yet complete, indicate that cracking of the cladding is not a problem in type 304 stainless steel rods cold swaged to reductions as high as 50 to 60%. At higher reductions, however, wall cracking may impose a serious limitation on swaged fuel rods. Hot swaging at temperatures of approximately 800°C also appears to aggravate the wall-cracking problem.

Several of the swageable grades of UO_2 produced commercially have been obtained and given a cursory evaluation. Densities achieved with three such oxides when swaged in type 304 stainless steel tubing (0.750-in. OD, 0.035-in. wall) to a reduction in area of 55% at room temperature and at 800°C are listed in Table 4.5.

A working design for swaging internally and externally cooled tubular fuel rods has been formulated and several capsules processed. One criterion of this design is that the fuel rods be fabricated, if possible, without the use of a mandrel for controlling the concentricity and size of the inner tube. It has been observed in capsules fabricated without a mandrel that the swaging-reduction schedule, as well as total reduction, has a marked

---

[10] R. E. Meadows and W. C. Thurber, Feasibility Study – Use of Small Diameter Wires in UO_2 Pellets for In-Pile Temperature Monitoring, ORNL CF-59-10-7 (in press).

[11] J. T. Lamartine and W. C. Thurber, Development of Swaged Stainless Steel Fuel Rods Containing UO_2, ORNL CF-59-10-8 (in press).

influence on the concentricity. From the sections of three initially identical capsules swaged through different reduction schedules, shown in Fig. 4.2, it can be seen that greater increments of reduction per pass produce more inner tube distortion. Uranium dioxide densities attained in the tubular capsules are slightly less than those achieved in solid, swaged rods.

Table 4.5. Densities Obtained From Various Commercial Swageable Oxides

Identification Code	Type	Surface Area (m^2/g)	O/U Ratio	Tapped Bulk Density (g/cm^3)	Swaged Density (% Theoretical Density at 55% Reduction in Area)	
					Room Temperature	800°C
A	High fired	0.067	2.0119	5.89	85.9	90.7
B	Fused and ground	0.05	2.0264	6.45	89.6	93.2
C	High fired	0.02	2.0405	5.0	88.3	86.6

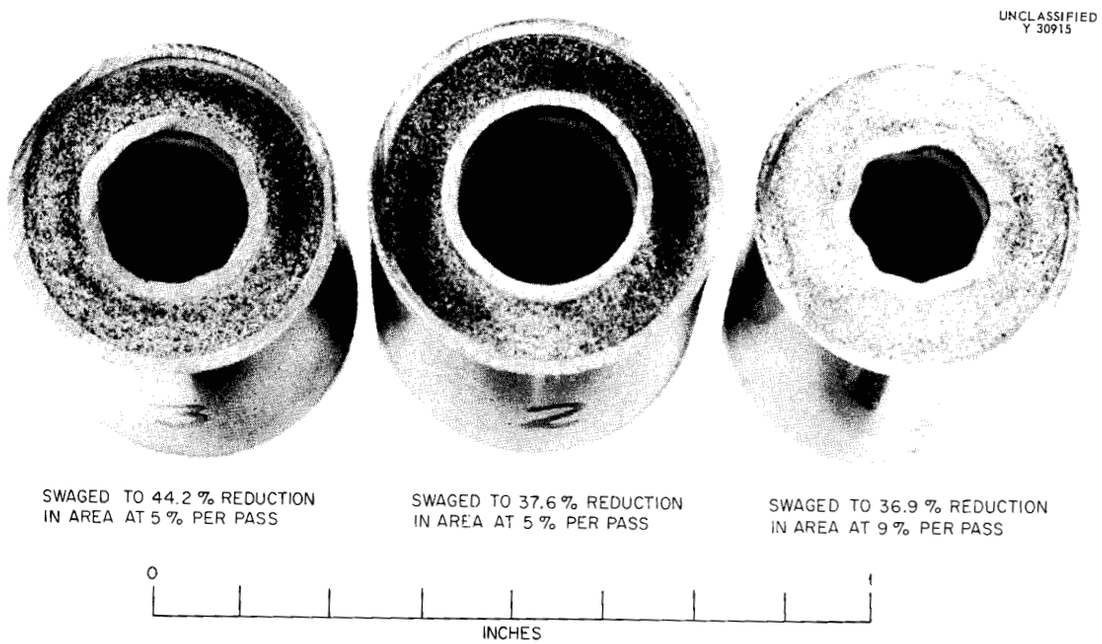

Fig. 4.2. Cross Sections of Swaged Tubular Fuel Capsules.

Metal Bonding of Stainless Steel-Clad UO_2 Fuel Rods

During the past year, a program was initiated to investigate the possibility of using a low-melting metal as the thermal bond between the fuel-and-sheath in stainless-steel-clad UO_2-pellet rods. The purpose of the metal bond is to reduce the large temperature drop associated with an inert-gas-filled annulus to more reasonable levels. Conventionally, the gap between fuel and cladding is initially filled with helium, but as burnup proceeds and fission-product gases, xenon and krypton, are released to the gap, the conductivity of the gas space is seriously degraded. With a metal-filled annulus it should be possible to reduce the temperature drop across the gap to a few degrees. Emphasis in this study has been placed on the use of lead because of its low absorption cross section and reasonable melting point.

Studies of the compatibility between UO_2 and type 304 stainless steel in contact with Pb, 0.7 Li–Pb, Bi, and 55 Bi–Pb at 650 and 750°F have shown no reaction between these materials after 500 hr. It should be noted that these test temperatures are somewhat above the anticipated reactor operating temperatures. Corrosion tests of lead and lead-type 304 stainless steel couples for 1300 hr in 525°F pressurized water have indicated a corrosion rate for lead of 30–65 mils/year. The lead, of course, would not be exposed to the primary coolant unless the integrity of the cladding was impaired.

Several stainless steel tubes (0.500-in. OD × 18-in. long) have been loaded with pellets and the clad-pellet annulus filled with lead. Subsequent ultrasonic inspection for continuity of the lead bond showed an excellent correlation with radiography, and results indicated that inspection of lead-bonded fuel rods should pose no particular problem.

To simulate the effects of hot spots, with attendant localized melting, in lead-bonded fuel rods, 1-in. sections of the rods were cycled from 1 to 15 times between 400 and 800°F by using an encircling-coil induction heater. Voids formed in the annulus, although no evidence of lead penetration into the pellets was noted. This phenomenon is being investigated further.

Lead-filled stainless steel capsules, each having had a 50-mil hole drilled in it, have been autoclaved at 650, 670, and 700°F to determine whether lead drainage would occur from leaking fuel tubes. None occurred at 650°F, but drainage was virtually complete at 700°F.

Compartmented Fuel-Plate Development

Although cylindrical UO_2 fuel rods are extensively specified in existing and planned power reactors, this shape suffers from high central temperatures associated with the limited heat-transfer surface and the relatively large thicknesses employed in such fuel bodies. Flat plates, however, offer the use of thinner fuel bodies having extended heat-transfer surface area. Consequently, flat-plate elements permit operation at higher specific power without raising the central temperature, which occurs in rod designs. However, the flat-plate design is structurally inferior, and the plates must be compartmented to compensate for the effects of fission-gas-pressure buildup and waterlogging in defective elements. Because of the significant thermal advantages, a program has been undertaken to evaluate the technical feasibility of manufacturing UO_2-bearing, flat-plate fuel elements by using stainless steel as the canning material.

The compartmented fuel plate consists of four main components: the grid which contains the fuel bodies, a frame which provides structural support for the grid, the cover sheets which seal the plates, and the UO_2 fuel bodies. To date, two methods of constructing the grid have been investigated: (1) an interlocked strip, or egg-crate construction, and (2) a spot-welded, bent-strip approach. An exploded view of an interlocked-strip plate is shown in Fig. 4.3. Figure 4.4 is a grid built up from bent strips by spot welding. The method of forming the strips is illustrated in Fig. 4.5.

One of the major areas of compartmental-fuel-plate technology which requires intensive study is that of joining the cover sheets to the grid-frame assembly. Every joint between rib and cover must be leaktight as well as structurally adequate to withstand internal pressure buildup. All the plates produced in this program have been assembled by brazing type 304 stainless steel components with electroless nickel alloy. The braze

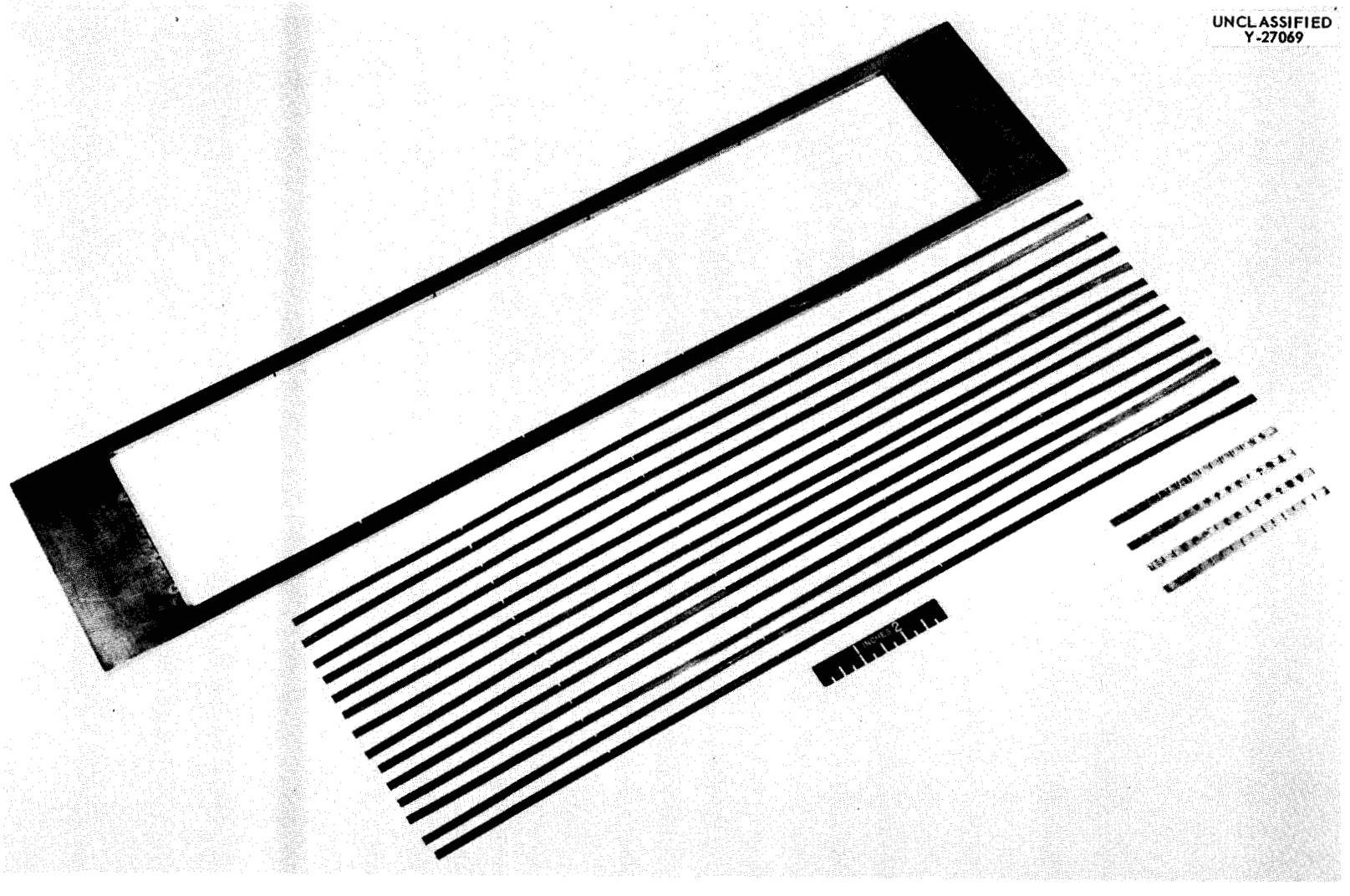

Fig. 4.3. Exploded View of Interlocked-Strip, Compartmented Fuel Plate.

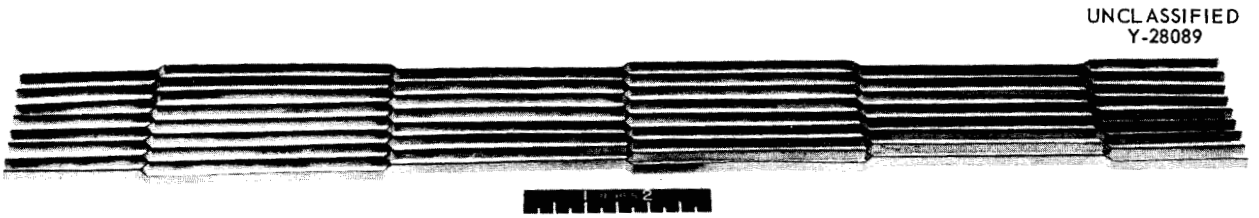

Fig. 4.4. Spot Welded, Bent-Strip Grid for Compartmented Fuel Plate.

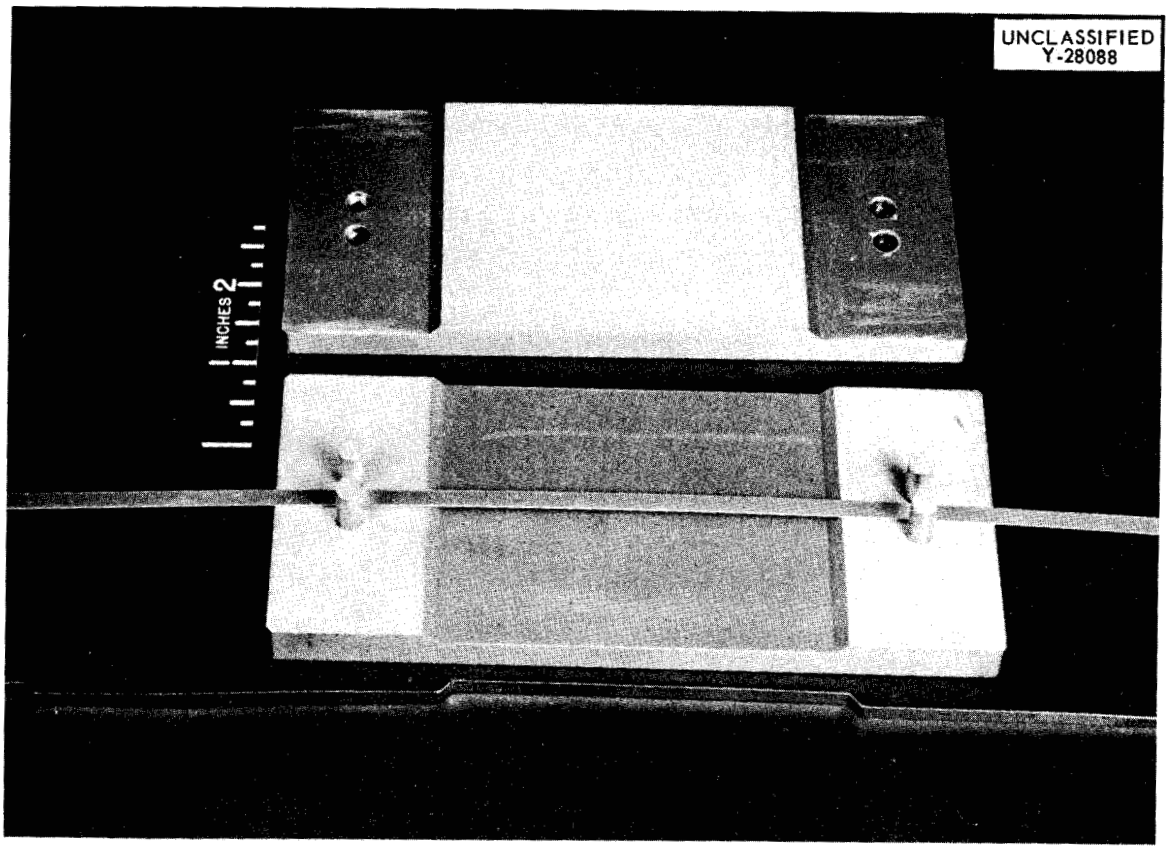

Fig. 4.5. Forming Die and Formed Strip Used in Manufacturing Bent-Strip Grid.

metal is preplaced on the grid, frame, and one side of the cover sheets by plating, prior to the brazing operation.

Resistance welding is an alternative method being investigated to join the various components of the flat-plate element together. This work has been contracted to Sciaky Brothers, Inc., where, at present, the feasibility of resistance welding 0.010-, 0.015-, and 0.020-in.-thick type 304 stainless steel cover sheets to 0.192-in.-thick type 304 stainless steel

plates is being determined. No results have been obtained from the program.

Five 4-in.-wide × 24-in.-long compartmented plates have been fabricated, one with an interlocking-rib grid and four with spot welded, bent-strip grids. Each plate was ultrasonically inspected for rib-to-cover-sheet bond integrity, leak checked for intercompartmental leakage, and finally sectioned and examined metallographically. Of the five plates, the one with the interlocking-strip grid was of the highest quality, with only 10 of its 75 compartments being interconnected. All the compartments in the four bent-strip plates were interconnected. The poor quality of these four plates has been attributed to misalignments in spot welding the grid. It is anticipated that this difficulty can be corrected by designing a suitable welding jig. An example of a good bond between the bent-strip ribs and cover plate is shown in Fig. 4.6.

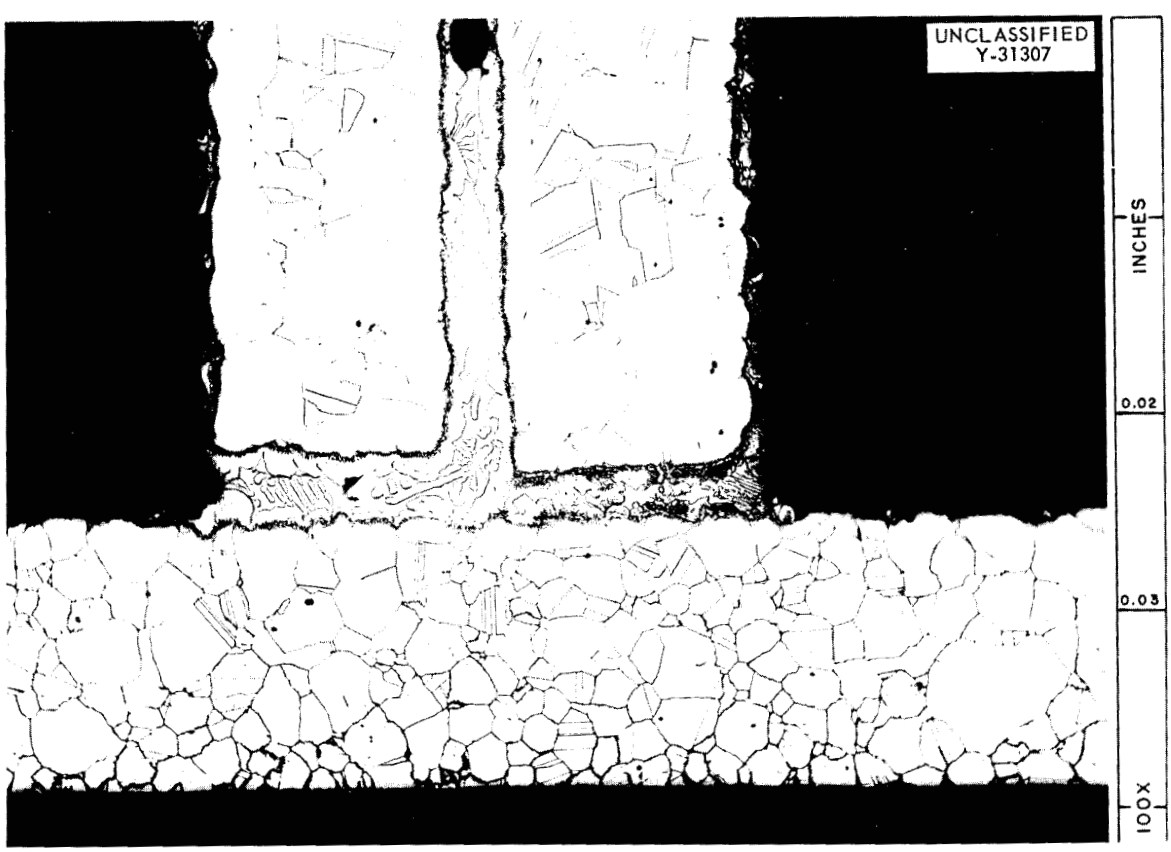

Fig. 4.6. Microstructure of a High-Quality Bond Between Bent-Strip Rib and Cover Plate Obtained by Brazing with Electroless Nickel. Etchant: 5% CrO_3, electrolytic (6 v, ~4 sec).

The ceramic fuel for these compartmented fuel plates is in the form of rectangular platelets, two being required per compartment. A limited amount of work has been done by the Ceramics Group to develop the manufacturing technology for producing them. Although only a few have been produced (Fig. 4.7), it appears that no extraordinary difficulties will be encountered in meeting the tentative specifications and dimensional tolerances.

FUEL ELEMENT DEVELOPMENT

C. F. Leitten

The primary aim of the fuel element development program is to advance reactor core technology and to reduce fuel-cycle cost. The scope of the effort during the past year has centered primarily on (1) improving the performance and service lifetime of aluminum-base-type fuel elements designed for application in low-temperature research reactors, and (2) investigating the potential of ferritic stainless steel for application in compact reactors which have high operating characteristics and low-cost

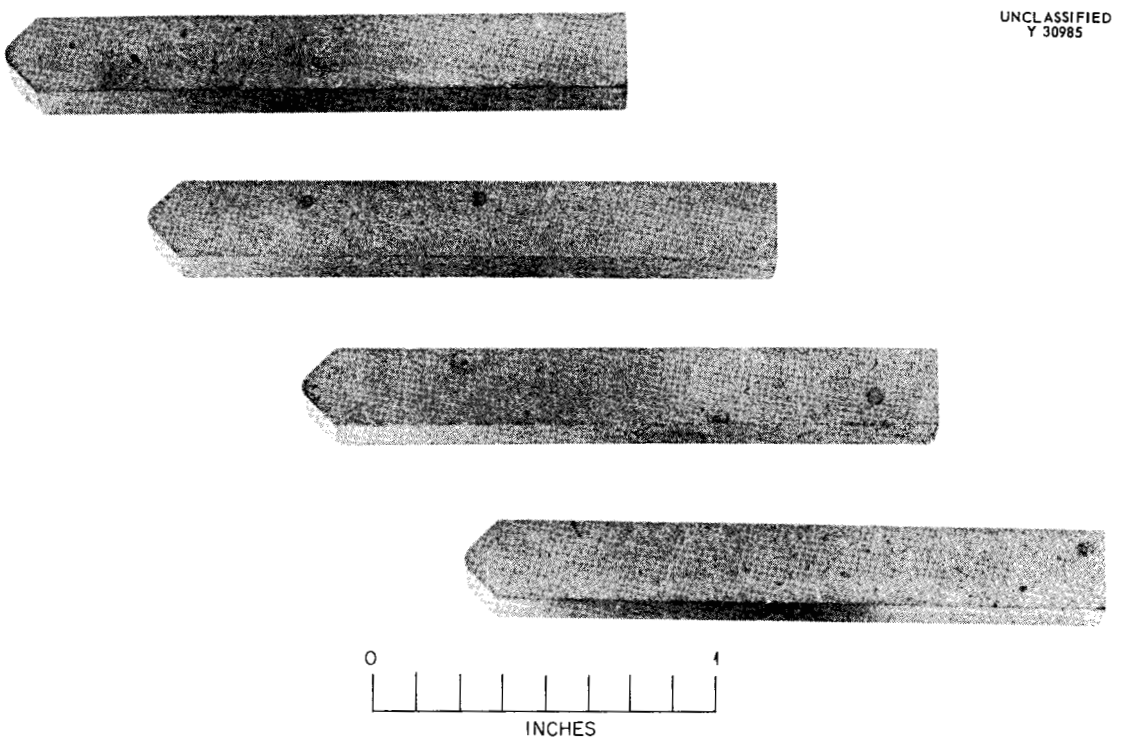

Fig. 4.7. Ceramic Fuel Bodies for Compartmented Fuel Plate.

performance. Progress in this general area of applied research is presented below.

Utilization of High-Strength Aluminum

D. T. Bourgette

As reported previously,[12] the substitution of an age-hardenable, high-strength aluminum for type 1100 aluminum increases the buckling resistance of the fuel element due to pressure differentials and decreases the susceptibility of the element to damage caused by mishandling during reactor operation. Recent work associated with this investigation has been directed toward the elimination of "flux annealing," which causes pitting on the surfaces of fuel elements and appears to have a deleterious effect on the corrosion-resistance of the material in pool-type reactors.

The substitution of vacuum-induction melting for the more conventional air melting of uranium-aluminum alloys has demonstrated that blister formation in the alloys, which has been attributed to occluded hydrogen during air melting, apparently can be eliminated. Thus, flux annealing becomes unnecessary. Table 4.6 lists the results of 208 composite plates fabricated at 600°C and heat treated at 610°C without prior flux annealing. Of the 128 plates clad with type 1100 aluminum, 10 showed blisters over the fuel portion of the plate. The balance was rejected because of misfit between the core and frame. The ten which were rejected because of blisters over the fuel region were examined extensively. There was no evidence that the blister formation was caused by evolution of hydrogen from the alloy. It is interesting to note that no blistering over the active portion was observed on plates clad with type 6951 aluminum; in fact, only 2.5% of the 80 plates prepared failed to pass all tests.

Results obtained from analyses of the segregation patterns in 1-1/2 × 4 × 10 in. vacuum-induction-melted castings of 14 wt % U–Al and 18 wt % U–Al alloys are graphically illustrated in Figs. 4.8 and 4.9, respectively. They closely conform with those reported previously for air-induction-melted alloys.[13]

---

[12] Met. Ann. Prog. Rep. Oct. 10, 1958, ORNL-2632, p 147 (classified).

[13] W. C. Thurber and R. J. Beaver, Segregation in Uranium-Aluminum Alloys and Its Effect on the Fuel Loading of Aluminum Based Fuel Elements, ORNL-2476 (Sept. 5, 1958).

Table 4.6. Data on Blister Formation in Alclad Fuel Plates Containing Vacuum-Induction-Melted U-Al Alloys. Composite Plates Heat Treated for 1 hr at 610°C with no Prior Flux Annealing

U Concentration in U-Al Alloy (wt %)	Clad and Frame Aluminum	Number of Plates Fabricated	Number of Plates Blistered	Location of Blisters
14	Type 1100	34	23	Core-frame interface
14	Type 1100	36	20	Core-frame interface, 8 Core-clad interface, 12
18	Type 1100	34	10	Core-frame interface
18	Type 1100	18	0	
14	Type 1100	6	0	
14	Alclad 6951	34	2	Core-frame interface
14	Alclad 6951	28	0	
18	Alclad 6951	18	0	

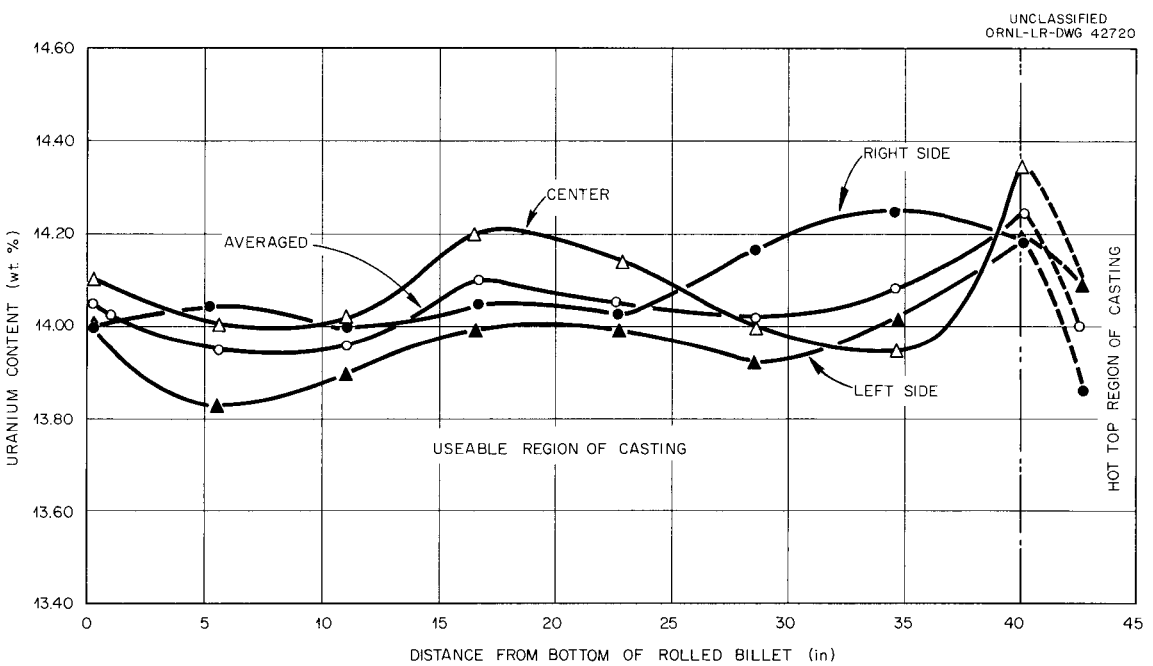

Fig. 4.8. Uranium Distribution in a Rolled Casting of Nominal 14 wt % U–Al Alloy Poured at 1150°C.

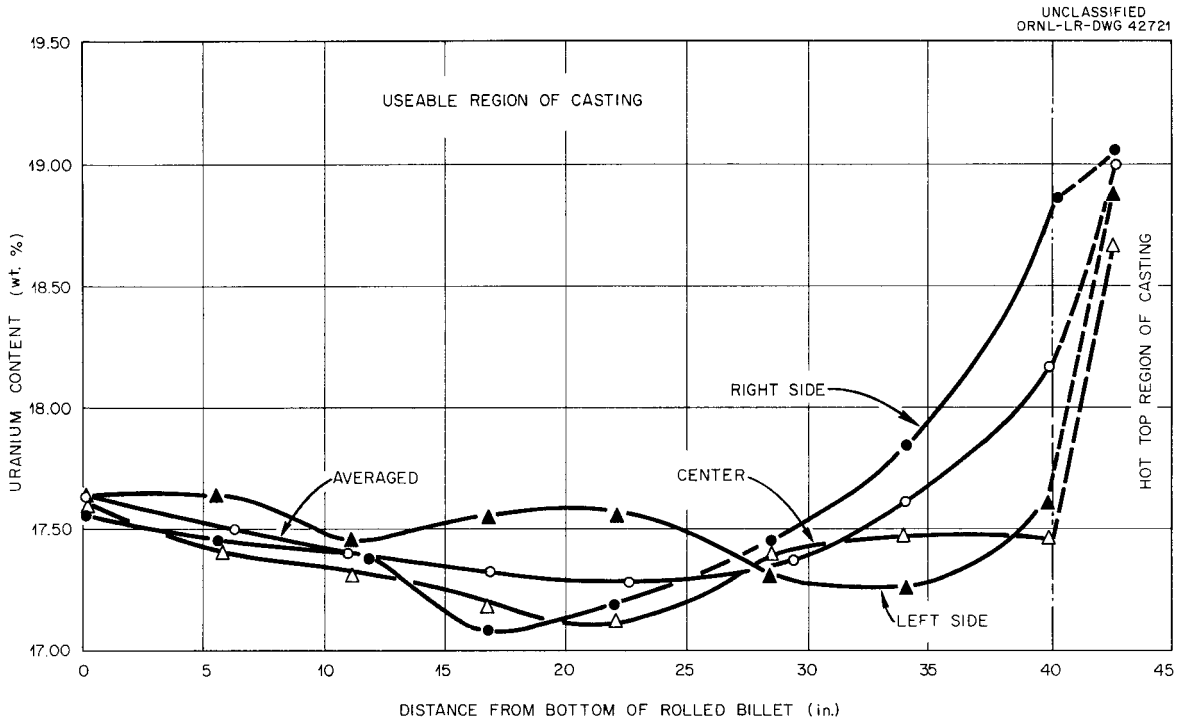

Fig. 4.9. Uranium Distribution in a Rolled Casting of Nominal 18 wt % U–Al Alloy Poured at 1150°C.

Type 6951 aluminum has been selected as the reference, age-hardenable aluminum for use in the makeup of future high-strength, plate-type elements for research reactor applications.

Uranium Contamination on Surfaces of Alclad Plates Containing Uranium-Aluminum Alloys

J. H. Erwin W. J. Kucera

The level of uranium contamination on the surfaces of Alclad ORR fuel plates has previously been reported to be 0.2 to 0.4 ppm (highly enriched in U^{235}).[14] At the same time, the amount of natural uranium in the aluminum stock was approximately 1 ppm; additional analyses have confirmed this latter value.

Although there is no reported solid solubility of uranium in aluminum, it is assumed that it does exist but is of such a low magnitude that it is difficult to detect with conventional equipment. Assuming that the solid

[14] Met. Ann. Prog. Rep. Oct. 10, 1958, ORNL-2632, p 147–48 (classified).

solubility is greater than 1.0 ppm, there exists the potential of diffusion of the uranium, which is in solution in the aluminum matrix of the uranium-aluminum alloy fuel core, into the type 1100 aluminum cladding. Preliminary data listed in Table 4.7 was obtained on the concentration of uranium in type 1100 aluminum cladding as a function of distances from the core-clad interface in composite plates containing both 14 and 18 wt % U–Al alloy

Table 4.7. Uranium Concentration in Aluminum Cladding of Composite Plates Containing 14 and 18% U-Al Alloys After the Indicated Treatment

Distance from Bond Interface (mils)	Uranium Concentration in Cladding (ppm)	
	14 wt % U–Al Alloy Plate	18 wt % U–Al Alloy Plate
	As Fabricated at 600°C	
18.5	0.15	
15.5	0.22	
13.5		0.39
12.5	0.13	
10.5		1.3
7.5		5.2
	After 3 hr Heat Treatment at 600°C	
18.5		
15.5	1.4	
13.5		8.3
12.5	2.9	
10.5		10.5
7.5		18.6
	After 6 hr Heat Treatment at 600°C	
18.5	6.1	
15.5	6.7	
13.5		31.8
12.5	17.0	
10.5		37.4
7.5		55.4

after 3 and 6 hr at 600°C. Although the results are somewhat scattered, there is a definite trend toward diffusion of uranium through the cladding. In the as-fabricated plate, at a distance of 13 to 16 mils from the core-clad interface, for example, the uranium concentration is approximately 0.3 ppm. However, after 3- and 6-hr heat treatments at 600°C, the uranium concentration was an order of magnitude greater.

The possibility of diffusion is vividly demonstrated in Fig. 4.10. In comparing an as-fabricated plate with a similar plate which was heat treated 14 days at 600°C, it is apparent that marked microstructural changes have occurred in the vicinity of the bonded interface. Although not yet identified, the precipitate at the grain boundaries is probably a complex compound containing uranium. Based on the data in Table 4.7 and the assumption that the solubility limit at 600°C is 30 ppm U, calculations indicated that a diffusion coefficient of 2×10^{-8} cm^2/sec best fits the data. It was then possible to relate the effect of diffusion of uranium on the contamination of plate surfaces as a function of cladding thickness and time at 600°C. This effect is graphically illustrated in Fig. 4.11.

Compatibility of Alclad Fuel Plates Containing UO_2 Dispersed in Aluminum

W. J. Kucera R. C. Waugh

One of the difficulties in incorporating UO_2 in aluminum and fabricating into Alclad plates for research reactors is the reaction of UO_2 with aluminum at the 600°C heat-treatments specified for manufacturing brazed fuel elements. Accompanying this reaction is warpage and growth of the fuel plate, which ultimately causes out-of-tolerance fuel elements.[15] An intensive study was made of three grades of UO_2, with the objective of understanding the mode of the reaction. Three grades of oxides were investigated: hydrothermal UO_2 reduced in hydrogen, hydrothermal UO_2 reduced in helium, and fused UO_2. The experiments and results have been reported in detail.[16] In general, all these oxides exhibited similar

[15]R. C. Waugh and J. E. Cunningham, The Application of Low-Enrichment Uranium Dioxide to Aluminum Plate-Type Fuel Elements, ORNL CF-56-8-128 (Aug. 20, 1956).

[16]R. C. Waugh, The Reaction and Growth of Uranium Dioxide-Aluminum Fuel Plates and Compacts, ORNL-2701 (Mar. 9, 1959).

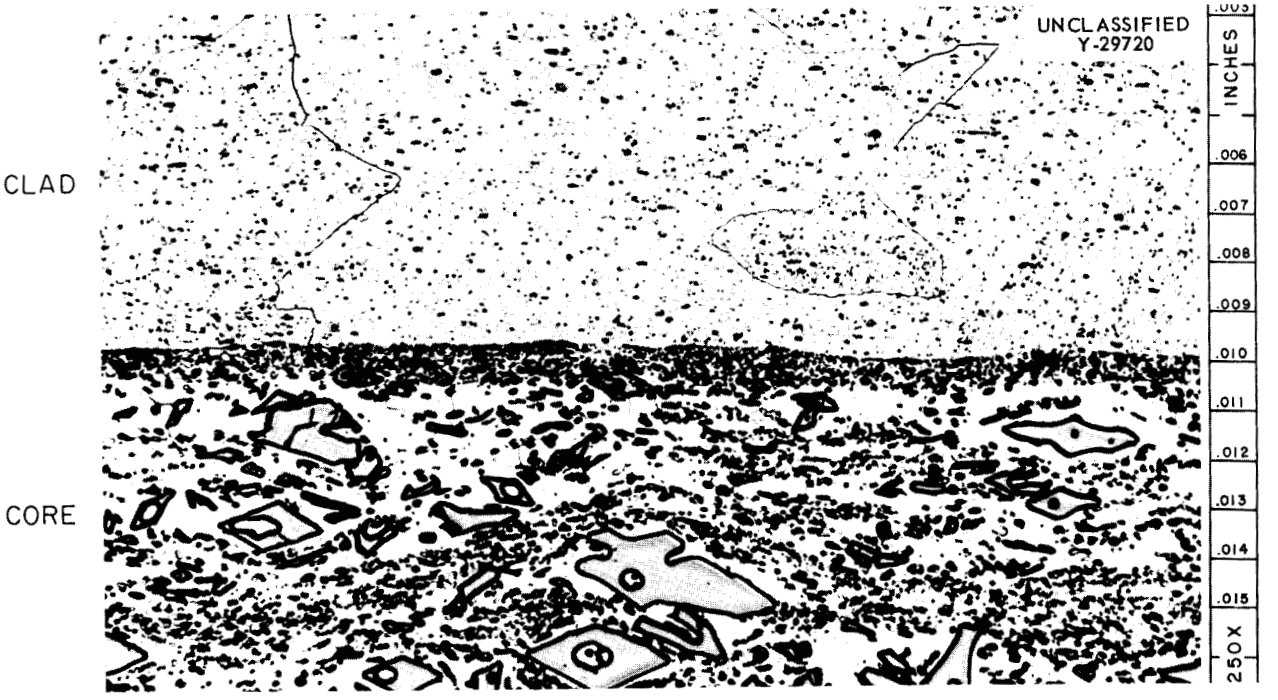

AS FABRICATED

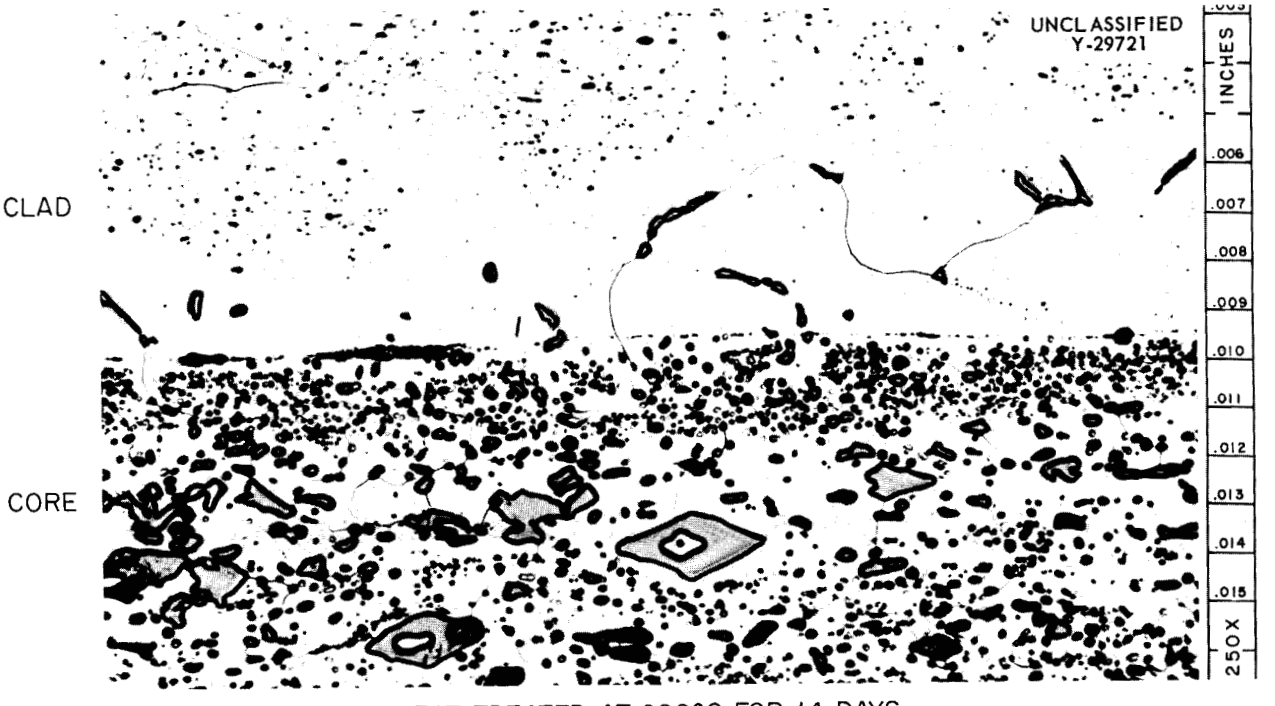

HEAT TREATED AT 600°C FOR 14 DAYS

Fig. 4.10. Comparison of Alclad Plates Containing 18 wt % U–Al Alloy After Fabrication at 600°C and After 14-Day Heat Treatment at 600°C.

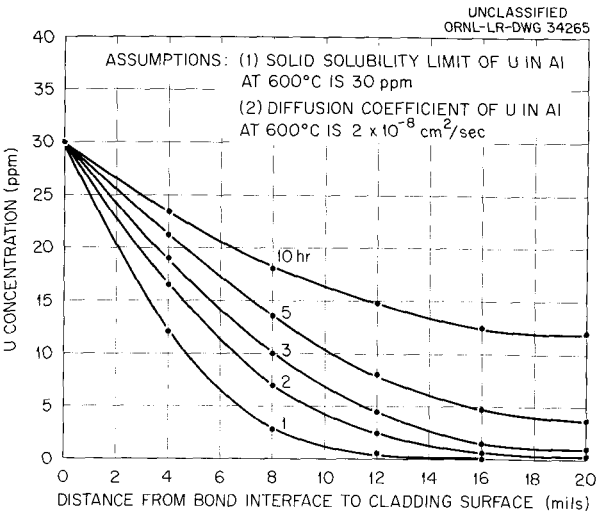

Fig. 4.11. Preliminary Analysis of the Effect of Diffusion of Uranium from the U-Al Alloy Core Through the Cladding of Aluminum Fuel Plates at 600°C.

reactions with aluminum at 600°C in a short period of time. As might be anticipated, temperature had an important effect and, at 500°C, long time periods were required for reaction to be observed. This report implied that gases, entrapped in this dispersion-type material, might be playing an important role.

A popular UO_2, Mallinckrodt high-fired UO_2 (with approximately 900 ppm titanium), was not included in the referenced report and has been investigated for comparison with the previously mentioned oxides. Miniature Alclad fuel plates containing 62 wt % of this UO_2 in aluminum were fabricated at 500°C and plate growths measured as a function of time at 500 and 600°C, respectively. One specimen was also heat treated for 24 hr at 550°C. The UO_2 was screened to -100 +325 mesh size prior to incorporation in the plate. As listed in Table 4.8, considerable growth was observed at 600°C after as little as 2 hr. On the other hand, no growth was observed after 48 hr at 500°C but was observed after 168 hr.

Table 4.8. Growth Studies in Alclad Plates Containing 62 Wt % Titanium-Stabilized UO_2 in Aluminum

Temperature (°C)	Time (hr)	Volume Increase (%)
500	16	0
500	24	0
500	48	0
500	168	2.08
550	24	13.24
600	1	0.91
600	2	4.08
600	4	7.40
600	24	30.25

Alclad Plates Containing Dispersions of U_3O_8 in Aluminum

W. J. Kucera

Reliable techniques have been developed for incorporating 20% enriched fuel in the form of U_3O_8 into plate-type fuel elements for research reactor applications. The present effort will culminate with the manufacture of two experimental loadings of U_3O_8-bearing elements for operation of the proposed reactor at the Puerto Rico Nuclear Center. Each element will contain approximately 1200 g of U_3O_8 having an isotopic enrichment of 20%. Mechanical means will be utilized rather than the conventional brazing process for joining the fuel plates into a flat-plate assembly. It is felt that this alteration in technique will improve the corrosion resistance in static-pool water and thereby extend the lifetime of the component.

The essential steps involved in the manufacture of Alclad plates containing U_3O_8 as the dispersoid are listed below:

1. Weighing of U_3O_8 and aluminum powder for each individual core.
2. Dry blending for 3 hr in an oblique blender.
3. Cold pressing at 31 tsi.

4. Sintering for 1 hr at 400°C in air.
5. Inserting into aluminum picture frame, and assembling of billet by welding cover plates to frame. Billet corners are left unwelded.
6. Hot rolling at 600°C to a total reduction in thickness of 92%.
7. Annealing for 1 hr at 500°C to determine presence of blisters.
8. Cold rolling to a reduction in thickness of 8%.
9. Fluoroscopically inspecting fuel core dimensions.
10. Shearing and machining to final size.

Aqueous Corrosion Tests of Aluminum-Base Fuels Containing High Concentrations of UAl_3, UC, and U_3O_8

W. J. Kucera

An aqueous corrosion study was conducted on the 48 wt % U–3 wt % Si–Al alloy, the 65 wt % U_3O_8–Al dispersion, and the 60 wt % UC_2–Al dispersion material. The samples consisted of segments (1/2 × 0.1 × 2 in.) sectioned from the fabricated fuel plate. Specimens were tested in the clad condition, with edges exposed and holes drilled through the specimen, and also in the completely unclad condition. Testing was conducted in high-purity aerated water. Table 4.9 gives the test conditions and the results of the corrosion tests.

The UC_2-Al corrosion tests were terminated after 120 hr due to catastrophic attack of the dispersion. Figure 4.12 shows the severe distortion and catastrophic attack experienced by an unclad sample of UC_2-Al after 48 hr in 60°C water. The U-Si-Al alloy and U_3O_8-Al dispersion tests were conducted for periods as long as 26 weeks. As shown in Fig. 4.13, the 48 wt % U–3 wt % Si–Al was susceptible to random blistering. It is postulated that the blistering may have been caused by attack on uranium carbide inclusions that may have been present in the alloy.

Figure 4.14 demonstrates the stability of a clad U_3O_8-Al sample tested for 26 weeks at 90°C. It is apparent that the material has satisfactory corrosion resistance.

Table 4.9. Aqueous Corrosion Tests on Aluminum-Base Fuel Materials

Type of Specimen (wt %)	Experimental Conditions			Remarks
	Condition	Time	Temperature (°C)	
60 UC_2-Al	Clad	48 hr	60	Cladding failed, peeled from core
	Unclad	120 hr	60	Specimen disintegrated
Silicon-modified 48 U-3 Si-Al	Clad	12 weeks	60	A few small blisters on exposed edges
	Unclad	26 weeks	60	Numerous blisters
65 U_3O_8-Al	Clad	26 weeks	90	Slight corrosion of U_3O_8, few pits in Al cladding
	Unclad	26 weeks	90	Minor attack at machining grooves

UNCLASSIFIED
Y 30811

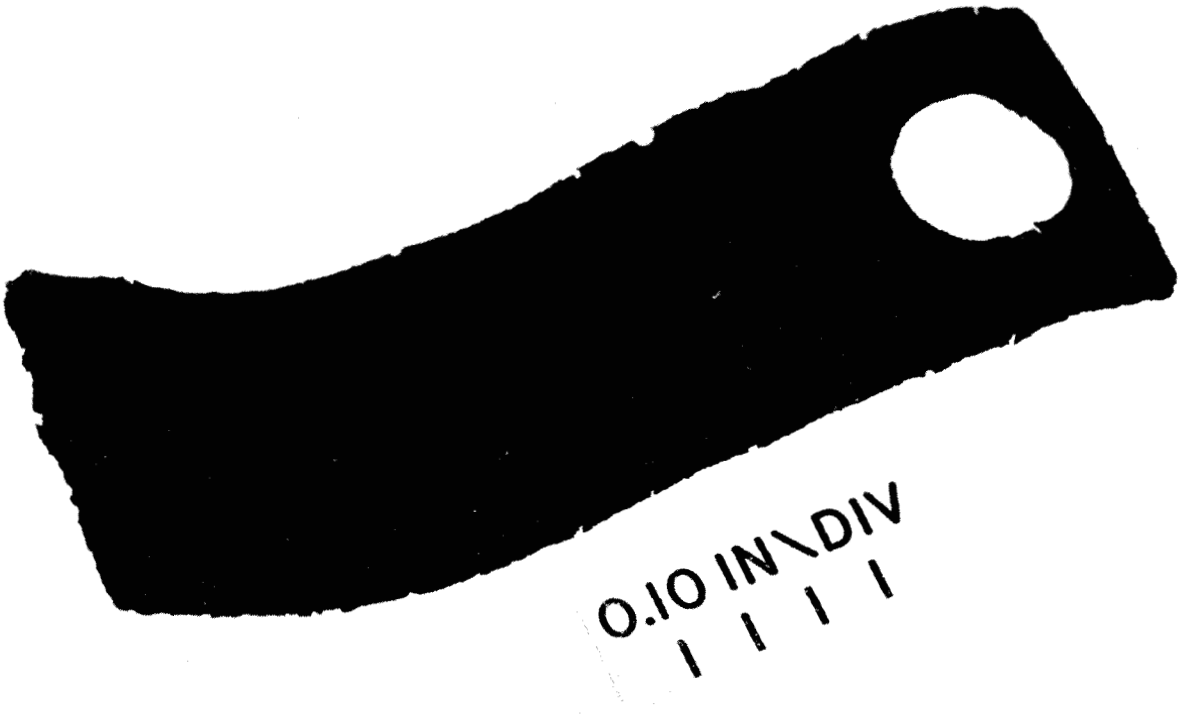

Fig. 4.12. Unclad 60 wt % UC_2–Al Specimen After Testing in High-Purity Water at 60°C for 48 hr.

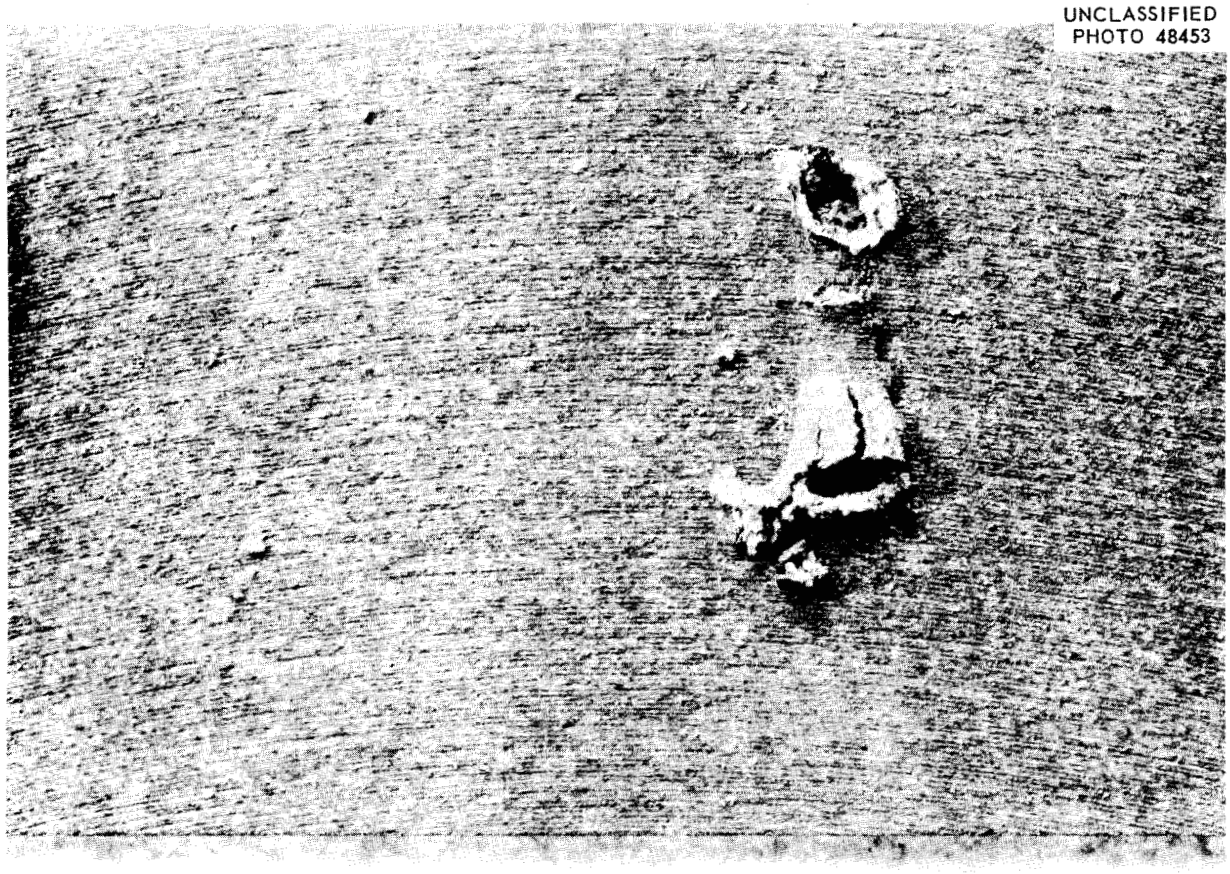

Fig. 4.13. Surface Appearance of an Unclad 48 wt % U–3 wt % Si–Balance Al Alloy Sample After Testing in High-Purity 60°C Water for 26 Weeks.

Ferritic Stainless Steel-Base Fuel Plates

J. H. Cherubini

A program was initiated to develop dispersions of UO_2 in ferritic stainless steel. Compared with austenitic stainless steel, the ferritic variety offers the following advantages: (1) higher thermal conductivity; (2) lower coefficient of thermal expansion; (3) lower thermal neutron cross section; and (4) low nickel concentration, thereby minimizing cobalt transmutation products.

Ferritic stainless steel, however, is more difficult to fabricate and weld, is easily sensitized, and has poor fatigue properties. Yet, it has sufficient promise as a structural material for fuel elements to warrant investigation.

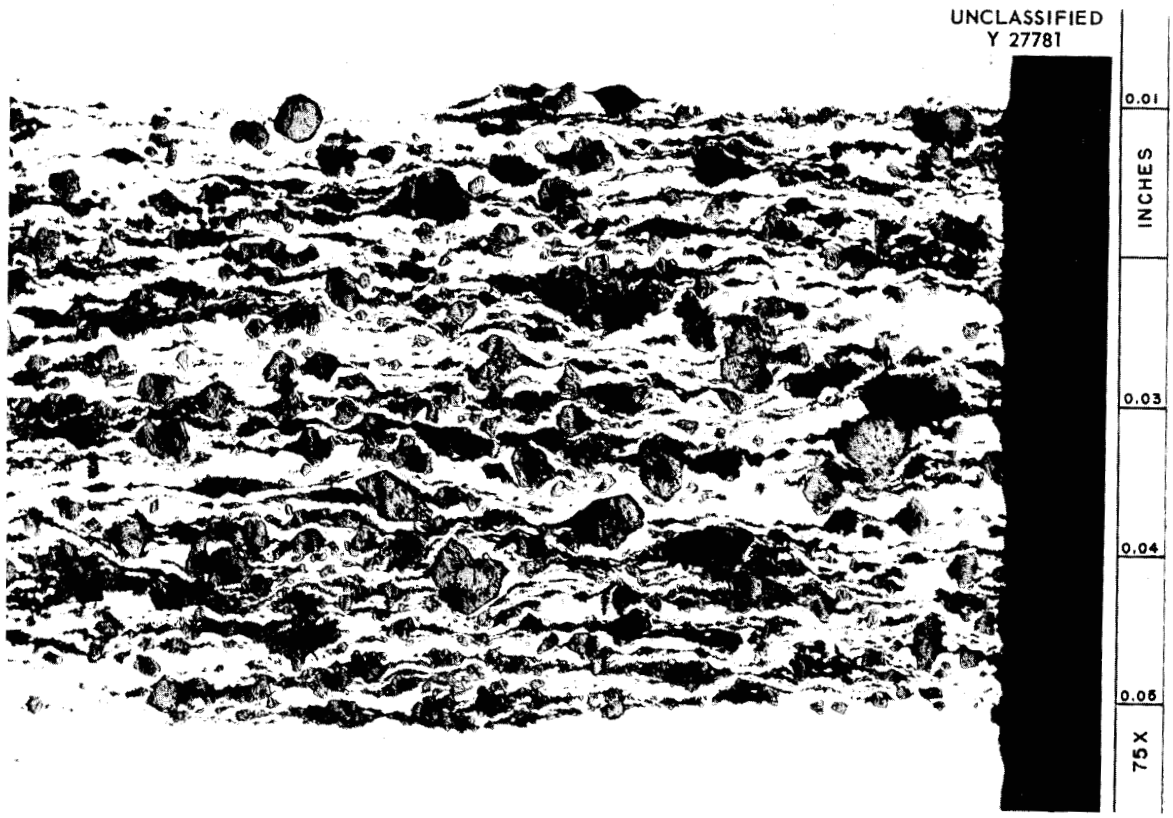

Fig. 4.14. Cross Section of 65 wt % U_3O_8–Al Dispersion Specimen After Testing in High-Purity Water at 90°C for 26 Weeks.

Type 430 stainless steel and the roll-cladding technique were selected as the reference material and fabrication method.[17] Plates were successfully prepared by using standard SM-1 procedures,[18] except that the final 20% hot reduction was executed at 700°C to refine the grain size.

A flatten-annealing temperature of 800°C was selected after annealing at 900°C proved deleterious because of apparent sensitization of the steel. A comparison between Figs. 4.15 and 4.16 illustrates the difference in grain growth and etchant attack of type 430 stainless steel after 1 hr of heat treatment at 800 and 900°C, respectively. To define this effect, hot-rolled material was heat treated 1 hr at 750, 800, 850, 900, and 950°C, air cooled, and Strauss tested. The specimens heat treated at

---

[17]J. H. Cherubini and C. F. Leitten, Selection of a Ferritic Type Stainless Steel as a Reactor Construction Material, ORNL CF-59-5-101 (June 16, 1959).

[18]J. E. Cunningham et al., Specifications and Fabrication Procedures for APPR-1 Core II Stationary Fuel Elements, ORNL-2649 (Jan. 29, 1959).

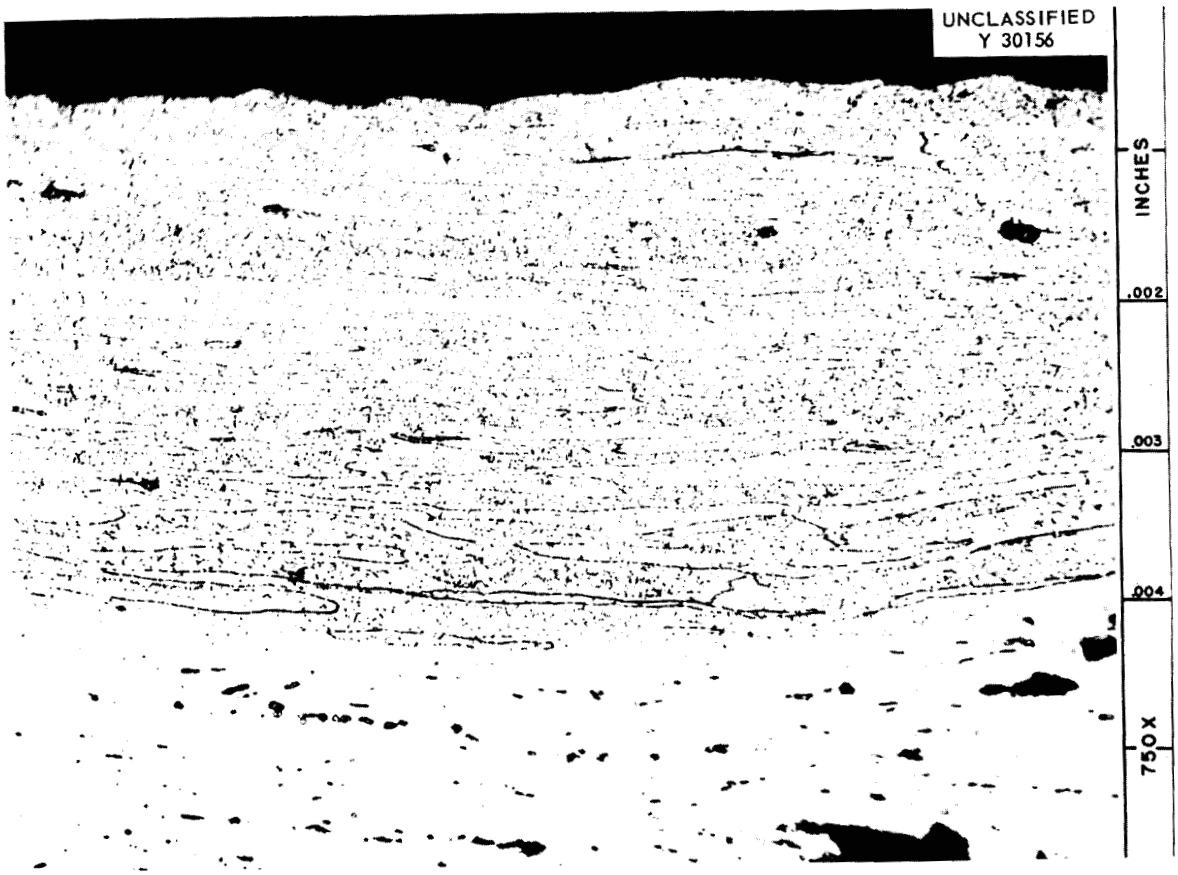

Fig. 4.15. Type 430 Stainless Steel, Cold Rolled and Annealed at 800°C for 1 hr. Etchant: oxalic acid. 750X.

750 and 800°C were microstructurally sound; those heat treated at 900 and 950°C had completely disintegrated. As shown in Fig. 4.17, the specimen heated at 850°C had partially disintegrated.

IRRADIATION TESTING

C. F. Leitten

Examination of Irradiated SM-1 Core I Fuel and Control-Rod Components

During March 1959, an on-site examination of the Core I component in the Army SM-1 reactor was conducted after the SM-1 had operated through approximately 10 of the designed 15 Mwyr of power. The examination revealed that swelling and clad failures had occurred in the iron-boron absorber sections. Scratches and possible cracks were also indicated

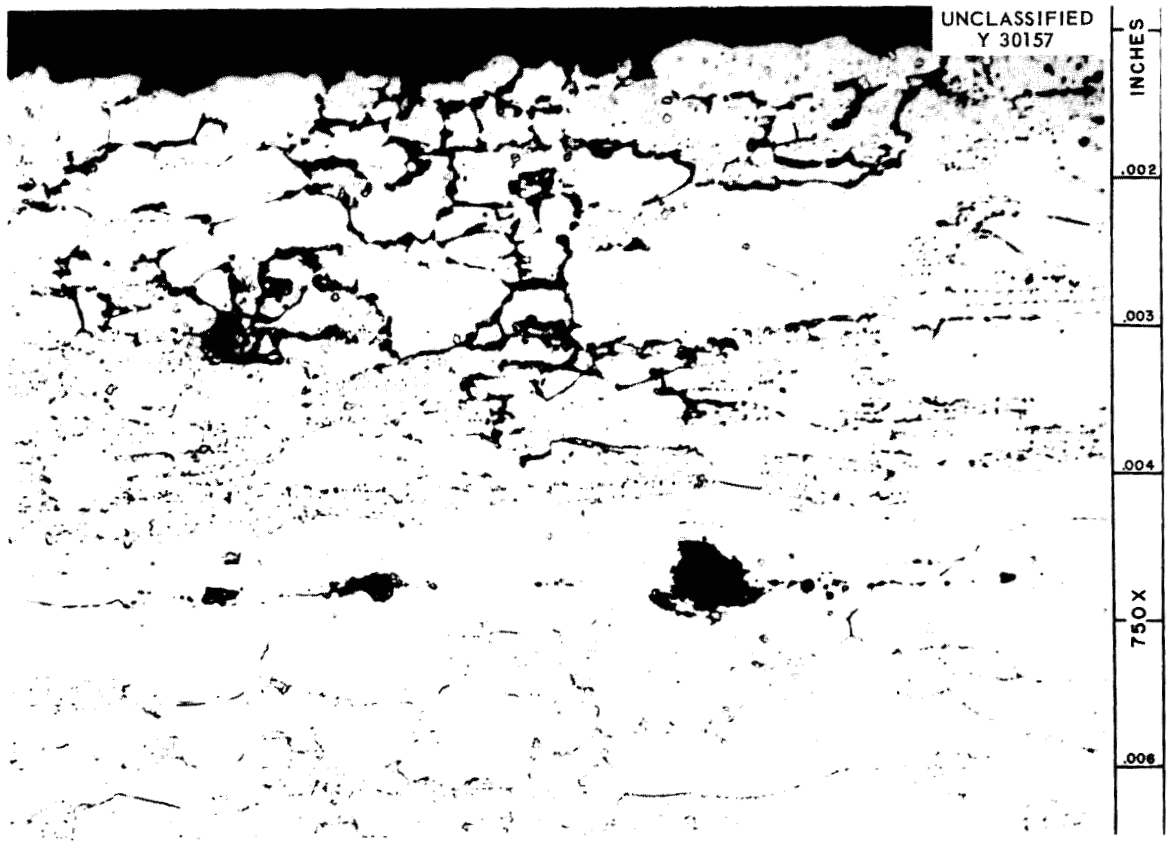

Fig. 4.16. Type 430 Stainless Steel, Cold Rolled and Annealed at 900°C for 1 hr. Notice the severe grain boundary attack by etchant, oxalic acid. 750X.

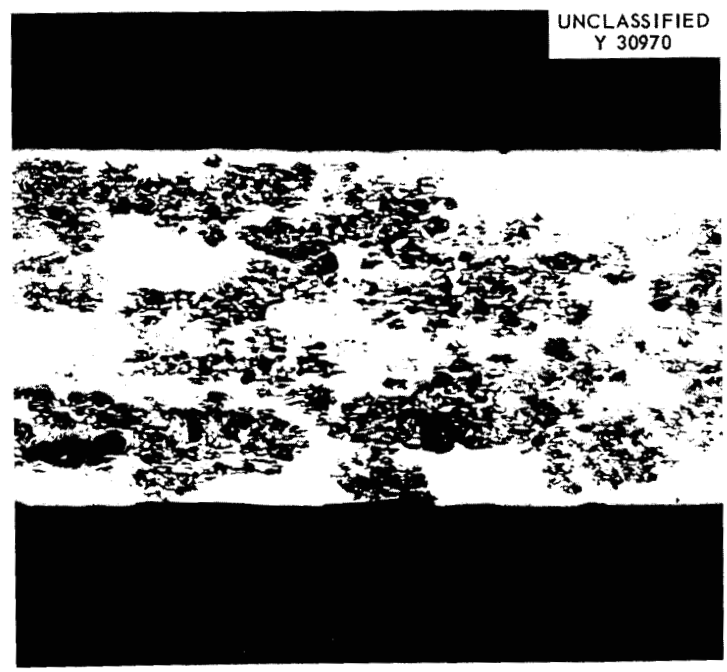

Fig. 4.17. Type 430 Stainless Steel, Annealed at 850°C for 1 hr, Water Quenched and Strauss Tested. Notice how attack had progressed from the edge and actually dissolved certain central areas. As-polished. 100X.

in the cladding of the fuel elements. Consequently, those fuel and absorber components with potential defects were returned to ORNL for hot-cell examination.

A visual hot-cell examination confirmed the failures observed in the iron-boron absorber sections; however, macroscopic examination of the surfaces of both the stationary and the movable control-rod fuel elements failed to reveal any definite evidence of defects in the fuel element cladding. These components will be inspected for dimensional stability and sectioned for additional studies of irradiation damage to the material.

Miniature Specimens of SM-1 Stainless Steel-Clad Absorber Plates Containing 3 wt % Enriched Boron Dispersed in Iron

Six of the 18 specimens forwarded to the MTR last year have completed their irradiation period.[19] Lithium analyses of two of these specimens revealed that the burnup, based on cobalt-wire monitoring, was low by a factor of approximately 3.5. All subsequent irradiation of this material was increased accordingly, with the objective of obtaining burnups ranging from 4 to 25% of the B^{10} atoms.

Miniature Alclad Plates Containing High Investments of 20% Enriched Uranium

Table 4.10 briefly outlines the present status of this program which was initiated last year.[20–22] The specimens which have completed irradiation testing in the beryllium reflector of the MTR have been returned to ORNL and visually examined. No gross warpage or blistering was noted on any of the irradiated specimens. These specimens will be examined for dimensional stability and possible microstructural changes.

---

[19] C. F. Leitten, Phase III Absorber Rod Sample Irradiation. Irradiation Request ORNL-MTR-28, ORNL CF-57-7-19 (July 5, 1957).

[20] C. F. Leitten and W. C. Thurber, Phase I – Foreign Reactor Fuel Sample Irradiation of a U-Si-Al Alloy. Irradiation Request ORNL-MTR-35, ORNL CF-58-2-109 (Oct. 13, 1958).

[21] C. F. Leitten and W. C. Thurber, Phase II – Foreign Reactor Fuel Sample Irradiation of UC_2-Al Dispersions. Irradiation Request ORNL-MTR-35, ORNL CF-58-10-20 (Oct. 17, 1958).

[22] C. F. Leitten and W. J. Kucera, Phase III – Foreign Reactor Fuel Sample Irradiation of U_3O_8-Al Dispersions. Irradiation Request ORNL-MTR-35, ORNL CF-58-10-30 (Oct. 18, 1958).

Table 4.10. Irradiation Status of Miniature Alclad Plates Containing High Investments of 20% Enriched Uranium

Capsule No.	Core Composition (wt %)	Desired Exposure $\times 10^{20}$ nvt	Irradiation Exposure $\times 10^{20}$ nvt	Desired Approximate Burnup (at. % U^{235})	Comment
ORNL-35-1	48 U–3 Si–bal Al	4.9	4.0	20	Sample returned to ORNL
ORNL-35-2	48 U–3 Si–bal Al	4.9	4.31	20	Sample returned to ORNL
ORNL-35-3	48 U–3 Si–bal Al	11.2	11.83	40	Sample returned to ORNL
ORNL-35-4	48 U–3 Si–bal Al	11.2	11.59	40	Sample returned to ORNL
ORNL-35-5	48 U–3 Si–bal Al	20.1	11.5	60	Sample under irradiation
ORNL-35-6	48 U–3 Si–bal Al	20.1	16.3	60	Sample under irradiation
ORNL-35-7	48 U–3 Si–bal Al	35.3	13.7	80	Sample under irradiation
ORNL-35-8	48 U–3 Si–bal Al	35.3	14.0	80	Sample under irradiation
ORNL-35-11	60 UC_2–Al	11.2	12.2	40	Sample completed irradiation
ORNL-35-12	60 UC_2–Al	11.2	12.7	40	Sample completed irradiation
ORNL-35-14	60 UC_2–Al	10.2	9.8	35	Sample completed irradiation
ORNL-35-15	60 UC_2–Al	20.1	21.3	60	Sample completed irradiation
ORNL-35-16	60 UC_2–Al	20.1	14.6	60	Sample under irradiation
ORNL-35-17	63 U_3O_8–Al	4.9	5.5	20	Sample completed irradiation
ORNL-35-18	63 U_3O_8–Al	4.9	5.0	20	Sample completed irradiation
ORNL-35-19	63 U_3O_8–Al	11.2	11.3	40	Sample completed irradiation
ORNL-35-20	63 U_3O_8–Al	11.2	11.6	40	Sample completed irradiation
ORNL-35-21	63 U_3O_8–Al	20.1	14.4	60	Sample under irradiation
ORNL-35-22	63 U_3O_8–Al	20.1	9.5	60	Sample under irradiation
ORNL-35-23	63 U_3O_8–Al	35.3	12.4	80	Sample under irradiation
ORNL-35-24	63 U_3O_8–Al	35.3	10.4	80	Sample under irradiation

Miniature Specimens of SM-1 Core II Absorber Plates Containing Various Percentages of Eu_2O_3 in Stainless Steel Clad with Stainless Steel

A series of miniature-sample irradiation experiments have been initiated to obtain radiation-damage information on Eu_2O_3 dispersions in type 304 stainless steel.[23] Such data are of interest, since this materials combination has been selected as the neutron absorber for Core II of SM-1.

Specimens containing 20, 30, and 40 wt % of Eu_2O_3 were dispersed in elemental type 304 stainless steel hermetically sealed within type 304L stainless steel by hot-roll bonding. The miniature plates will be irradiated in the beryllium reflector region of the MTR to total integrated fluxes corresponding to 1/2, 1, 2, and 3 core lives in the SM-1.

Full-Size, Plate-Type Elements Containing 20% Enriched U_3O_8-Al Dispersions

The irradiation testing of two 20%-enriched fuel elements, containing 37 vol % U_3O_8 dispersions in aluminum, roll clad with type 1100 aluminum, has been completed. The elements were irradiated in the active lattice of both the MTR[24] and the ORR to approximately 30 and 50% burnup of the U^{235} atoms, respectively.

A cursory examination of both of these irradiated fuel elements revealed no gross distortion of the elements or fuel-plate blistering. These elements will be inspected for dimensional stability and upon further sectioning in a hot cell, the individual fuel plates will be examined for possible dimensional and microstructural changes.

---

[23] C. F. Leitten, The Irradiation of Miniature, Eu_2O_3-Bearing Absorber Plates. Irradiation Request ORNL-MTR-39, ORNL CF-59-9-25 (Sept. 14, 1959).

[24] R. J. Beaver, Irradiation Experiment on Aluminum Fuel Element Containing U_3O_8 Dispersions, ORNL CF-56-12-116 (July 15, 1957).

BULK SHIELDING REACTOR (BSR) STAINLESS STEEL FUEL ELEMENTS

J. H. Erwin

Thirty-nine stainless steel plate-type fuel elements were fabricated for the Bulk Shielding Reactor (BSR). These elements will be used in experiments designed to obtain information on (1) high-energy gammas in pool-type reactors, (2) efficiency of a small stainless steel core for shielding studies, and (3) economics of stainless steel fuel elements for pool-type reactor application.

The fuel elements are similar in design to the SM-1 fuel components and consist of 20 plates containing 27 wt % of UO_2 dispersed in type 347 stainless steel, the blend being clad with type 347 stainless steel. Manufacturing procedures were generally based on specifications developed for fabricating fuel elements for Core II of SM-1 (ref 25).

The standard and the conrol-rod fuel units designed for operation in the BSR are illustrated in Fig. 4.18, with pertinent design information

[25] J. E. Cunningham et al., Specifications and Fabrication Procedures, for APPR-1 Core II Stationary Fuel Elements, ORNL-2649 (Jan. 29, 1959).

UNCLASSIFIED
Y 30768

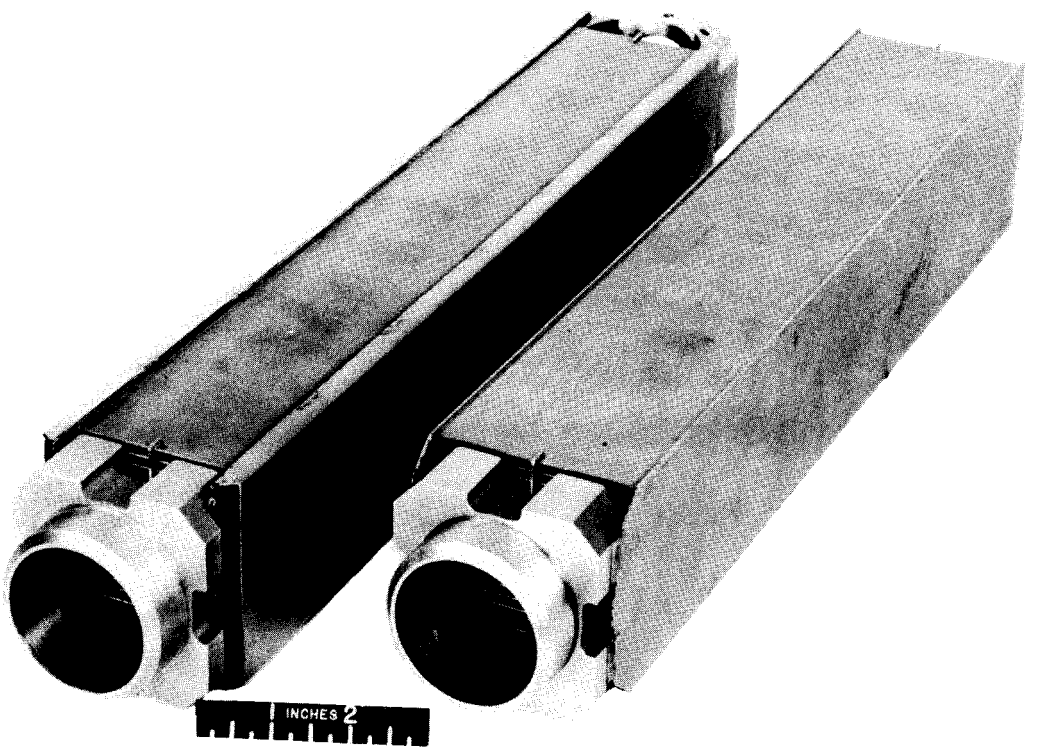

Fig. 4.18. BSR Stainless Steel Fuel Elements. Left, control-rod insertion unit; right, standard unit.

listed in Table 4.11. As shown, the control-rod unit has a channel section attached to the side plates through which the neutron-absorber plates are inserted. The neutron-absorber plate contains a mixture, 5 wt % boron dispersed in iron, which is prepared by powder metallurgy and clad by roll bonding with stainless steel.

One of the control-rod fuel elements was modified for application during testing of this stainless steel loading in the SPERT (Special Power Excursion Reactor Tests) facility. As shown in Fig. 4.19, channel sections are attached to the side plates as described previously, with the exception that the base of the channel is a composite fuel plate. Through these channel sections, a control plate is inserted which consists of a three-plate fuel element at one end and a neutron absorber at the other joined together as a unit. The neutron-absorber plate is simply a tube of rectangular cross section packed with 25 g of boron powder, highly enriched in B^{10}.

Rejections incurred at the various stages during manufacturing of the fuel components are listed in Table 4.12.

UNCLASSIFIED
Y 30767

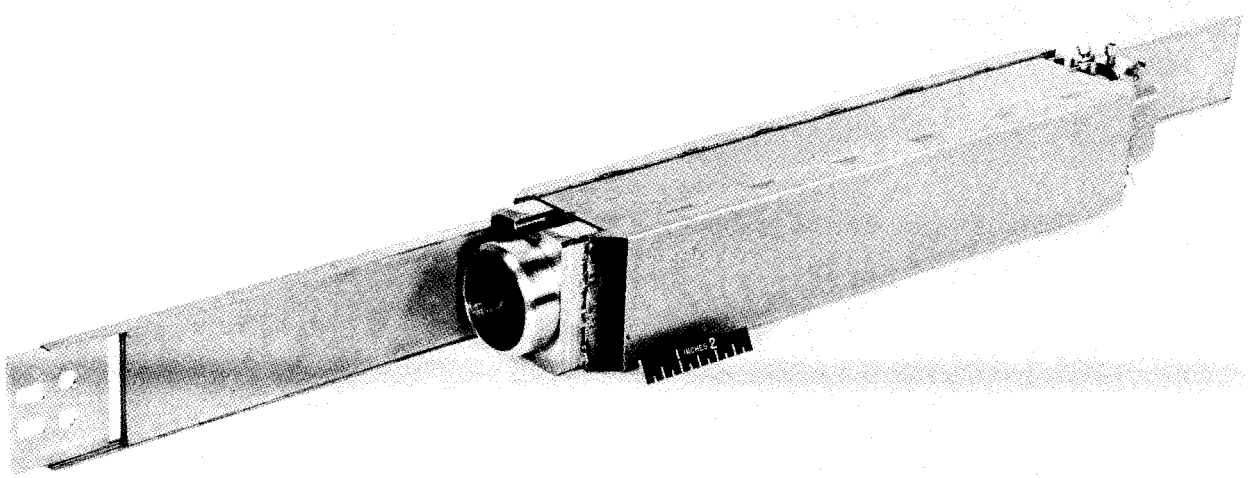

Fig. 4.19. BSR Test Element for SPERT Program.

Table 4.11. Pertinent Data on Stainless Steel Fuel and Neutron-Absorber Components for the Bulk Shielding Reactor

	Standard Fuel Element	Control-Rod Fuel Element	Neutron-Absorber Plate
Over-all size, in.	2.990 x 2.990 x 17-3/8	2.990 x 2.427 x 15-3/4	2.80 x 0.085 x 18
Number of fuel plates	20	20	
Material cladding	Wrought 347 stainless steel	Wrought 347 stainless steel	Wrought 347 stainless steel
Side plate	Wrought 347 stainless steel	Wrought 347 stainless steel	
Matrix	Powder 347 stainless steel	Powder 347 stainless steel	Elemental iron powder
Fuel or poison	UO_2 powder	UO_2 powder	Elemental boron powder
Brazing alloy	Coast Metals N.P.	Coast Metals N.P.	
Clad-core-clad thickness, mils	8-14-8	8-14-8	30-25-30
Core width and length, in.	2.56 x 15	2.00 x 15	2.5 x 14.87
Uranium-235 or boron-10 loading, g	290	224	4.66
Uranium-235 enrichment, %	93.7	93	
Boron-10 enrichment, %			90
Plate spacing, mils	122	122	
Metal-water ratio	0.26	0.26	

Table 4.12. Rejections Incurred During Manufacturing of Plate-Type BSR Stainless Steel Fuel Elements

Fuel Cores	
Number of compacts prepared	901
Number of compacts rejected	20
Percentage rejected	2.2
Composite Plates	
Number of plates fabricated	881
Number of plates rejected	31
Percentage rejected	3.5
Fuel Elements	
Number of fuel elements brazed	39
Number of fuel elements rejected	2
Percentage rejected	5.1

ADVANCED ENGINEERING AND DEVELOPMENT OF REACTOR MATERIALS

T. S. Lundy

R. E. Adams J. I. Federer R. C. Waugh

Fuel Irradiation Program

The ORR fuel irradiation program will investigate the effects of exposure temperature and fission burnup on thorium-base materials irradiated in temperature-controlled capsules. Initial test materials will be thorium alloys containing 0 to 10% fully enriched uranium. The specimens will be unclad pins, 1/8 in. in diameter and 1-1/2 in. long. The previously

planned systematic study on small plates of stainless steel–uranium dioxide[26] has been reduced in scope. Specimens of 25 vol % UO_2 dispersed in stainless steel will be irradiated at 1200°F to fission burnups of approximately 10, 20, and 30% of the U^{235}. These irradiations will be performed at the MTR (Materials Testing Reactor) in connection with the ORNL Fast Breeder Assistance Program.

The capsule to be used for the ORR irradiations is shown in Fig. 4.20. It provides double containment for the liquid metal and for any fission products that might be released from the specimens. The inner compartment contains specimens, thermocouples, and heaters immersed in sodium. Temperature control is achieved by maintaining a constant heat-generation rate in the capsule. The finned thermal barrier in the helium annulus provides the thermal conductivity required to obtain the desired temperature with the initial specimen fission-heating rate. Heaters will replace heat lost due to consumption of U^{235} and will compensate for normal flux variations. A mockup of the capsule was prepared in order to develop fabrication and inspection procedures.

Instruments for the capsule experiments have been designed, fabricated, and partially installed in the ORR. Chromel-Alumel thermocouples will be used in conjunction with a multipoint recorder to monitor and record specimen temperatures. One of the specimen thermocouples will control electrical power to the heaters. A liquid-detector device will be used in conjunction with an automatic withdrawal mechanism for removing the experiment from the reactor in the event that either water or sodium leaks into the helium-filled annulus.

A thin-walled aluminum access tube has been fabricated and installed in the reactor. The tube extends from the reactor pool through tank access flange V-8 to lattice position F-1. Installation and withdrawal of the experiment is made through this tube, which also serves as a conduit for thermocouple and heater wires from the experiment to a junction box just above the reactor pool.

A tubular capsule carrier about 2-1/2 in. in diameter and 23 in. long internally, with a minimum shielding of about 10 in. of lead, has been

---

[26] R. C. Waugh *et al.*, Met. Ann. Prog. Rep. Oct. 10, 1958, ORNL-2632, p 152 (classified).

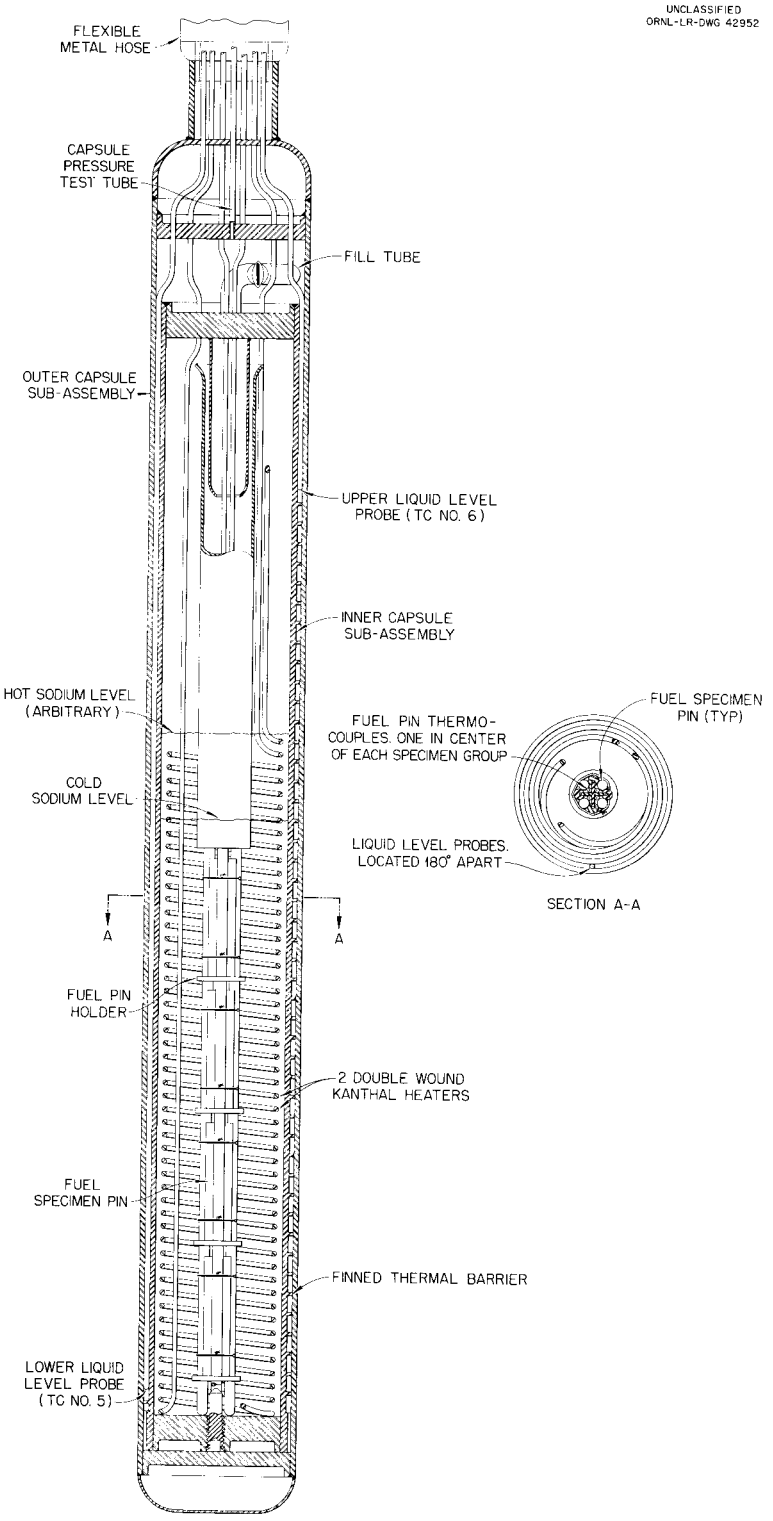

Fig. 4.20. Controlled-Temperature Fuel-Irradiation Capsule II Assembly.

designed and fabricated. The shielding will reduce the radiation intensity at the carrier surface to below the 200 mr/hr tolerance required for shipment of any experiment. The carrier was designed to be loaded under water and to facilitate the transfer of material between the carrier and the hot cells.

The equipment for a gamma-heating experiment has been fabricated and will soon be installed. Thin stainless steel disks, separated by a low-conductivity gas and brazed on their circumferences to the water-cooled capsule wall, have thermocouples placed along the radial dimensions. The gamma-heating rate will be calculated from the steady-state radial-temperature distribution of the disks and the thermal conductivity of the stainless steel.

Thorium and thorium alloyed with 1, 3, 6, and 10% depleted uranium have been prepared as arc-melted castings of about 1/2 in. diameter. The castings were swaged to the nominal specimen diameter of 1/8 in. Small sections of the swaged material were sealed under vacuum in quartz tubing and then heat treated for times of 0–5 hr at temperatures of 550–900°C. Hardness data and optical microscopy will be used to ascertain the treatments required to produce desired preirradiation microstructures — large grain sizes and uniform dispersion of secondary phases.

Intergranular Diffusion of Zirconium and Zircaloy-2 by Magnesium

J. I. Federer

Fuel elements clad with zirconium and Zircaloy-2 are difficult to chemically reprocess because the cladding materials are resistant to dissolution in many acids. It was previously reported that magnesium diffuses rapidly along the grain boundaries of these materials at 625°C, causing grain boundary embrittlement. About 2.5 hr are required to penetrate 0.03-in.-thick zirconium or Zircaloy-2, a nominal cladding thickness. Subsequent mechanical deformation was successful in removing the embrittled zirconium cladding from a uranium rod.[27]

---

[27]J. I. Federer, Met. Ann. Prog. Rep. Oct. 10, 1958, ORNL-2632, p 152–53 (classified).

Chemical dissolution tests were continued to determine whether magnesium penetration of zirconium and Zircaloy-2 would facilitate chemical reprocessing. Completely penetrated specimens, approximately 0.5 by 0.25 by 0.05 in., were exposed to the following acid solutions: 16 M HNO_3, 5 M HNO_3–2 M HCl, 6 M HCl, 4 M H_2SO_4, and 13 M HNO_3–0.04 M HF. All the solutions except the 13 M HNO_3–0.04 M HF intergranularly attacked magnesium-penetrated specimens, whereas control specimens of pure zirconium and Zircaloy-2 were attacked uniformly. The 13 M HNO_3–0.04 M HF solution uniformly attacked the penetrated and the control specimens. The rate of intergranular corrosion was much greater in 6 M HCl than in any of the other solutions, resulting in complete disintegration of penetrated zirconium and Zircaloy-2 specimens in about 50 and 120 hr, respectively. About 95% of the initial weight of the specimens was recovered in the form of small granular particles.

Thus, magnesium-penetrated zirconium and Zircaloy-2 can be disintegrated by intergranular corrosion in 6 M HF and by mechanical deformation. Both methods reduce the materials to small particles which may be more suited for permanent waste disposal than are bulky corrosive solutions resulting from conventional chemical reprocessing methods. (This work has been concluded, and a topical report is being prepared.)

CERAMIC MATERIALS

L. M. Doney

F. L. Carlsen, Jr.
S. D. Fulkerson
L. A. Harris
J. M. Kerr
R. A. Potter
C. E. Curtis
R. L. Hamner
M. P. Haydon
R. E. Meadows
A. J. Taylor

The major activities of the Ceramic Section during the past year have been in the role of direct support to the GCR (Gas-Cooled Reactor), MSR (Molten-Salt Reactor), and ANP (Aircraft Nuclear Propulsion) projects. For the most part, these activities have been concerned with the advancement of the technology of UO_2 and BeO for high-temperature applications

in power reactors. A small effort, however, was directed toward investigating the compatibility of various oxides in contact with selected metals at elevated temperatures and exploring the potential of ThO_2, Si-SiC, and bulk UC fuel bodies. Ceramic research consisted of x-ray structure analysis and phase equilibria studies on a variety of compounds as well as a preliminary investigation of the refractory properties of Sc_2O_3 and the oxides of the lanthanide elements. Accomplishments in each of these areas are summarized.

URANIUM DIOXIDE TECHNOLOGY STUDIES

Fabrication of GCR Fuel Bushings

A. J. Taylor

The primary task in the fuel program for the GCR is the investigation of the various factors which influence the irradiation behavior of the bulk UO_2 bodies. Numerous specimens were fabricated from a variety of powders and enrichments into several shapes and densities for in-pile testing. An attempt was made in the preparation of all test specimens to accurately allow for shrinkage during sintering so that the expensive operation of grinding to size could be eliminated. It was generally not possible to fabricate directly to the required dimensions because of powder variability and because only one die set was available for each of the various shapes required. Experience in the handling of powders having various sintering characteristics indicated that if the die were properly designed to match the characteristics of the powder, there would be no great difficulty in sintering pieces to within specified tolerances provided that the tolerances were not too tight. It has been demonstrated that the GCR reference fuel pellets, for example, can be consistently sintered to within ±0.3% of the diameter, while the miniature prototype fuel pellets can be maintained consistently within ±0.5% of the diameter.

In some instances, chemical analyses have indicated that the sintering methods employed in fabricating the UO_2 pellets have introduced impurities to the extent that the pellets do not meet purity specifications. Consequently, a study was initiated to determine the conditions under which the high impurity content of carbon and nitrogen is introduced into the

product. The objective of the study is to determine the necessary conditions to eliminate the impurity problem and to establish the nature of the equipment required. Samples of UO_2, sintered in various atmospheres in a graphite-susceptor induction-heated furnace, have been prepared and submitted for chemical analyses. The hope of being able to sinter in the same type of induction-heated furnace is related not only to the immediate need of a short-cycle furnace for the fabrication of the GCR test pellets, but is related as well to the original concept that a versatile, easily and economically built and maintained furnace is required for the continuous sintering of UO_2 and other refractory compounds.

The process for producing the type of UO_2 powder required for optimum fabrication behavior[28] has been refined to the point where reproducibility is generally quite good if the amount of material is large enough to allow the processing conditions to stabilize. The comparatively small quantity of enriched UO_2 powder being made available for fabrication into GCR test specimens has been the main reason for the variability of the finished product. While this process is ordinarily referred to as a continuous process, in reality it is not, because each lot of material must be carried completely through each step of the process before moving to the next step. However, the nature of the process and equipment is such that they may be coupled in series to minimize the handling problem. Refinements in the process are evolving rather slowly because it has been necessary to keep both the equipment and personnel doing work more akin to production than to development. Development work is lacking, not only to completely stabilize the parent process for handling the fluoride feed solution, but also to establish the conditions for a recycle process in which nitrate solutions will probably be used. Feed from the recycle should mesh with the parent process immediately after filtration of the ADU (ammonium diuranate) precipitate.

An interest has been expressed in the possibility of fabricating UO_2 shapes having a density of 97% of theoretical or better in large quantity. High-density UO_2 is of interest from the standpoints of greater uranium

---

[28] Met. Ann. Prog. Rep. Oct. 10, 1958, ORNL-2632 (classified).

density, improved fission-gas retention, and increased thermal conductivity. Laboratory techniques are available by which these high densities can be achieved, but they would increase fuel fabrication costs considerably if extended to a production basis. It is believed that higher density UO_2 can also be achieved by utilizing a process which is very close to current practice, provided that the necessary control over the powder-producing process can be maintained. This approach will require further investigation.

High-Temperature Compression Testing of UO_2

F. L. Carlsen, Jr.

Uranium dioxide bushings were compressed at 5000 psi at 1500°C for 1 hr, resulting in a permanent deformation of approximately 1% (ref 29).

Literature Survey on Thermal Conductivity

M. P. Haydon

A literature survey has reached proportions of about 800 references on thermal conductivity and related thermal properties. These represent reports from more than 75 sources. The thermal conductivity of UO_2 has been the prime object of search, but reports covering even remotely contributory factors to the measurement of this property of UO_2, as well as for other promising fuel element materials, have been collected. Cross references, an author file, and analyses of the assembled data and abstracts are planned in order to establish a useful information center for design engineers.

Figure 4.21 is a compilation of some of the reported thermal conductivities for UO_2, extrapolated linearly to theoretical densities. Variables affecting these measurements which are being studied at the various laboratories are the methods of fabrication of the UO_2, the stoichiometry, irradiation effects, and additives.

---

[29] GCR Quar. Prog. Rep. Sept. 30, 1959, ORNL-2835 (in press).

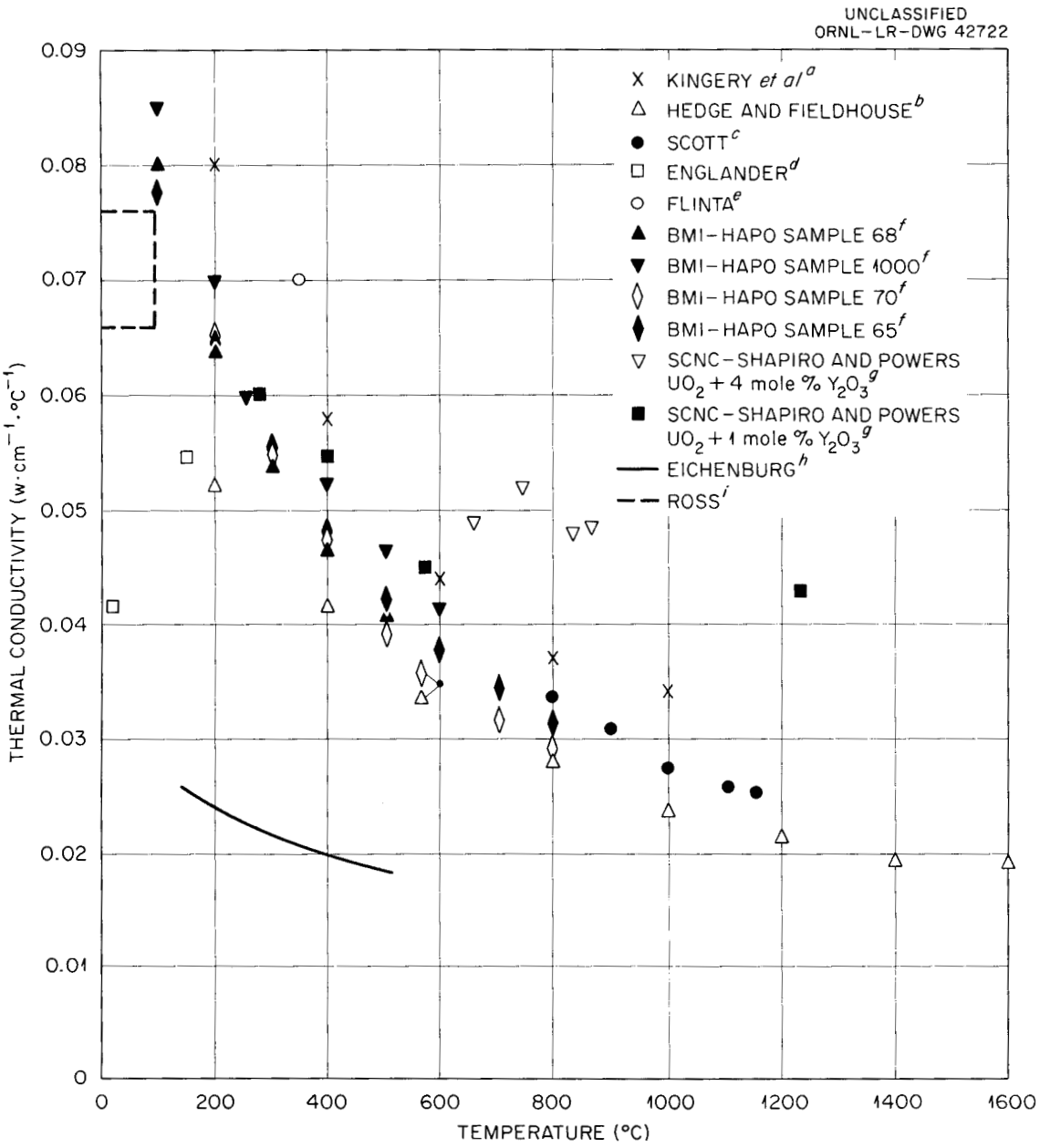

Fig. 4.21. Compilation of Reported Thermal Conductivities of UO_2, Extrapolated Linearly to Theoretical Density. The references are: (*a*) J. Am. Ceram. Soc. 37(2), 107–110 (1954). (*b*) AECU-3381; G022D3, Armour Research Foundation Report (Sept. 1956). (*c*) AERE M/R 2526 (1958). (*d*) CEA-79 (June 1951). (*e*) TID-7546, Book 2, p 516–525 (Mar. 1958). (*f*) BMI-1315, p 7–9 (Feb. 1959). (*g*) SCNC-296, p 28. (*h*) WAPD-200 (Sept. 1958). (*i*) CRFD-817, AEC of Canada, Ltd. (to be published).

Equipment for Thermal-Conductivity Measurement

S. D. Fulkerson

An apparatus for measuring thermal-conductivity coefficients as a function of temperature is now under construction. This apparatus is based on the radial-heat-flow method at steady-state conditions, originally developed by R. W. Powell.[30] Although this new apparatus is designed primarily for measuring UO_2 coefficients up to 1350°C, it should adapt itself quite well to a variety of other materials.

Fabrication of MSR Fuel Platelets

C. E. Curtis

Rectangular platelets of UO_2, approximately 2 in. long and 0.2 in. square, were successfully prepared for application in compartmented fuel plates which are of interest to the Maritime Ship Reactor Project. It was shown that it is possible to produce such platelets by usual methods of dry pressing and firing in an atmosphere of hydrogen-plus-nitrogen at 1750°C. However, very careful control of the raw materials of forming and firing will be necessary to hold the finished pieces to the tolerances specified (±0.001 in. to 0.003 in.). Otherwise, a final grinding operation will be necessary.

Extrusion of Uranium Dioxide

E. A. Fisher[31]

This work was performed according to Subcontract No. 1217 (between the Union Carbide Nuclear Company and The Electric Auto-Lite Company) under Prime Contract No. W-7405-eng-26.

Extrusion forming of ceramic products has been in common use for many years in the making of brick, sewer pipe, architectural tile, and porcelain specialty items. The materials contained from 30 to 100% clay — an important factor in promoting extrusion and for subsequent handling of the resultant product.

---

[30] R. W. Powell, Proc. Phys. Soc. (London) 51, 407 (1939).

[31] Electric Auto-Lite Company employee.

More recently, an extrusion-forming method has been used for the production of spark plug insulators from bodies containing 0 to 10% of clay. The problems encountered in extruding these oxide ceramics because of poor plasticity have been gradually overcome. High-speed equipment is daily turning out many miles of highly pure and uniformly dense tubular rod stock with excellent physical and electrical properties. Dimensional control of the finished product is extremely good.

Dry pressing is the standard method today for the fabrication of ceramic fuel bodies. The pellets are usually restricted to a length-to-diameter ratio of 1 or less because of frictional drag within the material as well as between the ceramic body and the die walls.

The principal aim of this work was to adapt previous experience in the extrusion of oxide ceramics to the development of the extrusion forming of UO_2. This was a scanning project to determine what additions were necessary to produce quality extrusions having high sintered density. It was shown that UO_2 can be extruded and sintered to high densities with no more difficulty than any other oxide. Extrusion properties of UO_2 were good when 1% CMC (carboxymethylcellulose) or Methocel were used, but were improved by using a mixture of 0.5% bentonite and 0.5% Methocel. Best results were obtained when the UO_2 was sintered in an inert atmosphere, argon being preferable.

If properly carried out, extrusion offers the following advantages when compared with conventional methods of dry-pressing and sintering of UO_2 powder:

1. Fuel rods or pellets of much greater length can be produced. Ultimately, a fuel rod could possibly be made in one piece.

2. Rods of very small diameter, not practical to form by pressing, can easily be extruded.

3. A high degree of uniformity is usually achieved. No density differential exists between the ends and the center of the rods.

4. Extrusion is readily adaptable to producing cored rods and the more complicated shapes.

5. The use of long rods should improve heat-transfer characteristics because of the elimination of the multiplicity of joints between pellets.

Compatibility of Graphite and UO_2

F. L. Carlsen, Jr.

The compatibility of UO_2 and graphite was studied, as previously reported.[32] The reduction of UO_2 by graphite has been observed at temperatures above and including 1300°C, under certain conditions. The approximate amount of reaction was determined by comparative-weight-loss and x-ray analytical methods. The reaction rate is a function of the UO_2 particle size, temperature, and gaseous environment.

Preparation of Hydrothermal Oxide Particles

T. S. Shevlin A. J. Taylor R. E. Meadows

A study is in progress covering the hydrothermal preparation of $UO_3 \cdot H_2O$ from $UO_4 \cdot 4H_2O$ in order to learn how to control the crystal size of the product. Controlling the grain size in UO_2 resulting from heating $UO_3 \cdot H_2O$ in H_2 is of consequence because dense grains of a rather large size are required in the preparation of dispersion-type fuel elements.

Direct observations in a capillary, plus PVT data from a 6-liter autoclave, are being used to follow the hydrothermal reactions which occur. To date the findings support the view that two types of competing reactions take place. This is not to say that there are but two reactions, but rather that there are at least two recognizable types.

One of these reactions is a complete dissolution of the $UO_4 \cdot 4H_2O$; this occurs on rapid heating. It has been directly observed in capillaries, and is also indicated by a change in autoclave pressure which shows the evolution of one mole of O_2 per mole of U in $UO_4 \cdot 4H_2O$. The evolution of this O_2 must mean that the U exists as UO_2^{++} ions in solution.

The other of these two reactions occurs on slow heating of the autoclave. Pressure-volume relationships in the autoclave indicate an oxygen release corresponding to 1/2 mole O_2 per mole of U in $UO_4 \cdot 4H_2O$. This indicates a decomposition of the $UO_4 \cdot 4H_2O$ to $UO_3 \cdot XH_2O$ and, in fact, this compound has been observed in the autoclave and identified as $UO_3 \cdot 1\text{-}1/2H_2O$. This $UO_3 \cdot 1\text{-}1/2H_2O$ is an intermediate between the $UO_4 \cdot 4H_2O$ starting material

---

[32] GCR Quar. Prog. Rep. Sept. 30, 1959, ORNL-2835 (in press).

and the $UO_3 \cdot H_2O$ final product. The intermediate compound from the reaction described must then be dissolved and finally precipitated from solution as $UO_3 \cdot H_2O$, which is wanted. This second reaction would have no further bearing on oxygen pressure in the autoclave except as it is affected by the rate of solution of $UO_3 \cdot 1\text{-}1/2H_2O$ or the rate of precipitation of $UO_3 \cdot H_2O$.

This recent knowledge of the effect of heating rate on the type of reaction opens the possibility of predicting and controlling the crystal-growth process and ultimately making an efficient process of it.

BERYLLIUM OXIDE TECHNOLOGY STUDIES

ANP Reactor Work

R. L. Hamner R. A. Potter

Development work being performed in support of the ANP Reactor Project has been reported elsewhere.[33]

Lithium-Release Experiments

R. A. Potter

Tests are being conducted to determine whether lithium from the $Be^9(n,\alpha)Li^6$ reaction will be released from BeO moderators at 1600°F in a CO_2 atmosphere. Beryllia powder containing approximately 0.05 wt % Li (carry-over from the ore) has been obtained and suitable pellets prepared. After being sintered at 1450°C, the lithium content was found, by spectroscopy, to be about 0.005 wt %.

Blocks of the oxide, approximately 4 × 4 × 1 in., are being fabricated. The reactivity worth of these pieces will be determined in a critical assembly. They will then be subjected to a 30-day heat treatment at 1600°F in CO_2, after which time they will be returned to the assembly and the reactivity again determined.

---

[33] ANP Semiann. Prog. Rep. Mar. 31, 1959, ORNL-2711, p 40–44 (classified); Oct. 31, 1959, ORNL-2840 (in press, classified).

Preparation of High-Density Beryllium Oxide Shot

M. P. Haydon

Experimental work in the GCR group indicates there may be a need to fill the central void in the fuel slug with a high-porosity material. Low-density BeO rods are being tested for this purpose. However, high core temperatures in the fuel slug present the possibility of the BeO rods undergoing additional sintering and shrinkage, thus leaving a gap in which powdery fragments from spalling UO_2 could accumulate. High-density BeO spheres which will not undergo further shrinkage have been suggested as a filler. An experiment is being designed in the Ceramics Laboratory to determine whether the BeO shot will work its way in between the slugs during thermal cycling and thus expand the column and whether UO_2 powder and chips will migrate downward through the shot. Five size fractions of BeO shot and a glass mockup of the EGCR fuel element have been prepared for this experiment.

CERAMICS RESEARCH

X-Ray Diffraction Studies

L. A. Harris

Although the diffraction equipment is heavily committed to service-type support work, some time was devoted to research during the past year. The research has been primarily directed toward structural analysis and phase equilibria relationship studies; results are summarized below.

<u>UO_2-Y_2O_3 System</u>. — Samples containing UO_2 and Y_2O_3 mixtures from zero up to and including 45 wt % Y_2O_3 were fired in an induction furnace at 1800°C, in a hydrogen atmosphere. Debye-Scherrer films were taken of all samples by using a 114.6-mm-dia camera and Cu Kα (1.5418 Å) radiation. Lattice parameters were calculated for the UO_2 phase in the above samples (Table 4.13). From the x-ray films, it was observed that a single-phase region of solid solubility of Y_2O_3 in UO_2 exists up to about 28 wt % Y_2O_3, and for higher percentages of Y_2O_3 there was a two-phase region consisting of a solid solution of Y_2O_3 in UO_2 and a solid solution of UO_2 in Y_2O_3.

Table 4.13. Lattice Parameters for the Solid Solution of Y_2O_3 in UO_2

Amount of Y_2O_3 (wt %)	Lattice Parameters* (Å)
0	5.4682
5	5.443
10	5.4188
22	5.3718
35	5.358
45	5.359

*The lattice parameter values are accurate to ±0.0005 Å and were calculated from Debye-Scherrer film data by the extrapolation method of Nelson and Riley.

Chemical analyses show that uranium is present as U(IV) and U(VI) ions, with the percentage of U(VI) ion increasing with Y_2O_3 additions.

$Ca_2Be_3O_5$ Compound. — A compound was observed to form at 60 mole % BeO in the CaO-BeO system. Optical examination of the above material which was quenched from 1475°C showed it to be an isotropic, single-phase material with an index of refraction n = 1.638 ± 0.003 (ref 34). The data obtained from a Cu Kα x-ray diffractometer pattern were indexed and tentatively found to best fit a face-centered-cubic unit cell whose lattice parameter is a_0 = 13.9 Å. The measured density is approximately 2.70 g/cm^3, as determined by the sink-and-float technique. Twenty-four molecules of $Ca_2Be_3O_5$ were calculated to fit this unit cell.

$LiYF_4$ Crystals. — Single crystals of $LiYF_4$ were obtained by mixing equal mole percentages of LiF and YF_3, firing to 650°C in vacuum, and allowing the material to cool slowly. The data from Weissenberg photographs (Cu Kα) were indexed and found to fit a tetragonal unit cell with lattice parameters a_0 = 5.26 ± 0.02 Å and c_0 = 10.94 ± 0.02 Å. The space group $I4_{1/a}$ was chosen on the basis of systematic extinctions observed in the single-crystal photographs. The compound $LiYF_4$ has a Scheelite type of

[34]Oral communication from T. N. McVay to L. A. Harris, July 7, 1959.

structure, with the Li^+ and Y^{+++} ions taking the places of the W^{6+} and Ca^{++} ions, respectively.

Rb_2ThF_6 Compound. — Data obtained from Cu Kα powder x-ray films of Rb_2ThF_6 were indexed and found to best fit a hexagonal unit cell whose lattice parameters are $a_0 = 6.847 \pm 0.002$ Å and $c_0 = 3.829 \pm 0.002$ Å. The calculated density is 5.56 g/cm^3, based on one molecule per unit cell and the space group $C\bar{6}2m$.

$Li_7U_6F_{31}$ Crystals. — Single crystals of $Li_7U_6F_{31}$ have been made available to the writer and H. Yakel, Jr., by the Reactor Chemistry Division for structure analysis. The data obtained from Cu Kα Debye-Scherrer films for $Li_7U_6F_{31}$ were indexed and found to best fit a tetragonal unit cell whose lattice parameters are $a_0 = 14.91 \pm 0.03$ Å and $c_0 = 6.50 \pm 0.03$ A. The space group $I4_{1/a}$ was chosen on the basis of systematic absences observed in single-crystal photographs. Future work is being planned to determine the structure of this phase in detail.

High-Temperature X-Ray Work. — An attempt was made to follow the $UO_2 \rightarrow U_3O_7 \rightarrow U_3O_8 \rightarrow UO_2$ transformation by high-temperature x-ray diffraction methods. A breakdown of the equipment has precluded the obtaintaining of any positive results; however, the $UO_2 \rightarrow U_3O_7$ transition was observed, but the temperature at which this took place could not be recorded.

Crystal Physics Program. — A double-crystal x-ray spectrometer attachment has been secured for work in cooperation with the Crystal Physics Group. This instrument has been set up in working order on a Norelco high-angle x-ray diffractometer. Single-crystal specimens of silicon have been chosen for initial examination in order to familiarize the users with the methods of obtaining "rocking curve" data. This method will be used to determine the perfection of single crystals grown by the Crystal Physics Group.

Refractory-Property Studies

C. E. Curtis

Lanthanide Oxides. — The oxides of 13 of the 14 rare-earth elements were successfully made into ceramic bodies (Pm_2O_3 was omitted).

Most refractory of the series, as shown by their sintered densities, were CeO_2, the first in the series, and Gd_2O_3, Tb_2O_3, Dy_2O_3, Ho_2O_3, and Er_2O_3, near the center; these were not completely sintered at 1600°C. On the other hand, theoretical density was approached at 1600°C by Pr_2O_3, Nd_2O_3, Sm_2O_3, Eu_2O_3 (near the first of the series), and by the last three oxides, Tb_4O_7, Yb_2O_3, and Lu_2O_3.

Complete stability toward air and boiling water was shown by sintered CeO_2 and by the last eight oxides of the series, including Gd_2O_3. Instability in air and in boiling water was exhibited by Nd_2O_3 and Pr_2O_3, while Sm_2O_3 and Eu_2O_3 were unstable in boiling water.

An effect due to firing in a hydrogen atmosphere was detected in the case of Lu_2O_3 only; it did not sinter well at 1600°C in hydrogen but was well sintered at this temperature in an oxygen atmosphere.

A report embodying these data is ready for publication in the Journal of the American Ceramic Society.

Scandium Oxide. — Preliminary tests have been made with 99.9% pure Sc_2O_3 in the form of dry-pressed cylinders, 1/4 in. in diameter and 1/4 in. high; these were fired in oxygen. The results indicate that temperatures of 1650 to 1700°C are necessary for complete sintering to 0% porosity. Scandium oxide is therefore in a class with Al_2O_3 as a refractory.

The sintering process in Sc_2O_3 in a hydrogen atmosphere is apparently more difficult than in oxygen at 1650—1700°C, since the cylinders fired in hydrogen still contained 3 vol % pores at 1700°C.

ThO_2-UO_2-Al_2O_3 Systems

C. E. Curtis

A study has been initiated to determine the various phases encountered in ThO_2-UO_2-Al_2O_3 systems. The first studies will be confined to the ThO_2 corner of the triaxial diagram (to approximately 8% UO_2 and 15% Al_2O_3). The results of heating various combinations at temperatures up to the melting point will be determined by x-ray, petrographic microscopy, and other techniques. It is proposed to determine melting points by both the electron-beam welder and the arc-image furnace. The above study is of interest to the thermal-breeder program.

STUDIES ON OTHER CERAMIC BODIES

Si-SiC Fuel Plates

J. M. Kerr

Eight Si-SiC fuel plates, four each of a 0.44-g loading and a 0.88-g loading of fully enriched UO_2, were sent to the Solid State Division for irradiation in the ORR. These were never irradiated because difficulties were encountered in getting a thermocouple that would not react with silicon. When a means of measuring the temperature has been established, these fuel plates will be available for irradiation. Eight Cr-Al_2O_3 fuel plates, four each of the above-mentioned fuel loadings, were also sent for irradiation. These were put into the ORR, but due to extreme gas leakage, were irradiated for only 1 hr. The final analysis has not been completed on these bars; so the exact cause of the leakage cannot be definitely established. It is thought that there were microcracks which allowed fission gas as well as particulate matter to escape.

Twelve cylindrical samples having a thin inner core of fully enriched UO_2 surrounded with Cr-Al_2O_3 have been prepared and are scheduled for irradiation testing early in 1960. These are not to be prototype fuel elements but are to be used solely to test the Cr-Al_2O_3 for its retention of fission gas and its behavior under irradiation.[35] These cylinders are to contain 0.5 g of fuel as UO_2 and are to be 0.750 in. long and 0.500 in. in diameter. The UO_2 will be added as -50 +70 mesh grains fired to 1750°C to achieve a high density. No further work is planned on the Cr-Al_2O_3 or Si-SiC cermets after the above assignment is completed.

Some work was done on Al_2O_3-clad fuel plates, but diffusion of UO_2 through the clad was quite serious at the firing temperatures necessary for attaining high-density Al_2O_3. At about this same time, it was learned that Al_2O_3 is damaged badly when irradiated in contact with fuel and, as a result, this work was stopped.

---

[35]Private communications to J. M. Kerr from P. E. Reagan, June 17, 1959.

Uranium Monocarbide

J. M. Kerr

Studies are being initiated to investigate the potential of bulk UC for fueling civilian power reactors.[36] The proposed program will call for studies on three types of fuel: (1) a cemented carbide using a non-carbide-forming metal binder, (2) a cemented carbide using a carbide-forming metal binder, and (3) a sintered double carbide. A high-temperature vacuum furnace heated by induction is under construction for this program.

Spherical Thorium Oxide Particles

C. E. Curtis

In view of the possible use of ThO_2 or $ThO_2 + UO_2$ in a "live bed" (suspended bed) breeder blanket, methods of forming strong, solid spheres of these materials seemed to merit investigation. By means of a "rolling" method it was possible to form such spheres of pure ThO_2, of $ThO_2 + UO_2$, of $ThO_2 + Al_2O_3$ and of ThO_2 + SiC. The Al_2O_3 and SiC were added to enhance the abrasion-resistance of the ThO_2. The smallest possible size of spheres producible by the rolling method that was employed is approximately 100 mesh (149 μ) with an upper limit for the diameter of perhaps 1/4 in.

Compatibility of Various Oxides with Selected Metals

J. M. Kerr

Some knowledge regarding the compatibility of various refractory metals and oxides can be valuable in designing apparatus for use at high temperatures. To obtain such information, a brief study was made in which oxides were heated in contact with several of the refractory metals in order to note the temperature at which they react. This investigation

---

[36]Private communication to J. P. Hammond from J. M. Kerr, July 6, 1959, "Program Outline; Fabrication Development for Cemented UC."

was intended to yield only the approximate temperature of reaction. The equipment and techniques utilized gave rapid, though not exact, results.

The furnace consisted of a resistance-heated metal strip connected to two water-cooled brass electrodes. A sight glass was positioned directly above the metal strip, and appropriate fixtures for pumping a vacuum and allowing gas to flow into the furnace were provided. The temperature of the metal strip was taken by an optical pyrometer, which was sighted on a spot immediately adjacent to the oxide material on the strip. Temperature corrections were made for deviations due to the pyrometer itself as well as those due to the sight glass. For three of the metals, tungsten, tantalum, and molybdenum, emissivity corrections were made. The rate of temperature increase was extremely rapid, and this must be taken into account when interpreting the results.

Generally, the data in Table 4.14 indicate that lower temperatures at which reactions were extreme were encountered with the eight oxides in contact with niobium and that thoria exhibited the least tendency toward reaction of any of the eight oxides with the five metals.

In many instances it was difficult to be sure that a reaction had taken place, rather than mere breakage and subsequent arcing of the metal strip. Metallography was used to check for reactions in these instances, and if any phases were present other than the oxide and metal, or if either phase were present in the other, reaction was presumed to have taken place. In all the oxide-metal combinations, except for those with rhenium, metallography proved most useful.

Although it must be emphasized that the temperatures of the various reactions reported in Table 4.14 are only approximate, they can be very useful in the design of equipment for high-temperature applications; they can serve as a preliminary point upon which the designer can base his initial design considerations. If more precise information is needed, these temperatures can also serve as points of departure.

Table 4.14. Approximate Temperatures (°C) for Initial and Fast Reactions Between Oxides and Metals*

Oxide	Metal										Remarks
	Niobium**		Tungsten		Tantalum		Molybdenum		Rhenium**		
	First	Fast	First	Fast	First	Fast	First	Fast	First	Fast	
Al_2O_3	No reaction up to 2000		Melted		2045	Melted	1805	Melted	Very slight, 1415	Melted	Electrically fused
BeO	1480	2135	2140	2310	2245	2355	No reaction up to 2130		Very slight, 920	2175	Hot pressed to a density of > 95%
MgO	1760	1855	2030	2495	1790	2000	1465	2130	1535	2260	Electrically fused
ThO_2	No reaction up to 2135		No reaction up to 2645		No reaction up to 2795		2155	2155	1350	None up to 2280	Sintered to 1800
TiO_2	Extreme, 1185	Reaction, 1515	1775	1780	1785	1785	1675	1845	1640	1775	Sintered to 1400
UO_2	Extreme, 2065	Reaction, 2065	1785	2600	2295	2420	No reaction up to 2155		Very slight, 925	2295	Electrically fused
Y_2O_3	No reaction up to 2000		1865	2165	Very slight, 1705	Very fast, 2410	1575	2135	1185	2220	Sintered to 1600
ZrO_2	2035	2135	2385	2390	1955	2125	1335	2010	Reaction, 1430	Continuous, 2230	Sintered to 1500

*All temperatures shown are ±50°C and are corrected for pyrometer and quartz-glass sight port.

**These have had no emissivity correction applied.

METALLOGRAPHY

R. J. Gray

W. H. Bridges
R. S. Crouse
C. K. H. DuBose
G. Hallerman
T. M. Kegley, Jr.
E. L. Long, Jr.
J. R. Riddle
J. E. VanCleve, Jr.

Dilatometry

J. R. Riddle

Thermal Expansion Data on Al-U_3O_8 Cermets. — The linear-expansion characteristics of U_3O_8-bearing aluminum compacts were investigated in the temperature range of 50 to 425°C. Wrought powder samples containing 0, 5, 10, 20, 30, 40, and 50 vol % U_3O_8 as the dispersed phase were machined from Alclad fuel plates. These fuel plates were prepared in accordance with the manufacturing procedures outlined in this part of the report, under "Alclad Plates Containing Dispersions of U_3O_8 in Aluminum." All specimens were completely decladded by machining, and determinations were made on samples oriented both parallel and transverse to the direction of rolling.

Results on the dilation behavior of wrought cermets containing from 0 to 50 vol % U_3O_8 dispersed in aluminum are presented in Table 4.15; twenty-four determinations were made. It should be noted that U_3O_8 additions to aluminum tend to reduce the linear thermal expansion by an amount which is approximately linear with the volume percentage of the U_3O_8 present. This effect is shown in Fig. 4.22.

In general, the data are in good agreement except at low concentrations of U_3O_8, where it is apparent that minor changes in the material are playing a more important role in the dimensional changes observed. In the low-uranium-content materials, the coefficient of expansion increased slightly with each run and, in most cases, there was a slight increase in the room-temperature length after testing. Blistering, due to the evolution of gases, was evident in these same samples during fabrication, and it is believed that entrapped gases may be the cause of some of the scatter in the data. Creep, due to the weight of the push rod that was resting on the sample, has also been proposed to account for this effect; however, samples held

Table 4.15. Thermal-Expansion Data on U_3O_8-Bearing Aluminum Powder Compacts

Specimen Composition (vol %)	Number of Runs	$Lo_1 - Lo_2$* (in.)	Average ΔL 50–425°C (mils/in.)	% Error $\left(\frac{Sx}{x} \times 100\right)$
		Oriented Parallel to Rolling Direction		
100 Al	10	+ 0.0001	9.73	1
95 Al–5 U_3O_8	6	- 0.0002	9.70	0.7
90 Al–10 U_3O_8	8	+ 0.0002	9.50	
80 Al–20 U_3O_8	7	+ 0.0006	8.80	0.3
70 Al–30 U_3O_8	9	+ 0.0007	8.15	0.6
60 Al–40 U_3O_8	9		7.90	0.1
50 Al–50 U_3O_8	10	- 0.0003	7.30	0.2
		Oriented Transverse to Rolling Direction		
100 Al	6	+ 0.0003	10.00	0.8
95 Al–5 U_3O_8	7	+ 0.0001	9.70	0.9
90 Al–10 U_3O_8	6	- 0.0003	9.35	0.8
80 Al–20 U_3O_8	7		8.55	0.6
70 Al–30 U_3O_8	7	+ 0.0004	7.80	0.3
60 Al–40 U_3O_8	7	+ 0.0001	7.00	0.1
50 Al–50 U_3O_8	6	+ 0.0011	6.40	0.2

*Lo_1 = Room temperature length before testing.

Lo_2 = Room temperature length after testing.

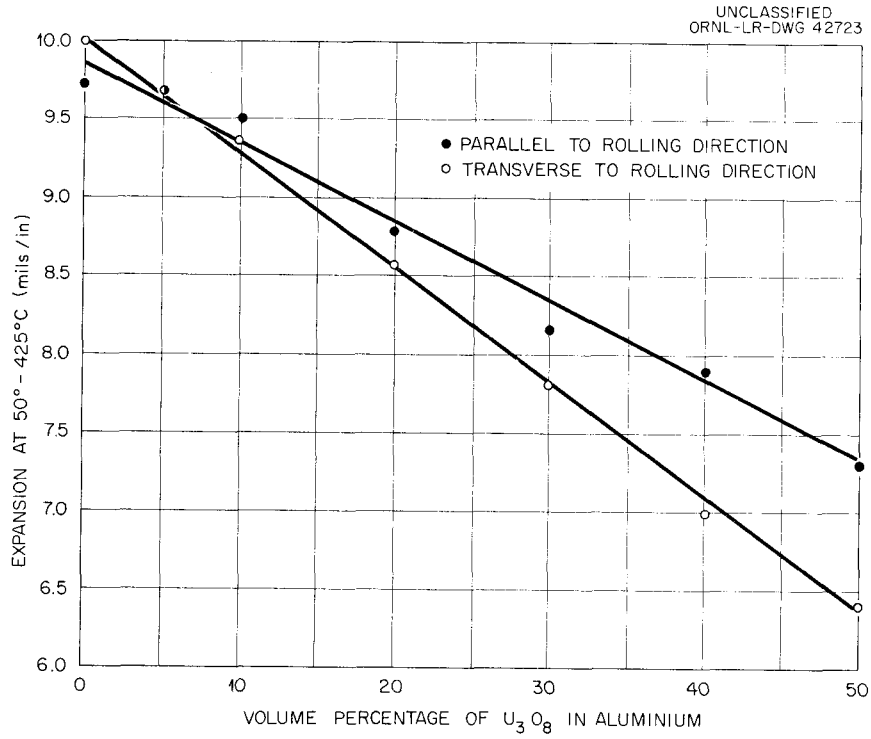

Fig. 4.22. The Effect of U_3O_8 Concentration on the Linear Thermal Expansion of Al-U_3O_8 Cermets in the Temperature Range of 50–425°C.

overnight between 400 and 525°C showed no tendency to creep. The cause may be associated with oxide introduced during the powder-metallurgy process, since the aluminum samples without U_3O_8 additions exhibited a lower coefficient of expansion than did cast material of the same purity. Samples are being prepared to test the effect of entrapped gases and to test the possibility that stress due to the weight of the push rod, combined with recrystallization, is a factor. The average coefficient of expansion for the various samples cut parallel to the direction of rolling is shown in Fig. 4.23.

Coefficient of Expansion in Transformer 58 Steel. — The linear thermal coefficient of expansion of a laminated 29-gage steel sheet containing 4.3% silicon was determined in directions parallel and transverse to the laminations, as shown in Fig. 4.24. This information was needed to facilitate the design of a motor capable of operating at 600°F for the GCR program.

Phase Transformations in Ni-Mo Alloy and Hastelloy B. — An investigation of the thermal expansion of Hastelloy B has revealed that an inflection occurs on both heating and cooling at about 600°C, as shown in

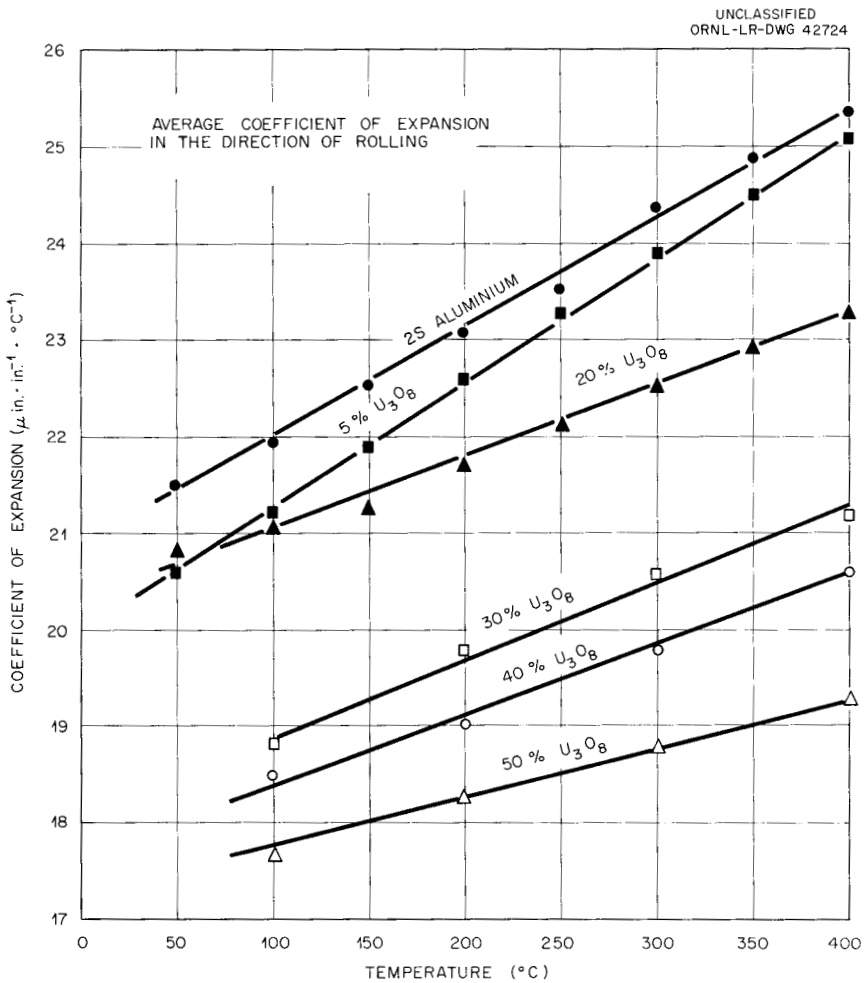

Fig. 4.23. Average Coefficient of Expansion Between Room Temperature and Indicated Temperature.

Fig. 4.25. The inflection is probably the result of a phase transformation related to the Ni-Mo system. In view of the uncertainties of the phases present in Hastelloy B (65% Ni, 28% Mo, 4-5% Fe, 2-3% other), dilatometric and x-ray diffraction investigations have been proposed as a means for following transformations in the Ni-Mo and the Ni-Mo-Fe systems; hence, attempts are being made to relate thermal expansion characteristics to phase transformations, the goal being to define the matrix in Hastelloy B in terms of the Ni-Mo system. If the matrix of Hastelloy B can be shown to transform by a mechanism analogous to the α-β reaction in the Ni-Mo system, then it may be possible to identify the precipitates that form within the matrix after

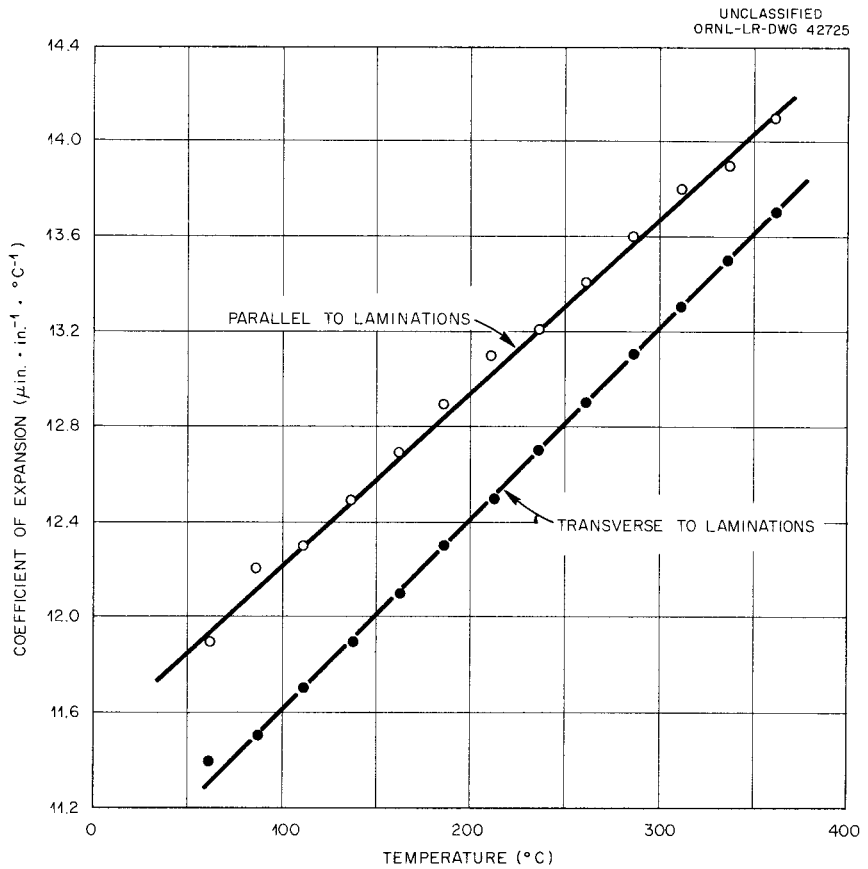

Fig. 4.24. Instantaneous Linear Thermal Coefficient of Expansion of Transformer 58 Steel.

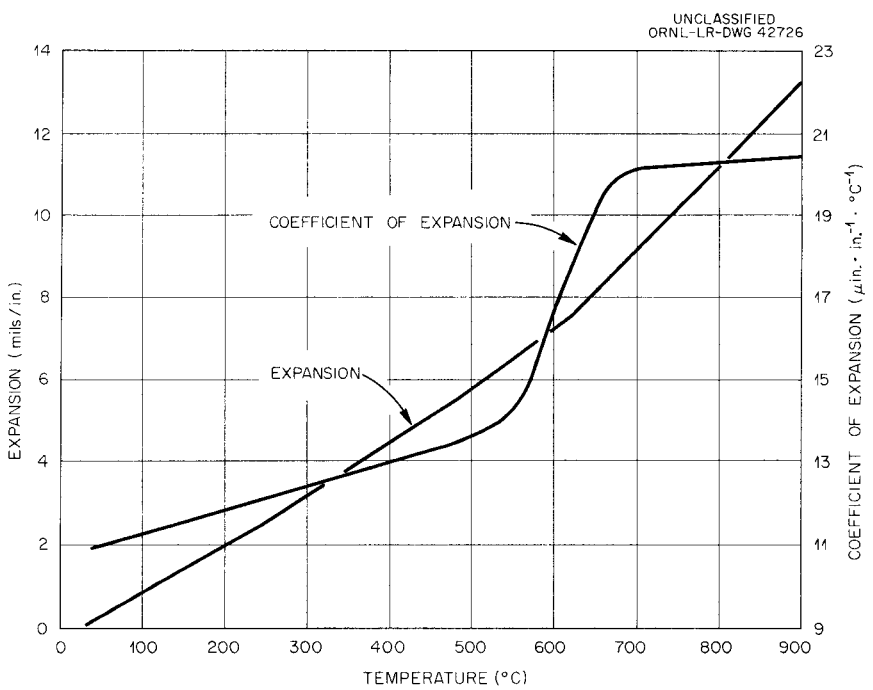

Fig. 4.25. Linear Thermal Expansion of Hastelloy B.

extended heat treatments. This information is needed to complete a report on the metallography of the isothermally heat-treated material.[37]

The thermal-expansion characteristics of three alloys are currently under investigation. One is a binary Ni-Mo alloy of the β composition (29 wt % Mo) while the other two are ternary alloys containing the same Ni-Mo ratio, but with 2-1/2% and 5% Fe additions as well. The quantitative characteristics of the binary alloy have been determined over the temperature range of 700-900°C, as shown in Fig. 4.26. According to E. E. Stansbury of the University of Tennessee, the low-temperature phase is β, a body-centered tetragonal structure; and the high-temperature phase is α, a face-centered cubic structure.[38] On heating, the material transforms to solid-solution α at a constant temperature of about 865°C. During the transformation, the volume increases by 0.8%, in an endothermic reaction. On cooling at rates of 1–2°C/min, the material transforms to the low-temperature phase (Ni_4Mo) at (790 ± 5)°C, in an exothermic reaction, as evidenced by the rise in temperature shown in Fig. 4.26. At

[37]J. R. Riddle and R. J. Gray, Metallography of Isothermally Heat Treated Hastelloy B, ORNL-2496 (to be published).

[38]E. E. Stansbury, private communication.

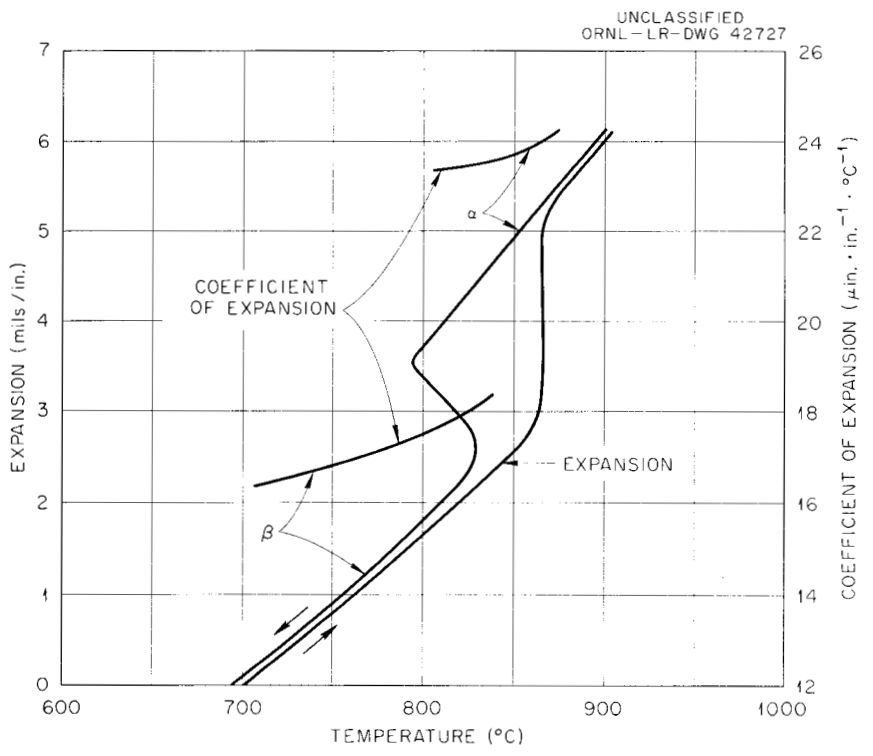

Fig. 4.26. Thermal Expansion Characteristics of the α-β Transformation in the Ni-Mo System.

extremely slow cooling rates, the material transforms to β at slightly higher temperatures (a sample held at 820°C transformed to β in about 3 hr) in a less spontaneous reaction. Alpha can be retained by quenching according to hardness data. Samples quenched from 950°C show a DPH (diamond pyramid hardness) of 180–210, while furnace-cooled samples show a DPH of 380–460. In both cases, the microstructure is that of a homogeneous material. It has also been shown that the material reverts to the low-temperature phase without supercooling when the material was not previously completely transformed to the high-temperature phase during heating.

Although the thermal expansion characteristics of Hastelloy B and of the α-β transformation in the Ni-Mo system have been quantitatively determined, the relationship between these transformations is not yet apparent. From limited data obtained on the ternary alloy containing 5% iron, it is evident that an inflection occurs in the thermal expansion curve much like that of Hastelloy B but at a slightly higher temperature. A parallel investigation is being conducted by E. E. Stansbury at the University of Tennessee, using x-ray diffraction techniques to identify the phases in these ternary alloys.

Electron Microscopy

E. L. Long, Jr. W. H. Bridges

The electron microscope continues to be utilized primarily as a service instrument to almost every program of the Division. The Ceramics Group has submitted a number of samples of BeO for general examination as to the characteristics of the powders. The Mechanical Properties Group submitted for topographical examination samples that had been tested in various atmospheres. They were examined for differences that might explain creep behavior. The Corrosion Engineering, Welding and Brazing, Materials Compatibility, and High-Temperature Alloy Development Groups have submitted miscellaneous samples for general microstructural examination, usually for the appearance and distribution of precipitates in the grain boundaries.

Grain Boundary Structure in Heat-Treated Inconel. – Typical of such samples were two specimens of Inconel, both of which were annealed in hydrogen at 1650°F. The specimen illustrated in Fig. 4.27 was annealed for 60 hr, while the specimen shown in Fig. 4.28 was annealed for 120 hr. In

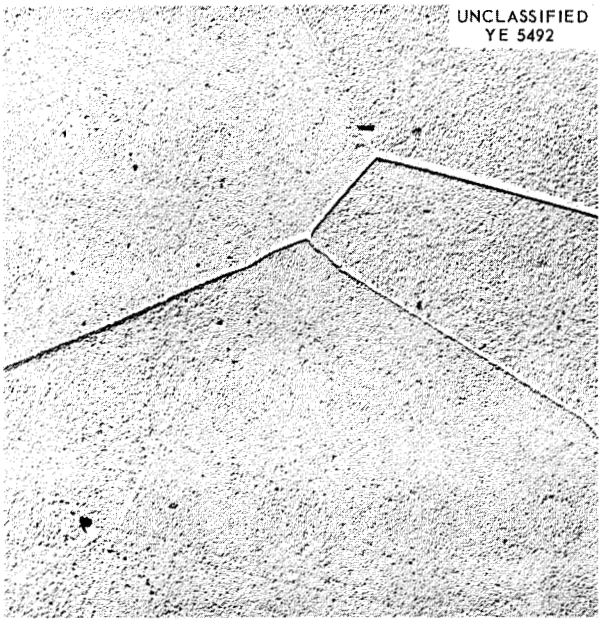

Fig. 4.27. Inconel Annealed for 60 hr in Hydrogen at 1650°F. Etchant: 10% oxalic acid. Palladium-shadowed carbon replica; 6200X. Reduced 12%.

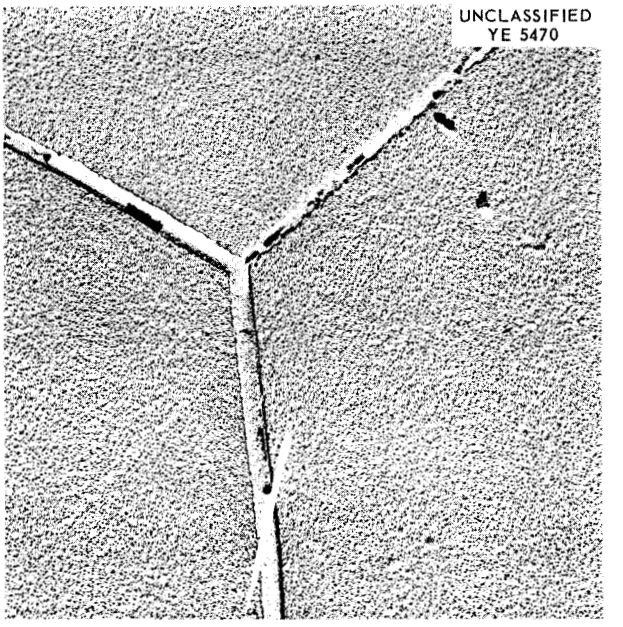

Fig. 4.28. Inconel Annealed for 120 hr in Hydrogen at 1650°F. Note broad grain boundary compared to the 60-hr anneal. Etchant: 10% oxalic acid. Palladium-shadowed carbon replica; 6200X. Reduced 12%.

the specimen treated for the longer time, the grain boundaries are somewhat wider and are not as clean.

Topography of Irradiated Zirconium Samples. — The Reactor Experimental Engineering Division requested an examination for topological differences in oxide films of zirconium exposed to reactor radiation and directly to fission-recoil neutrons. Typical electron micrographs are shown in Figs. 4.29 and 4.30. The specimen which was exposed to the fission recoils and fragments has a more eruptive appearance than does the other, which indicated that radiation had an apparent effect on the formation of the oxide film.[39]

Microstructure of Reaction Products in Heat Treated UO_2-Aluminum Powder Fuel Plates. — The Fuel Element Development Group submitted samples of UO_2-Al fuel elements to ascertain, if possible, whether there was a reaction zone surrounding the UO_2 particles. If there were, it might explain the warpage of the fuel elements observed during heating. Not just

[39]W. C. Yee, A Study on the Effect of Fission Fragments on the Oxidation of Zirconium, ORNL-2742 (in press).

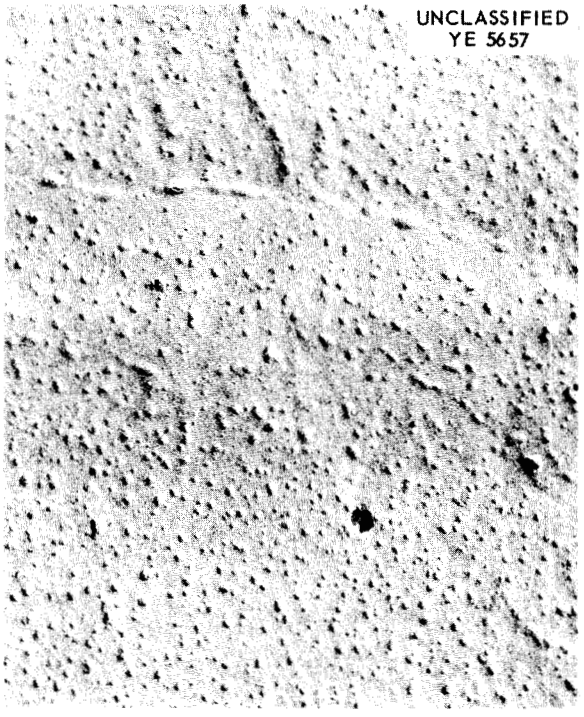

Fig. 4.29. Surface of Zirconium Oxidized While Being Exposed to Reactor-Induced Radiation. Palladium-shadowed carbon replica; 11,350X.

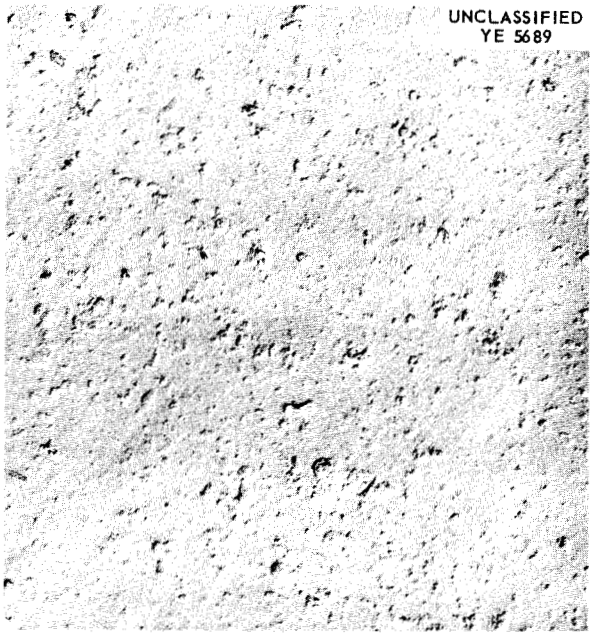

Fig. 4.30. Surface of Zirconium Oxidized While Being Exposed to Reactor-Induced Radiation and Fission-Recoil Neutrons and Fragments. Palladium-shadowed carbon replica; 11,350X. Reduced 10%.

one reaction zone was found, but zones of all three U-Al compounds were found. The various reaction zones can be seen in Fig. 4.31. Two of the zones are very distinct, and the third is still visible. From U-Al couple studies and phase diagram considerations, the various zones are identified as UAl_4, UAl_3, and UAl_2, each of which also contains Al_2O_3. The UAl_4 zone appears as a continuous region adjacent to the aluminum matrix. The UAl_3 zone has a lamellar structure, and the reaction has shown some tendency to be orientation dependent, as can be seen in Fig. 4.32. The UAl_2 zone was seen only seldomly, as it is apparently very thin and is visible only when cut through at a high angle. A typical micrograph of a reacting UO_2 particle is shown in Fig. 4.33. Here, the UAl_2 zone is not seen. The complete study has been reported by R. C. Waugh.[40]

Thorium Oxide Films on Th-U Alloy Samples. — Recently, some thin films from thorium-uranium alloy samples that were in evacuated quartz tubes were

[40]R. C. Waugh, The Reaction and Growth of Uranium Dioxide-Aluminum Fuel Plates and Compacts, ORNL-2701 (Mar. 9, 1959).

Fig. 4.31. As-Fabricated Al-UO_2 Element. Etched with a mixture of 85 parts H_3PO_4, 15 parts H_2SO_4. Faxfilm, palladium-shadowed carbon replica.

submitted for examination and identification. Figure 4.34 is an electron diffraction pattern of this film and was identified as thorium dioxide. Figure 4.35 is a transmission electron micrograph taken directly through a thin portion of the film. In addition to the general extinction contours,

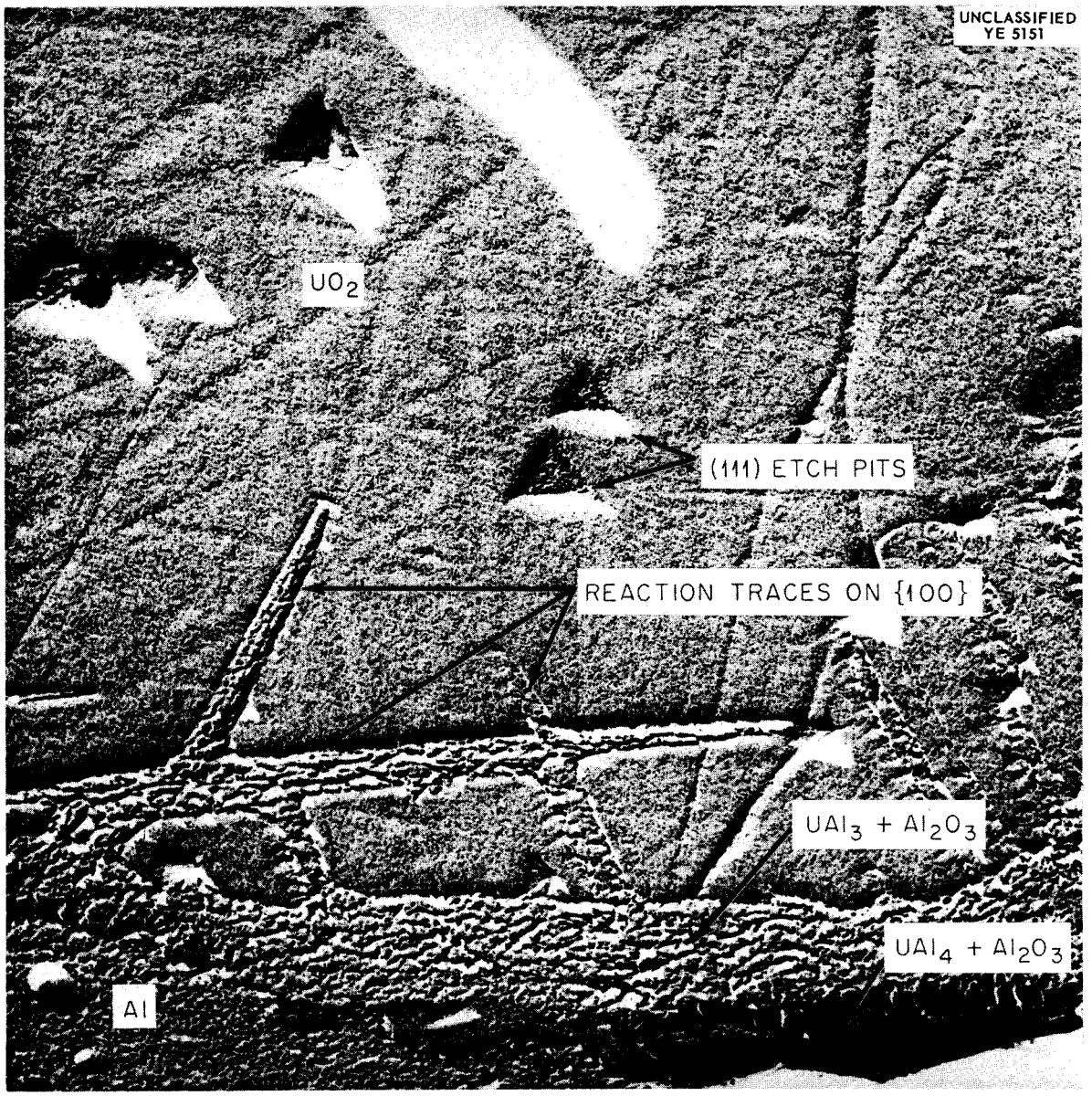

Fig. 4.32. As-Fabricated Al-UO_2 Element. Etched with a mixture of 20 parts H_2O_2, 5 parts H_2SO_4, 75 parts H_2O. Faxfilm, palladium-shadowed carbon replica. 16,000X. Reduced 14%.

there can be seen a series of straight interference bands; these do not change as the illumination is changed. An analysis of the bands is underway to determine whether they are just interference bands related to the thickness of the grains or whether they are related to the structure thickness of the crystals.

Topology of Anodized Aluminum. — The work reported in last year's report has been continued on a very limited scale. The primary facts determined so

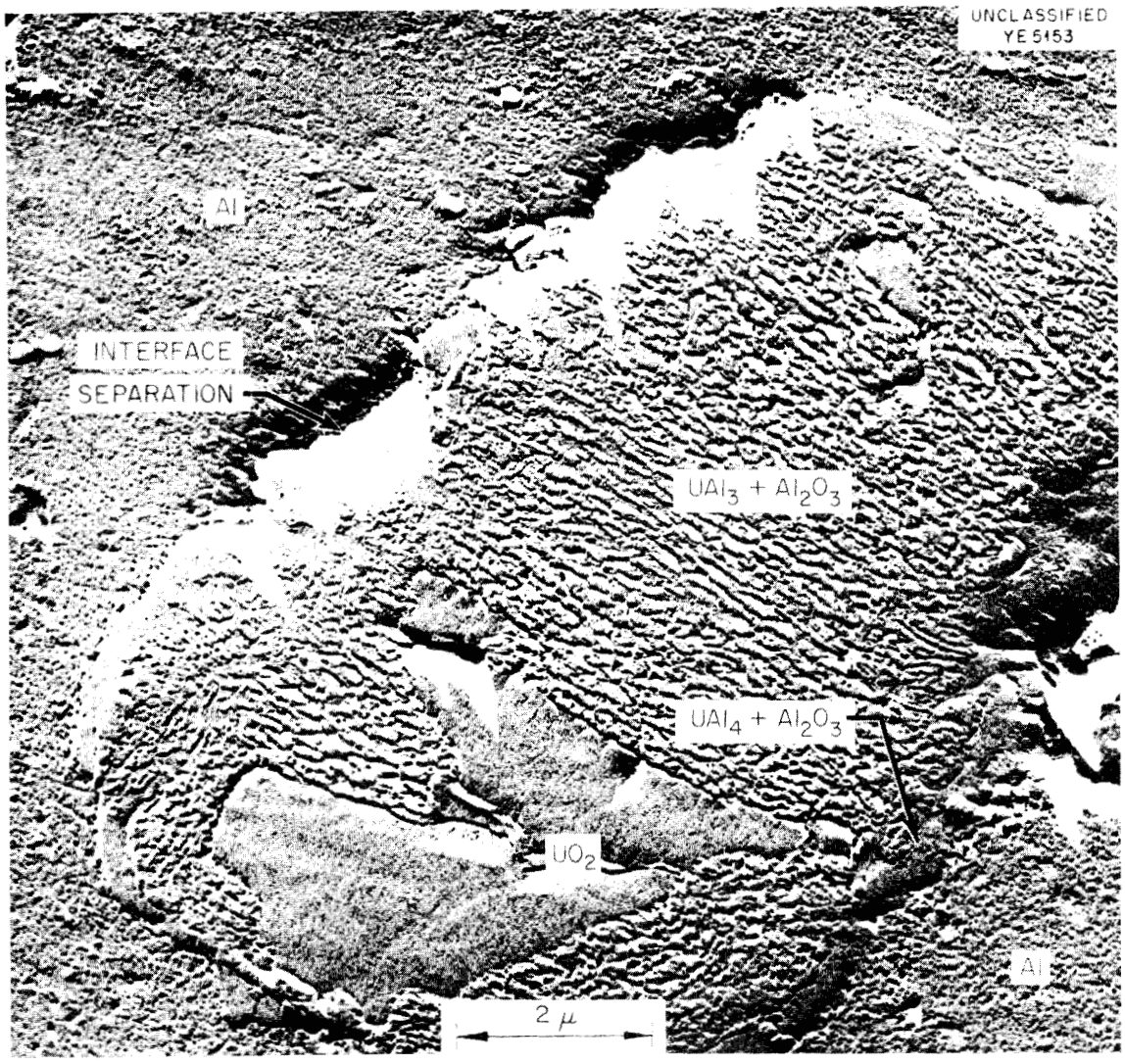

Fig. 4.33. Aluminum-Uranium Dioxide Element Heat Treated 30 min at 600°C. Etched with a mixture of 20 parts H_2O_2, 5 parts H_2SO_4, 75 parts H_2O. Faxfilm, palladium-shadowed carbon replica. Reduced 15%.

far are in direct agreement with those of Welch[41] in that the spacing of the furrows is directly related to the impressed voltage of anodization. The beginnings and endings of lines, with the accompanying adjustment of adjacent lines, do not seem to be related to any disorder of the substrate material, as the same spacings are seen on cold-worked and annealed aluminum anodized at the same voltage.

[41] N. C. Welch, J. Inst. Metals 85, 129–35 (1956–57).

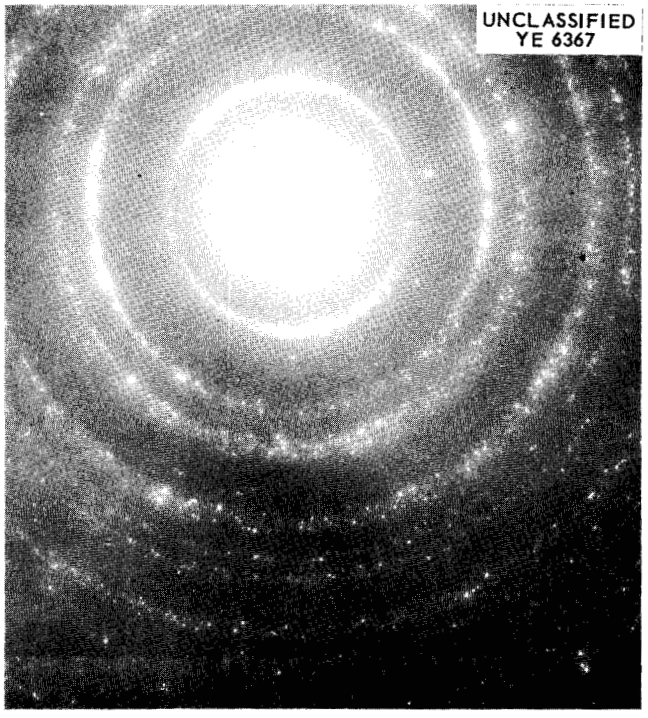

Fig. 4.34. Electron Diffraction Pattern from Thin Film of ThO_2. 12,500X.

Measured d Values	ThO_2 d Values from ASTM Index
3.21	3.22
2.80	2.79
1.98	1.97
1.68	1.68
1.28	1.28

Metallography of Ceramic Fuel Materials

R. J. Gray C. K. H. DuBose

U_3O_8-Bearing Materials. — The general appearance and crystal shape of U_3O_8 particles in powder form are illustrated in Fig. 4.36. This particular powder was prepared from $UO_3 \cdot H_2O$ by calcining at 1000°C in air. This type of U_3O_8 powder retains the morphological characteristics of the $UO_3 \cdot H_2O$ and is used primarily in the fabrication of dispersion-type fuel elements. A cross section of the U_3O_8 in an aluminum-powder matrix of a fuel plate that had been hot rolled at 590°C, then cold rolled from 0.072 in. to 0.060 in. after flux annealing 1/2 hr at 600°C, is shown in Fig. 4.37. It is evident that the U_3O_8 powder retained much of the original shape. The fine grain size of this powder is shown in Fig. 4.38. The etchant for showing the

Fig. 4.35. Transmission Electron Micrograph of Thin Film of ThO_2. 25,000X.

Fig. 4.36. U_3O_8 Powder Prepared from $UO_3 \cdot H_2O$. Reduced 11%.

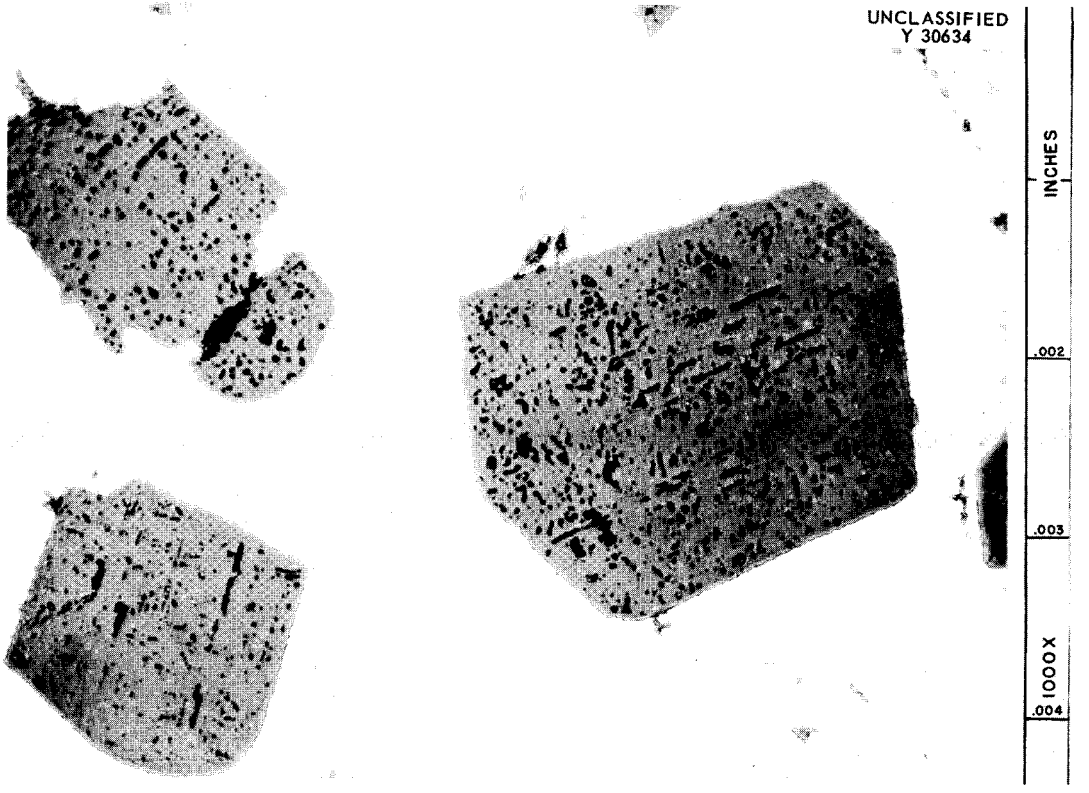

Fig. 4.37. U_3O_8 Powder in Aluminum Matrix of Fuel Plate. As-polished. Reduced 8.5%.

Fig. 4.38. U_3O_8 Powder in Aluminum Matrix of Fuel Plate. Etched to show grain size in U_3O_8.

grain size consisted of 70 parts H_2O_2 (30%), 10 parts H_2SO_4, and 20 parts H_2O. The etchant did not attack the aluminum during the 20-min immersion period.

Figure 4.39 is another photomicrograph of U_3O_8 powder compacted in aluminum powder and roll clad in an aluminum plate as described above. This U_3O_8 powder, however, exhibits two apparent degrees of porosity in the as-polished condition; one powder is very dense while the other is quite porous. These powders are representative of two different manufacturing techniques. The dense powder was made by the "dead-burn process" and the history of the other powder was not available. The sequence of operations generally employed in the preparation of "dead burnt" oxide is dissolution of UO_3 in HNO_3, precipitation by peroxide addition, calcination at 1000°C, screening to − 80 mesh size, high firing at 1180°C in air for 4 hr, and screening to − 100 mesh size. The two types of powders also had distinctly

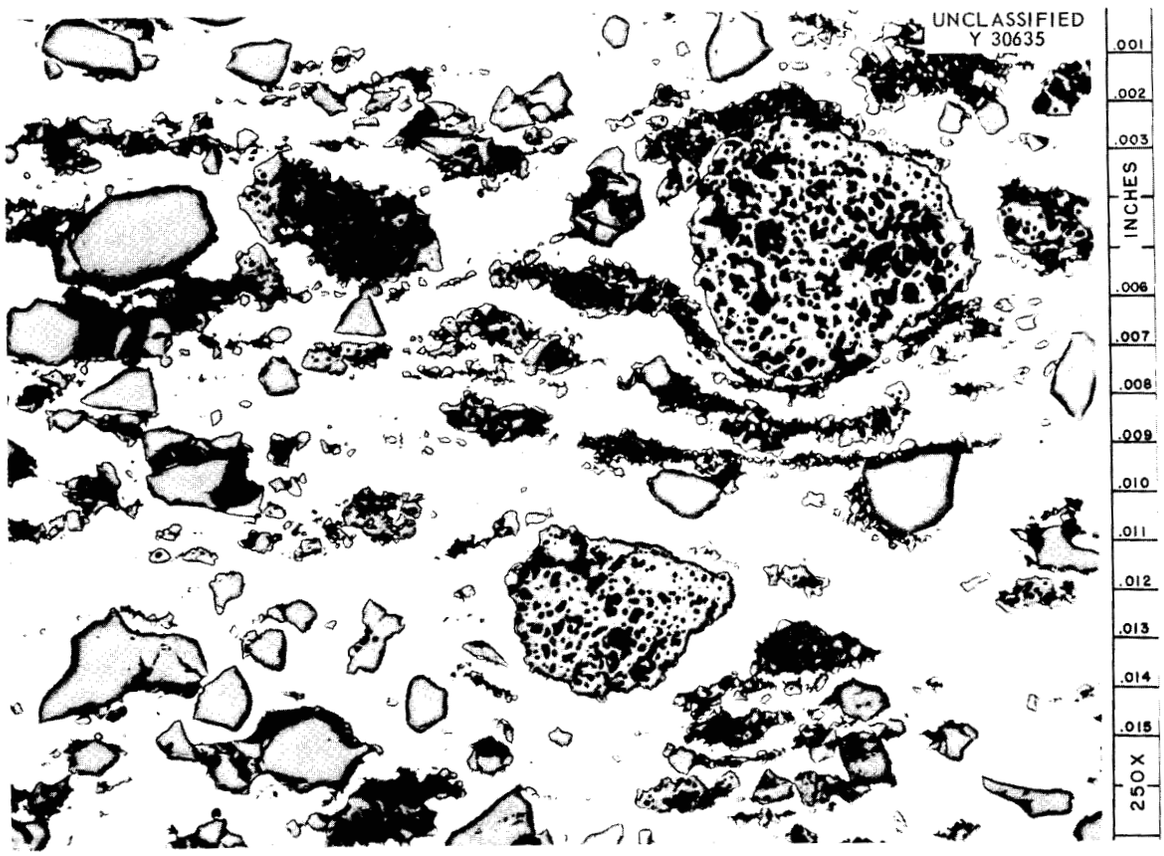

Fig. 4.39. U_3O_8 in Aluminum Matrix As-Polished. Note difference in porosity of ceramic particles.

different etching characteristics. The porous powders, for example, were polycrystalline, as shown in Fig. 4.40, whereas the dense powders were almost all single crystals. A few of the dense crystals did show twinning characteristics, as shown in Fig. 4.41. The origin of this twinning is not known.

UO_2-Bearing Materials. – Several types of UO_2 powder have been studied. Figure 4.42 shows the microstructure of fused UO_2. This product was prepared from UO_2 powder which had been cold pressed at 8000 psi, sintered for 1 hr at 1750°C in hydrogen, and finally arc melted in argon. The elongated grains are obviously the result of rapid cooling on the water-cooled copper hearth in the arc furnace. The microstructure of fused UO_2 was obtained by etching with 70 parts H_2O, 10 parts H_2SO_4, and 20 parts H_2O_2 (30%) (ref 42)

[42] D. R. Stenquist et al., Correlation of Surface Characteristics with the Sintering Behavior of Uranium Dioxide Powders, HW-51712 (July 25, 1957).

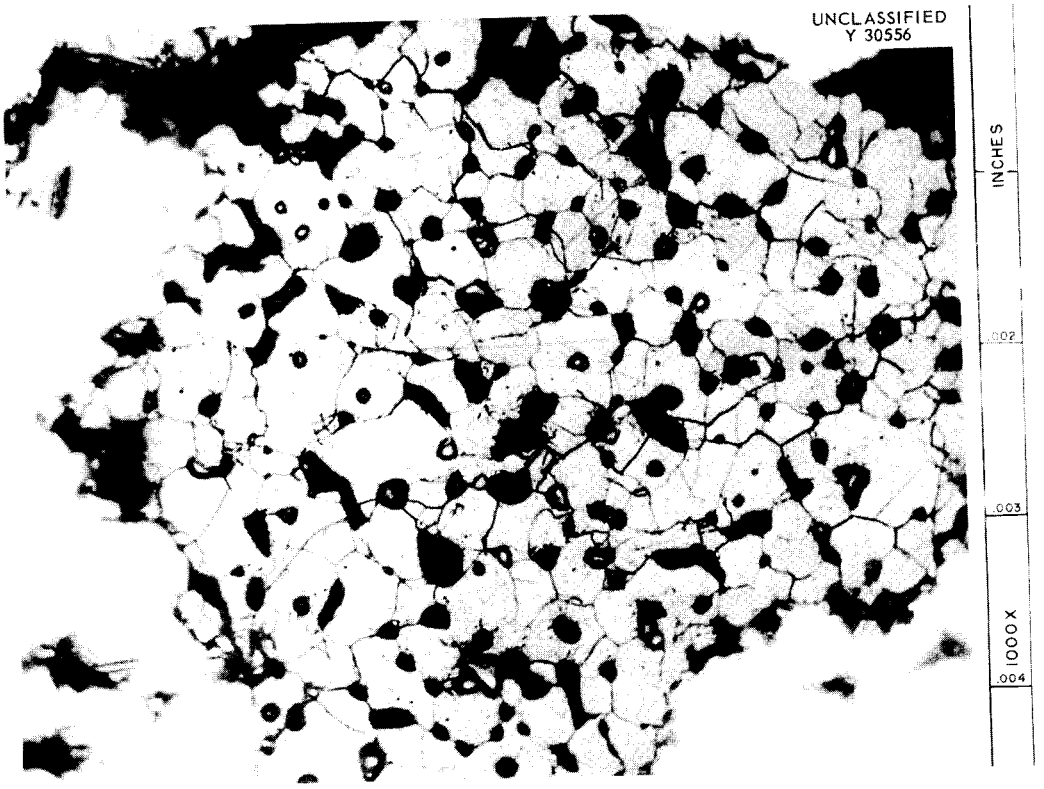

Fig. 4.40. Etched Porous Ceramic Particles. Note that these particles are polycrystalline. Reduced 11%.

Fig. 4.41. Etched Dense Particles. Note evidence of twinning. Reduced 10%.

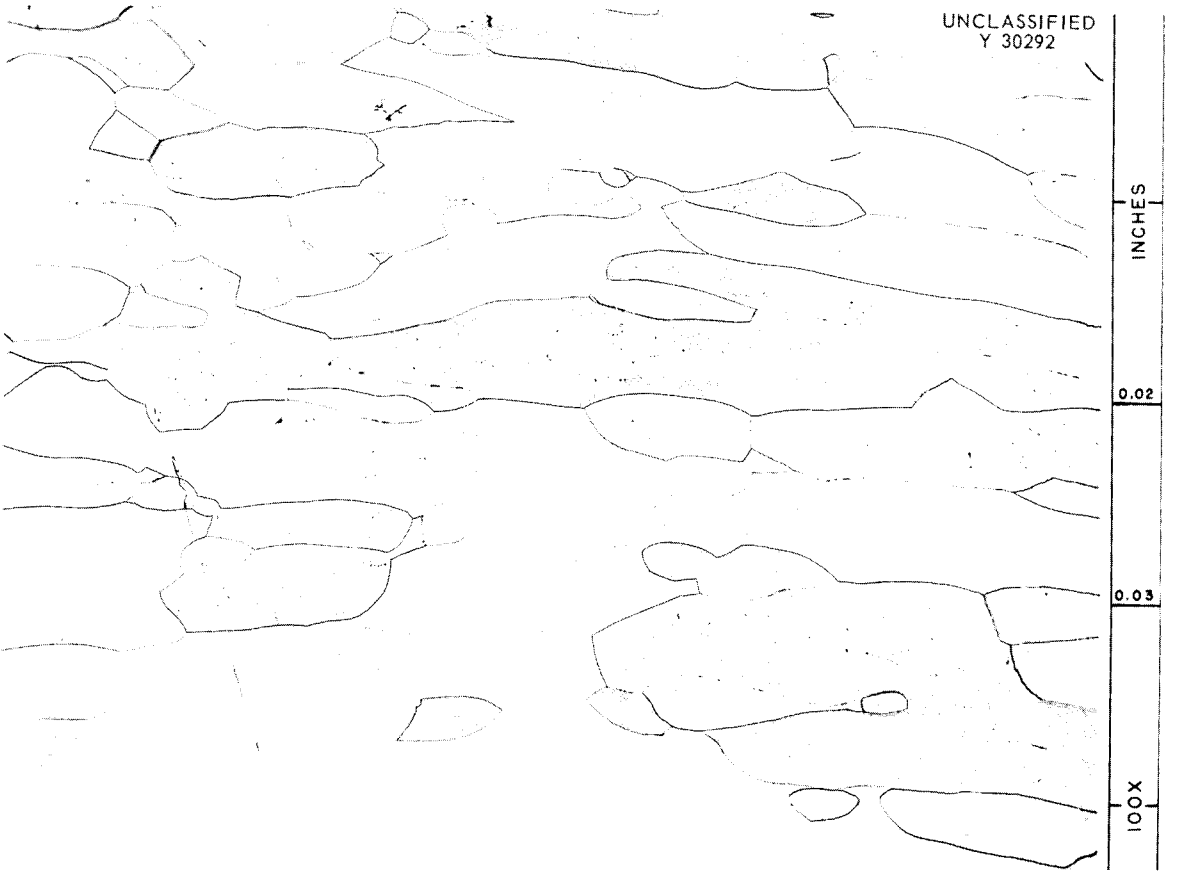

Fig. 4.42. UO_2 Powder Compacted, Sintered, and Arc Melted.

at room temperature. By heating the etchant to 80°C, a subgrain structure and pits appeared, as shown in Fig. 4.43. An electron micrograph (Fig. 4.44) of this specimen showed these subgrains and pits to be typical etch pits, thus making it possible to make orientation determinations of the cubic UO_2, if desired.

Metallographic examination of fused UO_2 samples received from a commercial vendor revealed the Widmanstätten precipitate, as shown in Figs. 4.45 and 4.46. These two specimens have O/U ratio of 2.089 and 2.141, respectively. According to Clayton and Aronson,[43] U_4O_9 cannot be detected by x ray when the O/U ratio of the oxide body is less than 2.10. Because U_4O_9 was identified in the sample illustrated in Fig. 4.46, the second phase observed in both samples is tentatively identified as U_4O_9.

---

[43]J. C. Clayton and S. Aronson, "Densities of Uranium Oxide in the Region UO_2-U_4O_9," Bettis Tech. Rev. (October 1958).

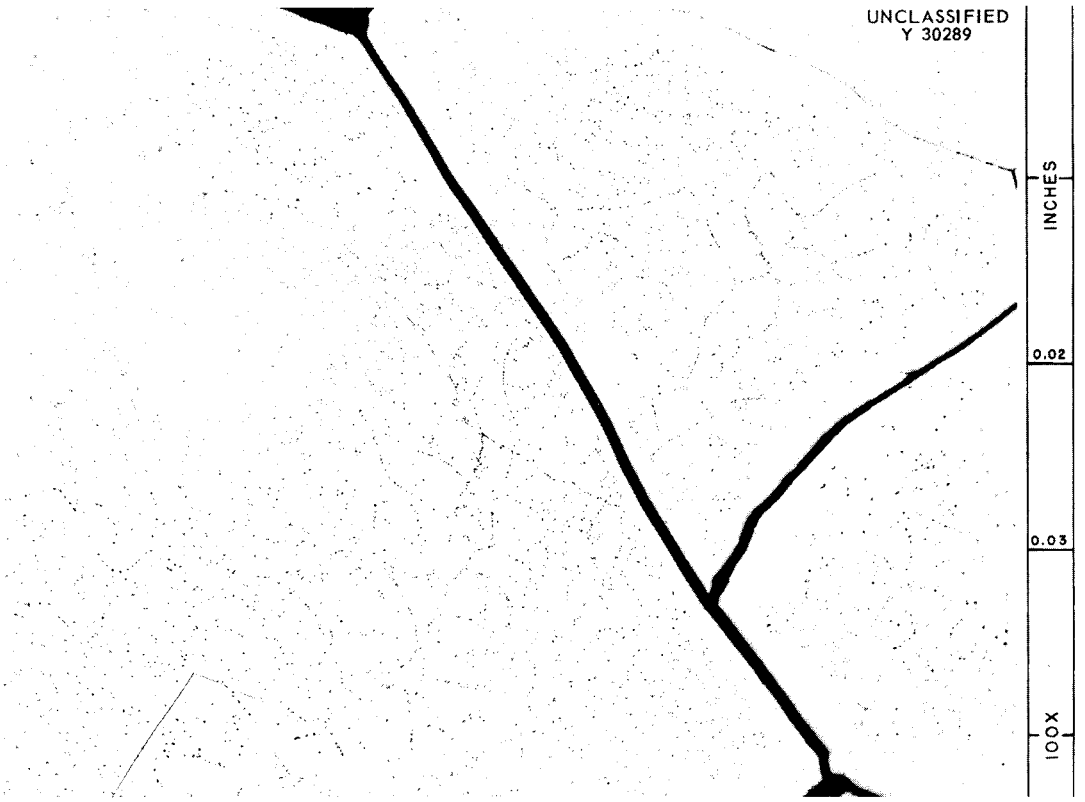

Fig. 4.43. UO_2 Powder Compacted, Sintered, and Arc Melted. Etched to show grain boundaries, subgrain boundaries, and etch pits. Reduced 8.5%

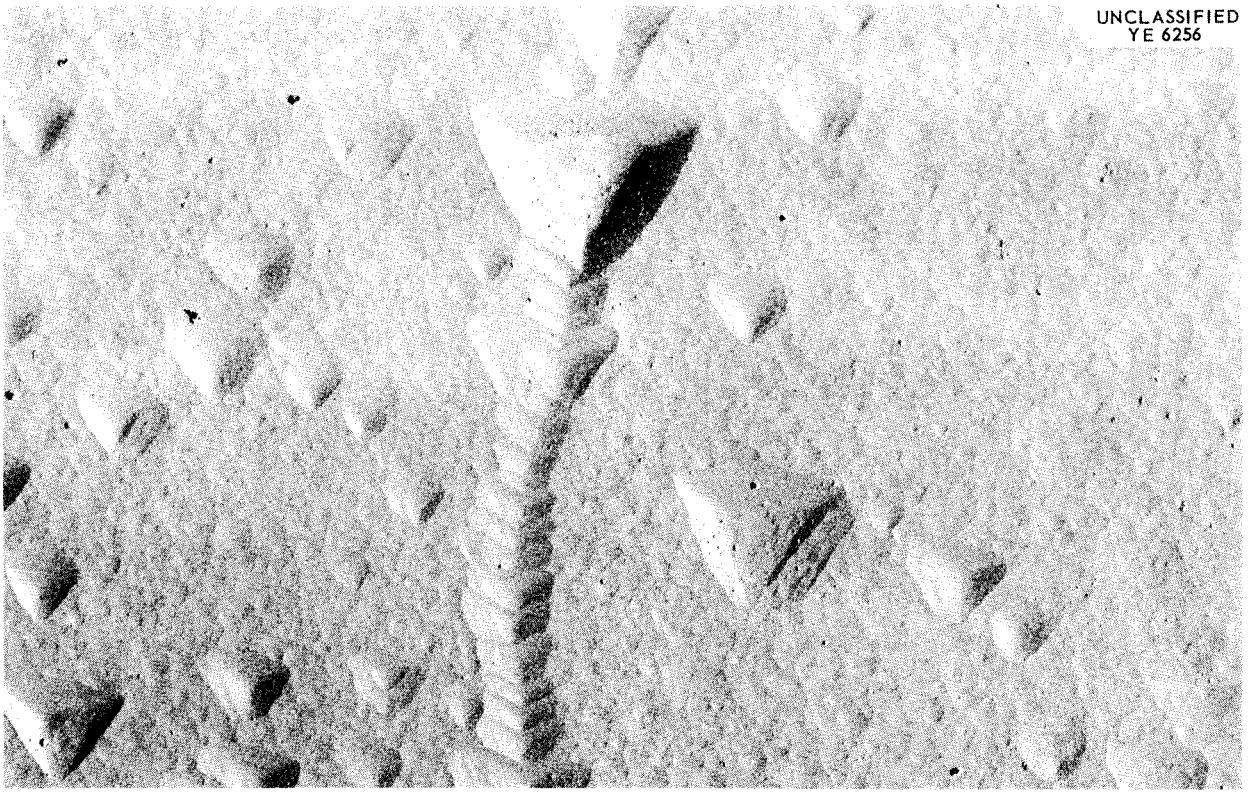

Fig. 4.44. Electron Micrograph Showing Etch Pits and Subgrain Boundary. 9700X. Reduced 6.5%.

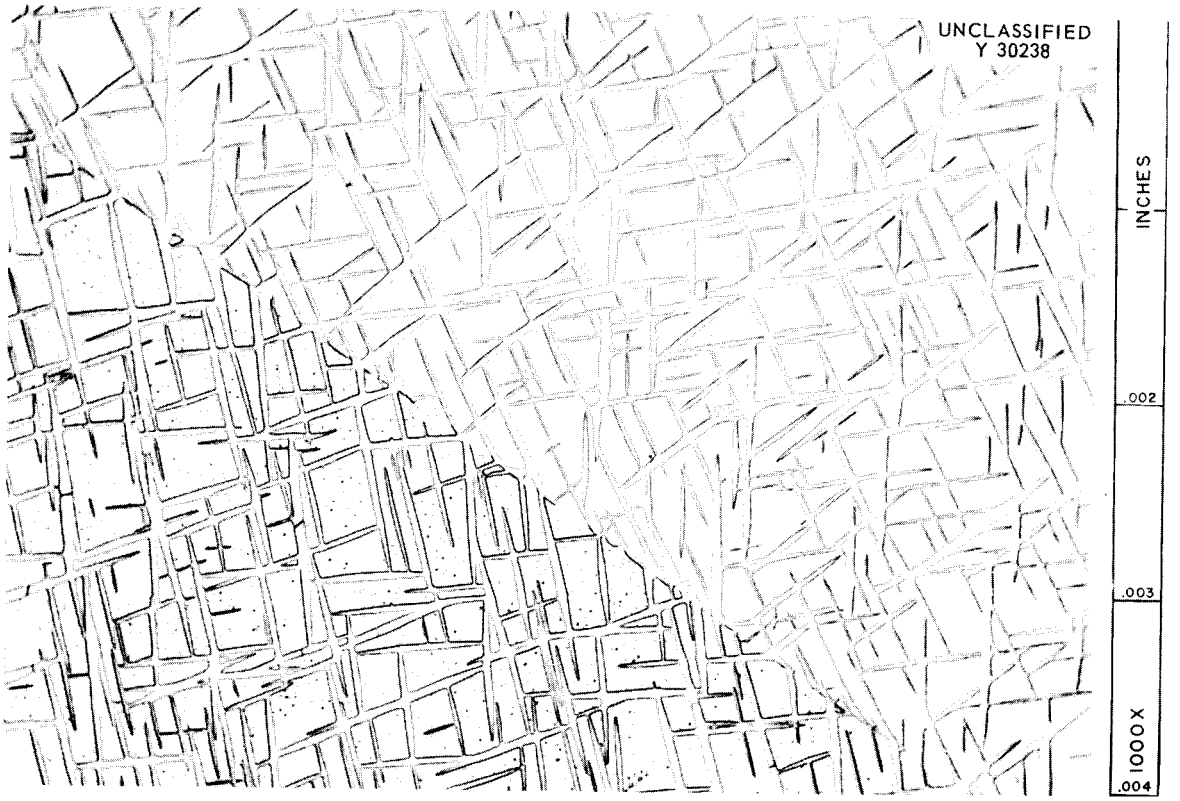

Fig. 4.45. Fused UO_2 with O/U Ratio of 2.089.

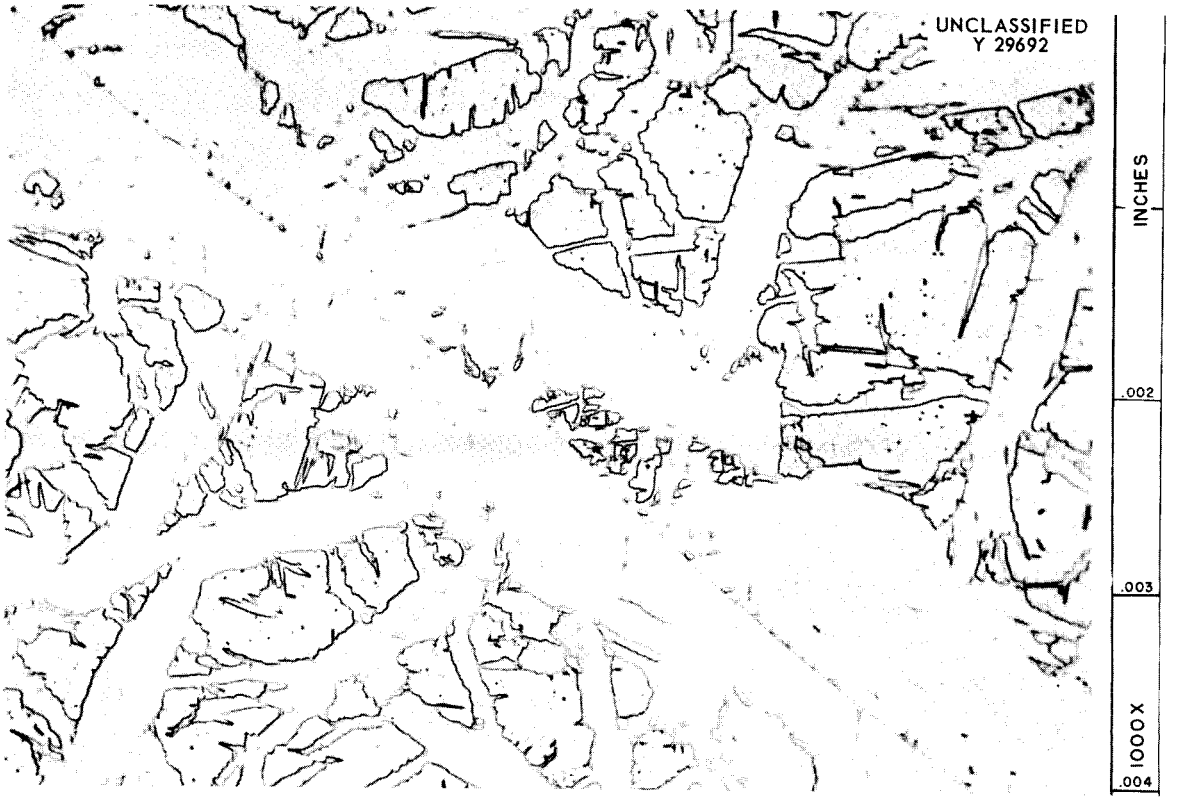

Fig. 4.46. Fused UO_2 with O/U Ratio of 2.141.

Plastic deformation in UO_2 (ref 44) can be readily detected by metallography, as shown in Fig. 4.47. The UO_2 powder was hot swaged in a tube at 800°C to 80% reduction. This longitudinal view shows elongation of the grains in the direction of hot working.

Other evidence of plastic deformation of UO_2 powder appears in a dispersion of UO_2 in type 304 stainless steel fuel plates. Figure 4.48 is a photomicrograph of such a plate and shows the individual etching characteristics of the fuel powder and the stainless steel matrix. The hot-rolling temperature and deformation were sufficient to produce an equiaxed, recrystallized stainless steel matrix with some plastically deformed UO_2, as shown by the elongated grains.

---

[44]A. R. Hall et al., The Plastic Deformation of Uranium Oxides, AERE/MR-2648 (August 1958).

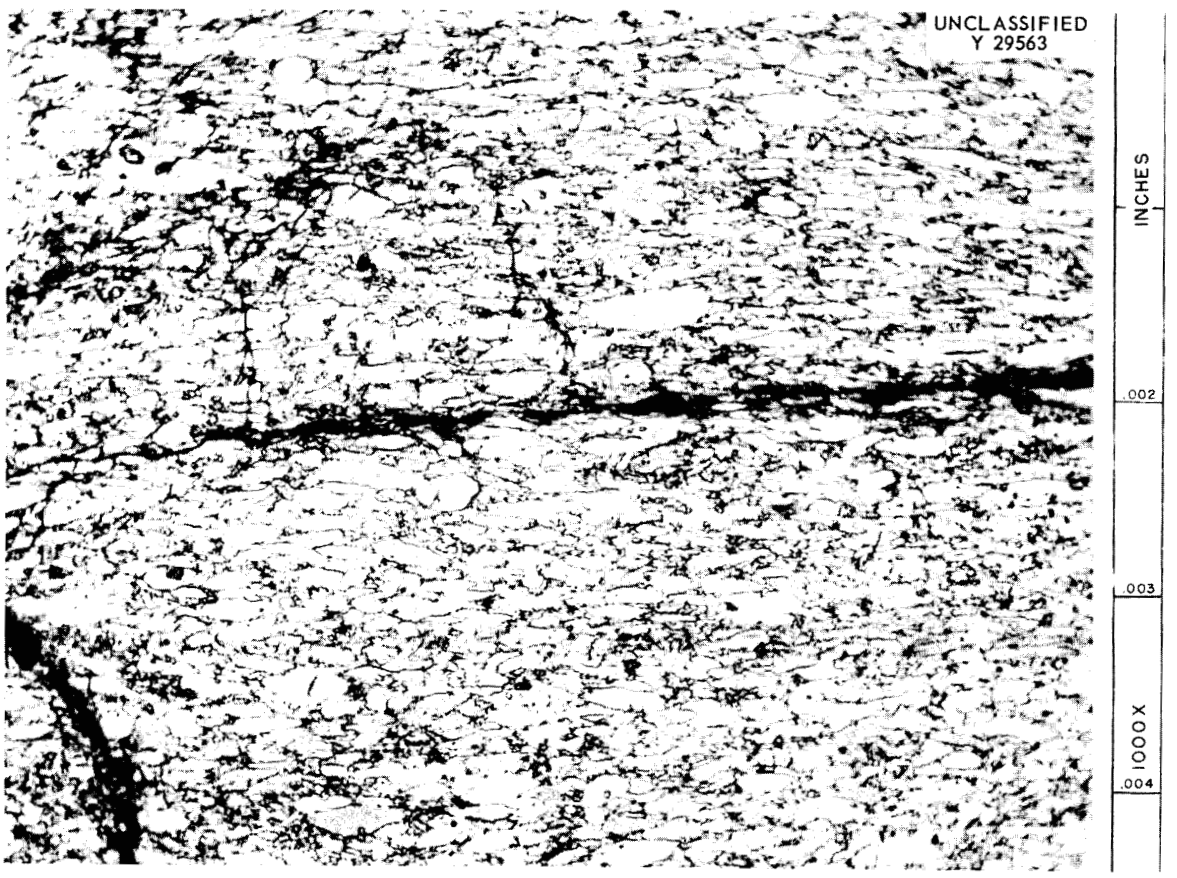

Fig. 4.47. UO_2 Powder Reduced 80% by Swaging in a Tube at 800°C. Note elongation of grains.

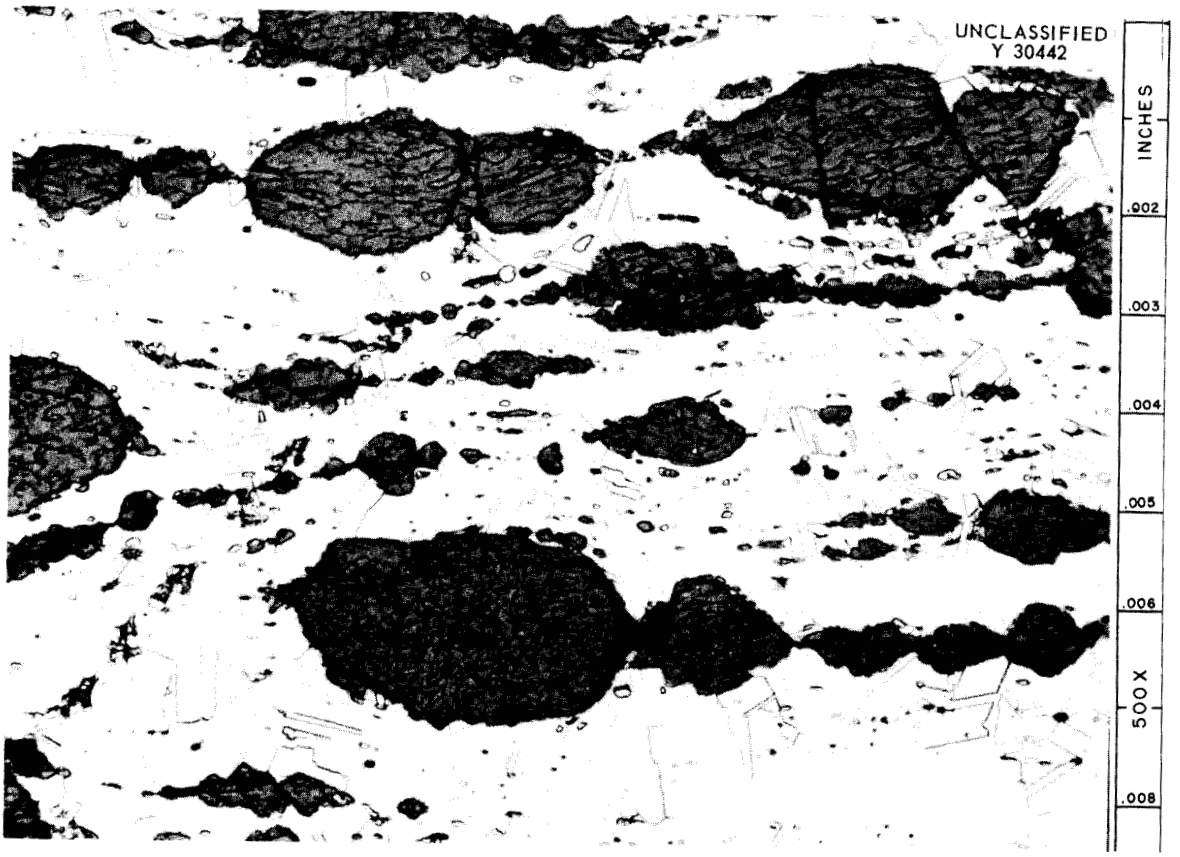

Fig. 4.48. UO_2 Powder Hot Rolled in a Type 304 Stainless Steel Fuel Plate. Note elongation of grains in the UO_2 particles.

Metallography has proved to be very useful in the examination of ceramic fuel materials. The general appearance of the particles, grain size, shape, the presence of second phases, and assistance offered in fundamental studies can be obtained. Such a study of several ceramic fuel materials will be published.[45]

Reactor Support Activities

Metallographic assistance is required in the implementation of many phases of the over-all development effort underway at the Laboratory on various reactor projects and, for the most part, the results of this support effort appear elsewhere in the report. Consequently, only project-support work in the field of metallography which is not covered elsewhere in the report is presented below.

---

[45]R. J. Gray and C. K. H. DuBose, Metallography of Ceramic Fuel Materials, ORNL-2827 (to be published).

Homogeneous Reactor Project (T. M. Kegley, Jr.). – Examination of a type 347 stainless steel corrosion specimen which had been exposed for 1 hr at 1200°C in a wet hydrogen atmosphere revealed surface decarburization. The evidence of decarburization, which resulted in the formation of ferrite (martensite) at the specimen surface, is illustrated in Fig. 4.49(a). The presence of subsurface oxide particles was also noted on examination of the specimen in the as-polished condition, as shown in Fig. 4.49(b). This

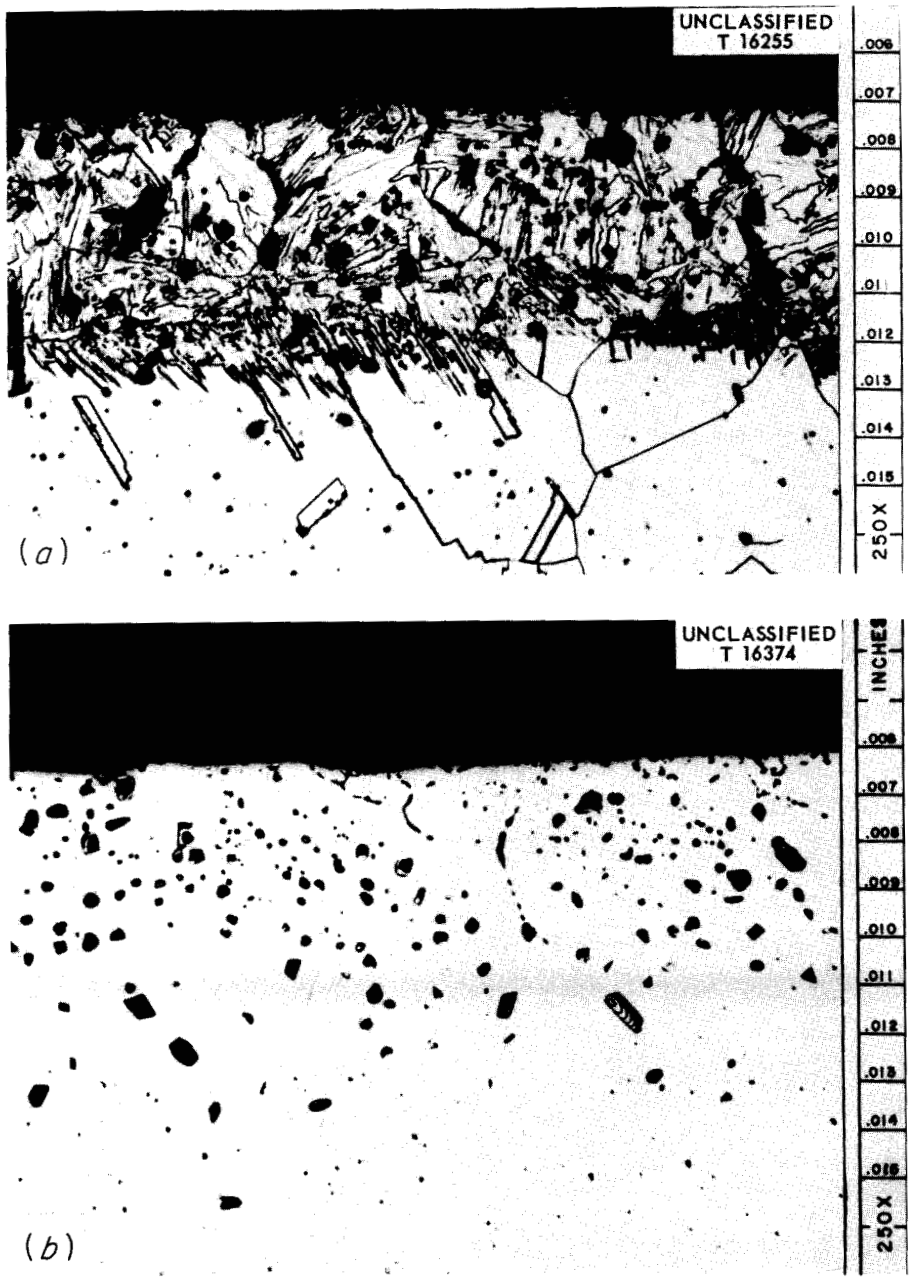

Fig. 4.49. Microstructure of Type 347 Stainless Steel Corrosion Specimen Exposed to Wet Hydrogen for 1 hr at 1200°C. (*a*) As-etched with glyceregia, showing decarburization; (*b*) as-polished condition showing subsurface oxide particles.

internal oxidation phenomenon was undoubtedly associated with decarburization.

A loop pin of cast stainless steel, type 347, exhibited extensive corrosion after exposure to a highly acid solution of uranyl sulfate. Figure 4.50 shows the loop pin and a photomicrograph of a patch of metal found in the corroded portion of the pin.

A pinhole developed in the housing of a canned-rotor pump after about 650 hr of operation, 238 of which was with uranyl sulfate. A type 347

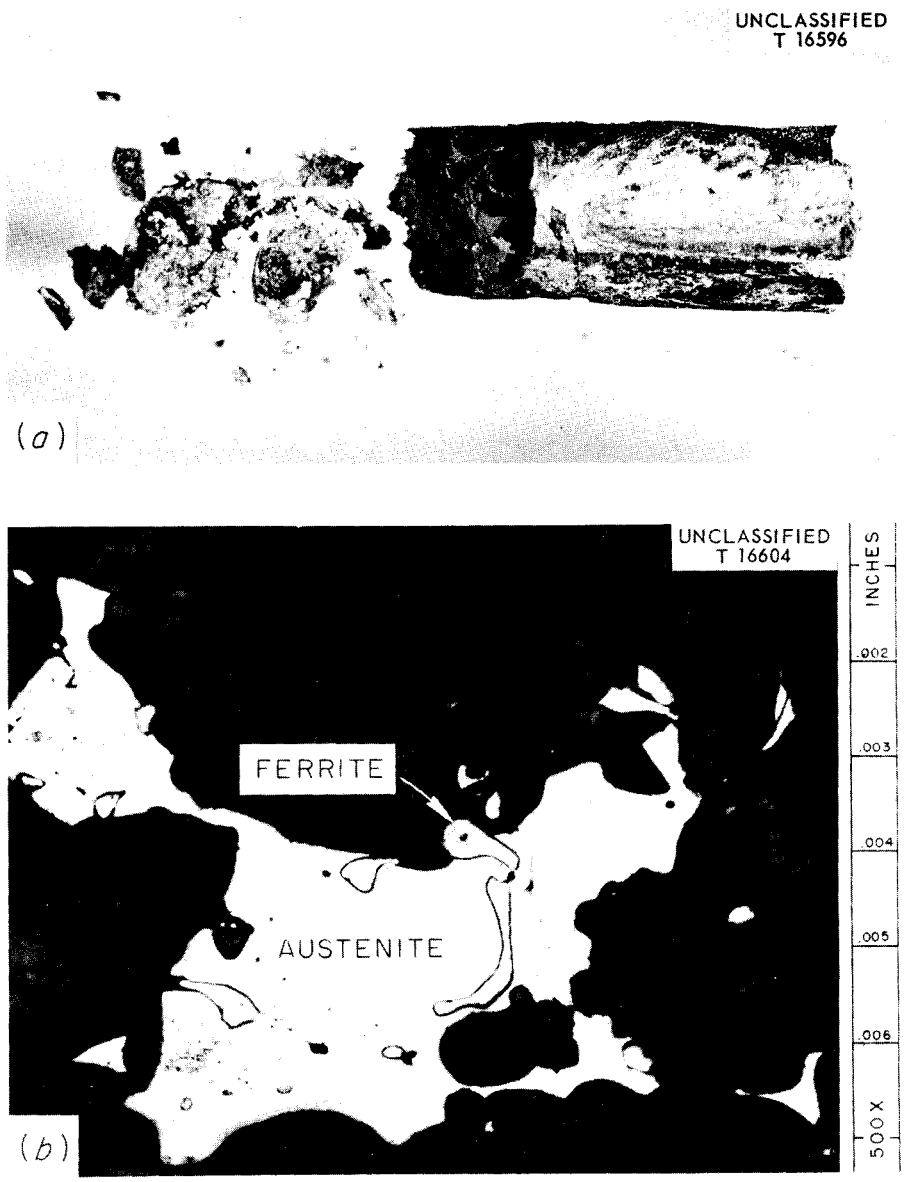

Fig. 4.50. Cast Type 347 Stainless Steel Loop Pin from Dynamic Corrosion Loop. (*a*) Corroded loop pin, 4.5X; (*b*) patch of metal found in corroded portion of pin. Etched with glyceregia.

stainless steel thermal spacer, which rested against the corroded inside surface of the housing, was corroded severely, as shown in Fig. 4.51(a). The transgranular cracks found in the "threads" of the thermal spacer are illustrated in Fig. 4.51(b).

Many Zircaloy-2 toroid pins, which had been exposed to thorium oxide slurry and hydrogen, were examined. Some of the Zircaloy-2 pins were

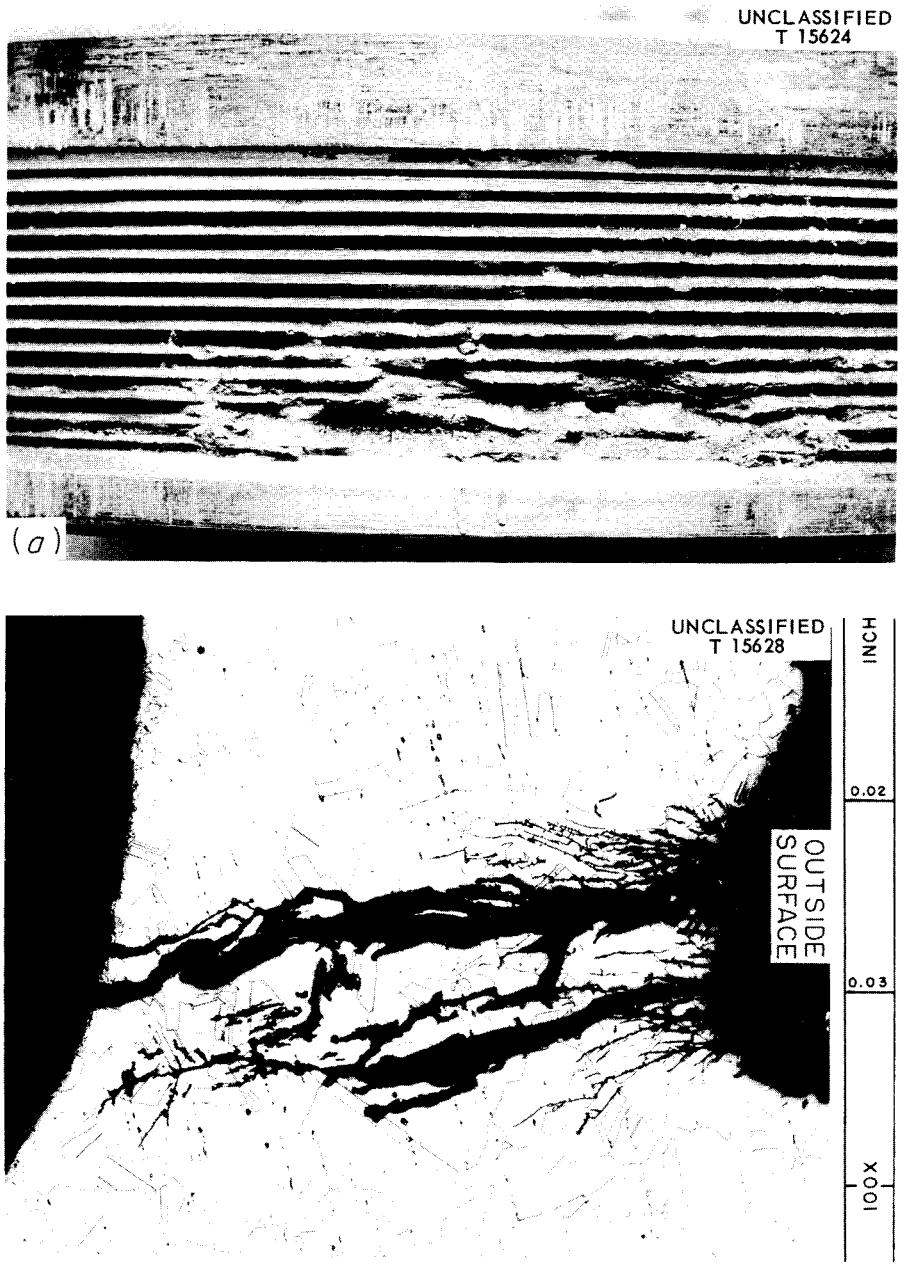

Fig. 4.51. Thermal Spacer of Type 347 Stainless Steel from Canned-Rotor Pump. (*a*) Corroded surface, 2.5X; (*b*) transgranular cracks found at base of "thread" of thermal spacer; etched with aqua regia.

cracked severely, as shown in Fig. 4.52(a). A section taken through a cracked area in one of the pins is shown in Fig. 4.52(b). The cracking was associated with the formation of hydrides within the Zircaloy-2 metal.

Aircraft Nuclear Reactor Project (R. S. Crouse). – As previously reported,[46] cycling tests were performed for the study of the effect of

---

[46]R. S. Crouse, Met. Ann. Prog. Rep. Oct. 10, 1958, ORNL-2632, p 181 (classified).

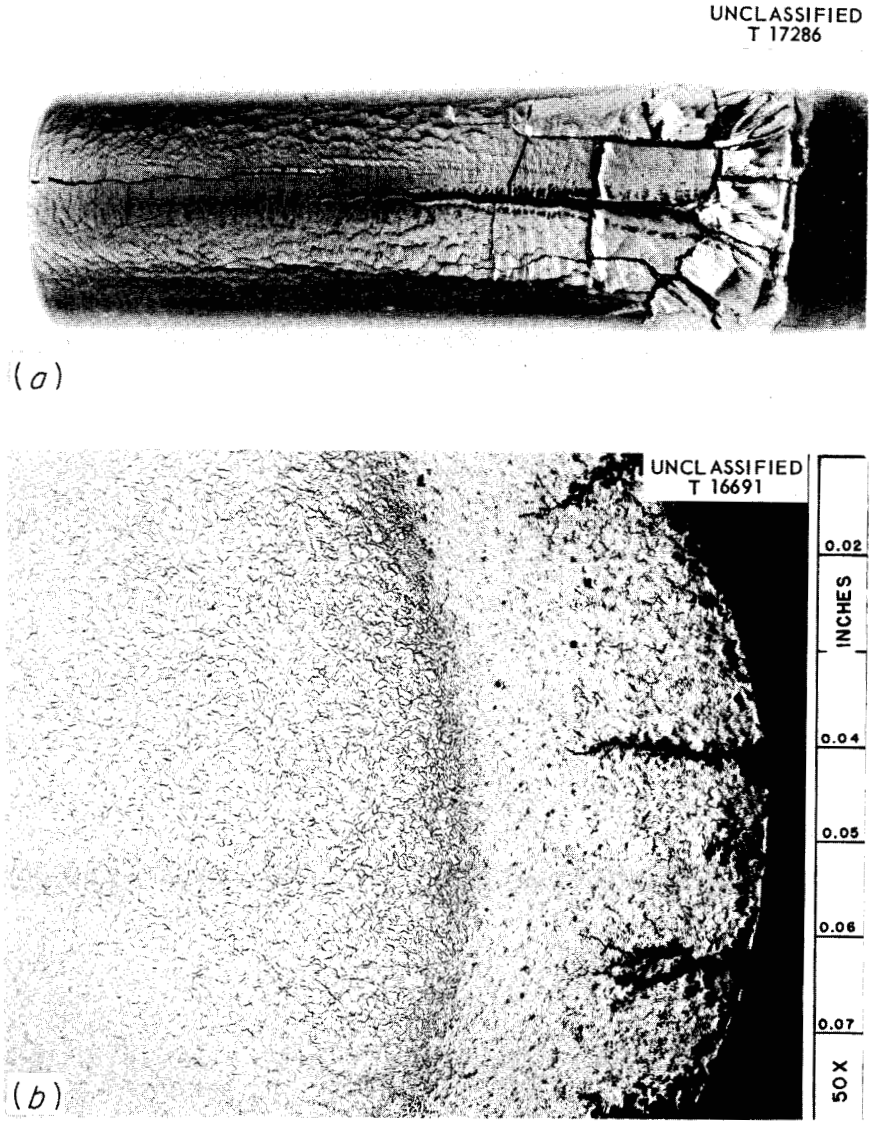

Fig. 4.52. Cracked Zircaloy-2 Toroid Pins. (*a*) Cracked surface of a pin, 10X; (*b*) section taken through cracked region of a pin, chemically polished and etched with 46 glycerine–46 HNO_3–8 HF.

drastic thermal fluctuations on Inconel tubing in various ART (Aircraft Reactor Test) heat exchanger designs. Rapid thermal fluctuations were accomplished by merely making vast temperature changes in the molten fluoride coolant. Additional tests have been completed. Test conditions and results are summarized in Table 4.16.

Gas-Cooled Reactor Project (R. S. Crouse). — Static-pot and natural-convection loop tests are underway to examine the compatibility behavior of certain structural alloys in contact with other environmental materials while under simulated reactor operating conditions. The alloys under test include types 304, 310, 316, and 410 stainless steels, Croloy 2-1/4, Croloy 3M, T-1 steel, and an Fe-Cr-Al alloy.

Table 4.16. Results of Thermal Cycling Tests on Inconel Tubing

Test No.	Time (hr)	Temp. (°F)	Max. Temp. (°F)	Frequency (cycles/sec)	Number of Cycles	Remarks
XIV	610	420	1700	1	2.2×10^6	New design; no definite cracking; void formation and "hydraulic wedging"
XV	214	568	1700	1	7.7×10^5	Same condition and results as Test XIII;* moderate cracking to 6 mils
XVI	75	570	1700	0.1	2.7×10^4	Same conditions and results as Test X;* heavy cracks to 150 mils deep

*Met. Ann. Prog. Rep. Oct. 10, 1958, ORNL-2632, Table 45, p 183 (classified).

In the static-pot tests, the alloys are in contact with graphite, in helium gas at 1400°F. In the natural-convection tests, the alloys and graphite are separated, in a helium-gas stream at 1000–1400°F. In both tests, the extent of carburization or decarburization is of primary importance and is determined by metallographic examination and microhardness tests.

At present, not enough microhardness data are available for analysis and conclusions. Microstructurally, carburization and decarburization are detected, but the relationship to the test conditions and thermal history has not been correlated.

Molten-Salt Reactor Project (R. S. Crouse). – Metallographic service for the Molten-Salt Reactor Program consists in the examination of thermal-convection and forced-circulation loops. The loops are constructed of Inconel or INOR-8, and the present emphasis is upon fuels containing various amounts of BeF_2.

Several of the INOR-8 thermal-convection loops and one forced-circulation loop have shown what appears to be a diffusion zone, or deposit, along the surface exposed to the fuel. This is the only evidence of any effect of the fuel on INOR-8 and may occur regardless of time of temperature. It is seldom thicker than 1/2 mil and is usually found only in the hot zone. Figure 4.53 shows an example of such a zone that was taken from loop 1212. This loop operated 8760 hr at 1250°F with fluoride mixture 125. Although the evidence is not complete, it appears that fuels containing BeF_2 are the ones responsible for the phenomenon.

Maritime Reactor Project (R. S. Crouse). – Several samples of UO_2 powder compacts were polished and examined. These compacts had wires of different metals inserted in them and were heated to a very high temperature. The samples were ground down until a good section was obtained and then were polished on the vibratory polisher for about 8 hr. Good definition was obtained this way, and the interface between the UO_2 and the insert was sharp. Table 4.17 is a compilation of the tests and the results of these examinations. Figure 4.54 shows the evidence of liquation and movement of gold into the UO_2 body.

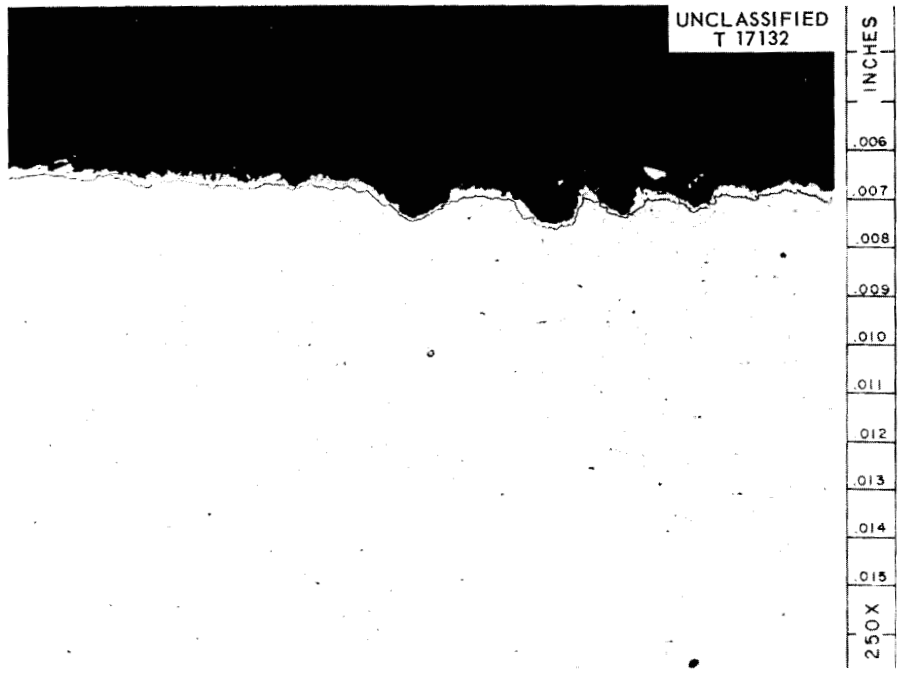

Fig. 4.53. Deposit or Diffusion Zone Found on INOR-8 Hot Zone After 8760 hr at 1250°F with Fuel 125. As-polished.

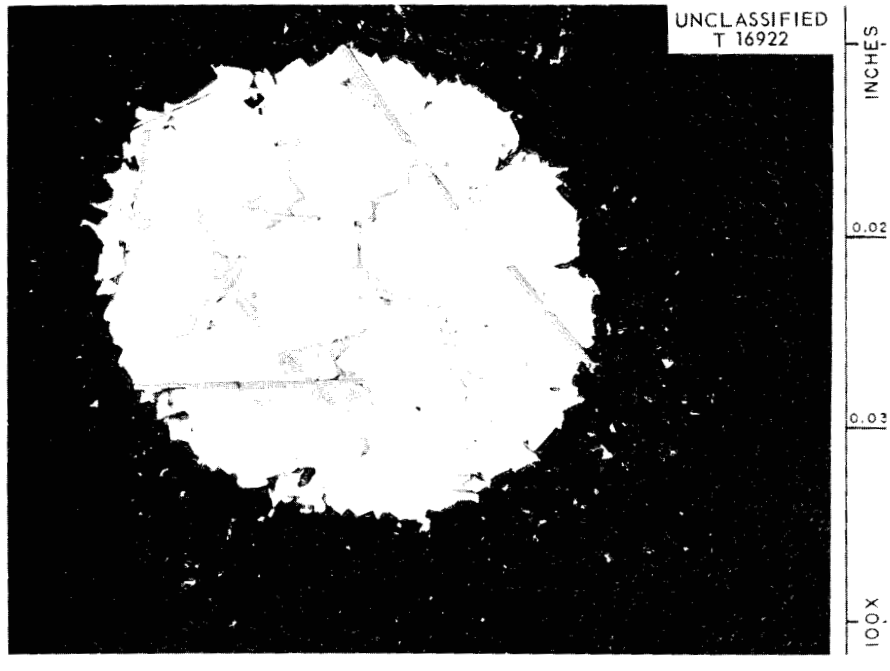

Fig. 4.54. Gold Wire in UO_2 Pellet After 2 hr at 1800°C. As-polished.

Table 4.17. Metallography of Bulk UO_2 Samples Containing Various Metal Pyrometer Wires

Insert	Time (hr)	Temperature (°C)	Results
Cu	2	1050	No change in wire shape
Cu	2	1100	Wire filled hole
Cu	2	1195	Wire filled hole
Cu	2	1800	Wire disappeared
Ni	2	1300	Wire melted partially, seemed to react with UO_2
Ni	2	1800	Wire disappeared
Fe	2	1490	Wire loose; lost in mounting
Fe	2	1535	Wire filled hole
Fe	2	1635	Wire had cast structure
Fe	2	1800	Wire disappeared
Au	2	1075	Wire filled hole
Au	2	1800	Wire filled hole; needle-like second phase; some Au in pellet surrounding wire (see Fig. 4.54)

A successful chemical polish[47] for nickel has been very useful in assisting the activities measurements program.[48] This polish consists of 60 parts CH_3COOH, 40 parts HNO_3, and 0.5 part HCl, and results in scratch-free microstructures. Figure 4.55 shows a specimen which was hand polished and then immersed in the reagent. When bubbles cover the surface, the polishing is complete and the sample should be removed immediately. Edges,

[47]P. A. Jacquet, "Electrolytic and Chemical Polishing," Met. Revs. 1(2) (1956).

[48]R. S. Crouse, Met. Ann. Prog. Rep. Oct. 10, 1958, ORNL-2632, p 183 (classified).

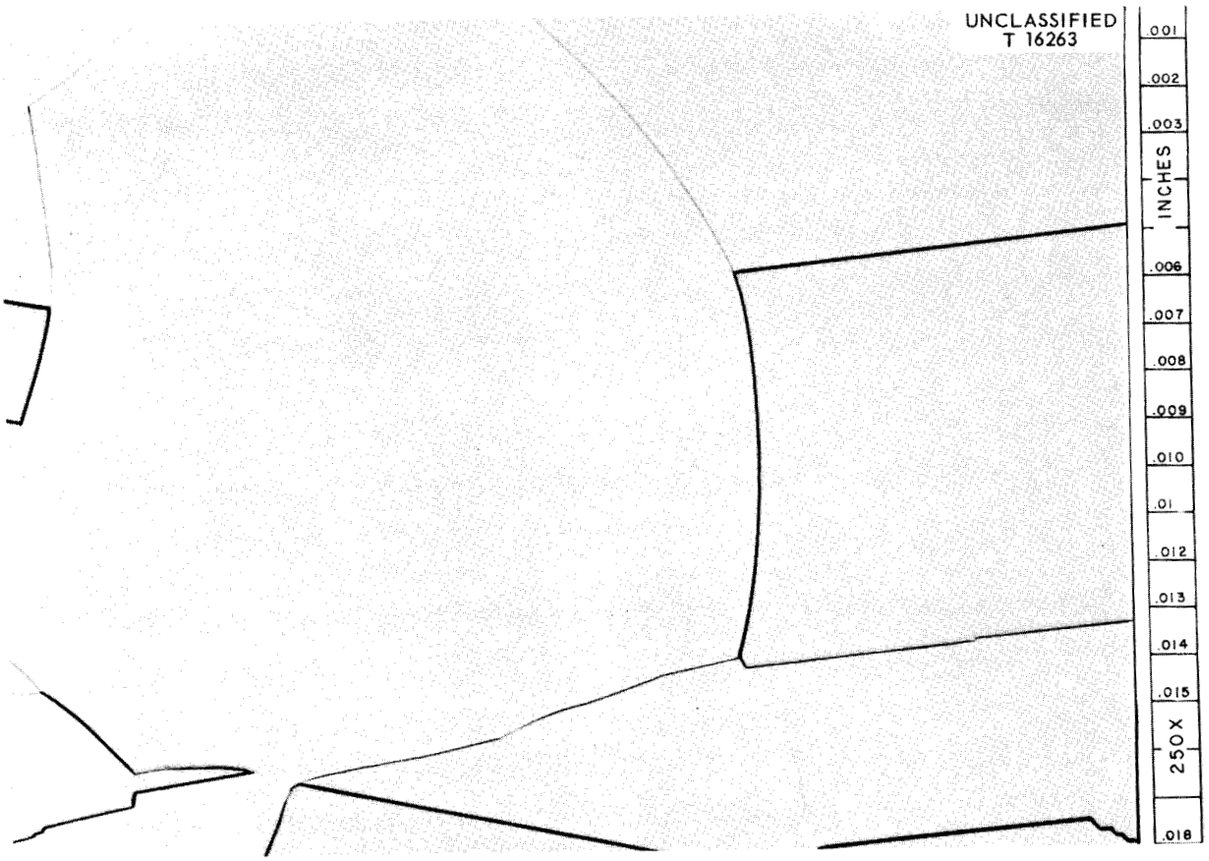

Fig. 4.55. Chemically Polished Nickel.

of course, are unsuitable for examination, but the general microstructure is good.

Equipment Development

Hot-Hardness Tester (G. Hallerman). – During the past year, some effort was devoted to the establishment of design criteria for a micro-hot-hardness tester. A literature survey and direct communications with people connected with the problems in hot-hardness testing revealed that there was no equipment in operation that met general requirements.

The preliminary design of the apparatus is now completed. It incorporates features of other testers with a number of important modifications which were conceived at this Laboratory. The unit will permit, for example, the making of a series of impressions on a single specimen without the need for breaking the vacuum or turning off the heating elements. Synthetic sapphire instead of diamond will be used as a penetrator since diamond is

susceptible to oxidation and the formation of carbides at elevated temperatures. The geometry of the indenter will be a 136°-square-based pyramid. Indentations will be made by using small loads (200–1000 g) in order to permit the testing of a variety of specimens, such as brittle and multiphase materials. The proposed design offers a certain amount of flexibility for possible future changes.

The possibility of building a second, simpler unit capable of making routine hot-hardness measurements is also being considered. This apparatus would use loads applied in standard-hardness measurements, since the problems in hot-hardness testing become more prominent with low loads. While the latter equipment would handle the bulk of routine work, the microtester would be reserved for hard, brittle materials, which require low loads, and for specimens in which the hardness of individual phases is to be determined.

Ultrasonic "Jack Hammer" (G. Hallerman). – Preliminary investigations were made to improve operation of the ultrasonic jack hammer.[49] Contact was established with Columbia University, where a similar apparatus is in operation.[50] To improve the performance of the unit, a better method of preparing the pointed stylus is under investigation. Also, a hooding arrangement, placed over the specimen during extraction, is being considered. This arrangement, with purified argon passing through it, may be necessary to prevent oxidation of the extracted particles caused by the frictional heat of the vibrating stylus.

Hot-Stage Microscopy (J. E. VanCleve, Jr.). – Development work on the hot-stage microscope, reported previously,[51] was begun early in the year. There was one major shortcoming with the commercial unit: the extreme difficulty in obtaining the high degree of vacuum necessary to halt the formation of thin oxide films on reactive metals at elevated temperatures. These thin films obscure the surface and make the examination extremely difficult or impossible.

---

[49]C. Hays, Met. Ann. Prog. Rep. Oct. 10, 1958, ORNL-2632, p 186 (classified).

[50]G. L. Kehl, H. Steinmetz, and W. J. McGonnagle, Laboratory Methods 55(329), 151 (1957).

[51]J. E. VanCleve, Jr., and J. R. Riddle, Met. Ann. Prog. Rep. Oct. 10, 1958, ORNL-2632, p 189 (classified).

The furnace windings were surrounded with a thick ceramic insulating material that released a large quantity of gas on each heating cycle and either obscured the viewing window or reacted with the sample. The more salient features of several different types of furnaces were examined in an effort to eliminate this problem. It was decided that, due to the gassing problem and the limited space available within the furnace chamber, the most promising furnace would be one of the solar type. Consequently, a focused-beam heat lamp was purchased.

Cold-Stage Microscopy. — The cold-stage unit, as designed by J. R. Riddle, was received after fabrication, and several experiments were tried.

An effort was made to study the topographical changes in the polished surface of a sample of cerium during the low-temperature transformation. The sample was cycled between room temperature and liquid-nitrogen temperature.

The surface changes proved to be quite subtle and defied analysis, without a permanent record for a more leisurely examination. A 35-mm camera was purchased and adapted to the unit. Preliminary tests were satisfactory; however, a higher priority program necessitated halting work on this project, and it will be resumed at some later time.

Metallography of Irradiated Materials

High-Radiation-Level Examination Laboratory. — A list of all the equipment considered necessary to make a complete metallographic analysis within the confines of a hot cell in the high-radiation-level examination laboratory was prepared. These items are schematically located within a 6- × 6-ft working area in order to provide ease of viewing and access. The majority of the items were approved and purchased.

Upon receipt of the equipment, and with the assistance of the Engineering Division, the adaptation for remote operation was undertaken; this work is presently underway.

A darkroom complex was fitted into the allocated space, and again, equipment requirements were listed. These items will be purchased in the future.

The gamma hot cells operated by the Solid State Division offer problems similar to those which will be encountered in the new facility. A

training program is presently underway in these cells. The tenure of each man in the program was estimated to be from three to four months, and by moving men in and out, it would be possible to train from twelve to fifteen men before construction is finished.

These "trained" men would not be fully competent hot-cell operators but would at least have some idea of the type work which they would be doing. The program also allows the men to reach a decision as to whether they prefer this type of work before any permanent assignment change takes place. The attitudes of the men are observed and evaluated by the more experienced cell-men, and any man who shows temperament difficulties, such as inordinate fear of radiation, may be advised against such work.

Experience with Vibratory Polishers and Design for Hot-Cell Applications (E. L. Long, Jr.). — The vibratory polishers have been in operation for over 2-1/2 years and are now considered as standard metallographic equipment in this laboratory. Six polishers are operating in the ORNL Metallographic Laboratory, two polishers have been installed in the Y-12 Metallographic Laboratory, and three are planned for an additional small laboratory. Eleven are necessary for the operation of the three laboratories, considering the variety of samples that require various abrasives and vehicles. An estimated 90% of the samples processed through these laboratories are now polished by vibratory polishers.

One innovation has been made which has increased the flexibility of the polishers. Twenty-four-hour timers were installed, which allows the technicians to use the polishers 24 hr/day or any portion of the 16-hr period at night; this was formerly thought of as overtime expense.

With the advent of the proposed HRLEL (High-Radiation-Level Examination Laboratory), the feasibility of making remotely operated vibratory polishers was investigated. Several designs were considered and one fulfilled the following requirements:

1. That the polishing cloths should be easily replaceable by remote manipulation.
2. That the clamping devices, bowl weights, and other equipment should be easily operable by means of the Mark VIII or IX manipulators.
3. That the design criteria should be sufficiently flexible, allowing for the alteration of the vibratory system without impairing the polishing action and, if possible, permitting improvements.

A prototype polisher was fabricated and met the above requirements and has operated satisfactorily for over 500 hr. The assembled prototype polisher is shown in Fig. 4.56. An exploded view of the remote vibratory polisher is shown in Fig. 4.57. The three major components for remote operation are the adapter plate with the toggle clamps, the polishing bowl, and a hoop and O-ring which holds the polishing cloth.

A typical hot-cell operation for changing cloths would involve mounting a new cloth on the hoop, which is held in place with a steel O-ring. The new cloth, hoop, and O-ring are considered as a replaceable unit that

UNCLASSIFIED
Y 30914

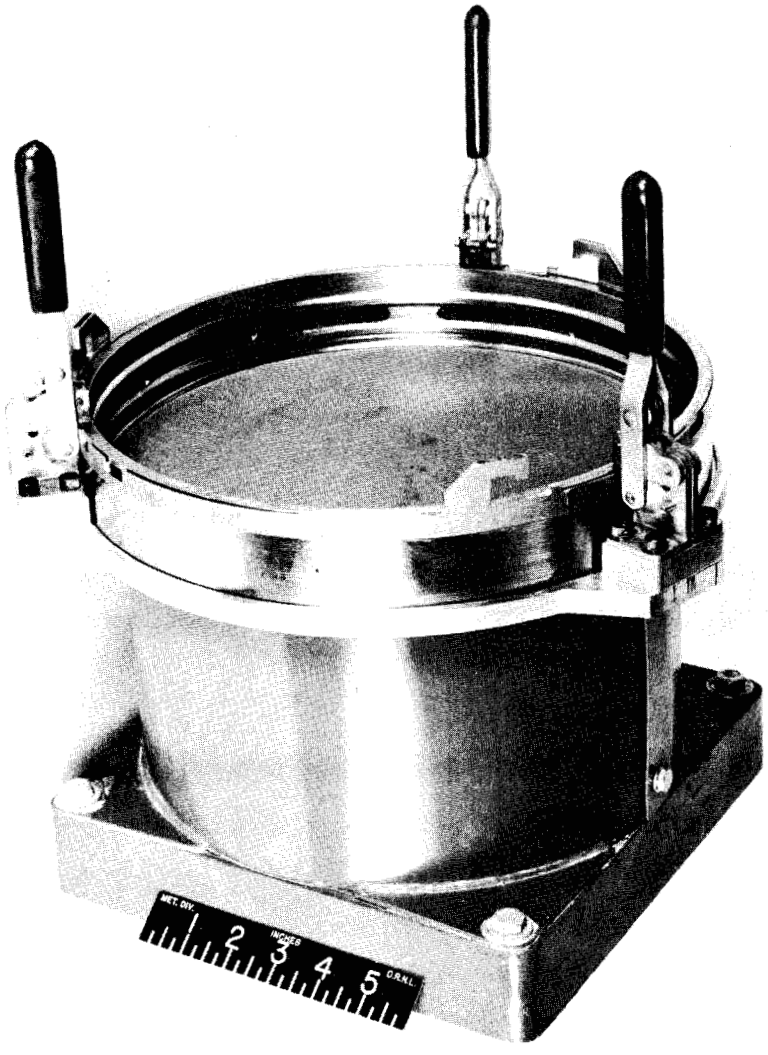

Fig. 4.56. The Assembled Prototype Vibratory Polisher Designed for Remote Operations.

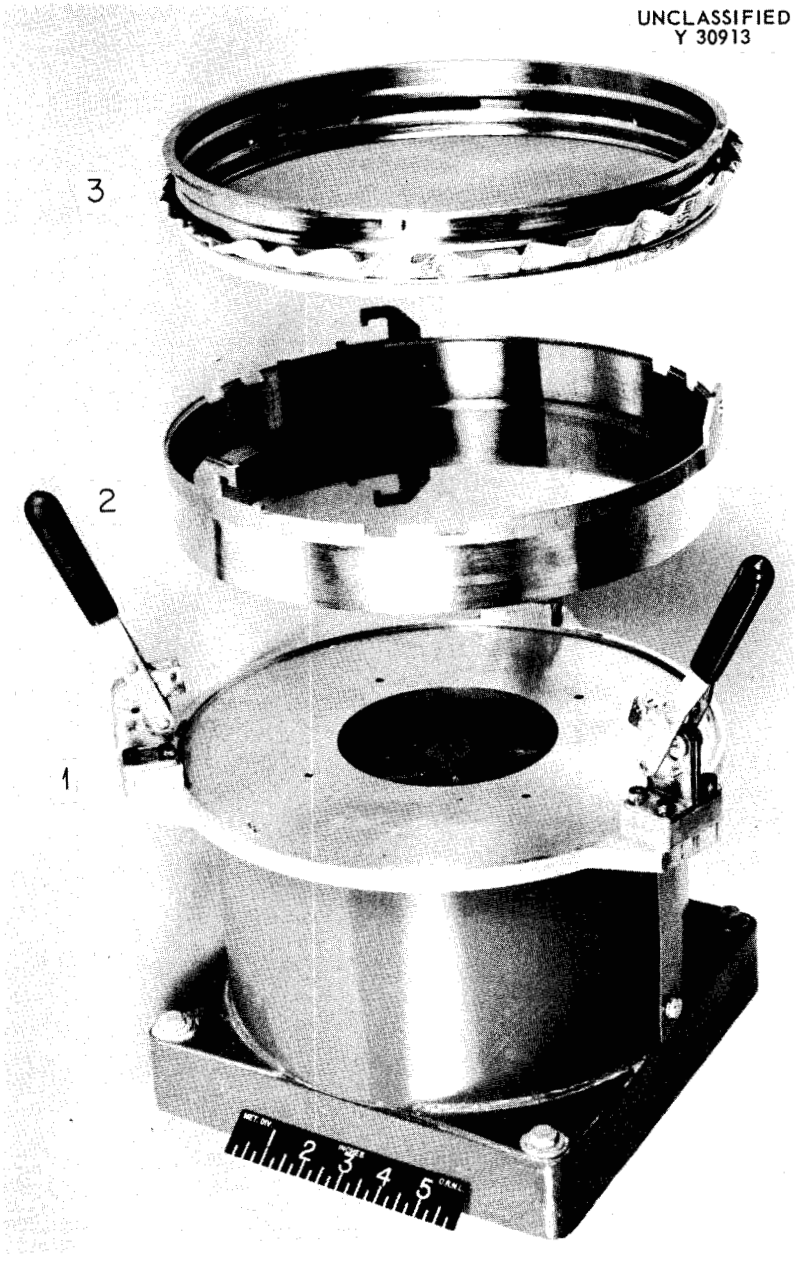

Fig. 4.57. An Exploded View of the Prototype Vibratory Polisher Showing the Three Major Components for Remote Operation: (1) Adapter Plate with Toggle Clamps; (2) Polishing Bowl; (3) Hoop, Cloth, and Steel O-Ring.

can be assembled and kept clean in a plastic bag outside the hot cell. The clean hoop and O-ring holding the cloth can be taken into the cell, removed from the plastic bag, placed in a polishing bowl with the manipulators, and clamped to the bowl and adapter plate with the toggle clamps. The polishing bowl itself can be removed for cleaning, as required, by using a lifting spider on the three hooks on the lip of the bowl. At

present, a finalized design that will establish tolerances ensuring the interchangeability of all components in the hot cells is being fabricated.

To complement the polishing process, remote sample holders were designed. The holder is shown in Fig. 4.58, without and with the sample inserted. The samples are held in place by a three-prong spider arrangement. The specimen is simultaneously positioned and secured by pushing the holder onto the specimen. The advantages of this type of holder are that ultrasonic cleaning is facilitated, since all small crevices are eliminated; also, in-cell operation is simplified, since Allen screws are not required for securing the specimen in place and since the specimen is self-aligned.

UNCLASSIFIED
Y 31023

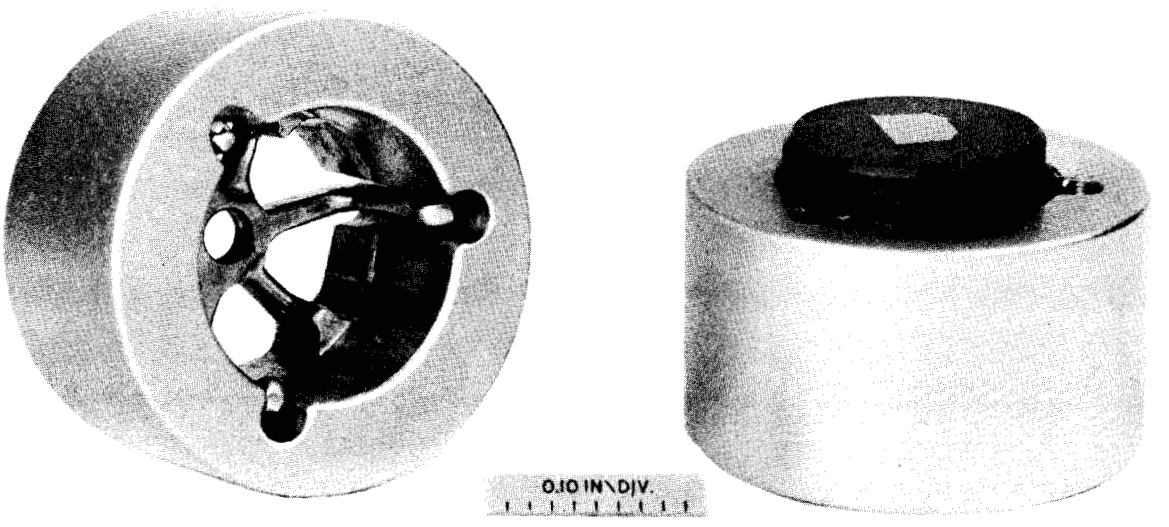

Fig. 4.58. Remote Specimen Holder for Vibratory Polisher. Note three-prong spider arrangement for holding and aligning specimen.

PUBLICATIONS

Allen, J. W., and R. W. McClung, An Electronic, High-Resolution, X-Ray Imaging System, ORNL-2671 (Aug. 11, 1959).

Adamson, G. M., R. S. Crouse, and W. D. Manly, Interim Report on Corrosion by Alkali-Metal Fluorides: Work to May 1, 1953, ORNL-2337 (Mar. 20, 1959).

Allen, J. W., Eddy-Current Testing in Practice, ORNL-2655 (Apr. 16, 1959).

Beaver, R. J., and J. E. Cunningham, "Recent Developments in Aluminum-Base Fuel Elements for Research Reactors," Fuel Elements Conference Held at Gatlinburg, Tenn., May 14–16, 1958, TID-7559 (Part 1) p 40 (August 1959).

Borie, B., "X-Ray Diffraction Effects of Atomic Size in Alloys. II," Acta Cryst. 12(4), 280 (1959).

Bridges, W. H., and E. L. Long, "A Technique for the Easy Removal of 'Direct' Replicas for Electron Microscopy," Am. Soc. Testing Materials, Spec. Tech. Publ. No. 245, (1958).

Clausing, R. E., P. Patriarca, and W. D. Manly, "Aging Characteristics of Hastelloy B," Trans. Am. Soc. Metals 51, 123–35 (1959).

Coobs, J. H., "Advanced Materials Development," Information Meeting on Gas-Cooled Reactors Oak Ridge National Laboratory October 21–22, 1958, TID-7564, p 363–72 (December 1958).

Cunningham, J. E., and R. J. Beaver, "Stainless-Steel Uranium Dioxide Fuel Components for Army Power Package Reactor," Nuclear Metallurgy, vol 5, p 29–40, IMD Special Report Series No. 7, Metallurgy Society of AIME, New York, 1958.

Cunningham, J. E., R. J. Beaver, R. D. Robertson, and E. C. Edgar, Specifications and Fabrication Procedures for APPR-1 Core II Stationary Fuel Elements, ORNL-2649 (Jan. 29, 1959).

Curtis, C. E., and A. G. Tharp, "Ceramic Properties of Europium Oxide," J. Am. Ceram. Soc. 42(3), 151–56 (1959).

Douglas, D. A., and J. R. Weir, The Recrystallization and Grain Growth of Inconel, ORNL-2406 (Nov. 3, 1958).

Evans, R. M. (ed.), Oak Ridge National Laboratory Reactor Material Specifications, TID-7017 (Oct. 29, 1958).

Franco-Ferreira, E. A., and P. Patriarca, The Inert-Gas-Shielded Metal-Arc Welding of Titanium, ORNL-2612 (Feb. 16, 1959).

Harris, L. A., "The Crystal Structures of Na_3ZrF_7 and Na_3HfF_7," Acta Cryst. 12(2), 172 (1959).

Harris, L. A., "Preliminary Study of the Phase Equilibria Diagram of ThO_2-SiO_2," J. Am. Ceram. Soc. 42(2), 74–77 (1959).

Hoffman, E. E., ORNL-2675 (Jan. 16, 1959) (classified).

Hoffman, E. E., Corrosion of Materials by Lithium at Elevated Temperatures, ORNL-2674 (Mar. 9, 1959) (classified).

Jansen, D. H., E. E. Hoffman, and D. M. Shepherd, Lead-Lithium Shielding Alloy – Metallurgical Studies, ORNL-2404 (Mar. 9, 1959).

Kennedy, C. R., and D. A. Douglas, High-Temperature Mechanical Properties of Hastelloy B and Hastelloy W, ORNL-2402 (Nov. 13, 1958).

Kennedy, C. R., W. O. Harms, and D. A. Douglas, Multiaxial Creep Studies on Inconel at 1500°F, ORNL-2622 (Jan. 19, 1959).

Kerr, J. M., "Preliminary Tests on Clay Sinters to Retain Reactor Wastes," Am. Ceram. Soc. Bull. 38(7), 374–77 (1959).

Leitten, C. F., Jr., R. J. Beaver, W. J. Kucera, and J. E. Cunningham, Specifications and Fabrication Procedures for SM-1 Core II Control Rod Fuel Elements, ORNL-2726 (July 29, 1959).

Leitten, C. F., Jr., R. J. Beaver, and J. E. Cunningham, Specifications and Fabrication Procedures on Europium-Bearing Absorber Rods for Reactivity Control in Core II of SM-1, ORNL-2733 (July 29, 1959).

Leitten, C. F., Jr., R. J. Beaver, and A. E. Richt, "Stainless Steel Clad Dispersion of Boron in Iron for Pressurized Water Reactors," J. Nuclear Materials 2, 136–44 (1959).

Long, E. L., and R. J. Gray, "Better Metallographic Techniques ... Polishing by Vibration," Metal Progr. 74(4), 145–48 (1958).

Manly, W. D., and J. H. Coobs, "Materials Selections and Development Work," Information Meeting on Gas-Cooled Reactors Oak Ridge National Laboratory October 21–22, 1958, TID-7564, p 138–64 (December 1958).

McClung, R. W., The Immersed Ultrasonic Inspection of Metal Plate, ORNL-2650 (Mar. 20, 1959).

McHargue, C. J., and L. K. Jetter, "Preferred Orientation in Uranium, Thorium, Zirconium and Beryllium," Progr. in Nuclear Energy, Ser. V 2, 430–59 (1959).

Metallurgy Division, ANP Materials Meeting November 16–18, 1954, ORNL-2685 (Mar. 12, 1959) (classified).

Nance, R. A., and J. W. Allen, Eddy-Current Measurement of Metal Thickness and Cladding Thickness, ORNL-2672 (Mar. 31, 1959).

Patriarca, P., and R. L. Heestand, "A Bulk UO_2-Stainless Steel Fuel Element for a Gas-Cooled Reactor," Fuel Elements Conference Held at Gatlinburg, Tenn., May 14–16, 1958, TID-7559 (Part 1) p 191 (August 1959).

Sax, N. I., and H. Steinmetz, Determination of Oxygen in Lithium Metal, ORNL-2570 (Oct. 15, 1958).

Slaughter, G. M., P. Patriarca, and R. E. Clausing, Welding of Nickel-Molybdenum Alloys, ORNL-2760 (Aug. 11, 1959).

Smith, G. P., G. F. Petersen, and W. M. Ewing, Densities of Some Molten Salt Mixtures Containing Nitrates, ORNL-2762 (Aug. 6, 1959).

Swindeman, R. W., and D. A. Douglas, The Failure of Structural Metals Subjected to Strain-Cycling Conditions, ORNL-2619 (Oct. 23, 1958); Trans. Am. Soc. Mech. Engrs. Ser. D, 81(2), 203–12 (1959).

Swindeman, R. W., and D. A. Douglas, Improvement of the High-Temperature Strength Properties of Reactor Materials After Fabrication, ORNL-2687 (May 8, 1959); J. Nuclear Materials 1, 49–57 (1959).

Tennery, V. J., Review of Thermal Conductivity and Heat Transfer in Uranium Dioxide, ORNL-2656 (Apr. 9, 1959).

Thompson, E. G., The Effect of Simulated Weld Thermal Cycles on the Properties of Hastelloy B, ORNL-2582 (Oct. 14, 1958).

Thurber, W. C., Deformation Textures in Uranium-Aluminum Alloys, ORNL-2635 (Nov. 4, 1958).

Thurber, W. C., and R. J. Beaver, Development of Silicon-Modified 48 wt % U–Al Alloys for Aluminum Plate-Type Fuel Elements, ORNL-2602 (Mar. 9, 1959).

Thurber, W. C., and R. J. Beaver, "Silicon-Modified Uranium-Aluminum Alloys for Foreign Reactor Application," Nuclear Metallurgy, vol 5, p 57–62, IMD Special Report Series No. 7, Metallurgy Society of AIME, New York, 1958.

Waugh, R. C., The Reaction and Growth of Uranium Dioxide–Aluminum Fuel Plates and Compacts, ORNL-2701 (Mar. 9, 1959).

White, J. K., R. W. McClung, and J. W. Allen, Implications of Ultrasonic Attenuation to Nondestructive Testing, ORNL-2651 (Mar. 30, 1959).

PAPERS PRESENTED AT SCIENTIFIC AND TECHNICAL MEETINGS

Allen, J. W., "Recent Developments in Nondestructive Testing," Annual Quality Control Convention, Cleveland, Ohio, May 25–27, 1959.

Allen, J. W., and R. W. McClung, "An Electronic, High-Resolution, X-Ray Imaging System," Society for Nondestructive Testing, Cleveland, Ohio, Oct. 27–31, 1958 [Nondestructive Testing, 16(5), 412 (1958)].

Beaver, R. J., "Stainless Steel-Clad Dispersions of Boron in Iron for Pressurized Water Reactors," Control-Rod Materials Meeting, Pleasonton, Calif., Feb. 12–13, 1959.

Borie, B. S., "Short Range Order in the Alloy Copper–16 Atomic Percent Aluminum," Annual Pittsburgh X-Ray Conference, Mellon Institute, Pittsburgh, December 1958.

Cathcart, J. V., "The Effect of In-Pile Radiation on the Oxidation of Nb," 8th Annual AEC Corrosion Symposium, Hanford, Wash., May 12–15, 1959.

Clausing, R. E., P. Patriarca, and W. D. Manly, "Aging Characteristics of Hastelloy B," National Metals Congress of American Society for Metals Congress of American Society for Metals, Cleveland, Ohio, Oct. 26–31, 1958.

Coobs, J. H., "Advanced Materials Development," Information Meeting on Gas-Cooled Reactors, Oak Ridge National Laboratory, Oct. 21–22, 1958.

Cunningham, J. E., "Dispersion-Type Elements," First International Symposium on Nuclear Fuel Elements, Columbia University, New York, Jan. 28–29, 1959.

Cunningham, J. E., and R. J. Beaver, "Stainless Steel–Uranium Dioxide Fuel Components for Army Package Power Reactor," AIME-IMD Nuclear Metallurgy Symposium, National Metals Congress, Cleveland, Ohio, Oct. 27–31, 1958.

Curtis, C. E., "Further Studies in the Sintering of Rare Earth Oxides," Rare Earth Symposium, National Convention of American Ceramic Society, Chicago, Ill., May 17–21, 1959 [Am. Ceram. Soc. Bull. 38(4) 171 (1959)].

DeVan, J. H., and A. M. Smith, "Effects of Contaminants Outgassed from Graphite on Structural Materials in High-Temperature Gas," 1959 Annual Meeting American Nuclear Society, Gatlinburg, Tenn., June 15–17, 1959 [Trans. Am. Nuclear Soc. 2(1) 26 (1959)].

Federer, J. I., R. E. Adams, and R. C. Waugh, "Application of Magnesium Diffusion to the Reprocessing of Zirconium-Clad Fuel Elements," American Nuclear Society, Detroit, Mich., Dec. 8–10, 1958.

Kennedy, C. R., and D. A. Douglas, "Multiaxial Creep Studies on Inconel at 1500°F," American Society for Engineers, New York, Nov. 30–Dec. 5, 1958.

Leitten, C. F., Jr., "Development of Eu_2O_3-Bearing Stainless Steel Dispersions," Control-Rod Materials Meeting, Pleasonton, Calif., Feb. 12–13, 1959.

Manly, W. D., and J. H. Coobs, "Materials Selections and Development Work," Information Meeting on Gas-Cooled Reactors, Oak Ridge National Laboratory, Oct. 21–22, 1958.

McClung, R. W., "The Immersed Ultrasound Inspection of Metal Plate," Society for Nondestructive Testing, Cleveland, Ohio, Oct. 27–31, 1958 [Nondestructive Testing 16(5), 410 (1958)].

Nance, R. A., and J. W. Allen, "Eddy-Current Measurements of Metal Thickness and Cladding Thickness," Society for Nondestructive Testing, Cleveland, Ohio, Oct. 27–31, 1958 [Nondestructive Testing 16(5), 410 (1958)].

Scott, J. L., "Liquid-Metal Diffusion," 8th Annual AEC Corrosion Symposium, Hanford, Wash., May 12–15, 1959.

Scott, J. L., and H. W. Leavenworth, "The Solubility and Rate of Diffusion of Nickel in Lead," AIME International Symposium on Physical Chemistry of Process Metallurgy, Pittsburgh, Pa., Apr. 27–30, 1959.

Slaughter, G. M., P. Patriarca, and R. E. Clausing, "Welding of Nickel-Molybdenum Alloys," Spring Technical Meeting of American Welding Society, Chicago, Ill., Apr. 6–10, 1959.

Smith, G. P., and C. R. Boston, "Absorption Spectra of Fused-Salt Solutions," Symposium on Fused Salts, New York Academy of Sciences, New York, Apr. 13, 1959.

Swindeman, R. W., and D. A. Douglas, "The Failure of Structural Metals Subjected to Strain-Cycling Conditions," American Society for Engineers, New York, Nov. 30–Dec. 5, 1958 [Trans. Am. Soc. Mech. Engrs. Ser. D, 81(2), 203 (1959)].

Taylor, A. J., "Development of UO_2 as a Fuel for a Gas-Cooled Reactor," The American Ceramic Society, Southeastern Section, Summer Meeting, Gatlinburg, Tenn., June 26, 1959.

Thurber, W. C., and R. J. Beaver, "Silicon-Modified Uranium-Aluminum Alloys for Foreign Reactor Application," AIME-IMD Nuclear Metallurgy Symposium, National Metals Congress, Cleveland, Ohio, Oct. 27–31, 1958.

Tolson, G. M., A. Taboada, and R. Stepp, "Radiographic Inspection of Thin-Walled Small-Diameter Tubing," American Society for Metals, National Exposition and Congress, Cleveland, Ohio, Oct. 27–31, 1958 [Nondestructive Testing 16(5), 416 (1958)].

Toner, D. F., "Studies of Thermal-Gradient Mass Transfer," 8th Annual AEC Corrosion Symposium, Hanford, Wash., May 12–14, 1959.

Waugh, R. C., "The Reaction and Growth of Uranium Dioxide–Aluminum Fuel Plates and Compacts," 1959 Annual Meeting of American Nuclear Society, Gatlinburg, Tenn., June 15–17, 1959 [Trans. Am. Nuclear Soc. 2(1) 46 (1959)].

White, J. K., R. W. McClung, and J. W. Allen, "Implications of Ultrasonic Attenuation to Nondestructive Testing," Society for Nondestructive Testing, Cleveland, Ohio, Oct. 27–31, 1958 [Nondestructive Testing 16(5), 419 (1958)].

Woods, J. W., and D. A. Douglas, "Some Materials Problems in Operating a Metal Clad Uranium Dioxide Fuel Element Above 1200°F," 1959 Annual Meeting American Nuclear Society, Gatlinburg, Tenn., June 15–17, 1959 [Trans. Am. Nuclear Soc. 2(10) 46 (1959)].

Yakel, H. L., and M. L. Picklesimer, "Structural Changes During Aging of Zr-Nb Alloy," Summer Meeting of the American Crystallographic Association, Cornell University, Ithaca, N.Y., July 19–24, 1959.

METALLURGY DIVISION
AT
THE OAK RIDGE NATIONAL LABORATORY

SEPTEMBER 1, 1959

DIRECTOR — J. H. FRYE, JR.
ASSOCIATE DIRECTOR — B. F. BYRUM, SEC.; W. D. MANLY*; L. M. ROWE, SEC.
ASSISTANT DIRECTOR — J. E. CUNNINGHAM*; M. B. WHITE,* SEC.

ADMINISTRATIVE ASSISTANT
L. E. BANKER
M. J. BOLINGER, SEC.

FUNDAMENTAL METALLURGY
B. S. BORIE*
B. L. BALLARD,* SEC.

PHYSICOMETALLURGICAL RESEARCH
L. K. JETTER*

STRUCTURE OF METALS
C. J. MCHARGUE
J. C. OGLE

THEORY OF ALLOYING
J. O. BETTERTON, JR.
G. D. KNEIP, JR.
D. S. EASTON
J. O. SCARBROUGH

X-RAY DIFFRACTION
H. L. YAKEL, JR.
O. B. CAVIN
L. A. HARRIS
R. M. STEELE

MICROSTRESSES IN CRYSTALS
B. S. BORIE*
C. J. SPARKS, JR.
J. C. RICHTER

HIGH-TEMPERATURE REACTIONS
G. P. SMITH, JR.
M. D. MONTGOMERY,* SEC.
C. R. BOSTON
J. J. MCBRIDE
W. M. EWING

REACTIONS AT METAL SURFACES
J. V. CATHCART
G. F. PETERSEN
R. E. PAWEL
J. J. CAMPBELL
J. E. EPPERSON

FUNDAMENTAL CERAMICS STUDIES
G. W. CLARK
C. B. FINCH
T. L. BOSWELL

DEFORMATION OF CRYSTALLINE SOLIDS
R. O. WILLIAMS

HRP METALLURGY
G. M. ADAMSON, JR.
F. LOVING,[2] SEC.
F. W. COOKE
W. J. LEONARD
C. H. WODTKE
C. M. SMITH, JR.

ZIRCONIUM ALLOY DEVELOPMENT
M. L. PICKLESIMER
M. D. MONTGOMERY,* SEC.
P. L. RITTENHOUSE
R. L. STEPHENSON
P. J. JONES
G. C. NELSON
J. J. WOODHOUSE, JR.

DIVISION SERVICES

PROCUREMENT AND MAINTENANCE
R. J. STEERE
R. B. PRATT[1]
K. P. BAYNE
M. E. BOTHWELL
J. S. CORUM[2]
C. E. DUNN

BUDGET
R. G. CARDWELL, JR.
P. A. MARTIN

CONSULTANTS
N. CABRERA, UNIV. OF VA.
J. F. ECKEL, VPI
J. F. ELLIOTT, MIT
N. J. GRANT, MIT
J. L. GREGG, CORNELL UNIV.
W. O. HARMS, UT
W. D. JORDAN, UNIV. OF ALA.
**J. H. KOENIG, RUTGERS
O. C. KOPP, UT
J. KORRINGA, OHIO STATE
**H. LEIDHEISER, JR., VA. RES. INST.
T. N. MCVAY
R. S. MATEER, UNIV. OF KY.
L. MITCHELL, GA. TECH.
J. W. PIRADOS, UT
T. S. SHEVLIN, OHIO STATE
**C. S. SMITH, UNIV. OF CHICAGO
E. E. STANSBURY, UT
J. B. WAGNER, YALE UNIV.
**H. A. WILHELM, IOWA STATE COL.

**MEMBER, ADVISORY COMMITTEE

*MULTIPLE LISTING
[1]ON LOAN FROM E AND M
[2]ON LOAN FROM IND. REL.
[3]ON LOAN FROM REED
[4]ON LOAN FROM ACF
[5]ON LOAN FROM TVA
[6]ON LOAN TO SOLID STATE
[7]ON LOAN FROM APDA

REACTOR METALLURGY
W. D. MANLY*
L. M. ROWE, SEC.

METALLURGY REPORTS OFFICE
M. R. HILL
F. R. FINN
G. B. HARRIS
L. M. PYATT

MECHANICAL PROPERTIES
D. A. DOUGLAS, JR.
J. R. MORRISON, SEC.
C. W. DOLLINS
C. R. KENNEDY
H. E. MCCOY, JR.
W. R. MARTIN
R. W. SWINDEMAN
J. R. WEIR, JR.
J. W. WOODS
F. L. BEELER
K. W. BOLING
E. BOLLING
V. R. BULLINGTON
J. T. EAST
V. G. LANE
B. MCNABB, JR.
E. B. PATTON, JR.
C. K. THOMAS
C. W. WALKER

NONDESTRUCTIVE TEST DEVELOPMENT
J. W. ALLEN
M. D. MONTGOMERY,* SEC.
R. W. MCCLUNG
R. A. NANCE
D. E. CONNER
R. A. CUNNINGHAM, JR.
W. J. MASON

HIGH-TEMPERATURE ALLOY DEVELOPMENT
H. INOUYE
B. L. BALLARD,* SEC.
D. O. HOBSON
T. K. ROCHE
W. J. WERNER
J. W. BARNETT
J. F. NEWSOME
J. E. POPE

ELECTRON BEAM MELTING LABORATORY
T. HIKIDO
G. E. ANGEL

GAS-COOLED REACTOR PROJECT
J. H. COOBS
A. E. GOLDMAN
E. A. WICK[4]
R. M. EVANS

WELDING AND BRAZING
P. PATRIARCA
M. D. MONTGOMERY,* SEC.
R. G. GONNELLY
E. A. FRANCO-FERREIRA
R. G. GILLILAND
R. L. HEESTAND
A. P. LITMAN
J. J. PRISLINGER
G. M. SLAUGHTER
J. W. TACKETT
J. D. HUDSON
R. G. SHOOSTER
L. C. WILLIAMS

MATERIALS COMPATIBILITY
E. E. HOFFMAN*
D. B. POE,* SEC.
W. H. COOK
J. R. DISTEFANO
D. H. JANSEN
J. L. GRIFFITH
J. W. HENDRICKS
R. E. POTTER
L. R. TROTTER

LIQUID METAL RESEARCH
J. L. SCOTT
B. L. BALLARD,* SEC.
D. F. TONER
R. A. BOWMAN

CORROSION ENGINEERING
J. H. DEVAN
E. Q. TAYLOR, SEC.
A. J. ROSENBERG
R. C. SCHULZE
G. M. TOLSON
G. D. BRADY
E. J. LAWRENCE
J. B. PHILLIPS
M. A. REEDEN

SHERWOOD PROJECT
R. E. CLAUSING
J. P. GORDON
D. E. ROSSON

REACTOR PROJECTS COORDINATORS

ANP	E. E. HOFFMAN*
GCR	J. H. COOBS
MSR	A. TABOADA
SHERWOOD	R. E. CLAUSING

APPLIED METALLURGY
J. E. CUNNINGHAM*
M. B. WHITE,* SEC.

PROCESS METALLURGY
R. J. BEAVER
M. B. WHITE,* SEC.
L. L. HALL

FABRICATION
J. H. ERWIN
H. J. WALLACE
G. H. CALLAWAY
N. H. FLICKINGER
G. D. GOLDSTON
W. W. PROAPS

ALLOY PREPARATION
D. T. BOURGETTE*
J. B. FLYNN
H. W. HOOVER
L. QUEENER

FUEL ELEMENT DEVELOPMENT
C. F. LEITTEN, JR.*
M. M. MARTIN
J. W. GEER

APPR PROJECT
C. F. LEITTEN, JR.*
J. N. HIX
C. HAMBY

FAST-BREEDER ASSISTANCE PROJECT
R. J. BEAVER*
D. T. BOURGETTE*
J. H. CHERUBINI
A. L. LOTTS
S. A. RABINOWITZ
R. C. WILLIAMS[7]
W. R. JOHNSON
E. R. TURNBILL

HIGH-FLUX ISOTOPE REACTOR
J. E. CUNNINGHAM*
J. H. ERWIN
W. J. KUCERA
T. D. WATTS
T. W. COFFEY

MARITIME SHIP REACTOR PROJECT
W. C. THURBER
J. T. LAMARTINE
C. W. HOLLAND

REACTOR PROJECTS COORDINATORS

APPR	C. F. LEITTEN, JR.*
FBAP	R. J. BEAVER*
HFIR	J. E. CUNNINGHAM*
MSRP	W. C. THURBER

BUILDING PLANNING COORDINATION
E. S. BOMAR
L. K. JETTER*

LONG-RANGE FUEL RESEARCH
J. P. HAMMOND
M. B. WHITE,* SEC.
J. A. BURKA
D. L. MCELROY
M. A. WHEELER

RADIATION METALLURGY
T. S. LUNDY
D. B. POE,* SEC.
R. E. ADAMS
J. I. FEDERER
R. A. PADGETT, JR.
J. H. TERRY

HRLEL STUDIES
A. R. OLSON
D. T. JONES[1]
W. C. ULRICH[1]
J. E. VANCLEVE, JR.
M. D. ALLEN

POST IRRADIATION EXAMINATION LABORATORY
R. E. MCDONALD
C. M. FITZPATRICK
B. W. MCCOLLUM
G. A. MOORE
W. J. SCHILL

CERAMICS
L. M. DONEY
A. S. HOBBS, SEC.
N. A. BROWN[2]
F. L. CARLSEN
C. E. CURTIS
S. D. FULKERSON
R. L. HANNER
M. P. HAYDON
J. M. KERR
R. E. MEADOWS
R. A. POTTER
J. M. ROBBINS
A. W. SEIFERT
A. J. TAYLOR
B. R. CHILCOAT
J. A. GRIFFIN
F. P. JEFFERS
W. M. PARKS

METALLOGRAPHY
R. J. GRAY
W. J. SHOCKLEY
R. S. CROUSE
E. L. LONG, JR.
W. H. BRIDGES
G. HALLERMAN
T. M. KEGLEY, JR.
J. R. RIDDLE
L. A. AMBURN, JR.
N. M. ATCHLEY[4]
E. R. BOYD
B. F. DAY
W. E. DENNY
C. K. H. DUBOSE
W. H. FARNER
R. L. FITZGERALD
J. B. FRENCH
J. C. GOWER
E. P. GRIGGS
T. J. HENSON
D. M. HEWETTE
J. T. HOUSTON
E. H. LEE
B. C. LESLIE
R. J. LOCKETT
B. J. REECE
L. G. SHRADER[6]
H. R. TINCH
C. E. ZACHARY

INTERNAL DISTRIBUTION

1. C. E. Center
2. Biology Library
3. Health Physics Library
4. Metallurgy Library
5–7. Central Research Library
8. Reactor Experimental Engineering Library
9–28. Laboratory Records
29. Laboratory Records, RC
30. L. B. Emlet (K-25)
31. J. P. Murray (Y-12)
32. G. M. Adamson, Jr.
33. J. W. Allen
34. R. J. Beaver
35. M. Bender
36. J. O. Betterton, Jr.
37. A. M. Billings
38. D. S. Billington
39. A. L. Boch
40. E. G. Bohlmann
41. S. E. Bolt
42. E. S. Bomar, Jr.
43. B. S. Borie
44. W. F. Boudreau
45. D. T. Bourgette
46. G. E. Boyd
47. E. J. Breeding
48. J. R. Brown
49. W. D. Burch
50. J. V. Cathcart
51. R. H. Chapman
52. R. A. Charpie
53. R. D. Cheverton
54. H. C. Claiborne
55. G. W. Clark
56. R. E. Clausing
57. E. L. Compere
58. J. H. Coobs
59. W. B. Cottrell
60. R. S. Crouse
61. F. L. Culler
62. J. S. Culver
63. J. E. Cunningham
64. D. G. Davis
65. R. J. Davis
66. J. H. DeVan
67. R. R. Dickison
68. L. M. Doney
69. D. A. Douglas, Jr.
70. J. R. Engel
71. J. L. English
72. J. H. Erwin
73. J. I. Federer
74. D. E. Ferguson
75. J. D. Flynn
76. J. Foster
77. A. P. Fraas
78. J. H. Frye, Jr.
79. C. H. Gabbard
80. W. R. Gall
81. R. J. Gray
82. R. J. Greeley
83. B. L. Greenstreet
84. J. C. Griess
85. E. E. Gross
86. P. A. Haas
87. J. P. Hammond
88. P. H. Harley
89. C. S. Harrill
90. T. Hikido
91. J. W. Hill
92–117. M. R. Hill
118. E. C. Hise
119. C. J. Hochanadel
120. E. E. Hoffman
121. H. W. Hoffman
122. A. Hollaender
123. A. S. Householder
124. H. Inouye
125. G. H. Jenks
126. L. K. Jetter
127. D. T. Jones
128. W. H. Jordan
129. S. I. Kaplan
130. P. R. Kasten
131. C. P. Keim
132. M. T. Kelly
133. C. R. Kennedy
134. F. Kertesz
135. B. W. Kinyon
136. J. O. Kolb
137. R. B. Korsmeyer
138. K. A. Kraus
139. M. E. Lackey
140. J. A. Lane
141. C. G. Lawson

142. C. F. Leitten, Jr.
143. R. E. Leuze
144. S. C. Lind
145. R. S. Livingston
146. R. A. Lorenz
147. M. I. Lundin
148. T. S. Lundy
149. R. N. Lyon
150. H. G. MacPherson
151. W. D. Manly
152. L. A. Mann
153. W. L. Marshall
154. J. P. McBride
155. H. C. McCurdy
156. H. F. McDuffie
157. C. J. McHargue
158. H. A. McLain
159. R. A. McNees
160. J. R. McWherter
161. A. J. Miller
162. E. C. Miller
163. R. L. Moore
164. J. G. Morgan
165. K. Z. Morgan
166. E. J. Murphy
167. F. H. Neill
168. M. L. Nelson
169. L. G. Overholser
170. L. F. Parsly, Jr.
171. P. Patriarca
172. F. N. Peebles
173. A. M. Perry
174. D. Phillips
175. M. L. Picklesimer
176. S. A. Reed
177. P. M. Reyling
178. D. M. Richardson
179. G. W. Rivenbark
180. R. C. Robertson
181. M. W. Rosenthal
182. G. Samuels
183. H. C. Savage
184. H. W. Savage
185. L. D. Schaffer
186. J. L. Scott
187. H. E. Seagren
188. C. L. Segaser
189. E. M. Shank
190. E. D. Shipley
191. M. D. Silverman
192. O. Sisman
193. M. J. Skinner
194. C. O. Smith
195. G. P. Smith, Jr.
196. A. H. Snell
197. I. Spiewak
198. F. J. Stanek
199. R. W. Stoughton
200. E. Storto
201. J. A. Swartout
202. A. Taboada
203. E. H. Taylor
204. D. G. Thomas
205. W. C. Thurber
206. D. S. Toomb
207. D. B. Trauger
208. W. E. Unger
209. R. Van Winkle
210. F. C. VonderLage
211. M. S. Wechsler
212. A. M. Weinberg
213. K. W. West
214. G. D. Whitman
215. G. C. Williams
216. J. C. Wilson
217. C. E. Winters
218. H. L. Yakel, Jr.
219. M. M. Yarosh
220. F. C. Zapp
221. J. Zasler
222. T. N. McVay (consultant)
223. T. S. Shevlin (consultant)
224. C. S. Smith (consultant)
225. E. E. Stansbury (consultant)
226. H. A. Wilhelm (consultant)
227. J. H. Koenig (consultant)
228. W. O. Harms (consultant)
229. H. Leidheiser (consultant)

EXTERNAL DISTRIBUTION

230. Brig. Gen. K. A. McCrimmon, OCE, US Army, Washington, D.C.
231. Col. D. G. Williams, APB-DRD, AEC, Washington, D.C.
232. Capt. E. D. Peisotto, APR-DRD, AEC, Washington, D.C.
233. Lt. D. A. Pistenma, APB-DRD, AEC, Washington, D.C.

234. M. A. Rosen, APB-DRD, AEC, Washington, D.C.
235. Capt. L. P. Crocker, APB-DRD, AEC, Washington, D.C.
236. Major J. T. Rhett, OCE, US Army, Washington, D.C.
237. Major W. E. Ray, NPFO, ERDL, Ft. Belvoir
238. M. Eisenbud, NYO, AEC, New York
239. Capt. R. L. Harris, NYO, AEC, New York
240. K. Kasschau, Alco Products, Inc., Schenectady, N.Y.
241. J. F. Haines, Alco Products, Inc., Schenectady, N.Y.
242. J. G. Gallagher, Alco Products, Inc., Schenectady, N.Y.
243. R. D. Robertson, Alco Products, Inc., Schnectady, N.Y.
244. E. C. Edgar, Alco Products, Inc., Schnectady, N.Y.
245. J. M. Simmons, DRD, AEC, Washington, D.C.
246. R. C. Dalzell, DRD, AEC, Washington, D.C.
247. Preston Eddy, MSR, DRD, AEC, Washington, D.C.
248. D. E. Baker, GE, Hanford
249. Capt. James W. Barnette, U.S. Am. Engrs., East Ocean, N.Y.
250. D. F. Cope, Reactor Div., ORO
251. Ersel Evans, GE, Hanford
252. J. L. Gregg, Cornell University
253. R. L. Maxwell, University of Tennessee
254. M. J. Whitman, AER Reactors Branch, Washington, D.C.
255. N. Cabrera, University of Virginia
256. J. F. Eckel, Virginia Polytechnic Institute
257. J. F. Elliott, Massachusetts Institute of Technology
258. N. J. Grant, Massachusetts Institute of Technology
259. W. D. Jordan, University of Alabama
260. O. C. Kopp, University of Tennessee
261. J. Korringa, Ohio State University
262. R. S. Mateer, University of Kentucky
263. L. Mitchell, Georgia Institute of Technology
264. J. W. Prados, University of Tennessee
265. J. B. Wagner, Yale University
266. Division of Research and Development, AEC, ORO
267–746. Given distribution as shown in TID-4500 (15th ed.) under Metallurgy and Ceramics category

Reports previously issued in this series are as follows:

ORNL-28	Period Ending March 1, 1948
ORNL-69	Period Ending May 31, 1948
ORNL-407	Period Ending July 31, 1949
ORNL-511	Period Ending October 31, 1949
ORNL-583	Period Ending January 31, 1950
ORNL-754	Period Ending April 30, 1950
ORNL-827	Period Ending July 31, 1950
ORNL-910	Period Ending October 31, 1950
ORNL-987	Period Ending January 31, 1951
ORNL-1033	Period Ending April 30, 1951
ORNL-1108	Period Ending July 31, 1951
ORNL-1161	Period Ending October 31, 1951
ORNL-1267	Period Ending January 31, 1952
ORNL-1302	Period Ending April 30, 1952
ORNL-1366	Period Ending July 31, 1952
ORNL-1437	Period Ending October 31, 1952
ORNL-1503	Period Ending January 31, 1953
ORNL-1551	Period Ending April 10, 1953
ORNL-1625	Period Ending October 10, 1953
ORNL-1727	Period Ending April 10, 1954
ORNL-1875	Period Ending October 10, 1954
ORNL-1911	Period Ending April 10, 1955
ORNL-1988	Period Ending October 10, 1955
ORNL-2080	Period Ending April 10, 1956
ORNL-2217	Period Ending October 10, 1956
ORNL-2422	Period Ending October 10, 1957
ORNL-2632	Period Ending October 10, 1958